WOODHEAD PUBLISHING IN MATERIALS

Blast protection of civil infrastructures and vehicles using composites

Edited by Nasim Uddin

CRC

WP

Blast protection of civil infrastructures and vehicles using composites

© Woodhead Publishing Limited, 2010

Related titles:

Lightweight ballistic composites: military and law-enforcement applications
(ISBN 978-1-85573-941-3)
Ballistic composites need to be lightweight, durable and exhibit high impact resistance and damage tolerance. This important book reviews these requirements, how the materials used for ballistic composites meet them and their range of applications. The first part of the book explores material requirements and testing. There are chapters on bullets and bullet fragments, material responses to ballistic impact, standards and specifications, modelling and test methods. Part II reviews the range of materials used, production methods and applications. Topics discussed include high-performance ballistic fibres and ceramics, non-woven ballistic and prepreg composites, and their uses in body armour, and in vehicle and aircraft protection.

Military textiles
(ISBN 978-1-84569-206-3)
Textiles and garments provide the barrier between the soldier and the surrounding environment. As the battlefield becomes increasingly complex, there is a need to develop intelligent textile fibres, structures and clothing systems, while maintaining comfort and functionality. With an expert editor and international team of authors, this important book, addresses these developments. Chapters discuss key themes such as how fabrics can be tailored to protect against extremes of heat and cold, ballistic impact, and against nuclear, biological and chemical threats.

Textiles for protection
(ISBN 978-1-85573-921-5)
In today's climate there is an increasing requirement for protective textiles, whether for personal protection, protection against the elements, chemical, nuclear or ballistic attack. This comprehensive book brings together the leading protective textiles experts from around the world. It covers a wide variety of themes from materials and design, through protection against specific hazards, to specific applications. This is the first book to give a complete coverage of textiles for protection.

Details of these and other Woodhead Publishing books can be obtained by:

- visiting our website at www.woodheadpublishing.com
- contacting Customer Services (e-mail: sales@woodheadpublishing.com; fax: +44 (0) 1223 893694; tel.: +44 (0) 1223 891358 ext.130; address: Woodhead Publishing Limited, Abington Hall, Granta Park, Great Abington, Cambridge CB21 6AH, UK)

If you would like to receive information on forthcoming titles, please send your address details to: Francis Dodds (address, tel. and fax as above; e-mail: francis.dodds@woodheadpublishing.com). Please confirm which subject areas you are interested in.

© Woodhead Publishing Limited, 2010

Blast protection of civil infrastructures and vehicles using composites

Edited by
Nasim Uddin

CRC Press
Boca Raton Boston New York Washington, DC

WOODHEAD PUBLISHING LIMITED
Oxford Cambridge New Delhi

© Woodhead Publishing Limited, 2010

Published by Woodhead Publishing Limited, Abington Hall, Granta Park, Great Abington Cambridge CB21 6AH, UK
www.woodheadpublishing.com

Woodhead Publishing India Private Limited, G-2, Vardaan House, 7/28 Ansari Road, Daryaganj, New Delhi – 110002, India
www.woodheadpublishingindia.com

Published in North America by CRC Press LLC, 6000 Broken Sound Parkway, NW, Suite 300, Boca Raton, FL 33487, USA

First published 2010, Woodhead Publishing Limited and CRC Press LLC
© 2010, Woodhead Publishing Limited
The authors have asserted their moral rights.

This book contains information obtained from authentic and highly regarded sources. Reprinted material is quoted with permission, and sources are indicated. Reasonable efforts have been made to publish reliable data and information, but the authors and the publishers cannot assume responsibility for the validity of all materials. Neither the authors nor the publishers, nor anyone else associated with this publication, shall be liable for any loss, damage or liability directly or indirectly caused or alleged to be caused by this book.

Neither this book nor any part may be reproduced or transmitted in any form or by any means, electronic or mechanical, including photocopying, microfilming and recording, or by any information storage or retrieval system, without permission in writing from Woodhead Publishing Limited.

The consent of Woodhead Publishing Limited does not extend to copying for general distribution, for promotion, for creating new works, or for resale. Specific permission must be obtained in writing from Woodhead Publishing Limited for such copying.

Trademark notice: Product or corporate names may be trademarks or registered trademarks, and are used only for identification and explanation, without intent to infringe.

British Library Cataloguing in Publication Data
A catalogue record for this book is available from the British Library.

Library of Congress Cataloging in Publication Data
A catalog record for this book is available from the Library of Congress.

Woodhead Publishing ISBN 978-1-84569-399-2 (book)
Woodhead Publishing ISBN 978-1-84569-803-4 (e-book)
CRC Press ISBN 978-1-4398-2771-0
CRC Press order number: N10154

The publishers' policy is to use permanent paper from mills that operate a sustainable forestry policy, and which has been manufactured from pulp which is processed using acid-free and elemental chlorine-free practices. Furthermore, the publishers ensure that the text paper and cover board used have met acceptable environmental accreditation standards.

Typeset by Toppan Best-set Premedia Limited
Printed by TJ International Limited, Padstow, Cornwall, UK

© Woodhead Publishing Limited, 2010

Contents

Contributor contact details *x*
Preface *xiii*

Part I Introduction 1

1 Blast threats and blast loading 3
D. C. WEGGEL, The University of North Carolina at Charlotte, USA

1.1 Introduction 3
1.2 Basics of high explosives 3
1.3 Some important explosive properties and physical forms 7
1.4 A generic explosive device 10
1.5 Blast waves in free air 11
1.6 Blast loading categories 15
1.7 Blast-induced load types and load cases 17
1.8 Threat assessment for design 22
1.9 Simplified blast load computation 24
1.10 Numerical examples of simplified blast load computation 32
1.11 Additional resources 37
1.12 References 41

2 Standards and specifications for composite blast protection materials 44
M. CHALK, Solent Composite Systems Ltd, UK

2.1 Introduction 44
2.2 Why do we want standards? 44
2.3 Who is responsible for applying standards? 45
2.4 How should we interpret standards? 45
2.5 What is relevant for standards for composite blast protection products? 48
2.6 When will composite blast protection standards be used? 50
2.7 Where can standards be applied for the use of composites? 51

© Woodhead Publishing Limited, 2010

2.8 The future for standards and specifications for composite blast protection 51
2.9 Conclusion 52
2.10 Sources of further information and advice 53
2.11 References 53

3 Processing polymer matrix composites for blast protection 54
H. TAN and K. M. PILLAI, University of Wisconsin–Milwaukee, USA

3.1 Introduction 54
3.2 Liquid composite molding (LCM) 58
3.3 Modeling of the mold-filling stage in liquid composite molding 60
3.4 Permeability measurement in liquid composite molding 74
3.5 Summary 78
3.6 References 78

4 High energy absorbing composite materials for blast resistant design 88
M. YANG, University of Texas, USA; and P. QIAO, Washington State University, USA

4.1 Introduction 88
4.2 Advanced and new materials for impact and energy absorption 89
4.3 Design philosophy for blast protection 101
4.4 Case studies of blast absorbing materials 103
4.5 Summary and concluding remarks 111
4.6 References 114

5 Modeling the blast response of hybrid laminated composite plates 120
A. E. BOGDANOVICH, 3TEX, Inc., USA

5.1 Introduction 120
5.2 Synopsis of 3D Mosaic analysis approach 126
5.3 Numerical simulations of a structural response for blast loading: input 132
5.4 Formulation of the 3D dynamic boundary value problem 134
5.5 Numerical results of the blast response for the four panels 140
5.6 Comparison of the blast response characteristics for the four panels 178

© Woodhead Publishing Limited, 2010

5.7 Comparison of the blast response characteristics for a longer time interval 191
5.8 Effect of internal material damping 195
5.9 Comparisons of theoretical and experimental results 201
5.10 Summary and conclusions 205
5.11 Acknowledgements 208
5.12 References 208

6 Response of composite panels to blast wave pressure loadings 212
K. Lee, Old Dominion University, USA; and S. W. Lee, University of Maryland, USA

6.1 Introduction 212
6.2 A comprehensive methodology for damage assessment 214
6.3 A simplified methodology for failure assessment 216
6.4 Numerical tests on flat laminated composite panels 223
6.5 Conclusions and future trends 231
6.6 References 232

Part II Applications 233

7 Ceramic matrix composites for ballistic protection of vehicles and personnel 235
J. J. Schuldies, Industrial Ceramic Technology, Inc., USA; and R. Nageswaran, Smaht Ceramics, Inc., USA

7.1 Introduction 235
7.2 Technology overview 236
7.3 Technology approach for improved ballistic protection 238
7.4 Impact of improved ceramic composites for ballistic protection 240
7.5 References 242

8 Developing mine blast resistance for composite based military vehicles 244
M. French and A. Wright, QinetiQ, UK

8.1 Introduction 244
8.2 Occupant injury mechanisms 251
8.3 Integrated vehicle survivability 252
8.4 The use of composite materials in vehicles 255
8.5 Mine blast loading of composite vehicle structures 259

© Woodhead Publishing Limited, 2010

8.6 Conclusion 267
8.7 References 267

9 Blast protection of buildings using fibre-reinforced polymer (FRP) composites 269
P. A. Buchan and J. F. Chen, The University of Edinburgh, UK

9.1 Introduction 269
9.2 Consequences of an explosion 271
9.3 Assessing if a building requires protection from blast 272
9.4 General design guidance for blast protection of buildings 272
9.5 Retrofitting buildings for blast protection 275
9.6 Retrofitting buildings for blast protection using fibre-reinforced polymer (FRP) composites 277
9.7 Future developments and trends 291
9.8 Sources of further information and advice 292
9.9 Conclusions 293
9.10 References 294

10 The use of composites in blast-resistant walls 298
L. A. Louca and A. S. Fallah, Imperial College London, UK

10.1 Introduction 298
10.2 Use of composites in strengthening applications 308
10.3 Use of composites in replacement applications 315
10.4 Use of composites in conjunction with metals 333
10.5 Concluding remarks 336
10.6 References 338

11 Using composite behavior to improve the blast resistance of columns in buildings 342
M. P. Rutner, Weidlinger Associates, Inc., USA

11.1 Introduction 342
11.2 Design specifications 342
11.3 Objectives 344
11.4 Simulation and experiment 344
11.5 Modeling 345
11.6 Results and discussion 355
11.7 Observed failure mechanisms 360
11.8 Mitigation of the failure mechanisms 361

© Woodhead Publishing Limited, 2010

11.9 Comparative investigation of performance and residual capacity of the load bearing column 369
11.10 Establishing parameters affecting blast resistance of columns 371
11.11 Summary and conclusions 371
11.12 Acknowledgements 372
11.13 References 373

12 Retrofitting using fiber-reinforced polymer (FRP) polymer composites for blast protection of buildings 375
G. S. URGESSA, George Mason University, USA

12.1 Introduction 375
12.2 Retrofitting structures for blast protection and the advantages of fiber-reinforced polymer (FRP) composite retrofits 376
12.3 The history of fiber-reinforced polymer (FRP) composites as retrofits for out-of-plane loadings 378
12.4 Full scale blast testing of fiber-reinforced polymer (FRP) retrofitted masonry walls 381
12.5 Fiber-reinforced polymer (FRP) connection systems 384
12.6 Equivalent non-linear single degree of freedom model for fiber-reinforced polymer (FRP) retrofitted structures 385
12.7 Resources for fiber-reinforced polymer (FRP) composites 387
12.8 References 387

13 Retrofitting to improve the blast response of masonry walls 390
L. MORADI, University of Alabama at Birmingham, USA

13.1 Introduction 390
13.2 Types of masonry walls 391
13.3 Blast load 391
13.4 Finite element models 393
13.5 Resistance function approach 396
13.6 Response model development 406
13.7 Summary 408
13.8 Notation 409
13.9 References 410

Index *413*

© Woodhead Publishing Limited, 2010

Contributor contact details

(* = main contact)

Editor

Dr Nasim Uddin
Associate Professor of Civil Engineering
University of Alabama at Birmingham
Hoehn 321
1075 13th Street South
Birmingham
AL 35294-4440
USA

Email: nuddin@uab.edu

Chapter 1

Dr David C. Weggel
Associate Professor of Civil and Environmental Engineering
The University of North Carolina at Charlotte
Cameron Building
9201 University City Blvd
Charlotte
NC 28223-0001
USA

Email: dcweggel@uncc.edu

Chapter 2

Matthew Chalk
Solent Composite Systems Ltd
Victoria Barracks
Albany Road
East Cowes
Isle of Wight
PO32 6AA
UK

Email: matt@solentcomposites.com

Chapter 3

Hua Tan* and Krishna M. Pillai
Mechanical Engineering Department
University of Wisconsin–Milwaukee
3200 N. Cramer Street
Milwaukee
WI 53211-3029
USA

Email: huatan@uwm.edu; krishna@uwm.edu

© Woodhead Publishing Limited, 2010

Chapter 4

M. Yang
Department of Civil and Environmental Engineering
University of Texas – San Antonio
San Antonio
TX 78249-0668
USA

Email: mijia.yang@utsa.edu

P. Qiao*
Department of Civil & Environmental Engineering
Washington State University
PO Box 642910
Spokane Street
Sloan 120
Pullman
WA 99164-2910
USA

Email: qiao@wsu.edu

Chapter 5

Dr Alexander E. Bogdanovich
3TEX, Inc.
109 MacKenan Drive
Cary
NC 27511
USA

Email: bogdanovicha@3tex.com

Chapter 6

Keejoo Lee*
Department of Aerospace Engineering
Old Dominion University
4750 Elkhorn Ave
Norfolk
VA 23529-0247
USA

Email: kxlee@odu.edu

Sung Won Lee
Department of Aerospace Engineering
University of Maryland
3181 Glenn L. Martin Hall
College Park
MD 20742
USA

Email: swlee@umd.edu

Chapter 7

J. J. Schuldies*
Industrial Ceramic Technology, Inc.
37 Enterprise Dr
Ann Arbor
MI 48103
USA

Email: ICT2311@aol.com

R. Nageswaran
SMAHT Ceramics, Inc.
181 West 1700 South
Salt Lake City
UT 84115
USA

Email: Rama@SMAHTCer.com

Chapter 8

Dr M. French* and A. Wright
QinetiQ
Room 2012
Building A5
Cody Technology Park
Farnborough
Hampshire
GU14 6EN
UK

Email: AJWright1@QinetiQ.com; Mafrench@QinetiQ.com

© Woodhead Publishing Limited, 2010

Chapter 9

Mr P. A. Buchan* and Dr J. F. Chen
Institute for Infrastructure and Environment
Joint Research Institute for Civil and Environmental Engineering
School of Engineering
The University of Edinburgh
The King's Buildings
Edinburgh
EH9 3JL
UK

Email: philipbuchan@hotmail.com; J.F.Chen@ed.ac.uk

Chapter 10

Dr Luke A. Louca* and Dr Arash S. Fallah
Skempton Building
Department of Civil and Environmental Engineering
South Kensington Campus
Imperial College London
London
SW7 2AZ
UK

Email: l.a.louca@imperial.ac.uk; arash.soleiman-fallah@imperial.ac.uk

Chapter 11

Dr Marcus P. Rutner
Weidlinger Associates, Inc.
Applied Science Department
375 Hudson Street 12F
New York
NY 10014-3656
USA

Email: rutner@wai.com

Chapter 12

G. S. Urgessa, Assistant Professor
Department of Civil, Environmental and Infrastructure Engineering
George Mason University
4400 University Drive
MS 6C1
Fairfax
VA 22030-4444
USA

Email: gurgessa@gmu.edu

Chapter 13

L. Moradi
Director of Engineering
Center for Biophysical Sciences and Engineering (CBSE)
Faculty, Department of Civil, Construction, and Environmental Engineering
University of Alabama at Birmingham (UAB)
1530 3rd Avenue South
Birmingham
AL 35294
USA

Email: moradi@uab.edu

© Woodhead Publishing Limited, 2010

Preface

Recent events throughout the world have drawn attention to the vulnerability of infrastructure to acts of terrorism. Protecting society against terrorism requires a well-planned layered approach that combines innovative intelligence with effective protective strategies. The development of protective measures against explosions encompasses not only creating new methods for designing new structures but also improving the capability of existing structures so that they will perform efficiently and effectively under anticipated dangers and threats. These threats include acts by criminals, terrorists, and subversives; and engineers require materials, methods, and guidance on designing structures to resist or contain these hostile acts.

Fiber-reinforced polymer (FRP) composites materials are ideal for structural applications where high strength-to-weight and stiffness-to-weight ratios are required. The protection of vehicles and facilities from blast effects and ballistic impacts using FRP is the primary objective of this book. FRP composites are now being utilized instead of steel plates due to their higher strengths, better corrosion resistance and far greater ease of transportation, handling and installation. The biggest advantage of FRPs is their tailorability. They can be more easily arranged according to the specific site conditions than other materials and so optimized for performance. FRP retrofitting can be applied quickly, is non-intrusive and provides a dramatic increase in the ability of a building to resist an explosion. The apparent high purchase cost of FRPs compared to other materials has been an obstacle in some decisions to implement this technique. However, a direct comparison on a unit price basis may not be appropriate. When installation, transportation, and life cycle costs are included in the cost comparison FRPs can compete with conventional materials in most cases.

Numerous research efforts, current and past, have focused on the development of blast shields and ballistic armor for military vehicles, government buildings, and, in some cases, commercial and private vehicles. Many of these R&D efforts have successfully demonstrated concepts that provide excellent protection for vehicles and buildings against blast effects and

© Woodhead Publishing Limited, 2010

ballistic penetrations. Typical approaches used in these concepts consist of layered structures made up of fiber-reinforced composite materials combined with metal plates or ceramic plates. These concepts usually result in very heavy and costly systems. On the other hand, the use of innovative composite materials and designs has significant potential to reduce vulnerability of transportation vehicles and infrastructure. This up and coming new generation of composite materials and structures offers outstanding damage tolerance under harsh conditions, and hence is the focus of this book.

With the upsurge in terrorism in recent years and the possibility of accidental blast threats, there is growing interest in manufacturing blast 'hardened' structures and retrofitting blast mitigation materials to existing structures. Composites provide the ideal material for blast protection as they can be engineered to give different levels of protection by varying the reinforcements and matrices. While a good number of technical publications exist, there are very few, if any, widely available documents providing engineers with the information required to design structures for enhanced protection using FRPs. In an effort to fill this apparent gap, we have thus elicited voluntary contributions – from the experts in the field – that cover some very significant portions of this broad topic, namely:

- threat issues – blast threats, types of damage
- materials selection issues – selection criteria for blast protection composites, testing of blast protection composites
- innovative methods of composites application for blast protection – vehicles, buildings, walls, columns
- retrofitting method for blast protection using composites – buildings
- analysis and design tool for blast protection using composites – blast simulation and modeling, response of composites to blast wave pressure loadings
- recent advances in composites materials – ceramic matrix composites, blast absorbing materials
- standards and specification for composites blast protection materials
- processing composites for blast protection

Contributions have been reviewed and raise critical issues for existing theories and practices dealing with structures affected by blast and impacts. Furthermore, contributions seek to help both students and public- or private-sector professionals in understanding how the innovative composites materials can help facilities owners and agencies cope with blast threats.

Part I discusses general technical issues with chapters on topics such as blast threats and types of blast damage, processing polymer matrix composites for blast protection, standards and specifications for composite blast protection materials, high energy absorbing composite materials for blast

© Woodhead Publishing Limited, 2010

resistant design, modeling the blast response of hybrid laminated composite plates and the response of composite panels to blast wave pressure loadings.

Chapter 1, titled 'Blast threats and blast loading' by Dr David C. Weggel, provides a background on explosive substances and some of their important properties and describes a generic explosive device. Explosive effects, namely blast waves in free air, blast loading categories, blast-induced load types, and considerations for threat determination, are then covered to set the stage for practical blast load computation appropriate for initial design. Simple numerical examples are presented for the more common explosive threat scenarios that civil or mechanical engineers may face. Moreover, additional resources are provided to assist the designer in achieving a satisfactory design. This chapter primarily considers solid high explosives and their effects after detonation. However, much of what is described here can be extended to other substances inlcuding fuels, flammable gases, propellants, and seemingly innocuous materials such as suspended dust – when they are under suitable conditions to deflagrate or detonate.

In Chapter 2, 'Standards and specifications for composite blast protection materials' by Matthew Chalk, current blast performance standards are reviewed by summarizing how they are interpreted for the use of protection systems produced using composite materials and products. The development of industry standards is also discussed together with how these are interpreted to encourage the use of composite technology to provide appropriate blast protection. Examples are considered across several industry sectors and comments made about the effectiveness of resulting standards with regard to the use of composites. Conclusions are drawn about the future development of standards and specifications that would encourage the implementation of composite solutions to solve explosion and blast protection problems.

Chapter 3, 'Processing polymer matrix composites for blast protection' by Hua Tan and Krishna M. Pillai, discusses the processing of polymer composites for blast protection applications. The background of polymer composites is introduced as well as the manufacturing processes for polymer composites. Of the many possible technologies available to fabricate such composites, the liquid composites molding (LCM) processes are discussed in the greatest detail. Mold-filling simulations are very important for optimizing mold designs in LCM. The modeling of LCM in terms of the physics of resin flow in porous media, the corresponding heat and mass transfer issues, and modeling the resin cure, are reviewed extensively. The research progress made on modeling the resin flow through dual-scale fiber performs, used extensively in LCM, is also reviewed. Since the permeability of fiber preforms is a very important parameter needed for simulating mold-filling in LCM, the permeability measurement is reviewed in detail.

© Woodhead Publishing Limited, 2010

In Chapter 4, 'High energy absorbing materials for blast resistant design' by Mijia Yang and Pizhong Qiao, a review of high-energy absorbing materials, with special attention to blast resistant materials, is presented. The design philosophy for blast absorbing materials is briefly introduced, and four cases of blast resistant materials (i.e., multilayer composites, sandwich panels, magneto-rheological fluids, and porous shape memory alloys) are provided. In particular, new design concepts related to high energy absorbing materials (lattice and truss structures, hybrid sandwich composites, metal foams, magneto-rheological fluids, porous shape memory alloys) are discussed. Recent studies on experimental evaluation and constitutive modeling of strain rate-dependent polymer matrix composites are also presented. Four case studies of blast absorbing materials are illustrated and discussed, and their mechanisms for blast energy absorption and dissipation are revealed. This review as well as case studies presented will help the readers in better identifying viable energy absorbing materials under impact in general and blast resistant materials in particular and designers in selecting high and effective energy absorbing materials, particularly for structures under blast loadings.

In Chapter 5, 'Modeling the blast response of hybrid laminated composite plates' by Dr Alexander E. Bogdanovich, three-dimensional (3-D) dynamic analysis approach was developed for a highly transient loading of thick layered hybrid blast mitigation panels and illustrated on several applications. The panels may include layers of traditional composites or novel 3-D textile composites along with ceramics, metals, light metallic and polymeric foams, Balsa wood and other popular materials. The approach is suitable for 3-D transient analysis of sandwich constructions with composite skins and lightweight foam cores, including composite sandwiches made of through-thickness integrally stitched fabric preforms and cores. The analysis approach is based on the 3-D dynamic variational theory developed earlier by this author. The 3-D displacement field is represented in terms of triple series, containing products of the chosen single-coordinate basis functions. Time variations of displacements, strains and stresses are computed for any point of the structure by a direct point-wise summation of respective triple series. The applicability and accuracy of the approach is illustrated by four specific blast loading problems solved for representative composite, sandwich and hybrid panels that include layers of ceramic, steel and aluminum foam. The comparisons include time variation of the back-face deflection and time variation of the strain measured by the surface bonded strain gauges. A very good agreement between theoretical and experimental results is obtained. Various practical applications and anticipated benefits provided by the presented analysis approach are discussed in the conclusion to the chapter.

© Woodhead Publishing Limited, 2010

Chapter 6, 'Response of composite panels to blast wave pressure loadings' by Drs Keejoo Lee and Sung Won Lee, provides a summary of a comprehensive methodology developed at the University of Maryland for assessment of damage of composite structures under high explosive blast pressure loading. A simplified methodology is then introduced to obtain structural responses at various blast wave pressure loadings and predict structural collapse based on these responses. Results of numerical tests on flat laminated composite panels show that the simplified methodology which does not require the computationally expensive failure analysis including the progressive material damages can predict the structural failure with reasonable accuracy. Accordingly, the simplified methodology could be used as a first screening tool for the design study, and then the full analysis including material damage and failure could be conducted to provide detailed local damages of selected designs. In addition, a graphical user interface (GUI) can be implemented to facilitate building up a design library for composite panels under blast wave pressure loading. However, the simplified methodology developed has been validated for structural collapse analysis of flat composite plates only for a limited number of cases. More extensive studies are needed to ascertain the validity of the methodology. It is also recommended that the future work include investigation of alternate panel geometries such as curved panels as well as sandwich panels.

Part II reviews applications including ceramic matrix composites for ballistic protection of vehicles and personnel, using composites to protect military vehicles from mine blasts, blast protection of buildings using FRP matrix composites, using composites in blast resistant walls for offshore, naval, and defense related structures, using composites to improve the blast resistance of columns in buildings, retrofitting using FRP composites for blast protection of buildings, and retrofitting to improve the blast response of concrete masonry walls.

Conventional armor materials are typically made of steel, aluminum, or other hard metals. Although these metallic materials primarily perform a structural function, they provide reasonably good ballistic protection at appropriate thicknesses (or areal densities). Often, this approach results in parasitic weight, which not only reduces fuel efficiency but also diminishes mobility in action. Recognizing that rapid deployment, enhanced fuel mileage, and reliable ballistic (and blast) protection are the keys to dominating future battles, new and innovative approaches involving lighter materials such as ceramics and polymers have become absolutely essential. Conventional ceramics, such as alumina, boron carbide, silicon nitride, and silicon carbide, have been investigated for application in ballistic protection armor systems and are being used, selectively, due to their low weight and

© Woodhead Publishing Limited, 2010

high mechanical properties. However, limitations such as multiple-hit capability have been recognized which necessitate developing newer and more advanced materials. Chapter 7, 'Ceramic matrix composites for ballistic protection of vehicles and personnel' by John J. Schuldies and Rama Nageswaran, proposes the use of ceramic whisker-reinforced ceramic composites be considered for next-generation armor systems. Specifically discussed is a commercially available alumina-based composite (CRYSTALOY©) which is reinforced with single crystal silicon carbide whiskers. Currently used in applications such as metal removal cutting tools, metal extrusion dies, and other wear, corrosive and high temperature parts, it forms the technology basis to develop an improved armor system. Data is provided to support the premise that developing a ceramic–matrix composite having improved ballistic performance is feasible.

Chapter 8, 'Developing mine blast resistance for composite based military vehicles' by Drs Mark French and Andrew Wright, is designed to provide an overview of mines used in warfare, their influence on the design of military vehicles, the use of composite materials to improve the design of armoured fighting vehicles (AFVs), and the research being undertaken to assess the performance of composite materials exposed to mine blast. A description of two research programmes, Advanced Composite Armoured Vehicle Protection (ACAVP) and Composite Design for Armoured Fighting Vehicles (CAFV), for evaluation of composites for military vehicles is provided, together with details of the modeling approaches that can be used to design vehicles against the mineblast threat.

Chapter 9, 'Blast protection of buildings using fiber-reinforced polymer matrix composites' by Mr P A Buchan and Dr J F Chen, discusses the consequences of a blast load on a building and general guidance for blast protection. It considers different retrofitting methods before concentrating on FRP retrofitting of columns, beams, slabs and walls. Existing research has overwhelmingly indicated that FRP and polymer retrofitting can significantly increase the blast resistance of a structure, by increasing the structural strength and ductility plus reducing fragmentation. However, there is a significant lack of understanding of the fundamental behaviour of FRP retrofitted structures under blast loading. Further research is required before the technologies can be widely applied in practice.

The use of fibrous laminated composites in blast protection has been discussed in Chapter 10, 'The use of composites in blast-resistance walls' by Drs Luke A. Louca and Arash S. Fallah. Different ply settings, i.e. unidirectional (UD), woven roving (WR) and chopped strand mat (CSM) lamina, are considered. Three examples of the use of composites viz. in strengthening existing corrugated blast walls and their connections, in replacement of blast walls by composite sandwich panels and the use of fiber metal laminates (FMLs) are discussed. The examples are selected to

© Woodhead Publishing Limited, 2010

reflect the range of applicability of composites in blast resistant design which includes offshore and marine industries. The problem of connecting composite and hybrid parts is addressed. The results included are adopted from the literature on the topic or are the results of analyses conducted by authors or by their affiliated research group. It is established that composites can be best used in conjunction with other materials. These materials can be metallic (such as aluminum) or non-metallic (such as Balsa wood). Hybrid settings can be used for low and moderate blast loading levels. The problem of designing hybrid parts using FRP composites for use in high-pressure–high-impulse blast has not yet been fully solved and further research is required to propose set-ups which can eliminate the drawbacks of current designs.

Chapter 11, 'Using composite behavior to improve the blast resistance of columns in buildings' by Dr Marcus P. Rutner, focuses on the investigation of a load-bearing column subjected to a near-proximity vehicle-borne explosive threat. The design of ground floor columns of high rise buildings has to fulfill architectural demands, such as to supporting long-spanned framing, which often result in a non-redundant structure. Additionally, standoff distances from the street curb line to the building's ground-floor column may be insufficient and no restrictions on vehicle access within short distances to the column may be possible. This hazard requires the local resistance design approach to protect the structure of progressive collapse. This chapter investigates the response of a representative steel column when subjected to a nearby explosive event. It discusses how composite construction technology can improve the blast response of the steel column. Additionally, structure-specific and load-dependent design parameters are derived to provide a high level of security.

Chapter 12, 'Retrofitting using fiber-reinforced polymer (FRP) composites for blast protection of buildings' by Dr Girum Solomon Urgessa, focuses on the history of the use of FRP composite retrofits for out of plane loadings, overview of blast tests using FRP retrofits and notes on the analysis of FRP strengthened (retrofitted) structures. Section 12.2 presents the need for retrofitting structures and the advantages of using FRP composites when compared to other retrofitting techniques. Section 12.3 discusses the history of FRP composites in structural engineering as a retrofit material for out of plane loadings including blast. The section also provides important research publications and findings in the area. Section 12.4 provides a case study of a full-scale blast test conducted on masonry walls retrofitted using FRP. Section 12.5 reviews existing knowledge on FRP connection systems and the challenges involved in transferring blast loads to surrounding strengthened structural components. Section 12.6 outlines an equivalent non-linear single degree of freedom model approach for the analysis of FRP retrofitted structures. Section 12.7 provides a brief commentary on

© Woodhead Publishing Limited, 2010

major professional organizations regarding FRP composites and available reference manuals and books.

Chapter 13, 'Retrofitting to improve the blast response of masonry walls' by Dr Lee Moradi, provides the formulation for the resistance of membrane retrofit concrete masonry walls to lateral uniform pressure. Resistance functions are provided for three separate cases: Unreinforced concrete masonry walls with and without membrane retrofit, unreinforced concrete masonry walls with and without membrane retrofit, and with arching action, and unreinforced concrete masonry walls with a membrane retrofit catcher system. The chapter provides the proper formulation to determine the response of membrane retrofit concrete masonry walls to blast and environmentally induced pressures in a cost-effective manner. The results may be used in high-risk areas to enhance the construction of new buildings using unreinforced concrete masonry walls, as well as to retrofit similar walls in existing buildings or homes. For arching action to develop, care must be taken to ensure gaps are not present between the wall and its top and bottom interfaces.

The book should appeal to all those concerned with protecting structures from the effects of blasts in both military and civil sectors. With its team of expert contributors reflecting many years of specialized experience, including the private, governmental, and academic perspectives, the book will be standard reference in many fields of engineering such as FRP composites, engineering mechanics, numerical analysis, material science and engineering, and structural engineering. It can serve as the text for a disaster mitigation course on blast containment and homeland security.

© Woodhead Publishing Limited, 2010

1

Blast threats and blast loading

D. C. WEGGEL, The University of North Carolina at Charlotte, USA

Abstract: This chapter provides a background on explosive substances and some of their important properties and describes a generic explosive device. Explosive effects – blast waves in free air, blast loading categories, and blast-induced load types – and considerations for threat determination are then covered to set the stage for practical blast load computation appropriate for initial design. Simple numerical examples are presented for the more common explosive threat scenarios that civil or mechanical engineers may face. Finally, additional resources are provided to assist the designer in achieving a satisfactory design.

Key words: explosives and high explosives (HE), blast waves in air, blast loads on structures, blast-induced load types, simplified blast load computation, numerical examples of simplified blast load computation.

1.1 Introduction

This chapter provides a background on explosive substances and some of their important properties and describes a generic explosive device. Explosive effects – blast waves in free air, blast loading categories, and blast-induced load types – and considerations for threat determination are then covered to set the stage for practical blast load computation appropriate for initial design. Simple numerical examples are presented for the more common explosive threat scenarios that civil or mechanical engineers may face. Finally, additional resources are provided to assist the designer in achieving a satisfactory design.

This chapter primarily considers solid high explosives and their effects after detonation. However, much of what is described here can be extended to other substances – fuels, flammable gases, propellants, and seemingly innocuous materials such as suspended dust – when they are under suitable conditions to deflagrate or detonate.

1.2 Basics of high explosives

1.2.1 Explosions and high explosives

An explosion is the sudden outward projection of a quantity of matter. Explosions can be caused by a number of phenomena, such as rupture of a container under high internal pressure or combining cool water with a

© Woodhead Publishing Limited, 2010

molten material (AMC, 1972). This chapter, however, will primarily be concerned with explosions resulting from the detonation of high explosives (HEs). Explosives are, quite simply, substances capable of detonating. They can be detonated by directly exposing them to high enough ambient temperatures or by an indirect mechanical process that produces adequate heat within its mass (Cooper, 1996). Explosives that have particularly high output (i.e., those capable of a very large energy release) are called HEs.

If a mass of material is impacted such that the material remains elastic, the waves that propagate through the material are called *sound waves*; they travel at the *sound velocity* in the material, a constant that is (linearly) proportional to the change in pressure (stress) in the material with respect to its change in density. If, however, the mass of material is impacted such that the material behaves plastically, the induced waves propagate at shock velocity, a velocity that is greater than the sound velocity and that increases non-linearly with increasing pressure (stress). The resulting shock wave is known as a 'jump process' or a discontinuity of state – pressure, density, energy – in the volume of material. As a result, an equation of state (EOS) relating the pressure–density–energy behavior of the material now becomes necessary to describe the complex shock wave propagations in the material. The material under consideration could be any gas, liquid, or solid.

When a HE charge detonates, it undergoes extremely fast, exothermic chemical reaction, producing gaseous (and some solid) products at very high temperatures and pressures. The self-sustaining 'reactive' shock wave, also known as a detonation wave, forms from rapid volumetric expansion of the explosive material at the reaction front and propagates through the explosive material at shock velocity. The detonation wave in the explosive trinitrotoluene (TNT) can have a pressure, temperature, and propagation velocity of 200 000 atm, 3000 deg K, and 7000 m/s, respectively (AMC, 1972). The gaseous explosive products, in turn, create a shock wave (or blast wave) in the surrounding medium. If this medium is air, the blast wave and its effects are generally termed 'airblast'. A blast wave in air is an 'unreactive' shock wave and therefore attenuates with distance from the source. The blast wave propagates faster than the sound velocity in air, and its front, a compression wave, is characterized by a sudden increase in ambient pressure. This pressure increase is also called an 'overpressure' from airblast because it is increased over ambient pressure. At a much slower rate, the gaseous products of detonation (of the original explosive substance) may mix with air and experience additional burning, which is called afterburn or gaseous burning, and is usually manifested by a fireball.

The materials considered in this chapter are solid HEs (or solid–liquid HEs) and the surrounding medium, through which 'unreactive' (inert) shock waves are transmitted to structures, is air. (For naval structures, the media would be both air and water.) While detonation physics within the

© Woodhead Publishing Limited, 2010

explosive mass and in the air immediately around it is quite complex, the far-field effects of a detonation – the pressure pulse at a point due to passage of the shock front – can be greatly simplified using empirical results.

1.2.2 Traditional uses

High explosives were developed for heavy civil work such as mining and large-scale excavation through rock. They were intentionally designed to be unstable (high sensitivity) under normal conditions (i.e., nitroglycerin, or NG) so that their explosive effects could be initiated with a small impact, current, or spark. After numerous accidents brought about by these high sensitivities, explosives manufacturers developed HEs with lower sensitivities so that a more deliberate initiation process (detonation) was required. For example, the initiation stimulus would be supplied by a blasting cap that would detonate a small explosive booster, which would then detonate the main explosive charge.

HEs are also used in a wide range of military applications, ranging from heavy civil work to use in various weapons including large bombs and warheads. Militaries have great interest in both creating highly lethal and controllable weapons systems on the one hand, and in defeating or resisting explosive effects on the other. As a result, a number of militaries have supported a large body of work to study blast loads and blast effects on structures, among other things. Much of the material presented in this chapter is based on decades of blast research conducted primarily by the US and British militaries.

1.2.3 Composition and oxidation

Most explosives contain carbon, hydrogen, nitrogen, and oxygen and are thus called CHNO explosives (Cooper, 1996). When an explosive detonates (or a fuel or propellant burns) a chemical reaction known as oxidation is occurring. Oxidation is a decomposition process in which the molecules of a substance (material) combine with oxygen to form new substances. A burning material is undergoing the exothermic chemical reaction of oxidation. Heat (energy) is produced because the molecules of the final (burned) substances possess less internal energy than the molecules of the initial (unburned) substance; the energy produced in this decomposition is called the *heat of reaction*. If a material is in an environment where it can completely oxidize, the products will go to their most oxidized state, and the energy produced is called the *heat of combustion*. For typical HEs, most or all of the oxidizer is in the explosive molecules, but further oxidation can also be provided by another source, such as the surrounding air or another substance added to the 'pure' explosive.

© Woodhead Publishing Limited, 2010

When a material burns and produces heat faster than the material can conduct it out of its volume, the accelerated rate of material burning is known as a *thermal explosion*. This condition can be completely described by laws of chemical reaction rates and heat conduction (AMC, 1972). In a more extreme scenario, a reaction wave can propagate through the unreacted material volume and set up a flow condition in the material. When the reaction wave propagates quickly, but at a velocity below the sound velocity in the material, the phenomenon is called a *deflagration*. If, however, the reaction wave propagates in the material at shock velocity (i.e., faster than the sound velocity in the material), the phenomenon is called a *detonation*. The energy released in this situation is called the *heat of detonation*. The detonation wave is known as a 'reacting' shock wave because it is maintained by the rapid chemical reaction in the explosive material. A coupled, thermal–hydrodynamic model is now required to completely describe the detonation phenomena. Since the mathematics and physics are quite complex for even the most simplified detonation models, this chapter will present graphical procedures based on semi-empirical studies to estimate blast pressures.

1.2.4 Confinement, size, shock sensitivity, and density effects

An explosive can be characterized by its unreacted density ρ_0 and its two Chapman Jouguet (CJ) state parameters: detonation velocity D_{CJ}, and detonation pressure P_{CJ}. In general, higher CJ parameters indicate more energetic explosives. Since burning reaction rates are a function of pressure and temperature and the reaction rate increases with pressure, strong confinement can cause burning to transition to detonation for most explosives and many propellants (Mader, 1998). On the other hand, if a burning explosive material is unconfined, it usually will not transition to detonation. For example, a small amount of unconfined black powder will simply burn if ignited under normal atmospheric conditions. If, however, it is adequately confined in a metal tube and then ignited, burning can transition to detonation, resulting in what is commonly called a pipe bomb. Confinement is often provided for military weapons by precision metal casings that can be designed for the dual purpose of producing the desired primary fragmentation after detonation.

Effective confinement can be provided by the bulk of the explosive material itself. This is related to the observation that, for a cylindrical bare explosive charge detonated at one end, the detonation velocity will increase with an increase in the diameter of the cylinder; the so-called infinite diameter detonation velocity is approached asymptotically at larger diameters and is a constant for a particular explosive substance under constant

© Woodhead Publishing Limited, 2010

confinement. For these larger explosives, the slower conduction of heat away from the explosive's reaction zone and the larger mass acting to confine it increase the pressure in the explosive material, which in turn increases the rate of chemical reaction. The increased rate of reaction leads to further increases in pressure, temperature, and density until the upper limit of detonation velocity is attained in the explosive. Conversely, there is a critical charge diameter for each explosive substance below which a detonation will not occur. This diameter is about 1 cm for TNT, 10 cm for ammonium nitrate, and 160 cm for some rubber-base composite propellants (AMC, 1972).

The way an explosive material is handled will also influence its behavior. For example, a piece of cast (solid) TNT will probably simply burn with a linear velocity of 1 cm/s if it is lit by a match; however, if it is strongly shocked, it will detonate with a linear velocity of approximately 700 000 cm/s (AMC, 1972). Confinement and charge size of a particular explosive material and its sensitivity to shock have obvious implications for its safe storage and transport as well as for the design of effective explosive devices.

Finally, the CJ parameters – detonation velocity and detonation pressure – are dependent on the unreacted density of the explosive. The detonation velocity for most explosives over reasonable ranges of density is nearly linearly related to unreacted density, as observed for TNT and pentaerythritol tetranitrate (PETN) (Cooper, 1996). If the unreacted density and either one of the CJ parameters of an explosive charge are known, the other CJ parameter can be computed from

$$P_{\mathrm{CJ}} = \frac{\rho_0 D_{CJ}^2}{\Gamma + 1} \qquad [1.1]$$

where Γ is the ratio of specific heats (constant volume and constant pressure) of detonation product gases, which if unknown can be estimated to be equal to three for unreacted explosive densities ranging from 1.0 to 1.8 g/cm^3 (Cooper, 1996). Further, an explosive's EOS, representing the expansion of its gaseous detonation products, can be scaled with respect to density for modest density changes. One such technique is presented by Lee *et al.* (1968) and applied by Zapata and Weggel (2008).

1.3 Some important explosive properties and physical forms

1.3.1 Heats of combustion, detonation, and afterburn

As described earlier, detonation refers to the extremely fast liberation of energy (heat) as an explosive material oxidizes at the reaction front propagating through its mass at supersonic velocity. Most explosives have

© Woodhead Publishing Limited, 2010

their oxidizers as a part of the same molecules as the fuel (Cooper, 1996); that is, detonation (or burning) does not rely on oxygen in the surrounding air. The heat of combustion is the theoretical upper limit for full oxidation of the explosive substance; it equals, respectively, the heat of detonation plus the heat of afterburn, thus

$$\Delta H_c = \Delta H_d + \Delta H_{ab} \quad [1.2]$$

The heat of detonation of an explosive is the maximum energy available for detonation, the energy that is liberated during the creation of the detonation products. Under the right conditions these detonation products (such as free carbon and carbon monoxide) will expand, mix with air, and burst into flame. The additional energy released during this reaction can be up to the heat of afterburn ΔH_{ab}. The visible fireball or burning gases of an explosion are associated with this slower energy release. The heat of detonation for most explosives is approximately one-third of the heat of combustion (US Department of the Army, 2008); therefore, as indicated by Eq. 1.2, the heat of afterburn will be approximately two-thirds the heat of combustion. Finally, it is emphasized that Eq. 1.2 represents an upper limit to the oxidation reaction; for example, the oxidation given by ΔH_d may not be attained because of improper detonation or the oxidation given by ΔH_{ab} may be incomplete in a low-oxygen environment.

1.3.2 TNT equivalency

Since there has been a great deal of practical experience with the blast effects of TNT charges, it has become the traditional reference explosive. To simplify and consolidate blast computations, pure explosives and explosive mixtures of varied chemical compositions are commonly assigned a TNT-equivalent weight (or mass). This can be accomplished by relating peak pressures, peak positive impulses, or heats of detonation of the explosive charge under consideration to those of a TNT charge of similar shape and under similar conditions.

If pressures will govern the structural design, it is preferable to use the TNT-equivalent weight based on comparisons of peak pressures

$$W_{P_{TNT}} = \left(\frac{P}{P_{TNT}}\right) W \quad [1.3]$$

where P is the peak pressure produced by detonation of weight W of the explosive under consideration and P_{TNT} is the peak pressure produced by detonation of the same weight of TNT. This can also be interpreted as the weight of TNT required to produce the same peak pressure as the weight W of the explosive under consideration.

© Woodhead Publishing Limited, 2010

If peak positive impulse (area under the pressure–time pulse) will govern the structural design, TNT equivalence is based on the analogous equation

$$W_{i_{\mathrm{TNT}}} = \left(\frac{i}{i_{\mathrm{TNT}}}\right) W \qquad [1.4]$$

where i is the impulse produced by detonation of weight W of the explosive under consideration and i_{TNT} is the impulse produced by detonation of the same weight of TNT.

When TNT equivalence based on pressure or impulse measurements is unavailable, it can be estimated by comparing the heats of detonation of the two explosives, thus

$$W_{\mathrm{TNT}} = \left(\frac{\Delta H_{\mathrm{d}}}{\Delta H_{d_{\mathrm{TNT}}}}\right) W \qquad [1.5]$$

where ΔH_{d} is the heat of detonation of the explosive under consideration, H_{dTNT} is the heat of detonation of TNT, and W is the weight of the explosive under consideration.

Table 1.1 lists densities, heats of detonation, and TNT equivalencies based on pressure, impulse, and heat of detonation ratios for a number of

Table 1.1 Representative densities, heats of detonation, and TNT-equivalencies for common explosives

Explosive	ρ_0^1 (g/cc)	ΔH_{d} (MJ/kg)	TNT-equivalent weight based on			
			P	*i*	Pressure range (MPa) for *P*, *i*	ΔH_{d}
Ammonia dynamite[4]	1.30	NA[2]	0.70	0.70[3]	NA[2]	–
ANFO[5]	NA[2]	NA[2]	0.87	0.87[3]	0.03–6.90	–
HMX	1.80–**1.90**	6.78	1.25	1.25[3]	NA[2]	1.15
NG dynamite[6]	NA[2]	NA[2]	0.90	0.90[3]	NA[2]	–
PETN	1.67–**1.78**	6.90	1.27	1.27[3]	0.03–0.69	1.17
RDX	1.63–**1.81**	6.78	1.10	1.10[3]	NA[2]	1.15
TNT	1.53–**1.65**	5.90	1.00	1.00	Standard	1.00
Tetryl	1.50–1.73	6.32	1.07	1.07[3]	0.02–0.14	1.07
Tritonal	1.72	NA[2]	1.07	0.96	0.03–0.69	–

[1] Bold value is theoretical maximum density
[2] Data not available
[3] Estimated value
[4] 20% strength
[5] 94/6 ammonium nitrate/fuel oil
[6] 50% strength

© Woodhead Publishing Limited, 2010

high explosives. Within this table, PETN is observed to have the highest heat of detonation and the highest TNT-equivalent weight irrespective of the method used to compute its TNT equivalency. A TNT equivalency factor of 1.3 will generally provide a conservative estimate of the TNT-equivalent charge weight for a HE charge when other data are unavailable (ASCE, 1999).

1.3.3 Physical forms

While some HEs are used in their pure liquid or solid forms, explosive products are typically pure explosives blended with one or more explosive or inert materials to achieve the desired mechanical, thermal, sensitivity, and output properties. As described in detail in Cooper (1996), explosive products can take the following physical forms:

- pressings
- castings
- plastic bonded, machined
- putties
- rubberized
- extrudable
- binary
- blasting agents
- slurries and gels
- dynamites

Attractive HEs are stable, have relatively high (detonation) output velocity and pressure, are insensitive to low-velocity impact, and have low toxicity (Cooper, 1996). With the exception of ANFO, the solid–liquid composite explosive comprising ammonium nitrate and fuel oil, this chapter primarily considers solid HEs. However, explosives of all physical forms, states (solid, liquid, or gas), and chemical compositions can be given a TNT-equivalent weight.

1.4 A generic explosive device

A generic explosive device is shown in Fig. 1.1. It consists of a 'train' of explosives: an initiating charge of primary explosive (typically contained within a blasting cap), a booster charge, and the main HE charge of secondary explosive. Primary charges are typically sensitive explosives (i.e., lead azide, mercury fulminate) that can be initiated by a mechanical shock, small spark, or other thermal source but have relatively low explosive output. The HE charges (i.e., TNT, RDX, dynamite) tend to be relatively difficult to initiate (insensitive) but have high explosive outputs suitable for the task

© Woodhead Publishing Limited, 2010

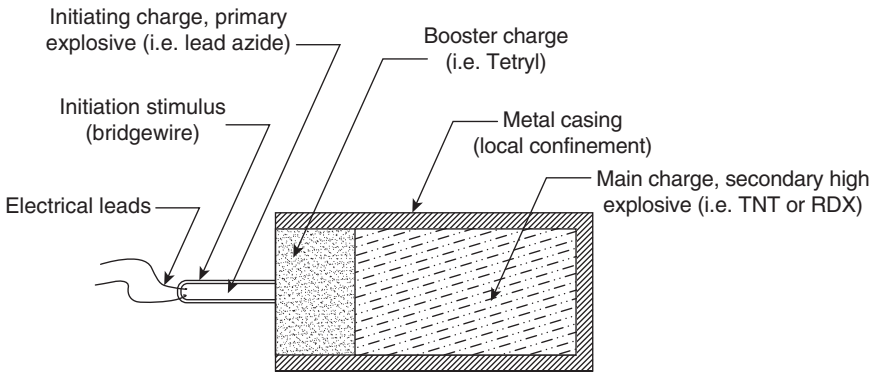

1.1 A generic explosive device.

for which the overall explosive device is designed (AMC, 1972). Often the main HE charges need a booster charge, typically one of the more sensitive secondary explosives (e.g., PETN, tetryl), to be effectively detonated.

1.5 Blast waves in free air

1.5.1 Ideal free-air explosion

In this section an ideal explosion in free air is assumed to occur at sea level under normal atmospheric conditions, where P_0 = 101 kPa (14.7 psi) is atmospheric pressure and a_0 = 340 m/s (1116 ft/s) is the sound speed in air. An 'ideal explosion' results from detonating a bare (i.e., without a casing to locally confine the explosive charge), spherical or hemispherical, TNT charge at its center of mass. 'Free air' implies there are no reflecting surfaces to obstruct passage of the enlarging, spherical shock wave as it propagates radially outward through the air medium.

1.5.2 Shock pressure and impulse

After the shock wave has propagated through the air some radial distance from the center of explosion (also known as the 'center of burst'), the air immediately behind the shock front is highly compressed relative to ambient conditions, and behind this compressed air, at a distance known as the positive wavelength L_w^+, the air is rarefied relative to ambient conditions. The resulting pressure–time pulse, shown by the solid curve in Fig. 1.2, is produced by the shock wave propagating at supersonic speed by a fixed point relative to the center of the explosion. At time t_a, the time of arrival of the shock front after detonation, a near-instantaneous increase in ambient pressure (i.e., an overpressure) occurs due to the highly compressed air of the shock front; this pressure is called the peak incident (or side-on) pressure

© Woodhead Publishing Limited, 2010

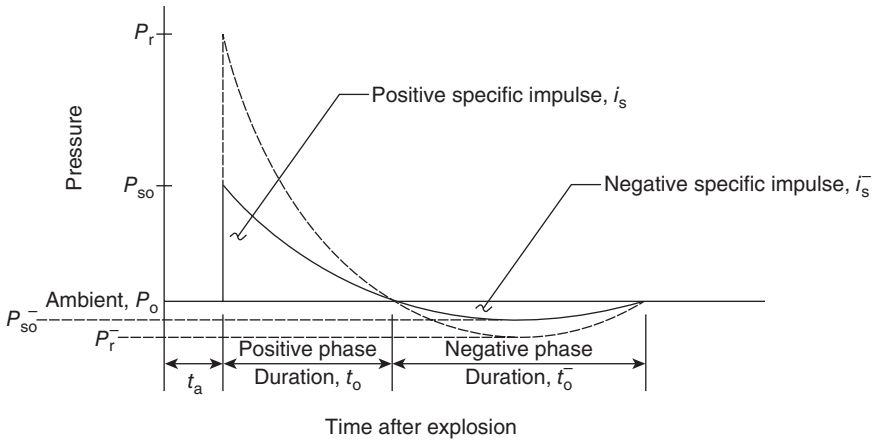

1.2 Incident and reflected blast pressure pulses.

P_{so}. The positive pressure decays back to ambient pressure over the period known as the positive phase duration t_0. The pressure further decays to a level below ambient pressure during the longer, negative phase duration t_0^-, resulting from the rarefaction of air a distance behind the shock front; negative pressure is associated with a reversal of air particle flow over a distance equal to the negative wavelength L_w^- and can be characterized as a 'suction' pressure. The maximum pressure amplitude of the negative phase is known as the negative incident pressure P_{so}^-. As the shock wave expands outward, its supersonic propagation velocity U and incident overpressure decrease and its wavelength and positive phase duration increase; this is due to spherical divergence, as well as dispersive effects. Peak positive pressures relatively near the explosion can be several orders of magnitude greater than atmospheric pressure but occur over durations that last only milliseconds.

The area under the pressure–time pulse over the positive phase is referred to as the positive specific incident impulse or, simply, the positive incident impulse i_s (MPa-ms). Similarly, the area under the pressure–time pulse of the negative phase is called the negative incident impulse i_s^-. The positive phase of the pressure pulse is typically more important than the negative phase for the design of rigid structures or rigid structural components. However, for relatively flexible structures, the negative-phase pressure pulse may also have to be included.

The modified Friedlander equation can be used to approximate the positive phase of the incident pressure pulse over time

$$P_s(t) = P_{so}\left[1 - \left(\frac{t - t_a}{t_0}\right)\right] e^{-(t-t_a)/\theta} \qquad [1.6]$$

© Woodhead Publishing Limited, 2010

for $t_a \le t \le t_a + t_0$ where t is time relative to detonation of the charge and θ (ms) is a time constant of the pressure pulse.

The positive incident impulse is the integral of the positive phase of the pressure pulse, thus

$$i_s = \int_{t_a}^{t_a+t_0} P_s(t)\,dt \qquad [1.7]$$

If t begins at the time of arrival, t_a can be set equal to zero and, substituting Eq. 1.6 into Eq. 1.7, the positive incident impulse can be written

$$i_s = \int_0^{t_0} P_{so}\left[1-\frac{t}{t_0}\right]e^{-t/\theta}\,dt \qquad [1.8]$$

which after integration is

$$i_s = \theta P_{so}\left[1-\frac{\theta}{t_0}\left(1-e^{-t_0/\theta}\right)\right] \qquad [1.9]$$

If the shock front impinges an infinitely large, perfectly rigid, reflecting surface at a normal angle of incidence, the incident pressure is magnified because the shock wave's propagation through the air is suddenly arrested and then redirected by the surface. The resulting normally reflected peak pressure P_r is two to approximately 13 times larger than the peak incident pressure P_{so}, where the higher end of this range is approached as incident pressures increase. The reflected pressure pulse is shown by the dashed curve in Fig. 1.2. In general, the peak reflected pressure at any angle of incidence can be written as a function of the peak incident pressure

$$P_{rx} = C_{r\alpha}P_{so} \qquad [1.10]$$

where $C_{r\alpha}$ is the reflected pressure coefficient that varies with angle of incidence α and P_{so}. Figure 1.3 is a plot of $C_{r\alpha}$ as a function of α for 20 values of P_{so}, ranging from 0.001 to 34.47 MPa.

As shown in Fig. 1.2, the reflected pressure pulse has approximately the same positive and negative phase durations as the incident pressure pulse; therefore the reflected positive impulse i_r will also be approximately two to 13 times greater than the incident impulse. Therefore, if $t_a = 0$, the positive phase of the reflected pressure and the positive reflected impulse are, respectively, given by

$$P_r(t) = P_r\left[1-\left(\frac{t}{t_0}\right)\right]e^{-t/\theta} \qquad [1.11]$$

and

$$i_r = \theta P_r\left[1-\frac{\theta}{t_0}\left(1-e^{-t_0/\theta}\right)\right] \qquad [1.12]$$

© Woodhead Publishing Limited, 2010

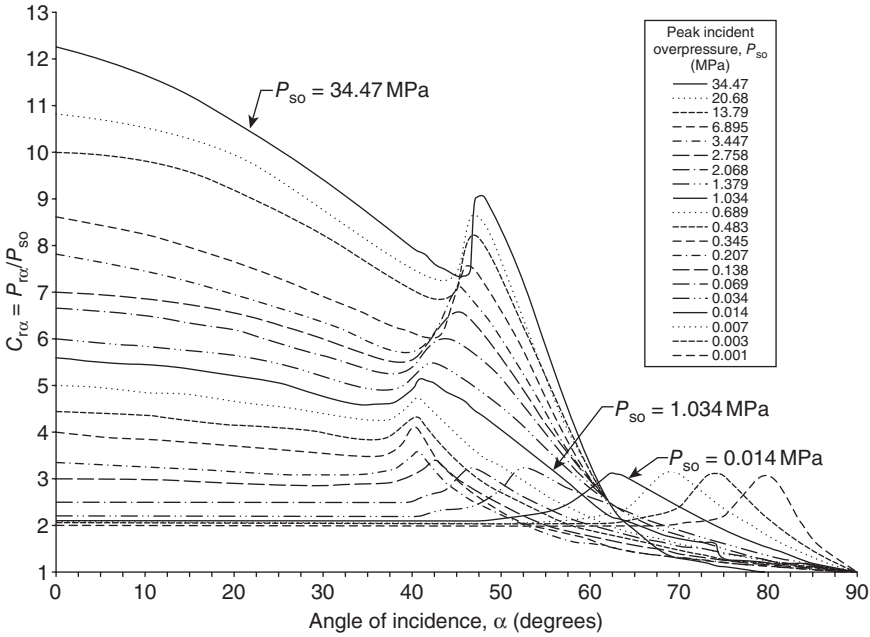

1.3 Reflected pressure coefficient (US Department of the Army, 2008).

Curves will be presented in Section 1.9.3 for the computation of several important positive phase blast parameters – including P_{so}, P_r, $C_{r\alpha}$, t_0, i_s, and i_r – as a function of TNT-equivalent charge weight and standoff (the distance between the explosive charge and the target).

1.5.3 Blast wind and gaseous burning

Air particles within the shock wave travel at particle velocities significantly lower than the supersonic velocity of shock front propagation U. This is illustrated effectively by the 'bead model' as presented in Cooper (1996). The dynamic pressure q associated with these particle velocities is commonly called the 'blast wind,' and it applies a drag pressure to objects in its path. When clearing effects, a function of the actual finite dimensions of a building, are considered for blast load computations for frontal normally reflecting walls, the reflected pressure can be reduced to the stagnation pressure – the sum of the drag pressure and the incident pressure – and the reflected pressure duration can be reduced to the clearing time t_c. Application of this procedure, as defined in US Department of the Army (2008), shows that the normally reflected pressure P_r and impulse i_r will yield conservative blast loads. As a result, these are the only loads that will be considered in more detail in this chapter.

© Woodhead Publishing Limited, 2010

For most explosives, just after detonation, gaseous burning – the oxidation of detonation products with the surrounding air mass – is typically manifested by a fireball. Except for very close-in unconfined explosions, the pressures produced by this energetic afterburn are small relative to those produced by the shock wave. The afterburn, however, could ignite the surroundings (including the structure) or set off other explosive events if the conditions are right.

1.6 Blast loading categories

1.6.1 Introduction

Blast loads can be categorized according to the confinement of the environment around the explosive device. This is not to be confused with the 'local confinement' provided by the casing around an explosive charge. Table 1.2, adapted from US Department of the Army (2008), provides a clear distinction of blast loading categories based on charge confinement, proximity to the ground surface, and 'venting' characteristics.

1.6.2 Unconfined explosions

Unconfined explosions, also known as 'external' explosions, produce shock waves that propagate through the air. A free-air explosion occurs when no obstructions are in the air medium to modify the radially propagating incident blast wave between the explosion and the target. An air explosion occurs a distance above the ground (as per US Department of the Army (2008), usually about two to three times the height of the structure under

Table 1.2 Blast loading categories

Charge confinement	Category	Pressure loads
Unconfined (external) explosions	1. Free-air explosion	Unreflected shock
	2. Air explosion	Reflected shock
	3. Surface explosion	Reflected shock
Confined (internal) explosions	4. Fully vented	Internal shock Leakage
	5. Partially confined	Internal shock Internal gas Leakage
	6. Fully confined	Internal shock Internal gas

Source: Adapted from US Department of the Army (2008).

© Woodhead Publishing Limited, 2010

consideration) such that the shock wave reflecting off the ground surface merges with the unreflected incident shock wave propagating directly toward the target. Ideal free-air and ideal air explosions are defined to be those occurring from detonation of bare, spherical TNT charges. A surface explosion occurs on or very near to the ground surface; that is, the 'height of burst' (HOB) is within a meter or two of the ground. Shock wave reflections off the nearby ground surface reinforce the incident wave front to form a hemispherical blast wave that propagates outward toward the target. If the ground surface were a perfect reflecting surface, the charge weight would be effectively doubled relative to a free-air explosion; however, due to the energy expended in ground cratering, a multiplier of approximately 1.7 is more realistic. An ideal surface explosion is defined to be one occurring from detonation of a bare, hemispherical TNT charge.

1.6.3 Confined explosions

Confined explosions, also known as internal explosions, produce shock pressures, leakage, and gas pressure build up, depending on whether the chamber is fully vented, partially confined, or fully confined; see Table 1.2. Depending on the geometry and frangibility of the confining structure, confined explosions can produce complex shock pressures due to reflections and interactions of shock waves within the structure. *Leakage* is the term given to incident and reflected shock waves and detonation products that form a shock wave that exits the confining structure.

A fully vented explosion occurs when an explosive is detonated inside a fully vented structure (cubicle), one that is completely open to the atmosphere on one or more sides. As shown in Table 1.2, the confining structure would, in general, be subjected to complex internal shock pressures and leakage. Another example of a fully vented explosion is when the target structure is in a relatively enclosed urban environment, surrounded by the reflecting surfaces of adjacent buildings and other structures.

A partially confined explosion produces complex internal shock pressures and leakage but is sufficiently confining such that a slower build up of gas pressure from afterburn (of detonation products) also occurs. The gas pressure dissipates by 'venting' to the atmosphere. The magnitude of the peak gas pressure is a function of TNT-equivalent charge weight, free volume of the chamber, and vent area; the magnitude of the corresponding gas impulse is also a function of these parameters and the inertia of the vent covers. The fundamental frequency for most confining structures (containment cells) is usually high enough that the gas pressure load can be considered quasi-static.

Finally, a fully confined explosion is a limiting case of the partially confined explosion. A complex shock environment is created but, unless the

© Woodhead Publishing Limited, 2010

containment cell fails, fully confined explosions experience no leakage and have very long gas pressure durations since no venting occurs.

1.6.4 Representative blast loading categories

This section will focus on three representative blast loading categories: unconfined free-air explosions, unconfined surface explosions, and partially confined explosions. The unconfined surface explosion is representative of a car bomb or satchel charge detonated near the ground surface but exterior to the target facility (structure). An explosive charge thrown into a public trashcan by an aggressor would likely be considered a partially confined explosion. A fully confined explosion would result if an explosive charge made its way inside a sealed luggage hold as contraband and was detonated.

The schematic in Fig. 1.4a shows an example of a free-air explosion. The shock wave propagates outward unobstructed, as represented by successively bigger spheres, until impinging the roof of the building. The line segment extending from the charge to Point A shows incident shock wave propagation along an angle of incidence $\alpha = 0$; the pressure reflected normally off the building's roof P_r will be many times greater than the incident pressure P_{so}, depending on the magnitude of P_{so}. The incident shock wave propagating along a general angle of incidence α relative to the roof (the line segment from the charge to Point B) will result in a reflected pressure $P_{r\alpha}$ greater than the incident pressure but typically not as large as the normally reflected pressure.

Figure 1.4b depicts an unconfined surface explosion that will produce an incident shock front that is nearly planar if the standoff R_G is relatively large. This implies that the incident and reflected pressure distributions will be nearly uniform over the front wall if it is an infrangible surface normal to shock wave propagation.

Finally, Fig. 1.4c shows an example of a partially confined explosion. Shock pressures will reflect and interact within the chamber in a complex manner, while a nearly uniform, quasi-static gas pressure will build up and slowly decay as it vents out the door opening.

1.7 Blast-induced load types and load cases

1.7.1 Traditional load types and load combinations

Before discussing the several blast-induced load types, it is emphasized that all traditional civil engineering load types (dead loads, live loads, snow loads, wind loads, seismic loads, etc.) and load combinations (as provided in model building codes, for example) must still be adequately considered

© Woodhead Publishing Limited, 2010

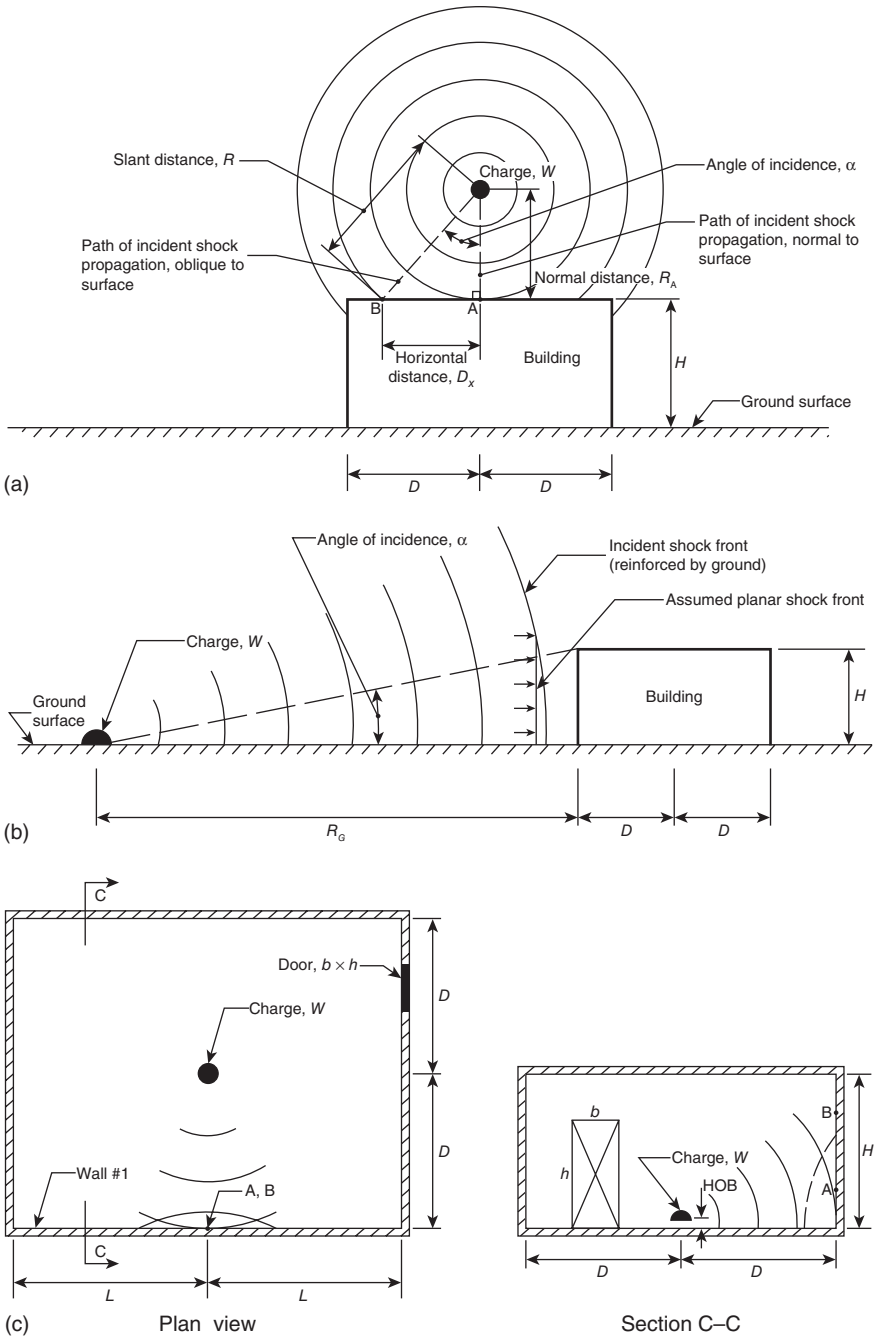

1.4 (a) Free-air explosion; (b) surface explosion; (c) partially confined explosion.

© Woodhead Publishing Limited, 2010

when designing a protective structure. Depending on the magnitude of relevant blast loads relative to traditional load types, blast loads may only control the design of (local) structural elements while wind or seismic loads control the (global) design of the structure's lateral force resisting system. This would likely be the case when the blast threat is the detonation of a small, close-in explosive device such as a satchel charge. Similarly, all traditional load types (and load combinations) must be applied in the design process of structures and components common to the field of mechanical engineering. In either field, it is important to note that a structure can probably be designed much more effectively (i.e., economically and aesthetically) when blast-induced load types are considered early in the design process.

1.7.2 Blast-induced load types

The intent of this section is to make the designer aware of all the blast-induced load types that should be considered in the design or retrofit of a structure. Some will be more critical than others for a particular threat, thus governing particular aspects of design. For example, air shock is the blast-induced load type that usually controls the design of an above ground structure to a surface explosion at larger standoffs. Shock pressures and gas pressure are the blast-induced load types that will likely control for partially or fully confined explosions occurring in a containment vessel such as a blast resistant luggage hold. However, some of the more extreme load types, such as resistance to direct shock or explosive cutting, may not be deemed practical to design for directly. In this case, local damage or failure of a component would likely be tolerated while global integrity of the system is maintained.

A brief description of each blast-induced load type is given below.

- **Air shock (airblast)** – shock pressures transferred through the air to the structure; pressures can be local or global.
- **Stagnation pressure** – blast wind (dynamic pressure) plus incident shock pressure transferred through the air to the structure; pressures are more likely to be global than local.
- **Ground shock** – shock pressures transferred through the ground to the structure's foundation; pressures can be local or global.
- **Direct shock** – very high shock pressures 'directly transferred' to a structural component; pressures are highly localized, from contact or near-contact charges.
- **Fragmentation** – usually small missile impacts (fragments) transferred through the air to the structure; impacts are usually relatively local, from close-in explosions.

© Woodhead Publishing Limited, 2010

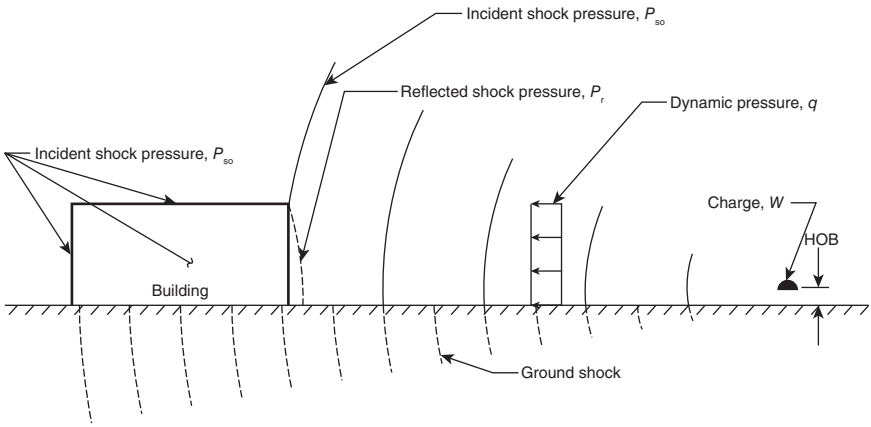

1.5 Load types for an above ground structure subjected to a surface explosion.

- **Gas pressure (gaseous burning)** – quasi-static gas pressures transferred through the air to the structure; pressures are local to the structure for very close-in unconfined explosions and global within the blast chamber for partially or fully confined explosions.
- **Jetting (explosive cutting)** – a jet material (usually a metal) at very high velocity and pressure is stressed into plastic flow and directly impinges the member; jet pressures are highly localized, from shaped charges.

Generally, after the design threat scenario(s) have been determined from a threat assessment, each of the blast-induced load types listed above should be evaluated for its relevance to the design. For example, Fig. 1.5 is a schematic of an above ground structure subjected to a near surface explosion at a considerable standoff. (The HOB is sufficiently small such that a surface explosion can be reasonably assumed.) For the initial design of this building, airblast (and possibly ground shock) will be the governing load type. The front wall, assuming it is infrangible under the applied airblast pressures, should be designed to resist the uniform normally reflected pressure P_r. The lower incident pressures P_{so} are typically used to approximate airblast pressures on surfaces that are roughly aligned along the radial travel of the shock front. The roof and side walls of this structure are surfaces that are so aligned. (US Department of the Army (2008), however, provides detailed guidance that will produce more representative pressure estimates for roofs and side walls.) The rear wall may also be designed to resist the incident blast load at the larger standoff given by the standoff of the front wall plus the depth of the building.

© Woodhead Publishing Limited, 2010

If the building has a frangible front façade, for example, the reflected pressure would be lower than if the façade were infrangible, since the incident blast pressure is not as drastically reflected by the frangible surface. (While less conservative, the reduced reflected pressures could be considered in the design process as per US Department of the Army, 2008.) However, appropriate consideration now has to be given to blast pressures entering the building through openings in the building envelope and loading both structural and non-structural interior components. Floor slabs can be particularly vulnerable to load reversals (upward loading) if this has not been specifically considered in design. Similarly, non-structural components such as infill walls, fixtures, and ductwork can be sources of secondary fragmentation that can cause further internal damage and injuries or fatalities to building occupants. Quantitative treatment for the reduction of blast loads on frangible elements and externally-generated blast loads entering openings in the building envelope are beyond the scope of this chapter. However, procedures amenable to hand calculations or spreadsheet implementation are presented in US Department of the Army (2008).

Close-in detonations can cause cratering on the front side of elements (the side facing the explosion) and spalling on the back side of elements (the side away from the explosion). In the case of close-in detonations, blast pressures will be very concentrated and non-uniform and may be accompanied by fragmentation impact. Designs to resist very close-in detonations, including contact charges and shaped charges, will typically require use of advanced analytical methods (i.e., hydrocodes) for analysis and/or representative blast testing.

For an explosive charge with $HOB = 0$, approximately 33% of the explosive energy is coupled to the ground to form a ground crater; for $HOB = 2.5r$, where r is the radius of a spherical charge, only approximately 1% of the energy is coupled to the ground (Cooper, 1996). Using dimensional analysis, the geometry of a ground crater (along with observed damage to surrounding structures) is often used to estimate the explosive yield (weight and explosive composition) of a terrorist charge. Beyond the crater, a shock wave propagates through the ground in much the same way it does through the air. Soil and rock formations and their component properties (e.g., stiffness, density, and compressibility) vary widely and, along with explosive yield, determine whether ground shock will be significant. Typically ground shock will be important only for close-in explosions from large charges.

Loading from fragmentation can become significant for close-in charges that have a metal casing or, in the case of an improvised explosive device, contain sharp, dense objects intentionally packed around the mass of the explosive. These fragments are referred to as primary fragments. Limited data for close-in explosions indicate that loading from fragmentation and airblast combined is much higher than for airblast or fragmentation alone.

© Woodhead Publishing Limited, 2010

Secondary fragments are not produced by the explosive device itself but are generated by airblast pressures or primary fragments impacting local objects. For example, rocks, soil, and other objects ejected during the formation of a ground crater are secondary fragments. Pieces of the 'shell' of a containment vessel or debris from structural or non-structural components of a building are additional examples of secondary fragments.

Quantitative treatment of ground shock/direct shock, fragmentation, cratering/spalling, and explosive cutting is beyond the scope of this chapter but guidance to compute these loads is provided in US Department of the Army (2008) and other technical references.

1.7.3 Blast-induced load cases

Blast-induced load cases consist of the critical load types resulting from a matrix of explosive charge sizes (TNT equivalent weight) versus charge locations. This matrix is the result of a thorough threat assessment, as discussed in the next section. For example, a number of charge sizes and locations will typically need to be considered for the design of the building shown in Fig. 1.5. Often it is more likely that a small explosive device (i.e., a satchel charge) can be placed closer to the building than a larger car bomb; this would be the case if an effective 'keep out' perimeter, consisting of walls, bollards, and the like, was established to limit vehicle approach toward the structure. The blast load distributions and intensities of these two threats will typically vary significantly and must be adequately considered. Further, when a charge is located such that its blast wave will propagate roughly parallel to a structural element, incident design pressures are appropriate. However, if the charge is moved to a location where blast wave propagation will be normal to the element, the higher reflected design pressures become appropriate.

1.8 Threat assessment for design

1.8.1 Introduction

An early requirement in protective design is to determine the blast threat (a design basis threat) so the associated blast-induced load cases can be defined for design. Producing a reasonable and thorough threat assessment can be one of the more difficult aspects of protective design or analysis. This section will provide an introduction to a threat assessment procedure.

1.8.2 Accidental or intentional explosions

Explosions are either accidental, or they are planned and executed by aggressors (terrorists, criminals, or subversives). The designer should

© Woodhead Publishing Limited, 2010

determine whether the structure is to be designed to resist accidental blast loads, intentional blast loads, or both. An accidental explosion could occur in a petrochemical facility, for example, when a combustible material becomes the unintended fuel source for a burning, deflagration, or explosive event. As a result, petrochemical facilities have been traditionally designed to resist accidental explosions; modern petrochemical facilities are more likely to be designed to resist intentional explosions as well. For accidental explosions, the explosive composition, weight, and the effective standoff are probably easier to estimate based on historical accidents in similar facilities. ASCE (1997) and US Department of the Army (2008) provide excellent guidance on threat assessment and designing facilities for unintentional explosions.

1.8.3 Threat assessment of aggression

As detailed in Chapter 1 of ASCE (1999), the threat assessment when an aggressor is involved can be performed using the eight-step procedure outlined below.

1. Identify and categorize assets: people, information, equipment, etc.
2. Determine importance (value) of asset(s): mission criticality, replaceability, relative value.
3. Determine the likelihood of aggression: aggressors' interest in the asset(s).
4. Review history of aggression: likelihood of future aggression based on past incidents.
5. Estimate potential for aggression: an intelligence estimate of future aggression from local law enforcement or a government agency.
6. Evaluate accessibility: evaluate security and other protective measures in place or planned for implementation.
7. Account for effectiveness of law enforcement: estimate the capabilities of local law enforcement.
8. Address deterrence: assess the likelihood that aggressors will be deterred by visible security and protective measures.

Once the eight steps above have been addressed, the two 'threat design criteria' – threat severity level and level of protection – can be developed. Based on the threat severity level and potential aggressor tactics, the design basis threat can be determined from two matrices supplied in ASCE (1999) in Appendix A. The design basis threat would be a minimum charge weight to consider in the blast-induced load cases described in Section 1.7.3. The level of protection is a measure of the toughness of the structure subjected to load cases from the design basis threat.

© Woodhead Publishing Limited, 2010

When the federal government is the building owner/lessee or presides over product development, it is very likely the design team will be provided with the design basis blast threat (or threats) as well as the product's required level of protection. Federal authorities typically know what to expect. On the other hand, private building owners or product developers are more apt to either rely on the design team for threat definition and performance requirements or to cite a federal document to do so. They are more inclined to have unrealistic expectations of a structure's level of protection to a given blast threat. Stated another way, an arbitrarily-chosen design threat that is too high may result in a perceived very low level of protection or an uneconomical structure. Therefore, a knowledgeable design team should provide rational guidance early in the design process to private sector owners regarding expectations of threat definition and level of protection for a given cost.

1.9 Simplified blast load computation

1.9.1 Primary parameters

For unconfined explosions, there are six primary parameters required to quantify airblast loads applied to a structure or structural component (i.e., the 'target').

1. **Explosive substance, unreacted density, and confinement** – This information may be needed to compute the TNT-equivalent weight of the charge, especially when the design charge is not initially designated as weight of TNT. For simplicity, the density of the explosive is often assumed to be its theoretical maximum density (TMD).
2. **TNT-equivalent weight** – The TNT-equivalent weight of the charge is a fundamental quantity in airblast computations. It is needed for blast load computations using empirical charts or in numerical simulations.
3. **Charge geometry** – Charge geometry is more important for close-in explosions. In the far field charge geometry becomes less important.
4. **Standoff** – The distance from the charge's center of mass to the target; this quantity is as fundamental as the TNT-equivalent weight of the charge.
5. **Angle of incidence** – The angle between a normal projected outward from the target and the direction of radial propagation of the shock front. The angle of incidence can have a pronounced influence on reflected pressures and impulses.
6. **Height of burst** – The distance between the explosive's center of mass and a reference reflecting plane, usually the ground surface.

© Woodhead Publishing Limited, 2010

The first three parameters define the properties of the explosive charge itself and the remaining three define the charge's orientation relative to the target and a primary reflecting surface, usually the ground. It is noted that the blast environment is made significantly more complex for unconfined (exterior) explosions by the presence of multiple reflecting surfaces typical of an urban environment. Furthermore, for more accurate blast load predictions, the flexibility and frangibility of reflecting surfaces (i.e., elements loaded by the blast wave) would need to be known *a priori*. The fluid structure interaction between a shock wave and a flexible (or frangible) structure is known as a coupled analysis. It is far too complex and expensive to be justified for initial design and would probably be justified only for certain military applications, high-profile projects that command a sizeable physical security design fee, or for mass-produced containment vessels.

For confined explosions the six parameters mentioned earlier will need to be supplemented with additional information including the following:

- orientation of major reflecting surfaces
- flexibility and frangibility of reflecting surfaces
- location, size, orientation of hallways, neighboring chambers, etc.
- blast chamber volume ('free' volume)
- area of openings, vents, and fenestration and inertia/frangibility of vent covers, window glass, and doors

Orientation of reflecting surfaces and information on their flexibility and frangibility is needed for accurate computation of shock pressures. Hallways, neighboring chambers, and openings influence shock wave reflection, interaction, and diffraction; leakage and the build up of gas pressures within the (main) blast chamber are also affected. The detailed treatment of blast effects from interior explosions is very complex and is the subject of ongoing research. Even the relatively simplified guidance provided in US Department of the Army (2008) is quite involved and limited in its application.

1.9.2 Blast scaling

It is convenient to scale airblast parameters according to the dimensional, 'cube-root' scaling law

$$Z = R/W^{1/3} \qquad [1.13]$$

where Z is the 'scaled distance' with units of m/kg$^{1/3}$, R is the distance (m) from the center of the explosive charge to the target, and W is the weight of the charge (kg); W is usually the TNT-equivalent weight. This scaling law indicates that two charges with similar geometry in the same ambient conditions, identical explosive composition, and different size (weight) will produce self-similar blast waves if their scaled distances are equal; the

© Woodhead Publishing Limited, 2010

distance R for each charge has to satisfy Eq. 1.13. Cube-root scaling is also known as Hopkinson–Cranz scaling, named for the two independent developers of the law.

1.9.3 Airblast (shock)

Kingery and Bulmash (1984) developed 'standard' airblast curves for positive-phase blast parameters for detonation of bare TNT charges. These curves were compiled from many sources, involving numerous blast tests and supplemental computations. They can be found in US Department of the Army (2008).

Figure 1.6 contains curves for the positive phase blast (shock) parameters for detonations of spherical, free-air, TNT charges as a function of scaled distance Z. The scaled distance is first computed by substituting the standoff and the TNT-equivalent charge weight into Eq. 1.13. Any of the desired blast quantities for this value of Z can be determined from the appropriate curve in the figure. The blast parameters that can be computed from this figure are:

- peak incident (side-on) overpressure P_{so} (MPa)
- incident (side-on) specific impulse i_s (MPa-ms)
- peak normally reflected overpressure P_r (MPa)

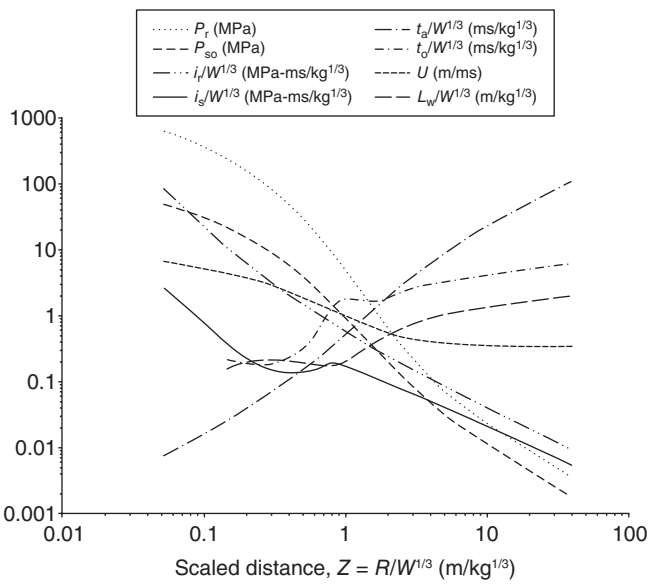

1.6 Positive phase shockwave parameters for a spherical TNT explosion in free air at sea level (US Department of the Army, 2008).

© Woodhead Publishing Limited, 2010

- normally reflected specific impulse i_r (MPa-ms)
- shock arrival time t_a (ms)
- positive phase duration t_0 (ms)
- shock front velocity U (m/ms)
- positive phase wavelength L_w (m)

It is noted that normally reflected pressure P_r corresponds to an angle of incidence of 0 degrees. The smallest scaled distance $Z = 0.054$ m/kg$^{1/3}$ corresponds to the radius of the spherical charge, the charge's surface. This implies that blast load parameters can be computed for charges in near-contact with the target; these computations should be made with caution, however, since the curves were extrapolated in the very low range of Z and other phenomena such as 'direct shock' and fragmentation may impose a more critical load than airblast. The largest value of scaled distance is $Z = 39.7$ m/kg$^{1/3}$, beyond which damage for the majority of structures is relatively superficial.

Figure 1.7 contains curves for the positive-phase blast (shock) parameters for detonations of hemispherical, TNT charges on the ground surface as a function of scaled distance Z. The same eight blast parameters can be computed from this figure as in Fig. 1.6. However, it is noted that pressures and impulses computed from Fig. 1.7 for a surface explosion at a given

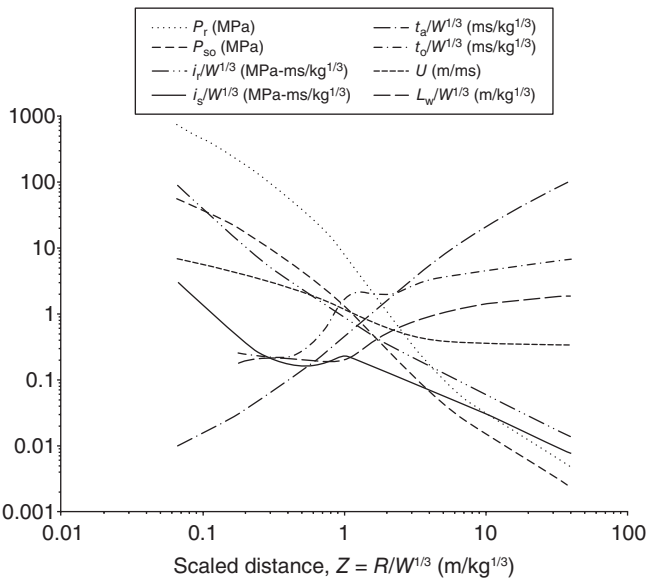

1.7 Positive phase shockwave parameters for a hemispherical TNT explosion on the surface at sea level (US Department of the Army, 2008).

© Woodhead Publishing Limited, 2010

scaled distance are higher than those computed from Fig. 1.6 for a free-air explosion. This is because the ground surface amplifies the shock wave for the surface explosion (given in Fig. 1.7), which could alternatively be obtained by roughly doubling the charge weight, computing the new value of Z, and using the curves of Fig. 1.6 for a free-air explosion.

The reflected pressure and impulse curves in these plots are based on reflections off an infinitely-large, rigid wall normal to the shock wave; this will typically yield conservative airblast loads. Reflected blast pressures from an identical explosion impinging a flexible structure can be substantially lower than reflected pressures impinging rigid reflecting surfaces. Estimating this reduced reflected pressure requires a coupled airblast/structural analysis or approximate computations like those presented by Kambouchev *et al.* (2007a,b). 'Clearing effects', a function of the finite size of an object obstructing blast wave propagation, can lead to further reduction of reflected pressures. Finally, the effect of angle of incidence on reflected pressures can be estimated from the curves in Fig. 1.3.

1.9.4 Interaction of shock fronts

Shock fronts for confined explosions (i.e., explosions that occur within the interior of a building or in a luggage hold) reflect off solid surfaces and interact in a complex manner. The reflected shock fronts can construct, interfere, and diffract around corners and through openings. Shock fronts reflecting off of frangible or flexible surfaces further complicate the situation, where relatively accurate pressure estimates would require a coupled fluid-structural analysis. Furthermore, if the potential for venting is significantly limited, a relatively slow rise in (quasi-static) gaseous overpressures will accompany and affect shock waves in the blast chamber. Fleisher (1996) and Weinstein (2000) demonstrate the complexities that result from shock front interactions in conjunction with the build up of gaseous pressures from explosions within luggage containers. In both references, the luggage containers were blast tested to verify the adequacy of initial design, to assist with design modifications, and to verify the final design of the containers. Partially confined explosions in an urban setting can also create a complex blast environment. Smith *et al.* (2001) performed experiments and numerical simulations on scale models of five generic street configurations to investigate the channeling effect that has been observed in terrorist vehicle bomb attacks in cities. They present several pressure and impulse plots to assist designers in accounting for the elevated blast loads associated with a built-up environment.

Shock front interaction could be the result of the detonation of multiple explosive charges simultaneously or in quick succession. Whatever the cause, although shock front interaction is typically quite complex, it should not be ignored. Analytical simulations or blast testing is recommended.

© Woodhead Publishing Limited, 2010

A numerical example is provided in Section 1.10, where very approximate blast pressures resulting from a confined explosion are computed for preliminary design. To approximately represent shock wave reflections and interactions, the reflected pressures and their corresponding impulses are multiplied by 1.75, as per US Department of the Army (2008).

1.9.5 Gas pressure

Confinement of detonation products for partially or fully confined explosions will lead to a relatively slow increase of gas pressure in the confining chamber. Peak gas pressure is a function of loading density, the ratio of explosive weight (mass) to the 'free' volume of the blast chamber. Free volume is the volume of the chamber (room) minus the volume of furnishings, structural elements, and other objects that occupy room space. Figure 1.8 is a plot of the maximum gas pressure P_g as a function of loading density for total vent areas A between $0 \le A/V_f^{2/3} \le 0.022$, where the term $A/V_f^{2/3}$ is the scaled total vent area.

As the total vent area approaches zero, as in a fully confined chamber (or containment cell), the duration of gas pressures approaches infinity. Practically speaking, at this lower venting limit most confinement chambers would either be breached or some venting would occur through seams or gaps in its walls.

The gas impulse i_g corresponding to the peak gas pressure can be obtained from Fig. 1.9. The gas impulse is scaled in the manner it was for shock impulses in Figs 1.6 and 1.7 and is a function of the scaled total vent area.

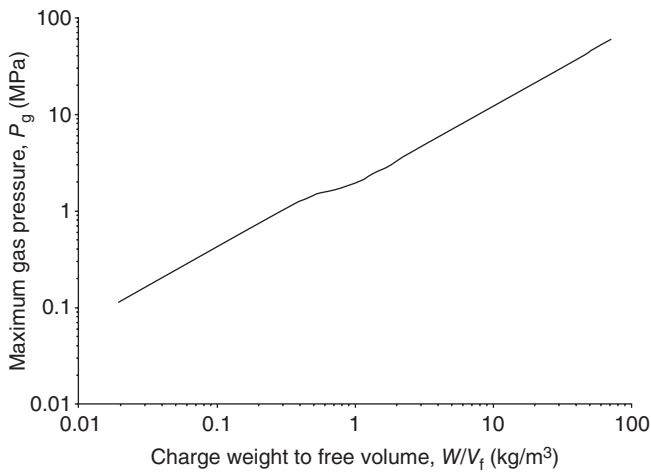

1.8 Peak gas pressure produced by a TNT detonation in a partially confined chamber (US Department of the Army, 2008).

© Woodhead Publishing Limited, 2010

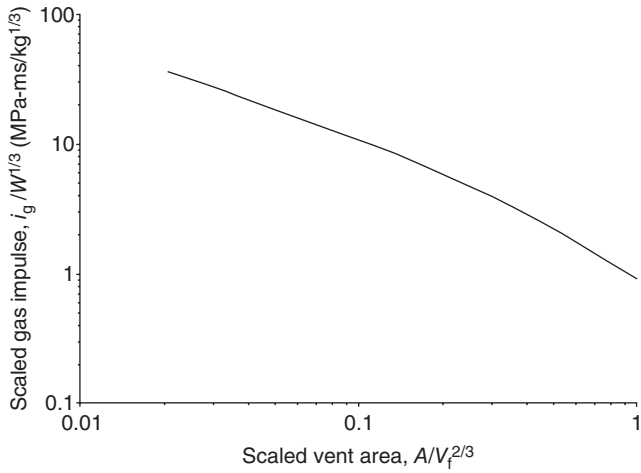

1.9 Scaled gas impulse for W/V_f = 0.032 kg/m^3 and vent opening without cover (US Department of the Army, 2008).

The curve in Fig. 1.9 is for weightless vent coverings and a loading density of up to 0.032 kg/m^3. Using the maximum gas pressure and its corresponding impulse, the approximate gas pressure pulse used for design can be specified, as discussed in the next section.

Figures 1.8 and 1.9 were generated to simplify gas pressure and impulse computations for design. However, gas pressure is shown in US Department of the Army (2008) and by other researchers to affect shock wave interactions. For example, Marconi (1994) performed a computational investigation to study the complex interactions of blast waves in a fully confined square room. Shock wave reflections and interactions were investigated, but the focus of the study was a Rayleigh–Taylor-type instability produced by the acceleration and densification of the hot gaseous core from detonation products at the center of the explosion. The interaction of reflected shock waves with the core appeared to promote this instability.

Vent design is also more complicated than the design curves suggest. Molkov (1999) studied actual deflagrations in domestic structures and industrial plants to assess safe vent area design with the overall goal of reducing overpressures due to deflagration. Molkov discussed system complexities and the hundred-fold scatter that can occur in vent design as determined by the various empirical formulae. Based on comparisons to actual deflagration data, Molkov was able to choose a suitable turbulence factor and discharge coefficient for use in a lumped parameter model to simulate the pressure–time behavior in vented enclosures. The deflagration dynamics also considered a range of vent release overpressures and inertia

© Woodhead Publishing Limited, 2010

of covers over the venting spaces. Molkov stated that vent design procedures can be improved with the appropriate turbulence factor and discharge coefficient for the facility of interest.

As the previous examples suggest, blast loads resulting from internal detonations or deflagrations are very complex. For the final design of containment chambers (or cells), it is recommended that hydrodynamic simulations, blast tests, or both be performed to verify the complex blast pressure environment and the integrity of the chamber.

1.9.6 Blast load simplifications for design

In general, explosions generate blast pressures on structures that vary temporally and spatially. The pressure distribution from a distant explosion is nearly uniform over a normal reflecting surface, so only the peak pressure and its time variation need to be computed. A close-in explosion, however, is more complex because it produces a pressure distribution that varies significantly in magnitude over the reflecting surface (i.e., the pressure is no longer uniform). In this case, reflected pressures and their time variations should be computed within several sub-regions of the reflecting surface so the pressure distribution can be more accurately represented. (In certain situations phasing of the individual pressure pulses may also be of concern.) Alternatively, the pressure pulses in each sub-region could be averaged to produce an 'effective' uniform pressure.

The primary blast loading parameters for design are usually incident or reflected peak (shock) pressures and their corresponding impulses. For initial design, it is usually adequate to represent the actual blast pressure–time pulse shown in Fig. 1.2 with the linearly-decaying triangular pulse shown in Fig. 1.10a. Since the negative phase will not typically affect design,

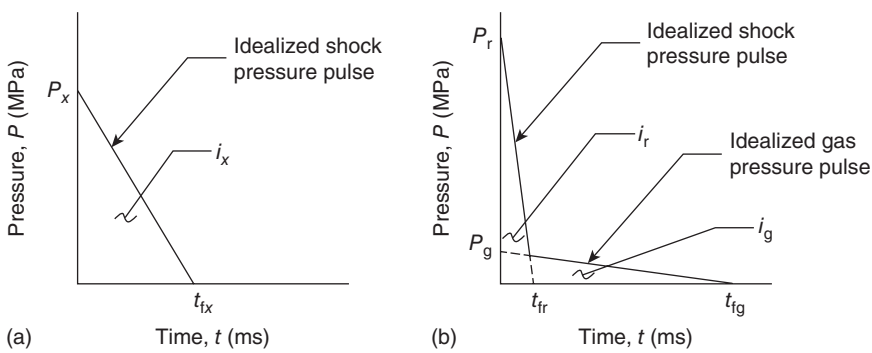

1.10 (a) Approximate pressure pulse for shock only; (b) approximate pressure pulse for shock plus gas.

© Woodhead Publishing Limited, 2010

it is ignored in the idealized pulse shown in Fig. 1.10a. The area under the triangle is by definition the positive impulse i_x, therefore the 'fictitious' pulse duration t_{fx} is computed from the peak pressure P_x and the impulse

$$t_{fx} = 2i_x / P_x \qquad [1.14]$$

In Eq. 1.14, P_x is either the peak incident or reflected pressure from the blast wave and i_x is the corresponding impulse. The peak pressure is assumed to be attained instantaneously and decays linearly to ambient pressure over the fictitious pulse duration.

The positive shock pressure pulse for rigid structures typically governs for design. In this case, the idealized blast load for the wall of a structure facing the charge is the triangular pressure pulse where the peak positive reflected pressure P_r and the reflected positive specific impulse i_r are used to determine the 'fictitious' pulse duration. For relatively flexible structures, consideration of the negative phase of the pressure pulse may be important if the 'suction' loading acts in phase with the rebounding structure. In design situations where the negative phase of the blast pressure–time curve is required, the more involved procedure given in US Department of the Army (2008) should be used.

For the design of structures subjected to partially confined explosions, the gas pressure should be combined with the appropriate reflected shock pressures to construct the complete pressure–time history. A simplified model, which uses two triangular pulses computed separately, produces the bilinear pressure–time curve for shock and gas (Fig. 1.10b). The fictitious pulse duration for gas t_{fg} is also computed using Eq. 1.14, where i_x is now the gas impulse i_g and P_x is the peak gas pressure P_g. It is noted that the peak gas pressure generally does not correspond with peak shock pressures but, for the purposes of design, the peak gas pressure is often assumed to start at time zero and decay linearly over t_{fg}. As shown in the figure, the two triangular pulses do not add together early in the time history but simply overlap.

1.10 Numerical examples of simplified blast load computation

Three examples are provided in this section to illustrate computation of important blast parameters that would be appropriate for initial design. Computation of blast loads from a free-air explosion, a surface explosion, and a partially confined explosion are presented.

1.10.1 Free-air explosion

Compute the peak incident and reflected pressures on the roof of the building at Points A and B for the free-air explosion shown in Fig. 1.4a.

© Woodhead Publishing Limited, 2010

Given:
W = 115 kg RDX charge
R_A = 5.0 m, D_x = 3.0 m, D = 4.0 m

Solution:
Convert the weight of RDX to TNT-equivalent weight; from Table 1.1 the factor to convert to TNT-equivalent weight based on peak pressure and impulse is 1.10, thus
$W_{TNT} = 1.10(115) = 126.5$ kg

Point A
$R = R_A$
$Z = R/W^{1/3} = 5.0/126.5^{1/3} = 1.00$ m/kg$^{1/3}$

From Fig. 1.6 (free-air explosion)
$P_{so} = 0.90$ MPa ***Ans.***
$P_r = 5.3$ MPa ***Ans.***

Point B
$R = \sqrt{5.0^2 + 3.0^2} = 5.8$ m $\alpha = \tan^{-1}(3.0/5.0) = 31$ deg
$Z = R/W^{1/3} = 5.8/126.5^{1/3} = 1.16$ m/kg$^{1/3}$

From Fig. 1.6 (free-air explosion)
$P_{so} = 0.67$ MPa ***Ans.***

From Fig. 1.3 (with $\alpha = 31$ deg and $P_{so} = 0.67$ MPa)
$C_{r\alpha} = 4.3$
Therefore from Eq. 1.10
$P_{r\alpha} = C_{r\alpha}P_{so} = 4.3(0.67) = 2.9$ MPa ***Ans.***

1.10.2 Surface explosion

For the surface explosion, compute idealized pressure–time pulses on the building shown in Fig. 1.4b for (a) the front wall (wall facing the charge), (b) the roof, and (c) the side walls. The pressure pulses should be appropriate for the initial design of localized structural elements. Also, compute the actual positive phase duration t_0 and the arrival time t_a at the location of the front wall.

Given:
W = 1000 kg TNT charge
R_G = 50 m, H = 10.0 m, D = 8.0 m

© Woodhead Publishing Limited, 2010

Solution:

(a) *front wall*: P_r, i_r, t_0, and t_a are evaluated at $R = R_G$

$Z = R/W^{1/3} = 50/1000^{1/3} = 5.0$ m/kg$^{1/3}$

$\alpha = \tan^{-1}(10.0/50.0) = 11.3$ deg (angle of incidence at the eave)

From Fig. 1.7 (surface explosion)

$P_{so} = 0.040$ MPa

$P_r = 0.10$ MPa

$i_r/W^{1/3} = 0.12$ MPa-ms/kg$^{1/3}$ $\quad i_r = 0.12(10.0) = 1.2$ MPa-ms

$t_0/W^{1/3} = 3.9$ ms/kg$^{1/3}$ $\quad t_0 = 3.9(10.0) = 39$ ms ***Ans.***

$t_a/W^{1/3} = 8.0$ ms/kg$^{1/3}$ $\quad t_a = 8.0(10.0) = 80$ ms ***Ans.***

Referring to Fig. 1.10a, the approximate pressure pulse to be applied uniformly to the front wall is defined by

$P_x = P_r = 0.10$ MPa ***Ans.***

$i_x = i_r = 1.2$ MPa-ms ***Ans.***

Therefore from Eq. 1.14

$t_{fr} = 2i_r/P_r = 24$ ms ***Ans.***

Check the planar wave assumption:

$R = \sqrt{50^2 + 10^2} = 51$ m

$Z = R/W^{1/3} = 51/1000^{1/3} = 5.1$ m/kg$^{1/3}$

From Fig. 1.3 (with $\alpha = 11.3$ deg and $P_{so} = 0.040$ MPa)

$C_{r\alpha} = 2.3$

Therefore

$P_{r\alpha} = C_{r\alpha}P_{so} = 2.3(0.040) = 0.092$ MPa

$P_{r\alpha}$ is close to the normally reflected pressure P_r so the planar wave assumption is reasonable.

(b) *roof*: P_{so} and i_s are evaluated at midpoint of the roof, $R = \sqrt{(R_G + D)^2 + H^2}$

$Z = R/W^{1/3} = 59/1000^{1/3} = 5.9$ m/kg$^{1/3}$

From Fig. 1.7 (surface explosion)

$P_{so} = 0.033$ MPa

$i_s/W^{1/3} = 0.05$ MPa-ms/kg$^{1/3}$ $\quad i_s = 0.05(10.0) = 0.50$ MPa-ms

Referring to Fig. 1.10a, the approximate pressure pulse to be applied uniformly to the roof is defined by

$P_x = P_{so} = 0.033$ MPa ***Ans.***

$i_x = i_s = 0.50$ MPa-ms ***Ans.***

$t_{fs} = 2i_s/P_{so} = 30$ ms ***Ans.***

© Woodhead Publishing Limited, 2010

(c) *side walls:* P_{so} and i_s are evaluated at the middle of the side walls,
$R = \sqrt{(R_G + D)^2 + (H/2)^2}$
$Z = R/W^{1/3} = 58/1000^{1/3} = 5.8$ m/kg$^{1/3}$

Since the scaled distance Z here is close to that of (b), the same approximate pressure pulse can be applied to the side walls, thus referring to Fig. 1.10a
$P_x = P_{so} = 0.033$ MPa ***Ans.***
$i_x = i_s = 0.50$ MPa-ms ***Ans.***
$t_{fs} = 2i_s/P_{so} = 30$ ms ***Ans.***

1.10.3 Partially confined explosion

For the partially confined explosion, compute the *combined* idealized shock and gas pressure–time pulse for a strip of Wall #1 centered directly across from the explosive charge; see Fig. 1.4c. Compute an average shock pressure and impulse for the wall based on computations at Points A and B, and approximately account for multiple shock wave reflections/interactions. The combined pressure pulse should be appropriate for the initial design of the local wall strip.

Given:
$W = 4.5$ kg TNT charge
$HOB = 0.30$ m
$D = 3.1$ m, $L = 3.8$ m, $H = 3.1$ m
$b = 0.9$ m, $h = 2.2$ m (door opening, assumed open)
Elev. $A = H/4 = 0.78$ m, Elev. $B = 3H/4 = 2.3$ m

Solution:
Point A (shock)
$R = \sqrt{3.1^2 + (0.78 - 0.30)^2} = 3.1$ m $\alpha = \tan^{-1}[(0.78 - 0.30)/3.1] = 8.8$ deg
$Z = R/W^{1/3} = 3.1/4.5^{1/3} = 1.90$ m/kg$^{1/3}$

From Fig. 1.7 (surface explosion)
$P_{so} = 0.32$ MPa
$P_r = 1.2$ MPa
$i_r/W^{1/3} = 0.39$ MPa-ms/kg$^{1/3}$ $i_r = 0.39(1.65) = 0.64$ MPa-ms

Point B (shock)
$R = \sqrt{3.1^2 + (2.3 - 0.30)^2} = 3.7$ m $\alpha = \tan^{-1}[(2.3 - 0.30)/3.1] = 33$ deg
$Z = R/W^{1/3} = 3.7/4.5^{1/3} = 2.24$ m/kg$^{1/3}$

© Woodhead Publishing Limited, 2010

From Fig. 1.7 (surface explosion)
$P_{so} = 0.20$ MPa
$P_r = 0.63$ MPa
$i_r/W^{1/3} = 0.30$ MPa-ms/kg$^{1/3}$ $\quad i_r = 0.30(1.65) = 0.50$ MPa-ms

Investigate the effects of angle of incidence on peak reflected pressure:
From Fig. 1.3 (with $\alpha = 33$ deg and $P_{so} = 0.20$ MPa)
$C_{r\alpha} = 3.1$
Therefore
$P_{r\alpha} = C_{r\alpha}P_{so} = 3.1(0.20) = 0.62$ MPa
$P_{r\alpha}$ is close to the normally reflected pressure P_r so P_r and i_r as computed above are reasonable.

Average shock pressures and impulses from Points A and B for an approximate uniform load on the wall strip. As per US Department of the Army (2008), multiply results by 1.75 to approximately account for shock wave reflections and interactions.
$\bar{P}_r = 1.75[(1.2 + 0.63)/2] = 1.6$ MPa
$\bar{i}_r = 1.75[(0.64 + 0.50)/2] = 1.0$ MPa-ms
$\bar{t}_{fr} = 2\bar{i}_r/\bar{P}_r = 1.3$ ms

Gas pressure and impulse
$V_f = 2(3.1) \times 2(3.8) \times 3.1 = 146.1$ m^3
$W/V_f = 4.5/146.1 = 0.031$ kg/m^3
$A = 0.90 \times 2.2 = 1.98$ m^2 (open doorway is the total vent area)
$A/V_f^{2/3} = 1.98/27.74 = 0.071$

From Fig. 1.8 (with $W/V_f = 0.031$ kg/m^3)
$P_g = 0.17$ MPa
$A/V_f^{2/3}$ is greater than 0.022, so P_g will be a conservative estimate from Fig. 1.8.

From Fig. 1.9 (with $A/V_f^{2/3} = 0.071$)
$i_g/W^{1/3} = 14.0$ MPa-ms/kg$^{1/3}$ $\quad i_g = 14.0(1.65) = 23.1$ MPa-ms
$t_{fg} = 2i_g/P_g = 272$ ms

Summary
The following six blast quantities can be used to construct the shock/gas bilinear pressure–time pulse, as shown in Fig. 1.10b.
$P_r = \bar{P}_r = 1.6$ MPa ***Ans.***
$i_r = \bar{i}_r = 1.0$ MPa-ms ***Ans.***
$t_{fr} = \bar{t}_{fr} = 1.3$ ms ***Ans.***
$P_g = 0.17$ MPa ***Ans.***

© Woodhead Publishing Limited, 2010

i_g = 23.1 MPa-ms ***Ans.***
t_{fg} = 272 ms ***Ans.***

The wall strip is 3.1 m wide, centered relative to a normal from the wall through the center of the explosive charge. The bilinear pressure pulse is applied uniformly to the 3.1 m × 3.1 m wall area. The gas pressure duration, approximately 0.3 s, indicates that the gas pressure can be assumed to be applied quasi-statically for most conventional wall systems.

1.11 Additional resources

The intent of this section is to make the designer aware of additional resources that can assist in the design/retrofit of a protective structure or a structural component.

1.11.1 Technical documents

A wealth of additional material is available to the interested designer. A partial list of documents addressing blast-induced loads and the design of protective structures is provided below.

- *Structures to Resist the Effects of Accidental Explosions*, UFC 3-340-02, US Department of the Army, 2008 (supersedes Army TM 5-1300, US Department of the Army, 1990).
- *A Manual for the Prediction of Blast and Fragment Loadings on Structures*, DOE/TIC-11268, US Department of Energy, 1992.
- *Protective Construction Design Manual*, ESL-TR-87-57, Air Force Engineering and Services Center, 1989.
- *Fundamentals of Protective Design for Conventional Weapons*, Army TM 5-855-1, US Department of the Army, 1986.
- *Design of Structures to Resist Nuclear Weapons Effects*, ASCE Manual No. 42, 1985.
- *Structural Design for Physical Security: State of the Practice*, ASCE, 1999.
- *Design of Blast-Resistant Buildings in Petrochemical Facilities*, ASCE, 1997.
- *Blast Effects on Buildings*, Mays and Smith (eds), 1995.
- *Protecting Buildings from Bomb Damage*, NRC, 1995.

1.11.2 Analytical methods for blast load computation and structural response

Blast loads can be predicted using semi-empirical or first-principle computer programs. When the blast domain has rigid boundaries that are not too complex (i.e., a rectangular or L-shaped room with vents or relatively simple street configurations as studied in Smith *et al.*, 2001), semi-empirical

© Woodhead Publishing Limited, 2010

ray tracing algorithms, such as BLAST-X, can be employed to predict blast pressures (shock and gas) with reasonable accuracy for design. However, as the blast domain becomes more complex (i.e., involving close-in explosions, a complex arrangement of reflecting surfaces, or the presence of frangible elements) or more detailed or accurate analyses are necessary, first-principle blast load simulations become necessary.

Hydrocodes or shock physics programs use first-principle physics and generally fall under the heading of computational fluid dynamics (CFD). Shock physics codes simulate shock physics phenomena by implementing a numerical algorithm, such as finite differences, to apply the conservation of mass, momentum, and energy within the system being modeled. Equations of state (EOSs), which relate the pressure–density–energy states of a material, are required for each material in the simulation. If explosives are involved, a burn model (representing the explosive's release of energy), the unreacted density of the explosive, and the two Chapman Jouguet (CJ) state parameters are also needed. These programs have a steep learning curve, require significant experience to produce consistently reliable results, and are very expensive to run (run times can take hours to days using high-performance computing systems). Until a high degree of confidence has been achieved with a particular program, results should be verified with blast tests or data from reputable sources.

First-principle structural response modeling falls under the heading of computational solid mechanics (CSM). The most common technique in CSM is the finite element method (FEM). General structures of various complexity can be modeled, considering non-linear material properties including failure definitions, large displacements/strains, and dynamic effects. When blast loads interact with flexible or frangible structural elements, a 'coupled analysis' should be performed. In theory, this type of analysis allows the analyst to predict more representative blast loads and structural responses by coupling the movement of reflecting surfaces relative to the incident and reflecting blast waves. Typically if the flexibility or frangibility of a reflecting surface is ignored, blast pressures will be over-predicted on that surface. A coupled analysis can reduce this conservatism. Table 1.3 gives a listing of computer programs for blast load prediction and structural response simulation. Abstracts from the corporate authors for many of the programs given in Table 1.3 are provided in NRC (1995).

1.11.3 Blast testing

General considerations

Using the curves presented in Section 1.9.3, blast loads on stand-alone, rigid, box-like structures for unconfined explosions can be computed with reasonable confidence. Experienced blast professionals using conventional materi-

© Woodhead Publishing Limited, 2010

Table 1.3 Representative computer programs for blast load prediction and structural response simulation

Program name	Purpose	Type	Corporate author
BLAST-X	Blast load prediction	Semi-empirical	Science Applications International Corporation (SAIC)
CONWEP	Blast load prediction	Semi-empirical	US Army Waterways Experiment Station
CTH	Blast load prediction	First-principle	Sandia National Laboratories
FEFLO	Blast load prediction	First-principle	SAIC
FOIL	Blast load prediction	First-principle	Applied Research Associates, Waterways Experiment Station
HULL	Blast load prediction	First-principle	Orlando Technology, Inc.
SHARC	Blast load prediction	First-principle	Applied Research Associates, Inc.
DYNA3D	Structural response	First-principle	Lawrence Livermore National Laboratory (LLNL)
EPSA-II	Structural response	First-principle	Weidlinger Associates, Inc.
FLEX	Structural response	First-principle	Weidlinger Associates, Inc.
ABAQUS®	Coupled analysis	First-principle	ABAQUS, Inc.
ALEGRA	Coupled analysis	First-principle	Sandia National Laboratories
ALE3D	Coupled analysis	First-principle	LLNL
AUTO-DYN®	Coupled analysis	First-principle	Century Dynamics
DYNA3D/ FEFLO	Coupled analysis	First-principle	LLNL/SAIC
FUSE	Coupled analysis	First-principle	Weidlinger Associates, Inc.
LS-DYNA®	Coupled analysis	First-principle	LLNL
MAZe	Coupled analysis	First-principle	TRT Corporation

Source: adapted from NRC (1995).

als can likewise be confident in performing relatively 'routine' structural designs to effectively resist blast loads. However, for complex blast environments subjected to unconfined explosions (i.e., an urban setting) or for structures/cells subjected to confined explosions, full-scale or model blast testing may be necessary. While blast testing tends to be quite expensive, it is necessary for validation and calibration of CFD and CSM computer programs, to provide confidence in simplified design procedures (blast load estimates and structural design), and ultimately to assess the performance of a specific structure to a particular blast threat. CFD and CSM programs can fill in the gaps of data obtained from blast testing once the analyst has confidence in the particular programs and their proper usage.

© Woodhead Publishing Limited, 2010

The three primary configurations for blast testing are: open-arena, shock tube, and blast chamber (or blast containment structure). As its name suggests, an *open-arena* is a vast expanse of flat land where blast tests can be performed, unobstructed by surrounding reflecting surfaces other than the ground. Open-arena tests are obviously preferable when measuring blast loads applied to solitary structures or responses of full-scale or model solitary structures. Rigid masses representing a built-up environment around the model test structure could be included if this is the anticipated environment around the prototype. This detailed level of testing would add to the expense.

A *shock tube* is a tubular chamber that focuses blast pressures on specimens attached to supports in the test zone. The pressures are generated at the other end of the tube by a compressed air/diaphragm system or simply by detonation of a HE charge. This type of testing is best suited for testing structural panels, typically when a detailed study of the blast pressure field is not the primary focus. A disadvantage of this type of testing is that clearing effects are not represented, especially if the specimen occupies the entire opening in the test zone; if not accounted for, the effect is more intense, more uniform blast pressures being applied to the specimen than desired. While more limiting, shock tube testing is typically less expensive than open-arena testing.

A *blast chamber* is a hardened room within which blast tests are conducted. There are some obvious limitations to charge size and test configurations if unconfined explosions are to be investigated. Reflections off of the chamber's walls could at best complicate or, worse, corrupt experimental results. However, this type of facility is ideal for testing the performance of containment cells.

Measurements from blast testing

Measurements of key quantities are required when conducting a blast testing program to investigate or verify blast loads and structural response and performance. There are many challenges in obtaining good data from blast testing; discussing them is beyond the scope of this chapter. However, the quantities that are commonly measured and some traditional measurement devices are highlighted for blast loading and structural response/performance.

Measurements of blast loads

- **Incident (side-on) pressures** – pressure pencils (piezo-electric, optical).
- **Reflected pressures** – flush-mount pressure transducers (piezo-electric, optical).

© Woodhead Publishing Limited, 2010

- **View/measure shock front shape and propagation** – high-speed video, laser imaging.
- **Temperature rise** – pyrometry gages, heat flux gages, thermocouples, laser imaging.

Measurements of structural response/performance

- **Dynamic displacements** – linear variable differential transformers (LVDTs) laser- or fiber optic-based imaging, high-speed video.
- **Peak dynamic displacements** – same as above, scratch tubes.
- **Permanent set** – post-test length/rotation measurements.
- **Shock (accelerations)** – shock transducers (piezo-electric).
- **Dynamic support reactions** – dynamic load cells (piezo-electric).
- **Strain** – strain gages (electrical resistance, piezo-electric).
- **Secondary fragmentation** – measurement of weight and number of fragments in various regions relative to the test specimen.
- **Structural performance** – all of the above supplemented with thorough visual and photographic evaluations (pre- and post-test comparisons).

1.11.4 Consulting a blast professional

Determining credible threats, computing blast-induced loads and determining critical design loads, and designing structures to resist these loads are challenging tasks, especially if they are to be performed economically. Further, if *detailed* blast load computations are necessary, one must be versed in the fields of thermochemistry, thermodynamics, and hydrodynamics. The design of general structures to resist blast-induced loads requires an intimate knowledge of structural materials (constitutive laws), nonlinear structural dynamics, and the performance of structural elements, connections, and systems. Under certain circumstances, physical testing to obtain or verify blast-induced loading, structural response, or structural performance will be needed for reliable designs. A reputable blast consultant will be expert in a number of these areas and will have reliable contacts in the others. Traditional structural (civil) and mechanical engineers tasked to design a protective structure should consider consulting with a reputable blast professional until they have acquired the appropriate expertise and the accumulated years of experience required to produce responsible designs.

1.12 References

AIR FORCE ENGINEERING and SERVICES CENTER (1989), *Protective Construction Design Manual*, ESL-TR-87-57, Tyndall Air Force Base, FL.

© Woodhead Publishing Limited, 2010

AMC, ARMY MATERIEL COMMAND (1972), *Engineering Design Handbook: Principles of Explosive Behavior*, National Technical Information Service, Springfield, VA, U.S. Department of Commerce.

ASCE (1999), *Structural Design for Physical Security: State of the Practice*, Reston, VA.

ASCE (1997), *Design of Blast-resistant Buildings in Petrochemical Facilities*, Reston, VA.

ASCE (1985), *Design of Structures to Resist Nuclear Weapons Effects*, ASCE Manual No. 42, Reston, VA.

COOPER P W (1996), *Explosives Engineering*, New York, NY, Wiley-VCH, Inc.

FLEISHER H J (1996), Design and explosive testing of a blast resistant luggage container, in Jones N, Watson A G and Brebbia C A (eds), *Structures Under Shock and Impact IV*, Southhampton, UK, WIT Press, 51–59.

KAMBOUCHEV N, NOELS L and RADONITZKY R (2007a), Fluid–structure interaction in the dynamic response of free-standing plates to uniform shock loading, *Journal of Applied Mechanics*, **74**, 1042–1045.

KAMBOUCHEV N, LUDONIC N and RADOVITZKY R (2007b), Numerical simulation of the fluid-structure interaction between air blast waves and free-standing plates, *Computers and Structures*, **85**, 923–931.

KINGERY C N and BULMASH G (1984), *Airblast parameters from TNT spherical air burst and hemispherical surface burst*, Technical Report ARBRL-TR-02555, US Army ARDC-BRL, Aberdeen Proving Ground, MD.

LEE E L, HORNIG H C and KURY J W (1968), *Adiabatic expansion of high explosive detonation products*, Report No. UCRL-50422, Livermore, CA, Lawrence Livermore National Laboratory.

MADER C L (1998), *Numerical Modelling of Explosives and Propellants, 2nd edn*, Boca Raton, FL, CRC Press.

MARCONI F (1994), Investigation of the interaction of a blast wave with an internal structure, *AIAA Journal*, **32**(8), 1561–1567.

MAYS G C and SMITH P D (eds) (1995), *Blast Effects on Buildings*, London, UK, Thomas Telford.

MOLKOV V V (1999), Explosions in buildings: modeling and interpretation of real accidents, *Fire Safety Journal*, **33**(1), 45–56.

NRC (NATIONAL RESEARCH COUNCIL) (1995), *Protecting Buildings from Bomb Damage*, Washington, DC, National Academy Press.

SMITH P D, WHALEN G P, FENG, L J and ROSE T A (2001), Blast loading on buildings from explosions in city streets, *Proceedings of the Institution of Civil Engineers: Structures and Buildings*, **146**(1), 47–55.

US DEPARTMENT OF THE ARMY (1986), *Fundamentals of Protective Design for Conventional Weapons*, Army TM 5-855-1, Washington, DC.

US DEPARTMENT OF THE ARMY (1990), *Structures to Resist the Effects of Accidental Explosions*, Army TM 5-1300, Washington, DC.

US DEPARTMENT OF THE ARMY (2008), *Structures to Resist the Effects of Accidental Explosions*, UFC 3-340-02, Washington, DC.

US DEPARTMENT OF ENERGY (1992), *A Manual for the Prediction of Blast and Fragment Loadings on Structures*, DOE/TIC-11268, Washington, DC.

WEINSTEIN E M (2000), Design and test of a blast resistant luggage container, in Brebbia C A and Jones N (eds), *Structures Under Shock and Impact VI*, Southampton, UK, WIT Press, 67–75.

© Woodhead Publishing Limited, 2010

ZAPATA B J and WEGGEL D C (2008), Computational airblast modelling of commercial explosives, in Jones N and Brebbia C A (eds), *Structures Under Shock and Impact X*, Southampton, UK, WIT Press, 45–54.

© Woodhead Publishing Limited, 2010

2

Standards and specifications for composite blast protection materials

M. CHALK, Solent Composite Systems Ltd, UK

Abstract: This chapter considers current blast performance standards and how they are interpreted for the use of protection systems produced using composite materials and products. The development of industry standards is discussed and how these are interpreted to encourage the use of composite technology to provide appropriate blast protection. Examples are considered across several industry sectors and comments made about the effectiveness of resulting standards with regard to the use of composites. Conclusions are drawn about the future development of standards and specifications that would encourage the implementation of composite solutions to solve explosion and blast protection problems.

Key words: standards and specifications, blast and explosion protection, composite, certification, performance engineering.

2.1 Introduction

This chapter provides a comprehensive summary of current test, engineering and performance standards related to explosions and blast events and explains how these standards are interpreted for the use of composite materials and products. It should be pointed out that blast protection standards and specifications vary between industries, countries and amongst different product types and that, although there is a wealth of experimental test and engineering data for the use of composite products in blast scenarios, this has resulted in very little in the way of standards specifically directed towards composite products. This chapter considers the many different blast standards and their common technical themes and how these may be applied to those industries that are adopting composite products to deliver blast protection for their personnel, infrastructure and equipment.

2.2 Why do we want standards?

The definition of a standard is an authorised measure or an established and accepted level of achievement and a specification is identified as a requirement or detailed summary of requirements. In this chapter, we will mainly consider standards because they describe the achievement level rather than a specification which serves to detail the measurable elements of such a standard.

© Woodhead Publishing Limited, 2010

Historically, standards have been derived in response to an event or scenario that has required some level of control that has hitherto been unavailable. Quite often standards are driven by social needs or political imperatives and they serve to apply a measure or to set an acceptable level of achievement that should be maintained in the future.

For blast performance, many of the standards were derived following catastrophic events and have sought to qualify and quantify the extent and effect of an explosion event and put forward some targets for any protection system to meet. Well known examples of the catastrophic events affecting different industries include the Lockerbie bombing of Pan Am flight 103 in 1988 (aircraft), the Piper Alpha platform disaster in 1988 (oil and gas) and a vast number of worldwide terrorist bombings that have affected the design and construction of many of our public buildings including government buildings, railway stations and airports. All of these tragic events have resulted in their respective industries conducting a thorough investigation of what took place in an effort to understand the key failure mechanisms so that corrective action can be taken in the future. It is this corrective action that many standards seek to address so that an achievement level is set and it is clearly understood when it has been met.

2.3 Who is responsible for applying standards?

In general, the ultimate responsibility for adherence to blast protection standards lies with the relevant government authority and the individual industry governing bodies, but the daily application of standards is carried out by the engineers and designers that are responsible for our vehicles, buildings, platforms and industrial plants. It is important that there is a traceable path from legislation via industry requirements through to product certification and testing that can demonstrate compliance of particular designs and products. Within this chain, it is common to find an independent authority with detailed knowledge and understanding of the performance requirements and the experience to assess whether a product will satisfy the needs of an industry. Within the oil and gas industry, this would include Lloyd's Register of Shipping, Det Norske Veritas (DNV) or Bureau Veritas. The construction industry would rely upon the appropriate national agencies responsible for building approvals and the aerospace industry would be governed by the FAA or CAA.

2.4 How should we interpret standards?

With regard to blast protection, there are many standards that apply to different products within a variety of industries. There are many examples for the use of glass and window products that were developed following

© Woodhead Publishing Limited, 2010

terrorist attacks such as the bombing in 1995 of the A.P. Murrah Federal Building in Oklahoma City, for which the following standards are relevant:

- ISO 16933:2007, Glass in Building – Explosion Resistant Security Glazing – Test and Classification for Arena Air-Blast Loading
- GSA-TS01-2003, US General Services Administration, Standard Test Method for Glazing and Window Systems Subject to Dynamic Overpressure Loadings
- GSA C/ISO EXV 25 and GSA C/ISO EXV 45
- ASTM International, F 1642-04, Standard Test Method for Glazing and Glazing Systems Subject to Airblast Loadings
- BS EN 13124 – 1:2001, Windows, doors, and shutters – Explosion Resistance – Test Method – Part 1 : Shock Tube
- BS EN 13123 – 2:2004, Windows, doors, and shutters – Explosion Resistance – Requirements and Classification – Part 2 : Range Test
- ISO 16935:2007, Glass in Building – Bullet-Resistant Security Glazing – Test and Classification
- German Standard DIN 52290 – blast resistant glazing using shock tube testing
- Navy Standard MIL-HDBK-1013, 'Evaluation and Selection Analysis of Security Glazing for Protection Against Ballistic, Bomb and Forced Entry'

This represents just a small sample of the standards in use today for this single product type and demonstrates that there is a wide range of possible requirements for blast performance of a product depending upon which standard is selected. However, they are all written around the common themes of blast loading and focus upon particular test methods to demonstrate compliance with the standard. The objective of the international standards for blast testing of glazing products is to have a repeatable and realistic set of tests appropriate for commercial use for a wide range of materials based upon an achievable set of criteria (Stephens, 2005). It is this approach that should be addressed for any standards developed for blast protection using composite technology and products.

There are other standards related to protection against high explosives which include military standards such as:

- Army Standard TM 5-853-3, 'Security Engineering Final Design'
- Department of Defense (DoD), 'Department of Defense Antiterrorism Construction Standards'
- Department of Defense (DoD), 'Unified Facilities Criteria (UFC) – DoD Minimum Antiterrorism Standards for Buildings'

© Woodhead Publishing Limited, 2010

There are also those standards that are issued to address the performance of specific products in the event of an explosion, which include the following:

- Determination of the Explosion Resistance of Litter and Recycling Bins – Test Method, HOSDB Publication No. 70 / 06, Version 1.1, August 2007
- ASTM E2639-09 Standard Test Method for Blast Resistance of Trash Receptacles
- ASTM F2247 Standard Test Method for Metal Doors Used in Blast Resistant Applications (Equivalent Static Load Method)
- WK1902 New Guide for Standard Test Method for Blast-Resistant Doors
- CWCT (1996) 'Standard and Guide to Good Practice for Curtain Walling' CWCT
- ISO 6517 Standard for Hardened Unit Loading Devices (HULDs) in Aircraft

In many ways, these and other industry standards attempt to qualify and quantify the effects of an explosion event whether caused by a flammable vapour cloud, a quantity of high explosive or by other events such as detonation of a dust cloud. The nature of such explosions is covered in other chapters within this book but the common features of impulse characteristics, pressure build up and release are addressed within the standards listed herein.

The individual standards aim to address the response of specific product types to the explosion events or to ensure that products satisfy the needs of specific industries. Many of these standards adopt an approach that attempts to relate specific small-scale explosion events that can be realistically and cost-effectively tested to those disastrous larger-scale events that have initiated the development of the standard in the first instance.

Examples of this approach to develop what can be described as an 'equivalence' include the Arena Satchel-Bomb Tests for the standard DIS 16933 where different charge sizes and separation distances are used to develop classification codes that can be used to compare product performance. A similar approach is written into ASTM F2247 for metallic blast resistant doors, and this allows the use of static load tests to assess the blast performance of metal doors, frames and restraining hardware (latches and hinges). However, the standard makes clear that this method requires knowledge of the principles of pressure, deflection and strain gauge measurement (ASTM, 2003). This conflicts with other recommendations that confirm that a simple conversion to uniform static pressure cannot be made because of the dynamic nature of the blast load case.

© Woodhead Publishing Limited, 2010

At the opposite end of the scale is the standard for Hardened Unit Loading Devices (HULDs), which are used to store luggage within the cargo hold of an aircraft. This standard states that even one blast test is not credible because it does not rigorously test the HULD. It is not surprising therefore that the deployment of HULDs in aircraft has not progressed to full-scale adoption because the costs of compliance with the standard are very high and there are barriers to their use related to the weight of the HULD that the standard does not seem to address (National Academy of Sciences, 1999).

2.5 What is relevant for standards for composite blast protection products?

The relevant parts of a standard for composite blast protection must seek to specify a performance requirement for the blast overpressure, the time to achieve that overpressure and the extent of any negative pressure or suction that occurs immediately following the blast wave. It is common also to state the magnitude or force of any drag loads that may occur as a result of the pressure wave causing a structure to be pushed in a particular direction. This has a large effect on the structural response of a protection system and the way it is connected to any neighbouring structure or anchor points. These details are commonly addressed within a standard and should be considered for any composite product as these are potentially the weak points in any protection structure.

The blast protection standard should also address those features that are specific to a blast event such as any ballistic impact or requirements for protection from fragments that may result from the explosion. The geometry effects of the protection structure and the blast wave should be considered since their interaction may have a significant effect on the nature and size of the loads. Finally, the standard should address any elements related to survivability and consider what may be acceptable levels of damage to the protection structure itself after an explosion has occurred, such as those outlined for protective glass (Johnson, 2004).

Other parts of any standard for composite products for blast protection should address any issues that are common to all composite products such as flammability, smoke and toxicity in the event of a fire, any weight constraints, residual strength following an explosion and/or fire, design lifetime during which the blast protection product is expected to meet the protection requirements and any waste disposal requirements to satisfy environmental standards related to 'End of Life' regulations.

At present, composite products are required to meet the current engineering standards for blast performance, which are written with steel or

© Woodhead Publishing Limited, 2010

concrete structures in mind. It is therefore quite common for suppliers of composite blast protection products to select those criteria within a standard that are relevant to their product and to ignore those that do not apply. This means that those products run the risk of being unacceptable to certain customers or industries because they cannot demonstrate full compliance with a standard that is aimed at products manufactured from more traditional engineering materials. For example, certain standards applied to shipping and vessels by the International Maritime Organisation (IMO) call for the use of non-combustible materials because the standard is written around metallic structures with ceramic insulation. Since composite products are combustible, they do not technically comply with this requirement.

From the author's experience of supplying blast protection products to protect against flammable gas cloud deflagrations and detonations on oil and gas installations, it is clear that a more pragmatic approach has emerged based upon protection against threats that have to be determined by the end user. This has resulted from recommendations made as a result of the Cullen enquiry into the Piper Alpha platform disaster (Cullen, 1990). In this case the recommendation is to move away from a single standard that hopes to address the needs of the industry to the use of a risk-based approach. In essence, each platform or onshore installation must be evaluated to qualify the risk areas that could cause an explosion or fire and to quantify these risks by assigning a value to the blast overpressure or drag load effect. This can vary for locations on an installation depending upon congestion and the potential amount of gas that could cause the explosion, and values typically range from 0.1 barg through to 1.5 barg overpressure with associated drag and suction loads.

It is therefore incumbent upon the designer or manufacturer of any composite protection system to carry out testing to demonstrate that their product will resist blast overpressures within the likely range of overpressures associated with a particular industry. Such testing is carried out by an independent test facility and is witnessed by a representative from a certifying authority. This ensures that the composite protection system is independently verified and has formal certification for blast performance.

For example, this approach and the resultant use of composite products to protect an LNG plant in the Arctic Circle in Norway against a wide range of explosion loads has been achieved by demonstrating compliance with national Norwegian oil industry (NORSOK) standards (Chalk, 2006).

It is also essential with this approach to gather load and strain data from the testing that can be used to validate composite engineering models. These engineering models are used to calculate the laminate and ply stacks required in order to satisfy a particular blast overpressure and span requirement. These calculations form part of the final product certification and are

© Woodhead Publishing Limited, 2010

used to verify the product performance without the need for repeated testing.

This approach allows the industry to assess and specify the risks for a particular oil and gas installation and encourages the supplier of composite systems to engineer their products to protect against damage arising from these risks. This avoids a 'one size fits all' approach and results in cost-effective products that are engineered to meet the risks identified by the owner of the installation. This encourages assessment of alternative strategies to address explosion risks; for example, if equipment can be installed in a larger space this reduces congestion and the resultant blast overpressure. Thus the owner of the installation can decide whether the cost of reducing congestion offers benefits by reducing performance loads and the resulting costs of any composite protection system.

The other benefit of this approach is that it promotes the use of alternative engineering solutions allowing composite products to compete directly with more traditional steel or concrete systems since they are assessed on their ability to satisfy the blast performance without constraints imposed by other criteria. In this manner, the oil and gas industry, which has relied upon the engineering of steel and concrete to construct its installations, has adopted the use of composite products to address blast protection needs. This drive to use composite products has also been assisted by the other benefits of light weight and long life, which offers advantages for platforms designed to support a limited weight and to remain in service with the minimum of maintenance for more than 30 years. Without the recommendations of the Cullen report, it is likely that the industry would still be installing heavy metallic or concrete products to meet a single explosion load criterion derived from standards borrowed from other industries. By adopting an approach that is guided by customer specifications rather than ruled by standards, the industry has been able to benefit from the use of composite protection systems. This places the onus on the engineers to understand the nature of the risks and develop a flexible engineering methodology that can deliver protection systems which are adapted to meet those risks. It is this approach that should be adopted more widely across other industries that require blast protection in order to benefit from the advantages of composite materials.

2.6 When will composite blast protection standards be used?

At the outset of a construction project that requires blast protection, the appropriate performance standards must be considered and agreed with all parties who have a 'duty of care' for a structure, such as the owners, personnel operating the completed project, engineers, designers, manufacturers

© Woodhead Publishing Limited, 2010

and construction contractors. The standards shall be clearly stated within the statement of requirements for a project and responsibility must be clearly delegated through the project organisation for meeting the standards. In practice, this generally relies upon the supplier of the composite product to demonstrate that the product will satisfy the blast performance requirements of an appropriate industry standard. It is also imperative if the supplier wishes to demonstrate performance by reference to a specific part of a standard that it is agreed with the project group that this is adequate to ensure the use of the product. This is particularly important where it is not possible or cost-effective to demonstrate full compliance to a particular standard.

2.7 Where can standards be applied for the use of composites?

The use of standards in blast protection is widespread albeit focussed on engineering materials other than composites. If the composites industry can develop standards demonstrating that their products deliver satisfactory performance against a range of explosion events then this would encourage industries to adopt the products. If this blast performance of composite technology could be governed by particular composite industry standards, a wider understanding of the benefits of composite products would be gained, allowing engineers familiar only with more traditional engineering materials to specify composite products for use in cladding of our buildings, protecting and supporting structural elements of ageing infrastructure that may be prone to explosion or as protection systems in their own right.

2.8 The future for standards and specifications for composite blast protection

As demonstrated in the earlier discussion, there are many standards for blast protection addressing the needs of particular industries, explosion scenarios or product types. However, many of these are not focussed on composite products. One option is to have specific standards that address blast requirements for composite products, but the present reality is that engineers must demonstrate by testing the performance of their products to protect against specific blast scenarios. This results in a clear understanding of the response of composite products to blast events that can contribute to a database for engineering future products.

One key issue is that the cost of demonstrating compliance with a standard by testing remains high and represents a barrier to the wider adoption of composite products and technology across a range of industries. Much

© Woodhead Publishing Limited, 2010

of the test data and information that does exist remains proprietary to individual companies that, having invested heavily to secure the data, are reluctant to share their knowledge across industries that could benefit from a clearer understanding of the advantages of composite materials to protect against blast scenarios. The composites industry and appropriate industry bodies can address this by conducting joint industry projects focussed on developing standards for the use of composite products to meet blast performance requirements, such as that for blast resistant cladding run by the Construction Industry Research and Information Association (CIRIA) and funded by the UK government department responsible for trade and industry (Alderson *et al.*, 1997).

By their nature, such initiatives must involve representatives from the entire supply chain to ensure that all the needs are understood and addressed. An appropriate approval or certifying authority must be involved as these organisations are largely responsible for preparing or accepting the standards that result from the work of the joint industry project.

2.9 Conclusion

At this time, there are a limited number of specific standards for composite products that protect against explosion or blast events. Those that exist are for specific applications where a composite product has been demonstrated to have clear performance advantages over metallic or concrete engineering solutions. In cases such as the use of composite litter bins, the standards have been initiated by government bodies (HOSDB, 2008) or standards agencies (ASTM, 2009) and were prepared to regulate the use of these innovative composite products. The oil and gas industry adopts a risk-based approach that encourages the use of composite blast protection products by compliance with performance specifications demonstrated by independently verified testing. This is an encouraging model for composite products and materials based upon the flexible interpretation of existing industry standards to accommodate new technologies and solutions.

Other industries take a more rigorous approach, insisting upon compliance to specific standards that may restrict the use of composite products because the standards were written before composite materials were demonstrated to offer a credible engineering alternative to steel and concrete.

In future, standards and specifications will be developed as individual industries embrace the opportunity to use the properties of composite materials to protect against explosions and blasts. However, it is not certain whether this will result in unique standards related to specific composite blast protection or the revision of existing standards to include composite products alongside established engineering alternatives.

© Woodhead Publishing Limited, 2010

2.10 Sources of further information and advice

- ISO standards can be purchased and downloaded in Europe at http://www.iso.org and in USA at http://webstore.ansi.org
- ASTM standards can be purchased and downloaded at: http://www.astm.org
- GSA standards can be downloaded free at: http://www.protectiveglazing.org
- BS EN standards can be purchased and downloaded at: http://www.bsiglobal.com

2.11 References

ALDERSON A S, AL-IZZI M S and WONG A F L (1997), Blast resistant GFRP cladding panels, *ICBEST, 97*, 15–17 April, Bath, UK, available at: http://www.bath.ac.uk/cwct/cladding_org/icbest97/paper13.pdf (last accessed October 2009).

ASTM (2003), *ASTM F2247-03 Standard Test Method for Metal Doors Used in Blast Resistant Applications (Equivalent Static Load Method)*, West Conshohocken, PA, http://www.astm.org.

ASTM (2009), *ASTM E2639-09 Standard Test Method for Blast Resistance of Trash Receptacles*, West Conshohocken, PA, http://www.astm.org.

CHALK M (2006), Fire and blast protection of critical safety equipment at Hammenfest, *Scandinavian Oil-Gas Magazine*, **34**(9), 12–14.

CULLEN W D LORD (1990), *The Public Inquiry into the Piper Alpha Disaster*, HM Stationery Office, London, UK.

HOSDB (2008), *The Selection, Positioning and Testing of Blast Resistant Litter Bins*, Guidance note 12/08, 2nd edn, Home Office Scientific Development Branch, Horsham, UK.

JOHNSON N F (2004), 'International Standards for Blast Resistant Glazing', ASTM International 19, Paper ID JAI 12892, http://www.astm.org.

NATIONAL ACADEMY OF SCIENCES (1999), *Assessment of Technologies Deployed to Improve Aviation Security: First Report*, National Academies Press, Washington, DC, available at: http://www.nap.edu/catalog/9726.html (last accessed October 2009).

STEPHENS R A C (2005), 'International Standard for Arena Testing of Blast Resistant Glazing', Glass Processing Days 2005.

© Woodhead Publishing Limited, 2010

3

Processing polymer matrix composites for blast protection

H. TAN and K. M. PILLAI, University of Wisconsin–Milwaukee, USA

Abstract: This chapter discusses the use of polymer composites for blast protection applications. The background of polymer composites is introduced together with the manufacturing processes. Of the many possible technologies available to fabricate blast resistance polymer composites, the liquid composites molding (LCM) processes are discussed in the greatest detail. The chapter then reviews the modeling of LCM in terms of the flow physics of resin flow in porous media, the corresponding heat and mass transfer issues, and modeling the resin cure. Since the permeability of fiber preforms is a very important parameter needed for simulating mold-filling in LCM, the permeability measurement is reviewed in detail as well.

Key words: polymer composites, liquid composite molding (LCM), dual-scale porous media, permeability measurement.

3.1 Introduction

Fiber-reinforced plastics (FRP) are composite materials made of polymer resins as matrix, and glass or carbon fibers as reinforcement. Due to their light weight, high strength, good corrosion resistance, and flexibility in design, FRP composites have now been widely used in automobile, aerospace, civil construction, shipbuilding, and military industries. The demand for advanced composite materials in past decades has been promoting the development of polymer composites.

As terrorist attacks have increased around the globe in recent years, blast protection products are beginning to be seen as having a rapidly growing market due to an increase in public safety concerns. The high strength to weight ratio obtainable from FRP composites makes them a good candidate for applications requiring blast protection, such as military vehicles, buildings and structures, and body armors [1–3]. A good example of polymer composites used for blast protection is FRP composites employed to retrofit or strengthen existing civil structures to improve their blast resistance [3].

Depending on the specific application of FRP composites for blast protection, different processes have been developed. Hand layup is the most

© Woodhead Publishing Limited, 2010

common means of retrofitting reinforced concrete structures to enhance their resistance to blast; the carbon fiber sheets are usually bonded to the external surface of the structures with polymeric resin in a layer-by-layer fashion by hand. The *in-situ* resin-infusion method has also been applied for retrofitting structures and is capable of achieving uniformity and good fabric compaction in contrast to the hand layup process. In the armor applications, FRP composites used for personal and vehicle protection are often manufactured by the automated processes including pultrusion, liquid composite molding (LCM), compression molding, and automatic fiber placement, where high-performance fibers such as aramid and carbon fibers are often used.

FRP composites are generally composed of two distinct phases: fibers and polymer resins. Fibers are the reinforcing phase bearing the structural loads and enhancing the stiffness of the composites. They are usually spun from a solution or a melt which orients the molecules of the materials. Typical fibers used in polymer composites are glass fibers, carbon (graphite) fibers, and aramids. The choice of type of fibers used in a particular application depends mainly on cost and performance. Generally, glass fibers are the cheapest, carbon fibers are the stiffest, while aramid fibers are the toughest. Readers interested in the details on properties of various fibers can refer to [4, 5].

Fibers used in FRP composites can be generally categorized into continuous (long) and discontinuous (short) fibers. Composites containing continuous fibers with high-performance resin are often called advanced composites, whereas composites containing discontinuous fibers are called engineering composites [4]. Continuous fibers are usually in the form of rovings, yarns, strands, or tows, each of which consists of thousands of filaments of diameters ranging from 5 to 20 micromenters, thus allowing them to be produced using textile machines. The yarns or tows are stitched, woven, braided, or knitted into one-, two-, or three-dimensional (1D, 2D, 3D) fabrics to create a textile preform. These fabrics are usually in the form of flat sheets (often called mats) that are rolled up for transport to the composites manufacturing sites. The fibrous preforms make skeletons of the FRP composites, which not only provide a mechanism for structural toughening of composites, but also facilitate the processing of composites into net or near-net shape structural parts. A 2D fabric consists of planar interlaced and interloped tows where the interlaminar strength is limited by the polymer matrix strength due to the lack of through-thickness fiber reinforcement, while the tows of a 3D fibrous preform are oriented in various in-plane and out-of-plane directions, providing additional reinforcement in the through-thickness direction. Two Dimensional fabrics are usually formed into shapes by molding or stitching, while 3D preforms are more suitable for creating net structural shapes. The architecture of fibrous preforms plays a

© Woodhead Publishing Limited, 2010

key role in composite manufacturing by facilitating processing steps including forming and resin infiltration. More details on textile preforms used for FRP composites can be found in Chapter 5 of [6].

Polymer resins in FRP composites are used primarily to bind the fibrous reinforcements together and hence allow the load to be transferred to the reinforcing fibers. The polymeric matrix protects the fibers from abrasion as well as environmental corrosion. Generally, polymer resins can be divided into two groups: thermoplastics and thermosets [4]. The major difference between thermoplastics and thermosets is that processing thermosetting composites involves a chemical reaction for cross-linking the polymer chains (called the curing reaction), whereas there is no chemical reaction for processing thermoplastics. The cross-links between the molecular chains of thermosets generate molecular structures in the form of 3D networks as opposed to the lack of such a molecular structure for thermoplastics. Unlike thermoplastics, the presence of cross-links in thermosetting resins improves stiffness, creep resistance, and thermal and dimensional stabilities; therefore most FRP composites use thermosetting resins. The cross-linking reaction of thermosets is irreversible, which means that once cured, the thermosets can no longer be remelted or reformed. However, the thermoplastics are capable of repeated reshaping and reforming due to the absence of cross-links in the molecular structure. Therefore, thermosets are not recyclable (except when used as fillers), unlike thermoplastics which are recyclable and hence environmentally-friendly.

Since the viscosity of thermoplastics in liquid state during processing is usually several orders of magnitude higher than that of thermosets, the processing conditions for thermoplastic composites are usually more challenging – often involving higher temperature and pressure. Therefore, the tooling system for manufacturing thermosetting composites is usually much cheaper than that for thermoplastic composites. Processing of a thermoplastic composite requires it to be heated, melted, shaped, and then cooled to solidify – all this can be accomplished very quickly in an injection molding machine, and this contributes to the fast (often less than a minute) production cycle. For thermosetting composites, the processing time is restricted by the curing of the resin that can range from a few minutes to a few hours.

Thermoplastic polymers can be either amorphous, where the molecules are randomly coiled, or crystalline, where the polymer molecules are packed in regular, repeating structural patterns. In reality, no polymer is completely crystalline: those with large concentrations of crystalline areas are said to be crystalline or, more accurately, semi-crystalline; those having large amorphous regions are said to be amorphous [4]. The thermoplastic properties are determined by the molecular structure which is strongly

© Woodhead Publishing Limited, 2010

affected by the cooling dynamics. Generally, an amorphous polymer has lower mechanical properties and is less resistant to corrosion than crystalline (semi-crystalline) polymers. The commonly used thermosets in FRP composites are epoxy, polyester, and phenolics, while the commonly used thermoplastics are polyethylene, polypropylene, and PVC. The details of the properties of these resins can be found in [4].

Sometimes, in order to enhance infiltration of fiber mats by polymer resin during molding operations, unidirectional or woven fabrics are pre-impregnated with the resin in a separate step prior to part fabrication. These fabrics which are often called prepregs are usually stored under cold conditions before use. Both thermoplastic and thermosetting prepregs are available from the market. The processing of composites using prepregs provides more controlled properties including higher stiffness and strength as opposed to the traditional on-line wetting processing. The prepreg technique also results in lower fabrication cost, shortened processing time, and reduced energy consumption. The disadvantages of prepreg materials include relatively high cost and limited shelf life. Prepregs are used in a wide variety of applications, including aerospace parts, sporting goods, electrical circuit boards, medical components, and industrial products. The manufacturing processes using prepregs include hand lay-up, compression molding, autoclave processing, and automated fiber placement.

There are a number of manufacturing processes available for making FRP composites including hand lay-up, spray-up, filament winding, pultrusion, LCM, compression molding, automatic fiber placement, and autoclave processing [5, 6]. Although these manufacturing techniques are different from each other in terms of applying heat and pressure, they all involve four basic steps: lay-up, wetting, consolidation, and solidification. In the lay-up step, fibers or fabrics are formed into the desired shape either manually (e.g., hand lay-up, spray-up) or automatically (e.g., filament winding, LCM, automatic fiber placement). In the wetting step, liquid resins impregnate the fibers. The wetting or impregnation of the fibers can take place either prior to the lay-up of the fiber structure (e.g., prepreg technique, filament winding, pultrusion) or after the lay-up step (e.g., LCM, compression molding). The purpose of this step is to make sure that the resin impregnates the fibers completely. In the consolidation step, the wetted fiber structure is placed under some compression to remove the entrapped air and achieve the desired fiber volume fraction of the final composite products. In the solidification step, thermosetting and thermoplastic matrices in FRPs are solidified through the cross-linking chemical reaction and the liquid-to-solid phase transformation by cooling, respectively. Solidification usually takes minutes for thermoplastics and may take up to a few hours for thermosets.

© Woodhead Publishing Limited, 2010

3.2 Liquid composite molding (LCM)

Among the various composites manufacturing processes, LCM has been recognized as a cost-effective and promising technology. In fact, LCM is not a single process but a generic set of technologies for manufacturing composite parts; it includes resin transfer molding (RTM), structural reaction injection molding (SRIM), vacuum assisted resin transfer molding (VARTM), and Seemann composites resin infusion molding process (SCRIMP).

Although a particular process of LCM may be different from the others in terms of specific processing techniques, these processes share many common features which allows one to classify them into the same category of composites manufacturing process. In a typical LCM process, the reinforcing fibers in the form of fiber preforms are placed in a closed mold; polymer resin as the matrix material in liquid form is then either injected under pressure, or sucked into the mold due to vacuum, to infiltrate the fiber mat. When the mold is filled with resin, the matrix material is allowed to undergo a solidification process (curing reaction) before the final part is removed from the mold. The fiber preform used in LCM can be made of glass, carbon, or aramid, depending on the specific application. The LCM mold is typically made of aluminum and steel. For RTM and SRIM, the mold is hard and double-sided as shown in Fig. 3.1, while one side of the mold is replaced by a flexible vacuum-tight bag for VARTM and SCRIMP as shown in Fig. 3.2. VARTM and SCRIMP are an adaptation of the RTM process; due to a reduction in tooling costs because of the use of the flexible

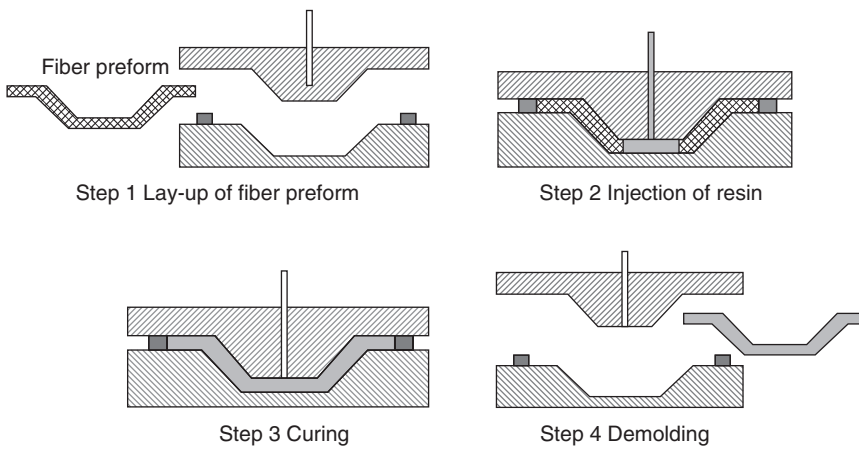

3.1 Manufacturing steps involved in RTM and SRIM.

© Woodhead Publishing Limited, 2010

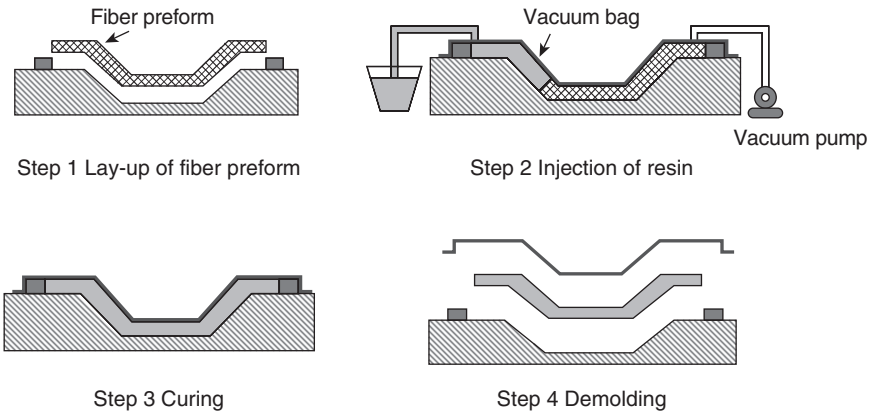

3.2 Manufacturing steps involved in VARTM and SCRIMP.

bag, they are very cost-effective in making large structures such as boat hulls, car bodies, and wind-turbine blades.

The SRIM process is different from the RTM process in terms of the resins used and the method of mixing resins before injection. In the SRIM process, two resins are mixed at high velocity in a mixing chamber and the resin is injected into the closed mold, which is similar to the reaction injection molding (RIM) process. In the RTM process, the resins are mixed by a static mixer and injected into the mold at a much slower flow rate. Therefore, the mold-filling pressure in SRIM is often several times higher than that in RTM. Resins used in SRIM must be able to fill the mold in a very short period of time without reacting and, once the mold is filled, it should cure quickly to allow fast solidification [6]. The process cycle time for SRIM is usually one to five minutes, depending on the size and geometry of the part. The resin viscosity for SRIM is quite low (10–100 cP) compared to RTM (100–1000 cP). Typical SRIM resins are low-viscosity polyurethane-based polymers [5]. For RTM, a wide range of resin systems can be used, including polyester, vinylester, epoxy, and phenolic. The most common resins used are the unsaturated polyester and epoxies.

VARTM and SCRIMP (a patented VARTM process) have been developed as a variant of the traditional RTM process to reduce the cost and design difficulties associated with large metal tools. Since one side of the mold is replaced by the vacuum bag, this eliminates the need for making a precise matched mold as required by RTM. The driving force for resin flow in VARTM is the pressure difference between the injection port (atmospheric pressure) and the vent (vaccum pressure) as shown in Fig. 3.2. Due to the relatively low pressure differentials of 1 atm, a resin distribution

© Woodhead Publishing Limited, 2010

medium with high permeability is often incorporated into the vacuum bag lay-up to facilitate the resin flow in the preform. Because of the low flow resistance in the distribution medium, the resin flows preferentially through the distribution medium and simultaneously flows across the thickness of the fiber preform placed underneath. The major advantage of VARTM over RTM is the lower tooling cost, and hence the fabrication of large-scale composites structures becomes more affordable using the former. Since one side of the mold is a flexible vacuum bag, surface quality and dimensional tolerances in the thickness direction are important issues for VARTM parts. VARTM has been applied to retrofit glass or fiber composites to steel, concrete, and masonry structures for blast protection [3].

Compared to the other composites manufacturing techniques, LCM processes have several advantages [7]. The pressure used during LCM is relatively lower than that required for the compression and injection molding processes, which means that investment in tooling and operating expenses is low. LCM ensures reasonable mass production rates of composites parts with moderate to high fiber volume fractions. Generally, the higher the fiber volume fraction of a composite is, the higher is its performance. Continuous fibers used in LCM lead to the production of net-shape parts, so material wastage and machining cost are reduced. Since the closed molding processes offer low volatile emission during processing, LCM processes are environmentally friendly.

3.3 Modeling of the mold-filling stage in liquid composite molding

The quality of the LCM product and the efficiency of the process depend strongly on the mold-filling stage of LCM. The mold-filling in the LCM is affected by several parameters including the location of resin inlet-gates and air vents, the resin infusion pressure, the applied clamp force, and the temperature of the resin mixture. The traditional trial-and-error methods to optimize the mold and process design can be too time-consuming and economically prohibitive. As a consequence, the numerical mold-filling simulations emerge as one of the most effective ways to optimize LCM technology. Successful computer simulations are able to improve the LCM mold design in virtual space without the need for the expensive and time-consuming trial-and-error approach to mold design.

In the following section, an overview of the traditional isothermal and non-isothermal mold-filling simulations of LCM based on single-scale porous-medium flow is presented, and then followed by an introduction to the modeling of dual-scale porous-medium flow in LCM.

© Woodhead Publishing Limited, 2010

3.3.1 Conventional mold-filling modeling and simulation in LCM

Traditionally, the fiber preforms are viewed as the porous media having a uniform pore-size. It is standard to assume that the pores in the fiber preform behind the flow front are fully saturated with resin, and the liquid resin flow impregnating the dry fiber preform during the mold-filling stage of LCM can hence be modeled using Darcy's law as

$$\mathbf{v} = -\frac{\mathbf{K}}{\mu}\nabla p \qquad [3.1]$$

where $\mathbf{v}$ is the volume-averaged velocity of resin in the fibrous porous medium, p is the pore-averaged resin pressure, $\mathbf{K}$ is the permeability tensor for the fiber preform, and μ is the resin viscosity. When the fiber preform is isotropic porous medium, the permeability becomes a scalar instead of a tensor. The resin is assumed to be incompressible, hence the continuity equation can be expressed as

$$\nabla \cdot \mathbf{v} = 0 \qquad [3.2]$$

Inserting Eq. 3.1 into Eq. 3.2 leads to an elliptic partial different equation (a Laplace equation) that has only one unknown variable as the pressure p. The resulting Laplace equation governs the pressure field in the region wetted by the resin. Introducing the proper boundary conditions, the pressure distribution as well as the flow-velocity distribution (through Eq. 3.1) can be obtained by solving the Laplace equation.

Over the past decades, the Darcy's law equation (Eq. 3.1) has been used to model the macroscopic flow behavior of LCM by many researchers. The modeling of mold-filling of LCM can be basically divided into two groups: isothermal and non-isothermal. For an isothermal mold-filling simulation, heat generation due to the exothermic chemical reaction of thermosetting resins and the subsequent heat transfer is neglected when the resin is impregnating the dry fiber preforms [8–48], whereas both are taken into consideration in non-isothermal simulation [6, 16, 34, 49–64]. The main tasks before the isothermal modeling simulations are to first obtain the velocity and pressure fields using Eqs 3.1 and 3.2, and then to track the flow front as resin moves in the mold cavity. For non-isothermal simulations, the additional focus is on modeling the thermochemical phenomena during mold filling in LCM.

Mold-filling of LCM is a typical problem of free-surface flow involving a moving boundary where the description and advancement of the moving boundary is the main concern. Generally, the moving boundary problems can be tackled using two algorithms: Lagrangian [11, 38, 40, 41, 44, 46, 48,

© Woodhead Publishing Limited, 2010

65] and Eulerian [8–10, 13–36, 39, 45, 47, 66–69]. In Lagrangian algorithms, a reference frame (often referred to as the material reference) is attached to the moving flow domain so the computational mesh deforms with motion of the fluid, and the boundary of the mesh coincides with the free surface of the fluid. Such algorithms can give an accurate description of the moving boundary; however, the frequent remeshing of the flow domain as the flow front advances leads to high computational costs, especially for 3D problems. In contrast to the Lagrangian algorithm, Eulerian algorithms employ fixed mesh to describe the moving fluid. Unlike the Lagrangian algorithms where the interface is defined explicitly, the Eulerian algorithms define the location and motion of the interface implicitly. Although the Eulerian method sometimes has less accurate representation of the moving interface, it is highly efficient computationally, especially for large problems with complex geometries, thus making it very attractive for practical engineering applications. As a result, most mold-filling simulations of LCM are based on the Eulerian algorithm because of this high computational efficiency.

Various front-tracking techniques based on the Eulerian algorithm have been proposed in the past decades. The most common are the marker-and-cell (MAC) method [66], the flow analysis network (FAN) method [67, 70], the pseudo-concentration method [68], and the volume of fluid (VOF) method [69, 71]. In the MAC method, the massless particles ('markers') are placed in the mesh cells which the invading fluid occupies at the beginning of the computation. The position of these markers is then updated from one time-step to the next based on the fluid velocity. The markers are used to track the movement of the fluid as well as to define the boundary of flow domain. In the FAN method, each node has its own control volume and a fill factor is assigned to each node to represent the fraction of the control volume that is filled with fluid. A unit value of fill factor corresponds to a completely filled control volume, whereas a zero value indicates an empty control volume. Control volumes with fill factor values between zero and one are partially filled with the fluid. The fill factor of a node is updated based on the net flow rates into the control volume associated with that node at each time-step. The pseudo-concentration and VOF methods are very similar to each other; in both the methods, flow fronts are tracked directly by solving the transport equation for the fractional volume function. The major difference between them is that the VOF method uses only one fluid whereas the pseudo-concentration method employs an additional fictitious fluid with a low viscosity (usually several orders of magnitude lower than the real fluid's viscosity) to represent the regions where the fluid has not yet reached. Reconstruction of the moving interface is necessary to ensure an accurate calculation of the fluid quantity flowing across the control volumes in the VOF method [71]. Due to robustness and efficiency, the VOF method has been widely used in mold-filling

© Woodhead Publishing Limited, 2010

simulations in the fields of die casting, polymer processing, and composites manufacturing.

With the help of these front-tracking techniques, a numerical method for solving different equations governing the transport and thermochemical phenomena has to be employed in order to simulate mold-filling in LCM. There are three common, basic classes of numerical methods for solving partial differential equations (PDEs): the finite difference method (FDM), the boundary element method (BEM), and the finite element method (FEM). Each method has been adapted in some form for certain specific problems encountered in the mold-filling simulation of LCM.

The finite difference method or FDM is the earliest numerical technique for solving fluid flow problems with simple geometries. Because of the simplicity and effectiveness of the method, FDM is relatively easy to program using computers and has been implemented in a wide variety of problems. However, this method suffers difficulties while handling irregularly-shaped geometries where the grid lines do not follow the orthogonal coordinate directions. A special technique called the 'boundary-fitted coordinate transformation' has been proposed to tackle the complex flow domains that are very common in most flows of engineering practice [72]. An irregular physical domain can be mapped onto a regular computational domain using this technique. The original PDEs transformed for the new computational coordinate system can then be solved through the conventional FDM. The disadvantages of this method are: (i) boundary-fitted grid generation for complex geometries is often time-consuming; (ii) the equation transformation increases both difficulty of programming and cost of solving the equations, and affects the accuracy of the solutions. Li and Gauvin [46] and Friedrichs *et al.* [42, 43] used the FDM combined with the boundary-fitted grid technique to conduct isothermal mold-filling simulation based on Darcy's law. In their method, the flow front was tracked using a Lagrangian algorithm. The physical domain saturated by the resin was mapped into the computational domain at each time-step. This remeshing processing involved in the boundary-fitted technique apparently increases the computational cost. Trochu and Gauvin [44, 48] compared the numerical predictions based on the method with the experimental results, and pointed out several limitations of this method including the high computational cost and the difficulty in handling the merging of flow fronts. Kuan and EI-Gizawy [45] and Panitapu *et al.* [47] developed FDM simulations based on the control volume method to track the flow fronts in the isothermal mold-filling simulations of LCM.

Unlike the FDM dealing directly with the PDEs, the boundary element method or BEM transforms the differential equations into integral identities which are applicable over the surface or boundary; as a result, the BEM only requires that the boundary or surfaces of the physical domain be

© Woodhead Publishing Limited, 2010

discretized. The integrals are then numerically evaluated to yield an algebraic system of equations. The advantages of the BEM include less data preparation time, high resolution of the solution, and less computer time and storage. The disadvantages include the relatively complex mathematics involved, difficulty in handling non-linear problems, and the fully dense solution matrix [37]. Um and Lee [40], Yoo and Lee [41], Schmidt *et al*. [38], and Soukane and Trochu [39] performed isothermal mold-filling simulations of LCM using the BEM; Darcy's law was employed along with mass conservation to construct the governing equation which was then solved using the BEM. The flow front was tracked using a Lagrangian algorithm [38, 40, 41], i.e., the positions of the boundary nodes were updated at each time-step as the flow front was advancing in the mold cavity. On the other hand, the Eulerian algorithm-based level set method was employed in [39] to track the moving interface.

The finite element method or FEM is a powerful numerical tool for solving the PDEs. This method is a generalization of the classical variational and weighted-residual methods. The basic idea of FEM is that the solution of a differential equation can be represented as a linear combination of a series of unknown parameters and functions in the entire domain. The parameters are then determined such that the differential equation is satisfied in a weighted-integral sense. Because of its ability to handle complex irregular geometries, the FEM has become the most popular numerical method for the solution of the boundary, initial, and eigenvalue problems arising in various fields of engineering. Many commercial simulation programs based on FEM have been developed for various purposes. The FEM is also the most widely used numerical method for the LCM mold-filling simulations [8–36, 49–64].

For the isothermal mold-filling simulation of LCM using FEM, there are two basic approaches: (i) use the Galerkin FEM to solve the governing equations and use the FAN (often referred to as the control-volume method) technique to track the flow front location, which is commonly referred to as the finite element/control-volume (FE/CV) method [8–10, 15, 16, 18–24, 29]; (ii) use the control-volume finite element method (CVFEM) to solve the governing equation and track the front using the FAN [11, 13, 14, 17, 24–26, 33, 35, 36]. The CVFEM is a variation of the FEM technique first proposed by Baliga and Patankar [73, 74]. (CVFEM ensures the strict conservation of various quantities (i.e., mass, momentum, and energy) which have physical meanings; such a connection to realism is often lacking in the Galerkin FEM. This method has been mainly used in fluid flow problems and has gained popularity in this field.) For the simplex element types (i.e. triangles and tetrahedrons) used in the finite element discretization, the two methods are exactly equivalent; however, the linear algebraic equations derived using the Galerkin FEM and CVFEM, respectively, are

© Woodhead Publishing Limited, 2010

different for the isoparametric elements (i.e., quadrilaterals, pentahedrons, and hexahedrons) [24]. The CVFEM leads to an unsymmetrical linear algebraic system for isoparametric elements with unequal opposite sides, while Galerkin FEM always results in a symmetrical system [24]. Phelan [24] pointed out that the mass cannot be strictly conserved during flow simulation under any conditions using the FE/CV method for isoparametric finite elements. In order to overcome the mass imbalance associated with the FE/CV method, Trochu *et al*. [27, 28] proposed to use non-conforming finite elements instead of the traditional conforming elements. Varma and Advani [29] presented an improved node-centered control-volume approach to improve the overall mass balance. Joshi *et al*. [15] developed a new scaling technique to ensure mass balance.

For both the FE/CV and CVFEM methods, a control volume can either be constructed around a finite element node by joining the midpoints of the surrounding finite element edges [8–10, 13–17, 21–26, 29–33, 35, 36], or be the finite element itself [27, 28, 49]. Conventionally, the transient mold-filling of LCM is treated as a continuous quasi-steady process with moving boundaries, so the whole process is divided into quasi-steady time-steps and the flow front progresses step by step. The FEM or CVFEM is first used to solve for the pressure field. The computed pressure field is then used to calculate flow rates (or Darcy velocities) and advance the flow front. The pressure field for the new domain is now computed and the procedure is repeated until the mold is full. This algorithm is often called the explicit mold-filling simulation, because time integration for the transient terms is evaluated numerically in an explicit manner. In order to ensure the stability of numerical solution based on the explicit time integration, the time-step increment is determined in such a manner so that only one control volume is filled at each time-step; the time-step size for each time-step is automatically determined in the simulation process based on the calculation of the mass flux and empty volume-fraction of a control volume that is filled fastest among all the boundary control volumes at that time-step. Obviously, this stability restriction makes the computational cost of the explicit algorithm very high for problems with complex geometries, especially in the case of 3D problems. In order to remove such a restriction on the time-step size, implicit algorithms have been proposed to speed up the computations [14, 18, 19, 21–23, 25, 26, 30–32].

Unlike the explicit method where a fill factor value is assigned explicitly to each node, the fill factor in an implicit algorithm is implicitly defined and a transient term in the form of the time derivative of the fill factor is included in the continuity equation. (In [44, 45, 51, 52], the concept of partial saturation was used instead of the fill factor. Numerically, the partial-saturation concept is identical to the fill-factor concept of the front-tracking algorithm FAN.) The time-step increment in the implicit algorithm

© Woodhead Publishing Limited, 2010

is determined manually before simulation. Proper selection of the time-step size is important for the implicit algorithm to achieve high computational efficiency with sufficient accuracy. It has been shown that compared to the explicit algorithm, the implicit algorithm is computationally efficient [14, 18, 19, 21–23, 25, 26, 30–32]; however, the implicit algorithm suffers a drop in accuracy when large time-step increments are used. In contrast to the implicit algorithm, Maier *et al*. [20] proposed a completely different numerical scheme to improve the computational efficiency of the traditional implicit method. Their method solves the algebraic equations only once for the complete filling cycle; however, the method cannot work for non-linear problems (e.g., when resin viscosity varies during the mold-filling process as a function of temperature and cure).

The non-isothermal mold-filling simulation using FEM has the additional task of modeling the thermochemical phenomena due to the chemical reaction of thermosetting resin, and developing a proper algorithm for decoupling the coupled momentum, energy, and species governing equations. The thermochemical phenomena in the mold-filling stage of LCM can be divided into two parts: modeling heat transfer inside the mold, and modeling the cross-linking reaction in resin. Since there are liquid (resin) and solid (fiber preform) phases involved in the mold-filling of LCM, the energy equations describing the heat transfer in LCM can be derived using either the two-phase model [6, 50, 52, 56, 57, 75] or the local thermal equilibrium model [16, 34, 49, 53, 55, 58–64, 75]. In the two-phase model, heat transfer is modeled for the resin and fiber preform separately and the heat transfer between the two phases is taken into account via a heat transfer coefficient. The energy equation for the liquid resin usually includes terms pertaining to transient heat accumulation, heat convection due to resin flow, heat conduction, heat generation due to the exothermic curing reaction in resin, and heat exchange between resin and fibers; the energy equation for solid fibers contains terms pertaining to transient heat accumulation, heat conduction, and heat exchange [50, 52, 56, 57, 75]. The energy balance in the fluid phase is

$$\varepsilon\rho_{\mathrm{r}}c_{\mathrm{pr}}\frac{\partial T_{\mathrm{r}}}{\partial t}+\rho_{\mathrm{r}}c_{\mathrm{pr}}(\mathbf{v}\cdot\nabla T_{\mathrm{r}})=\varepsilon\nabla\cdot k_{\mathrm{r}}\nabla T_{\mathrm{r}}+\varepsilon h_{\mathrm{v}}(T_{\mathrm{f}}-T_{\mathrm{r}})+\varepsilon\dot{\phi} \qquad [3.3]$$

and the energy balance in the solid phase is given by

$$(1-\varepsilon)\rho_{\mathrm{f}}c_{\mathrm{pf}}\frac{\partial T_{\mathrm{f}}}{\partial t}=(1-\varepsilon)\nabla\cdot k_{\mathrm{f}}\nabla T_{\mathrm{f}}+\varepsilon h_{\mathrm{v}}(T_{\mathrm{r}}-T_{\mathrm{f}}) \qquad [3.4]$$

where T is temperature, t denotes time, ε is the porosity of fiber mat, ρ is density, c_{p} is specific heat, k is thermal conductivity, h_{v} is the heat transfer coefficient from resin to fiber mat, $\dot{\phi}$ is heat generation rate by

© Woodhead Publishing Limited, 2010

chemical reaction. The subscripts r and f denote resin and fiber phases, respectively.

If it is assumed that the resin and fiber reach local thermodynamic equilibrium (i.e., temperatures of the two phases are identical at any position) as soon as the fiber is impregnated, then only one energy equation needs to be solved. This assumption is reasonable if the heat transfer coefficient between resin and fiber is large or the resin flows slowly through fiber preform [52, 57]. The energy balance based on local thermal equilibrium is

$$\rho c_{\mathrm{p}} \frac{\partial T_{\mathrm{r}}}{\partial t} + \rho_{\mathrm{r}} c_{\mathrm{pr}} (\mathbf{v} \cdot \nabla T_{\mathrm{r}}) = \nabla \cdot k \nabla T_{\mathrm{r}} + \varepsilon \dot{\phi} \qquad [3.5]$$

where ρ, c_{p}, and k are density, specific heat, and conductivity of the composite medium, respectively. Local equilibrium can be regarded as a special case of the two-phase model, and both methods have been used in modeling the mold-filling in LCM. Most non-isothermal mold-filling simulations of LCM are based on the energy equation obtained using the local thermal equilibrium model.

The species mass balance for chemical reaction is given in the form

$$\varepsilon \frac{\partial \alpha}{\partial t} + \mathbf{v} \cdot \nabla \alpha = \varepsilon \dot{m} \qquad [3.6]$$

where α is the degree of cure of the resin. $\dot{m}$ is the mass generation rate of the resin, which is usually a function of temperature and degree of cure depending on specific cure-kinetic model.

Because the energy and species equations are convection-dominated type PDEs, the conventional Galerkin FEM using the Eulerian fixed mesh can result in unstable solutions. Most researchers employ the streamline upwind Petrov–Galerkin (SUPG) method to stabilize the solutions [76]. Since the resin viscosity depends on temperature and degree of cure, the momentum, energy, and species equations are strongly coupled with each other. The resin flow depends on heat transfer and curing reaction through the resin viscosity, while the heat transfer and curing reaction in turn are affected by resin flow through the convection term. The iterative method has often been employed to decouple the governing equations [16, 34, 49, 50, 52–64]. At each time-step, the initial resin viscosity is evaluated using the temperature and degree of cure of the previous iteration step. The pressure and velocity fields can then be obtained by solving the momentum equation. Based on this velocity field, the energy and species equations are solved to update the temperature and degree of cure. A new round of calculations following the same order is carried out until the temperature and cure solutions converge. This iterative method works efficiently in solving the coupled governing equations and, for a sufficiently small time-step size, the solutions converge rapidly [49, 60].

© Woodhead Publishing Limited, 2010

3.3.2 Dual-scale modeling and simulation in LCM

In recent years, researchers have found that for some types of fiber mats, the predictions using Darcy's law do not match the experimental results and the wetted region behind the flow front is not fully saturated. For example, if a long rectangular-shaped mold stacked with fiber mats is injected with resin from the inlet-port located at one end of the mold under constant flowrate injection conditions as shown in Fig. 3.3, the inlet pressure predicted using Darcy's law should be linearly increasing with the time. For random fiber mats, the prediction matches the experimental results well, whereas the inlet pressure history is found to be deviating from the linear profile ('drooping') for the biaxial stitched fiber mats as shown in Fig. 3.4 [77]. For impregnation of the random mats, the entire wetting region behind the flow front is fully saturated, whereas there is obviously a partially saturated region behind the moving flow front for the biaxial fiber mat as shown in Fig. 3.5 [77]. A further study reveals that both macro- and micro-scale flows coexist and interact mutually during mold-filling in LCM due to the presence of dual length-scale in pore-sizes of the fiber preforms. A new concept of 'dual-scale porous media flow' is then put forward to address the modeling issues involved with the unsaturated flow of the dual-scale fiber preforms in LCM.

In the last decade or so, many such studies [77–87] have shown that the physics of resin flow in LCM cannot be explained using the conventional flow model for certain types of fiber mats such as woven or stitched fabrics. A careful examination of the microstructure of fiber preforms gives clues to the reason for discrepancy between the experiments on the one hand, and numerical prediction obtained from Eqs 3.1 and 3.2 on the other. The fiber tows (bundles of fibers) made of thousands of individual fiber filaments are either woven or stitched to form the fabrics used in LCM. The inter-fiber distance within the *intra-tow* region is of the order of micrometers, whereas the distance between the fiber bundles, also called gaps and constituting the *inter-tow* region, is of the order of millimeters. This order-of-magnitude difference in length scales of the pore-size in the same medium leads to its classification as a 'dual-scale' porous medium. Because of this dual-scale nature of fiber mats, when resin is injected into a mold, it quickly passes

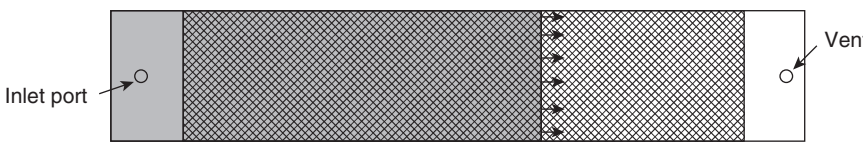

3.3 Schematic showing 1D flow in a flat rectangular mold under the constant flowrate injection conditions.

© Woodhead Publishing Limited, 2010

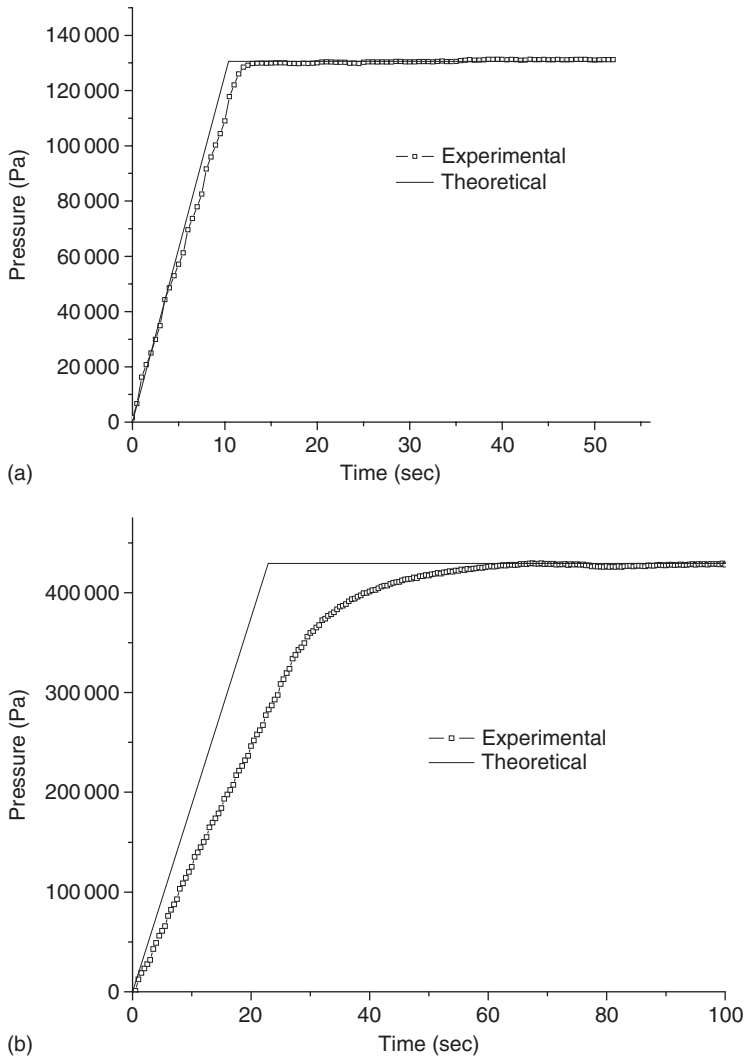

3.4 A comparison of the experimental inlet-pressure history with the theoretical prediction using Darcy's law: (a) random mat; (b) biaxial mat [77].

through the inter-tow channels without impregnating the tows due to high flow resistance inside the tows. After the front has passed, resin from the surrounding gap region continues to impregnate the tows gradually. This delayed impregnation of tows leads to the presence of a partially saturated region behind the macroscopic flow front during the mold filling of LCM process, as shown schematically in Fig. 3.6. Since the pore-size within a tow

© Woodhead Publishing Limited, 2010

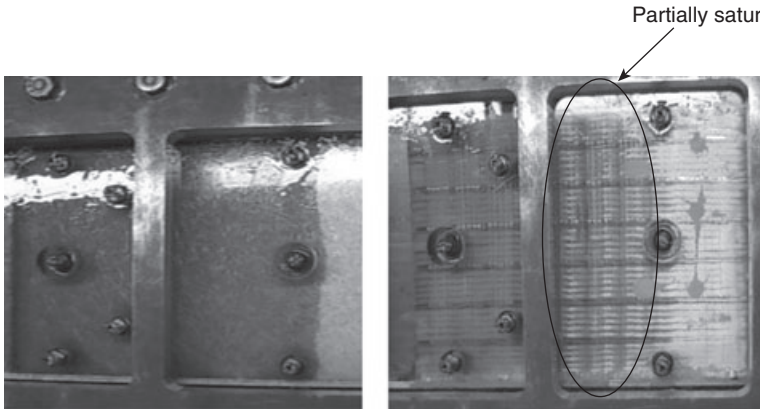

3.5 A snapshot of impregnation of fiber mats in 1D flow mold: (a) random mat; (b) biaxial mat [77].

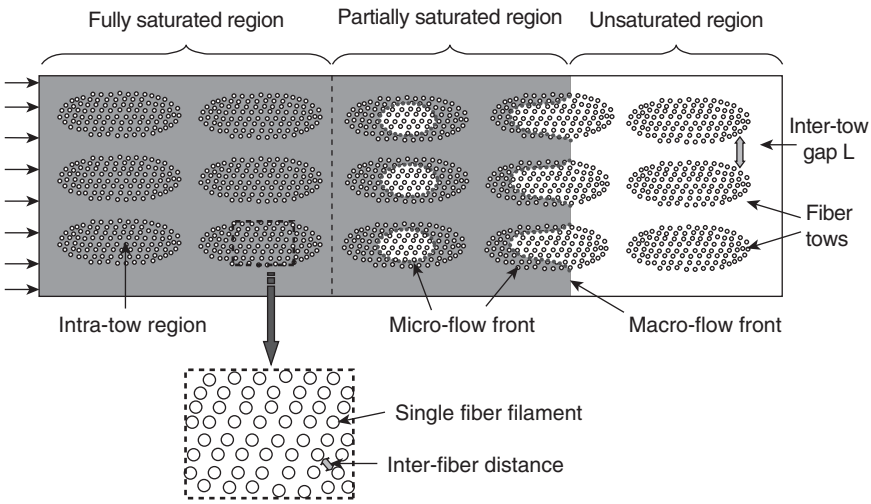

3.6 A schematic depicting the characteristic of a typical unsaturated flow within the dual-scale fiber preforms and highlighting the delayed impregnation of the fiber tows.

in the inter-fiber space is only the order of micrometers, the resin flow in the intra-tow region occurs at the micro-level, whereas the flow in the inter-tow region occurs at the macro-level. The coexistence of the macro- and micro-flows due to the dual-scale nature of the preforms has obvious influence on the mold-filling of LCM such as void formation [78, 80, 81, 84, 88–91], visible partially saturated region [77, 78, 82–86], and 'drooping' inlet

© Woodhead Publishing Limited, 2010

pressure profile under constant injection rates [7, 82–87, 92]. The presence of a partially saturated region behind the flow front for dual-scale porous media contradicts the key assumption of full saturation behind the flow front – such an assumption forms a crucial part of the conventional flow model based on Eqs 3.1 and 3.2 for mold-filling in LCM.

To understand the unsaturated flow in dual-scale fiber preforms of the LCM process, researchers have developed many different models. The dual-scale models can be classified into two groups: (i) tow-impregnation models where the focus is to study the mechanism of void formation due to the interaction between the micro- and macro-flows; (ii) global impregnation models where the primary aim is to capture the unsaturated flow characteristics during the transient mold-filling process in LCM with dual-scale preforms.

In the tow-impregnation models, flows in the inter- and intra-tow regions are usually modeled separately using a repetitive computational domain (often called the unit cell) that represents the mesoscopic fabric architecture and is made of a certain number of fiber tows and their adjacent inter-tow gap region. Such a computation domain is sometimes referred to as the unit cell that represents the periodic structure of the woven or stitched fabrics at mesoscopic level. For flow modeling at meso-level, each fiber tow in the unit cell is represented geometrically using a solid domain without modeling individual fiber filaments contained in the tow. A proper flow equation for the tow domain must be chosen to represent the micro-flow within the tows. Binetruy *et al*. [81, 88], Chang and Hourng [90], Lekakou and Bader [91], Parnas *et al*. [79], and Young [93] carried out transient tow-impregnation simulations using Darcy's law to model both inter- and intra-tow flows where the permeability of the inter-tow region is several orders of magnitude higher than that of the intra-tow region. On the other hand, Chang [94], Dimitrovova and Advani [95], and Yang *et al*. [96] employed the Stokes and Brinkman equations to model the inter- and intra-tow flows, respectively. There have been other variations to this basic model. For example, Dungan and Sastry [84] modeled the transient inter-tow flow using the analytical solution for a 2D flow through a channel bounded by liquid-absorbing, porous, parallel walls. Foley and Gillespie [97] incorporated the capillary pressure, the entrapped gas pressure, and wetting properties into Darcy's law to model the micro-flow infiltrating a tow. So far, the transient tow-impregnation models have not been applied to any full-fledged 3D mold-filling simulations.

The *transient* tow-impregnation models can provide a detailed understanding on how the local flows evolve in the intra-tows and inter-tow gaps within a unit cell; however, they require a relatively complicated domain, which includes details of the mesoscopic architecture of fabrics, ranging in dimensions from millimeters to centimeters. However, the length-scale

© Woodhead Publishing Limited, 2010

involved in LCM is usually on the order of meters. Therefore, except for a simple 1D mold-filling problem [78, 89, 91], the current tow-impregnation models are computationally prohibitive for use in a full-scale mold-filling simulation for dual-scale fiber preforms. (Although the mold-filling involving a radial flow is usually a 2D flow problem, it becomes a 1D flow for isotropic fiber mats due to the axial symmetry.)

Interestingly, the *steady-state* 'tow-impregnation' model (which more appropriately should be called the unit-cell flow model where both the inter- and intra-tow regions within a unit cell are under fully saturated flow while subjected to an external pressure gradient) can be used to predict the saturated permeability of fabrics as long as the periodic fabric structures are well represented in the computational domain [98–109].

Unlike the tow-impregnation models, the global impregnation models do not need detailed local (the inside tow) flow information, and instead use a lumped quantity to represent the mass exchange between the inter- and intra-tow regions and incorporate this term into the governing equation. The delay of impregnation within the tows at the micro-level acts as sinks of liquid in the macrosopic flow field within the gap region, so a new continuity equation at macro (gap) level was proposed by introducing a non-zero sink term [78, 83, 86, 89, 92, 110–115]:

$$\nabla \cdot \mathbf{v} = -S \qquad [3.7]$$

where S, the sink term, is equal to the volumetric rate of resin absorption by tows per unit volume. Equation 3.7 combined with the conventional Darcy's law equation (Eq. 3.1) completes the isothermal flow modeling in dual-scale porous media using the global impregnation model. Obviously, the sink term in Eq. 3.7 plays a key role in modeling the transient mold-filling in LCM with dual-scale preforms. Significant effort has been made to derive a suitable sink function since the sink model was first proposed by Parnas and Phelan [78]. Parnas and Phelan assumed the impregnation of liquid into the tows to be transversely radial and derived a mathematical expression of the sink term in the form of the position of the micro-front penetrating the tows. Using this model, they succeeded in predicting the experimentally observed phenomenon of jump in the inlet pressure for directional fiber mats at the end of the 1D mold-filling process. Chan and Morgan [89] have extended the same model to the case of bidirectional mats for integrating the tow-impregnation into the 1D global infiltration flow. Pillai and Advani [92, 116] developed a sink function using a two-layer model where they idealized the dual-scale porous medium as an array of low-porosity intra-tow regions interspersed with high-porosity inter-tow regions. They applied the model to a full-scale 2D mold-filling simulation and successfully replicated the drooping inlet-pressure profile typically witnessed in 1D flow experiments under constant injection rates for dual-scale

© Woodhead Publishing Limited, 2010

fiber mats. Pillai [110] later adopted the rigorous volume averaging method to derive the isothermal flow equations in dual-scale porous media and introduced an accurate terminology to describe such flows. Instead of explicitly including the sink term in the continuity equation as required in the regular sink model, Simacek and Advani [117] used 1D bar elements connected to the FEM mesh nodes to represent the sink term to avoid changing the governing equations. In this way, they incorporated the tow-saturation solution simultaneously into the full-scale isothermal mold-filling simulation.

The sink terms in previous sink models were mainly derived by applying Darcy's law to much simplified geometries [78, 83, 89, 92, 115, 116]. Unlike these analytical derivations for the sink term, Wang *et al*. [112, 113] obtained a sink function by conducting the transient tow-impregnation simulation within a unit cell that represents the mesoscopic architecture of a dual-scale fiber mat. The sink function, expressed in terms of the total tow saturation inside the unit cell as well as local gap pressure, was proposed based on the numerical results. A 1D dual-scale flow simulation was then carried out by incorporating the sink function into macro-flow equations, and some experimental observations characteristic of the dual-scale fiber mat flows were replicated.

Pillai and Jadhav [114, 115] carried out a *non-isothermal, reactive* flow simulation in a 2D dual-scale porous medium using the sink model where they reported significant differences in the average temperatures and cures within the gap and tow regions. In response to the need to accurately model temperature and cure within the gap and tow regions, Pillai and Munagavalasa [111] employed the mathematically rigorous volume-averaging method to develop sets of governing equations (see Tables 3.1

Table 3.1 The set of volume-averaged governing equations for the gap region

Mass	$\nabla\cdot\langle\mathbf{v}_g\rangle = -S$
Momentum	$\langle\mathbf{v}_g\rangle = -\dfrac{\mathbf{K}_g}{\mu_g}\nabla\langle P_g\rangle^g$
Energy	$\rho_g C_{p,g}\left[\varepsilon_g\dfrac{\partial}{\partial t}\langle T_g\rangle^g + \langle\mathbf{v}_g\rangle\cdot\nabla\langle T_g\rangle^g\right] = \nabla\cdot\mathbf{K}_{th}\cdot\nabla\langle T_g\rangle^g + \varepsilon_g\rho_g H_R f_c + Q_{conv} - Q_{cond}$
Cure	$\varepsilon_g\dfrac{\partial}{\partial t}\langle c_g\rangle^g + \langle\mathbf{v}_g\rangle\cdot\nabla\langle c_g\rangle^g = \nabla\cdot\mathbf{D}\cdot\nabla\langle c_g\rangle^g + \varepsilon_g f_c + M_{conv} - M_{diff}$

Note: C_p = specific heat; **D** = mass diffusion; f_c = reaction rate; H_R = heat generation per volume; **K** = permeability tensor; M_{conv} and M_{diff} = mass sink term due to convection and diffusion, respectively; P = pressure; Q_{cond} and Q_{conv} = thermal sink term due to conduction and convection, respectively; S = sink term; T = temperature; t = time; **v** = volume-averaged velocity; ε = porosity; μ = viscosity; ρ = density; the subscripts g and th denote gas and thermal, respectively

© Woodhead Publishing Limited, 2010

Table 3.2 The set of volume-averaged governing equations for the tow region

Mass	$\nabla \cdot \langle \mathbf{v}_{\mathrm{f}} \rangle = 0$
Momentum	$\langle \mathbf{v}_{\mathrm{f}} \rangle = -\dfrac{\mathbf{K}_{\mathrm{t}}}{\mu} \nabla \langle P_{\mathrm{f}} \rangle^{\mathrm{f}}$
Energy	$[\varepsilon_{\mathrm{t}} (\rho C_{\mathrm{p}})_{\mathrm{l}} + (1-\varepsilon_{\mathrm{t}})(\rho C_{\mathrm{p}})_{\mathrm{f}}] \dfrac{\partial T_{\mathrm{t}}}{\partial t} + (\rho C_{\mathrm{p}})_{\mathrm{l}} \mathbf{v}_{\mathrm{t}} \cdot \nabla T_{t} = \nabla \cdot \mathbf{K}_{\mathrm{th,t}} \cdot \nabla T_{\mathrm{t}} + \varepsilon_{\mathrm{t}} \rho_{\mathrm{l}} H_{\mathrm{R}} f_{\mathrm{c}}$
Cure	$\varepsilon_{\mathrm{t}} \dfrac{\partial c_{t}}{\partial t} + \mathbf{v}_{\mathrm{t}} \cdot \nabla c_{\mathrm{t}} = \nabla \cdot \varepsilon_{\mathrm{t}} \mathbf{D}_{\mathrm{t}} \cdot \nabla c_{\mathrm{t}} + \varepsilon_{\mathrm{t}} f_{\mathrm{c}}$

Note: notation as Table 3.1 with subscripts f, fiber phase, l, liquid phase, t, tow

and 3.2) for unsaturated dual-scale flows under non-isothermal, reactive flow conditions. They showed that the sink effect or delayed impregnation of fiber tows behind the macroscopic flow front profoundly changes the temperature and cure distributions within such dual-scale porous media, and leads to the formation of additional source and sink terms in the temperature and cure equations.

3.4 Permeability measurement in liquid composite molding

It is clear from Eq. 3.1 that the permeability of fibrous preforms is very important for the estimation of mold-filling velocity from a given pressure field. As a result, the permeability of the fiber preform plays an important role in numerical simulations. For a successful simulation, one needs to characterize the permeability of the fiber preform accurately so that resin velocity as well as mold fill-time can be correctly predicted.

Permeability is a property of the porous preform that correlates with the ease with which a fluid flows in the material: the more permeable the material, the faster the fluid flows through it for a given pressure gradient. Darcy's law (Eq. 3.1) is widely used for characterizing the permeability of fiber mats from flow experiments. Preform permeability depends on several factors including the fiber diameter, the fabric architecture, and the fiber volume fraction.

Various measurement techniques have been developed to estimate the permeability of fibrous media, but the most widely used methods are the 1D (unidirectional) and radial flows based techniques [118–145]. In the 1D flow experiment, a rectangular, flat mold with its length much larger than the width is used, and a test fluid, injected under the constant-flow-rate or constant-injection-pressure condition, flows along the mold length direction during the experiment [118–122, 124–129, 134–142, 144]. In the radial flow

© Woodhead Publishing Limited, 2010

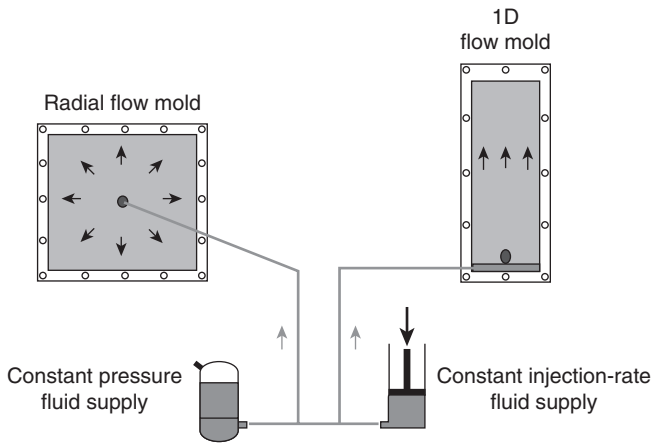

3.7 Schematic of permeability measurement based on 1D and radial flow techniques.

experiment, the injection from an inlet-port centered in the mold creates a radial, outward flow in the mold cavity [123, 130–145]. (A schematic of 1D and radial flow techniques is shown in Fig. 3.7.) Both the 1D and radial flow experiments can be carried out under either transient or steady-state conditions. The permeability measured after the fiber mats are fully wetted under steady-state conditions is often referred to as the *saturated permeability*, whereas the permeability measured through the transient flow is referred to as the *unsaturated permeability*. Research has shown that unlike saturated permeability, the unsaturated permeability may not be purely a function of fabric architecture, porosity, and fiber diameter, and may depend on the fluid properties as well as the flow rate [123, 127–129, 132, 136–138, 140, 142, 145]. In order to obtain the in-plane permeability tensor of an anisotropic fiber preform, the 1D flow experiment has to be conducted successively three times with different orientations of the fiber mat with respect to the flow direction [126, 127, 136–138, 141, 142, 144]; however, for permeability-measuring techniques based on the radial flow, only one single experiment is enough to determine the permeability tensor by observing the shape of the radial flow front during the fluid impregnation of the dry fiber preform in the experiment [130–145]. During the 1D flow experiment, if the fiber mats are not cut and stacked in the mold carefully, the gap between the side edges of the fiber mats and mold walls leads to a preferential flow along the gap channel during the experiment (often referred to as 'race tracking') which compromises the accuracy of the measurement [124, 126, 127, 138, 141, 142, 144, 146–148]. However, the radial flow experiment does not have such edge effects. The main drawback of the radial flow

© Woodhead Publishing Limited, 2010

experiment is the much larger mold deflection during the experiment compared to the 1D flow experiment [124, 126, 127, 136, 144].

Williams *et al.* [118] used both steady-state and transient 1D flow experiments to study permeability along the axis of an aligned fiber bundle and found that the saturated permeability was higher than the unsaturated permeability when measured with water and ethanol, and vice versa when measured with oil and epoxy. Gutowski *et al.* [119] investigated the axial and transverse permeabilities of the aligned graphite fibers under different consolidation states. Their study indicated that the permeability depends strongly on the fiber volume fraction, and the Kozeny-Carman's permeability model gives a good approximation of the axial permeability. Gauvin *et al.* [120] employed steady-state, unidirectional flow to study the permeability of three types of glass-fiber mats as a function of the fiber volume fraction. Trevino *et al.* [121] studied the in-plane permeabilities of different types of glass-fiber mats along and perpendicular to the flow direction as well as the transverse (across-the-thickness) permeability using the steady-state 1-D flow experiment. Gebart [122] proposed a theoretical model for predicting the permeability of unidirectional fiber mats and measured the permeability using the transient 1D flow experiment. Ferland *et al.* [124] developed concurrent methods to measure the unsaturated permeability using the 1D flow method. Hammond and Loos [125] investigated the relationship between the saturated and unsaturated permeabilities using the 1D flow experiment and found the two permeabilities to be close to each other. Gebart and Lidstrom [126], and Lundstrom *et al.* [127] developed a multi-cavity parallel flow technique to study the saturated and unsaturated permeabilities of anisotropic fiber mats; their study showed that the unsaturated permeability is slightly higher than the saturated permeability. Ma and Shishoo [128] measured the unsaturated and saturated permeabilities of five different glass fabrics using the 1D flow experiment: the saturated permeabilities were found to be higher than the unsaturated permeabilities in all the experiments. Ma and Shishoo found that the unsaturated permeability increases as the flow front moves forward, while Shojaei *et al.* [129] reported a completely different result: the unsaturated permeability decreases to a stabilized value as flow front is moving along the mold.

Most radial flow experiments are carried out under transient conditions to study the permeability tensor of the anisotropic fiber mats [130–133, 145]. Adams *et al.* [130] proposed to use the position and shape of the flow front combined with analytical approximation to study the permeability tensor of anisotropic fibrous materials. Chan *et al.* [131, 132] used the transient radial flow method to measure the permeabilities of isotropic and orthotropic performs. They reported that the measured permeabilities increased with the injection flow rate and attributed this to a preferential channeling

© Woodhead Publishing Limited, 2010

of the liquid through the large pores rather than through the micro-pores within fiber tows in the experiment. Young and Wu [123] measured the permeability of bidirectional woven glass fabrics, and found the measured permeability to vary with the injection flow rate due to deformation of the fiber mat. Hammami *et al.* [133] studied the permeability tensor of woven fabrics undergoing shear deformation. Han *et al.* [143] developed a new procedure to measure the saturated permeability of anisotropic fiber preforms using radial flow under steady-state condition instead of the conventional transient condition. Kim and Daniel [145] reported that both the saturated and unsaturated permeabilities of unidirectional fiber mats depend on the flow rate, and the saturated permeability is higher than the unsaturated permeability.

A number of researchers have tried to use both the 1D and radial flow methods to characterize the permeability of anisotropic fiber mats [105, 126, 134–142, 144]. Some of these studies showed that the 1D and radial flow experiments generated consistent results [126, 134, 137, 141], while some reported some inconsistency between the two methods [136, 140].

It is clear from the cited literature that there are many discrepancies, sometimes even conflicts, among the reported results. Since there are no commercially available permeability-measuring devices, researchers in this field have to develop their own experimental permeability-measuring set-ups. As a result, there have been variations in the permeability values for the same material, measured using different experimental set-ups owned by diverse research groups. Therefore it is very important to quantify the accuracy of a permeability-measuring device. Some efforts have been made in the past to achieve this objective. Lundstrom *et al*. [127] used a bank of capillary tubes to provide reference permeability in one of the cavities of their four-cavity permeability-measuring set-up to reduce errors in pressure and viscosity measurements. Parnas *et al*. [136] proposed using 3D woven fabrics as reference porous media for calibrating various permeability-measuring set-ups employing different methods. The possibility of change in permeability of these reference fiber-mats due to changes in mat porosity during transportation and handling, and due to race-tracking during mold-filling because of incorrect shearing and placement of these materials, has reduced the usefulness of such reference materials. Morren *et al*. [149] described an artificial porous medium created using the stereolithography technique where the numerically estimated permeability of the reference medium is used to calibrate the permeability-measuring devices. This may be one of the best attempts to create a reference (anisotropic) porous medium for calibrating the permeability-measuring devices. Unfortunately, the method suffers from the disadvantage of high cost. Pillai *et al*. [150, 151] proposed to use two reference media to evaluate the performance of the permeability-measuring experimental set-ups. For the 1D flow set-up, the

© Woodhead Publishing Limited, 2010

reference medium is an aluminum plate consisting of 25 parallel cylindrical holes of 1 mm diameter whose theoretical permeability is computed through the Hagen–Poiseuille flow equation. For the radial flow set-up, the reference medium consists of two concentric annular slits whose permeability is estimated analytically and numerically. When these two reference media are installed in the 1D and radial flow permeability-measuring devices, the experimentally measured permeability can be compared with the *exact* permeability of the reference media obtained through theoretical and numerical means. This will allow the calibration of the 1D and radial flow set-ups. These two newly proposed reference media have several advantages, including easy fabrication, low costs, and having a constant, analytically known permeability.

3.5 Summary

In this chapter, the use of polymer composites for blast protection applications was discussed. Of the many possible technologies available to fabricate such composites, the liquid composites molding (LCM) processes were discussed in the greatest detail. Mold-filling simulations are very important for optimizing mold designs in LCM. The modeling of LCM in terms of the flow physics of resin flow in porous media, the corresponding heat and mass transfer issues, and modeling the resin cure, were reviewed extensively. The research progress made on modeling the resin flow through dual-scale fiber performs, used extensively in LCM, was reviewed as well. Since the permeability of fiber preforms is a very important parameter needed for simulating mold-filling in LCM, permeability measurement was reviewed in detail.

3.6 References

1 MCCONNEL V (2006), Ballistic protection materials a moving target. *Reinforced Plastics*, **50**(11), 20–25.
2 THERMOPLASTIC COMPOSITE ARMOUR (2008), *Reinforced Plastics*, **52**(3), 6.
3 BUCHAN P A and CHEN J F (2007), Blast resistance of FRP composites and polymer strengthened concrete and masonry structures – a state-of-the-art review. *Composites Part B: Engineering*, **38**(5–6), 509–522.
4 STRONG A B (2006), *Plastics: Materials and Processing*, 3rd edn, Columbus, OH: Pearson Education.
5 MAZUMDAR S K (2001), *Composites Manufacturing: Materials, Product, and Process Engineering*, New York: CRC Press LLC.
6 GUTOWSKI T G (ED.) (1997), *Advanced Composites Manufacturing*, New York: John Wiley & Sons.
7 PARNAS R S (2000), *Liquid Composite Molding*, Cincinnati, OH: Hanser Gardner Publications.

© Woodhead Publishing Limited, 2010

8 BRUSCHKE M V and ADVANI S G (1989), Numerical simulation of the resin transfer mold filling process, *Proceedings Society of Plastics Engineers 47th Annual Technical Conference*, New York, 1–4 May, 1769–1773.
9 BRUSCHKE M V and ADVANI S G (1990), Mold Filling of Generalized Newtonian Fluids in Anisotropic Porous Media. *Transport Phenomena in Material Processing, ASME Trans*, Seattle, WA, **132**, 149–158.
10 BRUSCHKE M V and ADVANI S G (1991), RTM: filling simulation of complex three dimensional shell-like structures. *SAMPE Quarterly*, **23**(1), 2–11.
11 CHAN A W and HWANG, S-T (1991), Modeling of the impregnation process during resin transfer molding. *Polymer Engineering & Science*, **31**(15), 1149–1156.
12 CHANG W and KIKUCHI N (1994), Adaptive remeshing method in the simulation of resin transfer molding (RTM) process. *Computer Methods in Applied Mechanics and Engineering*, **112**(1–4), 41–68.
13 CHIU H-T and LEE L J (2002), Simulation of liquid composite molding based on control-volume finite element method. *Journal of Polymer Engineering*, **22**(3), 155–175.
14 JIANG S, YANG L, ALSOLIBY S, *et al.* (2007), Pcg Solver and its computational complexity for implicit control-volume finite-element method of RTM mold filling simulation. *Composites Science and Technology*, **67**(15–16), 3316–3322.
15 JOSHI S C, LAM Y C and LIU X L (2000), Mass conservation in numerical simulation of resin flow. *Composites Part A: Applied Science and Manufacturing*, **31**(10), 1061–1068.
16 LAM Y C, JOSHI S C and LIU X L (2000), Numerical simulation of the mould-filling process in resin-transfer moulding. *Composites Science and Technology*, **60**(6), 845–855.
17 LIM S T and LEE W I (2000), Analysis of the three-dimensional resin-transfer mold filling process. *Composites Science and Technology*, **60**(7), 961–975.
18 LIN M and HAHN H T (1996), Robust and efficient approach for RTM simulation. *Advanced Materials*, **74**, 75–76.
19 LIN M, HAHN H T and HUH H (1998), Finite element simulation of resin transfer molding based on partial nodal saturation and implicit time integration. *Composites Part A: Applied Science and Manufacturing*, **29**(5–6), 541–550.
20 MAIER R S, ROHALY T F, ADVANI S G, *et al.* (1996), Fast numerical method for isothermal resin transfer mold filling. *International Journal for Numerical Methods in Engineering*, **39**(8), 1405–1417.
21 MOHAN R V, NGO N D and TAMMA K K (1999), Three-dimensional resin transfer molding: isothermal process modeling and explicit tracking of moving fronts for thick geometrically complex composites manufacturing applications – part 1. *Numerical Heat Transfer; Part A: Applications*, **35**(8), 815–838.
22 MOHAN R V, NGO N D and TAMMA K K (1999), On a pure finite-element-based methodology for resin transfer mold filling simulations. *Polymer Engineering and Science*, **39**(1), 26–43.
23 MOHAN R V, NGO N D, TAMMA K K, *et al.* (1999), Three-dimensional resin transfer molding: isothermal process modeling and implicit tracking of moving fronts for thick, geometrically complex composites manufacturing applications – part 2. *Numerical Heat Transfer; Part A: Applications*, **35**(8), 839–858.
24 PHELAN F R J R (1997), Simulation of the injection process in resin transfer molding. *Polymer Composites*, **18**(4), 460–476.

© Woodhead Publishing Limited, 2010

25 SHOJAEI A, GHAFFARIAN S R and KARIMIAN S M-H (2003), Numerical simulation of three-dimensional mold filling in resin transfer molding. *Journal of Reinforced Plastics and Composites*, **22**(16), 1497–1529.
26 SHOJAEI A, GHAFFARIAN S R and KARIMIAN S M H (2002), Numerical simulation of three-dimensional mold filling process in resin transfer molding using quasi-steady state and partial saturation formulations. *Composites Science and Technology*, **62**(6), 861–879.
27 TROCHU F, BOUDREAULT J F, GAO D M, *et al.* (1995), Three-dimensional flow simulations for the resin transfer molding process. *Materials and Manufacturing Processes*, **10**(1), 21–26.
28 TROCHU F, GAUVIN R and GAO D M (1993), Numerical analysis of the resin transfer molding process by the finite element method. *Advances in Polymer Technology*, **12**(4), 329–342.
29 VARMA R R and ADVANI S G (1994), Three-dimensional simulations of filling in resin transfer molding. *ASME FED*, Chicago, IL, **200**, 21–27.
30 VOLLER V R and CHEN Y F (1996), Prediction of filling times of porous cavities. *International Journal for Numerical Methods in Fluids*, **23**(7), 661–672.
31 VOLLER V R and PENG S (1995), Algorithms for analysis of polymer filling of molds. *Polymer Engineering and Science*, **35**(22), 1758–1765.
32 VOLLER V R, PENG S and CHEN Y F (1996), Numerical solution of transient, free surface problems in porous media. *International Journal for Numerical Methods in Engineering*, **39**(17), 2889–2906.
33 WANG T J, LEE L J and YOUNG W B (1995), Control volume finite element method for mold filling simulation. *International Polymer Processing*, **10**(1), 82.
34 WU C H, CHIU H-T, LEE L J, *et al.* (1998), Simulation of reactive liquid composite molding using an Eulerian–Lagrangian approach. *International Polymer Processing*, 4, 398–397.
35 YOUNG W B, HAN K, FONG L H, *et al.* (1991), Flow simulation in molds with preplaced fiber mats. *Polymer Composites*, **12**(6), 391–403.
36 YOUNG W B, RUPEL K, HAN K, *et al.* (1991), Analysis of resin injection molding in molds with preplaced fiber mats. II: numerical simulation and experiments of mold filling. *Polymer Composites*, **12**(1), 30–38.
37 BECKER A A (1992), *The Boundary Element Method in Engineering: A Complete Course*. London, UK: McGraw-Hill International (UK) Limited.
38 SCHMIDT F M, LAFLEUR P, BERTHET F, *et al.* (1999), Numerical simulation of resin transfer molding using linear boundary element method. *Polymer Composites*, **20**(6), 725–732.
39 SOUKANE S and TROCHU F (2006), Application of the level set method to the simulation of resin transfer molding. *Composites Science and Technology*, **66**(7–8), 1067–1080.
40 UM M-K and LEE W I (1990), Numerical simulation of resin transfer molding process using boundary element method, *The 35th International SAMPE Symposium Proceedings*, Anaheim, CA, **35**, 1905–1916.
41 YOO Y-E and LEE W I (1996), Numerical simulation of the resin transfer mold filling process using the boundary element method. *Polymer Composites*, **17**(3), 368–374.
42 FRIEDRICHS B and GUCERI S I (1995), Hybrid numerical technique to model 3-D flow fields in resin transfer molding processes. *Polymer Engineering and Science*, **35**(23), 1834–1851.

© Woodhead Publishing Limited, 2010

43 FRIEDRICHS B, GUCERI S I, SUBBIAH S, *et al.* (1990), Simulation and analysis of mold filling processes with polymer-fiber composites. Tgmold. *Proceedings of Polymers and Polymeric Composites, ASME Winter annual meeting*, Dallas, TX, **19**, 73–90.
44 GAUVIN R and TROCHU F (1993), Comparison between numerical and experimental results for mold filling in resin transfer molding. *Plastics, Rubber and Composites Processing and Applications*, **19**(3), 151–157.
45 KUAN Y-D and EL-GIZAWY A S (2000), Numerical characterization of mold injection in resin transfer molding process. *Advances in Polymer Technology*, **19**(3), 173–179.
46 LI S and GAUVIN R (1991), Numerical analysis of the resin flow in resin transfer molding. *Journal of Reinforced Plastics and Composites*, **10**(3), 314–327.
47 PANITAPU R, JIANG S, MINAIE B, GOU J. (2004), *Time-Implicit Simulation of Filling Pattern in Resin Transfer Molding Using Control Volume Finite Difference Method. 49th International SAMPE Symposium*, Long Beach, CA, 16–20 May, **49**, 503–512.
48 TROCHU F and GAUVIN R (1992), Limitations of a boundary-fitted finite difference method for the simulation of the resin transfer molding process. *Journal of Reinforced Plastics and Composites*, **11**(7), 772–786.
49 BRUSCHKE M V and ADVANI S G (1994), Numerical approach to model non-isothermal viscous flow through fibrous media with free surfaces. *International Journal for Numerical Methods in Fluids*, **19**(7), 575–603.
50 CHAN A W and HWANG S-T (1992), Modeling nonisothermal impregnation of fibrous media with reactive polymer resin. *Polymer Engineering & Science*, **32**(5), 310–318.
51 CHANG W and KIKUCHI N (1995), Analysis of non-isothermal mold filling process in resin transfer molding (RTM) and structural reaction injection molding (Srim). *Computational Mechanics*, **16**(1), 22–35.
52 CHIU H-T, YU B, CHEN S C, *et al.* (2000), Heat transfer during flow and resin reaction through fiber reinforcement. *Chemical Engineering Science*, **55**(17), 3365–3376.
53 DESSENBERGER R B and TUCKER C L (1995), Thermal dispersion in resin transfer molding. *Polymer Composites*, **16**(6), 495–506.
54 HENZ B J, TAMMA K K, MOHAN R V, *et al.* (2005), Process modeling of composites by resin transfer molding: sensitivity analysis for non-isothermal considerations. *International Journal of Numerical Methods for Heat and Fluid Flow*, **15**(7), 631–653.
55 KANG M K, LEE II W, YOO J Y, *et al.* (1995), Simulation of mold filling process during resin transfer molding. *Journal of Materials Processing and Manufacturing Science*, **3**(3), 297–313.
56 LEE L J, YOUNG W B and LIN R J (1994), Mold filling and cure modeling of RTM and Srim processes. *Composite Structures*, **27**(1–2), 109–120.
57 LIN R J, LEE L J and LIOU M J (1993), Mold filling and curing analysis liquid composite molding. *Polymer Composites*, **14**(1), 71–81.
58 LIU B and ADVANI S G (1995), Operator splitting scheme for 3-D temperature solution based on 2-D flow approximation. *Computational Mechanics*, **16**(2), 74–82.
59 MAL O, COUNIOT A and DUPRET F (1998), Non-isothermal simulation of the resin transfer moulding process. *Composites Part A: Applied Science and Manufacturing*, **29**(1–2), 189–198.

© Woodhead Publishing Limited, 2010

60 NGO N D and TAMMA K K (1999), Non-isothermal '2-D flow/3-D thermal' developments encompassing process modeling of composites: flow/thermal/cure formulations and validations. *International Journal for Numerical Methods in Engineering*, **50**(7): 1559–1585.
61 SHOJAEI A, GHAFFARIAN S R and KARIMIAN S M H (2003), Simulation of the three-dimensional non-isothermal mold filling process in resin transfer molding. *Composites Science and Technology*, **63**(13), 1931–1948.
62 SHOJAEI A, GHAFFARIAN S R and KARIMIAN S M H (2004), Three-dimensional process cycle simulation of composite parts manufactured by resin transfer molding. *Composite Structures*, **65**(3–4), 381–390.
63 YOUNG W-B (1994), Three-dimensional nonisothermal mold filling simulations in resin transfer molding. *Polymer Composites*, **15**(2), 118–127.
64 YOUNG W-B (1995), Thermal behaviors of the resin and mold in the process of resin transfer molding. *Journal of Reinforced Plastics and Composites*, **14**(4), 310.
65 ZIENKIEWICZ O C and GODBOLE P N (1974), Flow of plastic and visco-plastic solids with special reference to extrusion and forming processes. *International Journal for Numerical Methods in Engineering*, **8**(1), 3–16.
66 HARLOW F H and WELCH J E (1965), Numerical calculation of time-dependent viscous incompressible flow of fluid with free surface. *Physics of Fluids*, **8**(12), 2182–2189.
67 GUTFINGER C, BROYER E and TADMOR Z (1974), Analysis of a cross head die with the flow analysis network (FAN) method. *Polymer Engineering and Science*, **15**(5), 381–385.
68 THOMPSON E (1986), Use of pseudo-concentrations to follow creeping viscous flows during transient analysis. *International Journal for Numerical Methods in Fluids*, **6**(10), 749–761.
69 HIRT C W and NICHOLS B D (1981), Volume of fluid (VOF) method for the dynamics of free boundaries. *Journal of Computational Physics*, **39**(1), 201–225.
70 TADMOR Z, BROYER E and GUTFINGER C (1974), Flow analysis network (FAN) – a method for solving flow problems in polymer processing. *Polymer Engineering & Science*, **14**(9), 660–665.
71 RIDER W J and KOTHE D B (1998), Reconstructing volume tracking. *Journal of Computational Physics*, **141**(2), 112.
72 WARSI Z U A and THOMPSON J F (1990), Application of variational methods in the fixed and adaptive grid generation. *Computers & Mathematics with Applications*, **19**(8–9), 31–41.
73 BALIGA B R and PATANKAR S V (1980), New finite-element formulation for convection–diffusion problems. *Numerical Heat Transfer*, **3**(4), 393–409.
74 BALIGA B R and PATANKAR S V (1983), Control volume finite–element method for two-dimensional fluid flow and heat transfer. *Numerical Heat Transfer*, **6**(3), 245–261.
75 TUCKER C L and DESSENBERGER R B (1994), Governing equations for flow through stationary fiber beds, in Advani, S G (ed.), *Flow and Rheology in Polymer Composites Manufacturing*, Amsterdam, the Netherlands: Elsevier, 257–324.
76 BROOKS A N and HUGHES T J R (1990), Streamline upwind/Petrov. Galerkin formulations for convection dominated flows with particular emphasis on the incompressible Navier-Stokes equations. *Computer Methods in Applied Mechanics and Engineering*, 199–259.

© Woodhead Publishing Limited, 2010

77 TAN H, ROY T and PILLAI K M (2007), Variations in Unsaturated Flow with Flow Direction in Resin Transfer Molding: An Experimental Investigation. *Composites Part A: Applied Science and Manufacturing*, **38**(8), 1872–1892.
78 PARNAS R S and PHELAN F R JR (1991), Effect of heterogeneous porous media on mold filling in resin transfer molding. *SAMPE Quarterly*, **22**(2), 53–60.
79 PARNAS R S, SALEM A J, SADIQ T A K, *et al.* (1994), Interaction between micro- and macro-scopic flow in RTM preforms. *Composite Structures*, **27**(1–2), 93–107.
80 SADIQ T A K, ADVANI S G and PARNAS R S (1995), Experimental investigation of transverse flow through aligned cylinders. *International Journal of Multiphase Flow*, **21**(5), 755–774.
81 BINETRUY C, HILAIRE B and PABIOT J (1997), Interactions between flows occurring inside and outside fabric tows during RTM. *Composites Science and Technology*, **57**(5), 587–596.
82 DE PARSEVAL Y, PILLAI K M and ADVANI S G (1997), Simple model for the variation of permeability due to partial saturation in dual scale porous media. *Transport in Porous Media*, **27**(3), 243–264.
83 SLADE J, PILLAI K M and ADVANI S G (2001), Investigation of unsaturated flow in woven, braided and stitched fiber mats during mold-filling in resin transfer molding. *Polymer Composites*, **22**(4), 491–505.
84 DUNGAN F D and SASTRY A M (2002), Saturated and unsaturated polymer flows: microphenomena and modeling. *Journal of Composite Materials*, **36**(13), 1581–1603.
85 BREARD J, HENZEL Y, TROCHU F, *et al.* (2003), Analysis of dynamic flows through porous media. Part I: comparison between saturated and unsaturated flows in fibrous reinforcements. *Polymer Composites*, **24**(3), 391–408.
86 BABU B Z and PILLAI K M (2004), Experimental investigation of the effect of fiber-mat architecture on the unsaturated flow in liquid composite molding. *Journal of Composite Materials*, **38**(1), 57–79.
87 KUENTZER N, SIMACEK S G, ADVANI, *et al.* (2006), Permeability characterization of dual scale fibrous porous media. *Composites Part A: Applied Science and Manufacturing*, **37**(11), 2057–2068.
88 BINETRUY C, HILAIRE B and PABIOT J (1998), Tow impregnation model and void formation mechanisms during RTM. *Journal of Composite Materials*, **32**(3), 223–245.
89 CHAN A W and MORGAN R J (1993), Tow impregnation during resin transfer molding of bi-directional nonwoven fabrics. *Polymer Composites*, **14**(4), 335–340.
90 CHANG C-Y and HOURNG L-W (1998), Numerical simulation for the transverse impregnation in resin transfer molding. *Journal of Reinforced Plastics and Composites*, **17**(2), 165–182.
91 LEKAKOU C and BADER M G (1998), Mathematical modelling of macro- and micro-infiltration in resin transfer moulding (RTM). *Composites Part A: Applied Science and Manufacturing*, **29**(1–2), 29–37.
92 PILLAI K M and ADVANI S G (1998), A model for unsaturated flow in woven fiber preforms during mold filling in resin transfer molding. *Journal of Composite Materials*, **32**(19), 1753–1783.
93 YOUNG W-B (1996), The effect of surface tension on tow impregnation of unidirectional fibrous preform in resin transfer molding. *Journal of Composite Materials*, **30**(11), 1191–1209.

© Woodhead Publishing Limited, 2010

94 CHANG C-Y (2003), Tow impregnation of unidirectional fibrous preform during resin transfer molding. *Journal of Reinforced Plastics and Composites*, **22**(11), 1003–1016.
95 DIMITROVOVA Z and ADVANI S G (2004), Free boundary viscous flows at micro and mesolevel during liquid composites moulding process. *International Journal for Numerical Methods in Fluids*, **46**(4), 435–455.
96 YANG J, JIA Y, SUN S, *et al.* (2006), Mesoscopic simulation of the impregnating process of unidirectional fibrous preform in resin transfer molding. *Materials Science and Engineering A*, **435–436**, 515–520.
97 FOLEY M E and GILLESPIE J W JR (2005), Modeling the effect of fiber diameter and fiber bundle count on tow impregnation during liquid molding processes. *Journal of Composite Materials*, **39**(12), 1045–1065.
98 NGO N D and TAMMA K K (2001), Microscale permeability predictions of porous fibrous media. *International Journal of Heat and Mass Transfer*, **44**(16), 3135–3145.
99 NGO N D and TAMMA K K (2004), Complex three-dimensional microstructural permeability prediction of porous fibrous media with and without compaction. *International Journal for Numerical Methods in Engineering*, **60**(10), 1741–1757.
100 NORDLUND M and LUNDSTROM T S (2005), Numerical study of the local permeability of noncrimp fabrics. *Journal of Composite Materials*, **39**(10), 929–947.
101 PHELAN F R, JR (1991), Modeling of microscale flow in fibrous porous media. *Journal of Thermoplastic Composite Materials*, **7**(3), 208–218.
102 PHELAN F R JR, LEUNG, Y and PARNAS R S (1994), Modeling of microscale flow in unidirectional fibrous porous media. *Journal of Thermoplastic Composite Materials*, **7**(3), 208–218.
103 PHELAN F R JR, and WISE G (1996), Analysis of transverse flow in aligned fibrous porous media. *Composites Part A: Applied Science and Manufacturing*, **27**(1), 25.
104 PILLAI K M and ADVANI S G (1995), Numerical and analytical study to estimate the effect of two length scales upon the permeability of a fibrous porous medium. *Transport in Porous Media*, **21**(1), 1–17.
105 RANGANATHAN S, ADVANI S G, WISE G M, *et al.* (1994), A numerical and experimental study of the permeability of fiber preforms. *10th Annual ASM/ESD Advanced Composites Conference*, Dearborn, MI, 7–10 November, 1994, 309–319.
106 SONG Y S, CHUNG K, KANG T J, *et al.* (2003), Prediction of permeability tensor for plain woven fabric by using control volume finite element method. *Polymers and Polymer Composites*, **11**(6), 465–476.
107 SONG Y S, CHUNG K, KANG T J, *et al.* (2004), Prediction of permeability tensor for three dimensional circular braided preform by applying a finite volume method to a unit cell. *Composites Science and Technology*, **64**(10–11), 1629–1636.
108 NEDANOV P B and ADVANI S G (2002), Numerical computation of the fiber preform permeability tensor by the homogenization method. *Polymer Composites*, **23**(5), 758–770.
109 SPAID M A A and PHELAN J F (1997), Lattice Boltzmann methods for modeling microscale flow in fibrous porous media. *Physics of Fluids*, **9**(9), 2468–2474.
110 PILLAI K M (2002), Governing equations for unsaturated flow through woven fiber mats. Part 1. Isothermal flows. *Composites Part A: Applied Science and Manufacturing*, **33**(7), 1007–1019.

© Woodhead Publishing Limited, 2010

111 PILLAI K M and MUNAGAVALASA M S (2004), Governing equations for unsaturated flow through woven fiber mats. Part 2. Non-isothermal reactive flows. *Composites Part A: Applied Science and Manufacturing*, **35**(4), 403–415.
112 WANG Y and GROVE S M (2008), Modelling microscopic flow in woven fabric reinforcements and its application in dual-scale resin infusion modelling. *Composites Part A: Applied Science and Manufacturing*, **39**(5), 843–855.
113 WANG Y, MOATAMEDI M and GROVE S M (2009), Continuum dual-scale modeling of liquid composite molding processes. *Journal of Reinforced Plastics and Composites*, **28**(12), 1469–1484.
114 JADHAV R S and PILLAI K M (2003), Numerical study of heat transfer during unsaturated flow in dual-scale porous media. *Numerical Heat Transfer; Part A: Applications*, **43**(4), 385–407.
115 PILLAI K M and JADHAV R S (2005), A numerical study of nonisothermal reactive flow in a dual-scale porous medium under partial saturation. *Numerical Heat Transfer; Part A: Applications*, **47**(2), 109–136.
116 PILLAI K M and ADVANI S G (1998), Numerical simulation of unsaturated flow in woven fiber preforms during the resin transfer molding process. *Polymer Composites*, **19**(1), 71–80.
117 SIMACEK and ADVANI S G (2003), A numerical model to predict fiber tow saturation during liquid composite molding. *Composites Science and Technology*, **63**(12), 1725–1736.
118 WILLIAMS J G, MORRIS C E M and ENNIS b c (1974), Liquid flow through aligned fiber beds. *Polymer Engineering & Science*, **14**(6), 413–419.
119 GUTOWSKI T G, CAI Z, BAUER S, *et al.* (1987), Consolidation experiments for laminate composites. *Journal of Composite Materials*, **21**(7), 650–669.
120 GAUVIN R, CHIBANI M and LAFONTAINE P (1987), Modeling of pressure distribution in resin transfer molding. *Journal of Reinforced Plastics and Composites*, **6**(4), 367–377.
121 TREVINO L, RUPEL K, YOUNG W B, *et al.* (1991), Analysis of resin injection-molding in molds with preplaced fiber mats. Part 1: permeability and compressibility measurements. *Polymer Composites*, **12**(1), 20–29.
122 GEBART B R (1992), Permeability of unidirectional reinforcements for RTM. *Journal of Composite Materials*, **26**(8), 1100–1133.
123 YOUNG W B and WU S F (1995), Permeability measurement of bidirectional woven glass fibers. *Journal of Reinforced Plastics and Composites*, **14**(10), 1108–1120.
124 FERLAND P, GUITTARD D and TROCHU F (1996), Concurrent methods for permeability measurement in resin transfer molding. *Polymer Composites*, **17**(1), 149–158.
125 HAMMOND V H and LOOS A C (1997), The effects of fluid type and viscosity on the steady-state and advancing front permeability behavior of textile preforms. *Journal of Reinforced Plastics and Composites*, **16**(1), 50–72.
126 GEBART B R and LIDSTROM P (1996), Measurement of in-plane permeability of anisotropic fiber reinforcements. *Polymer Composites*, **17**(1), 43–51.
127 LUNDSTROM T S, GEBART B R and SANDLUND E (1999), In-plane permeability measurements on fiber reinforcements by the multi-cavity parallel flow technique. *Polymer Composites*, **20**(1), 146–154.
128 MA Y L and SHISHOO R (1999), Permeability characterization of different architectural fabrics. *Journal of Composite Materials*, **33**(8), 729–750.

© Woodhead Publishing Limited, 2010

129 SHOJAEI A, TROCHU F, GHAFFARIAN S R, *et al.* (2004), An experimental study of saturated and unsaturated permeabilities in resin transfer molding based on unidirectional flow measurements. *Journal of Reinforced Plastics and Composites*, **23**(14), 1515–1536.
130 ADAMS K L, MILLER B and REBENFELD L (1986), Forced in-plane flow of an epoxy resin in fibrous networks. *Polymer Engineering and Science*, **26**(20), 1434–1441.
131 CHAN A W and HWANG S T (1991), Anisotropic in-plane permeability of fabric media. *Polymer Engineering & Science*, **31**(16), 1233–1239.
132 CHAN A W, LARIVE D E and MORGAN R J (1993), Anisotropic permeability of fiber preforms: constant flow rate measurement. *Journal of Composite Materials*, **27**(10), 996–1008.
133 HAMMAMI A, TROCHU F, GAUVIN R, *et al.* (1996), Directional permeability measurement of deformed reinforcement. *Journal of Reinforced Plastics and Composites*, **15**(6), 552–562.
134 PARNAS R S and SALEM A J (1993), A comparison of the unidirectional and radial inplane flow of fluids through woven composite reinforcements. *Polymer Composites*, **14**(5), 383–394.
135 PARNAS R S, SALEM A J, SADIQ T A K, *et al.* (1994), The interaction between microscopic and macroscopic flow in RTM preforms. *Composite Structures*, **27**(1–2), 93–107.
136 PARNAS R S, HOWARD J G, LUCE T L, *et al.* (1995), Permeability characterization. Part 1: a proposed standard reference fabric for permeability. *Polymer Composites*, **16**(6), 429–445.
137 AHN S H, LEE W I and SPRINGER G S (1995), Measurement of the 3-dimensional permeability of fiber preforms using embedded fiber optic sensors. *Journal of Composite Materials*, **29**(6), 714–733.
138 WANG T J, WU C H and LEE L J (1994), In-plane permeability measurement and analysis in liquid composite molding. *Polymer Composites*, **15**(4), 278–288.
139 GAUVIN R, TROCHU F, LEMENN Y, *et al.* (1996), Permeability measurement and flow simulation through fiber reinforcement. *Polymer Composites*, **17**(1), 34–42.
140 LEKAKOU C, JOHARI M A K, NORMAN D, *et al.* (1996), Measurement techniques and effects on in-plane permeability of woven cloths in resin transfer moulding. *Composites Part A Applied Science and Manufacturing*, **27**(5), 401–408.
141 LAI Y H, KHOMAMI B and KARDOS J L (1997), Accurate permeability characterization of preforms used in polymer matrix composite fabrication processes. *Polymer Composites*, **18**(3), 368–377.
142 PARNAS R S, FLYNN K M and DALFAVERO M E (1997), A permeability database for composites manufacturing. *Polymer Composites*, **18**(5), 623–633.
143 HAN K K, LEE C W and RICE B P (2000), Measurements of the permeability of fiber preforms and applications. *Composites Science and Technology*, **60**(12–13), 2435–2441.
144 LUNDSTROM T S, STENBERG R, BERGSTROM R, *et al.* (2000), In-plane permeability measurements: A Nordic round-robin study. *Composites Part A: Applied Science and Manufacturing*, **31**(1), 29–43.
145 KIM S K and DANIEL I M (2007), Observation of permeability dependence on flow rate and implications for liquid composite molding. *Journal of Composite Materials*, **41**(7), 837–849.

© Woodhead Publishing Limited, 2010

146 BICKERTON S and ADVANI S G (1999), Characterization and modeling of race-tracking in liquid composite molding processes. *Composites Science and Technology*, **59**(15), 2215–2229.

147 LAWRENCE J M, BARR J, KARMAKAR R, *et al.* (2004), Characterization of preform permeability in the presence of race tracking. *Composites Part A: Applied Science and Manufacturing*, **35**(12), 1393–1405.

148 YOUNG W-B and LAI C-L (1997), Analysis of the edge effect in resin transfer molding. *Composites Part A: Applied Science and Manufacturing*, **28**(9–10), 817–822.

149 MORREN G, GU J, SOL H, *et al.* (2006), Stereolithography specimen to calibrate permeability measurements for RTM flow simulations. *Advanced Composites Letters*, **15**(4), 119–125.

150 ROY T, TAN H and PILLAI K M (2007), A method to estimate the accuracy of 1-D flow based permeability measuring devices. *Journal of Composite Materials*, **41**(17), 2037–2055.

151 TAN H, ROY T and PILLAI K M (2007), Calibration of 1-D flow and radial flow based permeability measuring devices. In Vizzini A J, Joyce P J and Beckwith S W (eds), *SAMPE*. Baltimore, MD.

© Woodhead Publishing Limited, 2010

4

High energy absorbing materials for blast resistant design

M. YANG, University of Texas, USA; and P. QIAO, Washington State University, USA

Abstract: High blast absorbing materials have been consistently sought by the US Departments of Defense and Homeland Security, especially after 9.11. These materials can be used to effectively absorb blast wave energies and impact impulses and protect human lives and properties under extreme blasting events. The chapter reviews the current research status, outlines design philosophy for blast resistant design, and points to several case studies for using advanced materials and technology for blast mitigation, such as metal and foam sandwich panels, magneto-rheological fluids, and porous shape memory alloy.

Key words: blast absorbing materials, composites, sandwich, shape memory alloy, shear resistant fluids.

4.1 Introduction

High blast absorbing materials have been consistently sought by the US Departments of Defense and Homeland Security, especially after 9.11. These materials can be used to effectively absorb blast wave energies and impact impulses and protect human lives and properties under extreme blasting events.

Applicable examples, such as armors, temporary military shelters, body shells of tanks, etc., are frequently exposed to explosive forces. The materials used in these structures pose great demand for high energy absorption. During the 1990s, most of these structures were made from metal (e.g., steel) plates, some with ceramic tiles to blunt the projectiles. However, steel plates are heavy, which reduces the mobility of the structures designed. With recent advances in polymer matrix composites (PMCs) and high-strength foams, the materials used in blast resistant design have been significantly expanded.

4.1.1 Advanced composites as blast absorbing materials

Fiber composites, foams, magneto-rheological (MR) fluids, and porous materials are typical high energy absorbing materials. Fiber composites,

© Woodhead Publishing Limited, 2010

like carbon fibers, have relative higher stiffness and strength and lightweight compared to their steel counterpart. Foams and MR fluids are also typical energy absorbing materials. Crushing of metal cores in plasticity or shear damping in rheological fluids dissipate the input kinetic energy. Recently, a new type of foam, named coal-based carbon foam, has been invented (http://www.smdc.army.mil/FactSheets/Coal-basedCarbonFoam.pdf), and it shows a unique response to high energy blasts. The microstructure of the material resembles the structure of pumice, a common material used to absorb blast energy. A unique advantage of the coal-based carbon foam is that the strength of the material can be precisely controlled and matched to the strength of the specific energy mitigation needed. In addition, it can be integrated with highly elastic polymers and hardened materials to form a new and state-of-the art coal energy absorbing system (CEAS).

4.1.2 Multilayer and sandwich structures

Multilayer and sandwich materials are also typical armor structures used for blasting and impact protection (Qiao *et al.*, 2008). Sandwich systems represent a combination of different components and have the advantages of miscellaneous materials, e.g., low density of core, high bend resistance of face sheet and core combination, sound and vibration insulation, high energy absorption, high load-capacity at a low weight, etc. They have been used as the primary energy absorbing materials in naval and military structures.

4.2 Advanced and new materials for impact and energy absorption

New and advanced materials are increasingly being used to develop viable and high energy absorbing structures for impact and blast mitigation and protection. Polymer matrix composites and sandwich structures with inherent energy absorbing capability have been frequently employed in military applications to resist blast and ballistic impact. Novel lattice or truss structures with or without waiting links can also be considered in potential blast mitigation and armor design. Magneto-rheological (MR) fluids and porous shape memory alloys (SMA), commonly used in automobile and other industries for damping and energy dissipation, have found applications in blast and impact resistant design. In the following, a literature review on advanced and new materials for impact and energy absorption is provided, and the need for developing high energy and effective blast absorbing materials is briefly elaborated.

© Woodhead Publishing Limited, 2010

4.2.1 Literature review

Strain rate-dependent metal plates and polymer matrix composites

Metal plates and PMCs are the earliest materials used for personal protection for the defeat of arm projectiles and blasting, and as backing plates, usually with ceramics, against larger projectiles and blast fragments. PMCs combine the beneficial properties of both polymer resins (ability to absorb and mitigate kinetic energy) and high-performance fibers (high to ultrahigh elastic modulus and strength), possess higher specific strengths (ultimate tensile strength divided by density) than their metal counterparts, and are capable of providing equivalent ballistic protection at reduced weights. PMCs utilized for armor applications include fiberglass, aramid fiber, braided and woven composites, and polyethylene fiber composites. Shim *et al*. (1995) conducted research on modeling deformation and damage characteristics of woven fabric under small projectile impact, in which the deformation and damage of woven fabric composites were simulated. Ambur *et al*. (2001) developed numerical simulations of high-energy impact over thin metal plates, in which the penetration and perforation process of the projectile over the metal plate were analyzed. Lee *et al*. (2003) developed an advanced body armor system utilizing shear thickening fluids, which improves the ballistic penetration resistance of Kevlar® fabric composites. Hogg (2006) summarized current developments in using composites in armors and concluded that the current design of composite armor systems relies on experience, empiricism, and intuition to a great extent.

Under high-velocity impact, the deformation response of the PMC can be highly strain rate-dependent and non-linear. Most of the existing analytical models and numerical software, which assume the deformation of the materials to be independent of strain rate and often linear, are incapable of simulating strain rate-dependent deformation and non-linearity caused by the high strain rate impact (Goldberg *et al.*, 2008). Several studies have been conducted to experimentally characterize the strain rate-dependent behavior of resin or PMC and to develop associated constitutive models, which can be incorporated into the micromechanics models and the non-linear finite element analysis (e.g., non-linear finite element code LS-DYNA®) for the high-velocity impact analysis of PMC structures.

Polymer matrix is well known to have a strain rate-dependent deformation response. Daniel *et al.* (1995) studied the strain rate dependence and non-linearity of carbon/epoxy composites and concluded that the strain rate dependence and non-linearity are primarily driven by the epoxy matrix. The constitutive equations of metals based on plasticity and viscoplasticity were often adapted to model the non-linear and strain rate-dependent deformation of polymer (Bordonaro, 1995; Goldberg *et al.*, 2005). For example, the viscoplasticity theories were developed to account

© Woodhead Publishing Limited, 2010

for hydrostatic stress in the non-linear deformation response by applying variation of the Drucker–Prager yield criterion through modifying the definitions of the effective stress and effective inelastic strain (Li and Pan, 1990; Chang and Pan, 1997; Goldberg *et al.*, 2005). Using the above modification, Goldberg *et al.* (2005) developed the non-linear constitutive model to account for the strain rate dependence and non-linearity of the matrix and then implemented it into a micromechanics model to obtain the effective composite deformation response under different loading rates. Goldberg *et al.* (2008) further revised the analytical model in Goldberg *et al.* (2005) to account for the non-linear unloading behavior while still including the effects of hydrostatic stresses on the non-linear deformation.

Gilat *et al.* (2005) used small dogbone-shaped samples for tensile tests and short hollow cylinders for shear tests to obtain the stress–strain curves of epoxy resins at both low and high strain rates. Epoxy resins under tension, compression, and shear are experimentally characterized using a full field optical technique for strain measurement, and the stress–strain curves over a wide range of strain rates (10^{-5}/sec–10^{-1}/sec) and temperature (room temperature to 80 °C) are obtained in Littell *et al.* (2008). The full set of experimental data is useful for defining the internal state variables that can be used in the constitutive models for impact analysis (Goldberg *et al.*, 2005).

The experimental strain rate-dependent data of polymer matrix and strain rate-dependent, non-linear constitutive models are often implemented into micromechanics models to obtain effective composite properties, which are then input into the non-linear finite element code (e.g., LS-DYNA®) for impact and failure analysis of composite structures. Zheng and Binienda (2007) adapted the state variable-based viscoplastic equations and implemented them in strength of materials-based micromechanics models to predict the non-linear and strain rate-dependent deformation of the PMC. In their study, the state variable-based viscoplastic equations originally developed for metals were modified in order to account for the effects of hydrostatic stresses, which are significant in polymers. The polymer and composite models as rate-dependent shell elements were implemented into explicit finite element code LS-DYNA® as user defined materials (UMATs). Cheng and Binienda (2008) proposed a simplified methodology to model two-dimensional (2D) triaxially braided composite plates impacted by a soft projectile using an explicit non-linear finite element analysis code LS-DYNA®. The numerical finite element model captured the penetration threshold, deformation behavior, and failure of two different 2D triaxial braided composites with different fiber architectures.

The continuum models that only consider strain rate effects cannot provide answers about failure regime of PMCs and metal plates. For impact applications, one has to include the energy dissipation mechanisms. The

© Woodhead Publishing Limited, 2010

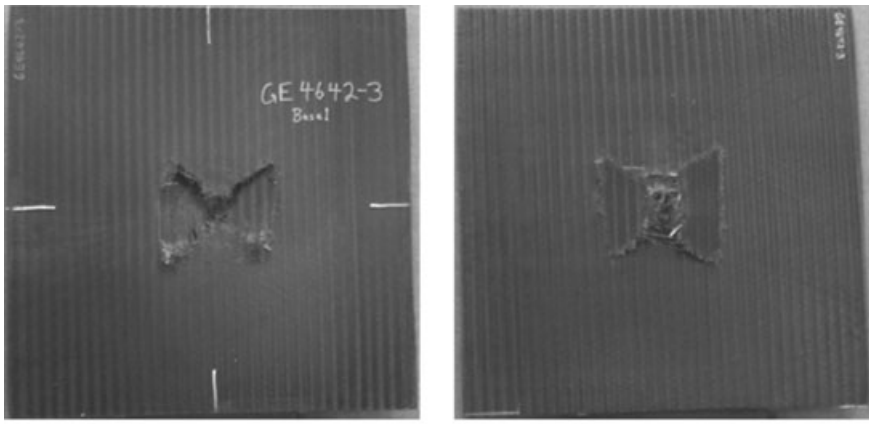

4.1 (a) and (b) The failure modes of a braided composite impacted by a projectile at 192 m/s (Cheng and Binienda, 2006).

energy dissipating mechanisms with this type of materials are: formation of inter-laminar cracks, breakage of fibers, shear-away of lamina bundles and debris, and plastic deformation. Figure 4.1 shows a typical multilayer braided composite system with different failure modes (Binienda, 2004; Cheng and Binienda, 2006). Predicting failure and energy dissipation capacity of composite materials is far from being achieved. Cox and Yang (2006) gave a general review for modeling failure mechanisms of structural composites and emphasize the difficult challenges of simulating diffuse and complex fracture patterns observed in these materials. Zhu *et al.* (2008) defined a new failure model capable of characterizing different failure modes of rate-dependent PMC laminates under high-velocity impact. Shear failure, delamination, and tearing failure were addressed, and the three-dimensional (3D) micromechanics model with damage (Zhu *et al.*, 2006) was implemented in the non-linear finite element code LS-DYNA® to analyze the penetration of composite laminates subjected to high-velocity impact. The new peridynamic method offers potential to resolve some of these challenges (see Xu *et al.*, 2008) by discarding the continuum assumption used in classical mechanics.

Composite and sandwich structures for blasting protection

Composite and sandwich structures are lightweight and capable of absorbing high impact energy absorption. These materials are sensitive to impact damage, and they absorb kinetic energy through induced large deformation and materials failure. The majority of impact studies on composite and

© Woodhead Publishing Limited, 2010

sandwich structures focused on the following four aspects: (i) dynamic response, (ii) contact mechanism of composite and sandwich structures with foreign objects, (iii) damage and failure modes of composite and sandwich structures under impact, and (iv) effects of anisotropy and special core structures on impact responses. In this section we review the literature particularly on damage and failure due to impact on composite and sandwich structures.

The impact damage and impact resistance of laminates and sandwich structures have been extensively investigated (see, e.g., Caprino and Teti, 1994; Thomsen, 1995; Tsai *et al.*, 1998; Turk and Hoo-Fatt, 1999). Dobyns and Porter (1981) proposed the prediction of the overall damage size of a carbon composite plate subjected to a low-velocity impact using elastic numerical results. Matemilola and Strong (1995) conducted an analytical study about impact-induced dynamic deformation and stresses in carbon fiber-reinforced polymer (CFRP) composites, which provides a stress analysis tool for further damage assessment. Davies *et al.* (1995) developed a simple mode-II fracture analysis for single circular delamination by treating glass fiber-reinforced polymer (GFRP) composite as an isotropic material and showed that a threshold force P_c could be used to find the initiation of delamination. Reid and Zhou (2000) performed several experiments on the initiation of delamination and damage size from the impact process, exhibiting that the critical delamination force or energy could be observed from the contact force history curve. Lim *et al.* (2004) captured the dynamic failure process of a foam sandwich subjected to a foreign object impact using a high-speed camera (Fig. 4.2), from which the failure mechanism involved in the impact event, i.e., core shear failure, debonding between the face sheets and core material, and face sheet tensile failure, was clearly depicted. Shipsha *et al.* (2003) studied failure mechanism and modeling of impact damage in sandwich beams through an experimental investigation, and the different failure modes involved were characterized. Lim *et al.* (2004) investigated failure modes of foam core sandwich beams under static and impact loads. Different failure modes of sandwiches with different density and face sheet dimensions under different impact velocities were characterized.

The dynamic response of sandwich structures with aluminum foam cores was analyzed in experiments performed by Nemat-Nasser *et al.* (2007). At high impact velocities, localized deformation of the metal foam was observed. The simulations using LS-DYNA® crushable foam material model did not predict the localized deformation but showed changes in the deformation as the impact velocity was varied, which was seen in the experiments.

Core crushing as an energy absorption mechanism is a special type of failure for honeycomb sandwich structures. Most earlier work on core

© Woodhead Publishing Limited, 2010

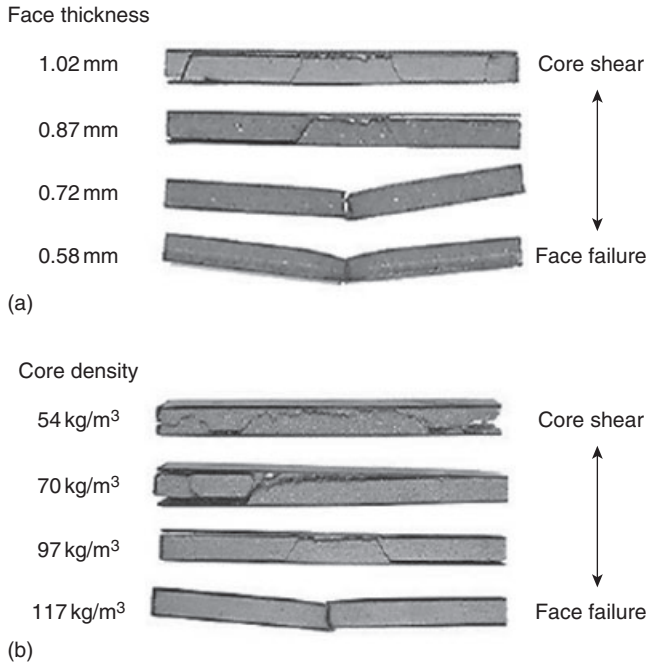

4.2 Failure modes of sandwich beams under impact forces (Lim *et al.,* 2004): (a) effect of face sheet thickness; (b) effect of core density (the sandwich beam is 90 mm in span and 150 mm in length; the core is made of PVC foam, and the face sheets are made of E-glass fiber reinforced epoxy).

crushing of aluminum honeycomb sandwich structure has been obtained by the aerospace and automotive industries. Magee and Thornton (1978) and Hexcel Corporation (1964, 1968) conducted extensive research characterizing the crushing behavior of honeycomb. An attempt to calculate the crushing strength of bare honeycomb (without face plates) went back to the work of McFarland (1963), in which the shearing of the walls in individual cells was modeled, but such a collapse model might not happen in reality. Wierzbicki (1983) predicted the mean crushing strength of an array of hexagonal cells from the known geometry of the cell and yield strength of the material and proposed a so-called folding element for aluminum structures. However, the research on crushing or indentation of honeycomb sandwiches with face sheet plates is limited, mainly because it is difficult to include the constraint effects of face sheets on honeycomb core structures. Wierzbicki *et al.* (1995) simplified the problem using a membrane on a rigid–plastic foundation and adopted a quasi-static model to simulate the impact response by assuming that the projectile is much heavier than the

© Woodhead Publishing Limited, 2010

face sheets. Closed form solutions were derived for the maximum deflection, the extent of plastic deformation, and the total energy absorbed as a function of the velocity and mass of projectile and the mechanical properties of the face plates and honeycomb core. A comprehensive experimental study in deformation and energy absorption of bare honeycombs and sandwich plates with honeycomb core was performed by Goldsmith and Sackman (1992). A cylindrical punch was used in static tests. In the dynamic tests, the blunt cylindrical strikers were launched with an initial velocity ranging from 10–40 m/sec. The resulting deflections of the face plates in both the static and dynamic tests are seven to 15 times larger than the thickness of face sheet plate, demonstrating that the membrane effect is very pronounced in such a case. Jamjian *et al.* (1994) derived a mathematical model of the impact problem and simulated this process. In their model, the face plate was considered to be rigid–plastic and bounded at infinity. The sheet plate deformation is in a combined bending/membrane mode, and the honeycomb core was modeled as a rigid–plastic foundation. The numerical predictions of the maximum indentation of the projectile into the face plate were found to be within 10% of the experimental results; those of the lateral extent of damage were within 5% of the test results.

Most recently, Yang and Qiao (2008) thoroughly evaluated the quasi-static crushing behavior of aluminum honeycomb materials using a combined experimental, analytical, and numerical approach. Based on their experimental characterization, the constitutive properties of the honeycomb cores under flat compression were approximated by an elastic perfectly-plastic material with inclusion of hardening after densification. Two different cell size materials were tested and compared, and the effect of strain rate on the maximal crushing stress was studied. The experimental results showed that the crushing platen stress is directly related to the relative density of core materials, and it can be associated with the strain rate, even though the effect of strain rates is not so dominant based on the conducted quasi-static tests. A simple physical model for the crushing wave length and stress was proposed and compared with the experimental data and available formulas in the literature. It is observed that the crushing wave length is close to the cell size and related to the geometric dimension and strain rate. The folding mechanism was also measured by the ARAMIS system (a photogrammetry technique), and the measured von Mises strains were compared with the numerical results from LS-DYNA®, demonstrating that the folding mechanism is initiated by two plastic hinge lines formed at the cell corners. Multilayer effect was also investigated, and it indicated that including the second layer slightly decreases the maximal crushing stress, but the simple superposition is still applicable for crushed multilayer sandwiches. Partial crushing due to small size cylindrical indenter was

© Woodhead Publishing Limited, 2010

further studied, and the experiment showed that the partial crushing process can be described by an elastic–plastic hardening material. Side impact process of honeycomb materials was also investigated, and the collapse band and its propagation process were captured.

Vaziri *et al.* (2006) studied metal sandwich plates with polymer foam-filled cores. The role of low-density structural polymeric foams filling the interstices of the cores of metal sandwich plates was analyzed to determine the strengthening of the cores and the enhancement of plate performance under crushing and impulsive loads. Two different types of sandwich structures, square honeycomb and folded plate steel cores, filled with two densities of structural foam were studied. The outcome suggested that plates with foam-filled cores can perform as well, or nearly as well, as plates of the same weight with unfilled cores. Vaziri and Hutchinson (2007) studied metal sandwich plates subjected to air shocks. Fluid–structure interaction was found to enhance the performance of sandwich plates relative to solid plates under intense air shocks.

Ceramic armors

Ceramic armors are used for the containment of blast fragments and prevention of bullet penetration. They were developed strictly for projectile resistance with a high hardness and compressive strength combined with an advantage of lightweight. The need for lighter protection materials for use by the military has given merit to the use of ceramic armor materials. Ceramics offer an advantage over steel in weight reduction, and over all metals in impact energy absorption. The most common ceramic materials used for armor applications are alumina, boron carbide, silicon carbide, and titanium diboride. In armor structures, ceramics are usually backed by metal plates, with or without a composite layer sandwiched between them (see Fig. 4.3). The energy dissipation mechanisms for this type of structure are: brittle failure and fragmentation of ceramics, delamination and delocalization of the fracture zone in the composites, and plastic deformation of the metal plate.

Lee and Yoo (2001) conducted an analysis of a ceramic/metal armor system, in which the strain rate effect was considered and the ballistic limits for different ceramic/metal back plate ratios were derived. Cheng *et al.* (2003) performed experiments for the ballistic impact on a boron carbide plate, and they found that the loss of impact resistance of boron carbide is due to the phase transformation to the glassy form.

An interesting aspect of the ballistic performance of armor grade ceramic tiles was experimentally investigated by Sarva *et al.* (2007). It was observed that restraining the impact-face of ceramic tiles with a membrane of suitable tensile strength, the ballistic performance is improved by 25% for

© Woodhead Publishing Limited, 2010

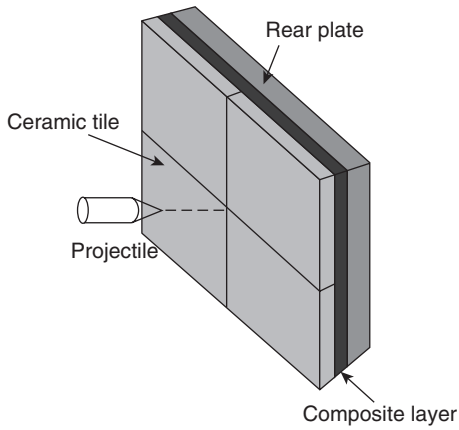

4.3 A layered armor composite system with ceramic facing (redrawn from Lopez-Puente *et al.,* 2005).

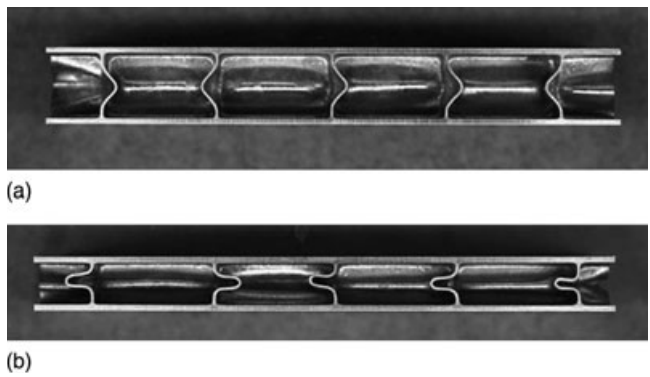

4.4 A square honeycomb sandwich energy absorbing system: (a) at plastic strain = 0.16; (b) at plastic strain = 0.47 (from Rathbun *et al.,* 2006).

a small increase in mass. The phenomenon is explained by the limiting effect the membrane has on the ejected material, which now works against the penetrator, eroding it and slowing it down. This type of effect would be a great and difficult benchmark test of numerical codes used in impact and penetration. New computational capabilities need to be developed to replicate the effects observed in Sarva *et al.* (2007).

Lattice and truss structures

Metal lattice or truss structures with or without waiting links can also be used in blast mitigation and armor design. Figure 4.4 shows a typical square

© Woodhead Publishing Limited, 2010

honeycomb sandwich system impacted by a blast wave with impulse levels of 3.8 kPa/s (Fig. 4.4a) and 4.6 kPa/s (Fig. 4.4b), and the main mechanism of energy absorption: the kinetic energy of incident waves is dissipated mainly through the plastic buckling of the core struts (Rathbun *et al.*, 2006).

Guruprasad and Mukherjee (2000) analyzed layered sacrificial claddings under blast loading, which could be compared with the honeycomb core sandwich behavior, absorbing the ballistic energy by the progressive crushing process. Evans *et al.* (2001) conducted research on multifunctional metal sandwich structures, primarily used for blast mitigation. Xue and Hutchinson (2004) studied blast resistant metal sandwich plates and compared the effect of different truss structures on impact resistance. Fleck and Deshpande (2004) also investigated the resistance of clamped sandwich beams due to shock loadings. The analysis of the type of failure of classical materials showed that localized failure is dominant in projectile impacts as well as blast impacts (Taylor and Vinson, 1990), which diminishes their effectiveness as armor systems. Therefore, lattice structures with waiting links are suggested to spread the localized damage and thus provide blast mitigation. The concept of lattice structures with waiting links has not yet been developed into products. The concept of lattice structure with waiting links was researched by Cherkaev and Slepyan (1995), who analyzed the loading responses of lattice structures with waiting links and explained the failure of a lattice structure under dynamic loading. Balk *et al.* (2001) further expanded the waiting link concept and simulated the delocalization of damages in a lattice structure. Slepyan and Ayzenberg-Stepanenko (2004) included the effect of cracks in the lattice structure and conducted studies on dynamic fracture propagation. Dancila and Armanios (2002) suggested a similar concept in composites. Preliminary validation of lattice structures with waiting links was presented in Ha and Dancila (2003). The waiting link concept could be transferred and applied to designing crystal lattices with a higher ballistic limit. Crystal lattice structures under dynamic loading were studied in, for example, Pouget (1992, 1993). Pouget (1992) conducted a study about the stability of non-linear structures in a lattice model for phase transformations in alloys. Pouget (1993) also studied the lattice dynamics and stability of modulated-strain structures for elastic phase transitions in alloys. Designing a new type of crystals with lattice structure of waiting links could provide a solution for new armor systems.

Magneto-rheological (MR) fluids

MR (magneto-rheological) fluids, having ferromagnetic ultrafine particles dispersed, are used as high energy absorbing materials. Normally, MR fluids behave like regular motor oils; however, when a magnetic field is present, they become viscous within milliseconds. The viscosity leads to

© Woodhead Publishing Limited, 2010

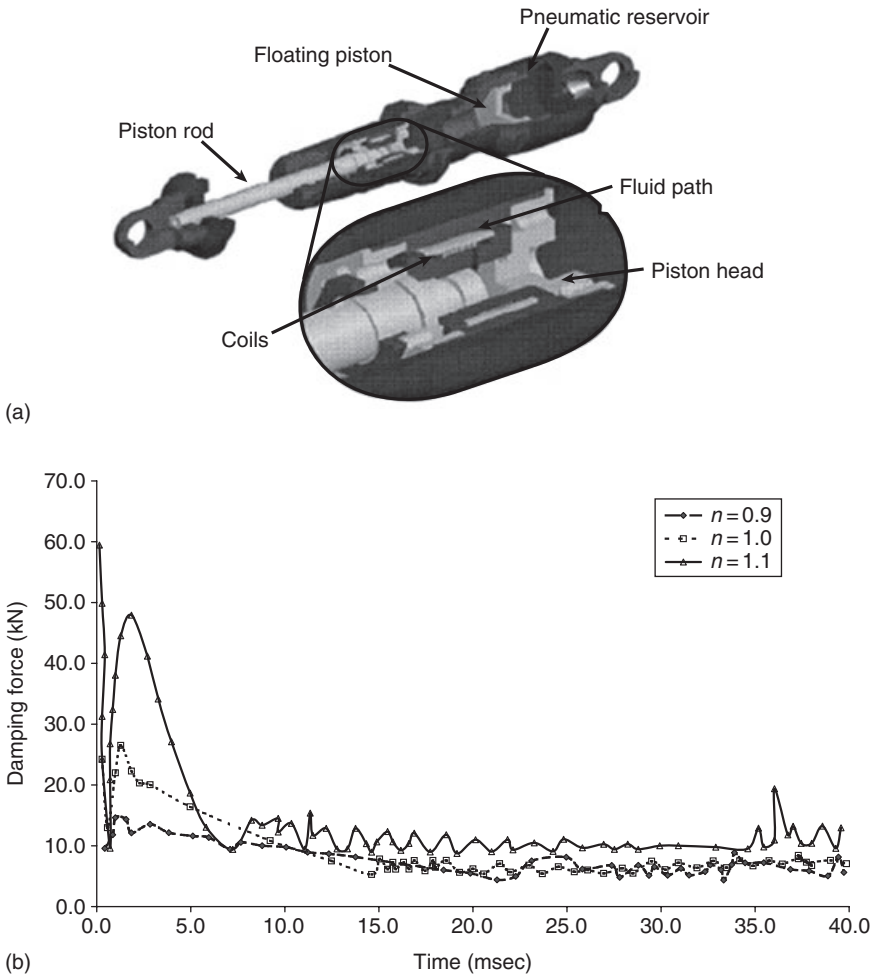

4.5 An impact damper MR fluid system (from Lee *et al.,* 2002): (a) an impact damper system; (b) damping force generated by the impact damper for different shear strain power indices (*n*).

energy dissipation when the MR fluid is sheared. Models for MR fluids relate the shear stress with a power of the shear strain. A subunitary power index corresponds to a shear-thinning fluid, whereas a supraunitary power index gives a shear-thickening fluid. Figure 4.5(a) shows an impact damper system (Lee *et al.*, 2002) which uses an MR fluid. The damping force generated by the damper for different shear strain power indices is shown in Fig. 4.5(b) (Lee *et al.*, 2002).

The majority of MR fluids are used in control devices, such as semi-active MR dampers used in earthquake mitigation (Yang *et al.*, 2004). Research

© Woodhead Publishing Limited, 2010

on MR dampers has focused on low velocity and frequency applications (Jolly *et al*., 1999). Ahmadian and Poynor, (2001); Ahmadian *et al.* (2002), and El Wahed *et al.* (2002) have shown the capability of MR fluids in handling impulsive loads for low velocities. It is still not known how to exploit MR fluids for high-velocity impulsive loads.

Porous NiTi shape memory alloys (SMA)

Miyoshi *et al*. (1999) designed porous NiTi SMA for high energy absorption applications. Since the density of porous NiTi is less than that of its solid version, it is much lighter. The porous NiTi, however, can absorb almost the same deformation energy as its solid counterpart does for the same volume. Kang *et al*. (2001) produced a ductile porous NiTi rod using spark plasma sintering (SPS) method, and its energy absorbing behavior was discussed in Zhao *et al*. (2005, 2006).

Figure 4.6 shows a porous NiTi SMA manufactured by SPS (Zhao *et al*., 2005), in which different porosities were realized. The hysteretic behavior of these materials shown in Fig. 4.7 gives the main mechanism that contributes to the energy dissipation in the material.

4.2.2 Problem significance

There is increasing interest in the use of blast resistant techniques for retrofit-hardening and strengthening of built infrastructure against the 'new' (man-made) hazard of terrorism. To meet this challenge, various materials associated with energy absorbing must be quantified and then considered as the basis for assessing different mitigation measures. Choosing suitable mitigation measures can greatly reduce the cost of blast event, protect human beings from attack, and warrant the normal functionalities of structures during a blast event.

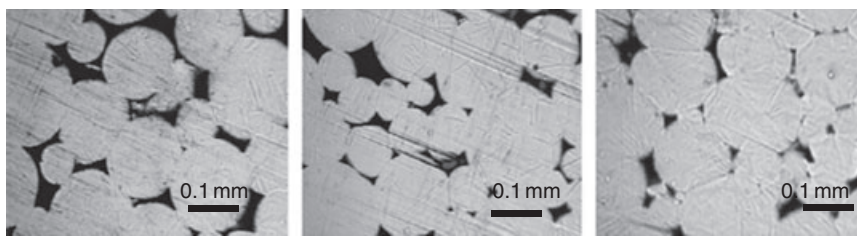

4.6 Porous SMA material system (from Zhao *et al.,* 2005).

© Woodhead Publishing Limited, 2010

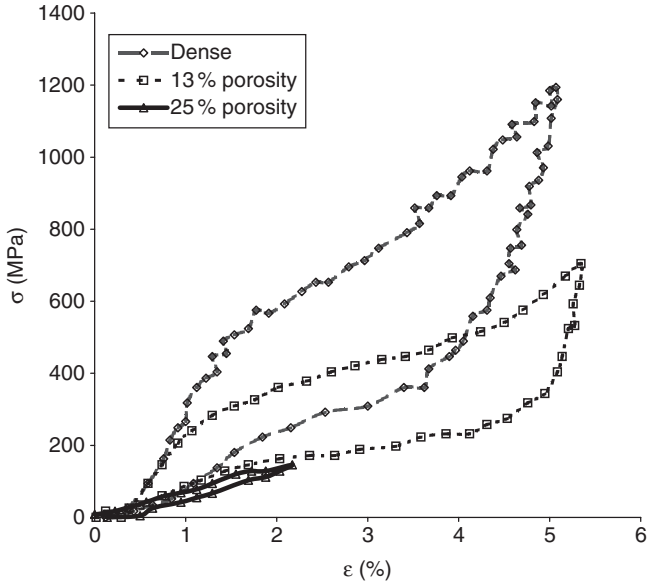

4.7 The hysteresis loops of the stress–strain curves for porous NiTi material (Zhao *et al.,* 2005).

4.3 Design philosophy for blast protection

An explosion in air is a process of a rapid release of energy generated by explosive. The energy sources can be chemical or nuclear materials, gases, or electricity. The explosive properties of air will cause the front of the pressure wave to shock up as the front moves. Without referring to different wave patterns, design of blast resistant materials requires certain energy absorbing capacity to safely contain the blasting energy.

Most of the blast resistant materials fall into two categories: one with a distinct yielding point, and the other without a distinct yielding point. Generally, both categories can be described using a pressure–volume curve (see Fig. 4.8). Under a blast loading, the loaded area is so great that the portion of the medium under consideration and its inclusion can be assumed loaded with the uniform lateral displacements confined. Therefore, the whole process can be approximated as a one-dimensional model, and the absorbed energy can be considered as the sum of dissipated energy and rebound energy. For a safe design, the absorbed energy must be greater than the kinetic energy transferred to the structure. Even though a design may have a suitable energy absorbing capacity, the dissipated energy depends on the deformation history of materials experienced in a structure.

Blast is an extraordinary type of dynamic load. As described in Beshara (1994), in the process of an explosion, the blast travels as an incident wave

© Woodhead Publishing Limited, 2010

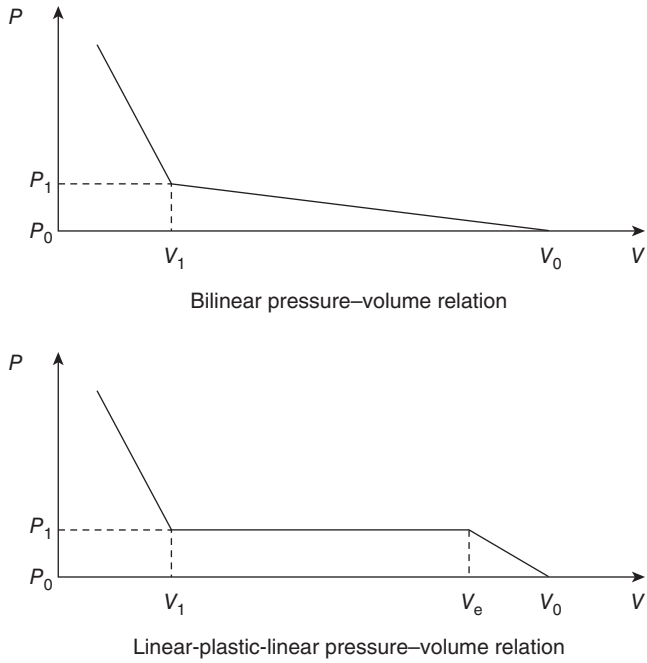

4.8 Two types of energy absorbing materials under blast.

until it strikes an object. Upon striking the object, a reflected wave is generated, and it travels back towards the point of explosion. At a point, some distance from the explosion center, the reflected wave meets the incident wave, producing a single vertical wave front called a 'Mach stem'. The structure below the intersection point of the reflected and incident waves experiences a single shock, whereas the surface above this point also experiences a shock history which is a resultant of the incident and reflected waves.

The pressure versus time plot of a typical blast wave is shown in Fig. 4.9. The pressure builds up to a peak value of the overpressure (P_0). The pressure then decays to a local ambient pressure (P_s) ambient in time (t_0), followed by a partial vacuum of very small amplitude, and it eventually returns to P_s. The portion of the pressure–time history below P_s is called the 'negative or suction phase', while the portion above P_s is called the 'positive phase'. In most blast studies, the negative phase of the blast wave is ignored, and only the parameters associated with the positive phase (see Fig. 4.9) are considered because the damage to the structure is primarily caused by the 'positive phase'.

In the positive phase, the pressure at any time (t) is described in terms of the peak overpressure (P_0), the dimensionless wave form parameter (α),

© Woodhead Publishing Limited, 2010

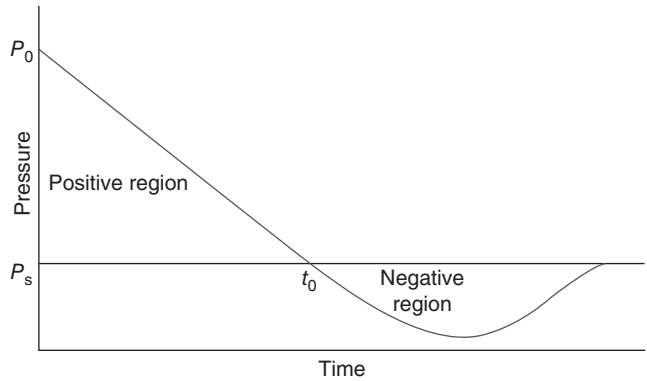

4.9 Pressure versus time plot of a typical blast wave (Sriram *et al.*, 2006).

and the positive phase duration time (t_0). These parameters for the pressure ($P(t)$) are related by Friedlander's equation as shown in Eq. 4.1, and the impulse per unit of projected area (I_s) is given by Eq. 4.2:

$$P(t) = P_0\left(1 - \frac{t}{t_0}\right)\exp\left(-\alpha\frac{t}{t_0}\right) \quad [4.1]$$

$$I_s = \int_0^{t_0} P(t)\,\mathrm{d}t = P_0 t_0\left[\frac{1}{\alpha} - \frac{1}{\alpha^2}(1 - \exp(-\alpha))\right] \quad [4.2]$$

4.4 Case studies of blast absorbing materials

In this section, four typical studies of blast absorbing materials (from fiber metal composite laminates, to metal–foam sandwich panels, to MR fluids, to porous SMA) are showcased. The experimental and/or numerical evidence of these materials under blast demonstrates the effective utilization of blast energy dissipation mechanisms within each blast resistant material, i.e., delamination and debonding in multilayer composites, transverse shear failure, fiber compressive breakage, matrix cracking, delamination, and core crushing in sandwich structures, increased viscosity with increasing applied current in MR fluids, and kinetic energy dissipation through the phase transformation in the porous SMA.

4.4.1 Multilayer composite structures under blast loading

Langdon *et al.* (2007) conducted a series of experiments on fiber metal laminates (FMLs), based on the stacked arrangements of metal alloy and

© Woodhead Publishing Limited, 2010

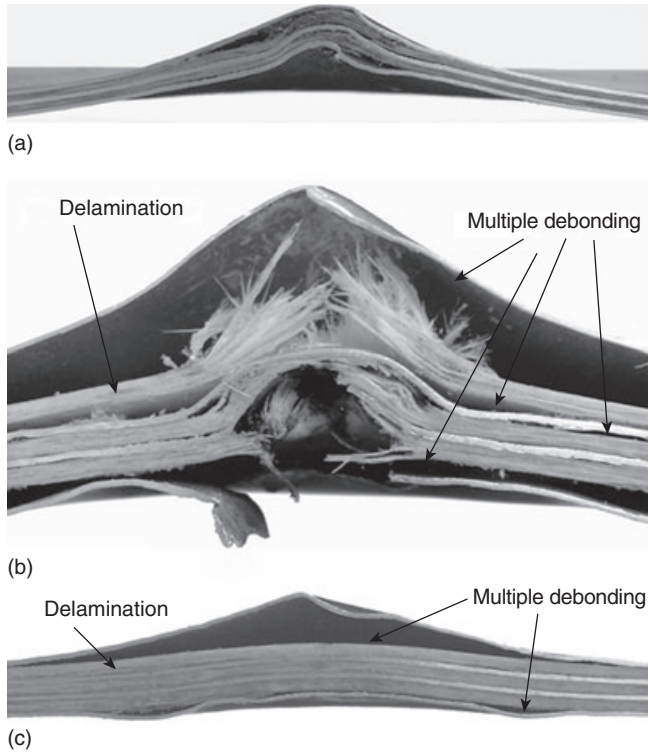

4.10 Failure of fiber metal laminates (FMLs) under explosive loading (Langdon *et al.*, 2007): (a) A3T22 (group A); (b) A4T34-4: Impulse = 14.65 Ns (group B_2); (c) A4T34-5: Impulse = 7.01 Ns (group B_2).

reinforced composite layers. The FML panels of 400×400 mm in size (300×300 mm of exposed area) were manufactured at the University of Liverpool from sheets 0.025 in. thick. The panels were clamped between two steel frames and mounted onto a ballistic pendulum and loaded by detonating PE4 plastic explosive on a polystyrene pad in the center of the panel. The PE4 was mould into a flat cylindrical shape.

Different cases were tested and photographed. One case using an A3T22 panel is shown in Fig. 4.10. From Fig. 4.10, it was observed that the A3T22 panels exhibited the full range of response from Mode I (open) failure with little debonding (Fig. 4.10a) to Mode II (shear) failure with petalling of the back face. Multiple debonding of all three aluminum layers is evident. Increasing impulse (see Figs 4.10b and 4.10c) often results in smaller debonded regions on the front face and increased debonded regions on the back face.

© Woodhead Publishing Limited, 2010

4.4.2 Design of metal and foam sandwich panels under blast

The behavior of a sandwich plate under blasting is, to some extent, similar to that under impulse impacts (Yang and Qiao, 2005, 2007). The analysis and design of a sandwich plate under blast loading, usually realized using commercial software, depend on the maximal impulse generated or the TNT magnitude used.

Sriram *et al.* (2006) simulated the sandwich plate under blasting using LS-DYNA® and considered a sandwich structure made of a foam core and two S2-glass/epoxy face sheets on either side of the foam core. The foam was made of Cymat aluminum foam. The dimensions of the foam and face sheet were 0.3 m × 0.3 m × 0.0159 m and 0.3 m × 0.3 m × 0.0015 m, respectively. The face sheets were modeled using material model 161 in LS-DYNA®. The foam was modeled using material model 126 with co-rotational element formulation 0. The sandwich composite was restricted for all degrees of freedom along the corners. ERODING SURFACE TO SURFACE was used to define the contact between face sheet and foam core. ERODING SINGLE SURFACE was selected to define the contact surface between the face sheets layers. The finite element model is illustrated in Fig. 4.11.

The blast impulse first accelerates the first face sheet, which in turn transfers the momentum of the blast wave to the subsequent face sheet and so on. The blast impulse is then transferred to the foam. The energy acquired by the foam is dissipated by crushing of the foam cells and its momentum

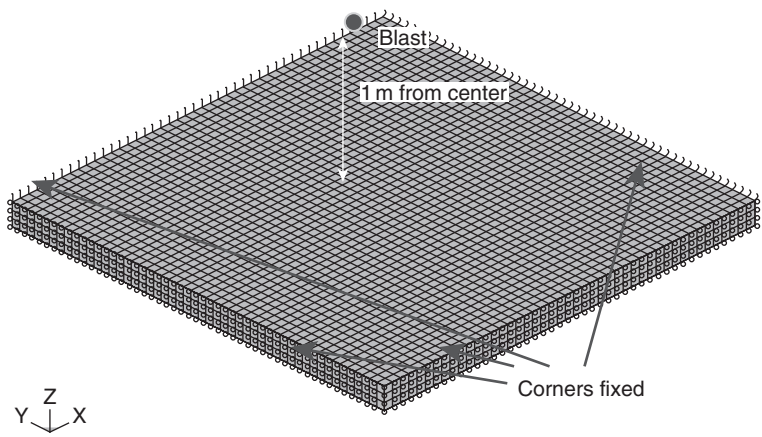

4.11 Foam restricted for all degrees of freedom along the corners (Sriram *et al.,* 2006).

© Woodhead Publishing Limited, 2010

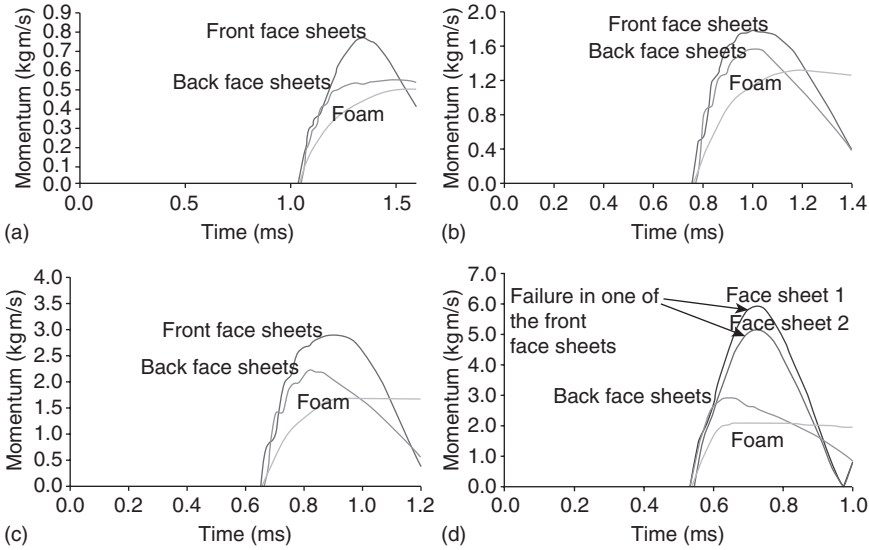

4.12 Momentum of face sheets and foam with different amounts of TNT (Sriram *et al.,* 2006): (a) TNT = 0.1 kg; (b) TNT = 0.3 kg; (c) TNT = 0.5 kg; (d) TNT = 1 kg.

4.13 Blast impact on sandwich composite at time of 1 ms, blast load of 5 MPa (Sriram *et al.,* 2006).

is thereby reduced. These findings are analogous to the conservation of momentum/impulse transfer with the steel plate.

The TNT charge was placed 1 m away from the sandwich composite, and the amount of charge was varied. The amounts of TNT considered were 0.1 kg, 0.3 kg, 0.5 kg, and 1 kg, respectively, and their generated resultant momentum versus time for different blast loads is shown in Fig. 4.12.

It can be observed from Figs 4.12a–4.12d that the momentum of the foam yields the core material and reaches a plateau after the blast wave reaches the core. The curve of the resultant momentum also shifts as the blast wave progresses from the top layer to the inner layers (face sheet 1 to face sheet 2 and so on), which is due to the failure which occurs between face sheet 1, face sheet 2, or delaminations between them.

The failure of the whole sandwich composite is shown in Fig. 4.13. It is clearly seen that many elements in the foam have fractured, which were

© Woodhead Publishing Limited, 2010

observed to have exhibited either tensile or shear failure. The region where erosion of elements was observed is shear-dominated because the sandwich composite is under compressive load.

Shear mode failure, compressive mode failure, matrix cracking, and delamination were extensively observed in the top face sheets as shown in Figs 4.14a–4.14d, respectively. Shear mode of failure is seen along the edges or corners (Fig. 4.14a). Compressive fiber failure happened at the center of the face sheet (Fig. 4.14b) as it experiences maximum pressure. Matrix crack patterns also happened at the center due to bending, since the matrix is the weaker of the two constituents (i.e., fiber and matrix) and cracks easily (Fig. 4.14c). Failure between the layers, such as delaminations, is shown in Fig. 4.14d.

Different failure patterns of the sandwich plate under different magnitudes of TNT are also shown in Fig. 4.15. From Fig. 4.15, the sandwich plate is massively damaged under 1 kg TNT explosive.

4.4.3 Design of magneto-rheological (MR) fluids under blast

Magneto-rheological (MR) fluid behaves like a Bingham fluid, and its instantaneous shear strength is proportional to the deformation rate of the fluid. For this type of material under blast impact, its energy absorption capacity depends on the shear rate of the blast wave as well as the propagation path of the blast waves.

The design of MR fluids under blast is realized through two different processes involved in a blast event: elastic interaction and plastic flow. Using the Bingham model, a plate under blast (Fig. 4.16) was simulated by Hu and Wereley (2008). Results similar to those shown in Fig. 4.16 have also been generated by the MR dampers widely used in system control.

It is a feature of MR fluids that the yielding stress and its damping ratio vary with the applied current as shown in Fig. 4.17 (Hu and Wereley, 2008). This characteristic means that MR fluids have a viable role in resisting intensive blast loads.

Yielding force versus displacement for a typical MR fluid is shown in Fig. 4.18 (Hu and Wereley, 2008). From Fig. 4.18, under blast impulse loadings, a large portion of the energy is absorbed through the hardening–loosen–hardening processes of MR fluids.

4.4.4 Design of porous NiTi shape memory alloys under blast

The deformation–displacement curve for porous NiTi shape memory alloys (SMA) exhibits hystersis loops (Lagoudas *et al.*, 2003). Its behavior under

© Woodhead Publishing Limited, 2010

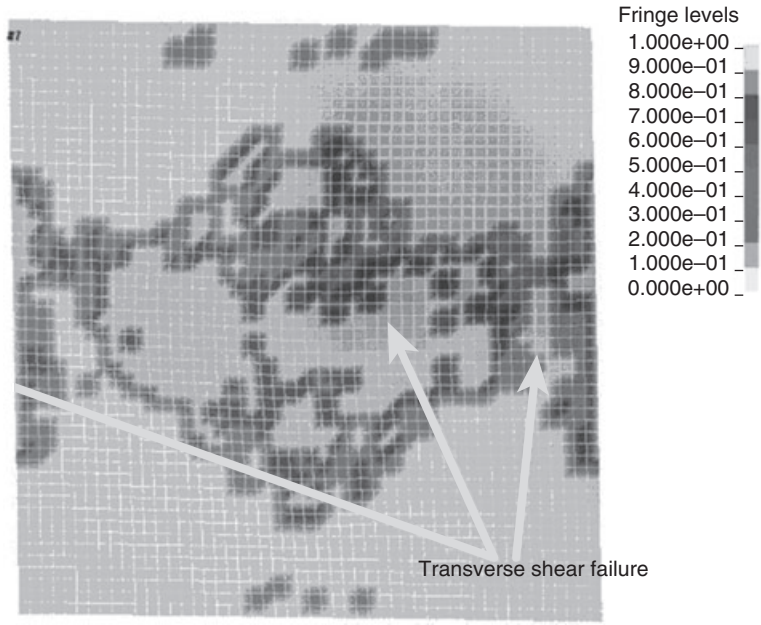

(a)

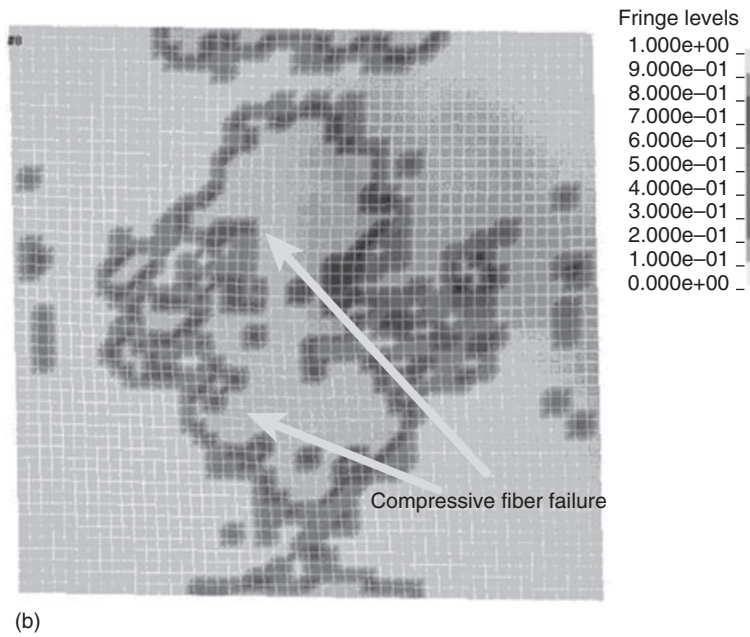

(b)

4.14 Failure modes in face sheet 1 at time of 1 ms, blast load = 5 MPa (0 = elastic & 1 = failure) (Sriram *et al.*, 2006): (a) shear mode failure; (b) compressive mode failure; (c) matrix cracking; (d) delamination.

© Woodhead Publishing Limited, 2010

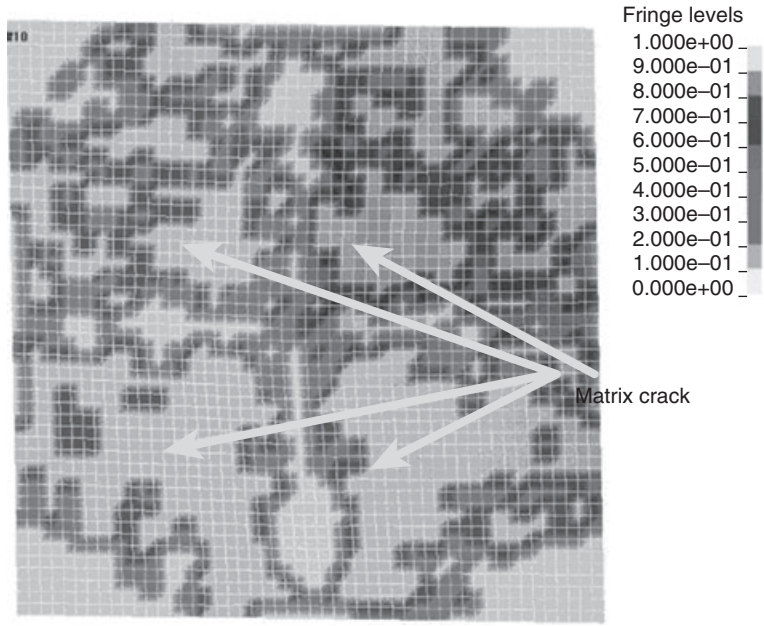

(c)

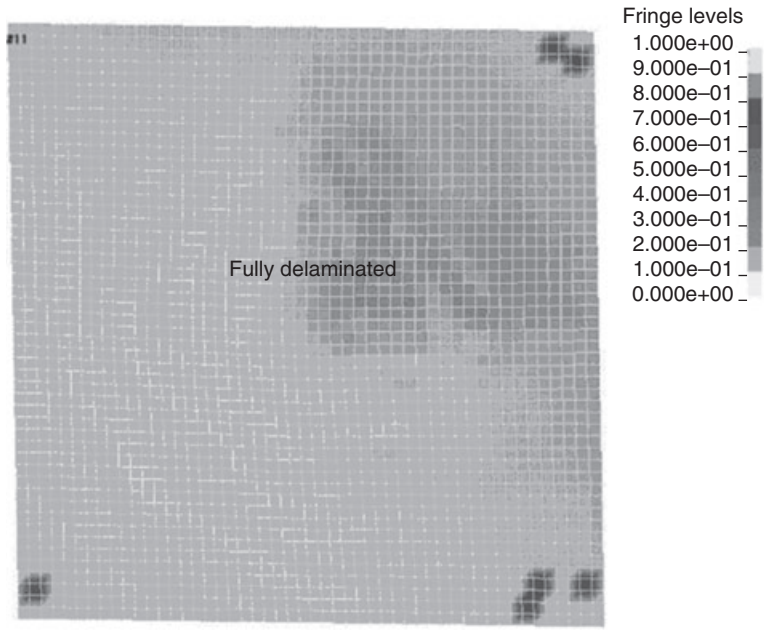

(d)

4.14 Continued

© Woodhead Publishing Limited, 2010

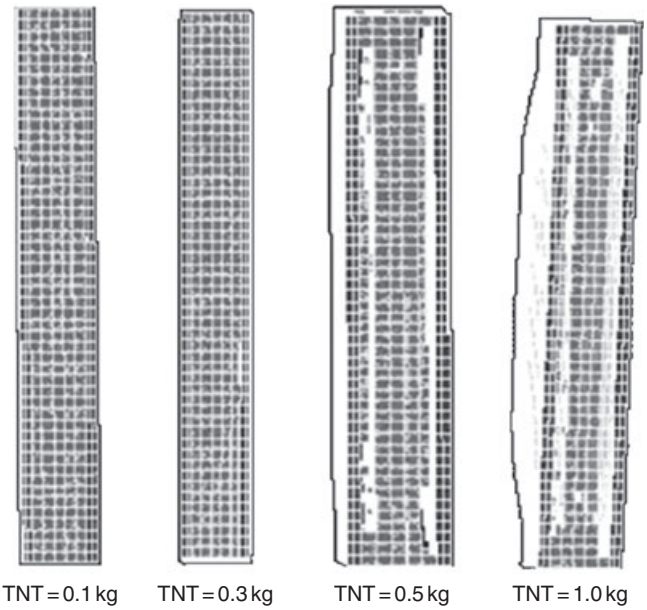

4.15 Sandwich composite showing dishing at t = 1 ms for different loads of TNT placed 1 m away from sandwich composite (Sriram *et al.,* 2006).

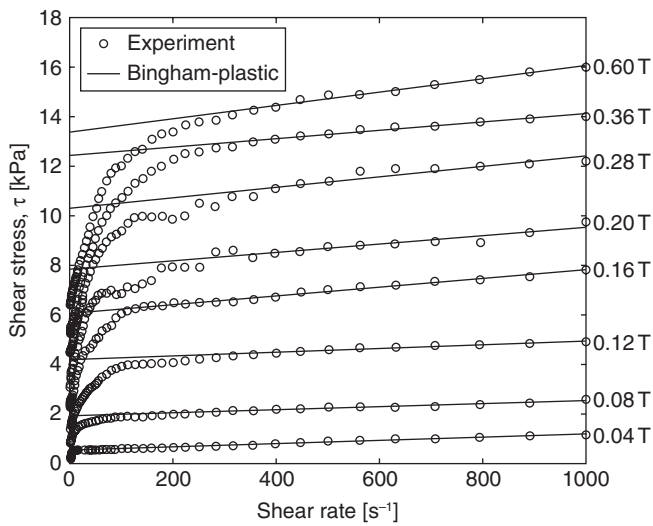

4.16 The Bingham-plastic behavior of magnetorheological fluids (Hu and Wereley, 2008).

© Woodhead Publishing Limited, 2010

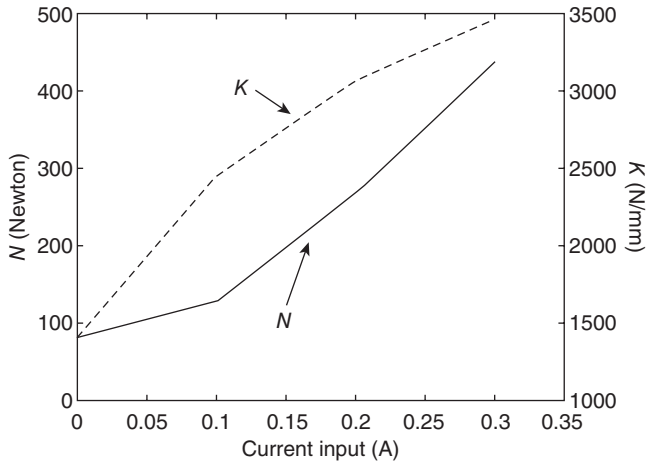

4.17 Variation of initial yielding force (*N*) and viscosity index (*K*) with applied currents (*A*) (Hu and Wereley, 2008).

blast also depends on the propagation path of the blast waves as shown in the MR fluids. These authors applied a square pulse with 800 MPa under adiabatic conditions to a SMA rod with an initial temperature of 320 K. The evolution of stress is shown in Fig. 4.19.

For blast types of loadings, it is useful to calculate the energy dissipated through the phase transformation. The energy dissipated through the SMA rod under the given adiabatic loading condition is shown in Fig. 4.20. As demonstrated in Fig. 4.20, about 85% of the input energy has been dissipated through the SMA phase transformation.

The same type of square pulses with 400 MPa is applied under twinning conditions to a SMA rod with the initial temperature of 295 K (Lagoudas *et al*., 2003). The evolution of stress is shown in Fig. 4.21. The energy dissipated through the SMA rod under the twinning loading condition is shown in Fig. 4.22. As exhibited in Fig. 4.22, about 85% of the input kinetic energy has been dissipated under twinning condition.

4.5 Summary and concluding remarks

In this chapter, a review of high energy absorbing materials, specially with attention to blast resistant materials, is presented. The design philosophy for blast absorbing materials is briefly introduced, and four cases of blast resistant materials (i.e., multilayer composites, sandwich panels, magneto-rheological fluids, and porous shape memory alloys) are provided. In

© Woodhead Publishing Limited, 2010

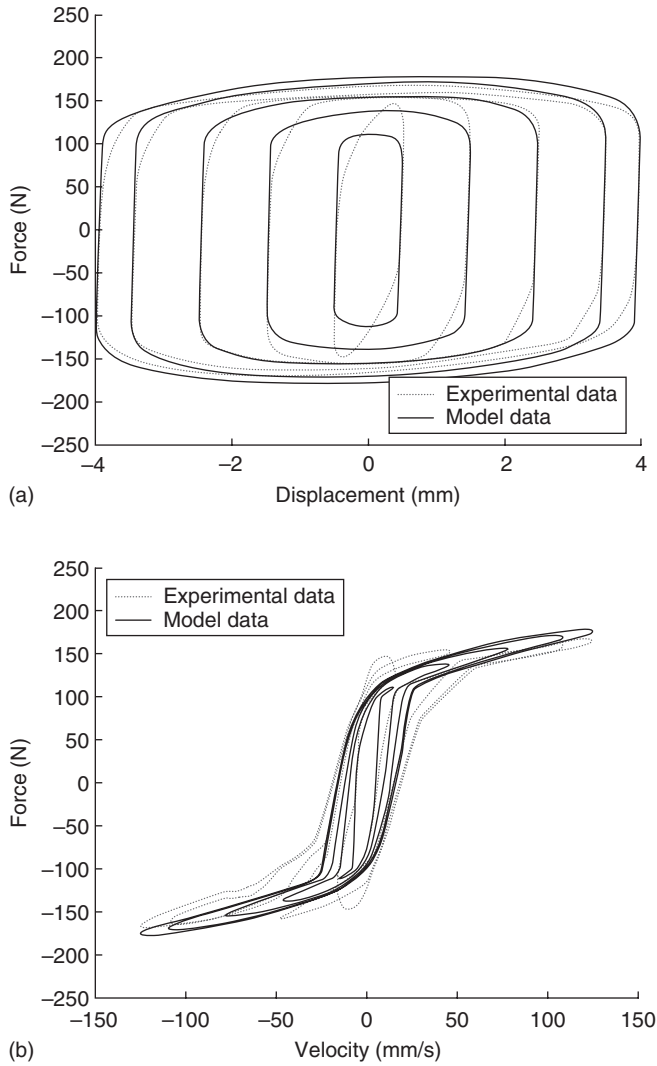

4.18 Typical force–displacement and force–velocity curves of a MR fluid through applied current cycles (Hu and Wereley, 2008): (a) force – displacement; (b) force – velocity.

particular, new design concepts related to high energy absorbing materials (lattice and truss structures, hybrid sandwich composites, metal foams, magneto-rheological fluids, porous shape memory alloys) are discussed. Recent studies on experimental evaluation and constitutive modeling of strain rate-dependent polymer matrix composites are also presented. Four

© Woodhead Publishing Limited, 2010

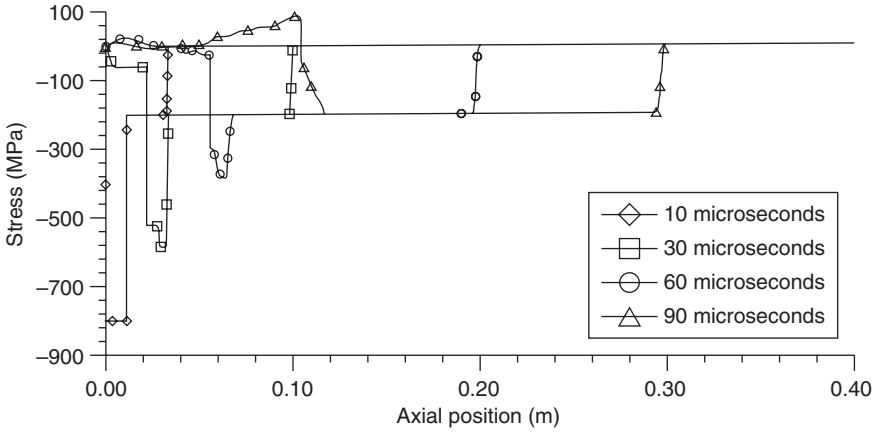

4.19 Stress evolution in a SMA rod under adiabatic conditions (Lagoudas *et al.,* 2003).

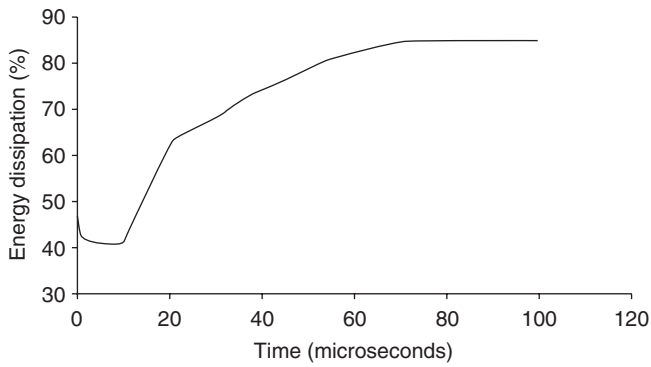

4.20 Energy absorbed in a SMA rod under adiabatic conditions (Lagoudas *et al.,* 2003).

case studies of blast absorbing materials are illustrated and discussed, and their mechanisms for blast energy absorption and dissipation are revealed. This review as well as case studies presented is intended to help the readers in better identifying viable energy absorbing materials under impact in general and blast resistant materials in particular and the designers in selecting high and effective energy absorbing materials, particularly for structures under blast loadings.

© Woodhead Publishing Limited, 2010

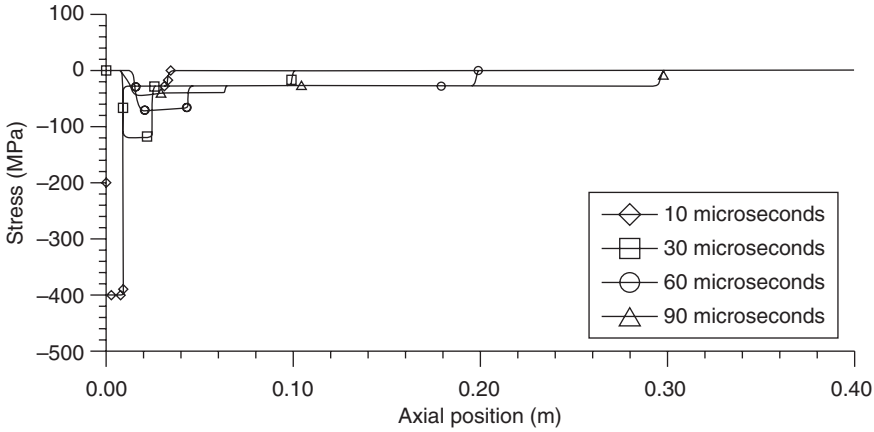

4.21 Stress evolution in a SMA rod under twinning conditions (Lagoudas *et al.,* 2003).

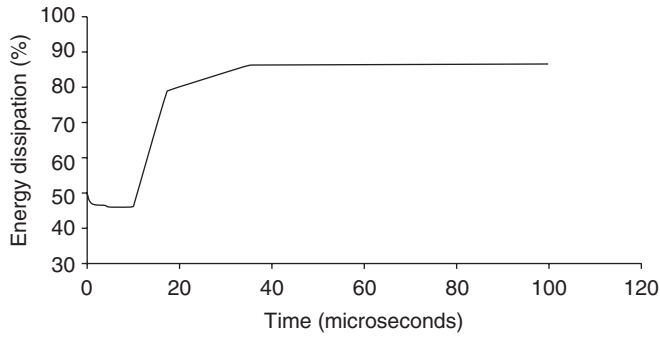

4.22 Energy absorbed in a SMA rod under twinning conditions (Lagoudas *et al.,* 2003).

4.6 References

AHMADIAN M and POYNOR J C (2001), An evaluation of magneto-rheological dampers for controlling gun recoil dynamics, *Shock and Vibration*, **8**(3–4), 141–146.

AHMADIAN M, APPLETON R and NORRIS J (2002), An analytical study of fire out of battery using magnetorheological dampers, *Shock and Vibration*, **9**(3), 129–142.

AMBUR D R, JAUNKY N, LAWSON R E and KEIGHT JR N F (2001), Numerical simulations for high-energy impact of thin plates, *International Journal of Impact Engineering*, **25**, 683–702.

BALK A M, CHERKAEV A V, SLEPYAN L I (2001), Dynamics of chains with non-monotone stress-strain relations. I. Model and numerical experiments, *Journal of the Mechanics and Physics of Solids*, **49**, 131–148.

© Woodhead Publishing Limited, 2010

BESHARA F B A (1994), Modeling of blast loading on aboveground structures – I. General phenomenology and external blast, *Computers & Structures*, **51**(5), 585–596.

BINIENDA W K (2004), *High energy impact of composite structures – Ballistic experiments and explicit finite element analysis*, Report, submitted to NASA Glenn Research Center, The University of Akron, Akron, OH.

BORDONARO C M (1995), *Rate Dependent Mechanical Behavior of High Strength Plastics: Experiment and Modeling*, PhD thesis, Rensselaer Polytechnic Institute, Troy, New York.

CAPRINO G and TETI R (1994), Impact and post impact behavior of foam core sandwich structures, *Composite Structures*, **29**, 47–55.

CHANG W J and PAN J (1997), Effects of yield surface shape and round-off vertex on crack-tip fields for pressure-sensitive materials, *International Journal of Solids and Structures*, **34**, 3291–3320.

CHENG J and BINIENDA W K (2006), Simulation of soft projectiles impacting composite targets using an arbitrary Lagrangian-Eulerian Formulation, *Journal of Aircraft*, **43**(6), 1726–1731.

CHENG J and BINIENDA W K (2008), Simplified braiding through integration points model for tri-axially braided composites, *Journal of Aerospace Engineering, Special Issue on 'Impact Mechanics and High Energy Absorbing Materials'*, **21**(3), 152–161.

CHENG M, MCCAULEY J and HEMKER K (2003), Shock-induced localized amorphization in boron carbide, *Science*, **299**(7), 1563–1566.

CHERKAEV A and SLEPYAN L (1995), Waiting element structures and stability under extension, *International Journal of Damage Mechanics*, **4**(1), 58–82.

COX B and YANG Q D (2006), In quest of virtual test for structural composites, *Science*, **314**, 1102–1107.

DANCILA D S and ARMANIOS E A (2002), Energy-dissipating composite members with progressive failure: concept development and analytical modeling, *AIAA Journal*, **40**, 2096–2104.

DANIEL I M, HSIAO H M and CORDES R D (1995), Dynamic response of carbon/epoxy composites, in Rajapakse YDS and Vinson JR (eds), *High Strain Rate Effects on Polymer, Metal and Ceramic Matrix Composites and Other Advanced Materials, AD-Vol. 48*, ASME, New York, 167–177.

DAVIES G A O, HITCHINGS D and WANG J (1995), Prediction of thresholds of glass fiber reinforced laminates, *Composite Structures*, **31**, 185–193.

DOBYNS A L and PORTER T R (1981), A study of the structural integrity of graphite composite structure subjected to a low velocity impact, *Polymer Engineering Science*, **21**, 493–498.

EL WAHED A K, SPROSTON J L and SCHLEYER G K (2002), Electrorheological and magnetorheological fluids in blast resistant design applications, *Materials and Design*, **23**(4), 391–404.

EVANS A G, HUTCHINSON J W, FLECK N A, ASHBY M F and WADLEY H N G (2001), The topological design of multifunctional cellular metals, *Progress in Materials Science*, **46**, 309–327.

FLECK N A and DESHPANDE V S (2004), The resistance of clamped sandwich beams to shock loading, *Journal of Applied Mechanics*, **71**, 386–401.

© Woodhead Publishing Limited, 2010

GILAT A, GOLDBERG R K and ROBERTS G (2005), *Strain Rate Sensitivity of Epoxy Resin in Tensile and Shear Loading*, NASA/TM-2005-213595, NASA Glenn Research Center, Cleveland, OH.

GOLDBERG R K, ROBERTS G D and GILAT A (2005), Implementation of an associative flow rule including hydrostatic stress effects into the high strain rate deformation analysis of polymer matrix composites, *Journal of Aerospace Engineering*, **18**, 18–27.

GOLDBERG R K, ROBERTS G D, LITTELL J D and BINIENDA W K (2008), Incorporation of nonlinear unloading effects into the strain rate dependent deformation analysis of polymer matrix materials utilizing a state variable approach, *Journal of Aerospace Engineering*, **21**(4), 235–248.

GOLDSMITH W and SACKMAN J L (1992), An experimental study of energy absorption in impact on sandwich plates, *International Journal of Impact Engineering*, **12**, 241–262.

GURUPRASAD S and MUKHERJEE A (2000), Layered sacrificial claddings under blast loading, Part I – Analytical studies, *International Journal of Impact Engineering*, **24**, 957–973.

HA K and DANCILA D S (2003), Energy-dissipating snap-resistant tether, *AIAA 41st Aerospace Sciences Meeting and Exhibit*, 6–9 January, Reno, NV.

HEXCEL CORPORATION (1964), *Design Data for the Preliminary Selection of Honeycomb Energy Absorption Systems*, Report No. TSB 122, Stamford, CT.

HEXCEL CORPORATION (1968), *Mechanical Properties of Hexcel Honeycomb Materials*, Report No. TSB 120, Stamford, CT.

HOGG P J (2006), Composites in armor, *Science*, **314**, 1100–1101.

HU W and WERELEY N M (2008), Hybrid magnetorheological fluid-elastomeric lag dampers for helicopter stability augmentation, *Smart Materials and Structures*, **17**(4), 045021.

JAMJIAN M, SACKMAN J L and GOLDSMITH W (1994), Responses of an infinite plate on a honeycomb foundation to a rigid cylindrical impactor, *International Journal of Impact Engineering*, **15**, 183–200.

JOLLY M R, BENDER J W and CARLSON J D (1999), Properties and applications of magnetorheological fluids, *Journal of Intelligent Material Systems and Structures*, **10**(1), 5–13.

KANG Y S, KIKUCHI K and KAWASAKI A (2001), Fabrication and characterization of functionally graded Ni/Al2O3/Ni compliant pad, *Proceeding of ISSPS*, 6–8 September, Singapore.

LAGOUDAS D, RAVI-CHANDAR K, SARH K and POPOV P (2003), Dynamic loading of polycrystalline shape memory alloy rods, *Mechanics of Materials*, **35**(7), 689–716.

LANGDON G S, CANTWELL W J and NUICK G N (2007), Failure characterisation of blast-loaded fibre–metal laminate panels based on aluminum and glass–fiber reinforced polypropylene, *Composites Science and Technology*, **67**(7–8), 1385–1405.

LEE M and YOO Y H (2001), Analysis of ceramic/metal armour system, *International Journal of Impact Engineering*, **25**, 819–829.

LEE D Y, CHOI Y T and WERELEY M N (2002), Performance analysis of ER/MR impact damper systems using Herschel–Bulkley model, *International Journal of Intelligent Material Systems and Structures*, **13**(7–8), 525–531.

LEE Y S, WETZEL E D and WAGNER N J (2003), The ballistic impact characteristics of Kevlar woven fabrics impregnated with a colloidal shear thickening fluid, *Journal of Material Science*, **38**, 2825–2833.

© Woodhead Publishing Limited, 2010

LI F Z and PAN J (1990), Plane-stress crack-tip fields for pressure-sensitive dilatant materials, *Journal of Applied Mechanics*, **57**, 40–49.

LIM T S, LEE C S and LEE D G (2004), Failure modes of foam core sandwich beams under static and impact loads, *Journal of Composite Materials*, **38**(18), 1639–1662.

LITTELL J D, RUGGERI C R, GOLDBERG R K, ROBERTS G D, ARNOLD W A and BINIENDA W K (2008), Measurement of epoxy resin tension, compression, shear stress-strain curves over a wide range of strain rates and temperatures, *Journal of Aerospace Engineering, Special Issue on 'Impact Mechanics and High Energy Absorbing Materials'*, **21**(3), 163–273.

LOPEZ-PUENTE J, ARIAS A, ZAERA R and NAVARRO C (2005), The effect of the thickness of the adhesive layer on the ballistic limit of ceramic/metal armours. An experimental and numerical study, *International Journal of Impact Engineering*, **32**(1–4), 321–336.

MAGEE C L and THORNTON P H (1978), *Design Consideration in Energy Absorption by Structural Collapse*, SAE Report No. 78-434.

MATEMILOLA S A and STRONG W J (1995), Impact induced dynamic deformation and stresses in CFRP composite laminates, *Composites Engineering*, **5**(2), 211–222.

MCFARLAND R K (1963), Hexagonal cell structures under post-buckling axial load, *AIAA Journal*, **1**, 1380–1385.

MIYOSHI T, ITOH M, MUKAI T, KANAHASHI H, KOHZU H, TANABE S and HIGASHI K (1999), Enhancement of energy absorption in closed-cell aluminum by the modification of cellular structures, *Scripta Materialia*, **41**(10), 1055–1060.

NEMAT-NASSER S, KANG W J, MCGEE J D, GUO W-G and ISAACS J B (2007), Experimental investigation of energy-absorption characteristics of components of sandwich structures, *International Journal of Impact Engineering*, **34**, 1119–1146.

POUGET J (1992), Stability of nonlinear structures in a lattice model for phase transformations in alloys, *Physical Review B*, **46**(17), 10554–10562.

POUGET J (1993), Lattice dynamics and stability of modulated-strain structures for elastic phase transitions in alloys, *Physical Review B*, **48**(2), 864–875.

QIAO P Z, YANG M J and BOBARU F (2008), Impact mechanics and high energy absorbing materials: review, *Journal of Aerospace Engineering*, **21**(4), 235–248.

RATHBUN H R, RADFORD D D, XUE Z, HE M Y, YANG J, DESHPANDE V, FLECK N A, HUTCHINSON J W, ZOK F W and EVANS A G (2006), Performance of metallic honeycomb-core sandwich beams under shock loading, *International Journal of Solids and Structures*, **43**(6), 1746–1763.

REID S R and ZHOU G (2000), *Impact Behavior of Fiber Reinforced Composite Materials and Structures*, CRC Press, Boca Raton, FL.

SARVA S, NEMAT-NASSER S, MCGEE J and ISAACS J (2007), The effect of thin membrane restraint on the ballistic performance of armor grade ceramic tiles, *International Journal of Impact Engineering*, **34**, 277–302.

SHIM V P, TAN V B C and TAY T E (1995), Modeling deformation and damage characteristics of woven fabric under small projectile impact, *International Journal of Impact Engineering*, **16**, 585–605.

SHIPSHA A, HALLSTROM S and ZENKERT D (2003), Failure mechanisms and modeling of impact damage in sandwich beams – a 2D approach. Part I. Experimental Investigation, *Journal of Sandwich Structures and Materials*, **5**(1), 7–32.

© Woodhead Publishing Limited, 2010

SLEPYAN L I and AYZENBERG-STEPANENKO M V (2004), Localized transition waves in bi-stable-bond lattices, *Journal of the Mechanics and Physics of Solids*, **52**, 1447–1479.

SRIRAM R, VAIDYA U K and KIM J E (2006), Blast impact response of aluminum foam sandwich composites, *Journal of Material Science*, **41**(13), 4023–4039.

TAYLOR W T and VINSON J R (1990), Modeling ballistic impact into flexible materials, *AIAA Journal*, **28**, 2098–2103.

THOMSEN O T (1995), Theoretical and experimental investigation of local bending effects in sandwich plates, *Composite Structures*, **30**, 85–101.

TSAI C Z, WU E and LUO B H (1998), Forward and inverse analysis for impact on sandwich panels, *AIAA J*, **36**(11), 2130–2136.

TURK M H and HOO FATT M S (1999), Localized damage response of composite sandwich plates, *Composites Part B: Engineering J*, **30**, 157–165.

VAZIRI A and HUTCHINSON J W (2007), Metal sandwich plates subject to intense air shocks, *International Journal of Solids and Structures*, **44**(6), 2021–2035.

VAZIRI A, XUE Z and HUTCHINSON J W (2006), Metal sandwich plates with polymeric foam-filled cores, *Journal of Mechanics of Materials and Structures*, **1**(1), 95–128.

WIERZBICKI T (1983), Crushing analysis of metal honeycombs, *International Journal of Impact Engineering*, **1**, 157–174.

WIERZBICKI T, ALVAREZ A and HOO FATT M S (1995), Impact energy absorption of sandwich plates with crushable core, AMD-205, *Proceedings of the 1995 joint ASME Applied Mechanics & Materials Summer Meeting*, 28–30 June, Los Angeles, CA.

XU J, ASKARI A, WECKNER O and SILLING S A (2008), Peridynamic analysis of impact damage in composite laminates, *Journal of Aerospace Engineering, Special Issue on 'Impact Mechanics and High Energy Absorbing Materials'*, **21**(3), 187–194.

XUE Z and HUTCHINSON J W (2004), A comparative study of impulse-resistant metal sandwich plates, *International Journal of Impact Engineering*, **30**, 1283–1305.

YANG G Q, SPENCER JR, B F, JUNG H-J and CARLSON J D (2004), Dynamic modeling of large-scale magnetorheological damper systems for civil engineering applications, *Journal of Engineering Mechanics*, **130**(9), 1107–1114.

YANG M J and QIAO P (2005), Higher-order impact modeling of sandwich beams with flexible core, *International Journal of Solids and Structures*, **42**(20), 5460–5490.

YANG M J and QIAO P (2007), Impact and damage prediction of sandwich beams with flexible core considering arbitrary boundary effects, *Journal of Sandwich Structures and Materials*, **9**(5), 411–444.

YANG M J and QIAO P (2008), Quasi-static crushing behavior of aluminum honeycomb materials, *Journal of Sandwich Structures and Materials*, **10**(2), 133–160.

ZHAO Y, TAYA M, KANG Y S and KAWASAKI A (2005), Compression behavior of porous NiTi shape memory alloy, *Acta Materialia*, **53**(2), 337–343.

ZHAO Y, TAYA M and IZUI H (2006), Study on energy absorbing composite structure made of concentric NiTi spring and porous NiTi, *International Journal of Solid and Structures*, **43**, 2497–2512.

ZHENG X and BINIENDA W K (2008), Rate dependent shell element composite material model implementation in LS-DYNA, *Journal of Aerospace Engineering,*

© Woodhead Publishing Limited, 2010

Special Issue on 'Impact Mechanics and High Energy Absorbing Materials', **21**(3), 140–151.

ZHU L F, CHATTOPADHYAY A and GOLDBERG R K (2006), A 3D micromechanics model for strain rate dependent inelastic polymer matrix composites, *47th AIAA/ASME/ASCE/AHS/ASC Structures, Structural Dynamics & Materials Conference*, 1–4 May, Newport, RI.

ZHU L F, CHATTOPADHYAY A and GOLDBERG R K (2008), A failure model for rate dependent polymer matrix composite laminates under high velocity impact, *Journal of Aerospace Engineering, Special Issue on 'Impact Mechanics and High Energy Absorbing Materials'*, **21**(3), 132–139.

© Woodhead Publishing Limited, 2010

5

Modeling the blast response of hybrid laminated composite plates

A. E. BOGDANOVICH, 3TEX, Inc., USA

Abstract: There has been a substantial increase in demand for a three-dimensional (3D) dynamic structural analysis tool capable of predicting explosive blast effects on protective armor and blast mitigation structures. The chapter describes a 3D analysis approach, based on 3D dynamic variational theory, developed for a highly transient loading of thick layered hybrid blast mitigation panels. Panels may include layers of traditional composites or novel 3D textile composites along with ceramics, metals, lightweight foams, Balsa wood or other popular materials. The approach is illustrated by solving four examples of the blast loaded panels and comparing their blast mitigation capabilities.

Key words: blast, shock wave, dynamic analysis, 3D analysis, composite, sandwich, layered media, material damping.

5.1 Introduction

5.1.1 Blast phenomena, their modeling and predictive analysis tools

The demand for 3D dynamic structural analysis tools capable of predicting explosive blast effects on protective armor and blast mitigation structures has increased substantially since the late 1990s. Commonly, these types of structures incorporate thick layers of various types of composites, ceramics, metals, lightweight foams, Balsa wood and other popular materials. The types of structures that require protection against blast attacks include ground vehicles, buildings, marine vessels, infrastructure systems, fixed wing and rotary wing aircraft, etc. Development of physically adequate and sufficiently accurate transient analysis methods and efficient computational tools aimed at predicting the effects of shock waves, along with the primary and secondary fragmentation caused by small and large bombs, is much needed.

It has been known for a while and repeatedly proved by the recent terrorist attacks and in the military operations that injuries/fatalities are caused by a combination of several factors: the blast overpressure, metallic bomb casing fragments and/or irregular objects filling the bomb, collapse of buildings, vehicles and other transportation systems, as well as secondary

© Woodhead Publishing Limited, 2010

debris of metal, concrete, brick, glass and fragments of other construction materials that are formed and accelerated by multiple propagated and reflected shock waves. Stationary or portable blast mitigation barriers used for building, ship and vehicle protection can greatly reduce fatalities. In general, the required predictive analysis tools should address a number of specific practical problems (see examples in Navy, 1990; ASCE, 1997; Bulson, 1997; Air Force, 1998; Bogosian *et al.*, 1999; Wesevich and Abernathy, 1999; Fertal *et al.*, 2001; Hansen *et al.*, 2002; Esper, 2003; Luccioni *et al.*, 2004). These include establishing relations between the 'ideal' or 'non-ideal' (such as ammonium nitrate and fuel oil – ANFO) explosive characteristics on the one side and the 'field-free' blast pressure history on the other, and correlating the field-free and the 'true' pressure pulse acting on the structural elements like front wall, back wall, side wall, roof, ceiling, etc. Notably, so-called 'reflected blast pressure' acting on the front wall may significantly exceed the peak field-free pressure.

There is a large bulk of literature on explosives, explosions, blast wave formation and propagation, dynamic blast loads, structural response and other related topics (see for example works by Baker *et al.*, 1983; Kinney and Graham, 1985; Zukas and Walters, 1998, where the authors provide excellent insight into this topic). From there one can learn, in particular, that the blast pressure versus time relationship is typically characterized by a peak pressure, impulse and shape. Though not physically accurate, it is commonly assumed in many popular analysis approaches and available computational tools that the blast pressure rises instantaneously to a peak pressure, while in reality the pressure rise may take microseconds, tens or even hundreds of microseconds. Then the blast pressure decays exponentially to ambient pressure. Importantly, there is a rather long time period when the pressure is below the ambient pressure. The 'negative' phase of blast pressure variation lasts for rather a long time, but the pressure magnitude is very small in comparison with the 'positive' pressure peak. Therefore, the negative phase can have only a minor effect on the overall dynamic response of an armor system or engineering structure. This is why the pulse shape of the type shown in Fig. 5.1, having only a 'positive' pressure branch, is commonly accepted. In practical analyses of engineering structures, this realistic type of incipient pressure pulse is often represented by a triangle with the peak pressure multiplied by the 'reflection factor' in the case of a front wall.

Typical structural materials are highly vulnerable to blast overpressure even if exposed to rather low-mass explosive charges at a relatively short standoff distances. Predecessors of total fracture and collapse of the structures exposed to blast overpressure are: initiation and growth of barely visible microcracks, their coalescence resulting in the formation of macrocracks, followed by the material fragmentation and spalling from the back

© Woodhead Publishing Limited, 2010

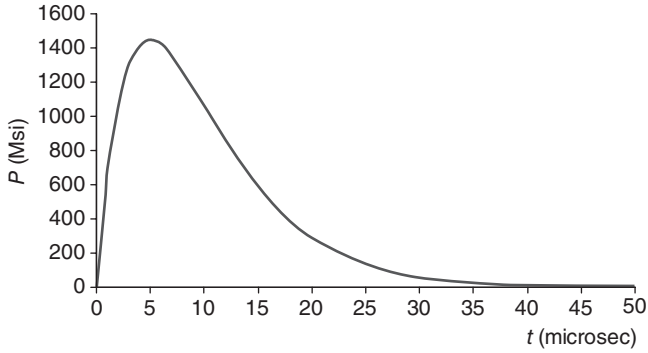

5.1 A typical pressure–time variation for an incident blast pulse. The pulse peak value, its duration time and shape have to be related (experimentally or theoretically) to the explosive characteristics and standoff distance.

free surface of the structure. All these complex phenomena occur during a very short initial time interval, typically from hundreds of microseconds to several milliseconds. There are many analytical and computational approaches aimed at this class of theoretical problems, ranging from rudimentary closed-form solutions to hydrocode and to commercial finite element codes (like ABAQUS®, ANSYS, DYNA 3D, LS-DYNA®, etc.). Also, many specialty analytical models and numerical analysis approaches aimed at the analysis of blast-induced phenomena are known. Examples can be found in the publications by Navy (1990), Yen and Jones (1997), Zukas and Walters (1998), Bogdanovich and Yushanov (1999a), Bogosian *et al.* (1999), Fertal *et al.* (2001), Hansen *et al.* (2002), Esper (2003), Librescu *et al.* (2004), Luccioni *et al.* (2004), Bogdanovich and Mungalov (2005), Yen *et al.* (2005), Park *et al.* (2006), Shukla *et al.* (2007), Tekalur *et al.* (2009).

One basic finite element analysis approach, which is often used for the blast response predictions of civil engineering structures, is described in Navy (1990). It assumes that each building component responds as the equivalent single-degree-of-freedom system. This approach was also recommended in some of the later blast resistant structures design manuals (see ASCE, 1997; Bulson, 1997). Implementation of hydrocode was illustrated by Luccioni *et al.* (2004) and Yen and Jones (1997) among many other authors. Examples of using commercial finite element codes can be found in works of Hansen *et al.* (2002), Esper (2003) and Yen *et al.* (2005) among many others.

Bogdanovich and Yushanov (2000a) developed an original 3D dynamic variational analysis approach, which can be viewed as the generalization of the 3D static analysis approach by Bogdanovich (2000). In that approach, inhomogeneous material or inhomogeneous structure are modeled in terms

© Woodhead Publishing Limited, 2010

of a 3D anisotropic mosaic solid, which assumes an arbitrary step-wise variation of elastic properties in all three coordinate directions. The approach presented in Bogdanovich and Yushanov (2000a) has been applied to the simulations of the transient response of multilayer panels made of dissimilar materials under blast loading by Bogdanovich and Yushanov (1999a) and by Bogdanovich and Mungalov (2005). This analysis approach and 3TEX's in-house computer code 3D MOSAIC will be implemented in this paper for the analysis of different layered composite panels exposed to highly transient blast pressure pulse.

5.1.2 Blast mitigation materials

Various new emerging materials show great potential for ballistic and blast protection of military and civilian personnel, ground vehicles, marine vessels, aircraft and civil engineering objects. An important place among them has been gained by composite materials reinforced with integral, non-crimp 3D orthogonal woven fabric preforms described in Mohamed *et al.* (2001). A substantial amount of experimental work has been devoted since the late 1990s to their performance characterization in the care of ballistic impact loading (Bogdanovich and Singletary, 2000; Singletary *et al.*, 2001; Gama *et al.*, 2004, 2005), (Bogdanovich *et al.*, 2005; Grogan *et al.*, 2007; LeBlanc *et al.*, 2007), blast loading (LeBlanc *et al.*, 2007; Shukla *et al.*, 2007; Tekalur *et al.*, 2009) and low-velocity impact loading (Baucom and Zikry, 2005; Baucom *et al.*, 2006). The principal benefits provided by 3D reinforcement architectures are, of course, related to the presence of trough-thickness yarns (aka 'Z yarns' or 'binder yarns'), which enable full delamination suppression, prevention of premature failure and significant increase of dynamic resistance and structural integrity. Specifically, it has been demonstrated that composite panels reinforced with a single-layer, relatively thick 3WEAVE® fabric produced by 3TEX, Inc. have much higher survivability under drop weight impact applied repeatedly at the same site of the structure (Mohamed *et al.*, 2001) and under closely spaced multiple ballistic hits (Bogdanovich *et al.*, 2005; Grogan *et al.*, 2007). Other tests showed substantially improved blast resistance of unitary 3D woven composites versus equivalent areal weight two-dimensional (2D) woven laminates.

A large volume of experimental data demonstrating impressive impact, ballistic and blast performance characteristics of 3D woven composites has given rise to significant practical interest in their application in various armor systems protecting military personnel, ground vehicles, naval ships, aircraft and rotorcraft. However, in order to go beyond initial success and develop optimized multifunctional structures, comprehensive theoretical work has to support the ongoing experimental studies. The first requirement is to achieve a profound understanding of the whole scope of 3D

© Woodhead Publishing Limited, 2010

transient deformation and dynamic failure processes in 3D woven composites and their behavior when integrated into various complex armor systems.

The majority of today's real-life armor systems include more than one material type; accordingly, individual materials are combined in a layered fashion. Specifically, the front face ceramic layer (alternatively, an assembly of ceramic tiles can be used) or a thin steel layer may be followed by a thin specialty rubber layer, by a much thicker (and relatively low-density) aluminum foam, or by a woven fabric reinforced composite layer. The rear, backing section is typically made of a relatively thick glass or hybrid fiber polymer matrix composite, which may contain many layers of plain weave of similar 2D woven fabric. Recently, thick 3D woven fabrics were introduced as the reinforcements for backing composite materials, as reported by Singletary *et al.* (2001), Bogdanovich *et al.* (2005) and Grogan *et al.* (2007). The initial success of their applications in a variety of protective armor systems has inspired continued theoretical and experimental studies of the dynamic behavior of this class of composite materials.

Another type of structural materials that attracts great interest in the context of blast mitigation is sandwich constructions. These materials have traditionally found a broad range of applications in the aerospace and marine industries due to their lightweight resulting from the use of low-density cores. The mechanical behavior and structural response of sandwich materials under quasi-static loadings have been studied in numerous publications (see notable books by Vinson (1999) and Davies (2001) and conference proceedings edited by Vautrin (1998) among numerous publications). Sandwich structures are often subjected to highly transient shock loading conditions, with the surface pressure spread over either the entire structure or some local area. However, there are few published experimental studies of the dynamic response of sandwich structures to localized shock wave loadings, as reported by Shukla *et al.* (2007) and Tekalur *et al.* (2009). The overall blast response of the sandwich should be dependent on the stiffness and strength of the skin material, compressive and shear moduli and strengths of the core, and on the bonding strength between the skins and core. Due to the specific nature of its construction, any sandwich has its through-thickness strength limited by the strength of the core or bonding strength between the skins and core. Thus, maximizing these strength characteristics without significant loss of the lightweight provided by a sandwich construction is a very important practical task.

In light of these considerations and with the aim of achieving better and better performances of layered and sandwich materials exposed to blast loading, several design advancements have been sought after in recent years. Among the most interesting is through-thickness stitching of the skin fabrics and foam core in an integral fashion (see Shukla *et al.*, 2007; Tekalur *et al.*, 2009). The stitching results in stiffening and strengthening of the core

© Woodhead Publishing Limited, 2010

and, also very importantly, in a significant increase in the core–skin joining strength in composite sandwiches. Materials of this type, named TRANSONITE®, are manufactured by Martin Marietta Composites using a pultrusion method with different fabric reinforcements of the skins, different foam core materials and different stitching patterns. In one particular product type, the aforementioned 3WEAVE® fabrics manufactured by 3TEX have been used for the skin reinforcement, and TRYMER™ 200 L foam core manufactured by Dow Chemical was used as the base core material. These materials have been stitched together using E-glass roving (different stitching densities can be applied) and then infused with polymeric resin in the pultrusion process. The type of sandwich material produced has great potential for applications where it is necessary to combine lightweight, high structural load-bearing capability, efficient blast mitigation ability, high damage tolerance and general survivability.

5.1.3 Scope of the chapter

This chapter will demonstrate several new specific applications of the 3D variational analysis approach and computational tool named 3D MOSAIC. The mathematical background and computational algorithms were described in the necessary detail by Bogdanovich (2000) and Bogdanovich and Yushanov (2000a). The approach incorporates several distinct and practically important features which make it advantageous over other versions of 3D hexahedral finite element analysis. Although the currently available 3D MOSAIC computer code is capable of solving 3D static and transient dynamic problems only for relatively simple structural shapes, the tool has proved valuable for rapid evaluation of different candidate materials and structural designs being considered for blast mitigation applications. It allows one to quickly formulate the necessary dynamic boundary value problems, run computationally efficient and exceptionally accurate analysis and assess convergence of the results. The latter task can be accomplished in three alternative ways: (i) by increasing the degree of the Bernstein approximation polynomial, which serves as the basis function, (ii) by refining the computational mesh, and (iii) by using both approaches (i) and (ii) simultaneously. The analysis enables the prediction of full 3D transient displacement, strain and stress fields at any point of the structure, including any interface between dissimilar materials. It allows one to apply the maximum allowable deflection criterion along with the maximum strain or maximum stress failure criterion for predicting transient structural response and material integrity performance for the known pressure pulse history. It is important to note that in the dynamic analysis, the computational tool to be used here preserves all of the inertia terms without neglecting or lumping any of them. This, in turn, enables keeping in the analysis all types

© Woodhead Publishing Limited, 2010

of multiscale 3D stress wave propagation processes. The material damping (energy dissipation) is also accounted for in the analysis for each constituent material. The next section provides necessary information on this analysis approach.

5.2 Synopsis of 3D Mosaic analysis approach

Following the original 3D Mosaic analysis concept originally proposed in Bogdanovich (1992, 1993) and further developed in Bogdanovich (2000) and Bogdanovich and Yushanov (2000a), we consider here a general problem of dynamic deformation of an arbitrary 3D mosaic parallelepiped, which may be composed of any number of solid, generally anisotropic material bricks assembled along the three coordinate directions x, y and z, as illustrated in Fig. 5.2. All of the bricks may have their distinct elastic properties, or some of them may have identical properties, depending on the composition of individual materials within the parallelepiped. In one important specific case, all of the bricks within some z-coordinate interval $z_n \le z \le z_{n+1}$ have identical properties, and we get a continuous homogeneous 'layer' within the mosaic body with its plane perpendicular to the z axis. Further, if the material properties of all of the bricks are identical for all of the z-coordinate intervals, namely $z_1 \le z \le z_2, \ldots, z_N \le z \le z_{N+1}$, we get traditional 'layered' or 'laminated' material, where material properties are constant within each individual 3D layer, but change from layer to layer (i.e., along the z-coordinate) in a step-wise manner. Furthermore, if properties of all of the bricks within all of the aforementioned z-intervals are identical, we arrive at a homogeneous 3D parallelepiped, containing only one kind of material.

Obviously, any special case of anisotropy of each individual brick material can be analyzed using this model. Specifically, in the case of one plane

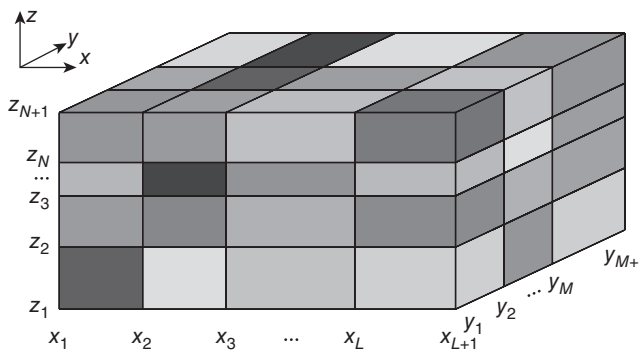

5.2 Generic 3D Mosaic solid model.

© Woodhead Publishing Limited, 2010

of elastic symmetry we have a monoclinic material, in the case of three planes of elastic symmetry – an orthotropic material, in the case of one plane of isotropy – a monotropic material, and in the case of three planes of isotropy – an isotropic material. This generality of the model allows one to apply it to any combination of solid materials like metals, concretes, ceramics, plastics, wood, unidirectional composites, cross-ply and angle-ply laminated composites, sandwiches, as well as to a variety of 2D and 3D textile-reinforced composites.

The stress–strain relations adopted for the *s*th generally anisotropic, linearly elastic brick in the mosaic parallelepiped are written as

$$\sigma_{ij}^{(s)}(\mathbf{r},t) = C_{ijkl}^{(s)}\varepsilon_{kl}^{(s)}(\mathbf{r},t), \quad i,j = 1,2,3 \qquad [5.1]$$

where $\sigma_{ij}^{(s)}(\mathbf{r},t)$ and $\varepsilon_{kl}^{(s)}(\mathbf{r},t)$ are coordinate- and time-dependent stress and strain fields, while $C_{ijkl}^{(s)}$ are coordinate- and time-independent material stiffness matrix components; $\mathbf{r} = \{x,y,z\}$ is a position vector and t is time variable. The strains $\varepsilon_{ij}^{(s)}(\mathbf{r},t)$ are related to the displacements $u_i^{(s)}(\mathbf{r},t)$ through conventional equations of linear elasticity:

$$\varepsilon_{ij}^{(s)}(\mathbf{r},t) = \frac{1}{2}\left(\frac{\partial u_i^{(s)}(\mathbf{r},t)}{\partial x_j} + \frac{\partial u_j^{(s)}(\mathbf{r},t)}{\partial x_i}\right) \qquad [5.2]$$

The construction of the 3D mosaic parallelepiped shown in Fig. 5.2 is fully determined by the location of the three sets of mutually orthogonal planes: $x = x_l$, $y = y_m$, $z = z_n$, where $l = 1, 2, \ldots, L + 1$, $m = 1, 2, \ldots, M + 1$ and $n = 1, 2, \ldots, N + 1$. The total number S of the bricks in the mosaic parallelepiped is expressed as $S = L \cdot M \cdot N$. The discretization planes that separate distinct material bricks are, essentially, physical interfaces, where one or more material properties may have a jump. This emphasizes again that a 'material' discretization mesh as shown in Fig. 5.2 has a different meaning than an 'element' discretization mesh used in conventional finite element analysis. A 'computational' mesh, which is necessary for the present analysis, is shown by thin lines in Fig. 5.3. This mesh can be uniform or arbitrarily non-uniform; it is determined by a set of three mutually orthogonal planes which divide each of the intervals $(x_1,x_2), \ldots, (x_L,x_{L+1})$ in the x direction, $(y_1,y_2), \ldots, (y_M,y_{M+1})$ in the y direction and $(z_1,z_2), \ldots, (z_N,z_{N+1})$ in the z direction into some numbers of sub-intervals. The discretization into such sub-intervals serves essentially the same purpose as the discretization into 3D hexahedral elements in conventional 3D finite element analysis. The entity contained between two adjacent computational planes in each of the three coordinate directions will be further termed a 'discrete element'. So, each material brick may now be viewed as an assembly of such discrete elements. Their number within the material brick depends on the number of discretization planes within the brick. Now it becomes

© Woodhead Publishing Limited, 2010

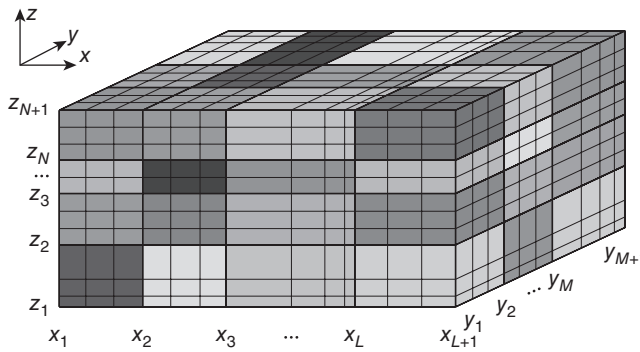

5.3 Two levels of discretization applied to 3D mosaic parallelepiped: thick lines show discretization into material bricks and thin lines into computational discrete elements.

obvious that a discrete element in the present analysis has the same meaning as a finite element in conventional 3D finite element analysis.

Further analytical derivations in the framework of the 3D Mosaic variational dynamic analysis approach involve Hamilton's variational principle.

$$\delta \int_{t_1}^{t_2} L(t)\mathrm{d}t = 0 \qquad [5.3]$$

where $L(t)$ is the Lagrange function incorporating kinetic energy $T(t)$, strain energy $P(t)$ and work of external surface forces $W(t)$:

$$L(t) = T(t) - P(t) + W(t) = \sum_{q=1}^{Q} [T^{(q)}(t) - P^{(q)}(t) + W^{(q)}(t)] \qquad [5.4]$$

Here, $T^{(q)}$, $P^{(q)}$ and $W^{(q)}$ are kinetic energy, strain energy and work of external surface forces determined for an individual discrete element, which is symbolized by index q in the mosaic parallelepiped. In order to obtain explicit expressions for these energy terms, the form of the 3D displacement field variation along coordinates x, y and z has to be specified first. A 3D displacement field is assumed for each individual discrete element in the form of triple series.

$$u_\alpha^{(q)}(x, y, z, t) = \sum_{i=0}^{I_q} \sum_{j=0}^{J_q} \sum_{k=0}^{K_q} U_{ijk}^{\alpha,q}(t) X_i(x) Y_j(y) Z_k(z); \quad \alpha = 1, 2, 3 \qquad [5.5]$$

Here, integers I_q, J_q and K_q define the initial number of degrees of freedom (dof) possessed by each discrete element in the mosaic parallelepiped; $U_{ijk}^{\alpha,q}(t)$ are undetermined time-dependent coefficients; $X_i(x)$, $Y_j(y)$ and

© Woodhead Publishing Limited, 2010

$Z_k(z)$ are three sets of basis functions, which are assumed here to be identical for all of the discrete elements.

A specific choice of the basis functions is required in order to take the next step in the analysis development. Of course, there are many different polynomial types (both interpolation and approximation ones) which can take the role of basis functions. Here, following Bogdanovich (2000), the basis functions are taken in the form of Bernstein approximation polynomials of an arbitrary degree. Their explicit form for a discrete element located between planes x_λ and $x_{\lambda+1}$, y_μ and $y_{\mu+1}$, z_υ and $z_{\upsilon+1}$ in written as follows:

$$X_i(x) = \begin{cases} B_i^I(x) = \dfrac{I!}{i!(I-i)!}\left(\dfrac{x-x_\lambda}{x_{\lambda+1}-x_\lambda}\right)^i\left(\dfrac{x_{\lambda+1}-x}{x_{\lambda+1}-x_\lambda}\right)^{I-i} & \text{for } x \in [x_\lambda, x_{\lambda+1}] \\ 0 & \text{else} \end{cases} \quad [5.6]$$

$$Y_j(y) = \begin{cases} B_j^J(y) = \dfrac{J!}{j!(J-j)!}\left(\dfrac{y-y_\mu}{y_{\mu+1}-y_\mu}\right)^j\left(\dfrac{y_{\mu+1}-y}{y_{\mu+1}-y_\mu}\right)^{J-j} & \text{for } y \in [y_\mu, y_{\mu+1}] \\ 0 & \text{else} \end{cases} \quad [5.7]$$

$$Z_k(z) = \begin{cases} B_k^K(z) = \dfrac{K!}{k!(K-k)!}\left(\dfrac{z-z_\upsilon}{z_{\upsilon+1}-z_\upsilon}\right)^k\left(\dfrac{z_{\upsilon+1}-z}{z_{\upsilon+1}-z_\upsilon}\right)^{K-k} & \text{for } z \in [z_\upsilon, z_{\upsilon+1}] \\ 0 & \text{else} \end{cases} \quad [5.8]$$

These equations apply to all discrete elements in the mosaic parallelepiped. The triad of integers λ, μ and υ defines the location of all computational boundaries within the body. From this point of view, the number q, which identifies a discrete element, can also be considered a function of these three integers, $q = q(\lambda,\mu,\upsilon)$. Therefore, in this analysis approach the displacement field representation in the form of triple series (Eq. 5.5) with the basis functions (Eqs 5.6–5.8) is established for each discrete element of the mosaic parallelepiped, as illustrated in Fig. 5.4. Obviously, each material brick may be discretized by as many planes in the x, y and z directions as necessary; the numbers of discretization planes in each direction is determined by integers λ, μ and υ.

The above basis functions (Eqs 5.6–5.8), called Bernstein basis functions, possess certain unique properties which make them very suitable for deriving all of the necessary equations in a very elegant closed form. The resulting equations, used in the computational algorithms, appear to be rather simple (see Bogdanovich, 2000). Our next task is to derive mathematical conditions that would ensure the necessary order of connectivity among all of the discrete elements and all of the material bricks in the mosaic

© Woodhead Publishing Limited, 2010

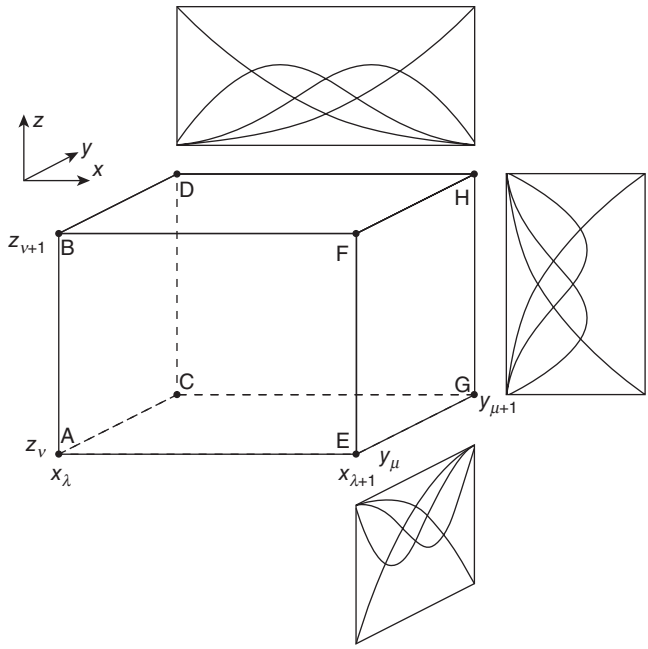

5.4 Schematics of Bernstein polynomial basis functions in *x*-, *y*- and *z*-directions for an individual discrete element.

parallelepiped. Specifically, when using basis functions 5.6–5.8, the displacement continuity conditions between any two adjacent discrete elements (including those which are separated by physical interfaces) are expressed through the following relations derived in Bogdanovich (2000):

$$\begin{aligned} U_{Ijk}^{\alpha,q(\lambda,\mu,\nu)}(t) &= U_{0jk}^{\alpha,q(\lambda+1,\mu,\nu)}(t) \\ U_{iJk}^{\alpha,q(\lambda,\mu,\nu)}(t) &= U_{i0k}^{\alpha,q(\lambda,\mu+1,\nu)}(t) \\ U_{ijK}^{\alpha,q(\lambda,\mu,\nu)}(t) &= U_{ij0}^{\alpha,q(\lambda,\mu,\nu+1)}(t) \end{aligned} \quad [5.9]$$

These relations shall be imposed in the solution algorithm for all those values of q, α, i, j and k which are involved in the formulation of the displacement continuity conditions for adjacent discrete elements. It is necessary to point out that the displacement continuity conditions are imposed here analytically and exactly, so there would be no computational displacement mismatch at any point of any interface between two adjacent bricks. Another important feature of this analysis approach is that the Bernstein basis functions (Eqs 5.6–5.8) enable one to exactly satisfy the external geometric boundary conditions of one important specific type, namely the condition of uniformly distributed (zero or non-zero) displacement along

© Woodhead Publishing Limited, 2010

some local surface element (see Bogdanovich (2000) for details of the derivations).

After adopting the displacement field representation in terms of Eqs 5.5–5.8, the following analytical expressions for the kinetic energy $T^{(q)}$, strain energy $P^{(q)}$ and work of external surface tractions $W^{(q)}$ are derived for each individual discrete element:

$$T^{(q)}(t)=\frac{1}{2}\sum_{i=0}^{I}\sum_{j=0}^{J}\sum_{k=0}^{K}\sum_{f=0}^{I}\sum_{g=0}^{J}\sum_{h=0}^{K}\sum_{\alpha=1}^{3}M_{ijk,fgh}^{\alpha\alpha,q}\frac{\mathrm{d}U_{ijk}^{\alpha,q}(t)}{\mathrm{d}t}\frac{\mathrm{d}U_{fgh}^{\alpha,q}(t)}{\mathrm{d}t}=\frac{1}{2}\dot{\mathbf{U}}^{(q)T}(t)\mathbf{M}^{(q)}\dot{\mathbf{U}}^{(q)}(t) \quad [5.10]$$

$$P^{(q)}(t)=\frac{1}{2}\sum_{i=0}^{I}\sum_{j=0}^{J}\sum_{k=0}^{K}\sum_{f=0}^{I}\sum_{g=0}^{J}\sum_{h=0}^{K}\sum_{\alpha=1}^{3}\sum_{\beta=1}^{3}U_{ijk}^{\beta,q}(t)K_{ijk,fgh}^{\alpha\beta,q}U_{fgh}^{\alpha,q}(t)=\frac{1}{2}\mathbf{U}^{(q)T}(t)\mathbf{K}^{(q)}\mathbf{U}^{(q)}(t) \quad [5.11]$$

$$W^{(q)}(t)=\sum_{i=0}^{I}\sum_{j=0}^{J}\sum_{k=0}^{K}\sum_{\alpha=1}^{3}U_{ijk}^{\alpha,q}(t)R_{ijk}^{\alpha,q}(t)=\mathbf{U}^{(q)T}(t)\mathbf{R}^{(q)}(t) \quad [5.12]$$

Here, $\mathbf{U}^{(q)}(t)$ is the vector of undetermined displacement coefficients, $\mathbf{M}^{(q)}$ is the mass matrix, $\mathbf{K}^{(q)}$ is the stiffness matrix and $\mathbf{R}^{(q)}(t)$ is the vector of external surface tractions; their explicit expressions can be found in Bogdanovich (2000). All non-zero elements of the mass matrix are determined as following:

$$m_{ijk,fgh}^{11,q}=m_{ijk,fgh}^{22,q}=m_{ijk,fgh}^{33,q}=\rho^{(q)}X_{if}Y_{jg}Z_{kh} \quad [5.13]$$

where

$$X_{if}=\int_{x_\lambda}^{x_{\lambda+1}}X_i(x)X_f(x)\mathrm{d}x,\ Y_{jg}=\int_{y_\mu}^{y_{\mu+1}}Y_j(y)Y_g(y)\mathrm{d}y,\ Z_{kh}=\int_{z_\nu}^{z_{\nu+1}}Z_k(z)Z_h(z)\mathrm{d}z \quad [5.14]$$

Now we have derived all the necessary terms for the Lagrange function (Eq. 5.3).

The next step in the algorithmic development includes modification of the primary displacement approximation (Eq. 5.5) by incorporating the internal displacement continuity conditions (Eq. 5.9) and external geometric boundary conditions which have to be formulated for each specific boundary value problem. Resulting from this, the kinematically admissible displacement field is obtained. Then, the initial Lagrange function (Eq. 5.4) is modified with respect to that kinematically admissible displacement field, as explained in Bogdanovich and Yushanov (2000a). After that, by applying Hamilton's variational principle (Eq. 5.3), a linear system of ordinary differential equations is derived. The system can be written in the following general form:

$$\mathbf{M}\ddot{\mathbf{U}}(t)+\mathbf{K}\mathbf{U}(t)=\mathbf{R}(t) \quad [5.15]$$

© Woodhead Publishing Limited, 2010

This system of equations is supplemented by respective initial conditions:

$$\mathbf{U}(t_0) = \mathbf{U}_0, \dot{\mathbf{U}}(t_0) = \mathbf{V}_0 \quad [5.16]$$

The initial value problem formulated by Eqs 5.15 and 5.16 is to be solved numerically, by direct integration; standard routines of different kinds are available for this purpose. The numerical integration results in computing time-dependent coefficients $U_{ijk}^{\alpha,q}(t)$ determined at some set of time instants $\{t_1, t_2, \ldots, t_T\}$. Intervals between the time instants here correspond to the numerical integration step, which is chosen by the analyst.

After the set of functions $U_{ijk}^{\alpha,q}(t)$ has been computed, the final steps of the analysis development can be made. The desired transient 3D displacement field $u_\alpha^{(q)}(x,y,z,t)$ for each discrete element is computed by direct summation of the triple series (Eq. 5.5). Obviously, this can be performed for any given triad of x, y, z coordinates belonging to each discrete element, including its boundaries, and for any time instant from the set $\{t_1, t_2, \ldots, t_T\}$. After that the transient 3D strain field is computed by substituting the displacement series (Eq. 5.5) into Eq. 5.2 and summation of the respective triple series; again, the strain field can be computed for any time instant from the above set and for any coordinate point. Finally, the desired transient 3D stress field is obtained by substituting the previously determined triple series for strains into Eq. 5.1 and summation of the obtained triple series for stresses. Again, this can be performed for any time instant from the same set and for any triad of coordinates. As should be clear from the above algorithm description, all displacement, strain and stress values are obtained in this analysis approach directly from their respective triple series with Bernstein basis functions. No extrapolations to the 'integration points' or other post-processing procedures of this kind are used or required. This feature makes the strain and stress post-processing much more economical and accurate.

A broad variety of 3D static and dynamic boundary value problems has been solved using this generic approach in the last decade (see for example papers of Bogdanovich and Yushanov (1999a, b, 2000a, b), Bogdanovich (2000, 2001, 2003, 2006, 2009), Bogdanovich and Mungalov (2005) and Tekalur *et al.* (2009). In Bogdanovich (2009), a novel 3D progressive failure analysis has been presented for a quasi-static loading. It is based on the same 3D Mosaic model and variational analysis approach. Its dynamic extension is currently under development.

5.3 Numerical simulations of a structural response for blast loading: input

The goal of predicting the dynamic transient response of some engineering structure exposed to virtual blast loading requires a lot of input data, which

© Woodhead Publishing Limited, 2010

are necessary for the formulation of the appropriate boundary value problem. This, in turn, requires the solving of several specific tasks of a very different nature. One of these is to determine the physical boundary conditions caused by the blast loading, including the determination of the pressure pulse shape, its application area and distribution over the area. The other task is to adequately formulate the necessary geometric boundary conditions at the ends of the structural component (if it is considered to be stand-alone), or to formulate the joining conditions within a specific assembly of structural components. Another important aspect of formulating an adequate set of boundary conditions may be accounting for the 'secondary' blasts caused by shock waves reflected from the nearby structural elements.

Next, the required input data naturally include various kinds of mechanical properties of all the materials involved (elastic and strength characteristics, plastic and/or viscoelastic properties, energy absorption characteristics, strain rate dependency, etc.). If micromechanical failure analysis is used, the characteristics of progressive damage and possible phase transformations during blast loading may be required. Obtaining all of these input data with the aim of performing reasonably accurate predictive blast analysis is a complex task in itself, which can be rarely solved to a full satisfaction. In practice, various compromises are inevitable in order to simplify the blast loading formulation, like idealizing the boundary conditions and reducing the amount of input data required for the materials. Specifically, multiple shock wave reflections are typically ignored, the real-life complex joints are modeled in terms of some relatively simple 'simply supported', 'clamped' or 'free' edge boundary conditions, and material behavior is idealized as 'elastic', 'rigid–plastic', 'viscous', etc., each of which represents one of the extreme and, possibly, not fully realistic material behaviors.

The necessary input data can be generated using theoretical means (special models for blast wave formation and propagation, predictive analysis results for material properties, etc.), experimental means (using field test data or lab simulation results) or by combining all available theoretical and experimental means. We will not dwell here on the very complex issue of specific blast model selection, generation of numerical results and their use in transient structural analysis. Instead, keeping in mind that the purpose of this work is mainly illustrative, we will work with some representative incident pressure histories of the type shown in Fig. 5.1. Of course, the shape of this curve and the specific time and pressure values shown on the axes are simply for illustration and can be adjusted to specific blast load history in each practical analysis case. Focusing on the 'initial', truly transient stage of the structural response, we will not consider here the stage when the incident pressure becomes negative.

Further, in the 3D transient analysis cases studied here, we will make certain suitable assumptions regarding the incident pressure distribution

© Woodhead Publishing Limited, 2010

over the loaded surface; we will apply relatively simple geometric boundary conditions and will keep mechanical properties of all incorporated materials linearly elastic or linearly-viscoelastic (with account taken for internal damping). The energy absorption effect can be additionally taken into account via respective 'damping coefficients' which are part of the input data set.

In summary, the principal objectives of this chapter are: (i) to formulate specific boundary value problems for some representative layered armor and blast mitigation systems, (ii) to perform numerical solutions of those problems and demonstrate convergence of numerical results, (iii) to illustrate and discuss important mechanistic aspects related to the highly transient nature of the results and the layered nature of the studied material systems, and (iv) to compare some of the numerical results with experimental data available from the shock tube tests.

5.4 Formulation of the 3D dynamic boundary value problem

5.4.1 Panel geometry and boundary conditions

Here we describe the principal 3D dynamic boundary value problem formulation which will be used for the first group of numerical examples. Consider a (generally thick and multilayer) flat square panel which is exposed to a pressure pulse $P(x,y,t)$ applied within some region on the top surface, as shown in Fig. 5.5. The panel schematic, coordinate system (its origin is located in the center of the bottom surface) and geometric boundary conditions imposed at the side edges are shown in the same figure. The transverse (z-directional) displacement $u_z(t)$ is assumed zero along all four side edges of the panel for all time moments; no other geometric boundary

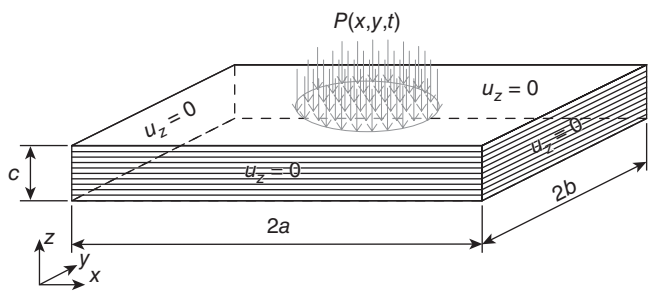

5.5 Schematic of a multi-layer panel exposed to a local pressure pulse with the coordinate system and boundary conditions at the side edges indicated.

© Woodhead Publishing Limited, 2010

conditions are imposed at the side edges. Owing to the symmetry of this boundary value problem, the analysis can be reduced to one-quarter part of the panel; for certainty we will consider here the right-back quarter. Accordingly, the following symmetry boundary conditions are imposed along the vertical symmetry planes:

$$u_x = 0 \text{ at } x = 0 \text{ for all } y \text{ and } z; u_y = 0 \text{ at } y = 0 \text{ for all } x \text{ and } z \qquad [5.17]$$

The incident pressure pulse $P(t)$ is represented by the following function:

$$P(t) = P_0 \cdot A \cdot t^n \cdot e^{-B \cdot t} \qquad [5.18]$$

where t is measured in μsec and P_0 in Pa (N/m^2). Numerical values of the parameters in Eq. 5.18 are taken as follows:

$$P_0 = 5.436 \text{ MPa}, n = 1, A = 1\,\mu\text{sec}^{-1}, B = 0.2\,\mu\text{sec}^{-1} \qquad [5.19]$$

The shape of the pulse is similar to what is shown in Fig. 5.1. The maximum pressure magnitude according to Eq. 5.18, $P_{\max}(t_0)$ = 10 MPa, is reached at t_0 = 5 μsec.

5.4.2 Description of Panel #1

The first example considers a composite panel (further called Panel #1) for which reinforcement consists of two plies of S-2 glass fiber 3D orthogonal woven fabric preform. Each preform ply is of 3.32 kg/m^2 (98 oz/yd^2) areal density. The preform was consolidated by epoxy–vinyl ester resin. The thickness of the composite panel is 5.6 mm. The side length of the square panel $2a$ = 40.6 cm. The computational 3D MOSAIC model developed for one-quarter part of the panel, with illustrative example of discrete element mesh, shown in Fig. 5.6.

A complete set of the effective elastic properties of the composite used here was predicted using the conventional stiffness averaging method. The

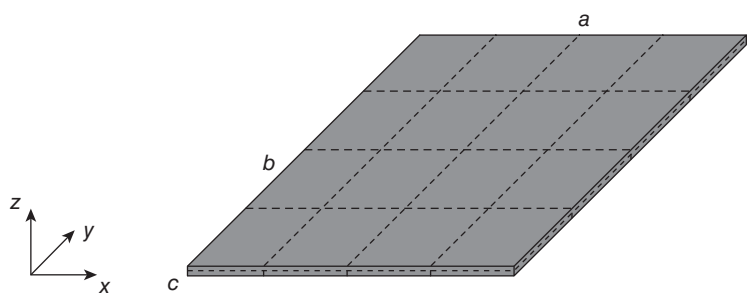

5.6 Computational model of two-layer S-2 glass 3D woven composite Panel #1 with discretization mesh example.

© Woodhead Publishing Limited, 2010

result is as follows (directions 1, 2 and 3 correspond to coordinate axes x, y and z in Fig. 5.6):

$$E_1 = 26.46\ \text{GPa}, E_2 = 26.74\ \text{GPa}, E_3 = 12.45\ \text{GPa}, G_{12} = 3.48\ \text{GPa}, G_{13} = 3.32\ \text{GPa},$$
$$G_{23} = 3.33\ \text{GPa}, \nu_{12} = 0.11, \nu_{13} = 0.34, \nu_{23} = 0.34; \text{density } \rho = 1800\ \text{kg/m}^3 \quad [5.20]$$

Here, index 1 corresponds to the warp, index 2 to the fill and index 3 to the Z fiber directions. Some of the characteristics listed in Eq. 5.20 were validated by experimental data (see details in Bogdanovich, 2003, 2006). The estimated areal density of the composite panel is 10.08 kg/m^2 (2.07 lb/ft^2).

5.4.3 Description of Panel #2

The second example considers a sandwich panel (further named Panel #2) which is composed of two S-2 glass 3D woven composite skins (each of which is identical to Panel #1 material) with a Balsa wood core between them. Construction of the panel is illustrated in Fig. 5.7a. Properties of the S45 standard Balsa core (treated as a transversely isotropic material with plane of isotropy 1–2) are taken as follows:

$$E_1 = E_2 = 0.054\ \text{GPa}, E_3 = 1.355\ \text{GPa}, G_{12} = 0.059\ \text{GPa}, G_{13} = G_{23} = 0.201\ \text{GPa},$$
$$\nu_{12} = 0.36, \nu_{13} = \nu_{23} = 0.014; \text{density } \rho = 600\ \text{kg/m}^3 \quad [5.21]$$

The thickness of each composite skin is 5.6 mm, the thickness of the core is 76.2 mm and the total thickness of the panel, denoted c, is 87.4 mm. The estimated areal density of this panel material is 65.88 kg/m^2 (13.51 lb/ft^2).

As before, the in-plane dimension of the square panel is $2a$ = 40.6 cm. Note that the panel is very thick; its length/thickness aspect ratio is only 4.65. Obviously, the geometry of this problem requires a full 3D analysis. The 3D Mosaic model developed for one-quarter part of the panel, with illustrative example of discrete element mesh, is shown in Fig. 5.7b.

5.4.4 Description of Panel #3

The construction of Panel #3, analyzed in the third numerical example, is shown in Fig. 5.8a. In this panel, a 9.0 mm thick ceramic hard face layer (made from CoorsTek CAP4 Al_2O_3 tiles each having $10 \times 10 \times 0.9$ cm dimensions) is on the top. That layer of bonded ceramic tiles is followed by the layer of 3D weave S-2 glass composite (identical to Panel #1 material). Below the composite there is a 50.8 mm thick Balsa wood core, which is followed by another layer of 3D weave S-2 glass composite having the same

© Woodhead Publishing Limited, 2010

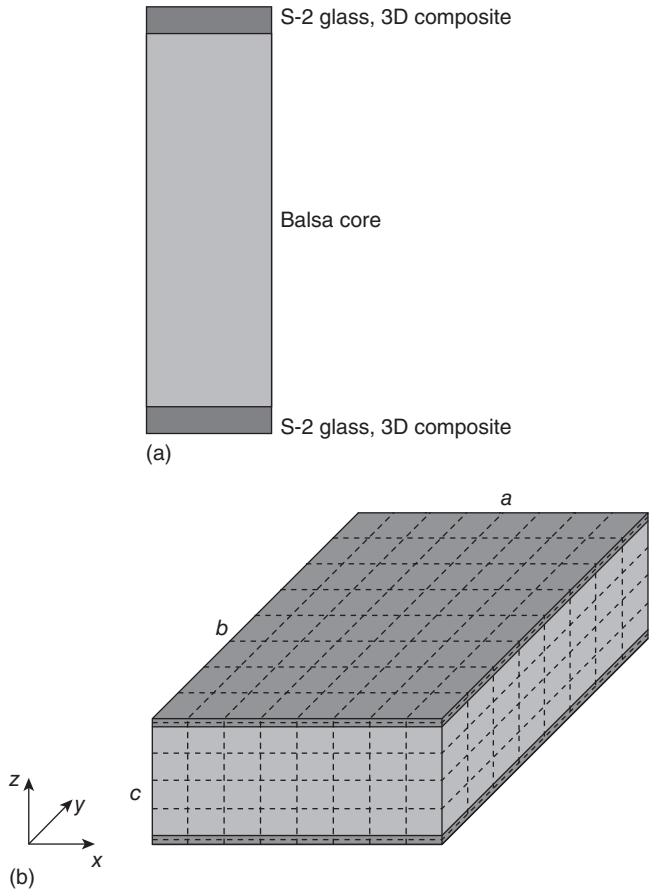

5.7 Cross-section scheme (a) and computational model (b) of the sandwich Panel #2 with discretization mesh example shown in (b).

properties and thickness as before. The total thickness of the panel in this case is 71.0 mm; the length to thickness aspect ratio is 5.72 (in-plane panel dimensions are the same as for Panel #1). The 3D Mosaic model developed for one-quarter part of the panel, with illustrative example of discrete element mesh shown in Fig. 5.8b.

The elastic properties of the Balsa core are same as in Eq. 5.21. The elastic properties of the ceramic material CAP4 Al_2O_3 (which is assumed to be isotropic) are as follows:

$$E = 350\ \text{GPa}, G = 143\ \text{GPa}, \nu = 0.22; \text{density}\ \rho = 3800\ \text{kg}/\text{m}^3 \quad [5.22]$$

The estimated areal density of this panel material is 84.84 kg/m^2 (17.39 lb/ft^2).

© Woodhead Publishing Limited, 2010

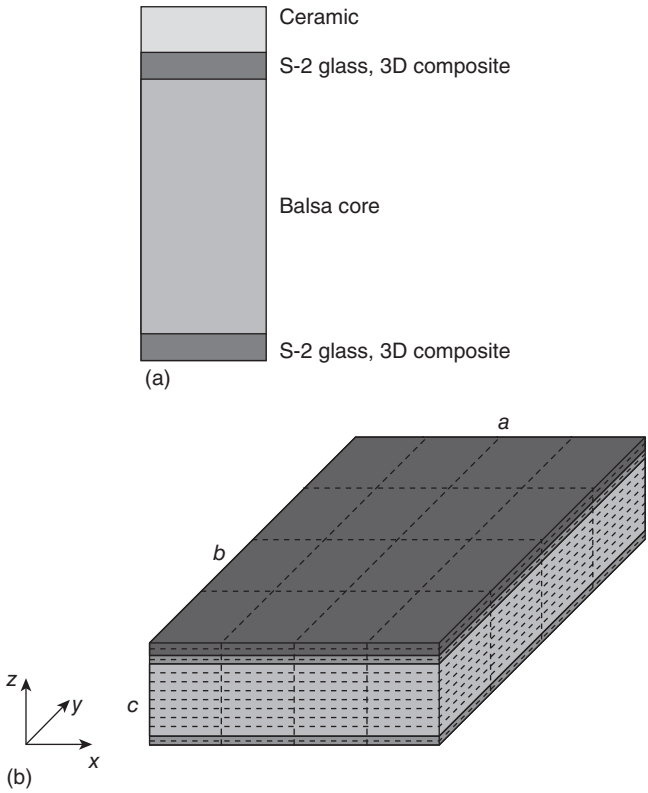

5.8 Cross-section scheme (a) and computational model (b) of the four-layer Panel #3 with discretization mesh example shown in (b).

5.4.5 Description of Panel #4

The construction of this panel is shown in Fig. 5.9a. The upper layer is 3.2 mm thick perforated steel (it serves as 'hard facing' instead of the ceramic layer in Panel #3). This is followed by a 5.1 mm thick composite layer which is reinforced with two plies of 3.25 kg/m^2 (96 oz/yd^2) areal density E-glass 3D woven fabric. Then there is a 25.4 mm thick layer of Al foam followed by a 38.1 mm thick layer of Balsa wood. The bottom layer is another 5.1 mm thick 3D woven E-glass fabric composite. The total thickness of the panel is 76.9 mm. The aspect ratio in this case is 5.28. The 3D Mosaic model of one-quarter part of the panel, with illustrative example of discrete element mesh, is shown in Fig. 5.9b.

The effective elastic properties of the 3D woven E-glass/epoxy-vinyl ester composite, predicted by the stiffness averaging method and used in this analysis, are as follows (as before, directions 1, 2 and 3 correspond to coordinate axes x, y and z):

© Woodhead Publishing Limited, 2010

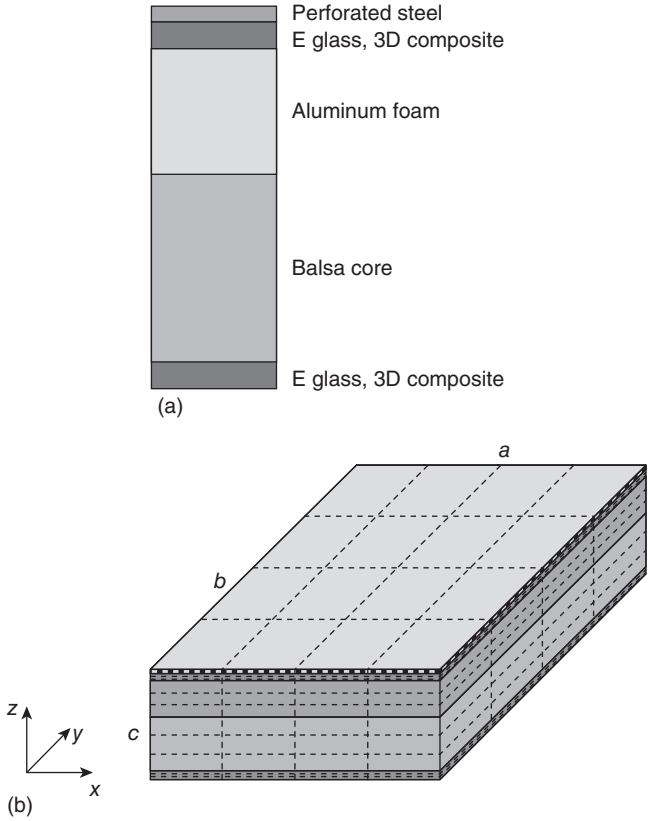

5.9 Cross-section (a) and computational model (b) of the five-layer Panel #4 with discretization mesh example shown in (b).

$E_1 = 23.56$ GPa, $E_2 = 23.47$ GPa, $E_3 = 10.45$ GPa, $G_{12} = 3.41$ GPa, $G_{13} = 3.25$ GPa, $G_{23} = 3.25$ GPa, $\nu_{12} = 0.13$, $\nu_{13} = 0.41$, $\nu_{23} = 0.41$; density $\rho = 1850\ \text{kg/m}^3$ [5.23]

Index 1 corresponds to the warp, index 2 to the fill and index 3 to the Z fiber directions of the fabric. Aluminum foam has the following effective properties (it is treated as isotropic linearly elastic material):

$$E = 4.5\ \text{GPa}, G = 2.25\ \text{GPa}, \nu = 0; \text{density } \rho = 600\ \text{kg/m}^3 \quad [5.24]$$

The properties of steel are taken as follows:

$$E = 207\ \text{GPa}, G = 79.6\ \text{GPa}, \nu = 0.3; \text{density } \rho = 7800\ \text{kg/m}^3 \quad [5.25]$$

The estimated areal density of this panel material is 84.84 kg/m^2 (17.39 lb/ft^2).

© Woodhead Publishing Limited, 2010

5.5 Numerical results of the blast response for the four panels

5.5.1 Convergence study and accuracy control of numerical results

One important aspect of this work is that a comprehensive convergence study has been performed as part of this analysis for all of the described Panels #1, #2, #3 and #4. Its purpose was to ensure that the computational parameters chosen (namely, the degree of the Bernstein basis functions and the number of discretization planes in the x, y and z directions) provide converged results for all displacement, strain and stress components everywhere in the structure, including all interfaces between dissimilar materials. Recall that one distinctive aspect of this analysis approach is that convergence of numerical results can be achieved either by increasing the degree of the basis functions, or by increasing the density of the discretization mesh or by applying both these approaches simultaneously. We skip here most of the details of the performed convergence studies and only present some selected illustrative results.

In the convergence studies conducted, the numbers of discretization planes of increasing density along coordinates x, y and z were used in combinations with different degrees of Bernstein basis functions. All of the meshes used were uniform, but the analysis is not so restricted; uniform meshes were used in these illustrative examples only for simplicity of description. Table 5.1 provides examples of the meshes used; the mesh code is explained in the table. Notations 2/4/2 for Panel #2, 1/1/1/1 for Panel #3, 2/2/2/2/2 for Panel #4, for example, indicate the numbers of discrete elements in the z direction within Layer 1, Layer 2 and Layer 3 in Panel #2, within Layer 1, Layer 2, Layer 3 and Layer 4 in Panel #3 and within Layer 1, Layer 2, Layer 3, Layer 4 and Layer 5 in Panel #4 (layers are counted from the bottom of the panel). In order to illustrate the accuracy of the numerical results obtained, the following comparisons between the computational results and some control data have been made.

(I). A comparison of the incident pressure history, $P(t)$, determined by Eqs 5.17 and 5.18, with the computed time variation of transverse normal stress component $\sigma_z(t,0,0,c)$ at the center of the upper (loaded) surface of the panel. Obviously, if it was possible to obtain an exact solution, the function $P(t)$ would be exactly equal to $\sigma_z(t,0,0,c)$ at all of the time instants. However, the analysis is approximate and the dynamic surface load is not imposed explicitly. Instead, it is taken into account in a 'soft' variational sense, through the term $W(t)$ in Eq. 5.4. Its explicit expression is provided by Eq. 5.12. Accordingly, any specific analysis results would necessarily show some numerical discrepancy between the input time function $P(t)$ and

© Woodhead Publishing Limited, 2010

Table 5.1. Description of computational meshes (numbers of uniform intervals and degrees of the basis functions) used for 1/4th part of Panels #1–#4 in numerical examples presented here

Mesh #	Mesh code	Used for panel #	Number of *x*-intervals	Number of *y*-intervals	Number of *z*-intervals	Degree of basis functions
1	4 × 4 × 1 (2)	1	4	4	1	2
2	8 × 8 × 1 (2)	1	8	8	1	2
3	12 × 12 × 1 (2)	1	12	12	1	2
4	16 × 16 × 1 (2)	1	16	16	1	2
5	20 × 20 × 1 (2)	1	20	20	1	2
6	8 × 8 × 2 (2)	1	8	8	2	2
7	4 × 4 × 3 (2)	1	4	4	3	2
8	4 × 4 × 1 (3)	1	4	4	1	3
9	4 × 4 × 1 (4)	1	4	4	1	4
10	4 × 4 × 1 (5)	1	4	4	1	5
11	2 × 2 × 2/4/2 (2)	2	2	2	2/4/2	2
12	2 × 2 × 2/4/2 (3)	2	2	2	2/4/2	3
13	2 × 2 × 2/4/2 (4)	2	2	2	2/4/2	4
14	4 × 4 × 1/1/1 (2)	2	4	4	1/1/1	2
15	4 × 4 × 2/4/2 (3)	2	4	4	2/4/2	3
16	8 × 8 × 2/4/2 (2)	2	8	8	2/4/2	2
17	4 × 4 × 1/1/1/1 (2)	3	4	4	1/1/1/1	2
18	4 × 4 × 2/8/2/2 (2)	3	4	4	2/8/2/2	2
19	4 × 4 × 3/3/3/3 (2)	3	4	4	3/3/3/3	2
20	4 × 4 × 2/2/2/2 (3)	3	4	4	2/2/2/2	3
21	4 × 4 × 1/1/1/1/1 (2)	4	4	4	1/1/1/1/1	2
22	4 × 4 × 3/3/3/3/3 (2)	4	4	4	3/3/3/3/3	2
23	4 × 4 × 2/2/2/2/2 (3)	4	4	4	2/2/2/2/2	3

the computed time function $\sigma_z(t,0,0,c)$. By evaluating the discrepancy in each specific numerical solution case, one can access the accuracy of that numerical solution. It is also worth mentioning that it is usually most difficult to compute the transverse normal stress component with sufficient accuracy. Therefore, if a numerical solution shows sufficiently close agreement between $P(t)$ and $\sigma_z(t,0,0,c)$, this shall be taken as a strong indication that the numerical solution obtained is sufficiently accurate.

(II). In a 3D analysis (and, especially, in a 3D transient analysis) of layered structures with material properties sharply varying from layer to layer, it is also advisable to compare the stress values (or their time functions) computed from the bottom and from the top of the interfaces. We designate the transient transverse normal and shear stresses computed from the bottom of some interface as $\sigma_z^-(t)$, $\sigma_{xz}^-(t)$, $\sigma_{yz}^-(t)$, and same stresses computed from the top of the interface as $\sigma_z^+(t)$, $\sigma_{xz}^+(t)$, $\sigma_{yz}^+(t)$. Therefore, the following continuity conditions have to be satisfied in the exact solution:

© Woodhead Publishing Limited, 2010

$$\sigma_z^-(t) = \sigma_z^+(t), \sigma_{xz}^-(t) = \sigma_{xz}^+(t), \sigma_{yz}^-(t) = \sigma_{yz}^+(t) \text{ for all } t \quad [5.26]$$

In the analysis approach used here, the continuity conditions (Eq. 5.26) are not imposed explicitly, but rather are expected to be satisfied more and more accurately when the overall energy functional minimization problem is solved more and more accurately. Hence, the discrepancies between computed pairs of transverse stresses from the top and from the bottom of all interfaces can be used as the other indicators of the accuracy of the numerical solution obtained. The solution convergence from this viewpoint will be illustrated further in the following sections.

(III). Typically, in a 3D static analysis of laminated plates, it is easy to reach any desired accuracy of computing all displacement components. It is more challenging to achieve sufficiently high accuracy when computing in-plane strains and in-plane stresses, and it is usually most difficult to achieve high accuracy when computing transverse shear and normal strains and stresses. In the case of a 3D transient dynamic analysis of laminated plates, the above general rule-of-thumb becomes not so obvious, especially when (i) the layers are anisotropic, (ii) significant property variation from layer to layer takes place and (iii) the principal geometric parameters (layer thickness versus in-plane dimensions) vary in a broad range. Indeed, the above factors influence the stress wave propagation and reflection processes in different directions and, particularly, affect the time intervals between consecutive stress wave reflections from the interfaces or from external boundaries of the body. All this may significantly influence the convergence rates of different displacement/strain/stress components in different layers of the structure. It is possible that even closeness of $\sigma_z(t,0,0,c)$ to $P(t)$ and sufficient closeness of the computed interfacial stresses from the top and from the bottom do not guarantee sufficiently high accuracy of the in-plane strains and stresses.

5.5.2 Numerical results for Panel #1

We start with the simplest example of a homogeneous composite Panel #1 and illustrate the most important convergence effects. Several discretization meshes, Nos 1–10, which are described in Table 5.1, were used in the convergence study. They correspond to the basis function degrees 2, 3, 4 and 5.

Figure 5.10 shows time variations of transverse displacement u_z, in-plane strain ε_x and stress σ_x, and transverse strain ε_z and stress σ_z obtained with different computational meshes for an initial, 50 μsec long time interval. As seen in Fig. 5.10a, the displacement convergence is obvious; Meshes 5, 6 and 10 provide practically identical results. At the same time, as Fig. 5.10b shows, it is not so easy to achieve the ε_x convergence. Although the trend

© Woodhead Publishing Limited, 2010

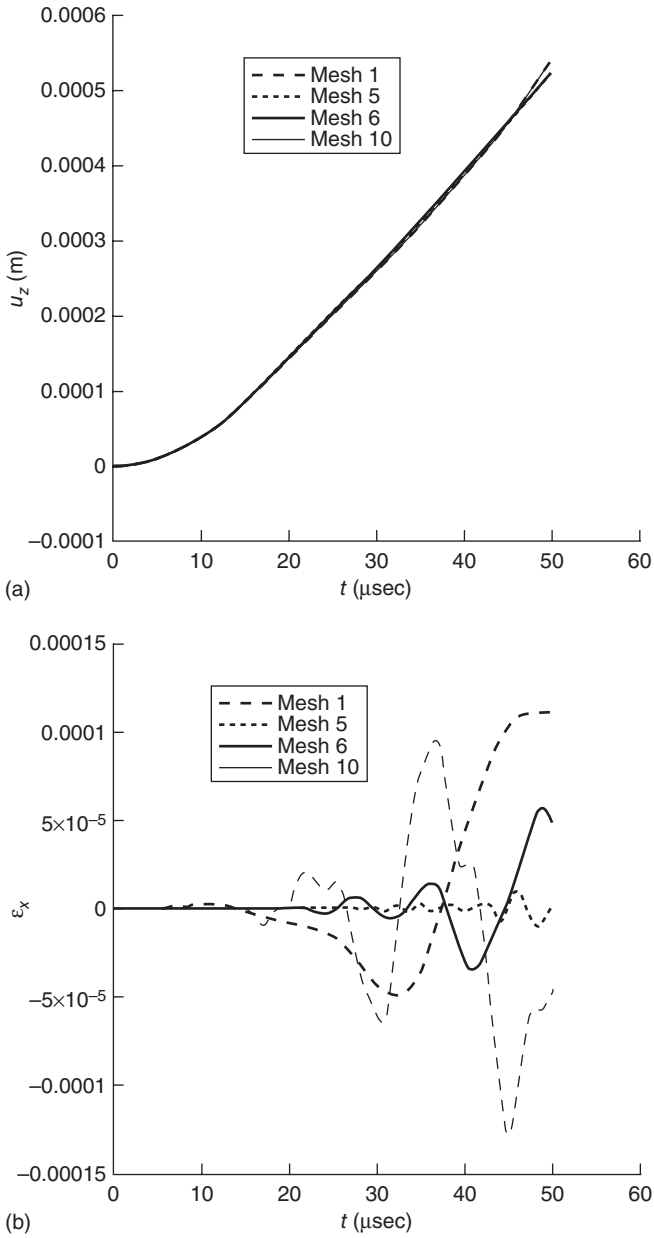

5.10 Convergence of the time variations of u_z (a), ε_x (b), σ_x (c), ε_z (d) and σ_z (e) computed at the center of the top surface of Panel #1 for [0, 50 μsec] time interval with different discretization meshes and degrees of basis functions.

© Woodhead Publishing Limited, 2010

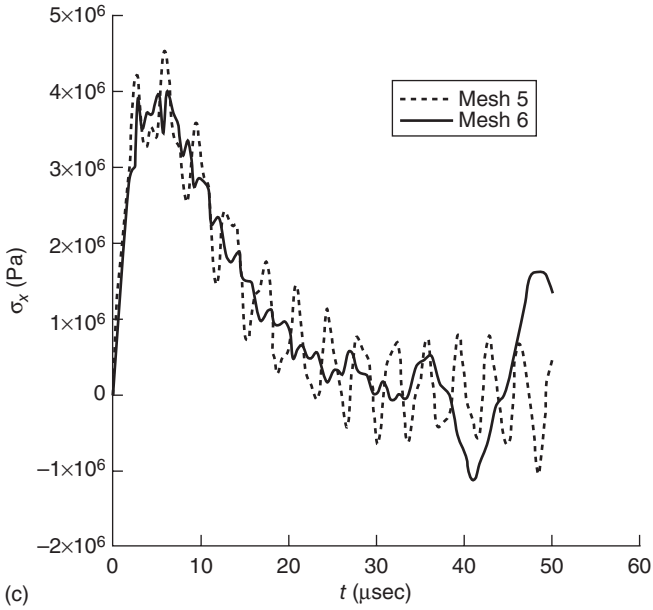

(c)

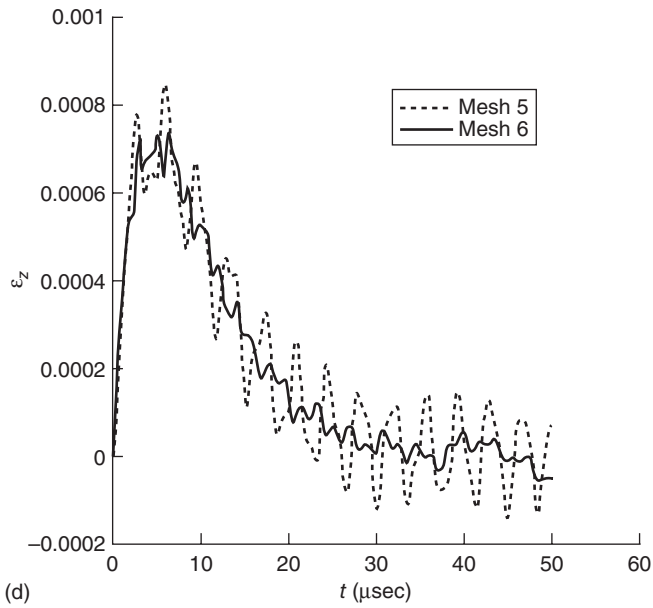

(d)

5.10 Continued

© Woodhead Publishing Limited, 2010

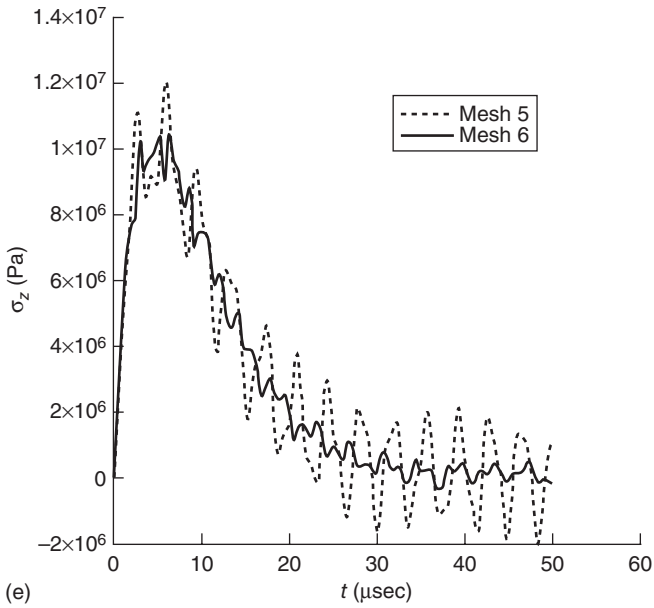

5.10 Continued

is obvious, it is possible that even Mesh 10 does not ensure a sufficiently accurate result. The conclusion therefore is that in order to achieve convergence of this strain component within an initial short time interval, a very dense in-plane discretization mesh has to be used. Also, as the result obtained with Mesh 10 shows, the desirable result is not achieved by simply increasing the degree of basis functions.

Figures 5.10c–5.10e show time variations of σ_x, ε_z and σ_z obtained with Meshes 5 and 6. The shape of these curves is very similar to the shape of the applied pressure pulse shown in Fig. 5.11, athough the pressure variation curve has no visible high frequency fluctuations. All three Figures, 5.10c–e consistently demonstrate that in the case of Mesh 6 the peaks of such fluctuations are much smaller than in the case of Mesh 5. So, Mesh 6 provides more accurate results for these three characteristics. In contrast to this, Fig. 5.10b shows that Mesh 5 provides more accurate result for ε_x than does Mesh 6.

Such a close similarity between the shapes of $\sigma_x(t)$, $\varepsilon_z(t)$ and $\sigma_z(t)$ as the one seen in Fig. 5.10 is not incidental of course. Obviously, $\sigma_z(t)$ at the loaded surface tries to get as close as possible to the shape of the applied pressure pulse $P(t)$. Eventually, with increasing mesh density and/or degree of the basis functions, the difference between these two functions becomes less and less visible. Further, when comparing the magnitudes of ε_z in Fig. 5.10d (the maximum is approximately 0.08%) and ε_x in Fig. 5.10b (the

© Woodhead Publishing Limited, 2010

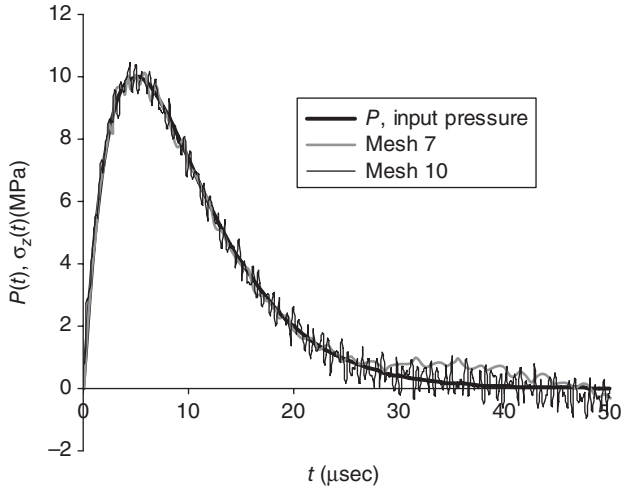

5.11 Comparison of transverse normal stress $\sigma_z(t)$, computed at the center of top (loaded) surface of Panel #1 with the use of Meshes 7 and 10, to the applied pressure pulse $P(t)$.

maximum is approximately 0.001% with Mesh 5), the difference appears to be about 80 times. Also worth mentioning is that in the boundary value problem under consideration, strain component ε_y is very close in magnitude to ε_x. Accordingly, in the constitutive equation (Eq. 5.1) that relates σ_z to the three strains ε_x, ε_y and ε_z, the latter strain has much greater magnitude than the other two. Now it becomes clear why the shape of $\varepsilon_z(t)$ is so similar to that of $\sigma_z(t)$. Further on, when considering the constitutive equation (Eq. 5.1) that relates σ_x to the three strains ε_x, ε_y and ε_z, the same reason explains why the shape of $\sigma_x(t)$ is so similar to that of $\varepsilon_z(t)$, and, consequently, why the shape of $\sigma_x(t)$ is so similar to that of $\sigma_z(t)$. Therefore, we can conclude that during the initial interval of transient deformation, the shapes of the dominating strain and stress components are forced to mimic the shape of applied pressure pulse $P(t)$.

Further, Fig. 5.11 shows the applied pressure pulse $P(t)$ in comparison with the predicted time variations of $\sigma_z(t)$ at the center of the plate. The latter variation was computed with Meshes 7 and 10. In the case of Mesh 10, the 'fluctuations' have larger spikes, but the average curve perfectly fits the $P(t)$ curve. In the case of Mesh 7, the fluctuations have much smaller spikes, but the average curve deviates from the $P(t)$ curve more significantly at the times beyond 25 μs. These results show that the first accuracy criterion discussed in Section 5.5.1 can be accurately satisfied by either increasing the number of discrete elements in the z direction or by increasing the degree of the basis functions.

© Woodhead Publishing Limited, 2010

Figure 5.12 illustrates the convergence of u_z, ε_x σ_x and ε_z for a longer time interval (500 μsec). As Fig. 5.12a shows, it is easy to get converged u_z; the differences when using Meshes 5, 6 and 10 are very small. However, as seen in Figs 5.12b–5.12d, the differences for ε_x, σ_x and ε_z are more pronounced. Although the general trends seen in all three curves in each of these figures are the same, local deviations from them are considerable. Specifically, at certain time instants all three curves are very close, while at other time instants two of them are very close but the third is more distant. Of course, by combining high density of the discretization mesh with high degree of the basis functions, it is possible to compute any transient strain and stress component for a given time interval with any desirable accuracy.

Finally, Fig. 5.13 presents time variations of u_z, ε_x, σ_x and ε_z for an even longer time interval (3000 μsec). Meshes 1 and 6 were used for comparison. It is worth mentioning that continuous computer run time was dramatically different: less than one hour for Mesh 1 and about 23 hours for Mesh 6. Although the numerical results obtained do not differ very much. Some details are different, but the predicted peak values of all four characteristics are quite close. This is important, because if this level of accuracy is viewed as acceptable, the analysis of more complex Panels #2, #3 and #4 can be performed for this long time interval with the meshes of 4×4 discrete elements in-plane and one element within each layer and second-degree basis functions used.

It is interesting to mutually compare results in Figs 5.12 and 5.13. The comparison of u_z shows that it reaches a value of 36 mm in Fig. 5.13a, while its maximum is only about 5.5 mm in Fig. 5.12a. The maximum of tensile ε_x in Fig. 5.13b is about 1.25%, while in Fig. 5.12b it is less than 0.3%. Interestingly, the maximums of compressive ε_x (reached at about 500 μsec) are very close, about 0.35%, in both cases. The same is valid in the case of σ_x – its maximum tensile value grows from 70 MPa to 375 MPa, while its compressive maximum, 110 MPa, remains the same. The results for ε_z show the opposite trend – tensile maximum, 0.28%, remains the same, while compressive maximum grows from 0.18% to 0.92%. So, the relative values of in-plane versus out-of-plain strains have reversed – within 500 μsec time the tensile ε_z and compressive ε_x were the highest strains, while within 3000 μsec time the tensile ε_x and compressive ε_z became dominant. This underscores again the complexity of the computed 3D transient stress/strain states.

In summary, the numerical results presented in Figs 5.10–5.13 for a homogeneous 3D woven composite plate, loaded with a very short and intensive blast pressure pulse, have demonstrated that good convergence can be obtained for all displacements, strains and stresses in the plate for the initial time interval (50 μs), intermediate time interval (500 μs) or for relatively long time interval (3000 μs). Depending on the purpose, the

© Woodhead Publishing Limited, 2010

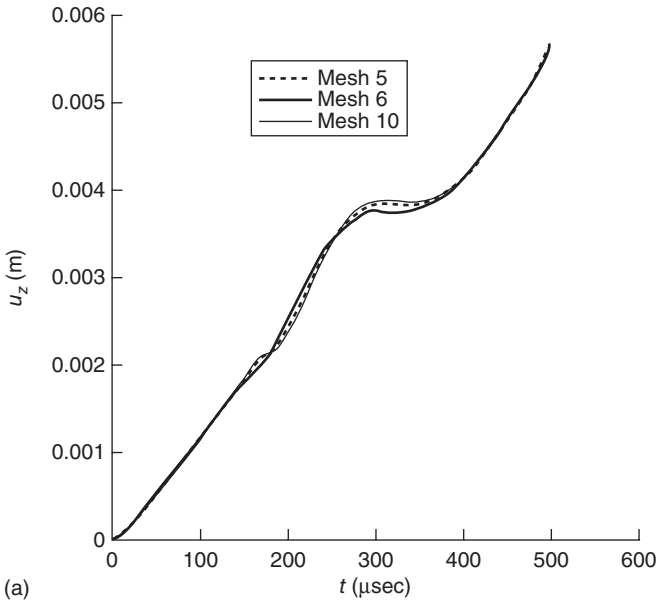

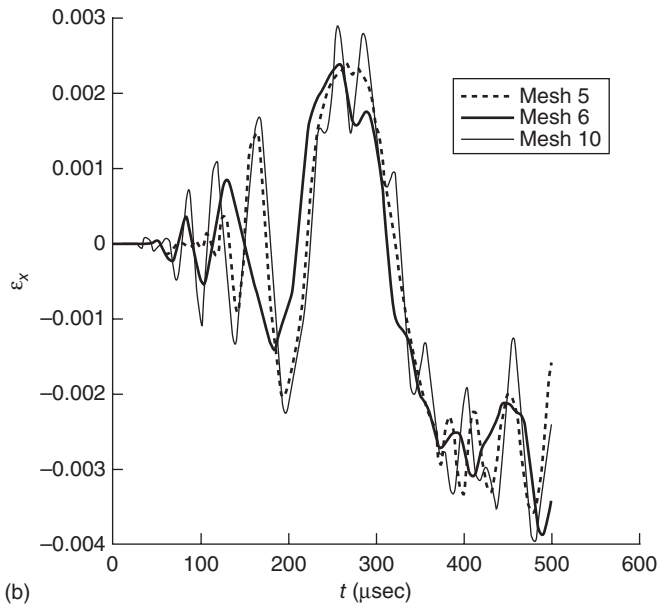

5.12 Convergence of the time variations of u_z (a), ε_x (b), σ_x (c) and ε_z (d) computed at the center of the top surface of Panel #1 for [0, 500 μsec] time interval with different discretization meshes and degrees of basis functions.

© Woodhead Publishing Limited, 2010

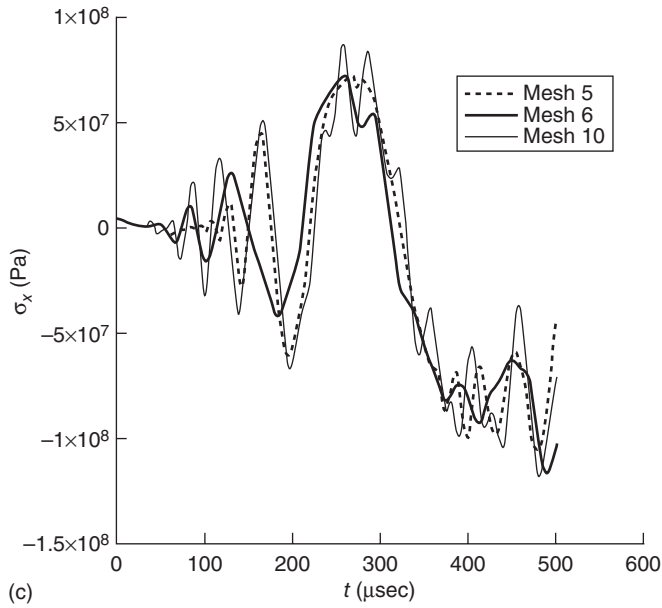

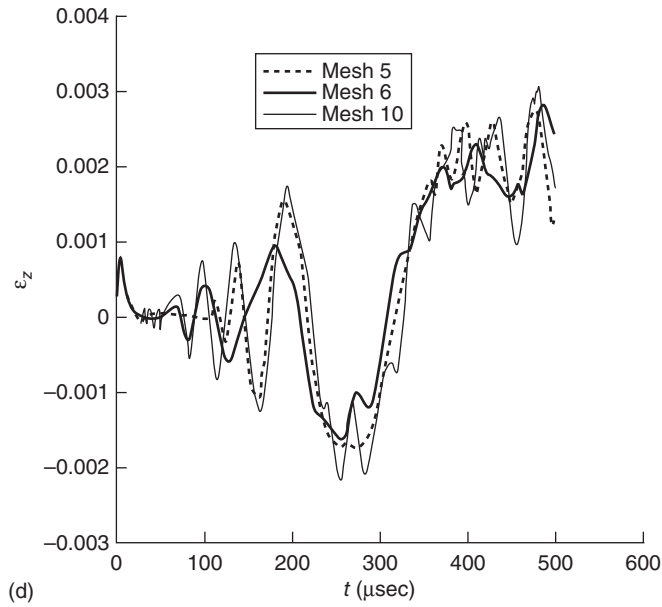

5.12 Continued

© Woodhead Publishing Limited, 2010

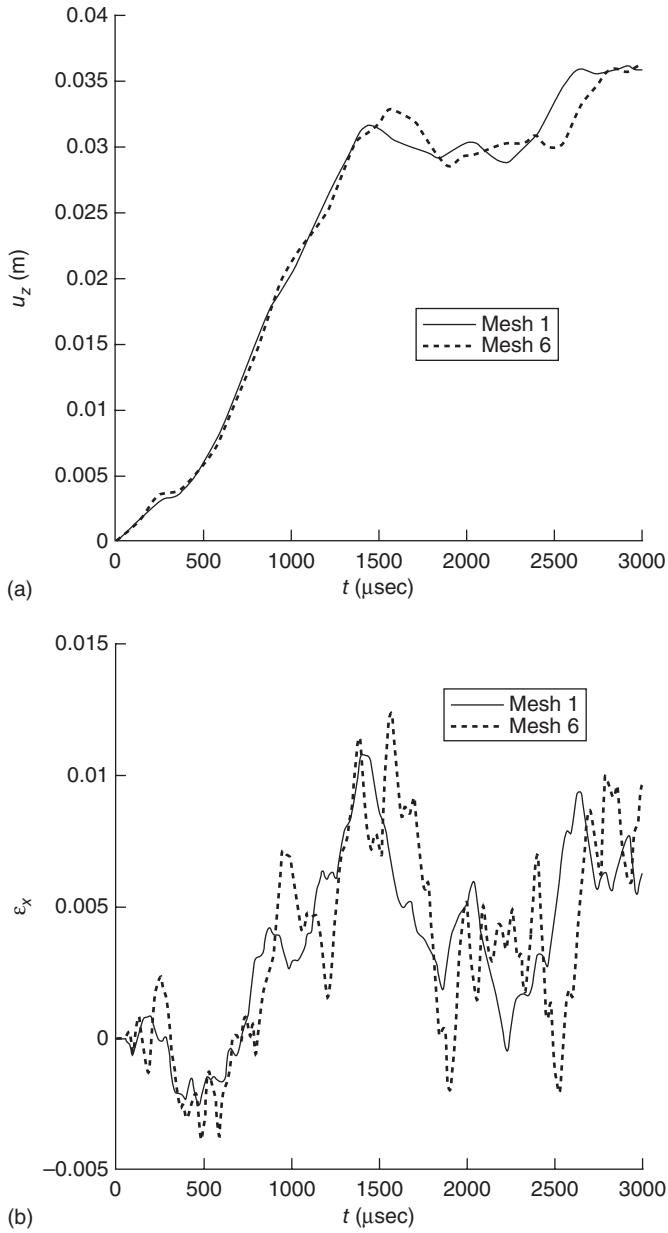

5.13 Time variations of u_z (a), ε_x (b), σ_x (c) and ε_z (d) computed at the center of top surface of Panel #1 for [0, 3000 μsec] time interval with Meshes 1 and 6.

© Woodhead Publishing Limited, 2010

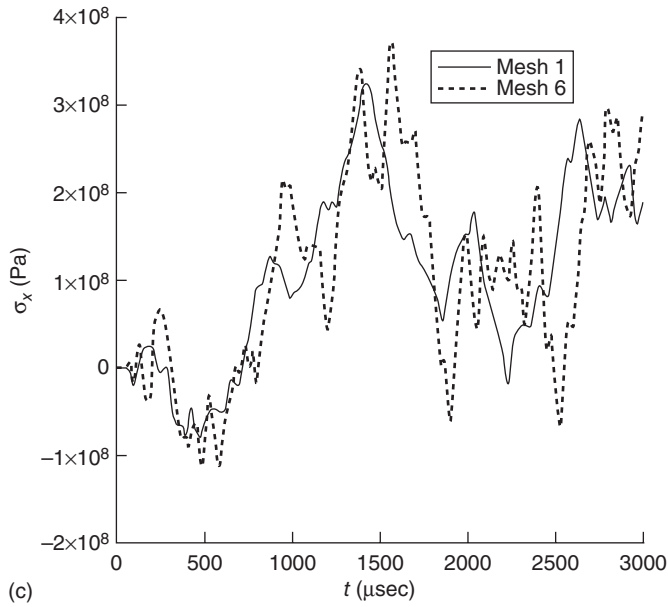

(c)

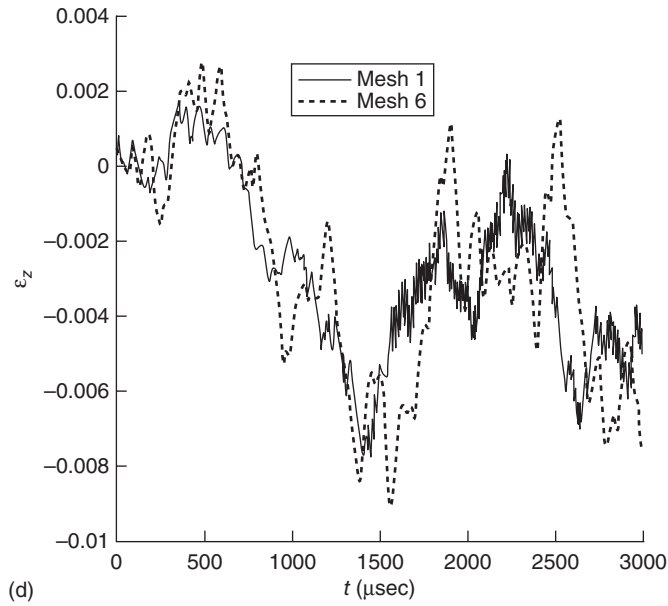

(d)

5.13 Continued

© Woodhead Publishing Limited, 2010

optimum computational meshes should be chosen differently for each of these intervals. If the in-plane strain/stress components are of interest within the initial time interval, the discretization mesh along the x- and y-coordinates shall be very dense, or the degree of the basis functions shall be very high. If the transverse strain/stress components are of primary interest, then the discretization along the z-coordinate shall be dense, or the degree of the basis functions shall be high. If the maximum strain/stress values are of interest for longer time intervals (measured in hundreds or thousands of μsec), than reasonably accurate results can be achieved with the use of relatively coarse discretization meshes (even with Mesh 1) and degrees of basis functions 2 or 3. In such cases, the computer run time is in hours. If more accurate results are required for time intervals in milliseconds, then numerical integration on a regular PC may take days and weeks of continuous computer run even for a simple homogeneous composite panel.

5.5.3 Numerical results for Panel #2

The most interesting feature of Panel #2 is its sandwich construction: it has relatively stiff 3D woven S-2 glass composite skins and a relatively soft, light and thick Balsa wood core (see Fig. 5.7a). Accordingly, the task to accurately predict strains and stresses at the interfaces between composite skins and Balsa is an additional one, not present in the case of Panel #1. Figures 5.14 and 5.15 show numerical results for the upper and lower interfaces in this panel. All numerical results were obtained with Mesh 15 (see Table 5.1).

First, Fig. 5.14a shows that the time variations of displacement u_z, computed at the center of the panel, are identical from the top and from the bottom of the upper interface. This is not a surprise, because the displacement continuity is analytically imposed in the algorithm. Figure 5.14b shows that the ε_x variations are also practically identical. This continuity condition was not imposed in the algorithm, so this result indicates that numerical solution performed with Mesh 15 is very accurate. Figure 5.14c shows time variations of σ_x stress. Due to the difference in elastic properties of the skin and core materials, under condition that ε_x is continuous at the interface, this stress component shall be discontinuous, which is actually seen in Fig. 5.14c. In fact, the σ_x values on the skin side are much higher than those on the core side. Further, as Fig. 5.14d shows, the transverse strain ε_z is discontinuous at the interface (naturally, with much higher values on the core side). This result is mechanistically obvious – the required continuity of transverse stress σ_z at the interface, combined with a mismatch of elastic properties, makes discontinuity of ε_z inevitable. Figure 5.14e illustrates that indeed σ_z computed from the top and from the bottom of the interface is

© Woodhead Publishing Limited, 2010

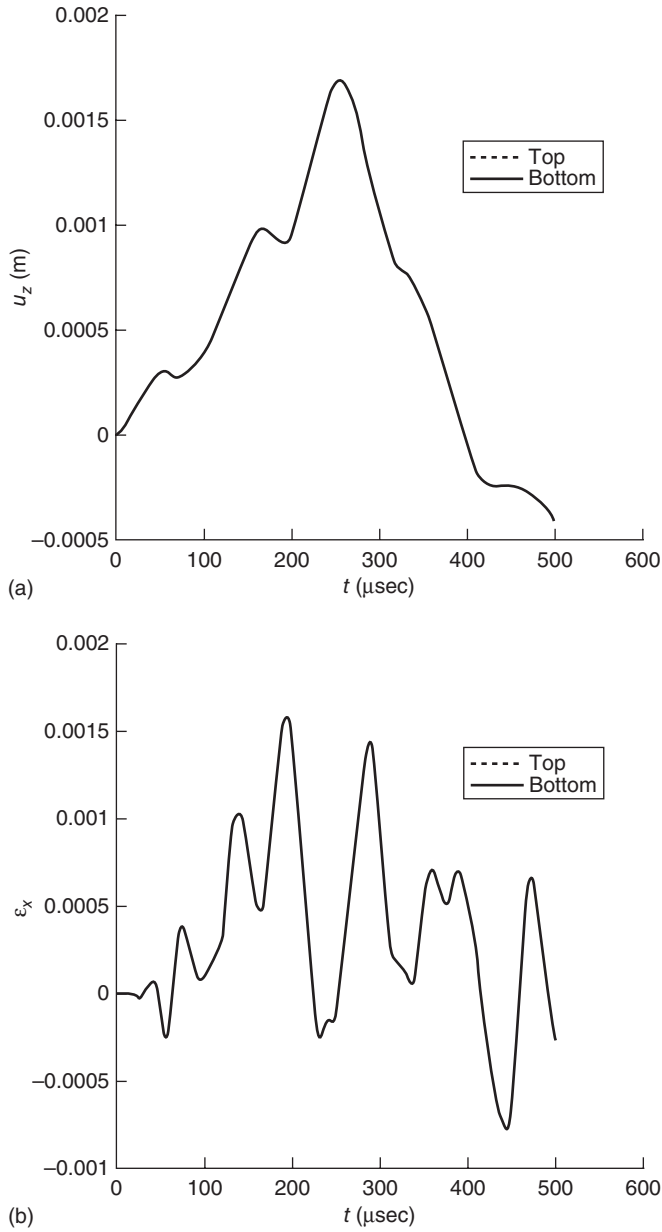

5.14 Time variations of u_z (a), ε_x (b), σ_x (c), ε_z (d) and σ_z (e) computed at the center of the upper interface, $z = 0.0818$ *m*, of Panel #2 'from the top' and 'from the bottom' (Mesh 15 used).

© Woodhead Publishing Limited, 2010

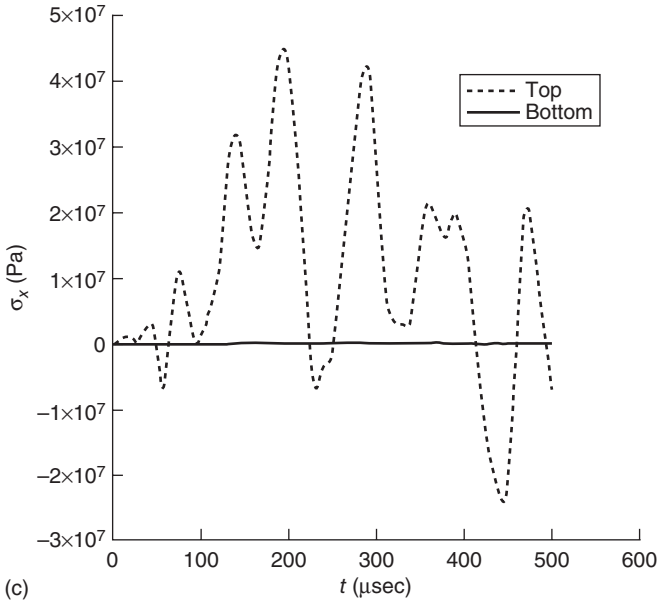

(c)

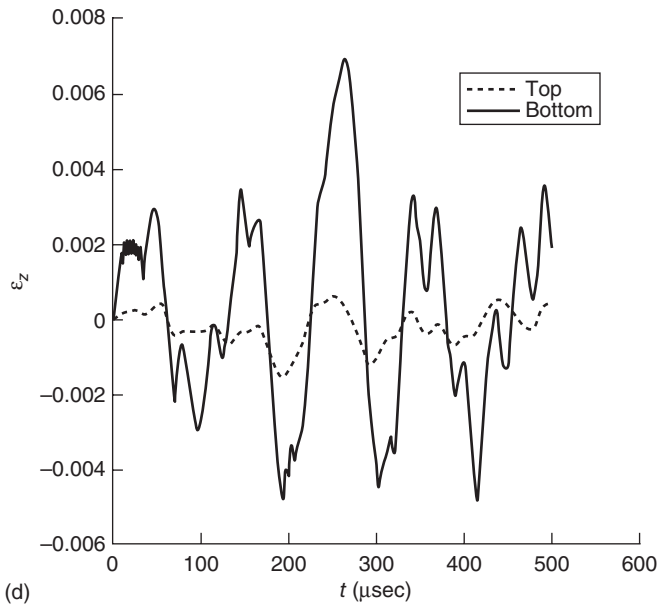

(d)

5.14 Continued

© Woodhead Publishing Limited, 2010

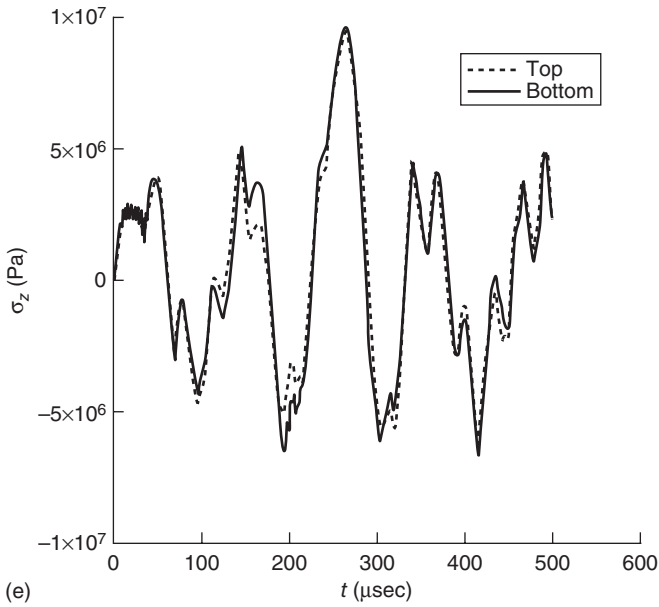

5.14 Continued

nearly continuous; only small deviations are seen near the spikes. As explained in Section 5.5.1, the continuity of transverse stresses is not imposed in the algorithm; it is satisfied in a 'soft' sense, when the overall variational problem of the functional minimization is solved more and more accurately.

Figure 5.15 shows respective results for the lower interface of the sandwich panel. The general trends here are similar to what was discussed for the upper interface – continuity of u_z is satisfied exactly (see Fig. 5.15a), continuity of ε_x is satisfied with very high accuracy (see Fig. 5.15b), in-plane stress σ_x is discontinuous with much higher stress values on the composite side (see Fig. 5.15c), transverse strain ε_z is discontinuous with much higher values on the core side (see Fig. 5.15d) and transverse stress σ_z is very close to being continuous (see Fig. 5.15e). All these results are in a full agreement with respective mechanistic requirements and do not require extensive discussion.

Therefore, the numerical results presented provide good evidence that the blast analysis of the sandwich panel can be accurately performed with Mesh 15, and all of the required continuity conditions for displacements, strains and stresses are satisfied either exactly or with high accuracy. This indicates that the obtained numerical solution is accurate overall.

© Woodhead Publishing Limited, 2010

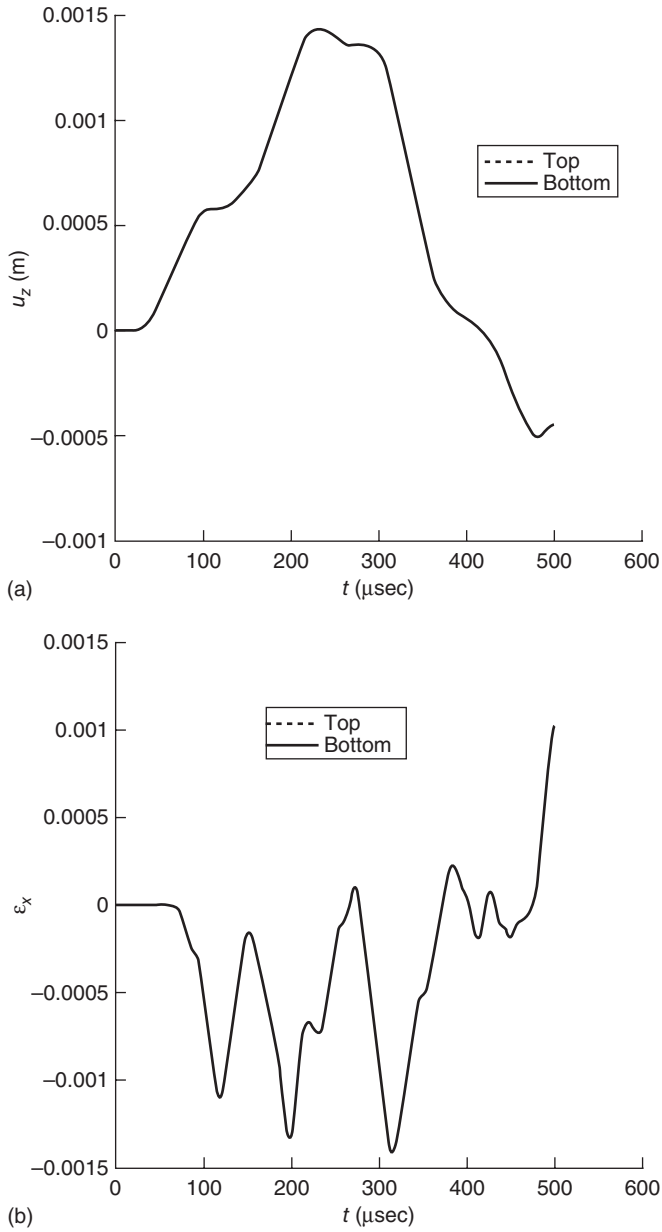

5.15 Time variations of u_z (a), ε_x (b), σ_x (c ε_z (d) and σ_z (e) computed at the center of the lower interface, $z = 0.0056$ *m*, of Panel #2 'from the top' and 'from the bottom' (Mesh 15 used).

© Woodhead Publishing Limited, 2010

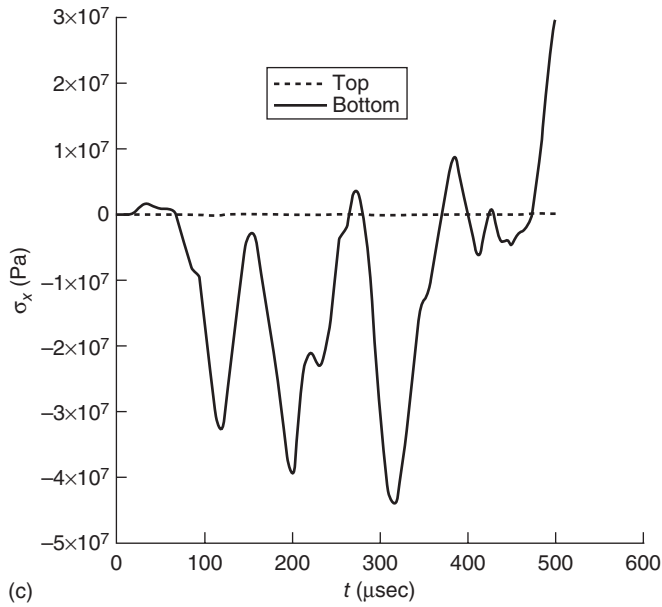

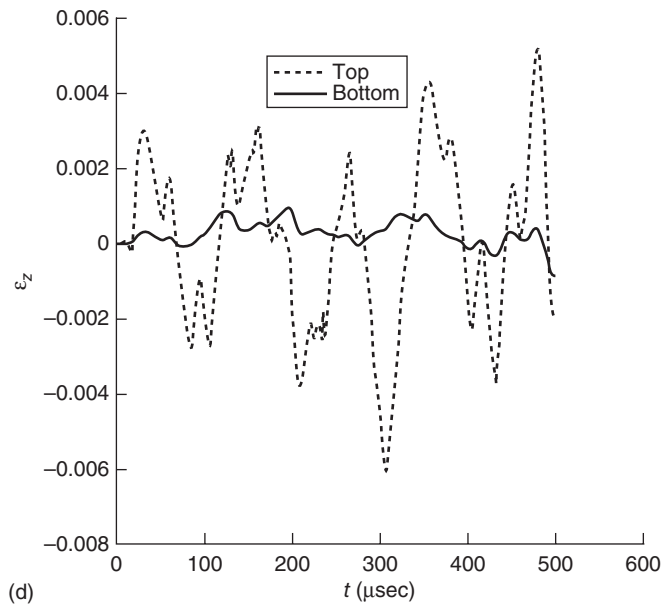

5.15 Continued

© Woodhead Publishing Limited, 2010

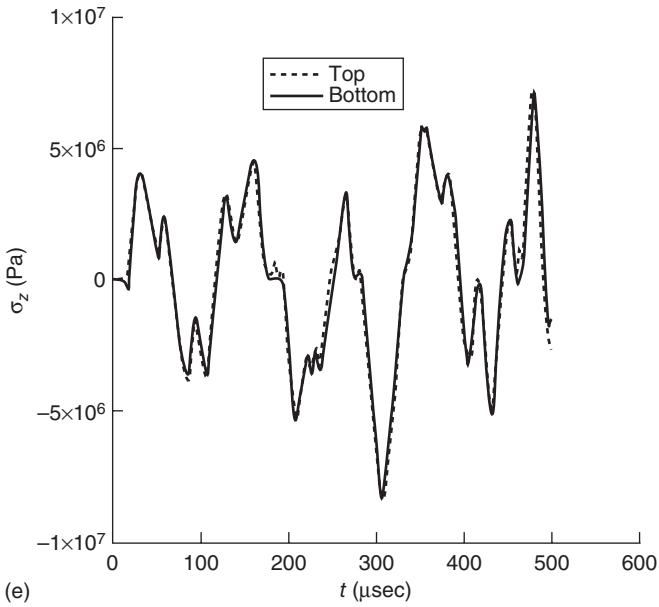

5.15 Continued

5.5.4 Numerical results for Panel #3

Panel #3 is even more interesting and complex in its transient behavior than Panel #2. It contains layers of such highly dissimilar materials as ceramic, 3D woven S-2 glass fiber composite and Balsa wood (see Fig. 5.8a). Accordingly, new aspects of the stress wave propagation from one layer to the other and stress wave reflection at the interfaces are added. Numerical results for this panel are presented in Figs 5.16–5.18; results in Fig. 5.16 correspond to the upper interface, results in Fig. 5.17 to the middle interface and results in Fig. 5.18 to the lower interface. All of the results have been obtained with Mesh 20 (see Table 5.1). Although adding the top layer of ceramic has changed significantly the stress wave propagation and reflection peculiarities seen in the results for Panel #2, the general trends discussed earlier remain similar.

Figure 5.16a shows that continuity of u_z is satisfied exactly, and no visible discontinuity of ε_x is seen in Fig. 5.16b. In-plane stress σ_x is discontinuous with much higher values on the ceramic side (see Fig. 5.16c). Transverse strain ε_z is discontinuous, but its values on the ceramic and composite sides are not as dramatically different (see Fig. 5.16d). The differences between the σ_z time variations at the top and at the bottom of the interface are seen mainly in the spikes, as seen in Fig. 5.16e.

© Woodhead Publishing Limited, 2010

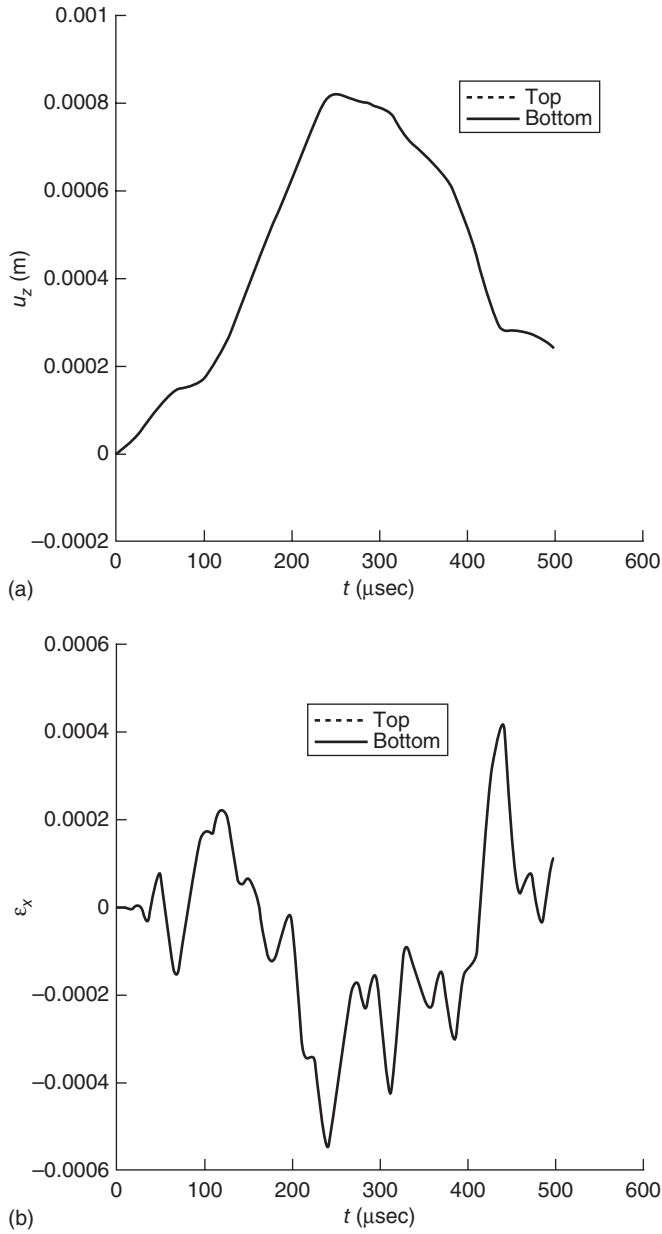

5.16 Time variations of u_z (a), ε_x (b), σ_x (c), ε_z (d) and σ_z (e) computed at the center of the first from top interface of Panel #3 'from the top' and 'from the bottom' (Mesh 20 used).

© Woodhead Publishing Limited, 2010

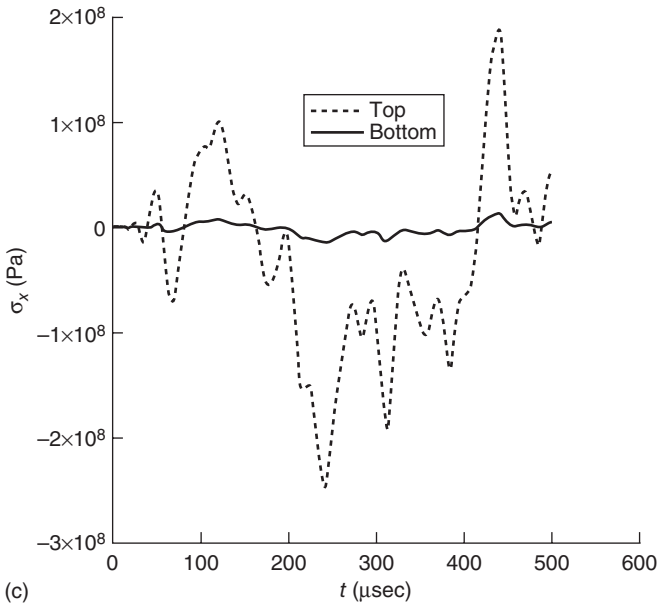

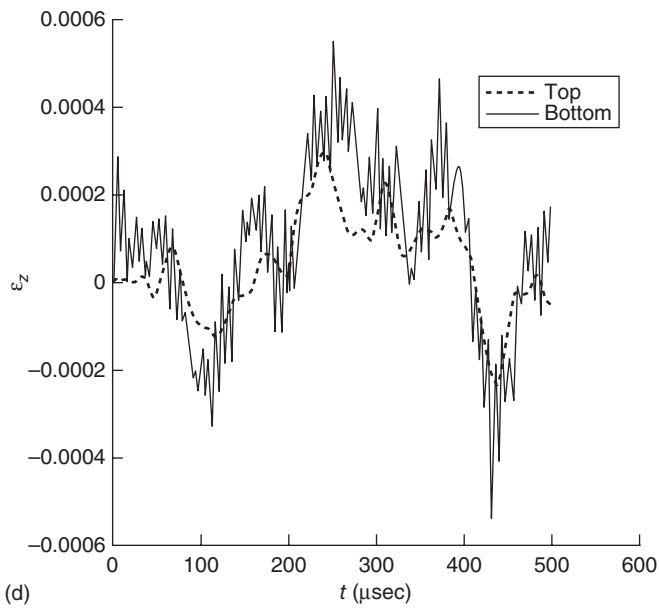

5.16 Continued

© Woodhead Publishing Limited, 2010

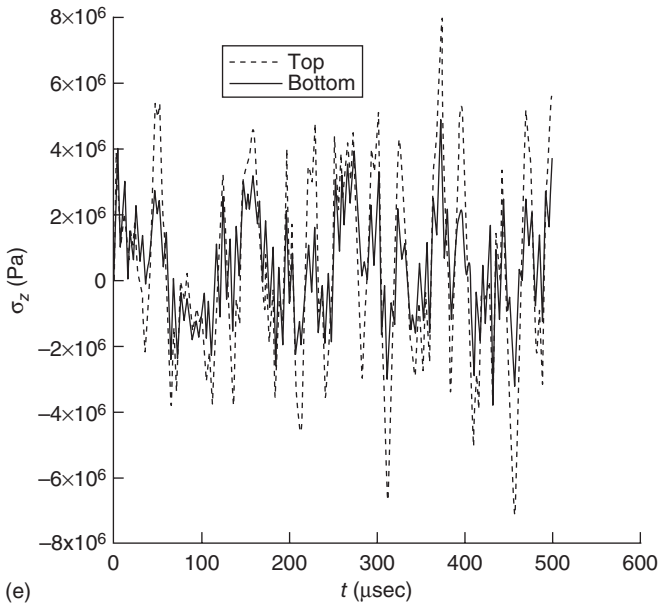

5.16 Continued

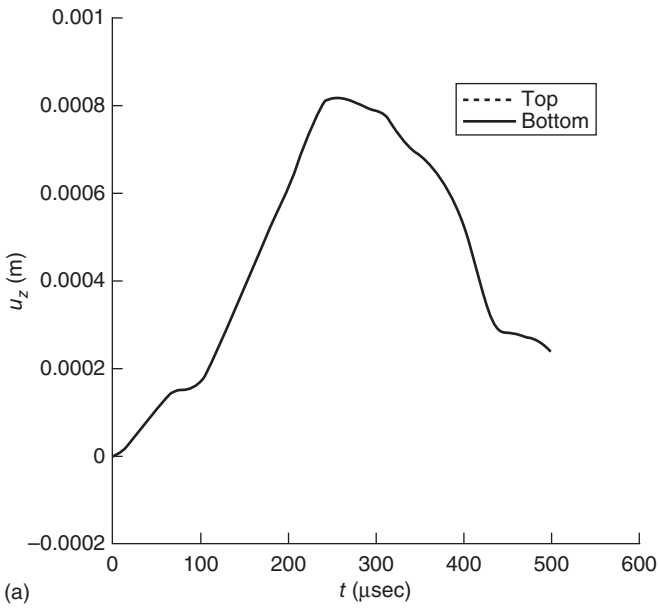

5.17 Time variations of u_z (a), ε_x (b), σ_x (c), ε_z (d) and σ_z (e) computed at the center of the second from top interface, $z = 0.0564$ *m*, of Panel #3 'from the top' and 'from the bottom' (Mesh 20 used).

© Woodhead Publishing Limited, 2010

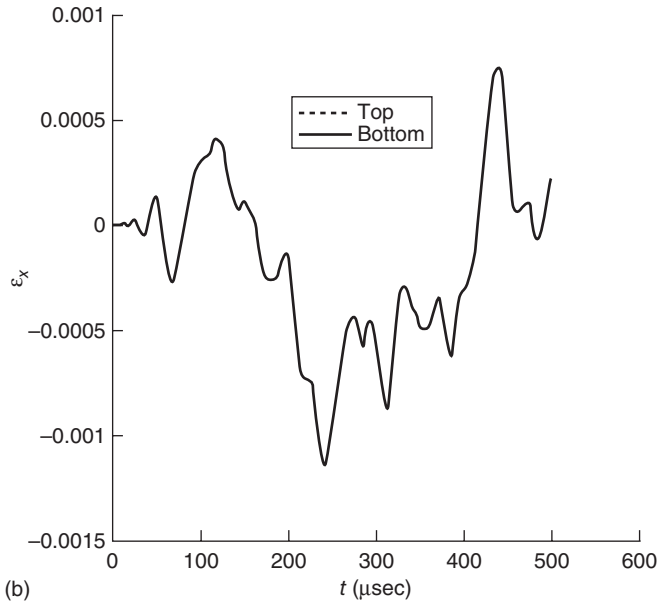

(b)

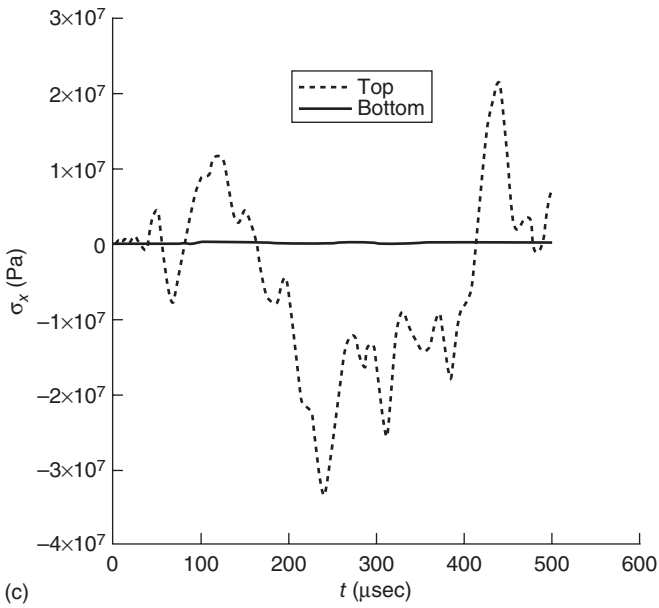

(c)

5.17 Continued

© Woodhead Publishing Limited, 2010

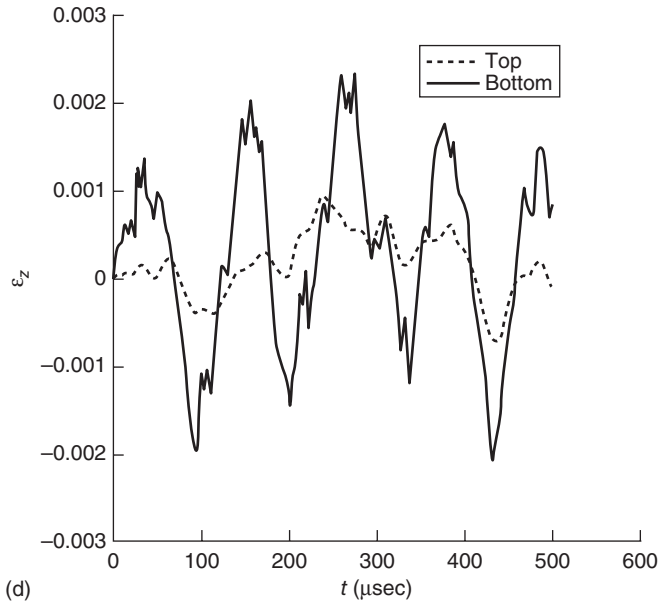

(d)

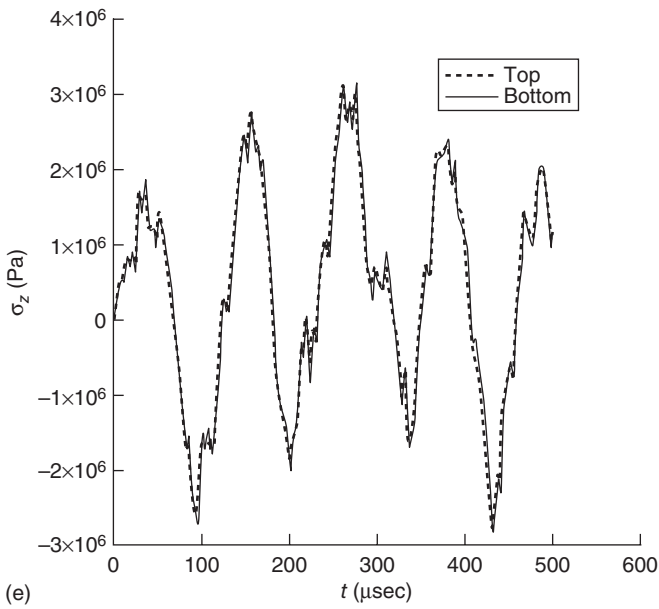

(e)

5.17 Continued

© Woodhead Publishing Limited, 2010

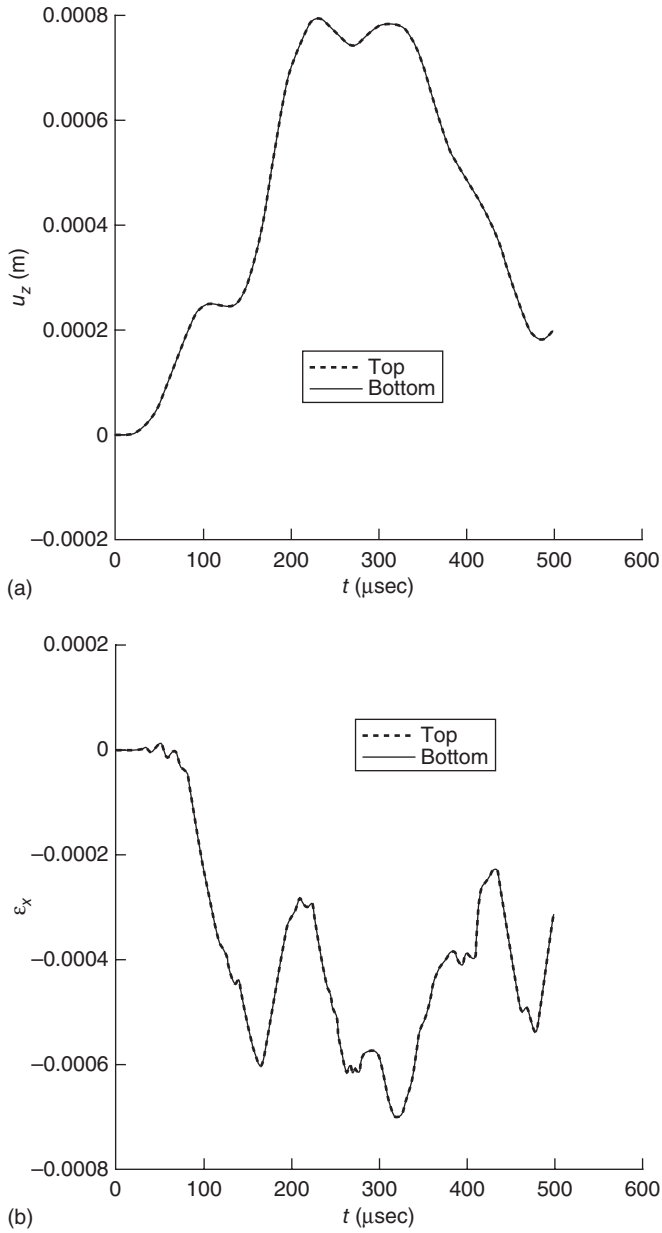

5.18 Time variations of u_z (a), ε_x (b), σ_x (c), ε_z (d) and σ_z (e) computed at the center of the third from top interface, $z = 0.0056$ *m*, of Panel #3 'from the top' and 'from the bottom' (Mesh 20 used).

© Woodhead Publishing Limited, 2010

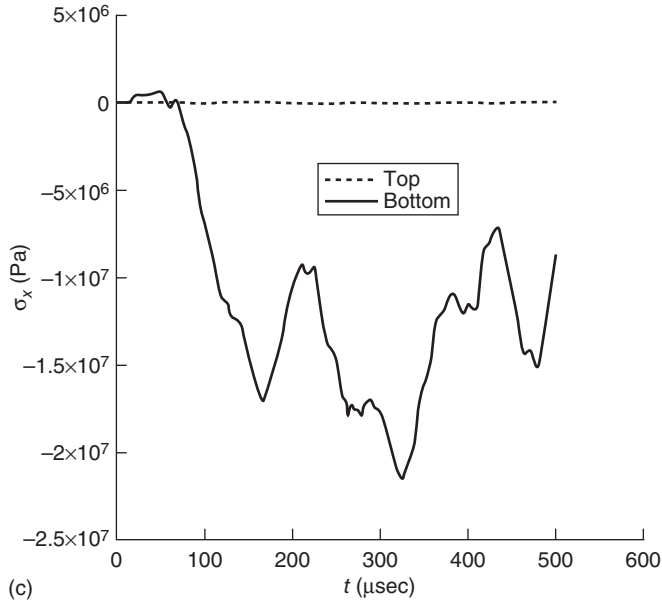

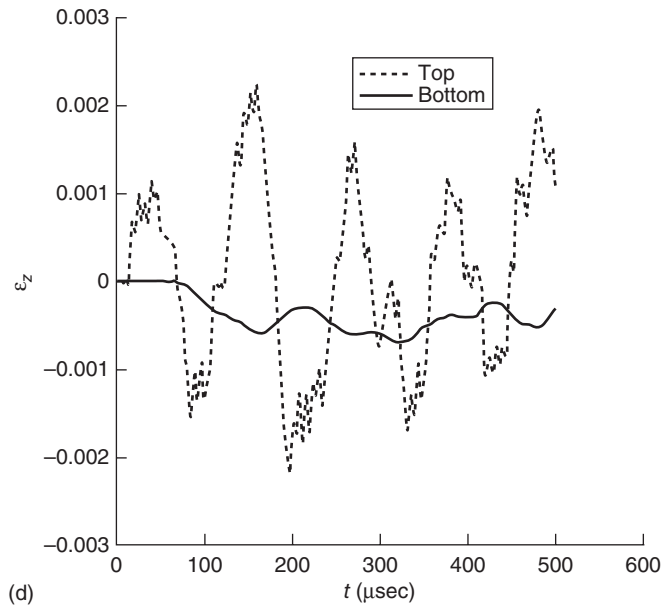

5.18 Continued

© Woodhead Publishing Limited, 2010

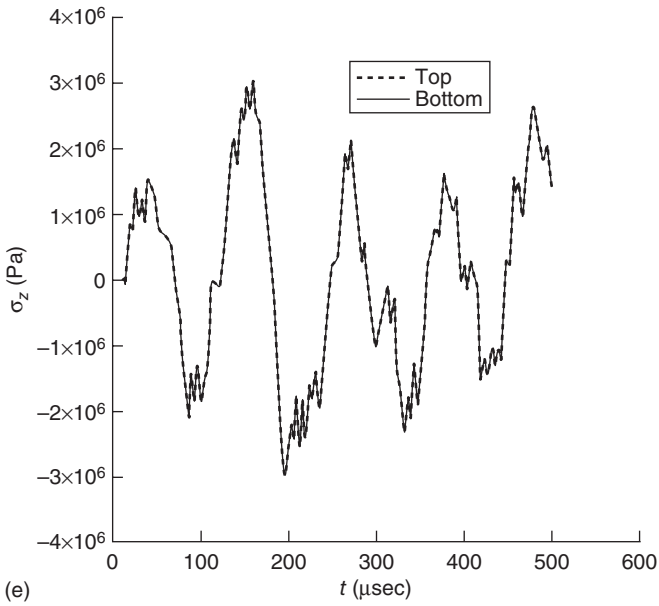

5.18 Continued

Results in Fig. 5.16d are especially interesting, because it illustrates how the differences in transverse (through-thickness) elastic modulus and density of the adjacent ceramic and polymer matrix composite affect the respective velocities of stress wave propagation and reflections from the interface and from the free outer surface. It is easy to calculate from material properties (Eqs 5.20 and 5.22) that the stress wave propagation speed in ceramic material (approximately 9600 m/sec) is 3.7 times greater than the stress wave propagation speed in the transverse direction of composite material (approximately 2590 m/sec). Further, considering that thickness of the composite layer is 5.6 mm, while thickness of the ceramic layer is 9.0 mm, we find that the stress wave runs one time through the thickness of the ceramic layer in 0.94 μsec, which is about 2.3 times less than one run time through the thickness of the S-2 glass composite layer (2.16 μsec). This is clearly seen in Figs 5.16d and 5.16e – the characteristic time between adjacent spikes in ceramic is significantly shorter than that in composite.

Figure 5.17 shows analogous results for the upper interface between composite and Balsa core. It is seen in Fig. 5.17a that the σ_z continuity at the interface is satisfied much more accurately than in the case of Fig. 5.16. Interestingly, all time variations shown in Fig. 5.17 are not similar, either quantitatively or qualitatively, to the ones in Fig. 5.14, where the upper interface between composite skin and Balsa core was also considered.

© Woodhead Publishing Limited, 2010

Figure 5.18 shows respective results for the lower interface between Balsa core and composite skin in Panel #3. As is seen in Fig. 5.18e, the $\sigma_z(t)$ continuity at the interface is satisfied very accurately. Also, one can recognize that most of the curves in Fig. 5.18 are significantly different from the respective curves in Fig. 5.15, where the lower interface of Panel #2 between composite skin and Balsa core was considered.

5.5.5 Numerical results for Panel #4

The construction of Panel #4 (see Fig. 5.9a) is substantially different from that of Panel #3. Firstly, a relatively thin (3.2 mm) facing layer of perforated steel is used in place of the ceramic layer. Secondly, a relatively thick (25.4 mm) layer of aluminum foam is added between the top composite layer and the Balsa wood. Thirdly, E-glass 3D woven fabric was used for both composite layers in place of the S-2 glass fabric composite used in Panels #1, #2 and #3. Numerical results for Panel #4 are presented in Figs 5.19–5.22. Mesh 23 was used in all cases.

Figure 5.19 shows results for the first from the top interface, which separates perforated steel and 3D woven E-glass composite. These results can

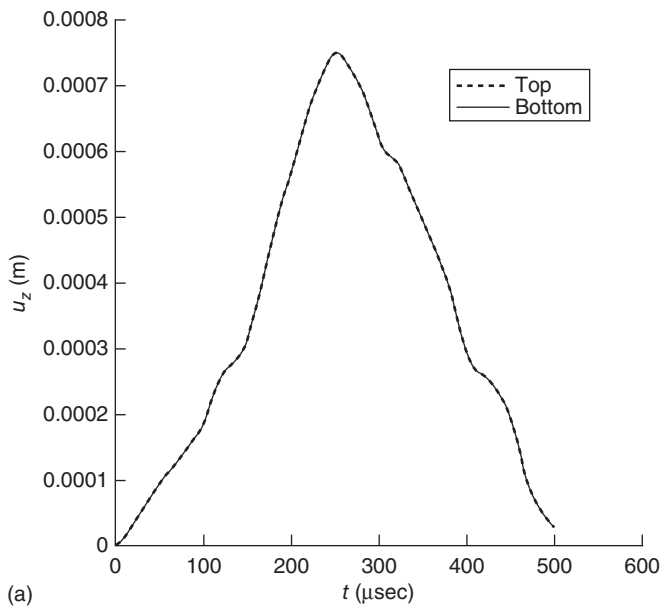

5.19 Time variations of u_z (a), ε_x (b), σ_x (c), ε_z (d) and σ_z (e) computed at the center of the first from top interface, $z = 0.0737$ *m*, of Panel #4 'from the top' and 'from the bottom' (Mesh 23 used).

© Woodhead Publishing Limited, 2010

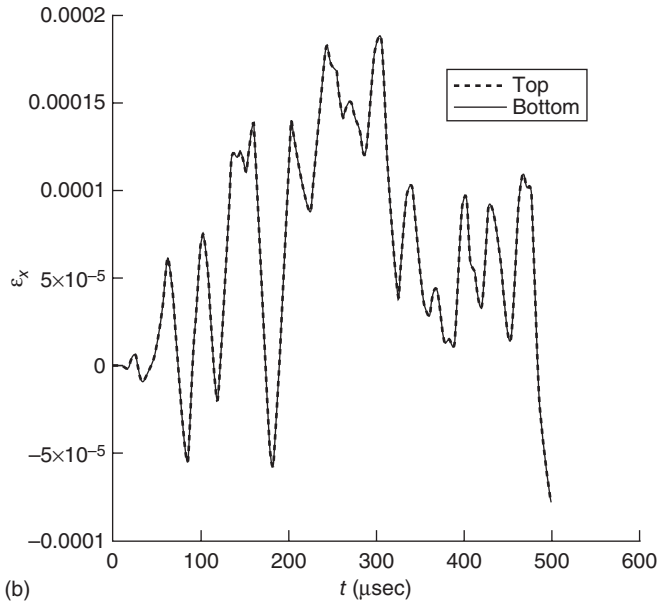

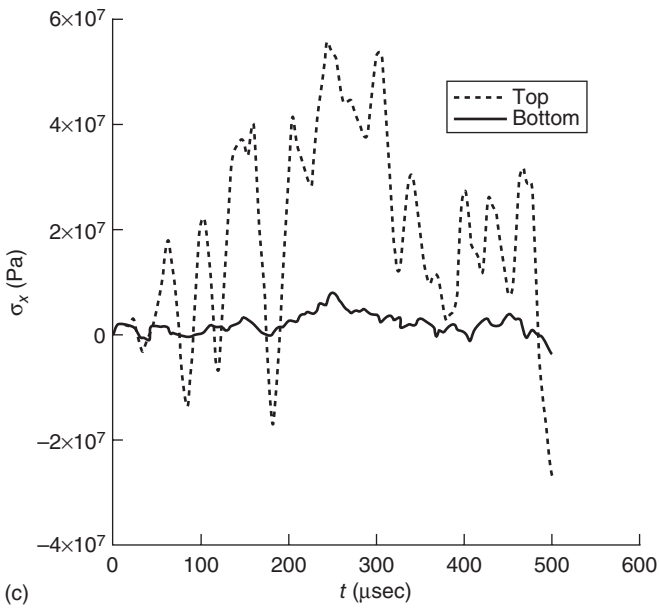

5.19 Continued

© Woodhead Publishing Limited, 2010

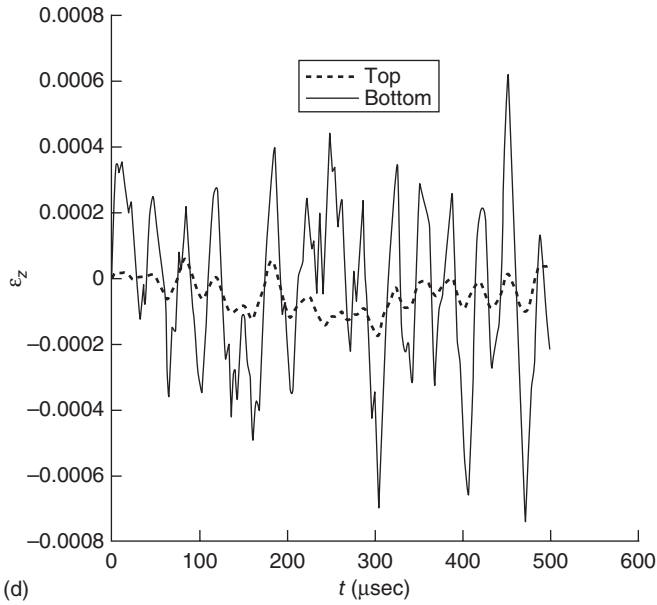

(d)

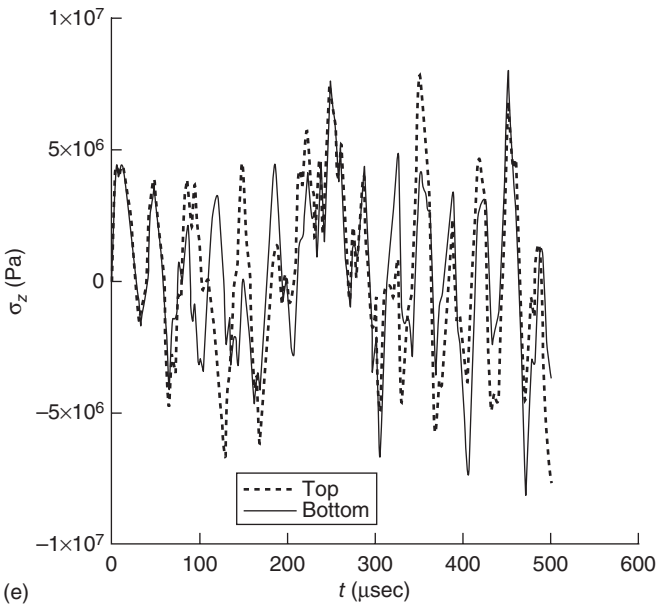

(e)

5.19 Continued

© Woodhead Publishing Limited, 2010

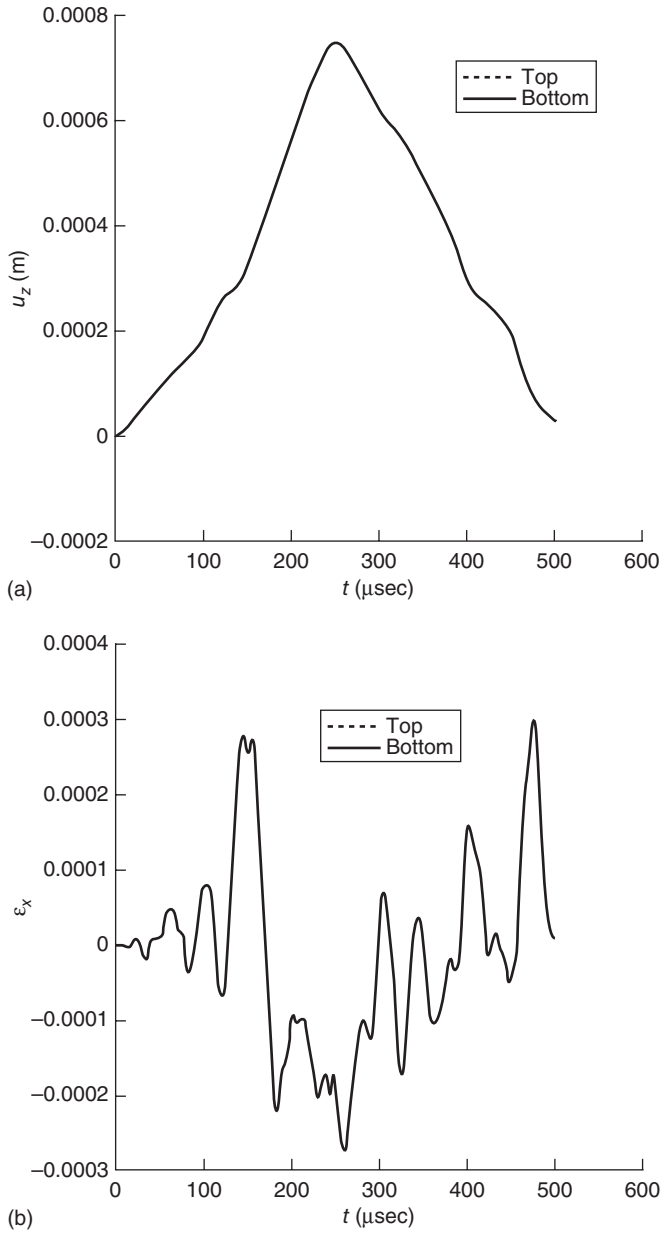

5.20 Time variations of u_z (a), ε_x (b), σ_x (c), ε_z (d) and σ_z (e) computed at the center of the second from top interface, z = 0.0686 *m*, of Panel #4 'from the top' and 'from the bottom' (Mesh 23 used).

© Woodhead Publishing Limited, 2010

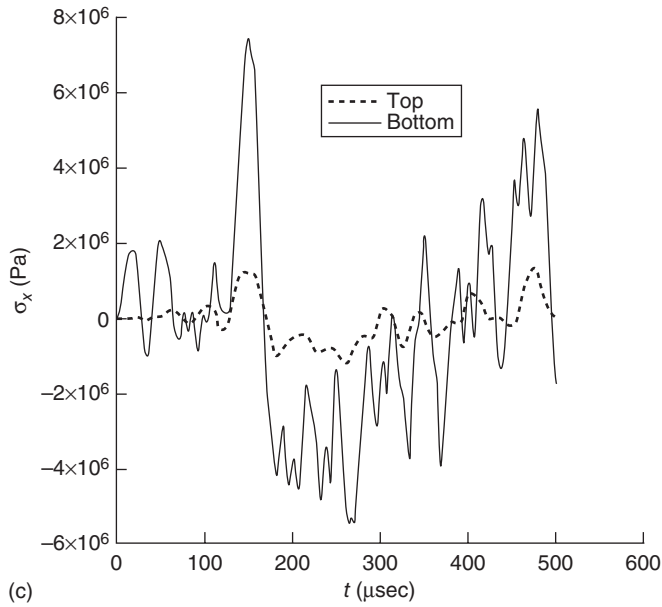

(c)

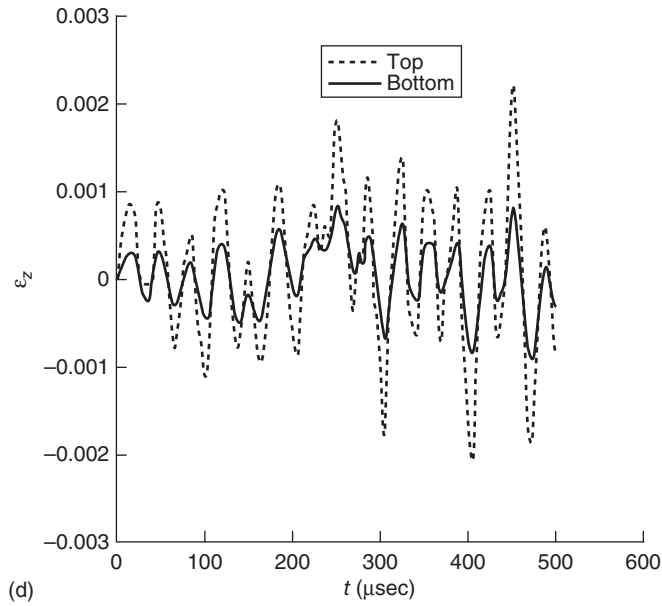

(d)

5.20 Continued

© Woodhead Publishing Limited, 2010

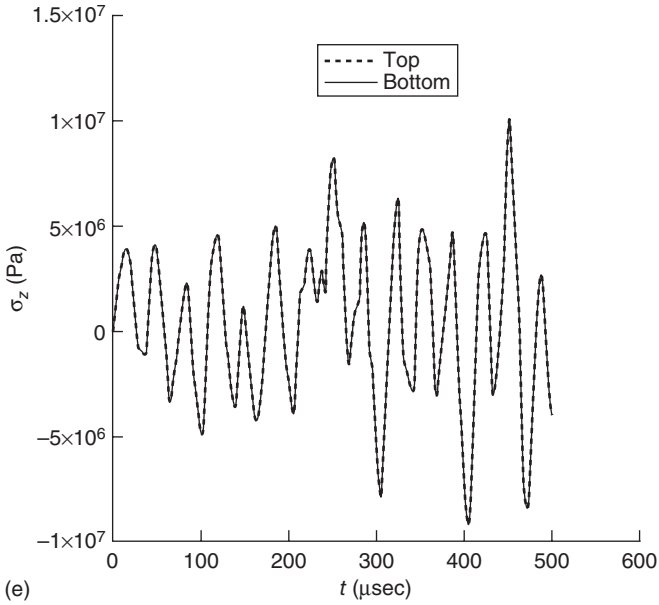

5.20 Continued

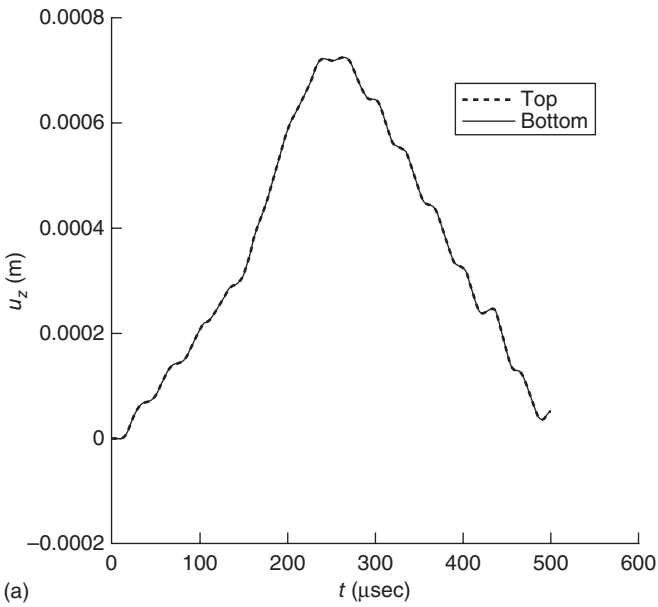

5.21 Time variations of u_z (a), ε_x (b), σ_x (c), ε_z (d) and σ_z (e) computed at the center of the third from top interface, $z = 0.0432$ *m*, of Panel #4 'from the top' and 'from the bottom' (Mesh 23 used).

© Woodhead Publishing Limited, 2010

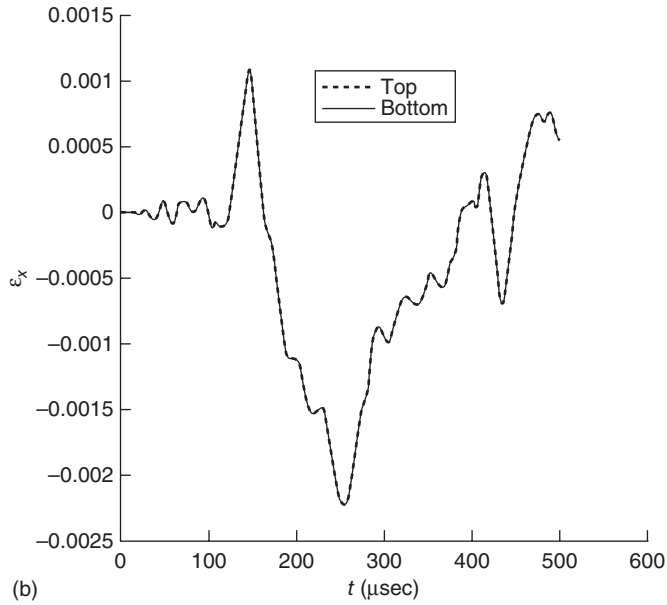

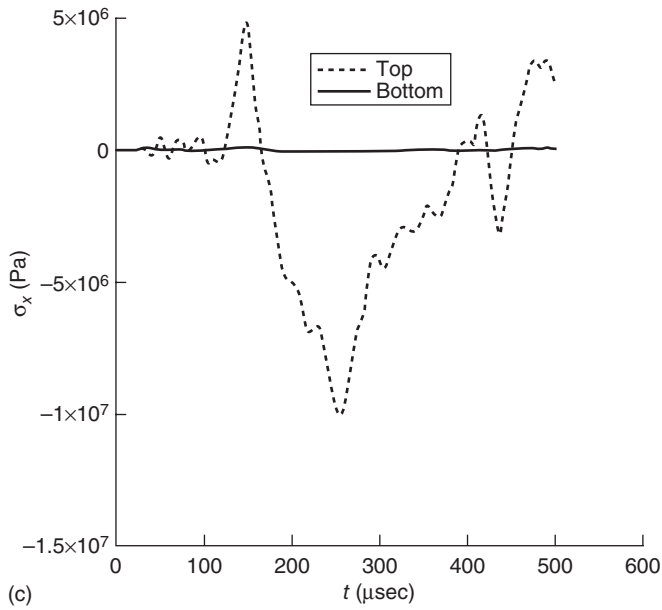

5.21 Continued

© Woodhead Publishing Limited, 2010

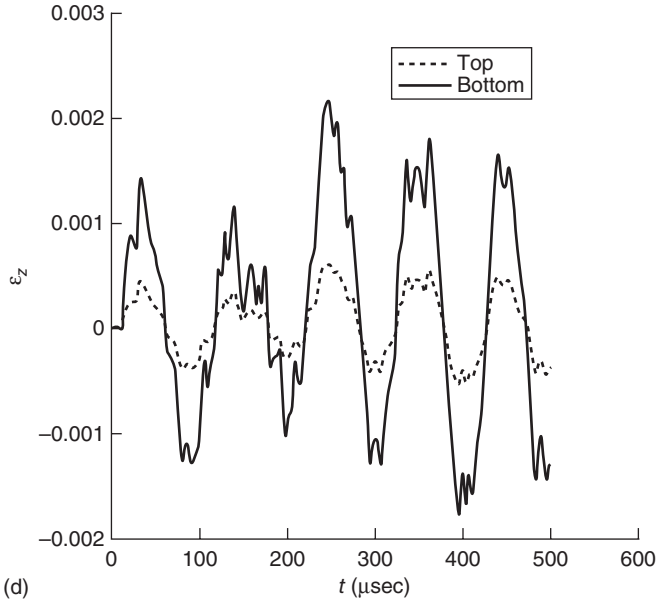

(d)

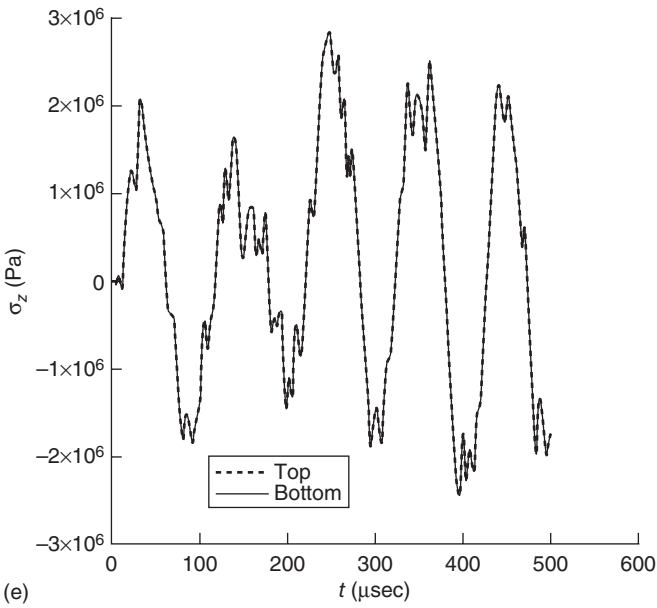

(e)

5.21 Continued

© Woodhead Publishing Limited, 2010

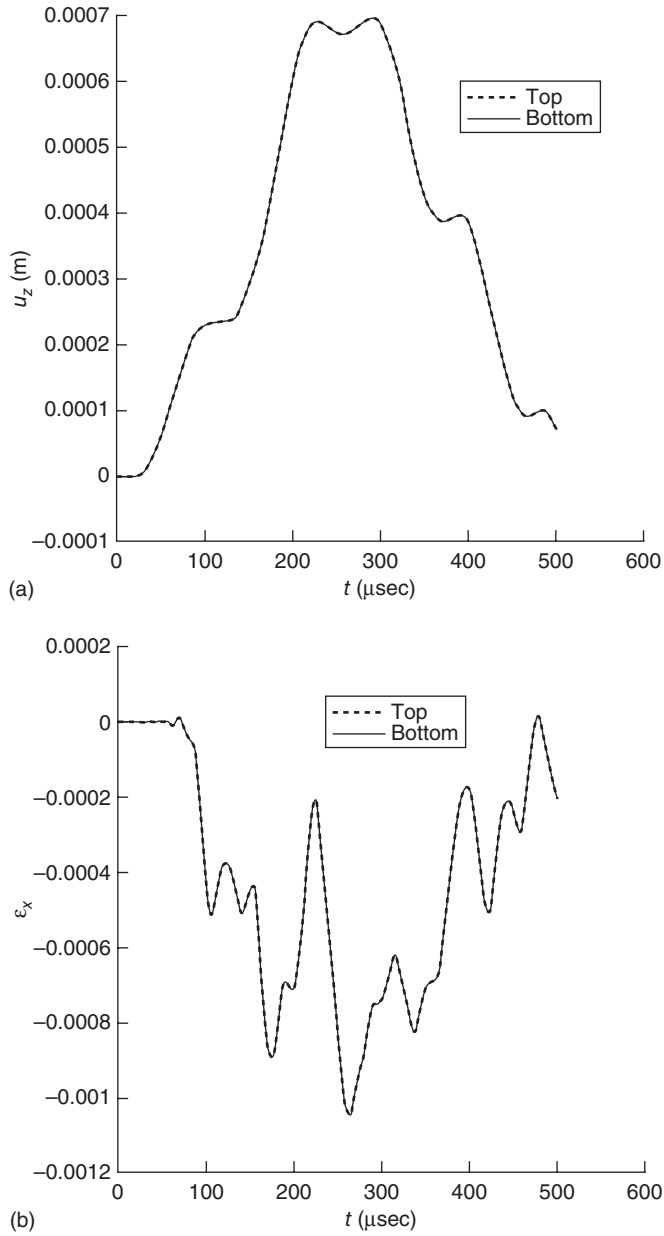

5.22 Time variations of u_z (a), ε_x (b), σ_x (c), ε_z (d) and σ_z (e) computed at the center of the fourth from top interface, $z = 0.0051$ *m*, of Panel #4 'from the top' and 'from the bottom' (Mesh 23 used).

© Woodhead Publishing Limited, 2010

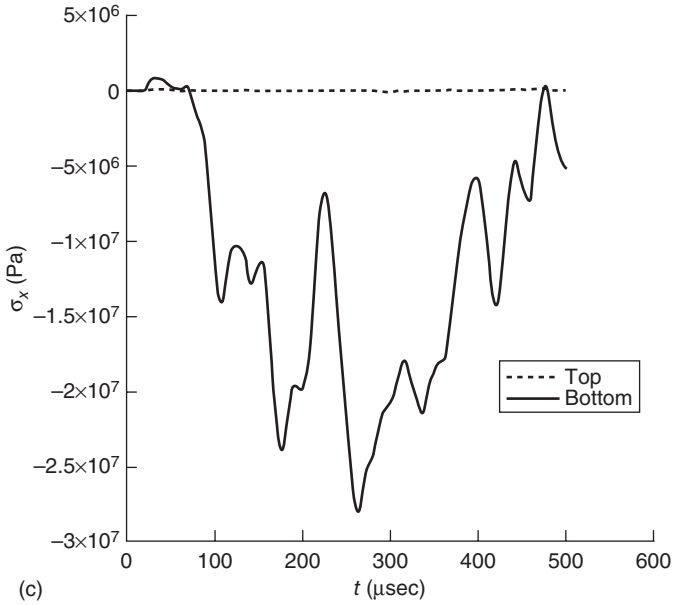

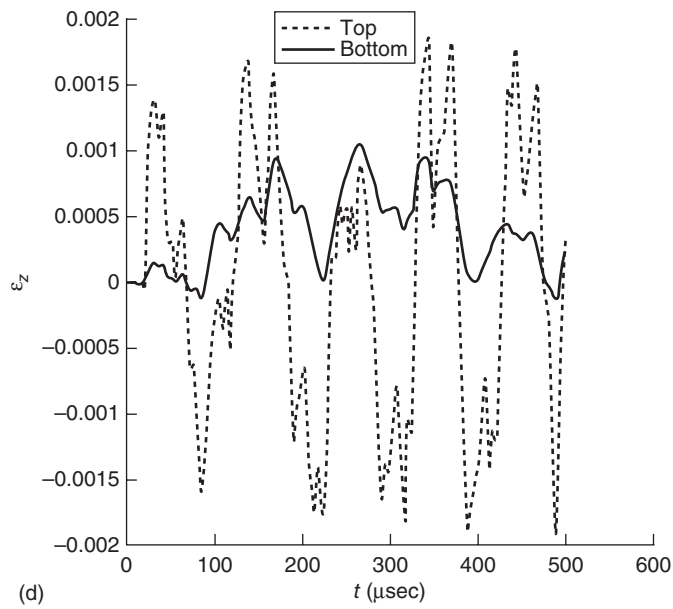

5.22 Continued

© Woodhead Publishing Limited, 2010

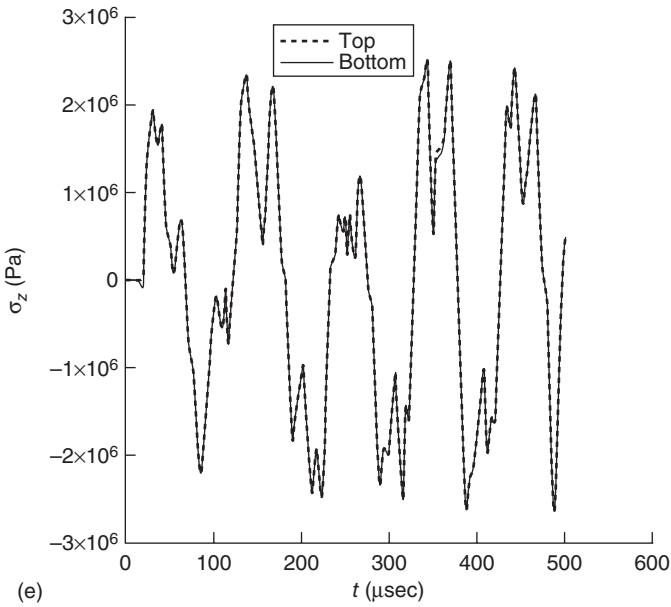

5.22 Continued

be compared to the respective results for Panel #3 in Fig. 5.16. In both cases σ_x is many times lower on the composite side. Also, in Fig. 5.19d ε_z is many times higher on the composite side. Note that the stress wave propagation speed in steel (approximately 5150 m/sec) is about 2.2 times greater than that in the transverse direction of the E-glass composite (approximately 2360 m/sec). Accounting for the difference in composite and steel layer thickness results in the time for one stress wave run through the thickness of the steel layer (0.62 μsec) being about 3.5 times smaller than that for the composite layer (2.16 μsec). This explains why the ε_z variation in Fig. 5.19d and the σ_z variation in Fig. 5.19e look like higher frequency processes on the steel side. Also, considerable differences between σ_z values from the top and from the bottom are seen in Fig. 5.19e.

Figure 5.20 presents respective results for the second from the top interface, which separates E-glass composite and lightweight aluminum foam. As Fig. 5.20c shows, σ_x is many times higher on the composite side. At the same time, as seen in Fig. 5.20d, the spikes of ε_z from the top and from the bottom are much closer than in the other cases (compared to Figs 5.14d, 5.15d, 5.17d, 5.18d and 5.19d). The other interesting effect is that the high-frequency oscillations seen in Fig. 5.20d have practically identical period from the top and from the bottom and occur 'in-synch'. It is also worth noting that excellent continuity of $\sigma_z(t)$ is observed in Fig. 5.20e.

© Woodhead Publishing Limited, 2010

Results in Fig. 5.21 correspond to the other new and interesting interface – between aluminum foam and Balsa wood. At this interface σ_x is much higher on the aluminum foam side, and ε_z is several times higher on the Balsa wood side. Excellent continuity of $\sigma_z(t)$ is seen in Fig. 5.21e.

Finally, Fig. 5.22 presents results for the lowest interface separating Balsa wood and E-glass composite. One can anticipate that these results should be very similar to the ones in Figs 5.15 and 5.18. Actually, there are some similarities; for example, σ_x is much larger on the composite side in all three cases, while ε_z is several times larger on the Balsa wood side. However, there are also significant differences; for example, ε_z on the composite side is mainly positive in Figs 5.22d and 5.15d, while it is mainly negative in Fig. 5.18d. Also, σ_x stress in Figs 5.22c and 5.18c is negative all of the time, while in Fig. 5.15c it sharply turns positive at about 450 μsec time instant. This emphasizes that the stress and strain variations at the interfaces in these complex inhomogeneous layered systems are determined not only by the nature of materials separated by the interface, but also by entire panel construction between the blast loading surface and the interface.

5.6 Comparison of the blast response characteristics for the four panels

Next we compare the time variations of u_z, ε_x, σ_x and ε_z for the four layered panels analyzed in detail above. These results will allow us to evaluate the blast mitigation ability of each of them in comparison with the other three.

Figure 5.23 presents a comparison of results for transverse displacement u_z corresponding to the center of the top (loaded) surface of each panel and to the center of the top surface of the lower composite layer in those panels. This comparison illustrates how the transient displacement varies through the thickness of each panel, and it becomes obvious from comparison of Figs 5.23a and 5.23b that the variation is very small. It is most obvious in the case of Panel #2, but even in this case the peak values differ by only 15%. Further, it is seen in Figs 5.23a and 5.23b that u_z of Panel #1 experiences nearly linear growth with time, and its value reaches 5.6 mm at 500 μsec time instant. Transverse displacement of Panel #2 reaches its peak (approximately 1.7 mm on the top surface) at about 250 μsec time instant. Transverse displacements of Panels #3 and #4 reach their almost identical peaks (0.8–0.9 mm on the top surface) at about the same time instant. So, if the objective is to minimize u_z and attenuate it through the thickness as much as possible, Panels #3 and #4 provide almost identical effect.

Figure 5.24a shows variations of in-plane strain ε_x at the center of the top surface of each panel. For Panel #1 the strain has highest positive value of about 0.3% and highest negative value of about 0.4%. However, Panel #2 shows about the same positive maximum value. Panels #3 and #4 show

© Woodhead Publishing Limited, 2010

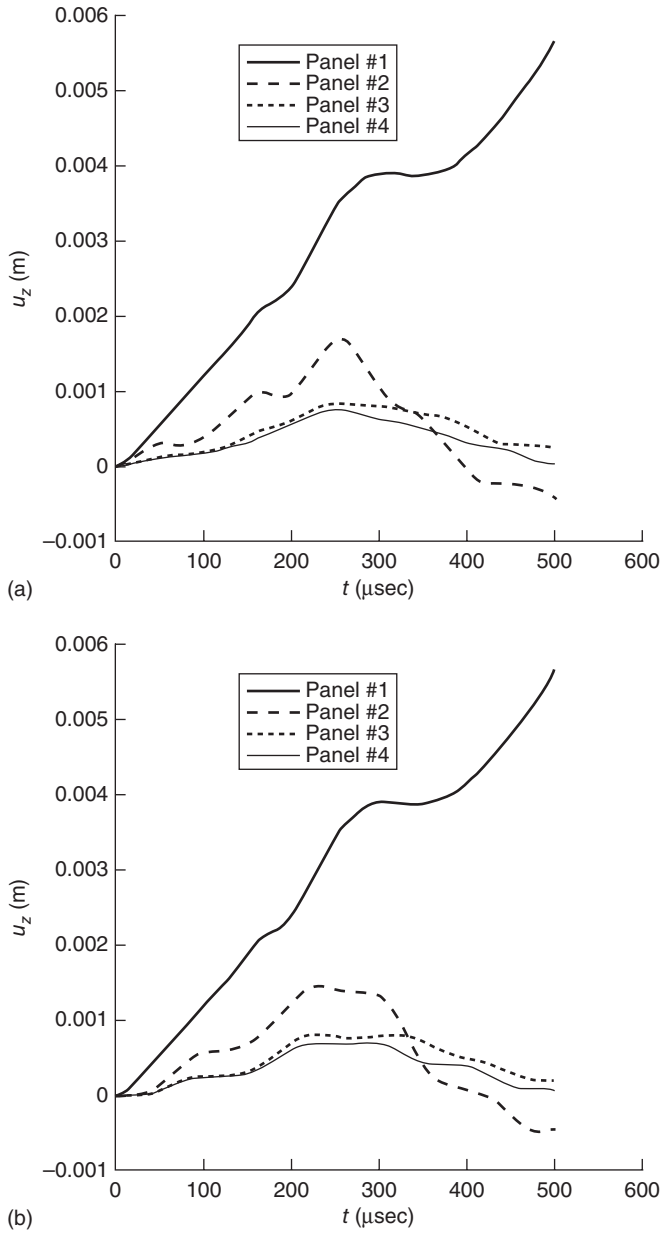

5.23 Time variations of displacement u_z computed for Panels #1–#4 at the center of top surface of the panels (a) and at the center of top surface of the lower composite layer (b). Mesh 10 used for Panel #1, Mesh 15 for Panel #2, Mesh 20 for Panel #3 and Mesh 23 for Panel #4.

© Woodhead Publishing Limited, 2010

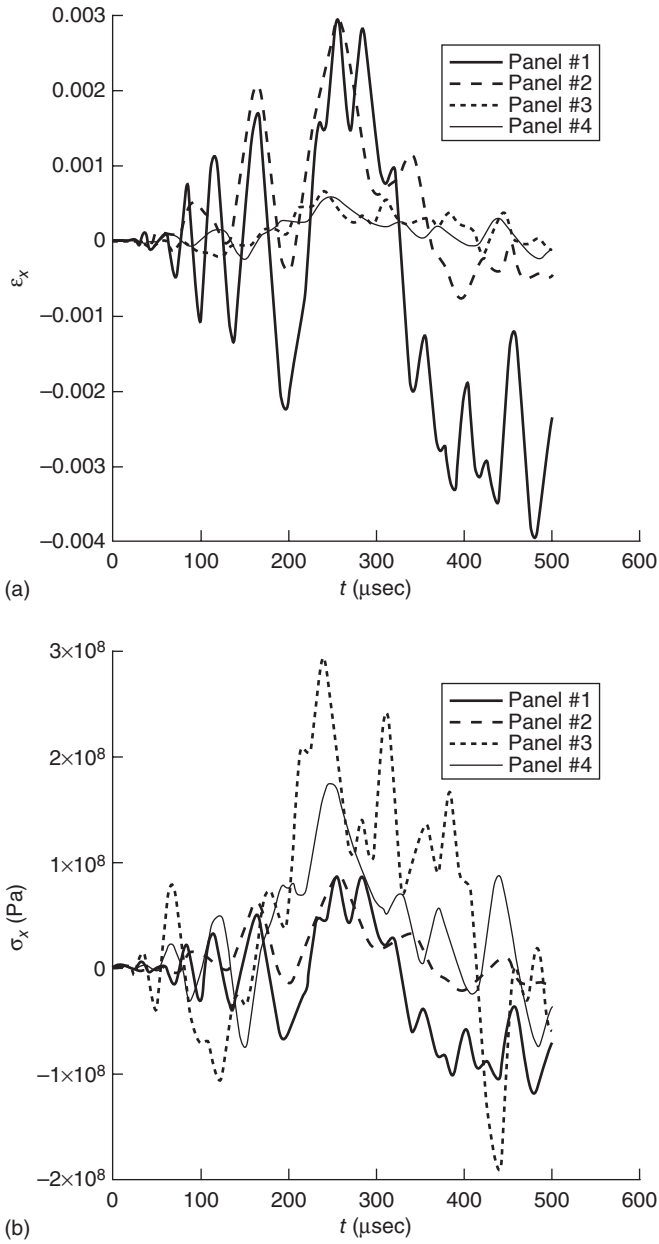

5.24 Time variations of ε_x (a), σ_x (b) and ε_z (c) computed at the center of top surface of Panels #1–#4. Mesh 10 used for Panel #1, Mesh 15 for Panel #2, Mesh 20 for Panel #3 and Mesh 23 for Panel #4.

© Woodhead Publishing Limited, 2010

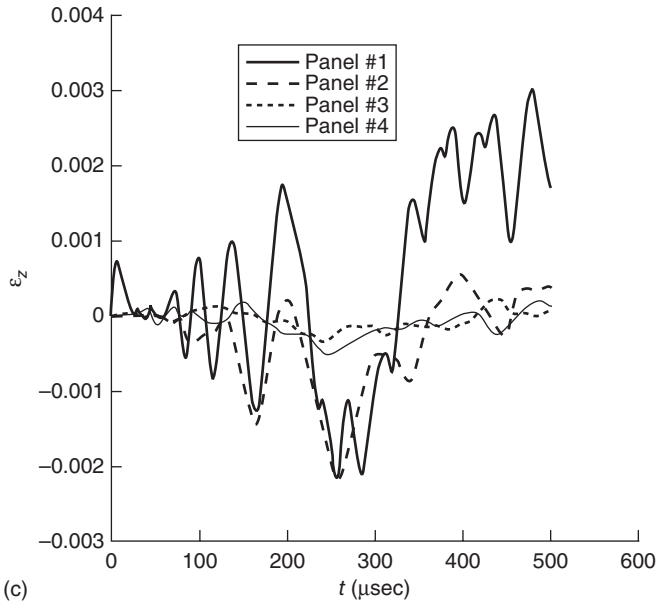

5.24 Continued

practically equal peak values of ε_x (about 0.06%), which is much lower than the peak value for Panel #2.

Results for σ_x in Fig. 5.24b are, as expected, totally different. The highest stress is reached in the ceramic layer of Panel #3 (approximately 300 MPa positive peak and nearly 200 MPa negative peak). The second highest tensile stress peak is obtained in the steel layer of Panel #4 (about 170 MPa), while the second highest compressive stress peak (about 115 MPa) belongs to the composite Panel #1. All other tensile and compressive stress peaks are under 100 MPa.

Fig. 5.24c shows time variations of transverse normal strain ε_z. The highest tensile values (about 0.3%) belong to Panel #1. All tensile strain peaks for Panels #2, #3 and #4 are relatively small (lower than 0.06%). The maximum compressive strain peaks of equal magnitude (about 0.21%) are seen for Panels #1 and #2. The highest compressive strain peaks for Panels #3 and #4 are much lower (less than 0.05%).

Figure 5.25 presents comparative results for the center of the top surface of the upper composite layer in Panels #1, #3 and #4. This comparison is important because it shows how well the ceramic layer in Panel #3 or the steel layer in Panel #4 protects this composite layer against blast pressure. Also, the 'backup layer' material (Balsa or aluminum foam) makes its effect by reducing flexural deformation of the composite layer. The curves

© Woodhead Publishing Limited, 2010

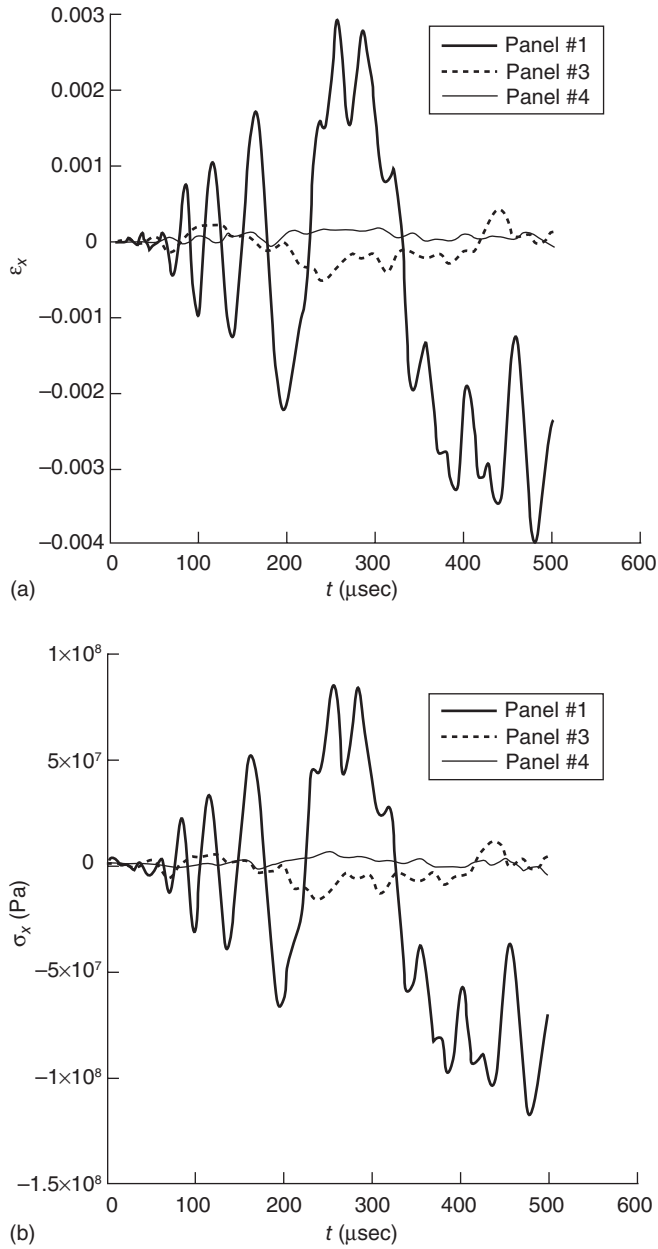

5.25 Time variations of ε_x (a), σ_x (b) and ε_z (c) computed at the center of top surface of the upper composite layer in Panels #1, #3 and #4. Mesh 10 used for Panel #1, Mesh 20 for Panel #3 and Mesh 23 for Panel #4.

© Woodhead Publishing Limited, 2010

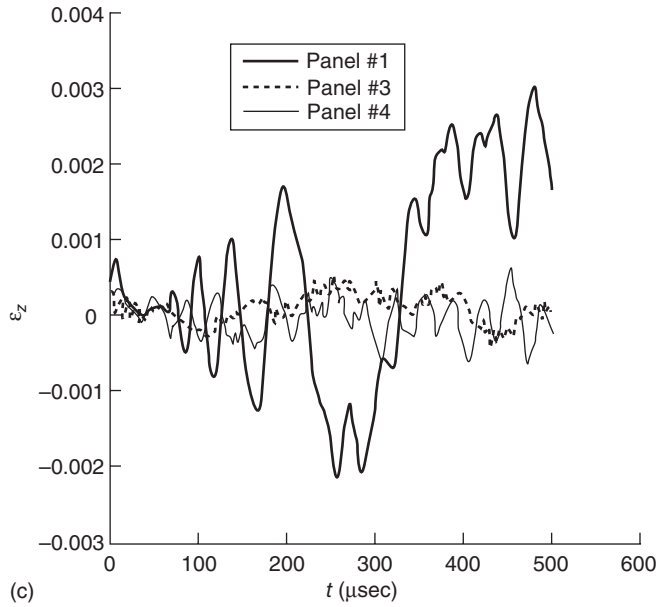

5.25 Continued

corresponding to Panel #1 in Fig 5.25 are, of course, the same as the curves for Panel #1 in Fig. 5.24. As Figs 5.25a–5.25c show, there is a dramatic reduction of ε_x, σ_x and ε_z reached in the top composite layer of both Panels #3 and #4, as compared to the unprotected and unsupported composite layer in Panel #1. It is counter-intuitive that all three characteristics are reduced to a lower level in Panel #4 than in Panel #3 (ceramic has higher modulus than steel). However, we do not immediately conclude that the steel layer in Panel #4 attenuates blast pressure better than the ceramic layer in Panel #3, because the backing effect of the aluminum foam core may be much stronger than that provided by the Balsa core. This interesting result requires better understanding and further study.

Results for ε_x, σ_x, ε_z and σ_z presented in Fig. 5.26 correspond to the center of the top surface of the Balsa core. They demonstrate how effectively the core material is protected by the other materials placed between the core and the blast loaded surface. As seen in Fig. 5.26a, the maximum peaks of both tensile and compressive ε_x are lower for Panel #3 than for Panel #4. The same is observed for σ_x in Fig. 5.26b. This trend is opposite to the one in Fig. 5.25, where the in-plane strain and stress were reduced more effectively in Panel #4. However, the highest tensile and compressive peaks of ε_z strain in Fig. 5.26c and of σ_z stress in Fig. 5.26d are very close in magnitude for the compared Panels #3 and #4.

© Woodhead Publishing Limited, 2010

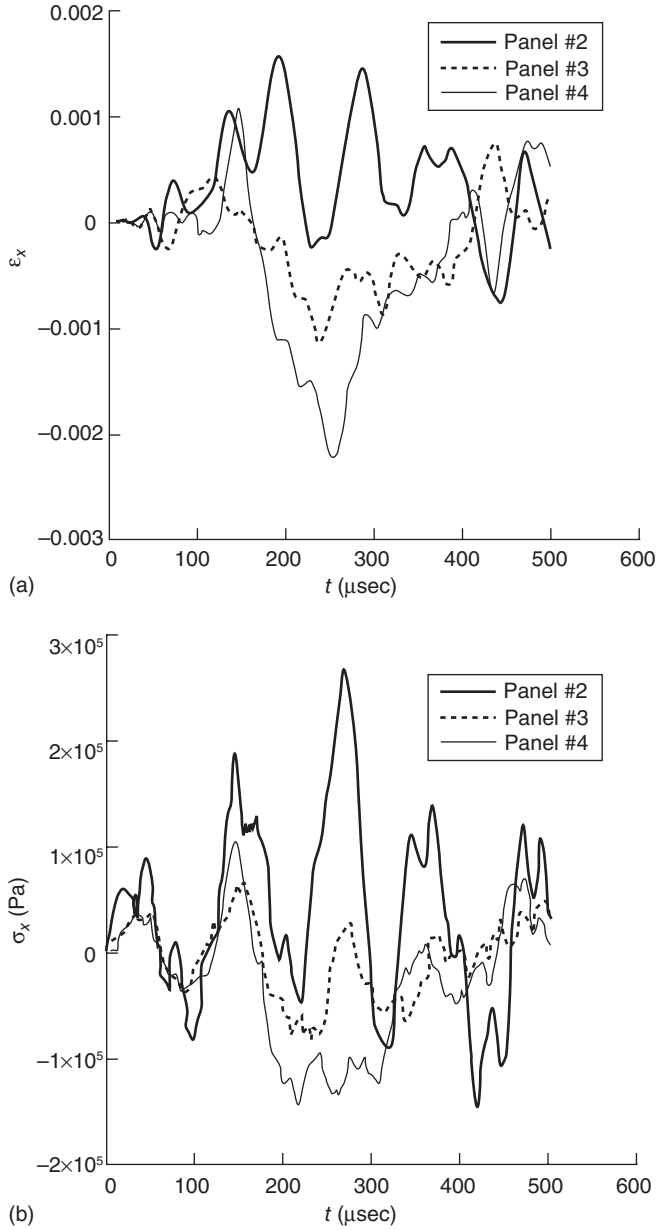

5.26 Time variations of ε_x (a), σ_x (b), ε_z (c) and σ_z (d) computed at the center of top surface of the Balsa wood layer in Panels #2, #3 and #4. Mesh 15 used for Panel #2, Mesh 20 for Panel #3 and Mesh 23 for Panel #4.

© Woodhead Publishing Limited, 2010

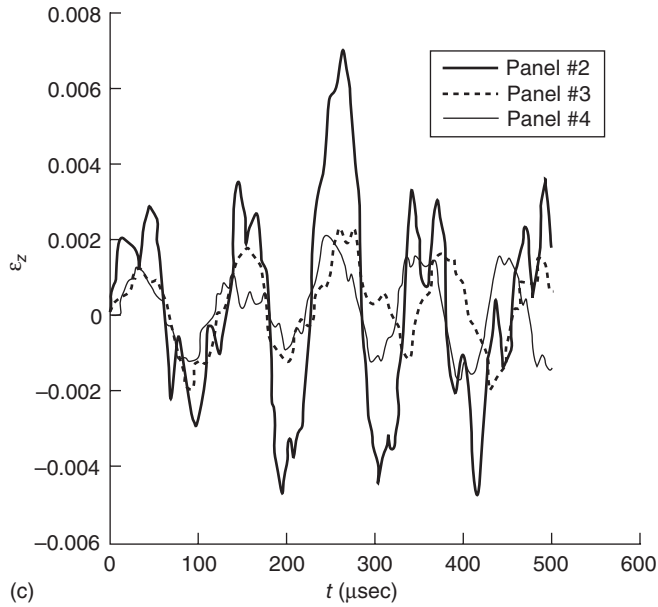

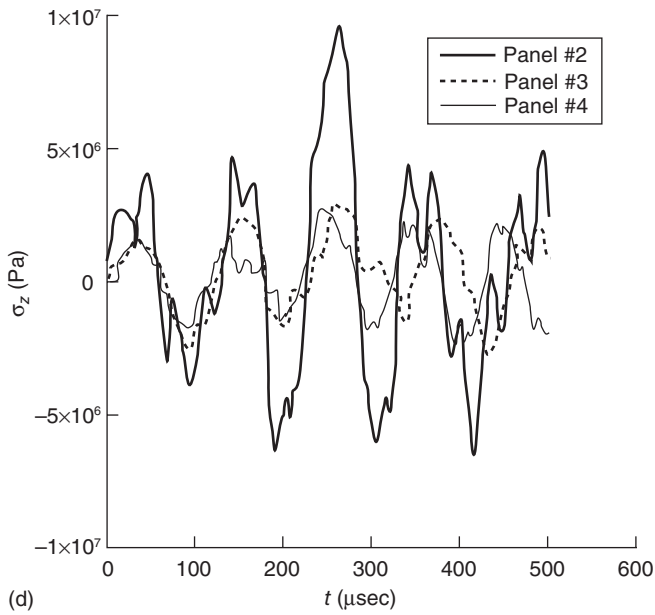

5.26 Continued

© Woodhead Publishing Limited, 2010

Figure 5.27 compares time variations of ε_x, σ_x, ε_z and σ_z at the center of the top surface of the lower composite layer in Panels #2, #3 and #4. These results are important because they indicate how much effect the incident blast pressure has on the backing layer, which is the last protecting material and, as such, has to survive without substantial damage. As is seen in Figs 5.27a and 27b, the highest tensile values of the in-plane strain and stress in Panel #2 start developing near the end of the analyzed time interval, i.e., after 450 μsec. Possibly, this manifests the start of catastrophic failure of the sandwich panel. The compressive in-plane strain and stress peaks developed earlier were limited to 0.14% for ε_x and 44 MPa for σ_x; these are about an order of magnitude lower than their respective ultimate values. So, this backing layer would undoubtedly survive the blast event. It is also seen in these figures that the effect of strain and stress attenuation is significantly stronger for Panel #3 than for Panel #4. This is in line with the results seen in Fig. 5.26, but in contrast to those shown in Fig. 5.25.

Further, results for ε_z in Fig. 5.27c indicate that intensive growth of compressive strain in Panel #2 starts just before 500 μsec. Nothing like that is seen for Panels #3 and #4. The tensile peak values are significantly higher in Panel #4, while compressive peaks have about the same magnitude in Panels #3 and #4. Results for σ_z in Fig. 5.27d show the highest tensile and compressive peaks for Panel #2. Several times lower peaks are seen for Panels #3 and #4. The σ_z peaks in the latter two panels are very close in magnitude.

It is interesting to further compare $\sigma_x(t)$ variations in Fig. 5.27d with respective incident pressure $P(t)$ variation at the center of the top surface shown in Fig. 5.10d; the latter one is applicable to all four panels. The incident pressure grows very fast and reaches its maximum value of 10 MPa at about 5 μsec. At 50 μsec it has already dropped to a very small value. The σ_z variations in Fig. 5.26d reach a first significant peak (interestingly, it is tensile for all three panels) at about 30 μsec. The following peaks have much higher magnitudes. In Panel #2 the highest compressive peak is reached at 310 μsec, while the highest tensile peak is reached at 470 μsec. The time when the latter peak has been reached is almost 100 times longer than the time when the incident pressure reached its peak. This emphasizes again the high complexity of this type of computational problems: in order to predict the transient structural response in a sufficiently long time interval, numerical integration has to be performed with equally high accuracy for the time period which may be tens and hundreds times longer than the time when incident pressure pulse reaches its maximum.

Further, when comparing Figs 5.10d and 5.27d, it becomes clear what capacity to attenuate blast pressure each of the Panels #2, #3 and #4 provides. While the incident pressure maximum is 10 MPa, the maximum peak values of σ_z reached in Panel #2 are about 8 MPa (in compression) and

© Woodhead Publishing Limited, 2010

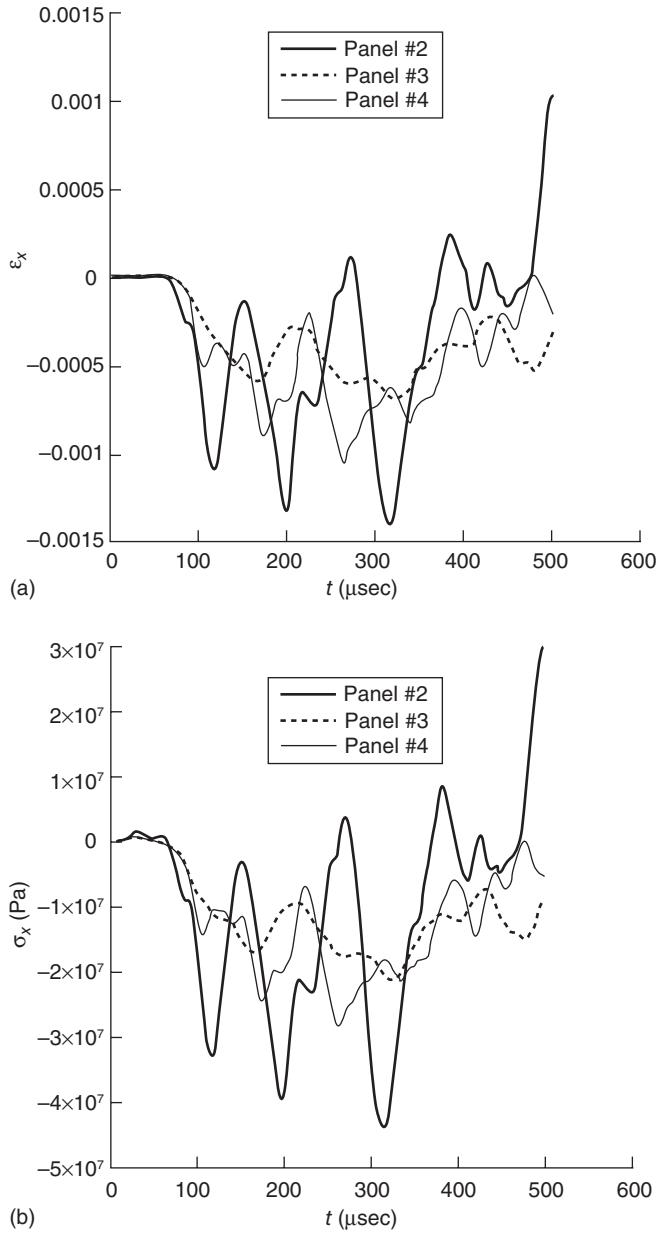

5.27 Time variations of ε_x (a), σ_x (b), ε_z (c) and σ_z (d) computed at the center of top surface of the lower composite layer in Panels #2, #3 and #4. Mesh 15 used for Panel #2, Mesh 20 for Panel #3 and Mesh 23 for Panel #4.

© Woodhead Publishing Limited, 2010

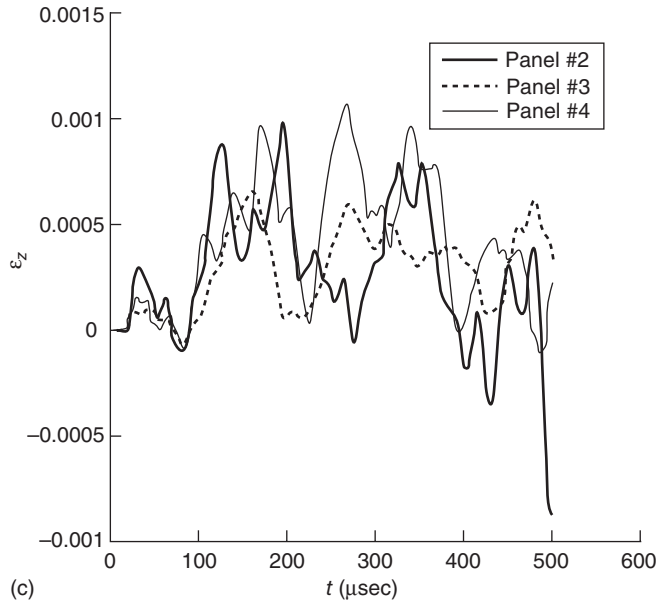

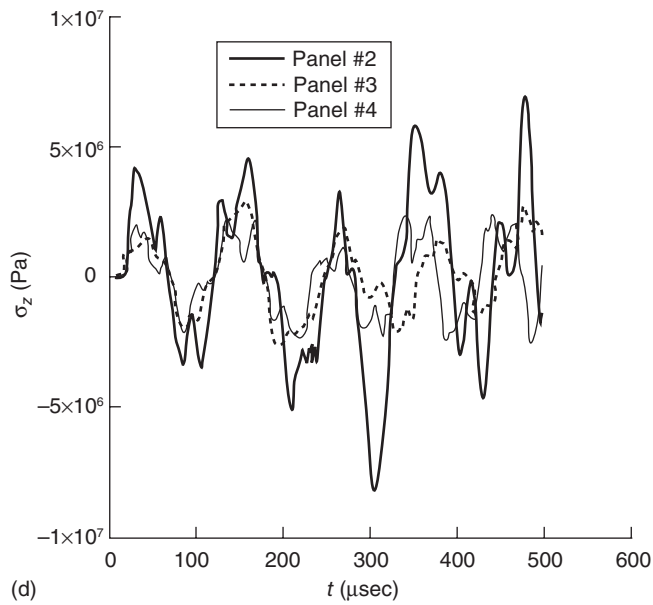

5.27 Continued

© Woodhead Publishing Limited, 2010

7 MPa (in tension). Both Panel #3 and Panel #4 show significantly lower magnitudes of the highest compressive and tensile σ_z peaks; both are in the range 2.5–3 MPa. As a reminder – all of these results have been obtained from a linearly elastic analysis, which does not account for internal damping, viscoelastic or plastic behavior of any material. The effect of damping will be studied in Section 5.8.

Figure 5.28 compares time variations of ε_x, σ_x and ε_z at the center of the bottom surface of the ceramic layer in Panel #3 and of the steel layer in Panel #4. It is seen in Figs 5.28a and 5.28b that the peak values of ε_x and σ_x show several times lower in the case of the steel top layer. The maximum tensile strain ε_x in ceramic is about 0.02%, while in steel it is twice as large. The maximum tensile σ_x in ceramic is about four times higher. It is also worth noting that the steel layer stays mainly under in-plane tension at this location, while the ceramic layer stays under in-plane compression. Figure 5.28c shows kind of inverse effect – ceramic is mainly under tension, while steel is most of the time under compression. The peak values of ε_z are still significantly higher in ceramic than in steel. Obviously, it is hard to explain these effects only by the difference in the properties and thicknesses of the steel and ceramic layers. Other materials, which are behind them, also make an important contribution to the overall transient deformation pattern.

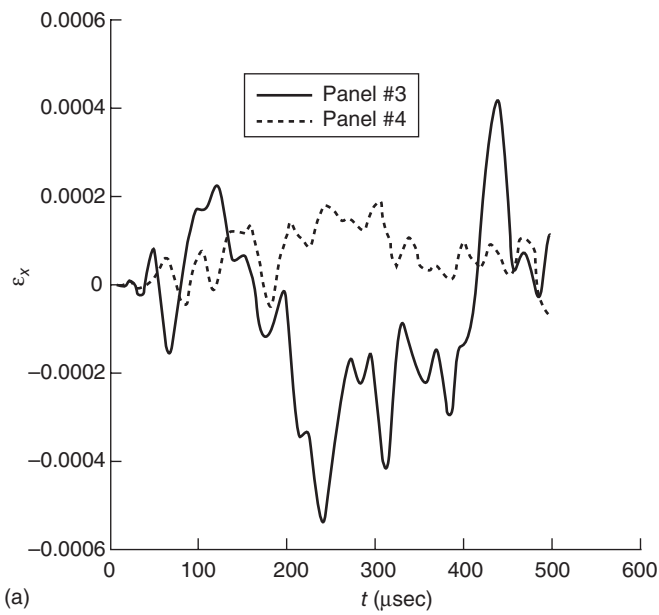

5.28 Time variations of ε_x (a), σ_x (b) and ε_z (c) computed at the center of bottom surface of ceramic layer in Panel #3 and steel layer in Panel #4. Mesh 20 used for Panel #3 and Mesh 23 for Panel #4.

© Woodhead Publishing Limited, 2010

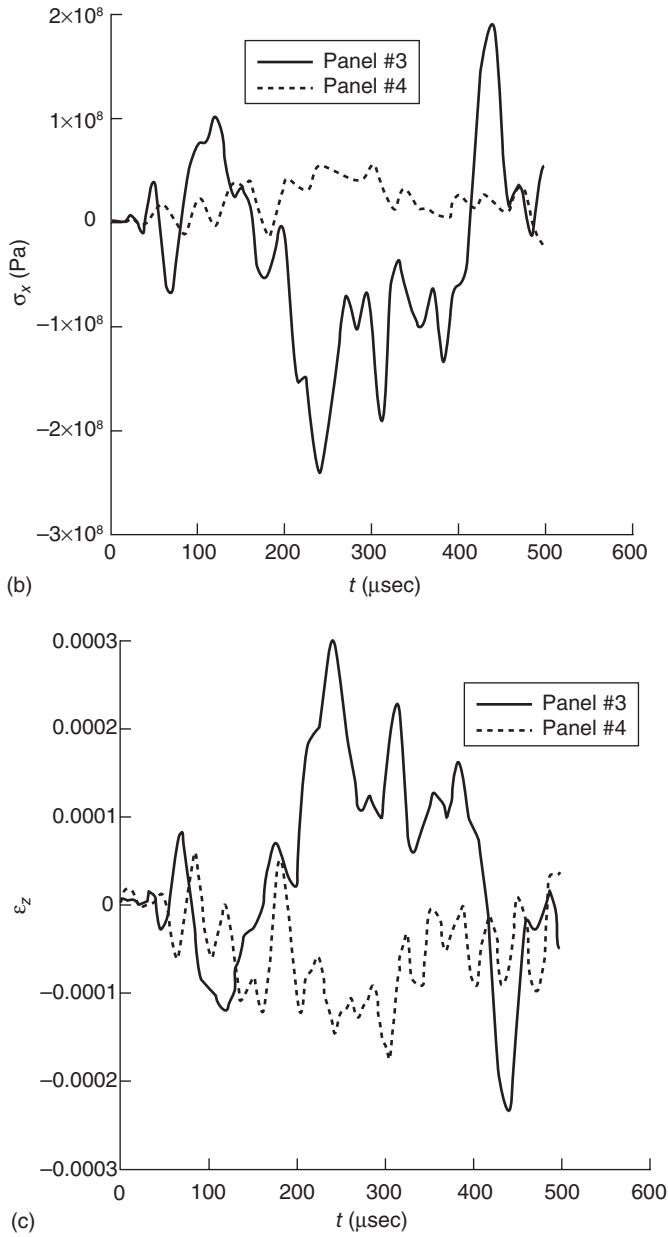

5.28 Continued

© Woodhead Publishing Limited, 2010

5.7 Comparison of the blast response characteristics for a longer time interval

Based on a reasonably close agreement between the numerical results obtained for Panel #1 with Meshes 1 and 6 (see Fig. 5.13), a series of computations has been performed for Panels #2, #3 and #4 for time interval [0, 3000 μsec] with the use of Mesh 13a for Panel #2, Mesh 16a for Panel #3 and Mesh 20a for Panel #4. Figure 5.29 presents comparative results for the time variations of u_z, ε_x, σ_x and ε_z at the center of the top surface of these three panels. Of course, in this time scale many fine details discussed above are not visible, but instead we get a more 'global' picture of the transient response, where bending deformations start playing significant role. This role is particularly manifested in a regular alteration of the positive and negative highest peaks of the displacement, strains and stresses, which happens with specific, relatively low frequency. Also, it is seen that for each material the highest peaks retain nearly constant magnitude when the time progresses.

Figure 5.29a reveals that the u_z peaks for Panels #3 and #4 are very close in both the tensile and compressive phases of transient deformation. The peaks computed for Panel #2 are about twice as high. A much greater

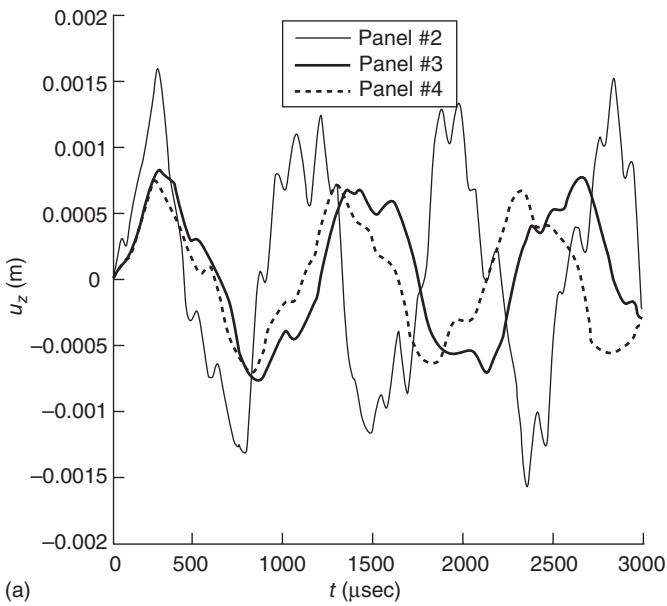

5.29 Time variations of u_z (a), ε_x (b), σ_x (c) and ε_z (d) computed at the center of top surface of Panels #2, #3 and #4 for [0, 3000 μsec] time interval. Mesh 14 used for Panel #2, Mesh 17 for Panel #3 and Mesh 21 for Panel #4.

© Woodhead Publishing Limited, 2010

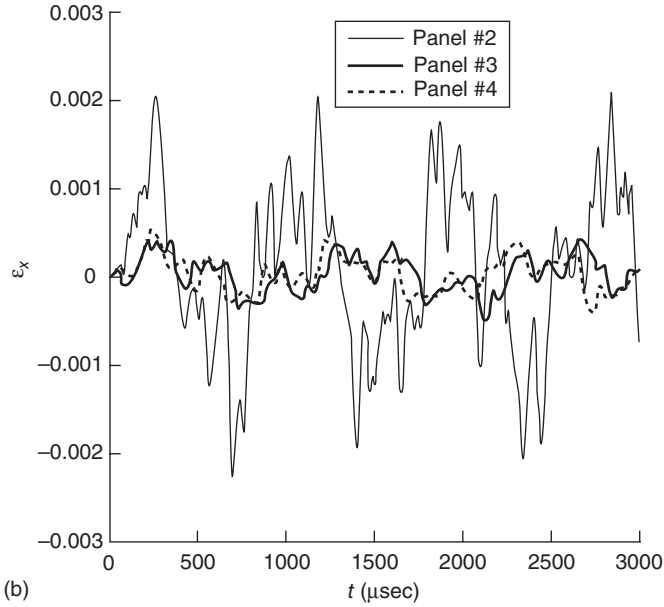

(b)

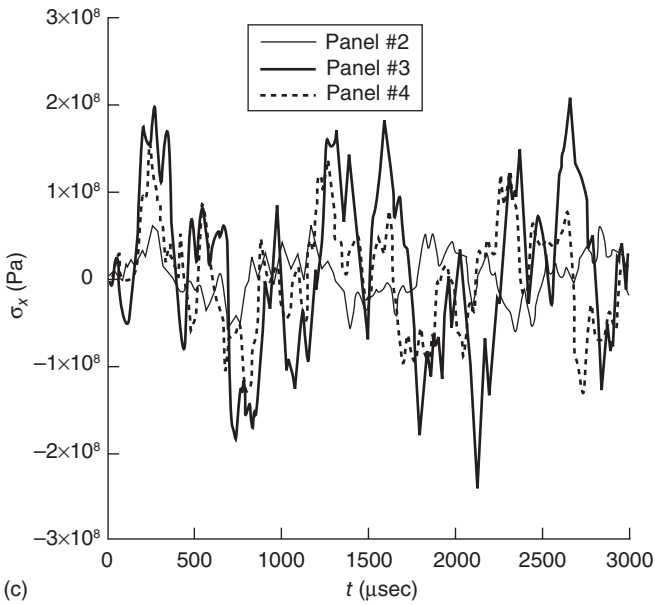

(c)

5.29 Continued

© Woodhead Publishing Limited, 2010

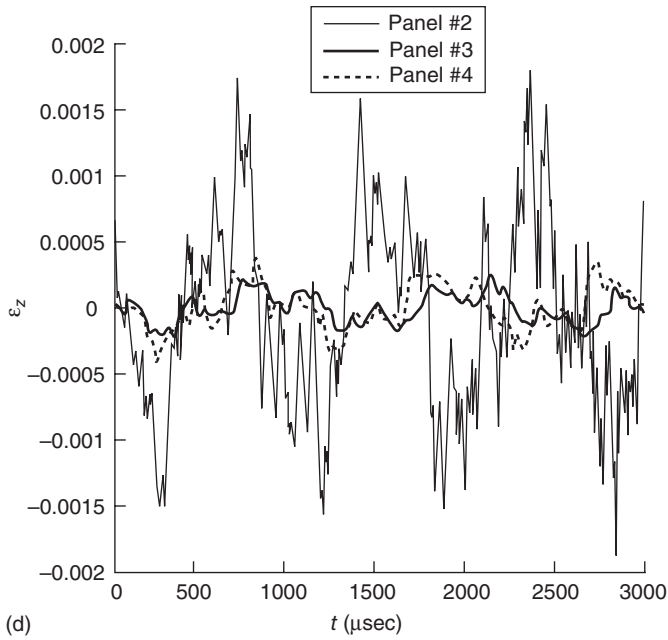

5.29 Continued

difference between strains ε_x and ε_z for Panels #3 and #4 on one side and Panel #2 on the other is observed in Figs 5.29b and 5.29d. At the same time, the differences between these strain components in Panel #3 and Panel #4 are relatively small. Figure 5.29c shows the expected effect – the in-plane stress is the highest in Panel #3 followed by significantly lower stress in Panel #4 and much lower stress in Panel #2. Obviously, the differences in elastic modulus of the top layer materials of these three panels prevail over the differences in the strains shown in Figs 5.29b and 5.29d.

Comprehensive numerical results presented above show clearly that the transient 3D stress/strain variations in complex hybrid laminated systems incorporating such dissimilar materials as ceramic, steel, polymeric composite, aluminum foam and Balsa wood may even be qualitatively counter-intuitive. The analysis itself is very complex, and the results are sometimes difficult to interpret. Obviously, each layer in the system makes its individual contribution (more or less pronounced depending on the mechanical properties of the material and the layer thickness) to the overall deformation in different stages of the transient deformation, and through that it influences the transient stress/strain states in all other layers.

To conclude this section we summarize in Tables 5.2 and 5.3 some of the numerical results, which are useful from the viewpoint of defeating high-intensity blast waves. Table 5.2 compares the maximal peak values of

© Woodhead Publishing Limited, 2010

Table 5.2 Summary of maximum transient magnitudes computed for displacement u_z(t), strains ε_x(t), ε_z(t) and stress σ_x(t) at the center of top (loaded) surface of Panels #1–#4 for time interval [0, 3000 μsec]

Panel #	Areal density		Max u_z (mm)	Max ε_x^+ (%)	Max ε_x^- (%)	Max ε_z^+ (%)	Max ε_z^- (%)	Max σ_x^+ (MPa)	Max σ_x^- (MPa)
	kg/m2	lb/ft2							
1	10.08	2.07	36	1.25	0.35	0.28	0.92	375	110
2	65.88	13.51	1.6	0.21	0.23	0.17	0.19	62	67
3	84.84	17.39	0.83	0.045	0.052	0.027	0.023	205	240
4	81.93	16.80	0.74	0.052	0.044	0.038	0.042	155	135

Note: Superscript '+' corresponds to positive (tensile) and superscript '–' corresponds to negative (compressive) strain and stress values.

Table 5.3 Summary of maximum displacement u_z(t) and strains ε_x(t), ε_z(t) values at the center of top (loaded) surface of Panels #1–#4 multiplied by respective ρ_A values

Panel #	Max $u_z \cdot \rho_A$	Max $\varepsilon_x^+ \cdot \rho_A$	Max $\varepsilon_x^- \cdot \rho_A$	Max $\varepsilon_z^+ \cdot \rho_A$	Max $\varepsilon_z^- \cdot \rho_A$
1	0.363	12.6	3.53	2.82	9.27
2	0.104	13.8	15.2	11.2	12.5
3	0.0704	3.82	4.41	2.29	1.95
4	0.0606	4.26	3.60	3.11	3.44

u_z, ε_x, ε_z and σ_x computed at the center of the top surface of all four panels for a time interval of 3000 μsec. It is seen that the maximum of u_z and the negative maximum of ε_x are the lowest in Panel #4; slightly higher maxima are reached in Panel #3. The positive maximum of ε_x, as well as both positive and negative maxima of ε_z are the lowest in Panel #3. Stress σ_x has significantly higher positive and negative maxima in Panel #3.

Considering that the four panels analyzed here have different areal density, ρ_A, some reasonable normalization of the computed transient response characteristics would help when making a decision about their comparative blast mitigation efficiency. One possible form of such normalization is used in Table 5.3, where the displacement and strain maxima are multiplied by the respective areal density of each panel. The smaller the computed displacement or strain characteristic is after such normalization, the better will be the resistance of the panel to blast if respective displacement or strain is chosen as the resistance criterion. Overall, even after normalization, Panels #3 and #4 are still more efficient than Panels #1 and #2. However, quite surprisingly, the lowest compressive ε_x

© Woodhead Publishing Limited, 2010

and the second lowest tensile ε_z belong to the 3D woven solid composite Panel #1, and this effect is achieved in spite of the much smaller thickness of Panel #1. It is also worth noting that solid composite Panel #1 shows about four times smaller normalized compressive ε_x and tensile ε_z than sandwich Panel #2, while the latter one shows 3.5 times lower normalized u_z. This result illustrates that the objective of reducing transient deflection and all strains to as low a level as possible would not have a unique solution, but rather require different combinations of materials in the layered protective panel depending on which particular characteristic has to be minimized.

5.8 Effect of internal material damping

The internal material damping effect can be accounted for in the analysis by using different approaches. One of them, direct and simple, is to formally generalize the system of dynamic equilibrium equations (5.15) by adding 'internal friction forces', which are directly proportional to the velocity vector $\dot{\mathbf{U}}(t)$:

$$\mathbf{M}\ddot{\mathbf{U}}(t) + \mathbf{C}\dot{\mathbf{U}}(t) + \mathbf{K}\mathbf{U}(t) = \mathbf{R}(t) \qquad [5.27]$$

Here, **C** is the time-independent 'damping matrix'. The second possible approach is to add an 'energy dissipation' term $D^{(q)}(t)$ to the Lagrange function (Eq. 5.4). This additional term can be ultimately expressed in the form similar to the other energy terms (Eqs 5.10–5.12), but of course with different expressions for the matrix components. The resulting system of dynamic equilibrium equations is obtained in the same form as Eq. 5.27, but with different matrix **C**. The third possible approach is to generalize the stress-strain relations (Eq. 5.1) by adding certain integral terms responsible for a viscoelastic behavior of the material. In this case, one has to undertake a long and difficult path of derivations in order to arrive at the resulting system of dynamic equilibrium equations, which appears to be a system of integral–differential equations instead of a system of differential equation (Eq. 5.27). The first and second approaches have been realized in 3D MOSAIC code.

In each of the aforementioned three cases, another serious problem emerges – how to relate the 'damping coefficients' (aka 'damping ratios') to the physically measurable material constants that characterize internal friction, energy dissipation or viscoelastic behavior, respectively. Delving into this problem would take us far beyond the topic of this paper; the readership is directed to fundamental books on structural dynamics, finite element analysis and viscoelasticity; see, for example books by Clough and Penzien (1975), Bathe (1996) and Christensen (2003), where these issues have been addressed in great detail.

© Woodhead Publishing Limited, 2010

Here, for purely illustrative purpose, we follow the first of the aforementioned approaches and assume that all damping coefficients in matrix **C** of the system of equations (5.27) have identical values; two particular values, 0.1 or 0.5, were chosen for numerical examples. These arbitrary numerical values were adopted without identifying their physical meaning. The analysis results are compared in Figs 5.30 and 5.31 for damping coefficients all equal to 0 (elastic solution), 0.1 and 0.5. Figure 5.30 shows results for initial time interval t = 50 μsec, while Fig. 5.31 shows results for a longer time interval, t = 500 μsec.

Time variations of u_z in Fig. 5.30a show no effect of damping on transverse displacement, while Figs 5.30b–5.30e show significant effect of damping on the strains and stresses. Particularly, the magnitude of ε_x gets lower and lower with increasing damping coefficient. The effect of damping on ε_z, σ_x and σ_z is totally different – the ultra high-frequency fluctuations are suppressed by damping, and the curves in Figs 5.30c–5.30e become smooth. However, damping does not affect the average time variations of these characteristics.

The results presented for time variations of the same characteristics during a longer period, shown in Fig. 5.31, also demonstrate no effect of

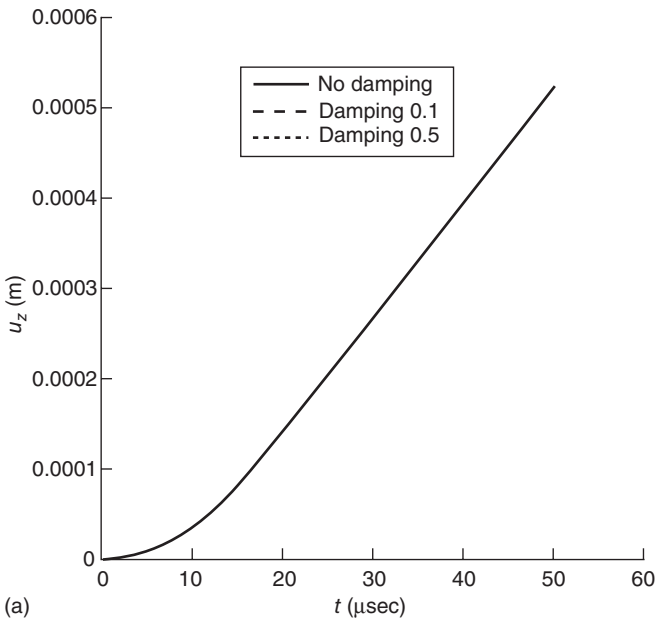

5.30 Time variations of u_z (a), ε_x (b), σ_x (c), ε_z (d) and σ_z (e) till t = 50 μsec computed at the center of the upper interface of Panel #1 with different values of the damping factor (Mesh 6 used).

© Woodhead Publishing Limited, 2010

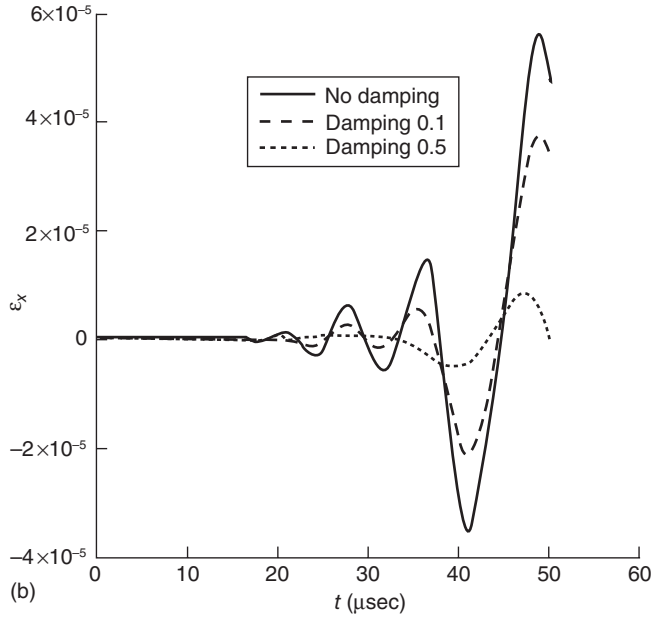

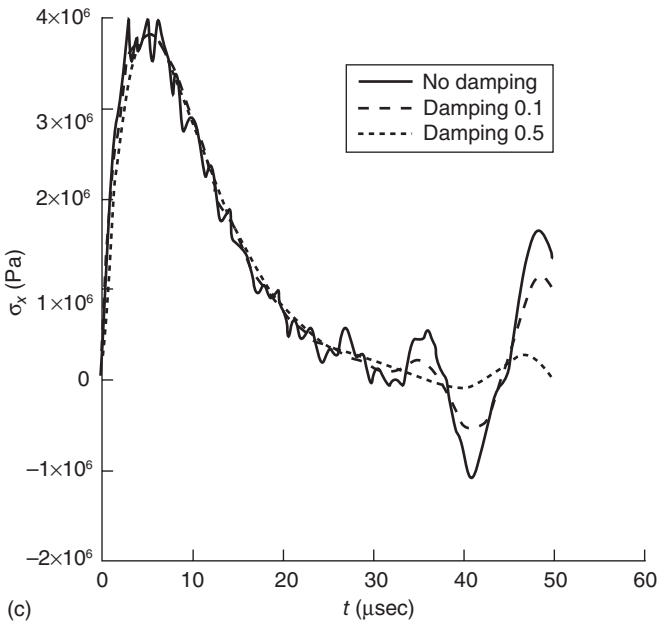

5.30 Continued

© Woodhead Publishing Limited, 2010

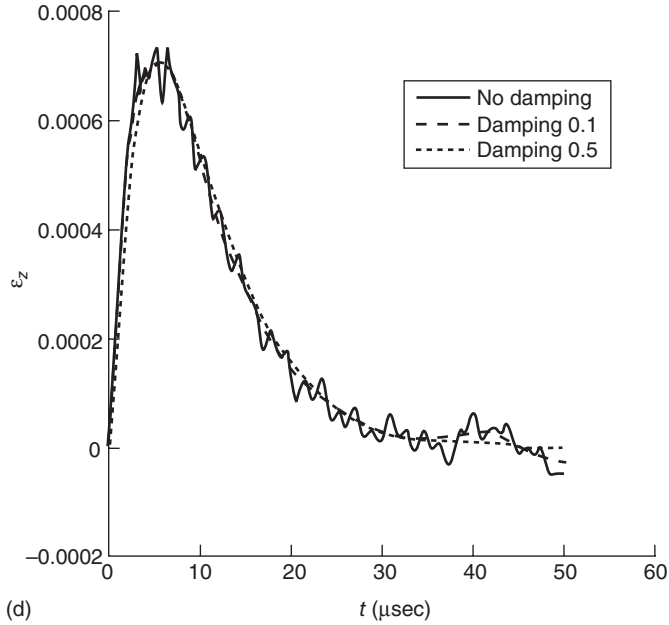

(d)

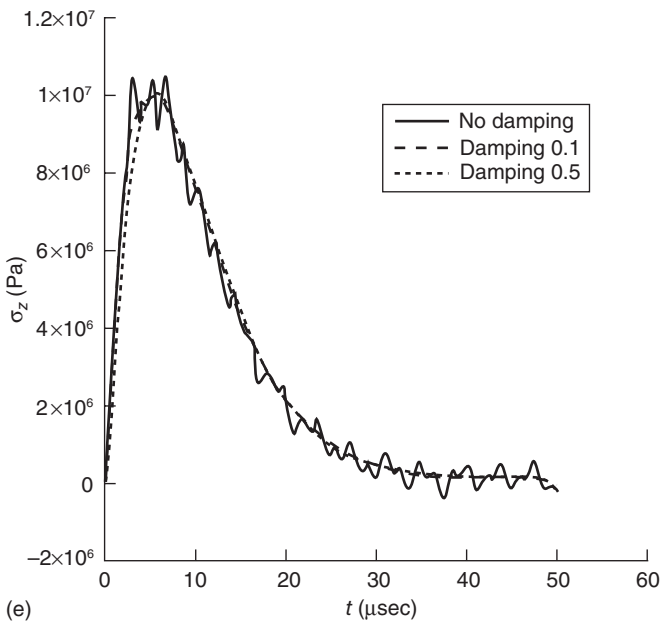

(e)

5.30 Continued

© Woodhead Publishing Limited, 2010

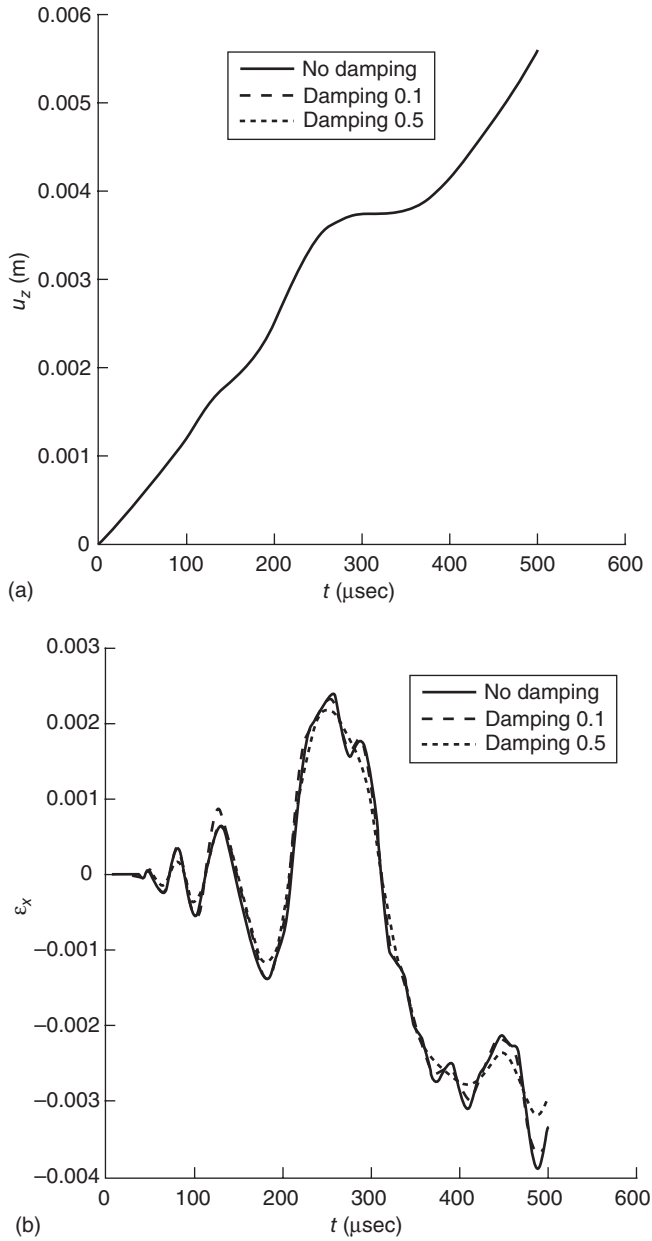

5.31 Time variations of u_z (a), ε_x (b), σ_x (c) and ε_z (d) till t = 500 μsec computed at the center of the upper interface of Panel #1 with different values of the damping factor (Mesh 6 used).

© Woodhead Publishing Limited, 2010

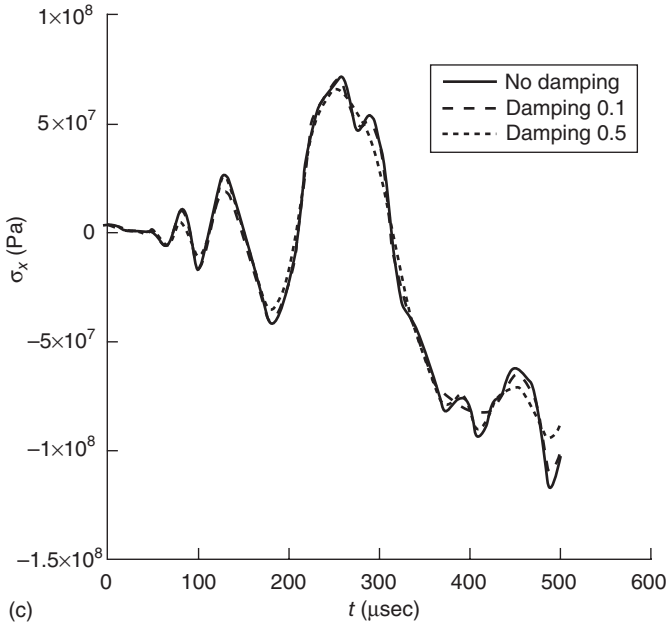

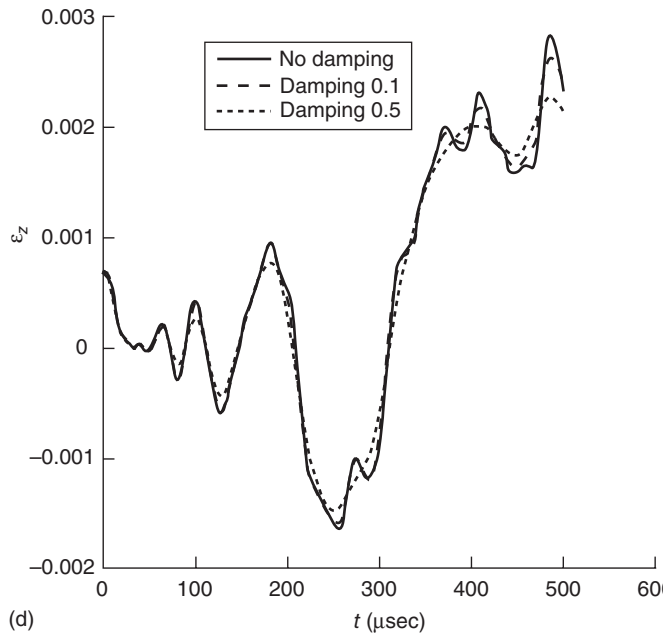

5.31 Continued

© Woodhead Publishing Limited, 2010

damping on u_z and some minor effect on ε_x, σ_x and ε_z. That minor effect is manifested mainly in suppressing ultra high-frequency fluctuations. To get a more insightful explanation of these effects, we would need first to identify what the values of damping coefficients 0.1 and 0.5 actually mean, and how they relate to the actual internal damping properties of the materials included in this analysis. We will not go into this problem in detail here.

5.9 Comparisons of theoretical and experimental results

5.9.1 Laboratory studies of shock wave loading

In the last few years, a collaborative research between 3TEX, Inc. and Dynamic Photomechanics Laboratory of the University of Rhode Island, has resulted in a large volume of ballistic and blast test data obtained for 3D woven composite, layered and sandwich panels. Those were 3D woven composite panels stand-alone, or combined with ceramic tiles on the strike face and various cores between the skins. Results of that research have been comprehensively described in several publications by Bogdanovich *et al.* (2005), Grogan *et al.* (2007), LeBlanc *et al.* (2007), Shukla *et al.* (2007) and Tekalur *et al.* (2009). The experimental data produced were extensively used for the validation of 3D Mosaic analysis approach and computer code.

In the shock tube experiments that involved the all-S-2 glass composite materials, reported by LeBlanc *et al.* (2007), the tested square panels were of in-plane size 0.3 m × 0.3 m with an approximate specimen thickness of 6.35 mm. The specimens having dimensions 0.22 m × 0.22 m of unsupported test section were held under fully clamped boundary conditions. The blast was applied over a circular area 76 mm in diameter.

Experimental results presented in a recent article by Tekalur *et al.* (2009) were obtained for several unstitched and stitched sandwich panels, made by Martin Marietta Composites using their TRANSONITE® technology and tested at the University of Rhode Island shock tube facility. In that case, 3WEAVE® E-glass fiber preforms were used as reinforcements for the skins, and the TRYMER™ 200 L polyisocyanurate foam, manufactured by Dow Chemical, was used as the base core material. TRANSONITE® technology includes two steps: (i) integral through-thickness stitching of the skin fabric preforms and the foam core and (ii) pultrusion of the obtained fabric-core sandwich structure. Detailed information on these materials can be found in Tekalur *et al.* (2009). In the experiments involving such sandwich materials, as reported by Shukla *et al.* (2007) and Tekalur *et al.* (2009), the rectangular specimens were tested under simply supported boundary conditions applied along two opposite sides of the specimen. The specimen

© Woodhead Publishing Limited, 2010

size was 0.30 m × 0.102 m. The span between supports was 0.152 m. As in the previous case, the blast load covered a 76 mm diameter circular central region of the specimen. Further experimental details can be found in the papers mentioned on the previous page.

The two aforementioned experimental shock tube test set-ups have been simulated by 3TEX using 3D Mosaic analysis approach and computer code. Some key results of the performed comparisons are described next section.

5.9.2 Example 1: Two-ply 3D woven S-2 glass composite plate

In this first example we compare some of the analysis results to experimental data for a solid 3D woven S-2 glass composite plate. Figure 5.32 shows smooth approximation of the experimental blast pressure history, which was used as the boundary condition, at the center of the plate, and computed time variation of the stress component σ_z $(t, x = a, y = b, z = c)$. As discussed earlier in the chapter, the latter function would be exactly the same as the input pressure history, if we had obtained an exact solution. However, as noted in Section 5.5.1, numerical solutions obtained with the 3D Mosaic analysis approach (as with any other approximate numerical analysis) inevitably deviate from the exact result. This is why we see certain discrepancies between the input pressure history and the computed function σ_z (t) in Fig. 5.32. The differences are mainly manifested in small

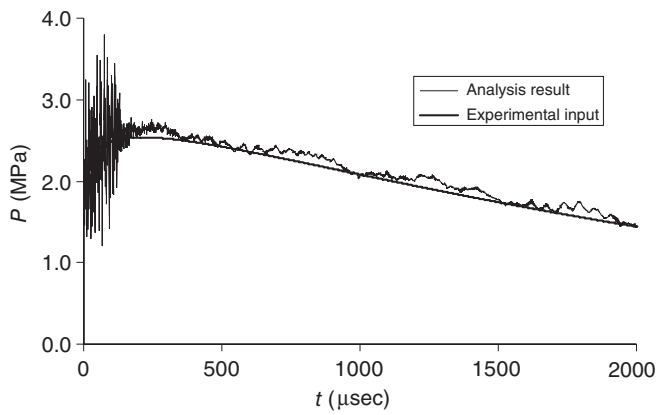

5.32 Smooth approximation of the experimental blast pressure history, used as input in the analysis, and computed time variation of stress, σ_z, at the center of the blast loaded surface.

© Woodhead Publishing Limited, 2010

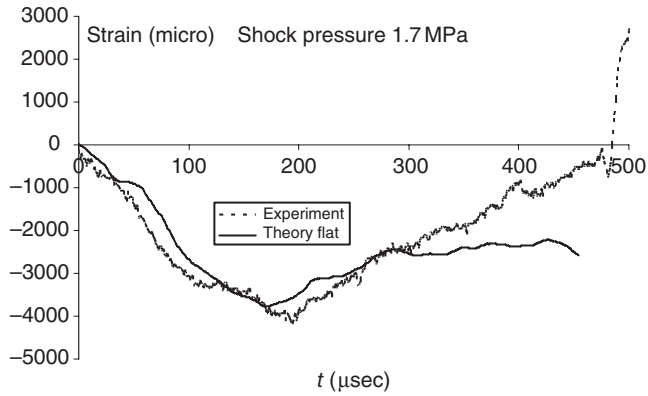

5.33 Experimental strain recorded by strain gage and strain history predicted by analysis.

irregular 'fluctuations' seen on the σ_z (t) curve. However, the overall closeness of the two curves is obvious, and this is an important indication that other transient displacements, strains and stresses should be in a very good agreement with experimental results.

One specific comparison between theoretically predicted and experimentally recorded strain is shown in Fig. 5.33. Keeping in mind the difficulties of reliably and accurately measuring transient strains under shock wave on one side, and the very high complexity of the 3D transient analysis performed here on the other, the agreement between theoretical and experimental results seen in this figure is very impressive. The characteristic negative strain in the first phase of deformation (prior to 500 μsec) is almost identical for both the experimental and theoretical curves. The second, positive strain phase (between 500 and 2000 μsec) seen in the experimental curve is also present in the theoretical curve, and the experimental peak values are very close to the theoretical ones. Some differences seen in Fig. 5.33 between the two curves can be attributed to two main reasons. One of these is that the actual clamping of the plate was not precisely simulated by the boundary conditions assumed in the analysis. The other lies in a possible difference between the 'reflected' pressure history and the actual incident pressure applied to the test specimen surface. The reflected pressure pulse, corresponding to a specific explosive amount, was measured in the 'calibration' experiments and then used as the input pressure pulse in the analysis. Further discussion of these effects can be found in LeBlanc *et al.* (2007) and Tekalur *et al.* (2009). In any case, our first comparison of the theoretical and experimental results obtained appeared to be very encouraging.

© Woodhead Publishing Limited, 2010

5.9.3 Example 2: Sandwich panel with 3D woven composite skins and stitched foam core

Experimental methodology of material testing in a shock wave tube was also applied to three types of TRANSONITE® sandwich samples: Sandwich 1 having unstitched foam core, Sandwich 2 with 'intermediately stitched' (four stitches per square inch) foam core, and Sandwich 3 with 'densely stitched' (eight stitches per square inch) foam core (see Tekalur *et al.*, 2009). Having three sandwiches with different stitch density allowed us to study its effect on the transient response under shock wave loading.

The shock wave loading of Sandwich 1, Sandwich 2 and Sandwich 3 test specimens was simulated using the 3D MOSAIC analysis approach. The experimental specimens were placed on rigid supports which were oriented in the y-direction. The specimen length outside each support was a_1 = 0.076 m. The support width was taken to be a_2 = 0.4 m. Although this parameter was not exactly determined and may slightly influence the analysis results, it is believed that the above value is small enough for making no significant effect of the support width on the structural response. The distance from each support to the center of the specimen is a_3 = 0.076 m. Another geometric parameter is associated with the loading area, which is assumed to be a square with side length $2a_0$ = 0.06751 m; this length was evaluated based on the requirement that the square area must be equal to the circular area having diameter d = 0.0762 m (which was the actual loading area in the shock tube experiments). Due to the symmetry of the boundary value problem under consideration, the analysis was reduced to one-quarter of the panel size, with respective symmetry conditions added. Further details of the boundary value problem formulation and computational aspects can be found in Tekalur *et al.* (2009).

A comparison between theoretical results provided by 3D MOSAIC dynamic analysis code and experimental data obtained in the shock tube tests is illustrated here for the case of Sandwich 3. The experimental data points for transverse displacement (aka deflection) $u_z(t)$ were determined from the sequence of high-speed camera frames, where the images of progressively deformed panel profile were used for the deflection measurements at the front and back surfaces of the sandwich (see details of the measurements in Tekalur *et al.*, 2009). It was assumed that the maximum of $u_z(t)$ seen in the images obtained corresponds to the center point of each surface. These experimental data points are compared in Fig. 5.34 with the theoretical predictions provided for $u_z(t)$ by 3D MOSAIC code. The deflection vs time variations were computed at the center of the panel, on the front (exposed to shock pressure) and on the back (load-free) surfaces. Excellent agreement between theoretical and experimental results for both front and back surfaces of this sandwich panel is observed. So, the second

© Woodhead Publishing Limited, 2010

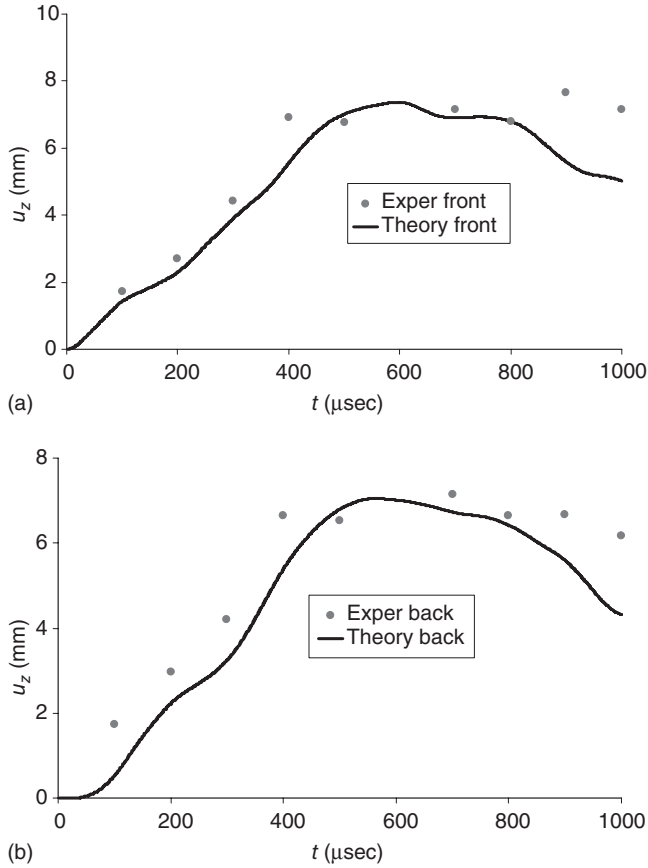

5.34 Theoretical (solid line) and experimental (dots) deflection vs time variations for the front (a) and back (b) faces of the stitched sandwich panel exposed to shock pressure loading.

comparison between the theoretical and experimental results obtained for the transient deflection of rather complex composite sandwich panel is also very encouraging. Other comparative studies of this kind are in progress and will be reported elsewhere.

5.10 Summary and conclusions

This chapter addressed several fundamentally important theoretical and experimental aspects of general structural response to blast loading and blast mitigation problems. The background discussions presented in the first part of the chapter addressed the determination of blast pressure pulse

© Woodhead Publishing Limited, 2010

for the analysis input, current state-of-the art armor and blast mitigation materials, selection of adequate analysis approaches and computational tools, material models, boundary and joining conditions. The principal aspects of 3D Mosaic analysis methodology have been described in sufficient detail.

The main focus of this chapter was on the implementation of the 3D Mosaic dynamic analysis approach and computer code for numerical simulations of a transient structural response to a high-intensity, short-time blast pressure pulse. Four square panels having different thicknesses and composed of very distinct materials were analyzed under identical blast pressure pulse. The first of these was polymeric composite reinforced with two layers of 3D orthogonal woven S-2 glass fabric. The second was a typical sandwich construction with 3D orthogonal woven S-2 glass composite skins and Balsa wood core. The third was a four-layer construction including layers of ceramic, 3D orthogonal woven S-2 glass composite and Balsa wood. The fourth was a five-layer construction that included layers of perforated steel, aluminum foam, Balsa wood and 3D orthogonal E-glass fiber composite.

A comprehensive convergence study has been conducted in order to ensure that numerical results obtained for all 3D displacement, strain and stress components are of sufficient accuracy. The convergence study was carried out using two alternative approaches: refinement of the discretization mesh and increasing degree of the Bernstein basis functions. The convergence study was performed separately for three important time intervals: initial (50 μsec), intermediate (500 μsec) and relatively long (3000 μsec). For each of these time intervals, the discretization meshes and the basis function degrees that provide sufficient accuracy of the computed deflection, strains and stresses were determined. Importantly, those discretization mesh and basis function degree parameters were found to be different for each of the three time intervals. It is also worth noting that during the initial time interval, an accurate prediction of the in-plane strains and stresses appeared to be a more difficult task than an equally accurate prediction of transverse strains and stresses.

After the convergence of numerical results was assessed, a comprehensive analysis of the central deflection, in-plane and out-of-plane strains and stresses was performed for the four aforementioned panel constructions. Again, this was performed separately for the three characteristic time intervals. The typical time variation curves were presented, and the maximum value of each studied displacement, strain and stress component was determined. Special attention was paid to the strain and stress variations (and, where applicable, to their continuity) 'from the top' and 'from the bottom' of each interface in the three layered panels. It was shown that the required (though not imposed as the explicit boundary conditions) continuity of

© Woodhead Publishing Limited, 2010

respective strain and stress components at the interfaces was satisfied with very high accuracy.

Having numerical results for all four panels during a relatively long (3000 μsec) time interval made it possible to determine maximum peak values of the transient deflection, strains and stresses caused by the applied blast pressure pulse. The obtained results also allowed us to mutually compare the peak values of the displacements, strains and stresses in the four studied panels and, consequently, determine their relative blast mitigation efficiency. It is interesting to note that, depending on the performance criterion (taken alternatively for deflection, some strain or stress component) the blast mitigation efficiency ranking changes from panel to panel. Even a solid 3D orthogonal woven composite may be the best in defeating certain strain or stress components.

The effect of internal material damping (energy dissipation) has been illustrated by comparing numerical results for the solid composite panel at three damping factor values (0, 0.1 and 0.5). The effect of damping is most visible in the early stage of transient deformation, when the ultra high-frequency small amplitude fluctuations are seen on the time variations of strains and stresses computed without damping, while they completely disappear when the damping with either coefficient 0.1 or 0.5 is taken into account. With growing time, the damping effect becomes less and less pronounced.

Finally, some comparisons between experimental data obtained at the University of Rhode Island shock tube test facility on the one hand, and numerical simulations results obtained with 3D MOSAIC computer code on the other, were described in the chapter. One example of such a comparison considered a clamped square 3D orthogonal woven S-2 glass composite plate loaded in its central part by a shock wave pressure. The transient in-plane strain, measured by a dynamic strain gage bonded on the back surface of the plate, showed very good agreement with computed strain time variation until the moment when the strain gage had separated from the plate. The second comparison example was presented for a simply-supported sandwich panel, in which 3D orthogonal woven E-glass skin preforms were integrally stitched with the foam core before being pultruded. The transient central deflections at the front (pressure pulse exposed) and back (load-free) surfaces of the panel, obtained from the high-speed camera monitoring, were found to be in a very close agreement with the respective central deflection values predicted by 3D MOSAIC computer code.

Overall, the 3D dynamic analysis tool 3D MOSAIC, introduced and implemented in this chapter, showed excellent capability to provide converged and accurate results for all 3D transient displacement, strain and stress components computed for the four thick and very distinct layered

© Woodhead Publishing Limited, 2010

armor panels. Although this computational tool has its limitations (in the first place, it currently does not solve structural components having complex geometries), it has its proven advantages. Where the code is applicable, it provides very accurate results for all 3D stress/strain components with high computational efficiency. The use of Bernstein basis functions of an arbitrary degree is at the core of its high computational efficiency and accuracy. The code can be especially useful for fast screening of candidate materials, fast screening of different designs of layered panels and determining the optimum combinations of constituent materials and layer sequences providing best blast mitigation solutions.

5.11 Acknowledgements

3D MOSAIC computer code used for generation of numerical results for this paper was developed by Intelligent Software Solutions, Inc. (Raleigh, NC, USA) under contracts from 3TEX, Inc. Special thanks to the code development leader Mr Alexander Birger.

The description of shock tube test facility and experimental data were kindly provided by Dr Arun Shukla and Dr Arjun S. Tekalur (University of Rhode Island, Kingston, RI, USA).

The author is grateful to Dr Dmitri Mungalov (3TEX) for assistance in illustrative material preparation.

5.12 References

AIR FORCE (1998), *Design and Analysis of Hardened Structures to Conventional Weapons Effects*, Technical Manual for Army, TM 5-855-1, incorporating the Air Force AFPAM 32-1147 (I), Navy NAVFAC P-1080, and Defense Special Weapons Agency DAHSCWEMAN-97 documents.

ASCE (1997), *Design of Blast Resistant Buildings in Petrochemical Facilities*, document prepared by the Task Committee on Blast Resistant Design of the Petrochemical Committee of the Energy Division, New York, ASCE.

BAKER W E, COX P A, WESTINE P S, KULESZ J J and STREHLOW R A (1983), *Explosion Hazards and Evaluation*, New York, Elsevier Scientific.

BATHE K-J (1996), *Finite Element Procedures*, Upper Saddle River, NJ, Prentice Hall.

BAUCOM J N and ZIKRY M A (2005), Low-velocity impact damage progression in woven E-glass composite systems, *Composites Part A: Applied Science and Manufacturing*, **36**(5), 658–664.

BAUCOM J N, ZIKRY M A and RAJENDRAN A M (2006), Low-velocity impact damage accumulation in woven S2-glass composite systems, *Composites Science and Technology*, **66**(10), 1229–1238.

BOGDANOVICH A E (1992), Three-dimensional analysis of anisotropic spatially reinforced structures, in Buckley JD (ed.), *Proceedings of the Sixth Conference on Advanced Engineering Fibers and Textile Structures for Composites, FIBER-TEX 1992*, Philadelphia, PA, NASA Conference Publication 3211, 1993, 271–304.

© Woodhead Publishing Limited, 2010

BOGDANOVICH A E (1993), Three-dimensional analysis of anisotropic spatially reinforced structures, *Composites Manufacturing*, **4**(4), 173–186.

BOGDANOVICH A E (2000), Three-dimensional variational theory of laminated composite plates and its implementation with Bernstein basis functions, *Computer Methods in Applied Mechanics and Engineering*, **185**(2–4), 279–304.

BOGDANOVICH A E (2001), Three-dimensional variational analysis of composite structures using Bernstein polynomial approximations, *Mechanics of Composite Materials*, **37**(5/6); Pt. 1, 525–538; Pt. 2, 539–552.

BOGDANOVICH A E (2003), Multiscale predictive analysis of 3-D woven composites, *CD Proceedings of 35th International SAMPE Technical Conference*, **35**, 28 September–2 October, Dayton, OH.

BOGDANOVICH A E (2006), Multi-scale modeling, stress and failure analyses of 3-D woven composites, *Journal of Materials Science*, **41**(20), 6547–6590.

BOGDANOVICH A E (2009), Progressive failure modeling and strength predictions of 3-D woven composites, *CD Proceedings of the 50th AIAA/ASME/ASCE/AHS/ASC Structures, Structural Dynamics, and Materials Conference*, 4–7 May, Palm Springs, CA, AIAA Paper 2009-2658.

BOGDANOVICH A E and MUNGALOV D D (2005), Three-dimensional blast response simulation of layered composite armor panels, in Reddy JN and Chandra N (eds), *CD Proceedings of the 3rd International Conference on Structural Stability and Dynamics (ICSSD)*, 19–22 June, Kissimmee, FL.

BOGDANOVICH A E and SINGLETARY J N (2000), Ballistic performance and applications of 3-D woven fabrics and composites, *CD Proceedings of the 9th European Conference on Composite Materials (ECCM9)*, 4–7 June, Brighton, UK.

BOGDANOVICH A E and YUSHANOV S P (1999A), 3D blast performance analysis of concrete walls with layered composite protection/retrofit, in Whitney JM (ed.), *Proceedings of the American Society for Composites, Fourteenth Technical Conference*, Lancaster, PA, Technomic, 151–160.

BOGDANOVICH A E and YUSHANOV S P (1999B), Progressive failure analysis of adhesive bonded joints with laminated composite adherends, *Journal of Reinforced Plastics and Composites*, **18**(18), 1689–1707.

BOGDANOVICH A E and YUSHANOV S P (2000A), Three-dimensional variational impact contact analysis of composite bars and plates, *Composites Part A: Applied Science and Manufacturing*, **31A**(8), 795–814.

BOGDANOVICH A E and YUSHANOV S P (2000B), Three-dimensional variational analysis of Pagano's problems for laminated composite plates, *Composites Science and Technology*, **60**(12–13), 2407–2425.

BOGDANOVICH A, COFFELT R, GROGAN J and SHUKLA A (2005), Integral 3-D woven S-2 glass fabric composites for ballistic armor systems, *Proceedings of 26th International SAMPE Europe Conference*, 5–7 April, Paris, France, 245–250.

BOGOSIAN D D, DUNN B W and CHROSTOWSKI J D (1999), Blast analysis of complex structures using physics-based fast-running models, *Computers and Structures*, **72**(1), 81–92.

BULSON P S (1997), *Explosive Loading of Engineering Structures*, London, UK, E & FN Spon.

CHRISTENSEN R M (2003), *Theory of Viscoelasticity*, 2nd edn, New York, Dover Publications.

CLOUGH R W and PENZIEN J (1975), *Dynamics of Structures*, New York, McGraw-Hill.

© Woodhead Publishing Limited, 2010

DAVIES J M (2001), *Lightweight Sandwich Construction*, Oxford, Wiley-Blackwell.

ESPER P (2003), Investigation of damage to buildings under blast loading and recommended protection measures, *Proceedings of 9th International Structural Engineering Conference*, 29 November–1 December, Abu Dhabi.

FERTAL M J, ROE E K and SCHUHMACHER C L (2001), Blast/FX™ explosive effects analysis software, *Technology Review Journal*, Spring/Summer, 57–69.

GAMA B A, HAQUE MD J, GILLESPIE J W (JR) and BOGDANOVICH A E (2004), Impact, damage, and energy absorption of a 3D orthogonal weave composite unit cell model, *Proceedings of 49th International SAMPE Symposium and Exhibition*, 16–20 May, Long Beach, CA.

GAMA B A, BOGDANOVICH A E, COFFELT R A, HAQUE MD J, RAHMAN M and GILLESPIE J W (JR) (2005), Ballistic impact damage modeling and experimental validation on a 3D orthogonal weave fabric composite, *Proceedings of SAMPE'05 Conference*, 1–5 May, Long Beach, CA.

GROGAN J, TEKALUR S A, SHUKLA A, BOGDANOVICH A and COFFELT R A (2007), Ballistic resistance of 2D and 3D woven sandwich composites, *Journal of Sandwich Structures and Materials*, **9**(3), 283–302.

HANSEN H-J, KRISTENSEN A, DAMKILDE L and THYGESEN U (2002), "Structural analysis of offshore structures exposed to blast loads," in Lund E, Olhoff N and Stegmann J (eds), *Proceedings of NSCM 15, 15th Nordic Seminar on Computational Mechanics*, 18–19 October Aalborg, Denmark, Aalborg University 237–240.

KINNEY G F and GRAHAM K J (1985), *Explosive Shocks in Air*, New York, Springer-Verlag.

LEBLANC J, SHUKLA A, ROUSSEAU C and BOGDANOVICH A (2007), Shock loading of three-dimensional woven composite materials, *Composite Structures*, **79**(3), 344–355.

LIBRESCU L, OH S-Y and HOHE J (2004), Linear and non-linear dynamic response of sandwich panels to blast loading, *Composites: Part B*, **35B**(6–8), 673–683.

LUCCIONI B M, AMBROSINI R D and DANESI R F (2004), Analysis of building collapse under blast loads, *Engineering Structures*, **26**(1), 63–71.

MOHAMED M H, BOGDANOVICH A E, DICKINSON L C, SINGLETARY J N and LIENHART R B (2001), A new generation of 3D woven fabric preforms and composites, *SAMPE Journal*, **37**(3), May/June, 8–17.

NAVY (1990), NAVFAC P-397 and Air Force AFR 88-22, *Structures to Resist the Effects of Accidental Explosions*, Technical Manual for Army TM 5-1300.

PARK H, LEE K, LEE S W and KIM K (2006), Dynamic analysis of nonlinear composite structures under pressure wave loading, *Journal of Composite Materials*, **40**(15), 1361–1383.

SHUKLA A, TEKALUR S A, ROUSSEAU C, BOGDANOVICH A and LEBLANC J (2007), Performance of 3D woven composites under shock loading, *CD Proceedings of 16th International Conference on Composite Materials (ICCM-16)*, 8–13 July, Kyoto, Japan.

SINGLETARY J, BOGDANOVICH A, COFFELT R, GAMA B A, GILLESPIE J W (JR), HOPPEL C R P and FINK B K (2001), Ballistic performance of 3D woven polymer composites in integral armor, in Hyer MW and Loos AC (eds), *Proceedings 16th Annual Technical Conference of the American Society for Composites*, Boca Raton, FL, CRC press, 168–179.

TEKALUR S A, BOGDANOVICH A E and SHUKLA A (2009), Shock loading response of sandwich panels with 3D woven E-glass composite skins and stitched foam core, *Composites Science and Technology*, **69**, 736–753.

© Woodhead Publishing Limited, 2010

VAUTRIN A (ed.) (1998), *Mechanics of Sandwich Structures*, Dordrecht, the Netherlands, Kluwer Academic.

VINSON J R (1999), *The Behavior of Sandwich Structures of Isotropic and Composite Materials*, Lancaster, PA, Technomic.

WESEVICH J W and ABERNATHY R L (1999), Inelastic structural component response comparisons between ANFO and TNT based on recent air blast data at scaled ranges of 1.4 to 68 ft/lb$^{1/3}$, *International Workshop on the Modeling of Non-Ideal Explosives*, 16–18 March, Socorro, NM.

YEN C-F and JONES M L (1997), *Composite Material Modeling for Blast Protection*, final technical report, accession number ADA 340968, March, Belvoir, VA, Defense Technical Information Center.

YEN C F, SKAGGS R and CHEESEMAN B A (2005), Modeling of shock mitigation sandwich structures for blast protection, in Reddy JN and Chandra N (eds), *CD Proceedings of the 3rd International Conference on Structural Stability and Dynamics (ICSSD)*, 19–22 June, Kissimmee, FL.

ZUKAS J A and WALTERS W P (1998), *Explosive Effects and Applications*, New York, Springer.

© Woodhead Publishing Limited, 2010

6

Response of composite panels to blast wave pressure loadings

K. LEE, Old Dominion University, USA; and S. W. LEE, University of Maryland, USA

Abstract: There is considerable demand for a reliable computational methodology capable of being used in design studies of composite structures to determine the level of blast protection. As an example, a summary of a comprehensive methodology developed at the University of Maryland for the assessment of damage to composite structures under high explosive blast pressure loading is provided. A simplified methodology is then introduced to obtain structural responses at various blast wave pressure loadings and predict structural collapse based on these responses. The results of numerical tests on flat laminated composite panels show that this simplified methodology, which does not require computationally expensive failure analysis including the progressive material damages, can predict structural failure with reasonable accuracy. Accordingly, the methodology could be used as a first screening tool for design study, and then a full analysis including material damage and failure could be conducted in order to provide detailed predictions of local damage to the selected designs.

Key words: structural failure assessment, composite panels, blast wave pressure loading.

6.1 Introduction

Thin, laminated composite structures are attractive for many lightweight applications such as military vehicles and civil infrastructures due to their durability, versatility and high mechanical performance. One of the technical challenges in their design is to determine the level of blast protection. They may undergo large deflection dynamic motion under high-pressure explosive blast loads and experience progressive material damages and even a structural collapse. Recently, Tekalur *et al.* (2008) conducted an experimental study of material behavior and damage evolution for E-glass vinyl ester and carbon composites subjected to static and blast loads. Their findings in the case of the blast loads were limited to qualitative descriptions of the different damage evolutions for the two composite materials. Perhaps more importantly, they acknowledged that the response of composites to explosive and air blast is a complex phenomenon to implement in a laboratory setting and, for this reason, is rarely studied experimentally. Accordingly,

© Woodhead Publishing Limited, 2010

there is considerable demand for a reliable computational methodology capable of being used in design studies to determine the level of blast protection required in composite structures subjected to blast load. The methodology must incorporate appropriate failure assessment techniques capable of identifying the types of material damage and predicting their onset and growth. In addition, the methodology must accurately describe the kinematics of large dynamic motion of thin, laminated composite structures.

Librescu and Nosier (1990) analytically showed that one must incorporate the transverse shear deformation effects in the description of thin composite plates subjected to blast shock wave. Türkmen and Mecitoğlu (1999) conducted a geometrically non-linear analysis of thin, laminated composite plates under normal blast shock waves based on the classical plate theory and the von Karman assumption. They used the Friedlander function to describe the exponentially decaying blast wave loading. The geometrically non-linear analysis was conducted ignoring in-plane stiffness and inertia effects. They presented a comparison between analytical and experimental results for the time history of a ply strain, which showed a considerable discrepancy after the first wave. Kazancı *et al.* (2004) improved the previous model by including in-plane stiffness and inertia effects. Recently, Kazancı and Mecitoğlu (2008) added the structural viscous damping effect. However, their analysis results for the strain time history still showed a considerable discrepancy. They suspected that the discrepancy was a result of excluding the higher vibration modes of the plate and also neglecting the aeroelastic interaction between the plate motion and blast loads. The discrepancy can be partly due to the fact that the geometrically non-linear analysis of thin plates was conducted ignoring transverse shear deformation. In addition, the progressive failure effect due to material damage was not taken into account in these works.

Padhi *et al.* (1998) examined progressive failure and ultimate collapse of laminated composite plates subjected to uniform transverse pressure under static loading conditions. The effect of aspect ratio for E-glass/polyester composite panels on their response was investigated. They applied strength-based failure criteria and carried out the stiffness reduction at integration points. A commercial finite element program, ABAQUS, was used for the analysis. More recently, Nayak *et al.* (2006) used a finite element model based on the first-order shear deformation theory to study the small deflection dynamic response of composite sandwich plates under the influence of initial stress due to the manufacturing process and assembly techniques. However, the study was carried out only for small deflection without accounting for material damage.

Park *et al.* (2006) developed a comprehensive methodology to assess damage and failure of composite structures under high explosive blast

© Woodhead Publishing Limited, 2010

pressure loadings. The methodology is based on the assumed strain non-linear shell element formulation that incorporates a geometrical non-linear formulation to handle composite structures undergoing large deflection as well as material non-linearity due to local material damages under blast wave pressure loading. The material damages can be accumulated to an extent that results in structural collapse. The developed methodology can be used for numerical prediction of the structural collapse in terms of time and blast load level. In general, the failure analysis requires a very small time increment to guarantee its accuracy, placing a heavy demand on computational resources and time. Accordingly, this presents an obstacle to the routine use of the comprehensive methodology for design study of composite panels if a full analysis including material damage and failure analysis is required.

Lee and Lee (2007) developed a simplified methodology to predict structural collapse of composite panels under blast wave pressure loading. In the simplified methodology, structural responses of a composite panel are systematically observed via conducting geometrically non-linear analyses under carefully chosen, blast wave pressure loadings. It is to be noted that, to obtain a quick reference response, the simplified methodology does not take into account the material non-linearity due to material damage and failure. A structural failure criterion is defined based on careful observation of the response of composite panels under blast wave pressure loadings. Full analyses including material damage and failure are then carried out under the corresponding impulse levels to validate the results of the simplified methodology.

The following section of this chapter provides a summary of a comprehensive methodology developed at the University of Maryland for assessment of damage to composite structures under high explosive blast pressure loading. A simplified methodology is then introduced to obtain structural responses at various blast wave pressure loadings and predict structural collapse based on these responses. Subsequently, validation of the simplified methodology is conducted by carrying out full analysis including material failure model. This is followed by concluding remarks.

6.2 A comprehensive methodology for damage assessment

In this section, a brief overview of a comprehensive computational methodology for assessment of damage and failure of composite structures under high explosive blast pressure loading is presented. Subsequently, a summary of validation studies on the comprehensive method is described.

© Woodhead Publishing Limited, 2010

6.2.1 Non-linear solid shell element formulation for dynamic problems

The non-linear solid shell formulation is based on the total Lagrangian description that employs Green's strain and the second Piola–Kirchhoff stress. In the solid shell element formulation, the composite plate is treated as a three-dimensional solid, allowing thickness change and transverse shear deformation. The kinematics of deformation is described by vector variables only, not including any rotational angles. For dynamic problems, the mass matrix remains constant during the analysis. For geometrically non-linear static cases, it has been shown that large load increments can be used with the solid shell element formulation (Park *et al.*, 1995).

The assumed strain formulation is combined with the solid shell formulation to alleviate element locking. In this approach, an assumed strain field is carefully chosen independently of the displacement-dependent strain field. These two strain fields are related to each other by satisfying a set of compatibility equations. The assumed strain field within an element is expressed by assumed strain shape functions and their parameters that are eliminated at element level. Accordingly, these additional assumed strain parameters do not increase the number of unknowns at global level. Detailed description of the assumed strain solid shell formulation has been provided by Park *et al.* (1995) and Kim and Lee (1988).

For the dynamic formulation, the trapezoidal rule is chosen for the time integration. The trapezoidal rule requires iterations in order to obtain the dynamic equilibrium state at an instant in time. An incremental form of equilibrium and compatibility equations based on incremental expressions for stress and strain vectors are used. The blast wave is treated as dynamic pressure loading applied over the plate surface and the time variation of the blast pressure is approximated by the Friedlander decay function.

6.2.2 Failure criteria for unidirectional and woven ply composites

The effect of material damages such as fiber failure, matrix cracking and fiber–matrix shearing failure on the behavior of composite structures is addressed via reducing the material stiffness corresponding to detected failures. The static failure criteria proposed by Hashin (1980), and Chang and Chang (1987) are modified to generate two separate dynamic failure criteria for unidirectional and woven ply composites. For woven composites, a single layer can be viewed as interlocks of two perpendicular fibers, resulting in little or no difference of material properties in the two fiber directions. The two perpendicular fibers affect failure mechanisms in the

© Woodhead Publishing Limited, 2010

woven composites. For example, the matrix domination in the transverse direction, common to the unidirectional ply, disappears. Accordingly, a failure model different from the unidirectional case is proposed. For instance, fiber breakages in both fiber directions are a major concern in woven composites. For relatively thick panels undergoing bending deformation under transverse pressure loading, the effect of delamination on the structural response can be ignored as the fiber breakage failure is predominantly responsible for the structural failure. Also, the contribution of transverse stresses toward fiber breakage failures is negligible compared with that of their in-plane counterparts. For progressive failure analyses, material failure check is performed at every equilibrium state. Once a failure is detected at a local material point, the in-plane elastic stiffness matrix of the intact material is degraded into a matrix of reduced values. In the dynamic failure criteria, the strain-rate effect on the material strength such as the longitudinal and shear strengths is taken into account based on the results of uniaxial and off-axis tension tests. The strain-rate effect on the constitutive equations is not considered due to a lack of reliable experimental data.

6.2.3 Validation

Various numerical analyses of composite panels were conducted under the static and dynamic loading conditions to validate the effectiveness of the comprehensive computational methodology in the previous study (Park *et al.*, 2006). The analysis results clearly exhibit the significant effect of material damages on the structural behavior of the composite panels. For example, the collapse of the composite panels occurs at lower pressure due to the dynamic effect compared with the static counterpart. It can be observed that the structural collapse occurs when the fiber breakage failure spreads along the boundary of the panel. Also, the analysis results are in good agreement with the available experimental data (Park *et al.*, 2006)

6.3 A simplified methodology for failure assessment

In this section, a simplified methodology to predict structural collapse based on numerically observed structural behavior of composite panels under blast wave pressure loading is introduced. The blast wave pressure loading is treated as an impulse for design study. A two-step approach is introduced to efficiently obtain structural responses under various blast wave pressure loadings. Subsequently, a structural failure criterion using the structural responses resulting from the two-step analyses is introduced.

© Woodhead Publishing Limited, 2010

6.3.1 Numerically observed structural responses of composite panels

In the previous study by Park *et al.* (2006), the comprehensive methodology was applied to the dynamic analysis of a square composite plate under blast wave pressure loading, and the results were compared with available experimental data, as shown in Fig. 6.1. The plate considered in this study is 914 mm long, 914 mm wide and 9.525 mm thick, clamped along two opposite edges and free along the remaining two edges. The plate consists of 15 plies with the layup sequence of $(0,45,0,45,0)_3$. The ply is a woven fabric made of S-2 glass fiber and SC-15 epoxy resin. Detailed description of the problem can be found in Park *et al.* (2006). Figure 6.1 shows the maximum displacement at the plate center versus impulse. One can observe that the numerical results correlate well with experimental data. As impulse increases from zero to 0.4 MPa-ms, a distinct geometrically non-linear stiffening effect is observed. As impulse increases further to 1.0 MPa-ms, the geometrically non-linear stiffening effect is not as evident as before, as it is somewhat mitigated by local material damage. This is more evident in Fig. 6.2, where maximum deflections obtained without considering the material damage are shown as the dotted line for comparison. One can observe that the material damage effect on material stiffness starts to appear at around 0.75 MPa-ms. These numerical results demonstrate that it is very important

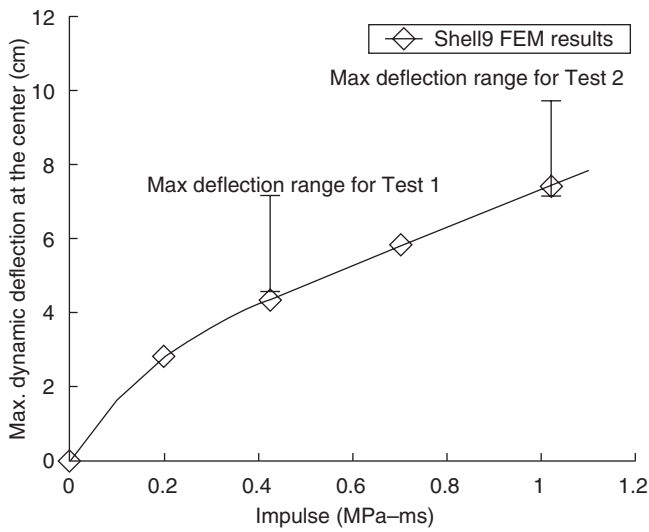

6.1 Comparison of the result between numerical analysis and test for the maximum displacement at the plate center (H Park *et al.,* 2006).

© Woodhead Publishing Limited, 2010

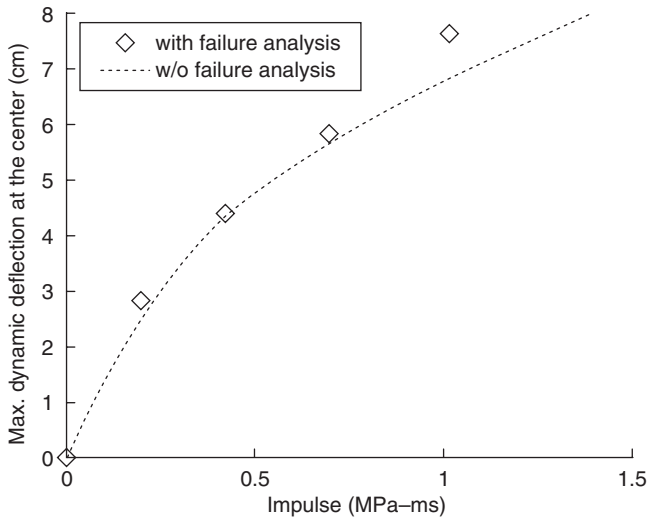

6.2 The maximum displacement at the plate center vs impulse with failure analysis and without failure analysis.

to take into account the material damage effect as well as the geometrically non-linear effect to accurately determine structural response.

Progressively accumulated material damage not only affects the structural response of a composite panel, but also sometimes results in a structural failure. Figure 6.3 shows the center displacement versus time for a composite panel undergoing large deflection under blast wave pressure loading. Detailed description of the problem can be found in Park *et al.* (2006). Analyses carried out with material damage effect are compared with those without material damage. One can observe that, according to the analysis with material damage effect, the panel structurally collapses before it reaches the first peak. It is also observed that the center deflection is slightly under-predicted when the effect of material damage and failure is considered. However, the center deflections are about the same order of magnitude, regardless of whether or not the material failure effect is included, at least up to the structural collapse. This suggests that, for the purpose of design study, one may be able to use the deflections obtained without considering material damage and failure as a quick reference.

As shown in Fig. 6.2, for the numerical results obtained with material failure effect, marked by diamonds, the diminishing geometrically non-linear stiffening effect is related to the softening effect of progressive material damage on its stiffness. For structural responses obtained without failure analysis, the geometrically non-linear stiffening effect appears up to higher impulse. For further investigation of the structural behavior observed

© Woodhead Publishing Limited, 2010

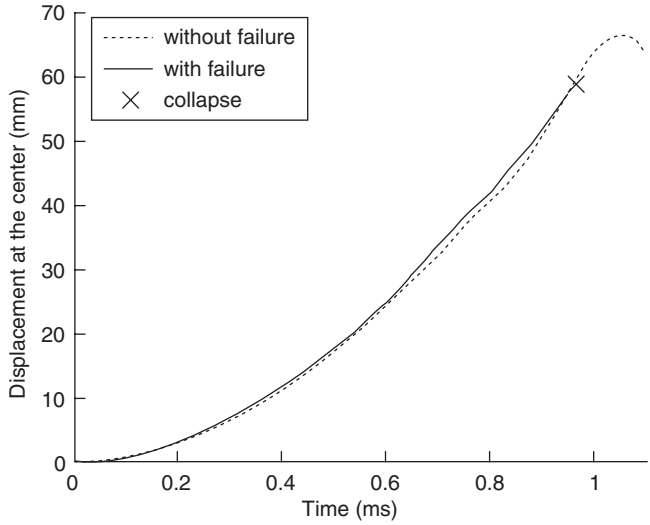

6.3 Deflection vs time for blast pressure wave load.

in Fig. 6.2, non-dimensional center deflection versus impulse is introduced to higher impulse in Fig. 6.4 where w is the center deflection at the first peak and h is the thickness of the panel. It is interesting that, even for the case without the effect of material damage and failure, the stiffening effect eventually starts to diminish beyond a certain level of impulse as shown in the figure. To investigate the phenomenon systematically, a response parameter, called 'slope' S is defined as

$$S = \frac{d(w/h)}{d(impulse)} \qquad [6.1]$$

The slope is calculated by using the quadratic interpolation along the impulse in Fig. 6.4 and plotted in Fig. 6.5. It is observed that the slope rapidly decreases at low impulse and the change of the slope becomes noticeably small as impulse increases.

Figure 6.6 shows deformed configurations at the first peak of the five impulse cases considered in Fig. 6.5. Note that for convenience, different scales are used for the horizontal axis and the vertical axis. One can observe that bending deformation is dominant for the low-impulse cases. However, as impulse increases, the dominant deformation mode changes from bending to in-plane stretching. The more gradual slope change observed at high impulse in Fig. 6.5, appears related to the deformation mode change. According to the dynamic analysis results for the composite panel including material damage and failure models, severe material damage is observed

© Woodhead Publishing Limited, 2010

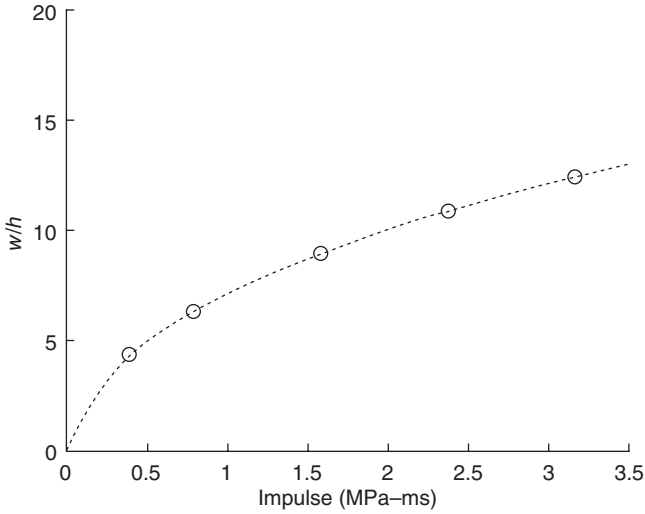

6.4 Non-dimensional *w*/*h* vs impulse for a panel subjected to blast pressure wave.

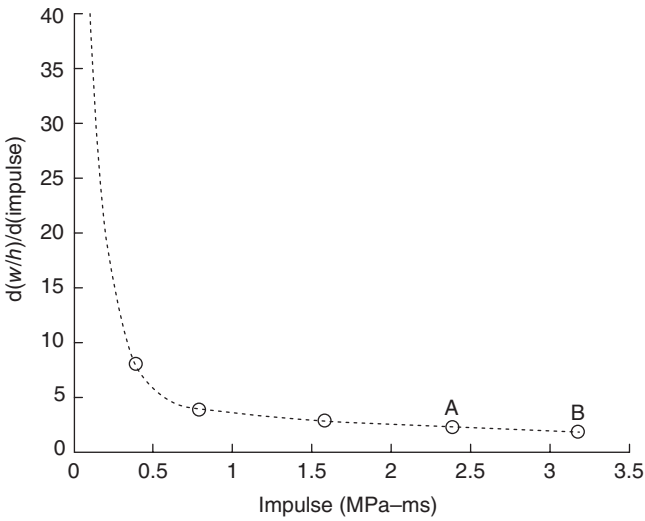

6.5 Slope vs impulse for a panel subjected to blast pressure wave.

at point A and structural failure is observed at point B in Fig. 6.5. One can say that the structural collapse occurs between A and B, which is near the onset of the minimal slope change. Also, the onset of the minimal slope change is perhaps related to the deformation mode change. The in-plane stretching mode under high impulse may induce high stresses in composite

© Woodhead Publishing Limited, 2010

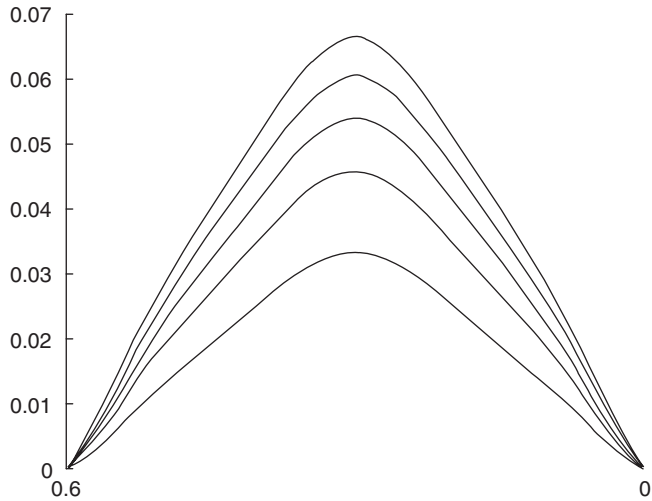

6.6 Deformed configurations of the plate centerline at the first peaks.

materials and eventually cause structural collapse through material damage and failure.

6.3.2 A two-step approach

In the present study, the blast pressure $P(t)$ is approximated by the Friedlander decay function as shown below:

$$P(t) = P_m\left(1-\frac{t}{t_p}\right)\cdot\exp\left(1-\alpha\frac{t}{t_p}\right) \qquad [6.2]$$

where P_m represents the initial magnitude of a pressure wave, while t_p and α determine time dependence and how fast it decays as time elapses. An impulse, I can be defined as

$$I = P_m t_p \int_0^1 (1-\tau)\cdot\exp(1-\alpha\tau)\,d\tau \qquad [6.3]$$

where $\tau = t/t_p$. For a given impulse, the three Friedlander parameters are not uniquely determined. For a givenα, high P_m corresponds to relatively short t_p; however, the resulting response is almost insensitive to the blast wave loading parameters. As long as t_p is sufficiently short, the blast wave pressure loading can be treated as impulse. Accordingly, in the present study, impulse is considered as a design input. For convenience, one may vary P_m only and fix the other two parameters.

© Woodhead Publishing Limited, 2010

In this section, a two-step approach that does not include the effect of material damage and failure is introduced to expedite determination of structural responses under various blast wave pressure loadings. In the present two-step approach, it is assumed that the blast load level ranges from 1.0 to 100.0 MPa in terms of the initial pressure. The first step is to carry out dynamic analyses under the blast wave pressure loads of 1, 10 and 100 MPa to examine response characteristics. Depending upon whether the first peak exists or not for each blast load level, the outcome of the first step is categorized as one of the following four cases:

Case I: Every response shows the first peak.
Case II: First two cases (1 and 10 MPa) only show an acceptable first peak.
Case III: First case (1 MPa) only shows an acceptable first peak.
Case IV: No first peak.

For Case I, the design study is terminated because the panel must be over-designed, probably too heavy for lightweight composite applications. For Case IV, the design study is also terminated because the panel is probably under-designed, not acceptable for armor purposes. These two cases are used for a quick sanity check. For Case II and III, the design study moves onto the second step as follows:

Case II: Obtain structural responses to 2, 4, 6, 8, 20, 40, 60 and 80 MPa
Case III: Obtain structural responses to 0.2, 0.4, 0.6, 0.8, 2, 4, 6 and 8 MPa

For Cases II and III, a total of 11 analyses are carried out for each case, composed of three runs for Step #1 and eight runs for Step #2. The resulting center deflections at the first peak, if any, are obtained.

6.3.3 A structural failure criterion

Using the previously introduced two-step approach, one obtains a set of the first peak displacements for some of the 11 impulse cases. Then, based on the previously introduced reasoning, a structural failure criterion is defined by assuming that a composite panel structurally fails once the change of the slope becomes less than a prescribed value as follows:

$$\frac{\Delta S}{S_1} < \varepsilon \qquad [6.4]$$

where S_1 is the initial slope at the lowest impulse level and ε is a prescribed value. In the present study, ε is set to 0.03. For higher safety factor, a designer can increase the prescribed value.

© Woodhead Publishing Limited, 2010

6.4 Numerical tests on flat laminated composite panels

In this section, the simplified methodology introduced to predict structural collapse of composite panels under blast wave pressure loading is validated by using the results of full analysis including material damage and failure model. In general, material damage of a composite panel is progressive and local, reducing the material stiffness of the affected region. Once sufficiently accumulated, the material damage affects the structural response of the panel in a significant manner. In this case, the accumulated damage may also induce structural collapse. Four examples of flat, composite panels made of woven and unidirectional plies are considered.

One can test the composite panel under various impulses and may determine a threshold impulse corresponding to structural collapse. However, defining structural collapse based on numerical analyses can be rather subjective and empirical. For example, if all material along the boundaries of the panel is damaged, the panel may start a rigid body motion. Even though the majority of the panel is intact, the panel loses its integrity and the original purpose, which can be considered as structural failure. Alternatively, the panel may experience slow and wide distribution of material damage over a wide area other than the boundaries. Once the majority of the material loses its initial stiffness, this can also be treated as structural failure. In this study, both cases are treated as structural failure. A structural failure is declared if two of the following three conditions are satisfied:

(A) Material damage including fiber breakage, matrix cracking and fiber/matrix shearing occurs at over 50% of material points.
(B) Fiber breakage occurs at over 40% of material points.
(C) Fiber breakage occurs at over 40% of boundary points.

6.4.1 All clamped panel with unidirectional plies

The plate is clamped at all edges and subjected to uniform transverse pressure loading. The ply material is E-glass/polyester and material constants are as listed in Table 6.1. The number of plies is five with the layup sequence of $[0/45/90/-45/0]_{total}$. The plate is 600 mm long, 600 mm wide and 3.43 mm thick. For numerical analysis, the full plate is modeled with an 8×8 element mesh. The plate is exposed to a normal blast shock wave. The blast wave loading is assumed to be uniform over the plate surface and the time variation of the blast pressure is described by the Friedlander decay function parameters of $t_p = 1.8$ ms and $\alpha = 0.35$. The initial pressure is listed in Table 6.2. The time increment of $\Delta t = 0.03$ ms is used.

Using the two-step approach, dynamic analyses of the plate are carried out. Figure 6.7 shows the resulting non-dimensional center deflection versus

© Woodhead Publishing Limited, 2010

Table 6.1 Mechanical properties of unidirectional E-glass/polyester laminate

Material properties	Value
Longitudinal modulus, E_x (GPa)	23.6
Transverse modulus, $E_y = E_z$ (GPa)	10.0
Shear modulus, $G_{xy} = G_{xz}$ (GPa)	1.0
Shear modulus, G_{yz} (GPa)	1.0
Poisson's ratio, $\upsilon_{xy} = \upsilon_{xz}$	0.23
Poisson's ratio, υ_{yz}	0.30
Density, ρ (kg/m^3)	1800
Quasi-static longitudinal tensile strength, X_T^{QS} (MPa)	735.0
Quasi-static longitudinal compressive strength, X_C^{QS} (MPa)	600.0
Quasi-static transverse tensile strength, Y_T^{QS} (MPa)	45.0
Quasi-static transverse compressive strength, Y_C^{QS} (MPa)	100.0
Quasi-static in-plane shear strength, SC^{QS} (MPa)	45.0

Table 6.2 Impulse and the initial pressure magnitude

Case #	Impulse (MPa-ms)	P_m (MPa)
1	0.161	0.2
2	0.322	0.4
3	0.484	0.6
4	0.644	0.8
5	0.804	1.0

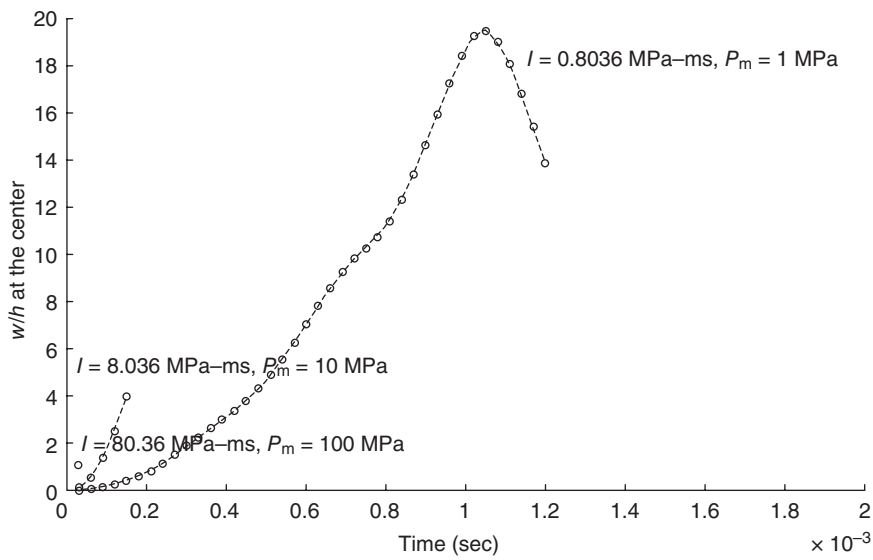

6.7 Non-dimensional center deflection vs time for three blast wave pressure loadings for Step 1.

© Woodhead Publishing Limited, 2010

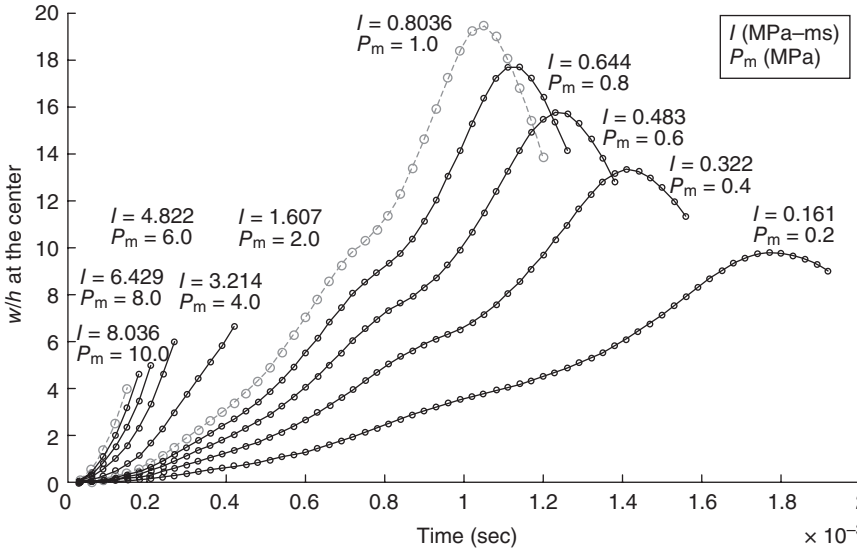

6.8 Non-dimensional center deflection vs time for 11 blast wave pressure loadings for Step 1 and Step 2.

time curves for Step #1. The first peak is observed only for the case where P_m = 1 MPa, which falls under Case III. Subsequently, dynamic analyses are carried out under the blast wave pressure loadings, predefined for Step #2. The resulting non-dimensional center deflections versus time curves are shown in Fig. 6.8. Note that these two figures are shown for reference purpose. The five first peaks corresponding to the lowest five impulses are obtained. The previously defined slope is calculated and shown in Fig. 6.9. Based on the structural failure criterion, the plate collapses at around 0.5 MPa-ms, which is validated by the results of dynamic analyses including material failure model, listed in Table 6.3. As shown in the table, structural failure occurs at 0.6 MPa or 0.5 MPa-ms due to accumulated matrix cracking over the panel and fiber breakage along the boundaries. From the third and fourth columns of the table, one may observe that fiber breakage becomes an increasingly significant part of the overall material damage. In addition, from the fifth column of the table, one may observe that the rapid increase in fiber breakage along the boundaries coincides with the structural collapse. Note that the percentage of fiber breakage along the boundaries is calculated by counting damaged material points out of all the material points that belong to elements adjacent to the boundaries. Figure 6.10 shows deformed configurations of the plate at its first peak for the five impulse cases. Note that proper modeling such as reasonable mesh size and time increment is a prerequisite in any case. For example, solution

© Woodhead Publishing Limited, 2010

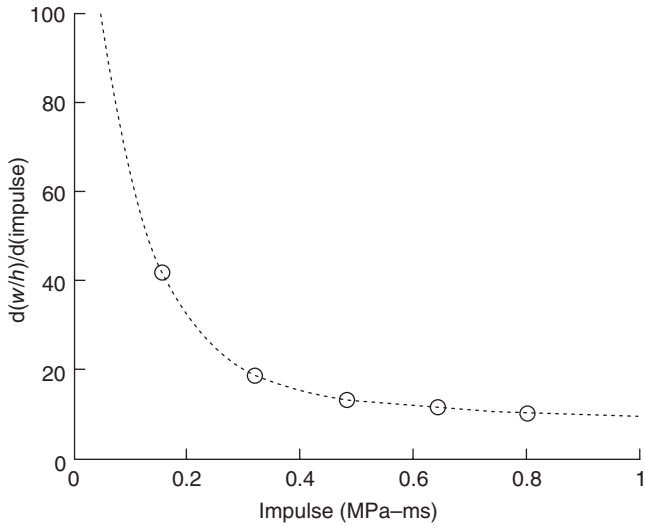

6.9 Slope vs impulse for the all clamped E-glass/polyester laminate panel.

Table 6.3 Analysis results using material damage model for unidirectional E-glass/polyester laminate

Impulse (MPa-ms)	Peak (ms)	Damage (%)	Fiber breakage (%)	Fiber breakage along boundary (%)
0.161	1.88	52.01	0.00	0.00
0.322	1.54	81.91	0.63	7.53
0.484	No peak	98.30	21.77	44.35
0.644	No peak	99.69	39.20	81.59
0.804	No peak	100.00	40.94	85.36

sensitivity to mesh size and time increment size must be checked as shown in Figs 6.11 and 6.12.

6.4.2 All clamped panel with woven plies

A plate, clamped at all edges, is 914 mm long, 914 mm wide and 9.525 mm thick. The plate consists of 15 plies with the layup sequence of $(0,45,0,45,0)_3$. The ply is woven fabric made of S-2 glass fiber and SC-15 epoxy resin and its material constants are provided in Tables 6.4 and 6.5. For numerical analysis, the full plate is modeled with an 8×8 element mesh. The blast wave loading is assumed to be uniform over the plate surface and the time

© Woodhead Publishing Limited, 2010

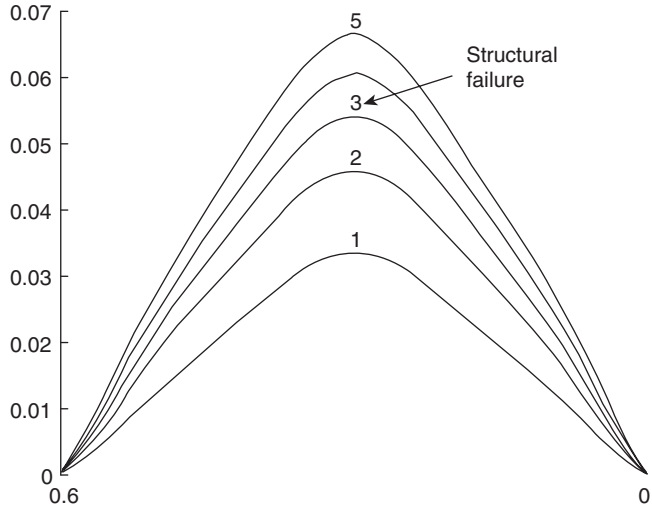

6.10 Deformed configurations of the plate centerline for the E-glass/polyester laminate panel.

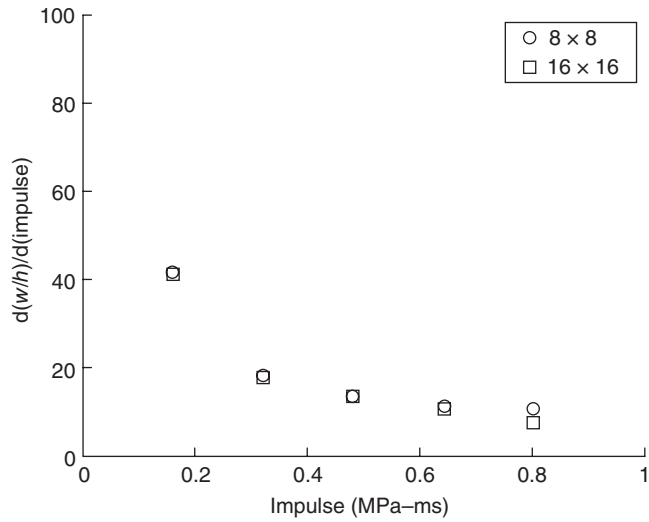

6.11 'Slope' vs impulse for two different meshes.

variation of the blast pressure is described by the Friedlander decay function parameters of $t_p = 1.3$ ms and $\alpha = 1.70$. The initial pressure is listed in Table 6.6. The time increment of $\Delta t = 0.03$ ms is used. Using the two-step approach and the structural failure criterion, structural collapse analysis of the plate is carried out. The resulting slope versus impulse data are shown

© Woodhead Publishing Limited, 2010

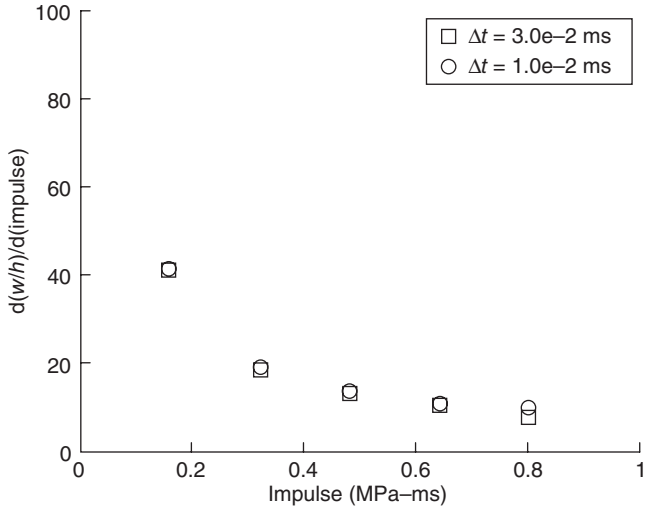

6.12 'Slope' vs impulse for two different time increments.

Table 6.4 Mechanical properties of woven fabric S-2 glass/epoxy laminated plate

Material properties	Value
Longitudinal modulus, E_x (GPa)	28.3
Transverse modulus, E_y (GPa)	28.3
Shear modulus, G_{xy} (GPa)	5.86
Poisson's ratio, υ_{xy}	0.23
Density, ρ (kg/m^3)	1800
Quasi-static longitudinal tensile strength, X_T^{QS} (MPa)	583.12
Quasi-static longitudinal compressive strength, X_C^{QS} (MPa)	402.12
Quasi-static transverse tensile strength, Y_T^{QS} (MPa)	583.12
Quasi-static transverse compressive strength, Y_C^{QS} (MPa)	402.12
Quasi-static in-plane shear strength, SC^{QS} (MPa)	95.06

Table 6.5 Strain-rate dependent strength properties of woven fabric S-2 glass/epoxy

Longitudinal tensile strength, X_T (MPa)	$X_T = 48.16 \log_{10}\dot{\varepsilon}_{11} + X_T^{QS} + 144.48$
Longitudinal compressive strength, X_C (MPa)	$X_C = 48.16 \log_{10}\dot{\varepsilon}_{11} + X_C^{QS} + 144.48$
Transverse tensile strength, Y_T(MPa)	$Y_T = 48.16 \log_{10}\dot{\varepsilon}_{22} + Y_T^{QS} + 144.48$
Transverse compressive strength, Y_C (MPa)	$X_C = 48.16 \log_{10}\dot{\varepsilon}_{22} + Y_C^{QS} + 144.48$
In-plane shear strength, SC (MPa)	$SC = 8.08 \log_{10}\dot{\varepsilon}_{12} + SC^{QS} + 24.24$

© Woodhead Publishing Limited, 2010

Table 6.6 Impulse and the initial pressure magnitude

Case #	Impulse (MPa-ms)	P_m (MPa)
1	0.40	1.0
2	0.79	2.0
3	1.59	4.0
4	2.38	6.0
5	3.17	8.0
6	3.97	10.0

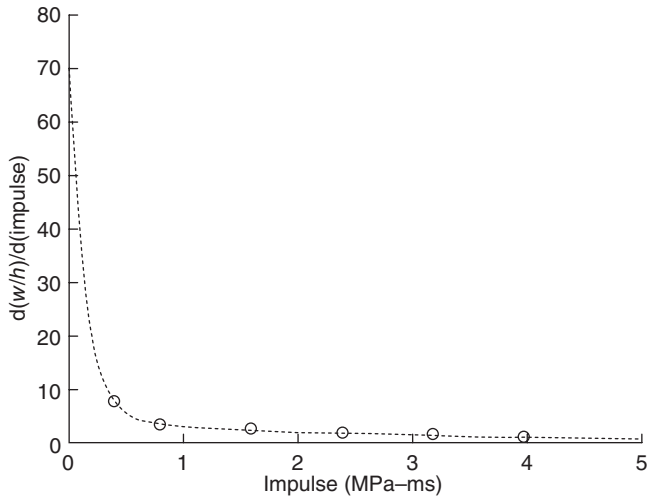

6.13 'Slope' vs impulse for the all clamped S-2 glass/epoxy laminated panel.

in Fig. 6.13. Based on the structural failure criterion, the plate collapses at around 2.4 MPa-ms, which is validated by the results of dynamic analyses including material failure model, listed in Table 6.7. As shown in the table, structural failure occurs at 6.0 MPa or 2.4 MPa-ms due to accumulated fiber breakage over the panel as well as along the boundaries.

6.4.3 Simply supported–free panel with woven plies

The plate geometry, ply layup sequence and material properties are identical to those in the previous example (Section 6.4.2). The plate is simply-supported along two opposite edges and free along the remaining two edges. For numerical analysis, the full plate is modeled with an 8 × 8

© Woodhead Publishing Limited, 2010

Table 6.7 Analysis results using material damage model for woven fabric S-2 glass/epoxy laminated plate (all clamped)

Impulse (MPa-ms)	Peak (ms)	Damage (%)	Fiber breakage (%)	Fiber breakage along boundary (%)
0.79	1.47	1.04	0.42	5.01
1.59	1.35	18.88	11.64	31.15
2.38	1.41	61.08	43.94	48.96
3.17	1.41	76.32	57.27	52.85
3.97	1.32	95.80	77.30	64.53

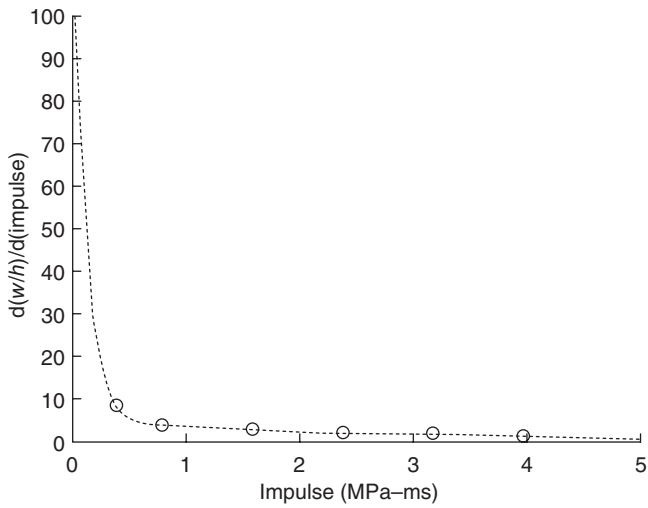

6.14 'Slope' vs impulse for the simply supported- free S-2 glass/epoxy laminated panel.

element mesh. The blast wave loading is assumed to be uniform over the plate surface, and the time variation of the blast pressure is described by the Friedlander decay function parameters of $t_p = 1.3$ ms and $\alpha = 1.70$. The time increment of $\Delta t = 0.03$ ms is used. Using the two-step approach and the structural failure criterion, structural collapse analysis of the plate is carried out. The resulting slope versus impulse data are shown in Fig. 6.14. Based on the structural failure criterion, the plate collapses at around 2.4 MPa-ms, which is validated by the results of dynamic analyses including material failure model, listed in Table 6.8. As shown in the table, structural failure occurs at 6.0 MPa or 2.4 MPa-ms due to accumulated fiber breakage over the panel as well as along the boundaries.

© Woodhead Publishing Limited, 2010

Table 6.8 Analysis results using material damage model for woven fabric S-2 glass/epoxy laminated plate (simply-supported–free)

Impulse (MPa-ms)	Peak (ms)	Damage (%)	Fiber breakage (%)	Fiber breakage along boundary (%)
0.79	1.74	1.08	0.00	0.00
1.59	1.38	44.05	8.85	30.00
2.38	1.38	77.21	40.30	27.50
3.17	1.32	94.47	56.15	25.00
3.97	1.38	100.00	60.37	60.00

6.5 Conclusions and future trends

Results of numerical tests on flat, laminated composite panels show that the simplified methodology, which does not require the computationally expensive failure analysis including the progressive material damages, can predict the structural failure with reasonable accuracy. Accordingly, the simplified methodology could be used as a first screening tool for the design study, and then the full analysis including material damage and failure could be conducted to provide detailed local damages of selected designs. In addition, a graphical user interface (GUI) can be implemented to facilitate building up a design library for composite panels under blast wave pressure loading.

However, the simplified methodology developed has been validated for structural collapse analysis of flat composite plates only for a limited number of cases. Accordingly, more extensive studies are needed to ascertain the validity of the methodology. It is also recommended that the future work include investigation of alternate panel geometries such as curved panels as well as sandwich panels. Also, it is to be noted that the simplified methodology can be used only when it is validated by a full analysis that incorporates geometrical and material non-linearities taking into account complete failure mechanism under blast wave pressure loading. This emphasizes the need to extend the capability of the full analysis methodology. Accordingly, it is strongly recommended that the future work include investigation of other material failure mechanisms associated with delamination. In addition, it is recommended that the future work include investigation of the structural response of composite structures under multiple hits of blast wave pressure loading. One may note that the structural responses have been obtained under prescribed blast wave pressure loadings. Based on more advanced simulation capabilities, one may pursue modeling the interactive phenomenon between thin, laminated composite structures and blast loads.

© Woodhead Publishing Limited, 2010

6.6 References

CHANG F K and CHANG K Y (1987), A progressive damage model for laminated composite containing stress concentrations, *Journal of Composite Materials*, **21**, 834–855.

HASHIN Z (1980), Failure criteria for unidirectional fiber composites, *ASME Journal of Applied Mechanics*, **47**, 329–334.

IANNUCCI L (2005), Progressive failure modeling of woven carbon composites under impact, *International Journal of Impact Engineering*, **32**, 1013–1043.

KAZANCI Z and MECITOĞLU Z (2008), Nonlinear damped vibrations of a laminated composite plate subjected to blast load, *AIAA Journal*, **44**(9), 2002–2008.

KAZANCI Z, MECITOĞLU Z and HACIOĞLU A (2004), Effect of in-plane stiffness and inertia on dynamic behavior of a laminated composite plate under blast load, *Earth & Space*, 484–491.

KIM Y H and LEE S W (1988), A solid element formulation for large deflection analysis of composite shell structures, *Computers and Structures*, **30**(1/2), 269–274.

LEE K and LEE S W (2007), A simplified methodology for structural collapse analysis of composite panels under blast wave pressure loading, *International Conference on Computational & Experimental Engineering & Sciences*, January 3–8, Miami, FL.

LIBRESCU L and NOSIER A (1990), Response of laminated composite flat panels to sonic boom and explosive blast loadings, *AIAA Journal*, **28**(2), 345–352.

NAYAK A K, SHENOI R A and MOY S S J (2006), Transient response of initially stressed composite sandwich plates, *Finite Element Analysis and Design*, **42**, 821–836.

PADHI G S, SHENOI R A, MOY S S J and HAWKINS G L (1998), Progressive failure and ultimate collapse of laminated composite plates in bending, *Composite Structures*, **40**(3–4), 277–291.

PARK H C, CHO C M and LEE S W (1995), An efficient assumed strain element model with six dof per node for analysis of geometrically nonlinear shells, *International Journal for Numerical Methods in Engineering*, **38**(24), 4101–4121.

PARK H, LEE K, LEE S W and KIM K (2006), Dynamic analysis of nonlinear composite structures under pressure wave loading, *Journal of Composite Materials*, **40**(15), 1361–1383.

TEKALUR S A, SHIVAKUMAR K and SHUKLA A (2008), Mechanical behavior and damage evolution in E-glass vinyl ester and carbon composites subjected to static and blast loads, *Composites: Part B*, **39**, 57–65.

TÜRKMEN H S and MECITOĞLU Z (1999), Nonlinear structural response of laminated composite plates subjected to blast loading, *AIAA Journal*, **37**(12), 1639–1647.

© Woodhead Publishing Limited, 2010

7

Ceramic matrix composites for ballistic protection of vehicles and personnel

J. J. SCHULDIES, Industrial Ceramic Technology, Inc., USA; and
R. NAGESWARAN, SMAHT Ceramics, Inc., USA

Abstract: Of growing interest to the US military is the use of lightweight ceramic composites that can offer improved ballistic protection to military personnel and tactical ground vehicles. New technology must be developed with minimum capital cost penalties and offer improved operational efficiency and tactical performance during military action. Conventional ceramics, such as alumina, boron carbide, silicon nitride, and silicon carbide, have been investigated for application in ballistic protection armor systems and are being used, selectively, due to their low weight and high mechanical properties. However, limitations such as multiple-hit capability have been recognized which necessitates developing newer and more advanced materials. This chapter proposes that the use of ceramic-whisker reinforced ceramic composites be considered for next-generation armor systems. Specifically discussed is a commercially available alumina-based composite (CRYSTALOY®) which is reinforced with single crystal silicon carbide whiskers. Currently used in applications such as metal removal cutting tools, metal extrusion dies, and other wear, corrosive and high temperature parts, it forms the technology basis to develop an improved armor system. Data are provided to support the premise that developing a ceramic–matrix composite having improved ballistic performance is feasible.

Key words: ceramic composites, ballistic performance, crack propagation, multi-hit capability, silicon carbide whiskers.

7.1 Introduction

Lightweight hybrid composites that can offer substantial ballistic protection to tactical ground vehicles and, in turn, to military personnel are of ever-growing interest to the US military. One of the major requirements for such a ballistic protection technology is the ability to defeat or protect against the 7.62 mm NATO M80 ball round and 7.62 mm NIJ IV or DIN C5-SF AP round threats. It is also an implicit requirement that such a technology be developed without any capital or operational cost penalties; rather, there must be associated gains in operational efficiency and tactical performance during military action. Therefore, there is a need to develop armor systems that are based on high mass efficiency ballistic-shield materials, innovative and functional hybrid designs, and reliable scaleable processing methods.

© Woodhead Publishing Limited, 2010

Conventional armor materials are typically made of steel, aluminum, or other hard metals. Although these metallic materials primarily perform a structural function, they provide reasonably good ballistic protection (Viechnicki *et al.*, 1991; Aghajanian *et al.*, 2001) at appropriate thicknesses (or areal densities). Often, this approach results in parasitic weight, which not only reduces fuel efficiency but also diminishes mobility in action. Recognizing that rapid deployment, enhanced fuel mileage, and reliable ballistic (and blast) protection are the keys to dominating future battles, new and innovative approaches involving lighter materials such as ceramics and polymers have become absolutely essential. Also recognized is the need for ceramic composite armor capable of surviving multiple hits.

7.2 Technology overview

Structural ceramics, such as alumina, were developed for armor applications in the USA during the 1960s. The primary use was for bullet-proof vests and helicopter seats. The objective was to stop small, armor-piercing projectiles at a lower weight (areal density) than armor systems employing metal protection. While high-alumina and alumina–zirconia ceramics have been successfully used for ballistic protection of military and tactical police personnel, they have also been used to protect critical parts of aircraft.

Metals and ceramics differ in the mechanisms which absorb the kinetic energy of projectiles. Ductile metals absorb energy primarily through plastic deformation. Ceramics dissipate energy through fracture mechanisms which include deformation of the projectile and the initiation of small cracks in the ceramic, leading to crack propagation and destruction of the ceramic. The ability of ceramics to provide ballistic protection depends on both physical and mechanical properties such as density, porosity, hardness, fracture toughness, elastic modulus, sonic velocity (velocity of sound in the ceramic), and mechanical strength. No single property correlates with ballistic performance due to the interaction of various stress factors during impact and the short time associated with the initiation and propagation of cracks.

While researchers, in the past, noted that reinforcement of ceramics may provide improved ballistic protection, the fabrication route would normally include hot-pressing with an increase in cost versus other densification routes such as sintering. Viechnicki *et al.* (1991) proposed the use of ceramic whiskers or fibers to reinforce ceramic armor materials. Other particulate reinforced compositions and cermets were also considered at that time. Evidently, the densification routes required to produce effective properties were too costly as very few of these ceramic systems are being used for armor applications.

© Woodhead Publishing Limited, 2010

7.2.1 Ceramic composite materials and ballistic results

Several recent studies (Karandiker *et al.*, 1994; Chin 1999; Parameswaran *et al.*, 1999; Medvedovski, 2002a; Ray *et al.*, 2003; Skaggs, 2003) have utilized monolithic ceramics such as alumina (Al2O3), boron carbide (B4C), silicon carbide (SiC), and titanium diboride (TiB2) for developing personnel and vehicular ballistic protection armor systems. Owing to their low specific gravity, and high stiffness, hardness, strength, and thermal stability, the ceramic-based systems have shown potential for improving upon current standards for ballistic performance, which includes multi-hit capability.

The manufacturing process for reaction bonded SiC (RBSC) is well known, and this ceramic composite, consisting of SiC, carbon and silicon, is used in numerous industrial applications. Its evaluation for armor applications has shown it has good ballistic properties and can be fabricated into shapes, while maintaining tolerances, eliminating the need for machining.

Recognizing the need for improved ballistic properties, efforts were made to develop a similar reaction bonded system replacing SiC with B4C, RBBC (Aghajanian *et al.*, 2001). Ballistic properties of this ceramic composite, as well as RBSC and hot-pressed B4C, were determined by the procedures specified in MIL-STD-662F. Both ball rounds and armor-piercing (AP) tests were conducted. Properties of RBSC and RBBC are shown in Table 7.1. The RBBC ceramic composite exhibits a 28% increase in fracture toughness (K_{Ic}) relative to the RBSC and a reduced density which is important for armor applications which are weight sensitive.

Ballistic properties are shown in Tables 7.2 and 7.3 with commercial hot-pressed (HP) B4C as the control. Threat levels of 7.62 mm M80 ball rounds and 7.62 mm AP M2 rounds were used for these tests.

However, cost issues and structural limitations have necessitated further research for newer and more advanced systems. Of late, ceramic-matrix composites (reinforced with whiskers or fibers) have emerged as the answer to the question surrounding the structural (toughness) issues of monolithic ceramics. Ceramic-based composites ranging from SiC (toughened)-Al2O3 to siliconized-B4C are being actively studied and touted for next-generation armor systems (Viechnicki *et al.*, 1991; Medvedovski, 2002b).

Table 7.1 Properties of reaction bonded SiC and reaction bonded B4C

Property	RBSC	RBBC
Density g/cc	3.06	2.57
Young's Modulus (GPa)	384	382
MOR (MPa)	284	278
K_{Ic} (MPa-m½)	3.9	5

© Woodhead Publishing Limited, 2010

Table 7.2 Ballistic test results with 7.62 ball threats

	System areal density	Mass efficiency	Normalized mass efficiency
	[kg/m^2(lbs/f^2)]	RHA equivalent	
HP B4C (control)	23.5 (4.82)	4.56	1.00
RBSC	23.9 (4.89)	5.11	1.12

Table 7.3 Ballistic test results with 7.62 AP M2 threats

	System areal density	Mass efficiency	Normalized mass efficiency
	[kg/m^2 (lbs/f^2)]	RHA equivalent	
HP B4C (control)	29.0 (5.59)	4.53	1.00
RBBC	30.2 (6.18)	4.85	1.07

7.3 Technology approach for improved ballistic protection

One such SiC (whisker)-reinforced Al2O3 composite named CRYSTALOY® (U.S. Pat. 5,177,037) is attractive for use as the hard front-face plate. Its desirable physical and mechanical properties are derived from the addition of discretely dispersed SiC whiskers in a matrix of ceramic powder. The degree of improvement in strength and fracture toughness obtained by whisker additions is substantial because the mechanism of microcrack initiation, propagation and coalescence to critical crack size, leading to catastrophic failure, is significantly suppressed in whisker-reinforced ceramic composites (Homeny *et al.*, 1987; Becher *et al.*, 1988; Homeny and Vaughn 1990; Krause *et al.*, 1990; Lillo *et al.*, 2003). Microcrack initiation is suppressed as the whiskers pin the grain boundaries of the ceramic matrix and prevent grain-growth during processing at elevated temperatures which, in turn, results in high hardness and strength. Another benefit of the SiC whisker addition is to produce a strain redistribution effect which reduces stress at localized areas similar to the effect of stress redistribution due to ductility in a metal. Any deleterious localized stresses are modulated in the presence of the whiskers, whereby, instead of a large and catastrophic crack, numerous small non-catastrophic cracks are formed.

To overcome the mechanical property limitations of conventional ceramics, CRYSTALOY® type ceramic composites provide new opportunities. By preferentially admixing discretely dispersed silicon carbide (SiC) whiskers in a matrix of ceramic powders, both physical and mechanical properties

© Woodhead Publishing Limited, 2010

Table 7.4 Ceramic composite properties

Ceramic composition	Al2O3[4]	CRYSTALOY® 2301* (Al203+SiCw)	Al2O3+ 30 wt% TiC[4]	CRYSTALOY® 2311* (Al2O3+ TiC+SiCw)	CRYSTALOY® 2321* (Non-oxide based +SiCw)
Density (g/cc)	3.9	3.6–3.8	4.3	3.9–4.1	3.8–3.9
Hardness[1] Hv	2000	2200–2500	2400	2400–2550	2500–2600
Module of rupture[2] (ksi/Mpa)	55/380	85–100/570–720	90/630	80–110	120–130/ 820–895
Fracture toughness[3] ($MN/m^{3/2}$)	3–4	8–11	4–5	7–9[5]	9–11[5]

*Typical SiCw (silicon carbide whiskers) volume loading range properties
[1]5 kg load
[2]4-point, Room Temperature
[3]SENB
[5]Indentation
[4]Catalog data

are enhanced as compared to an unreinforced alumina (Al2O3) matrix. Table 7.4 compares the mechanical properties of conventional ceramics, Al203 and Al203+TiC, with the properties obtained with the addition of single crystal silicon carbide whiskers.

Ceramic whiskers also exhibit an interesting elastic effect. As much as 3% strain with no observed permanent deformation has been reported (Milewski 1981) compared to less than 0.1% strain levels in polycrystalline bulk ceramics. This physical characteristic may play an important role in the toughening of brittle ceramics, thought to be accomplished through a load transfer stress-redistribution mechanism from the low-strength, low-strain tolerance matrix, to the high-strength, high-strain tolerance ceramic whiskers. Increasing the ceramic whisker volume content in a ceramic composite could conceivably produce a material having reduced sensitivity to small defects due to a greater propensity for stress redistribution and a reduction in localized stress effects. This may be important in achieving additional ballistic protection, such as multiple strikes.

The SiC whisker additions promote microcrack isolation, crack bridging, and crack deflection. An illustration of such mechanisms in operation can be seen in the photograph of Fig. 7.1 which shows a SiC(w)-toughened Al2O3 composite, produced by Industrial Ceramic Technology, Inc., with multiple surface-related cracks.

© Woodhead Publishing Limited, 2010

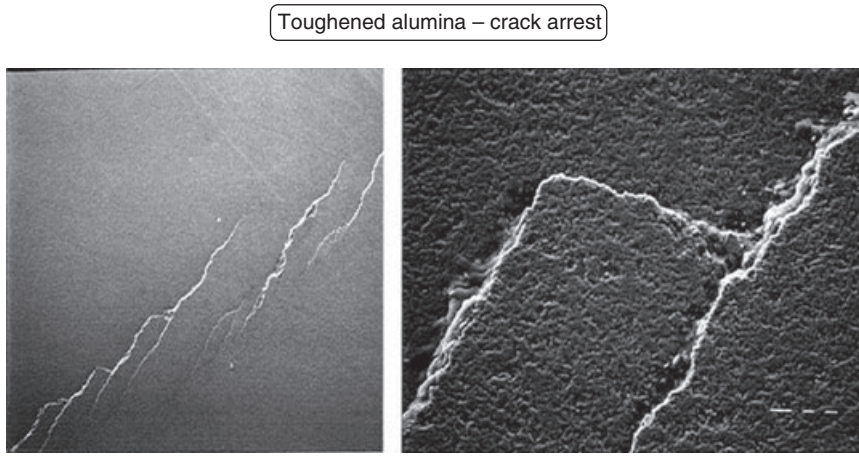

7.1 Illustration of the toughening effects of SiC (whiskers) in an alumina matrix composite (a) 35× (b) 400×.

Regardless of the nature of the ceramic-based front-face plate, it is now well-established that a polymeric (Kevlar®, aramid, fiberglass, or S2 glass) or metallic backing plate is vital for overall ballistic shielding. The hard ceramic frontal plate performs the role of blunting the projectile and inducing a destructive shock wave on the projectile upon impact. The softer (polymeric or metallic) backing material acts as a 'catcher' for residual broken fragments in preventing target penetration. Virtually all of the kinetic energy of the projectile must be absorbed through deformation and failure of the fiber-reinforced composite laminate. The laminate also serves to provide physical integrity to the armor system and provide environmental protection. The dynamic response of the ceramic–polymeric composite armor system will be strongly influenced by the stiffness of the composite. (Parameswaran *et al.*, 1999). Ideally, the polymeric composite needs to be stiff enough to support the ceramic during impact, but compliant enough to allow high fiber strain and energy absorption during deformation by the projectile fragments.

7.4 Impact of improved ceramic composites for ballistic protection

7.4.1 Primary military applications

The proposed advanced, lightweight composite armor technology is primarily targeted for military ballistic (and blast) protection applications, par-

© Woodhead Publishing Limited, 2010

ticularly in ground tactical vehicles such as Humvees and jeeps, and in a variety of FMTV (family of medium tactical vehicles) and security vehicles. With respect to the above tactical vehicles, the two major application areas are: (i) doors and cab-structure for protection against various assault rifle fires and (ii) roof and belly for protection against grenades, landmines, etc.

If successfully developed and utilized in these critical application areas, the technology will not only offer superior ballistic protection but also result in weight savings (reduced areal density) compared to the conventional metallic armor. In terms of specific numbers, at an areal density of 15 lbs./ft^2 or less, the proposed hybrid-composite armor is expected to offer equal or better protection than the current steel armor with typical areal density of 17 lbs./ft^2. Moreover, in application, this reinforced composite armor can be used either as a replacement for existing armor or as an 'add-on' (for which the reinforced-ceramic might be adequate by itself). In addition to mobile or moving-target protection, the proposed innovation could also find its way into stationary applications – for protection of shelters, bunkers, etc. against the 7.62 mm type ballistic threats.

7.4.2 Other possible military and law-enforcement applications

The ballistic-shield or ceramic component of the armor system should also be amenable to fabrication into smaller and complex shapes, which carries it over to other military and law-enforcement applications. Increased protection for ground troops is one of the potential areas of use for this armor system. Currently, there is a huge demand for 'stand-alone' or 'add-on' armor plates for additional chest and back protection.

Ballistic shields for machine gunners is another potential application for this system. The machine gunner is a critical component to an effective fire team due to his ability to lay down a large field of fire.

Typically, the machine gunner and assistant gunner are targeted more by enemy fire as they pose a larger threat, are more exposed to operate the gun, less mobile and are harder to conceal due to tracer fire and muzzle flash. The proposed hybrid-armor system could be used as shield elements that may be quickly mounted/dismounted to machine guns (such as on the bipod legs for M60 and M249 machine guns) to provide additional protection to the gunner firing from short duration positions.

As with the military body armor, complex shapes of just the reinforced-ceramic or the hybrid-composite itself can be fabricated and used for added protection for law-enforcement personnel against 7.62 mm and 5.56 mm rifle fire than is currently available. More coverage is of key importance for law enforcement because their tactical encounters typically occur in more open areas with less cover.

© Woodhead Publishing Limited, 2010

In conclusion, the benefits of the proposed technology to the military are many. However, it would suffice to say that it could make the difference between 'life and death' or 'few lives versus many lives' or, ultimately, 'a battle won instead of lost'. Financially, the ramifications of successful use of this armor technology are huge because of what can be gained in terms of 'saved lives' alone. Finally, it is also worth noting from the point of a market outlook that the armor industry is one of the fastest growing areas involving structural ceramics with a growth rate of almost 15% in recent years.

7.5 References

AGHAJANIAN MK, MORGAN BN, SINGH JR, MEARS J and WOLFFE RA (2001), A new family of reaction bonded ceramics for armor applications, *Pacific Rim*, **4**, 1–13.

BECHER PF, HSUEH C-H, ANGELINI P and TIEGS TN (1988), Toughening behavior in whisker-reinforced ceramic matrix composites, *Journal of the American Ceramic Society*, **71**(12), 1050–1061.

CHIN E (1999), Army focused research team on functionally graded armor composites, *Materials Science and Engineering*, **A259**, 155–161.

HOMENY J and VAUGHN W (1990), R-curve measurement in silicon carbide whisker-reinforced alumina composites, *Journal of the American Ceramic Society*, **73**(7), 2060–2062.

HOMENEY J, VAUGHN WL and FERBER MK (1987), Processing and mechanical properties of SiC-whisker-Al2O3-matrix composites, *Bulletin of the American Ceramic Society*, **67**(2), 333–338.

KARANDIKAR P, AGHAJANIAN M and MORGAN B (1994), Complex net-shape ceramic components for structural, lithography mirror and armor applications, *Ceramic Engineering and Science Proceedings*, **24**(3), 561–567.

KRAUSE RF, FULLER ER JR and RHODES JF (1990), Fracture resistance behavior of silicon carbide whisker-reinforced alumina composites with different porosities, *Journal of the American Ceramic Society*, **73**(3), 559–566.

LILLO TM, CHU HS, BAILEY DW, HARRISON WM and LAUGHTON DA (2003), Development of a pressureless-sintered SiC monolith and special-shaped SiC(whisker)-reinforced SiC matrix composite for lightweight armor application, *Ceramic Engineering and Science Proceedings*, **24**(3), 359–364.

MEDVEDOVSKI E (2002a), Alumina ceramics for ballistic protection, Part 1, *Bulletin of the American Ceramic Society*, **81**(3), 27–32.

MEDVEDOVSKI E (2002b), Alumina ceramics for ballistic protection, Part 2, *Bulletin of the American Ceramic Society*, **81**(4), 45–50.

MILEWSKI JV (1981), Whiskers, *Encyclopedia of Materials Science and Engineering*, Chapter 19.

RAY D, FLINDERS M, ANDERSON A and CUTLER RA (2003), Hardness/toughness relationship for SiC armor, *Ceramic Engineering and Science Proceedings*, **24**(3), 401–410.

PARAMESWARAN V, BENTLEY W, SHUKLA A and PROSSER RA (1999), A new approach for improving ballistic performance of composite armor, *Experimental Mechanics*, **39**(2), 103–110.

© Woodhead Publishing Limited, 2010

SKAGGS SR (2003), A brief history of ceramic armor development, *Ceramic Engineering and Science Proceedings*, **24**(3), 337–349.

VIECHNICKI D, SLARIN MJ and KLIMAN MI (1991), Development and current status of armor ceramics, *Ceramic Bulletin*, **70**(6), 1035–1039.

© Woodhead Publishing Limited, 2010

8

Developing mine blast resistance for composite based military vehicles

M. FRENCH and A. WRIGHT, QinetiQ, UK

Abstract: This chapter is designed to provide an overview of mines used in warfare, their influence on the design of military vehicles, the use of composite materials to improve the design of armoured fighting vehicles (AFVs) and the research being undertaken to assess the performance of composite materials exposed to mine blast. A description of two research programmes, ACAVP (Advanced Composite Armoured Vehicle Platform) and CAFV (Carbon Armoured Fighting Vehicle), for evaluation of composites for military vehicles, is provided, together with details of the modelling approaches that can be used to design vehicles to better withstand the mine blast threat.

Key words: fibre-reinforced composite, mine weapons, blast loading, armour design, spall, blast modelling.

8.1 Introduction

This chapter is designed to provide an overview of mines used in warfare, their influence on the design of military vehicles, the use of composite materials to improve the design of armoured fighting vehicles (AFVs), and the research being undertaken to assess the performance of composite materials exposed to mine blast.

8.1.1 The historical development of mines

As a defensive weapon, the use of mines (when described simply as a hidden underground device) can be traced back to Roman times, when the war elephant was the equivalent of the modern AFV. To counter the progress of the elephants and other siege engines, large earthenware jars were buried in the soil. Under the weight of the elephants, the jars broke and collapsed, significantly hindering their progress (Schneck, 1998). With the deployment of the first ever tanks by the British forces in the First World War, the ongoing cycle of threat and counter threat was taken up by the German forces with their deployment of the first anti-tank mines. These mines were the forerunners of the improvised explosive devices (IEDs) encountered in Iraq by the US-led coalition forces, whereby the insurgents

© Woodhead Publishing Limited, 2010

use mortar and artillery shells with either self-triggering pressure sensitive fuses or via command wire detonation. After the First World War, as other nations started to deploy tanks, the development of mines increased, leading to their widespread use in the Second World War. At this time anti-personnel mines were also developed, containing smaller quantities of explosive, which were deployed to prevent opposing forces from removing the anti-tank mines.

At a simplistic level, a land mine can be viewed as having two purposes: protective, to defend an area from an opposing force or to attack an opposing force; and tactical, to disrupt, turn, fix and block the enemy force. Mine fields are intended to prevent, slow down or channel the passage of opposition forces to benefit the defending force; the location of a mine field may, therefore, even be highlighted to act as a deterrent. Defensive mining of this sort was used extensively during the Second World War and resulted in considerable tank losses, estimated to be of the order of 20 % of all tank casualties.

When used as a method of attack, mines are generally deployed in locations where troops and vehicles have to pass, such as main roads, and their presence is hidden from opposing forces. This approach is favoured by insurgent, rebel or terrorist groups that do not deploy their own AFVs, and has been seen in recent conflicts in South Africa, the former Rhodesia, Bosnia and, most recently, Iraq. These mines also pose a serious threat to supporting logistics vehicles that, in a conventional conflict, would not expect to encounter mines.

8.1.2 Blast mines

The mines used in the Second World War, and in later conflicts such as Korea and Vietnam, employed the blast effect from high explosives in an effort to immobilise opposition tanks by damaging the wheels, tracks and associated components. Pressure-operated fuses were employed, which initiated the explosive in response to loading by the vehicle's wheel or track. Since the wheels or tracks are located at the sides of a typical AFV, the hull was not the main target and was likely to remain intact. Figure 8.1 shows a typical blast mine.

On detonation of an anti-tank blast mine, a high-pressure shock wave is formed within the explosive filling, which rapidly propagates away from the point of detonation as the material expands violently. In the case of a charge in free air, this rapid expansion forms a high-pressure region in the air adjacent to the charge surface, which propagates further until impinging on a target structure. The incident shock wave is characterised by an instantaneous increase from atmospheric pressure to a peak value, followed by a steady decay, as illustrated in Fig. 8.2.

© Woodhead Publishing Limited, 2010

8.1 TMM1 blast mine.

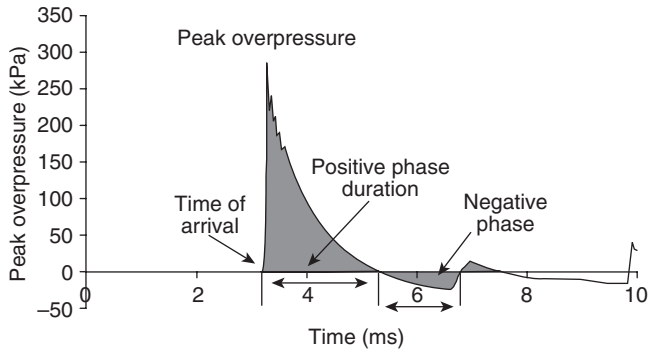

8.2 Typical shockwave associated with an explosive event, illustrating characteristic blast wave parameters.

Over time, the pressure reduces below atmospheric pressure, resulting in a negative phase region. As time passes, the pressure will oscillate one or more times between positive and negative phases. On reaching the target structure, the shock wave is reflected and a pressure applied to the target's surface. The magnitude of this reflected pressure will depend both on the magnitude of the incident pressure wave and the angle of incidence, where the magnitude of the incident wave is controlled primarily by the size of and distance from the explosive charge. The shock wave is followed by the explosive products expanding from the original position of the mine; these products and the surrounding air generate a blast wind. In the case of a confined or buried charge, the rapid expansion of the explosive will also accelerate any neighbouring materials, such as soil or fragments, toward the target (Fig. 8.3), generating a dynamic loading on the structure. In response to the applied loading, the vehicle structure will deform, and may

© Woodhead Publishing Limited, 2010

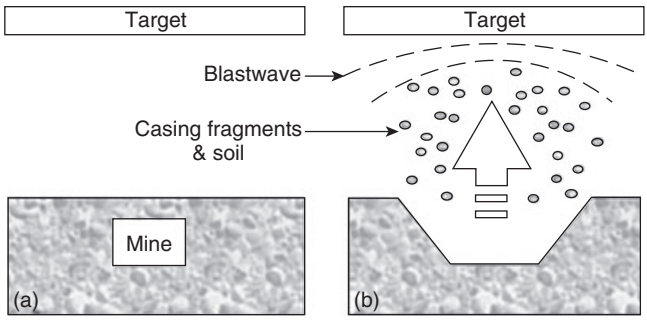

8.3 Schematic view of mine blast event: (a) prior to detonation; (b) post detonation.

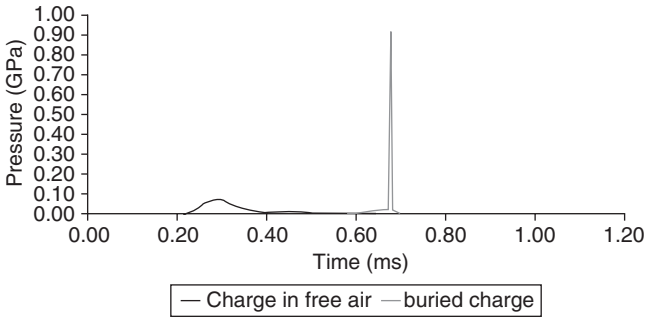

8.4 Comparison of pressure–time histories for free air and sub-soil blast events, with constant standoff distance.

rupture if the strength of the material is exceeded. The vehicle as a whole will then be accelerated in response to the applied impulse.

The loading applied to the structure can therefore be divided into two principal components: blast loading due to the explosive within the device, and particulate loading caused by the impact of soil and casing fragments to which energy has been transferred. The nature of the soil and the depth of burial can significantly influence the contribution from particulate loading as part of the overall load, with the soil's moisture content being of particular importance. The influence of burial on the loading experienced by the target structure is illustrated in Fig. 8.4, which clearly shows that particulate loading can represent a significant proportion of the total applied load. As the depth of burial is increased, the level of confinement and the contribution from particulate loading are increased, although a greater mass of soil must also be accelerated. For this reason, there is an optimum depth of burial, which will depend on both charge size and soil properties.

© Woodhead Publishing Limited, 2010

Fragments from the mine casing have traditionally been treated as minor threats to a vehicle's survivability, since the thickness of the belly plate designed to protect the vehicle from the shock has been sufficient to stop these fragments. As will be discussed in the following section, metal fragments can also form the main threat.

8.1.3 Shaped charge and fragmentation mines

As mine fusing systems developed, anti-tank mines were deployed with tilt-rod, magnetic and seismic fusing systems, which were used to initiate the mine under the belly of the vehicle, causing more severe damage to the hull and significantly increasing the risk of injuries and fatalities, especially if the hull is breached. While vehicle designs evolved to address this type of threat, new warhead types were also developed, using the Munroe shaped charge principle (which uses shaping of the explosive to focus the explosive energy on the metal liner) to form a high-velocity plasma jet or the Misznay Schardin principle (which uses a sheet of explosive that expands primarily perpendicular to its plane) which interacts with the metal liner to form a self-forging fragment, also termed an explosively formed projectile (EFP). Depending on the shape of the liner in the warhead, therefore, a range of effects can be generated. Figure 8.5 illustrates the influence of liner shape on weapon effects.

With a conical metal liner, the liner collapses as the detonation wave within the explosive moves along the warhead from the apex of the cone to the base. The metal remains a solid, but is termed a plasma as it possesses a sufficiently high velocity (7000–8000 m/s at the tip) that both it and the target material on impact behave as though they were liquids and flow hydrodynamically (Coutney-Green, 1991). The material at the base of the

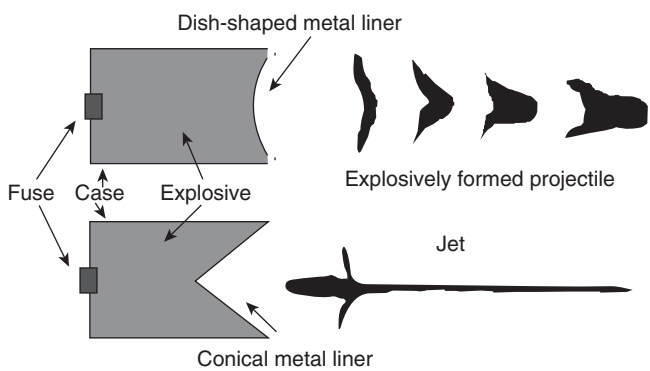

8.5 Effect of liner shape on weapon effects.

© Woodhead Publishing Limited, 2010

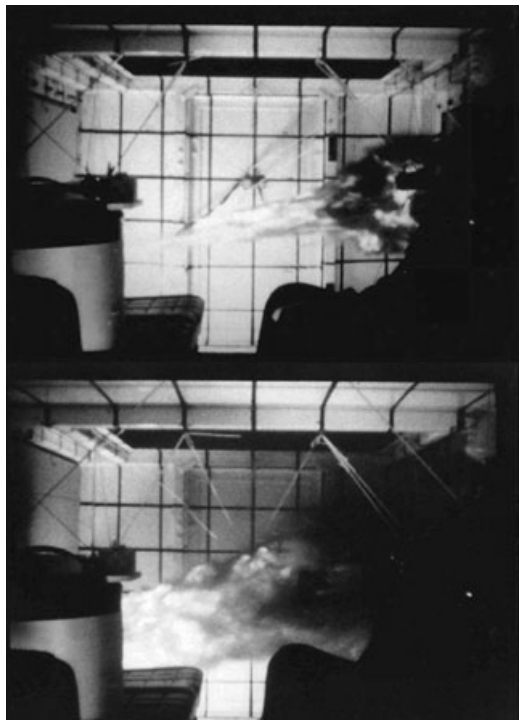

8.6 Effect of shaped charge warhead on vehicle interior.

cone forms a heavier, slower moving slug with a velocity of between 300 and 800 m/s. These weapons are commonly called shaped charges or chemical energy (CE) weapons, and include the ubiquitous rocket propelled grenade (RPG), which represents a prime example of an extremely portable, shoulder-launched CE weapon.

The narrower and longer the jet formed, the more penetrative the warhead. Associated with the hole created by the jet are a large number of fragments (termed spall) which scatter across the inside of the vehicle. This process is referred to as behind armour effects (Fig. 8.6). To mitigate the effect of spall a plastic spall liner is often employed, which is discussed in Section 8.3.1.

With a dish shaped liner, a self-forging projectile is created, which can remain effective at a significant distance from the target. The projectile is not formed instantly, and an optimum standoff distance is required to achieve maximum penetration capability. Similar to the shaped charge warheads discussed above, the projectile can generate significant behind armour effects.

© Woodhead Publishing Limited, 2010

8.7 TMRP-6 mine sectioned view.

Mines using the Misznay Schardin principle had been deployed in the Second World War, but their effectiveness was dramatically demonstrated in the Bosnian conflict, which saw widespread use of the former Yugoslav designed TMRP-6 mine (Fig. 8.7). This mine contains approximately 5 kg of explosive and produces a fragment, termed a slug, weighing in the order of 0.5 kg with an acceleration of over 2000 m/sec^2 (Beaver, 1996). The combination of large fragment mass and velocity results in a significant amount of kinetic energy, with the slug capable of penetrating 40 mm of armour from a distance of 800 mm.

In recent years, improvised versions of the above mine types have frequently been deployed, either buried or placed at the side of the road, by insurgent groups in Iraq and Afghanistan to attack members of the coalition forces. While many of these IEDs rely purely on blast effects to immobilise their targets, significant numbers of pre-fragmented or fragment-forming devices have also been employed.

The amount of explosive in a commercially available mine ranges from tens of grammes through to tens of kilogrammes. As discussed above, however, with asymmetric warfare, insurgents are looking to use improvised explosives to destroy vehicles. To do this, the amount of explosive is generally much greater, and mine attacks such those experienced by Israeli forces have utilised buried charges in excess of 100 kg. While it is possible to add thicker plates to the bottom of vehicles to resist this level of threat, this usually degrades the overall performance of the vehicle; the designer/user of the vehicle must take a more pragmatic view, understanding that

© Woodhead Publishing Limited, 2010

this level of threat is not the norm, and that vehicles should be designed to meet the more commonly occurring threats. Surveys of commercially manufactured blast mines indicate that the most likely encountered mine will weigh less than 10 kg; for this reason, many vehicles are designed to resist 10 kg of explosive under the belly of the hull. The use of stacked mines, however, is a growing threat, and mines comprising up to 20 kg of explosive are not uncommon.

8.2 Occupant injury mechanisms

In addition to concerns regarding vehicle integrity, the safety of military personnel is critical. Regardless of whether or not the vehicle's hull is ruptured by the applied loading, vehicle occupants will be exposed to mechanical effects such as shock, structural deformation and vertical impulse loading. In cases where hull rupture does occur, occupants may also be exposed to blast overpressure, weapon and secondary armour fragments, fire and gases. The effect of mines on vehicle occupants can be separated out into three types: primary, secondary and tertiary (Smith and Hetherington, 1994). Primary injuries relate directly to the pressure and duration of the blast wave; secondary injuries relate to the impact of fragments or other debris; and tertiary effects occur when the body suffers significant accelerations or decelerations (e.g. spine injury from collision with seat and head injuries caused by contact with the vehicle structure).

On the assumption that hull integrity can be maintained, the principal causes of occupant injury are related to local and global acceleration effects (NATO RTO, 2007). Severe lower leg injuries are very common in cases where the vehicle's inner floor or foot plates are in contact with or in close proximity to the bottom of the hull, which is rapidly accelerated by the blast. Pelvic and spinal injuries can also be severe in cases where the seat is mounted on the floor of the occupant area and, for this reason, seats in mine-protected vehicles are frequently mounted to the roof or sides.

Even when good measures have been taken to reduce the risk of injuries due to localised deformations of the vehicle's structure, life threatening injuries can occur as a result of global vehicle accelerations and decelerations, as the vehicle is thrown into the air. As well as pelvic and lumbar spine injuries, this form of loading can result in high neck loads, either as a direct result of the acceleration itself or, in the absence of an appropriate restraint system, due to contact with the vehicle's roof. In an effort to reduce these effects, sophisticated seating systems are frequently employed, which use a range of energy absorption mechanisms including hydraulic dampers, springs, crushable structures and foams.

© Woodhead Publishing Limited, 2010

8.3 Integrated vehicle survivability

There are many different ways of increasing the overall level of occupant protection against the range of threats to which modern AFVs are exposed. This concept is frequently discussed in terms of the 'survivability onion' (Fig. 8.8), which illustrates the different layers of survivability and the trade-offs necessary in vehicle design. In this model, installed armour, including any internal spall liner, effectively forms the last line of defence against attack, with other factors such as physical size and mobility also playing a significant role.

A common example of an AFV design trade-off is the vehicle ground clearance and associated vehicle height. In order to prevent being targeted by opposition forces, AFVs may be designed to be close to the ground, as this enables them to hide behind buildings and folds in the ground while maintaining sufficient ground clearance to traverse the terrain. For a given mass of explosive, however, the severity of a mine impulse on the vehicle's floor is inversely proportional to the cube root of the distance between the explosive and the vehicle. Addressing this reduction in protection by increasing the thickness of vehicle's floor will increase the overall weight of the vehicle, leading in turn to a reduction in mobility. Due to the need for compromise between a number of competing requirements, large sums of money have been invested to develop optimised mine resistant vehicles.

The improvement in protection made possible by increasing the distance between the mine and the vehicle's floor is one of the key design parameters used to increase occupant survivability, and is frequently used on mine

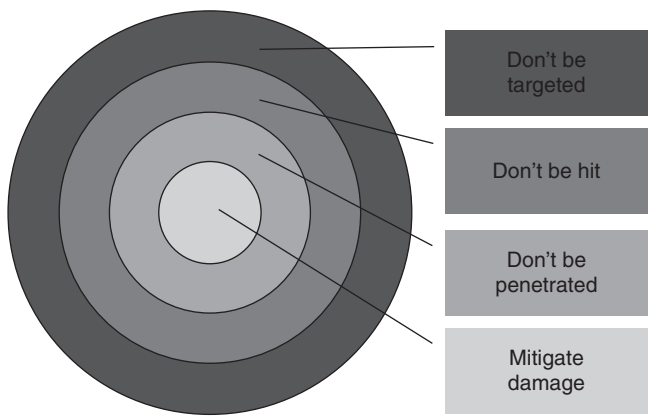

8.8 The survivability onion.

© Woodhead Publishing Limited, 2010

8.9 BAE Systems RG31 (image courtesy of BAE Systems).

resistant armoured patrol (MRAP) vehicles. Typical of this type of vehicle is the BAES RG31 (Fig. 8.9) which not only attempts to raise the height of the vehicle's floor but also uses shaping of the hull floor to form a 'V' shape hull, in an attempt to deflect the mine blast while simultaneously increasing the natural stiffness of the floor. This vehicle's design was based on the developments of the South African military research which produced the Casspir and Buffel vehicles. A key worker in this area has been Dr Vernon Joynt (Joynt, 2008), who has investigated the influence of vehicle shape and components such as wheels on the blast resistance of vehicles.

A second technique that may be employed, either in combination with a 'V' shaped hull or in isolation, is the use of an internal floor, separating the response of the outer hull from the floor of the occupant compartment. This is beneficial in reducing the risk of lower limb injuries caused by rapid floor deformations, and helping prevent primary blast injuries caused by pressure entering the occupant compartment. Use of an internal floor, however, requires either a reduction in internal volume, a reduction in ground clearance, or an overall increase in vehicle height. Increasing the vehicle's overall height, which raises the centre of gravity, can also lead to vehicle instabilities and increase the possibility of vehicle roll over.

8.3.1 Spall liners

Despite the improvements that can be made in occupant survivability, it is important to remember that protection can never be guaranteed, and that all vehicles are potentially vulnerable to threats which exceed those considered during their design. This is particularly relevant in the case of light

© Woodhead Publishing Limited, 2010

armoured vehicles, where the ability to carry the mass of applied armour is limited by the need to retain a high level of mobility and, in some cases, the strength and stiffness of the base vehicle chassis.

Even if the metallic hull of a vehicle is not penetrated by a projectile, the resulting shock on the metal structure can generate scabs of metal, also called spall, from the inside surface. These 'secondary projectiles' can, in themselves, cause injury both to vehicle occupants and equipment. This was seen in the first tanks produced during the First World War and led to the use of crude body armour being worn by the tank operators, principally to protect their faces from impact.

Due to the risk of threats penetrating the vehicle, a spall liner – this being either a woven fabric blanket or a solid plastic/composite plate – is generally required inside the metal hull of MRAP vehicles and AFVs. The purpose of the spall liner is to minimise the spread of primary and secondary projectiles within the vehicle in the event of an armour overmatch. Its effectiveness is measured in terms of the spread of fragments, which may be represented by a cone, as illustrated in Fig. 8.10. The smaller the cone angle of fragments, the higher the probability that a particular occupant will survive the penetration of the hull, and the better the spall liner's performance. Traditionally, the spall liner material is non-structural and non-metallic, and is attached to the metallic hull purely to mitigate damage due to the threat, protecting the crew and internal components.

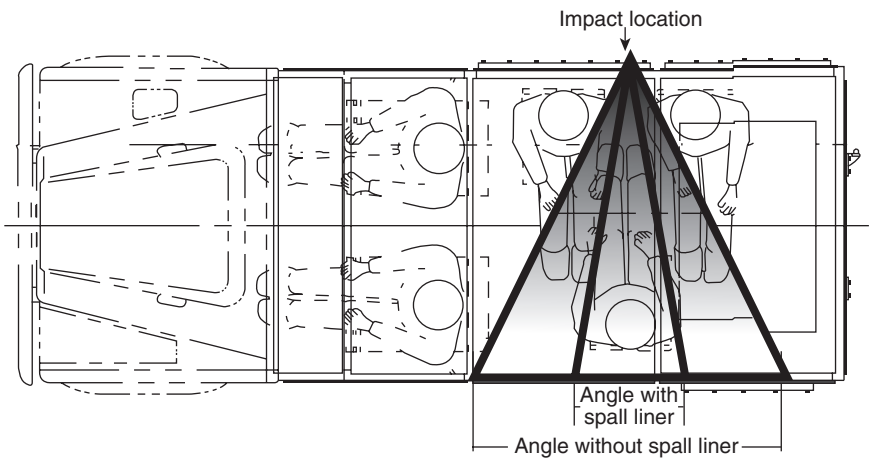

8.10 Illustration of debris cone within a vehicle resulting from an armour overmatch event.

© Woodhead Publishing Limited, 2010

8.3.2 Requirement for lighter weight armoured fighting vehicles (AFVs) driving the use of composite materials

The requirement for lighter weight vehicles is driving the investigation of composite materials for future AFV designs. As discussed earlier, protected vehicles must balance a range of competing requirements, including protection, mobility and load carrying capacity. The need to improve the survivability of the overall system, addressing all layers of the 'survivability onion', is therefore providing the impetus for the development of lighter-weight vehicle structures using composite materials. Traditionally, armour materials such as ultra high hardness steels, lightweight polymers and ceramics have been parasitic in nature, providing increased occupant protection at the expense of payload and mobility, and requiring stiffer base structures to support their added weight. For this reason, fibre-reinforced composite materials are of significant interest in the design of blast-protected vehicles, providing a unique combination of structural performance and occupant protection. Furthermore, the use of composite in place of a conventional metallic hull reduces or even eliminates the need for a dedicated spall liner, since the debris produced during an overmatch event is much less damaging than the relatively large secondary fragments produced when a metallic target is overmatched.

8.4 The use of composite materials in vehicles

The use of composite materials in military vehicles has been proposed for a number of years, but has been typically limited to spall liners and a limited number of components such as ammunition bins. One exception is the CAV 100 vehicle from NP Aerospace, which uses a composite pod on a metal chassis. In this case, the composite pod fulfils multiple roles, forming the structure of the rear of the vehicle as well as providing protection against ballistic, blast and fragmentation threats.

One of the reasons for the apparent reluctance to use composite materials is that current AFV manufacturers are not well-versed in the design and production methods needed to produce a composite hull. The incompatibilities of composite materials with existing metals processes include different design requirements (e.g. anisotropy and inhomogeneity), manufacture (processability, dimensional control, cycle times, temperature tolerance and assembly methods), and performance (coefficients of thermal expansion, electrical conductivity and ballistic efficiency). While substituting individual metal components with composite replacements can lead to both weight and cost reductions alongside improved durability, the dimensions of the composite components must conform to those of existing component

© Woodhead Publishing Limited, 2010

designs in order to allow interchangeability between units. This design approach may lead to a less than optimum design for the composite component, and the potential weight savings and performance improvements for the composite component may not be fully realised. In order to achieve the maximum advantage from composite materials, the complete vehicle design strategy must be re-evaluated to effectively demonstrate the advantages offered by composite materials. Moving from incremental, part-by-part substitutions to whole platforms shifts the emphasis from making composites compatible with metals to exploiting composites' unique benefits for solving system issues such as hull weight, hull stiffness and the financial cost per hull.

Shaped charge mines have not been a common threat, due in part to the variation in penetration capability they exhibit with standoff distance; EFP mines, which are less sensitive to this distance, are therefore a major threat to vehicles deployed against insurgents. EFP mines are easily manufactured and can be fired from distances in excess of 10 m from the target with potentially devastating effects. This has led to the use of increasingly heavy armour systems on the lower sides of vehicles. The need to retain the required level of vehicle mobility, however, means that overmatch is a significant possibility, and a composite spall liner is necessary to minimise behind armour effects. As the thickness of the spall liner increases, the use of a system which fulfils both structural and protective roles offers increasing benefits.

8.4.1 The development of a composite AFV

The Advanced Composite Armoured Vehicle Platform (ACAVP) was a materials demonstrator programme which showed that glass fibre composite materials could be used to form the hull of an AFV (French, 1999). In this application, the composite acts both as a structural material, capable of carrying the loads imposed from the suspension/running gear and associated equipment, and as a ballistic material to provide the required level of ballistic and spall protection. ACAVP was the first all composite hulled AFV to be produced that relied entirely on the composite hull material to carry directly the loads reacted at the hull suspension joint, without the need for supporting metallic structures. The ACAVP hull was manufactured using a variation of resin transfer moulding (RTM), called vacuum infusion moulding (VIM) to produce a glass fibre-reinforced plastic (GFRP) hull. The vehicle, illustrated in Fig. 8.11, was evaluated by the British Army between March 2000 and March 2001.

As well as forming an integrated structural spall liner, composite hulls can also improve performance against mine blast loading by eliminating the presence of weld joints, which are used in metallic hulls to join the belly to

© Woodhead Publishing Limited, 2010

8.11 The Advanced Composite Armoured Vehicle Platform (ACAVP).

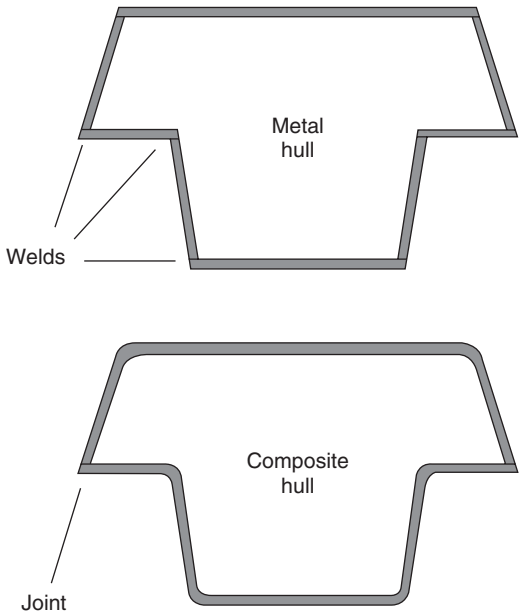

8.12 Location of joints in metal and composite hull designs.

hull side plates. Due to their location, these welds can be susceptible to cracking under the pressure of the mine, allowing the blast to enter the hull, as in Fig. 8.12.

Furthermore, composites can be easily shaped, at no additional cost, to form a 'V' shaped hull to deflect blast pressure. For metal hulled AFVS

© Woodhead Publishing Limited, 2010

subjected to a track-initiated mine blast, the 'V' reduces the blast pressure on the hull side plate belly joint, while simultaneously increasing the stiffness of the floor and reducing the level of deformation witnessed under loading from a belly mine attack (Ogorkiewicz, 1997). In the case of metallic hulls, a 'V' shaped profile can be created by welding or bending. For welded profiles, the apex of the 'V' effectively represents a potential weak point on the floor of the vehicle. For profiles formed by bending, heavy presses are required, while many metallic armour materials are not amenable to bending; this is particularly true in the case of deep 'V' profiles, which may be desirable for modern MRAP vehicles. By contrast, a composite hull bottom can be produced in one piece, including shaping, while the hull can also be designed such that the joints are above the region directly affected by the blast. This approach was used on ACAVP; Fig. 8.13 shows the top composite moulding being placed on the lower composite hull moulding.

A major conclusion from the ACAVP programme was that to make significant reduction in the weight of future AFVs the use of carbon fibre composites should be considered in place of glass fibre composites. This is a result of the GFRP material's relatively low modulus and the need to thicken the structure to provide adequate levels of stiffness. A material with a higher level of stiffness such as carbon fibre reinforced polymer (CFRP) can lead to further weight reductions, but the design also needs to offer adequate ballistic protection. For many ballistic threats it is recognised that this will require the use of CFRP in combination with a range of other

8.13 ACAVP lower hull moulding.

© Woodhead Publishing Limited, 2010

materials (for example ceramics and titanium). To assess these issues a European research programme called the Carbon Armoured Fighting Vehicle (CAFV) programme (Wright and French, 2008) has been conducted to explore the use of CFRP for AFVs.

8.4.2 Use of composites in civil protected vehicles

Composite materials are frequently used in discreetly armoured civilian vehicles due to the strict weight limits imposed by the use of original equipment manufacture (OEM) base vehicle components. This is particularly true in the case of protection against high-velocity rifle rounds, where substantial weight savings can be achieved through the use of armour solutions employing lightweight ceramic and composite materials in place of more traditional metallic armours. Due to the need to maintain an appearance as close as possible to that of the original base vehicle, and the limited amount of space available, composites are usually installed in vehicle doors. There is a need, however, to ensure strong integration between the installed composite armour and the surrounding metallic frame in order to prevent the composite from being forced into the vehicle under blast loading. This is particularly important in the case of lightweight polyethylene armours, which are non-structural, and tend to tear away from any securing bolts.

8.5 Mine blast loading of composite vehicle structures

In assessing the performance of composite materials against blast loading, and comparing their performance against metallic solutions, it is critical that the testing and associated loading applied to the material is representative of that experienced during a full-scale mine blast event. This is particularly true in the case of small-scale trials, which may be used as an initial assessment of various candidate materials due to the costs – financial and time – associated with full-scale mine blast testing. Scale testing is particularly relevant for composite materials due to the large number of possible variables, such as matrix type, reinforcement type and layup, which means there are many test panel material combinations to evaluate.

As described previously, much of the complexity associated with mine blast testing relates to the position of the mine, which is generally buried beneath a layer of soil, or at least partially buried such that the top surface of the mine is flush with the ground. To eliminate the variability of the soil, a number of test procedures have been developed that rely purely on the blast loading due to the explosive. These test procedures seek to represent the loading imparted by the soil using combinations of charge shape, confinement and standoff distance. A test procedure outlined in Allied

© Woodhead Publishing Limited, 2010

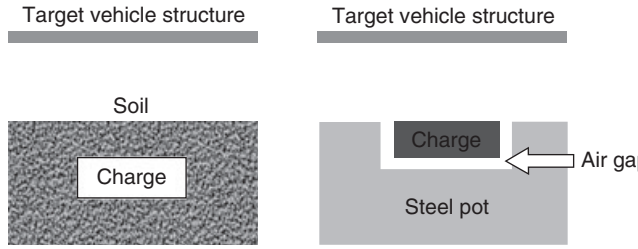

8.14 Position of mine relative to target structure for soil (left) and pot (right) blast test procedures outlined in AEP55 Vol. 2 (NATO, 2006).

Engineering Publication 55 Volume 2 (NATO, 2006), for example, recommends the use of a steel pot to partially confine the explosive charge: blast wave reflections within the pot act to increase the total momentum applied to the target, and compensate to some extent for the absence of particulate loading effects (Fig. 8.14). This approach was used on the CAFV project to validate the small-scale testing and modelling undertaken in the earlier phases of the programme.

The effect of blast loading on a composite target structure can be characterised in terms of the peak overpressure, impulse and blast focussing, as follows:

Peak overpressure

Provides a measure of the maximum instantaneous load experienced by the target structure. During blast loading, the impact of the high-pressure shock wave on the outer surface of the target generates a compressive stress wave within the material. If this instantaneous pressure exceeds the compressive strength of the target material, some degree of crushing failure may occur. The stress wave then propagates through the material until it reaches the rear face of the target, where it is reflected as a tensile wave. As before, if the amplitude of this wave exceeds the tensile strength of the material, further damage may occur. In composite materials, the compressive stress wave can cause crushing failure of the polymeric matrix, while the reflected tensile wave is responsible for localised through-thickness delamination. The floor of the vehicle's hull will normally experience the highest peak pressure values, which reduce substantially as they propagate through the hull to the roof.

Impulse

Provides a measure of the energy transferred to the target structure, and may be determined from the area underneath the pressure–time curve for

© Woodhead Publishing Limited, 2010

the blast loading event. To a large extent, impulse controls the level of target deflection, which can result in both tensile and compressive fibre failure in composite materials. The rate of energy transfer, as defined by the slope of the impulse–time curve, is also important as this controls the strain rate experienced by the target material.

Blast focussing

Simply describes the localisation of loading over a relatively small area of the target surface. In mine blast events, this localisation occurs as a result of both explosive charge geometry and confinement, but it can also be influenced by stand off distance (between the explosive and target), since the distance (and angle of incidence) between the detonation point and the target surface will vary with position across that surface. Where a target is subjected to a highly localised blast load, the substantial variation in peak pressure across the target surface can result in shear damage and through-thickness material failure, referred to as 'shock holing'. For more evenly distributed loading, through-thickness material failure is less likely to occur, although there will be a greater likelihood of failure around joints and corners.

8.5.1 Mine blast testing of composites

For composite AFVs, the effect of blast loading on the vehicle's structure can be assessed and quantified in a number of ways. Of greatest interest to vehicle designers are the threshold conditions for hull rupture, which can be defined as the combination of charge size and standoff distance required to cause through-thickness failure of the hull. In the event of hull perforation, blast pressure and gasses can enter the occupant area, significantly increasing the risk of primary blast injuries, while the likelihood of secondary injuries due to fragment impacts is also increased. During experimental assessment, one strategy for identifying threshold conditions for rupture can be by maintaining a constant explosive standoff distance and increasing the charge size. An alternative approach would be the use of a constant charge size and gradually reducing the standoff distance until rupture occurs. In general, it is advisable to use a set standoff distance and control the level of blast loading by changes in charge size, as the cube root relationship between standoff distance and peak overpressure can make it difficult to control the level of blast loading through changes in standoff distance. This procedure was used on the CAFV programme, where small-scale testing was undertaken using 800 mm × 800 mm targets. Figure 8.15 shows the steel frame used to hold the composite plates to be tested. The sketch provides details of the experimental set-up including the use of

© Woodhead Publishing Limited, 2010

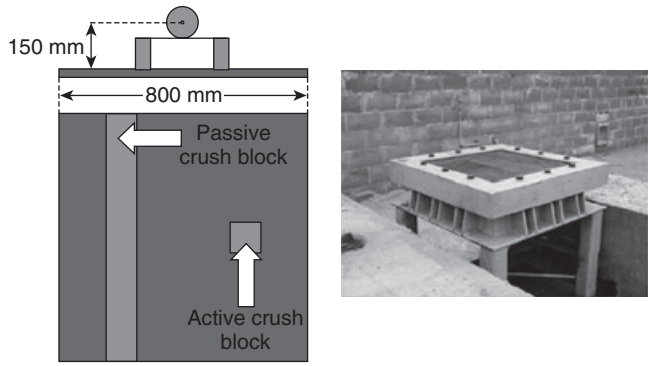

8.15 Small-scale trials arena used to screen candidate materials during CAFV research programme.

active and passive crush block to measure the deflection of the plates subjected to the blast load from the sphere of explosive. The location of the explosive was arranged to replicate the focussed blast loading from a steel pot as described in Allied Engineering Publication 55 Volume 2 (NATO, 2006).

By quantifying blast resistance in this manner, different materials can be compared on a weight-for-weight basis to identify a ranking of material performance which can be used to initiate the development of an optimised solution.

As well as considering the threshold conditions for rupture, vehicle designers must also take into account the effect of less severe blast loads on the residual strength and stiffness of the hull. The vehicle structure must be designed against a series of well-defined design loads, which relate to both the applied mass being carried and the loads imparted through the vehicle's running gear as a result of the stated mobility requirements. Depending on how close the applied loading conditions are to the threshold for rupture, significant material damage can occur, including global and localised delamination, matrix cracking and fibre fracture. This damage will have an adverse effect on the load carrying capacity of the hull and, depending on its extent, may render the vehicle incapable of undertaking future missions. For this reason, there is a need for non-destructive testing techniques which allow the residual strength of the hull to be accurately determined.

Finally, there is a need to determine the local and global deformations and accelerations of the hull in response to the blast load, and to assess their implications in terms of tertiary injuries to vehicle occupants. The overall mass of the vehicle will impact on the global vertical acceleration, while the stiffness of the materials used will influence the extent and rate

© Woodhead Publishing Limited, 2010

of localised hull deformations. As discussed previously, MRAP vehicles may employ an inner floor to reduce the risk of perforation into the occupant area and limit the extent of injuries due to floor accelerations. In the case of low-stiffness materials, therefore, it may be necessary to increase the distance between the outer and inner floor, leading to a corresponding reduction in internal space or increase in the overall height of the vehicle.

8.5.2 Design tools for composite vehicle structures for mine protection

Due to the cost of full-scale mine blast testing and the potentially large test matrix involved, dynamic finite element analysis (FEA), using software such as ANSYS AUTODYN® and LS-DYNA®, is frequently used to perform simulations of mine blast events on candidate hull designs and materials (Ansys Incorporated, 2007, a, b; Livermore Software Technology Corporation, 2007). The mine blast event may be explicitly represented using fully coupled blast and vehicle models, or implicitly represented using pressure histories applied to the base of the vehicle hull. While the latter approach does not take into account the interaction between the blast load and hull (the applied load at any given time will change in response to target deformation) or angle of incidence effects, it is much more computationally efficient than the former, since explicit blast models require a significant number of elements to achieve the desired level of accuracy.

The use of load curves is particularly beneficial when comparing the performance of a range of candidate materials against a well-defined set of standardised threats, such as those outlined in STANAG 4569 Annex B (NATO, 2004). Identical blast loads can be applied to a range of armour materials and/or designs in order to identify the most promising solutions for further investigation. Detailed blast models can be run to determine a set of pressure–time histories for each level of threat (Fig. 8.16) that can then be applied to a structural model of the hull, with the added advantage that different software packages can be used to run the blast and structural models. Care should be taken, however, where hull shape and standoff distance vary between candidate designs, as these effects cannot be accurately represented without the use of a coupled simulation approach. A fully coupled mine blast model is shown in Fig. 8.17 which illustrates the development of the blast load onto the hull floor using a half section of a vehicle hull. Figure 8.18 illustrates the effects of hull shaping on the spread of the blast pressure across the floor and the resulting transfer of moment which results in a global upward vehicle acceleration.

The results of this modelling can be used to assess the likely loading placed on vehicle occupants including spine loading which can lead to vertebrae damage. Within dynamic analysis models, material models are

© Woodhead Publishing Limited, 2010

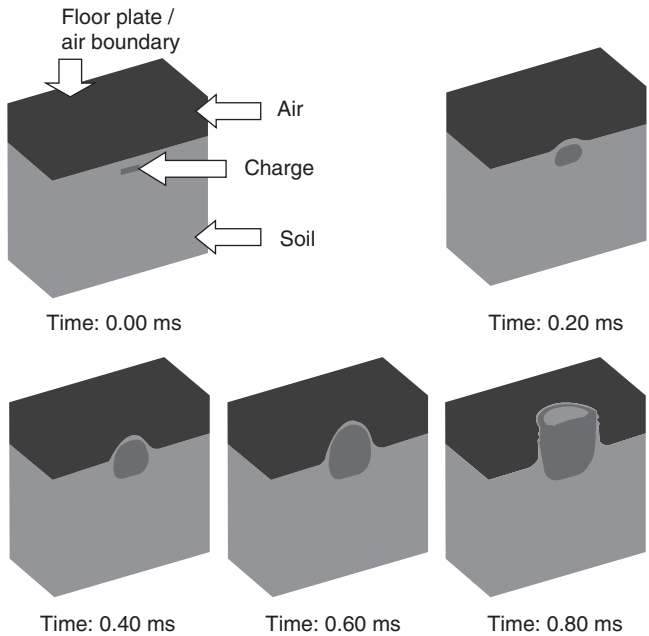

8.16 Blast only model used to generate load curves for application to structural hull model.

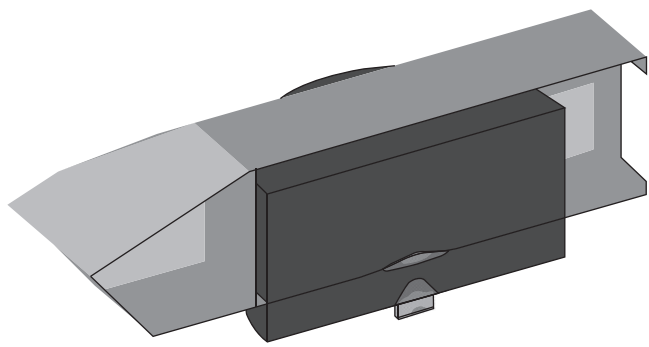

8.17 Example of fully coupled model.

required to describe the behaviour of the air, explosive, soil and composite target. While air and a large number of explosives are relatively well characterised, accurate descriptions of soil and composite material behaviour are more difficult to achieve. It is well known, for example, that the moisture content of the soil can have a significant effect on the degree of charge confinement and, therefore, the load applied to the vehicle hull (Fiserova,

© Woodhead Publishing Limited, 2010

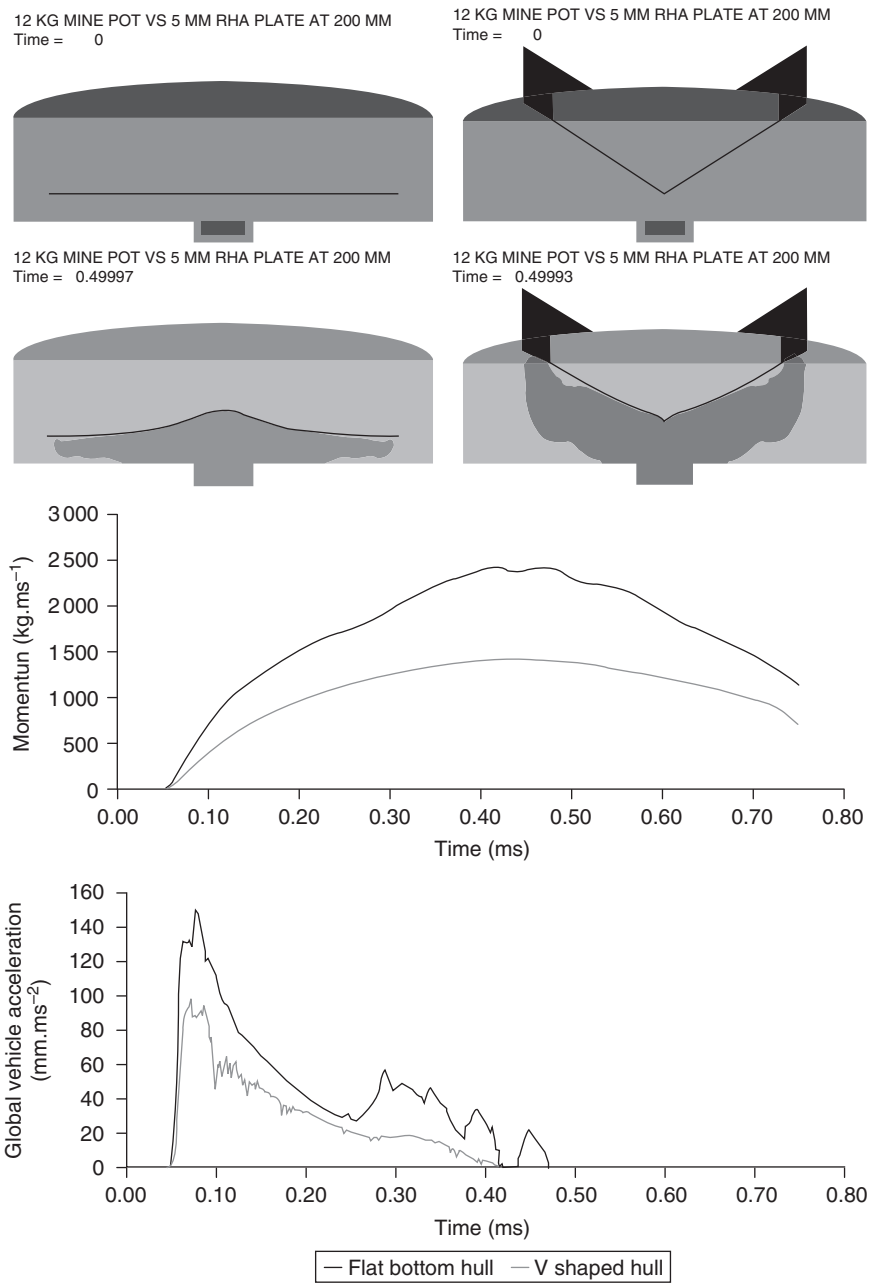

8.18 Fully coupled blast model used to investigate the effect of hull shaping on momentum transfer and global vehicle vertical acceleration.

© Woodhead Publishing Limited, 2010

2006; Grujicic *et al.* 2008). While some steps have been taken to account for the effect of moisture content on the constitutive properties of soils, research in this area is still at a relatively early stage.

The material models used to describe the composite vehicle hull should accurately describe the stiffness, strength and post-failure energy absorption characteristics of the laminate at a wide range of strain rates, and material characterisation is further complicated by the anisotropic nature of the laminate. While strength and stiffness are relatively well understood, and can be modelled with a reasonable degree of accuracy, modelling post-failure response and quantifying the energy absorbed presents a significant challenge. Composite materials are capable of absorbing large amounts of energy through failure mechanisms including fibre and matrix failure, fibre/matrix interface failure and delamination, and the energy absorbed through these mechanisms must be represented in order to accurately predict the threshold conditions for rupture. Due to the large number of variables for composite materials in terms of reinforcement materials, fabric constructions, matrices and layups, detailed characterisation of a number of candidate materials may be prohibitively expensive where a large number of candidate materials are under consideration. Simple brittle failure models, without a description of the energy absorbed through active failure mechanisms following the initiation of damage, are conservative in nature. This can lead to the over engineering of a composite vehicle's structure; experimental assessment is therefore still key to weight-efficient design and development of composite vehicle structures.

A further difficulty introduced when considering the response of full-scale vehicle structures to blast loading is the need to retain sufficient through-thickness resolution within the model to predict when catastrophic rupture of the hull is likely to occur, without using an excessively large number of elements. Unlike metallic vehicle structures, which are frequently modelled using shell elements, the relatively thick composite laminates used to construct an AFV hull can absorb an appreciable amount of energy due to through-thickness failure mechanisms. Since these failure mechanisms are influenced by the through-thickness transmission of stress waves within the laminate, they cannot be accurately represented using shell elements. For this reason, it may be beneficial to employ localised model refinement, where a refined solid element mesh is used to represent the region of the vehicle directly loaded by the blast, while a coarser shell element mesh is used to represent more global effects.

Despite the identified difficulties, numerical modelling is a useful tool in terms of the ability to compare the effect of experimental variables, key material properties and target variables on the response to blast loading. The potential contribution of finite element modelling to research and design can be summarised as follows:

© Woodhead Publishing Limited, 2010

- enables rapid, low-cost comparison of candidate materials (providing accurate material models are available);
- assists experimental design (scaling, charge size, boundary conditions, etc.);
- improves understanding of blast load/target interaction effects;
- allows assessment of structural design factors (joints, corners etc.);
- enables optimisation of vehicle geometry to minimise the effects of blast on vehicle occupants.

8.6 Conclusion

The threat from mines plays a major role in the design of AFVs from specialist mine resistant vehicles through to main battle tanks. The requirement to produce lighter vehicles necessitates that materials used in the design of AFVs must provide a multifunctional response in terms of being able to contribute to the vehicle's structural and ballistic requirements, including the need to minimise the overmatch of the armour and provide spall protection. This is a key discriminator when deciding between metallic and composite materials for the construction of a vehicle hull. The ACAVP and CAFV programmes have demonstrated the use of composites for the construction of future AFVs by providing evidence that alternatives to existing metallic hulls, in terms of both performance (defined by ballistic, blast and structural requirements) and cost are viable.

With the varied range of materials available to the AFV designer, the need for modelling tools to reduce the amount of costly physical testing is clearly beneficial. The modelling of blast against composites is still a relatively new area of research. Methods are still being developed to ensure the full range of energy absorbing mechanisms – displayed when a composite structure fails – are addressed in order to be able to predict both failure and damage growth.

Further work is also required to fully explore all potential benefits of composites for AFVs, with particular reference to optimised manufacturing processes to reduce costs, optimised structural design to reduce weight, and durability assessment. AFV manufacturers will remain reluctant to use composites for their vehicle designs until fully working composite vehicles have been successfully demonstrated over a period of time so that current unknown issues, such as long-term durability and associated whole life costs, have been determined. This is, therefore, a key requirement that needs to be addressed in future research programmes.

8.7 References

ANSYS INCORPORATED (2007a), *AUTODYN User's Manual Version 11*, Canonsburg, PA.

© Woodhead Publishing Limited, 2010

ANSYS INCORPORATED (2007b), *Composite Modelling in AUTODYN User Documentation*, Canonsburg, PA.

BEAVER P (1996), New mines spark call for vehicle standards, *Jane's Defence Weekly*, 4 September.

COUTNEY-GREEN P R (1991), *Ammunition for the Land Battle*, Brassey's (UK) Ltd, London, UK.

FISEROVA D (2006), *Numerical analyses of buried mine explosions with emphasis on effect of soil properties on loading*, PhD thesis, Cranfield University Defence College of Management and Technology, Cranfield, UK.

FRENCH M (1999), ACAVP – demonstrating the potential use of composite materials for future AFVs. In *4th European Advanced Fighting Vehicles Symposium*, 9–11 February, RMCS Shrivenham, UK.

GRUJICIC M, PANDURANGANA B, QIAO R, CHEESEMAN B A, ROY W N, SKAGGS R R and GUPTA R (2008), Parameterization of the porous-material model for sand with different levels of water saturation, *Soil Dynamics and Earthquake Engineering* **28**(1), 20–35.

JOYNT V (2008), The key four threats to MRV, *XIIIth European Armoured Fighting Vehicle Symposium*, May, Cranfield University, Cranfield, UK.

LIVERMORE SOFTWARE TECHNOLOGY CORPORATION (2007), *LS-DYNA Keyword User's Manual Version 971*, Livermore, CA.

NATO (2004), *Protection Levels for Occupants of Logistic and Light Armoured Vehicles*, Standardisation Agreement 4569 Edition 1, North Atlantic Treaty Organisation, Brussels, Belgium.

NATO (2006), *Procedures for evaluating the protection level of logistic and light armoured vehicles*, Allied Engineering Publication 55 Volume 2 Edition 1, North Atlantic Treaty Organisation, Brussels, Belgium.

NATO RTO (2007), *Test methodology for protection of vehicle occupants against anti-vehicular landmine effects*, RTO-TR-HFM-090, North Atlantic Treaty Organisation Research and Technology Organisation, Brussels, Belgium.

OGORKIEWICZ R M (1997), Improved mine protection shields armoured vehicles, *Jane's International Defense Review*, 030/004.

SCHNECK W C (1998), The origins of military mines Part II, *Engineer Bulletin*, **28**(4), 44–50.

SLOAN C E E (1986) *Mine Warfare on Land*, Brassey's Defence Publishers, London, UK.

SMITH P D and HETHERINGTON J G (1994), *Blast and Ballistic Loading of Structures*, Butterworth-Heinemann Ltd, Oxford, UK.

WRIGHT A and FRENCH M (2008), The response of carbon fibre composites to blast loading via the Europa CAFV programme, *J Mater Sci*, **43**: 6619–6629.

© Woodhead Publishing Limited, 2010

9

Blast protection of buildings using fibre-reinforced polymer (FRP) composites

P. A. BUCHAN and J. F. CHEN, The University of Edinburgh, UK

Abstract: The effect of blast loads on buildings is of relevance to engineers in the context of either blast protection against accidental or malicious explosions or intentional demolition of old buildings, with the former being the focus of this chapter. Explosions in the proximity of vulnerable buildings may cause considerable damage and loss of life. The US Department of State reported that globally in 2007 there were more than 14 000 terrorist attacks, killing more than 20 000 people. As a result there is often a requirement to increase the blast protection of many types of buildings which have typically not been designed to resist an explosion and to include blast protective design into new buildings. This chapter presents an overview of protecting buildings from explosions and then focuses on the use of fibre-reinforced polymer (FRP) composites for this purpose.

Key words: blast protection, blast retrofitting, polymer-matrix composites, FRP, buildings, explosions.

9.1 Introduction

The effect of blast loads on buildings is of relevance to engineers in the context of either blast protection against accidental or malicious explosions or intentional demolition of old buildings, with the former being the focus of this chapter. The behaviour of buildings under explosions has been of particular interest after accidental explosions such as at Ronan Point tower block in London in 1968. In this fatal incident the tower block suffered a partial collapse due to a natural gas explosion. As a result, building regulations in the UK were improved to ensure the safety and integrity of buildings in the event of an explosion (Pearson and Delatte, 2005). A focus on the behaviour of buildings under intentional explosions has occurred during World War II, through the Cold War and now as a result of global terrorism such as the attack on the Khobar tower in Saudi Arabia in 1996 (Fig. 9.1).

Buildings which are vulnerable to accidental explosions, terrorist attack or both are often government buildings, corporate headquarters, military establishments, transport terminals, public buildings, grain storage facilities, together with chemical, petroleum and nuclear plants. Attacks directed towards vulnerable buildings may cause considerable damage, loss of life

© Woodhead Publishing Limited, 2010

9.1 Partial collapse of Khobar tower after a terrorist attack, Dhahran, Saudi Arabia, 1996 (US Department of Defense).

and disruption to services. As a result there is often a requirement to increase the blast resistance of many types of existing buildings which have typically not been designed to resist an explosion and to include blast protection into new buildings.

The US Department of State reported that globally in 2007 there were more than 14 000 terrorist attacks, killing more than 20 000 people (Office of the Coordinator for Counterterrorism, 2008). Between 1998 and 2004, the most common terrorist tactic was the improvised explosive device, accounting for 50% of all international terrorist attacks based on the statistics from the National Consortium for the Study of Terrorism and Responses to Terrorism (START, 2008). The use of this technique is perhaps not surprising as a bomb provides a dramatic yet relatively straightforward and low-risk method of achieving a terrorist's objective. Few skills are required to manufacture a crude bomb, discreetly place it, and detonate from a remote location. As a result, this chapter focuses on the threat of an externally detonated terrorist device, although the same methodologies and techniques can be used to protect buildings from accidental explosions.

Most buildings are not designed to resist blast loads. Maintaining a sufficient standoff is the most effective and simple way of protecting a building from an explosion as the explosive pressure drops rapidly with distance.

© Woodhead Publishing Limited, 2010

However, this is often impractical or uneconomical in urban environments where space is at a premium. As a result the vulnerable exterior and interior of high-risk buildings may need to be retrofitted to increase the blast resistance of the buildings to these threats. A cost-effective technique for this purpose is retrofitting with fibre-reinforced polymer (FRP) composites. This technique has been shown to be effective in increasing the blast resistance of a building's structural components and enhancing the building's integrity so it can survive an explosion (Buchan, 2006; Buchan and Chen, 2006, 2007).

This chapter presents an overview of protecting buildings from explosions and then focuses on the use of FRP composites for this purpose. It concentrates on retrofitting existing buildings using FRP composites as often new buildings can be more easily designed to increase their blast resistance.

9.2 Consequences of an explosion

During an explosion at ground level, the blast pressure wave expands from its source hemispherically if no obstructions, except the ground, are present. However, the blast load from an external explosion on a building in an urban environment is often quite different from that experienced by an isolated building. Streets and buildings in built-up areas confine the blast pressure wave and prevent it from propagating hemispherically with the effect of increasing the pressure on a building. The blast pressure wave can also reflect from buildings and travel around corners. As a result all sides of a building can be affected by an explosion (Mays and Smith, 1995).

Humans coming into direct contact with a blast wave can suffer injury due to ear drum rupture and lung damage at low pressures or fatality at higher pressures (DePalma *et al.*, 2005). However, experience has shown that the majority of casualties sustained in an explosion in close proximity to a building are not a direct result of the explosive detonation, but are due to blunt trauma and penetration injuries. These are typically caused by shattered glass, non-secured objects and fragments of the building being propelled at a high velocity by the explosion.

The other main source of casualties during an explosion is structural collapse. It may not be possible to completely prevent localised damage to structural members such as columns, beams, walls or slabs, especially when the explosion is significant, but it is important to ensure that this does not initiate a progressive collapse. Progressive collapse occurs when an explosion damages a relatively small portion of a building which initiates a chain reaction of failures that then propagates. This results in a disproportionately large structural failure and also in a disproportionately large loss of life when compared to the size of the original explosion (Gould *et al.*, 2006).

© Woodhead Publishing Limited, 2010

Secondary consequences of an explosion against a building can be fire and smoke which can lead to further casualties. An explosion can disrupt critical fire, life safety, ventilation, water and power systems which can combine to hinder or prevent evacuation, contributing to additional casualties.

9.3 Assessing if a building requires protection from blast

The implementation of any type of blast protection to a building has an associated cost from increased requirements such as thicker walls, additional reinforcement or blast resistant glazing. This can typically be an increase of 5% in the total cost of a new commercial building (National Research Council, 1995). Before committing to these increased costs, the building owner or developer should first consider if their building requires protection from a potential explosion and to what extent.

Typically, explosive devices do not have to be large to be considered a threat to a building. Less than 20 kg will fit into a briefcase or backpack and may receive little notice from security staff. Explosive threats can be delivered to a building in several ways. These can include hand-carried charges in public areas in or around the building, packages delivered to a building's loading area or mail room and vehicles on public roads or parking areas around the building.

Normally a risk assessment is required to understand the probability of an attack and the potential consequences. The building owner or developer than has to decide what can be spent in order to protect the building. Protection is never an absolute concept and some losses may have to be accepted, while certain losses such as human life, specialist equipment or vital data may not (Elliott *et al.*, 1992).

From this process, a set of design objectives should materialise to define the level of protection to be provided while balancing the cost and potential losses. These objectives should include the type of threats to be designed against and standards to be met, for example, the size of device from which the building must survive and be subsequently repairable or the theoretical standoff distance for a particular device at which the glazing should remain intact. Providing protection against a higher blast pressure from a bigger or closer device will obviously be more expensive.

9.4 General design guidance for blast protection of buildings

The objective of blast protective design of buildings is to save lives by preventing fragmentation, preventing structural collapse and facilitating the

© Woodhead Publishing Limited, 2010

evacuation and rescue of survivors. Significant features can be incorporated into the design of new buildings to increase their blast resistance. It should be noted that architectural design can sometimes be in conflict with blast resistant design. To avoid costly redesigns and delays to the project schedule it is necessary that a blast consultant is involved from the beginning of the design process. Many of the methods used to protect new buildings can be used to retrofit existing buildings and improve their performance under blast.

Protective design does not just start at a building's entrance. A building can be designed so that the layout and security arrangements prevent attacks by placing obstacles in the way of a potential attacker, showing that the likelihood of success is remote. This can include visible security, bollards to protect standoff and entry controls. Areas at higher risk such as entrance areas, mail rooms and loading decks can also be placed in a separate building away from the main structure.

Through good design, a building can also conceal its most valuable assets such as areas of high occupancy. This can lead to a reduced impact because much of the energy is consumed in non-essential areas if the building is attacked. For example, targets that may be attractive to terrorists can be made to look anonymous or placed away from the building's exterior and public roads or entrances.

Essential services can also be distributed or duplicated over a large area of a building so that one explosion cannot cause significant disruption (Mays and Smith, 1995). This methodology has been successfully used in warship design to decrease the probability of one attack disabling the whole vessel.

As well as the direct effects of an explosion on the building structure, significant damage may be caused by the explosive pressure wave entering the building. Service systems such as computer, telecommunication, security, lighting, heating and ventilation systems are all relatively weak and vulnerable to explosive pressure waves. Although secondary to human life and building integrity, if the pressure wave can be prevented from entering the building it can significantly reduce the loss of functionality together with the time and cost to repair.

Unfortunately, many of the features that make a building desirable for human occupation are the same features that are undesirable during an explosion and can allow the pressure wave to enter a building. Windows and atriums provide a sense of space and natural light but are often the areas closest to the explosion and the most vulnerable part of the building's exterior. As a result of an explosion, broken glass may be projected over a large area and impinge on neighbouring buildings which are not the intended target. Broken glass is one of the main sources of casualties in an explosion and improving the window glazing can be an effective precaution

© Woodhead Publishing Limited, 2010

in urban areas where many potential targets exist. There have been considerable developments in blast resistant glazing options, and for an effective protective design it is now not necessary to design a fortress or bunker.

Standard glazing is typically plain annealed glass which is very brittle and breaks into deadly angular jagged fragments. Toughened monolithic glass breaks into small cubes on fracture, but these can still be lethal when projected at high speeds. Potential solutions include annealed or toughened laminated glass which has a high strain capacity and can absorb a large amount of energy without losing its integrity. Due to its ability to absorb energy, laminated glass also reduces the forces transmitted to its supports when compared to other options such as polycarbonates. This aids the frame and attachment design which must hold the glazing in place long enough to allow a flexible membrane to form, otherwise the window will free itself from its frame and become a projectile. There are also other solutions such as anti-shatter film and bomb blast net curtains. These are less effective than laminated glass but are cheaper and are often utilised in historic buildings where laminated glass is not suitable (Cormie, 2007).

It is important that a building's structural integrity is maintained to reduce the risk of progressive collapse. There are now guidelines available to assist in designing against progressive collapse which aim to increase the robustness and redundancy in a building (GSA, 2003; UFC, 2005). These guidelines typically recommend:

- the use of ties to keep the building together in the event of an abnormal load and so enhance continuity, ductility and structural redundancy;
- the creation of alternative load paths to allow the building to remain standing if a structural element is removed; and
- the design of key structural elements which, if removed, the building could not bridge, to resist a specified static pressure load.

The explosive charge weight and the standoff distance between the seat of an explosion and a target building are the two major factors which determine the severity of the blast load on the building. Doubling the distance between the seat of a bomb and a building can reduce the loading pressure by a factor of eight, while tripling the standoff cuts the loading pressure by 27 times. As a result, maximising the standoff is often the most effective and straightforward way of protecting a building from an explosion. Due to the exponential decay of the explosive pressure wave even a small increase in additional standoff can significantly reduce the effect of an explosion.

Standoff can be created between a potential explosion and the critical areas of a building with the use of open areas such as pedestrian zones, car parks or sacrificial buildings. These distances can be maintained with physical barriers such as bollards, fences and walls to control vehicles and entry

© Woodhead Publishing Limited, 2010

procedures to control pedestrians. However, in urban environments creating sufficient standoff is often impractical or uneconomical. If a sufficient standoff cannot be maintained, the size of threat may have to be reduced. For example, this could be achieved by reducing the size of delivery vehicles that can approach the building. If this cannot be satisfactorily achieved, the building may need to be enhanced to increase its resistance to these threats.

9.5 Retrofitting buildings for blast protection

9.5.1 Introduction

When considering a potential retrofitting method, the primary consideration is the effectiveness of the method, i.e. its ability to protect a building and occupants from an explosion. However, there are also secondary factors to be considered before a technique can be applied in practice. Many government and corporate buildings at risk of terrorist attack are historical, ornate and listed, which means retaining their appearance is essential. Unfortunately, many techniques used to protect buildings from blast are unattractive, clumsy, intrusive and as a result unsuitable. It is crucial that these symbolic buildings do not appear like a fortress, as this can affect public opinion and confidence.

A protective solution should also be economically viable. It is therefore desirable that it does not require a significant reduction of floor space, extensive interruption to existing services or require highly skilled technicians for application, which all contribute to the cost. A retrofit may not be required over the entire building but may just be required in areas which are identified as vulnerable. After retrofitting, the building should still be fit for purpose and have no major additional maintenance costs.

9.5.2 Reinforced concrete

The blast resistance of a building may be improved by increasing its mass with additional concrete and steel reinforcement. Concrete is often used as its mass per unit cost is favourable, it has good fire resistance and with the steel reinforcement it has the ability to absorb large amounts of energy. Unfortunately, this solution can still be expensive, add considerable gravity loads to the foundations of a building and require a considerable period of time to install. The possibility of spalling and fragmentation are also disadvantages when concrete and masonry are exposed to an airblast load because one of the main sources of injury in an explosion is high-velocity fragments. The loss of material also weakens the structural component which may affect the integrity of the building.

© Woodhead Publishing Limited, 2010

Additional mass is not necessarily a good method for protecting a building from very large blast loads. It is often preferable to use plastic behaviour and ductile systems which can also achieve the desired protection by absorbing the blast load energy as strain energy upon deformation. These methods require less material which may lead to lower costs. A ductile solution is less likely to make the building look like a fortress by more efficiently using the retrofit materials.

9.5.3 Catcher system

Catcher systems have been used on the rear of masonry walls subjected to blast loads to restrain fragments from entering the occupied space and so preventing casualties. In such a system, usually a fabric covers the entire surface of the wall and is securely anchored to the top and bottom with just enough tension to remove slack. The method uses lightweight materials, is easy to install and is relatively inexpensive. Aesthetic problems of the method can be avoided by hiding the fabric behind dry walls. However, special arrangements must be made for load bearing walls as this method provides no structural support and for walls with windows as the fabric must span continuously from floor to ceiling without interruption (Ward, 2004).

9.5.4 Steel stud walls

Steel stud walls can be applied to the interior of existing walls to increase their ductility and energy absorption. To maximise this ductility, the connection to the floor and ceiling must be well designed so they do not fail but instead the stud yields and failure occurs due to strain elongation. The disadvantages of this method are long installation times and loss of floor space.

9.5.5 Steel plates

In-situ enhancing of reinforced concrete (RC) structural components using externally bonded steel plates has previously been attempted. The mechanism of strengthening beams, walls and slabs with bonded steel plates is by increasing their flexural strength. RC columns can effectively be strengthened by steel jacketing. The addition of steel jackets strengthens RC columns in two different mechanisms. First, the steel jackets provide directly additional axial and flexural strength. Second, the steel jackets provide lateral confinement to the concrete which enhances the axial compressive strength and ductility (Teng *et al.*, 2002). The surface concrete can spall in steel plated concrete structures due to the volumetric expansion of the corroded steel, as it is poor at resisting weather attacks (Lau *et al.*, 2001). This

© Woodhead Publishing Limited, 2010

method is also usually time-consuming and requires regular maintenance which increases the through life costs.

9.5.6 Fibre reinforced polymer (FRP) composites

FRP composites are now being widely utilised instead of steel plates due to their higher strengths, better corrosion resistance and far greater ease of transportation, handling and installation. The biggest advantage of FRPs is their tailorability. They can be more easily arranged according to the specific site conditions than other materials and so optimised for performance. FRP retrofitting can be applied quickly, is non-intrusive and provides a dramatic increase in the ability of a building to resist an explosion. The apparent high purchase cost of FRPs compared to other materials has been an obstacle in some decisions to implement this technique. However, a direct comparison on a unit price basis may not be appropriate. Including installation and transportation in the cost comparison, FRPs can often compete with conventional materials. If the comparisons include through life costs, FRPs can be advantageous (Täljsten, 2003a).

9.6 Retrofitting buildings for blast protection using fibre-reinforced polymer (FRP) composites

9.6.1 Introduction

Externally bonded advanced FRP composites to retrofit buildings against explosions were initially used on military and diplomatic structures in the early 1990s. Before these buildings were retrofitted with FRP, the survivability offered was variable as they were built using a broad range of construction materials and methods. FRP composites became popular because of their superior properties, speed of application and cost-effectiveness compared with other methods. As a result, this has become an established method of increasing the resistance of buildings against explosions.

In this section, the choice of FRP composites and the application procedure are discussed. This is followed by how FRP composites can be used for increasing the blast resistance of typical building structural components and the typical failure mechanisms of such retrofitted members under blast.

9.6.2 FRP composite materials used to protect buildings from explosions

Many FRP and polymer materials have been used to retrofit building components against blast loads. The most commonly used materials are glass fibre-reinforced polymer (GFRP) and carbon fibre-reinforced polymer

© Woodhead Publishing Limited, 2010

(CFRP) composites. There is some debate about which material is the most economical, with raw glass fibres being cheaper to purchase but high-strength carbons saving on resin resulting in a potentially more economic total solution (Concrete Society, 2004). Carbon has been shown to have better durability characteristics, and its high stiffness provides more efficient confinement of columns with fewer wraps. It is possible to produce greater confinement of columns with a less stiff material by increasing the number of wraps, but this process requires longer installation times and may sometimes prove less economic.

Aramid fibre-reinforced polymers (AFRP) have also been used due to their superior impact resistance properties (Crawford and Morrill, 2003). This is important in protecting a building against primary fragments, generated from the bomb casing, and secondary fragments, generated from debris, moving at high velocity towards the building.

Spray-on polyurea and polyurethane materials have been successfully used for protecting non-load bearing walls instead of traditional FRP sheets. These materials have been shown to be ultraviolet and temperature stabile, flame resistant and cost-effective. As failure of FRP retrofitted walls can occur due to the brittle tensile failure of the FRP, the spray-on polyurea and polyurethane materials can be advantageous as they have significantly higher failure strains (Davidson *et al.*, 2004).

Other methods which have been attempted for protecting buildings from explosions include retrofitting with FRP rods and pre-stressed FRP sheets (Carney and Myers, 2003; Myers *et al.*, 2003, 2004).

9.6.3 Application procedure

Two main FRP systems are available for protecting buildings: pultruded plates and wet layups. Pultruded or prefabricated plates allow better quality control as they are prefabricated under factory conditions and can be used for bonding to beams or slabs or for filament winding of columns. However, the wet layup method is the most commonly used. This technique involves the *in-situ* addition of epoxy resin to the fibre sheets. This is a more versatile technique as the flexible fabric sheets can be fitted to building components of any shape or size.

Application of an FRP system starts with assessing the condition of the structure to be retrofitted and proper design of the required strengthening. The strength of the existing substrate material and its bond properties with FRP should be checked and tested whenever possible. Any holes or voids should be repaired with structural repair materials before applying the FRP. For concrete structures the surface has to be prepared to remove the weak surface layer of concrete and to expose the aggregate which provides an enhanced bond with the FRP. The concrete and masonry substrates

© Woodhead Publishing Limited, 2010

must be sound, clean and free from surface contaminants. This may be achieved using abrasive blasting, high-pressure washing, steam cleaning and surface grinding to expose coarse and fine aggregate and followed by vacuumed cleaning. Using the wet layup method, the FRP fabric should then cut into the desired dimensions with special cutting tools as the fibres tend to blunt normal scissors.

A solvent should be wiped over the roughened surface to remove contaminants and dust. Once the surface is dry, a polymer primer may, depending on the adopted adhesive system, then be applied to the structural component to fill in pores and promote bonding. A thin layer of resin should then be applied to the concrete or masonry. For FRP plates, a thin layer of resin should also be applied onto the plate which can then be applied to the structure. For wet FRP fabrics, the resin is applied to the fabric before installation using rollers, brushes or impregnation machines. Vacuum-assisted resin infusion may also be used *in situ*. Surplus adhesive from the sides of the plate should be removed while the adhesive is uncured. After the adhesive has cured, tapping the surface plate with a metallic object tests for voids. For aesthetic purposes the laminate may be coated with paint or wallpaper (Concrete Society, 2004; Ojha, 2001).

The wet layup procedure is not a particularly cost- or time-efficient method of applying the material to a large area such as a wall. As a result, spray-on polymers are now being used to protect non-load bearing walls. With this technique, a spray gun is used to spray the polymer mixture directly on to the target but, again, like the wet layup process the wall must firstly be prepared and cleaned. The advantage of the technique is the speed of application while disadvantages are in the protective clothing and spraying equipment required for application (Davidson *et al.*, 2004).

9.6.4 FRP retrofitted concrete columns

In the 1995 bombing of the Alfred P. Murrah Building in Oklahoma City the damage was caused by the shearing of three main load bearing columns at the ground level of the building which resulted in the collapse of the majority of the structure (Mlakar *et al.*, 1998). Subsequently FRP composites have been shown to increase the blast resistance of columns and so maintain the structural integrity, prevent progressive collapse and avert disproportionately large numbers of casualties.

In protecting buildings from progressive collapse, the shear capacity of a retrofitted column shall exceed its flexural strength. This avoids the brittle shear failure and allows a more ductile flexural response. Significantly less energy can be dissipated prior to shear failure compared with a flexural failure so the resistance to blast of a shear deficient column is low. Many methods may be deployed to increase the shear capacity in new building

© Woodhead Publishing Limited, 2010

design, such as increasing the stirrups in or the size of the column. For existing buildings, the use of composite hoop wraps is the most common method of increasing the blast resistance of concrete columns using FRP composites (Malvar *et al.*, 2007).

The hoop wraps have two functions. First they provide confinement to the concrete. The concrete column expands laterally under vertical compression. This lateral expansion increases in rate when the concrete is close to failure as micro-cracks are developed. For the concrete column to fail at the ultimate state, cracks have to develop sufficiently to allow the aggregate to slide over each other, resulting in more significant lateral expansion. This lateral expansion of concrete forces the FRP wraps to expand inducing a tensile hoop stress in the FRP. The FRP wrap in turn applies a confining pressure to the concrete to prevent its lateral expansion. The final failure is thus by FRP rupture. From this description, one would appreciate that FRP wraps with their main fibres horizontally orientated are most effective.

The confinement provided by the FRP hoop wraps enhances the concrete's uniaxial compressive strength. It also ensures that the flexure failure of the column is by the development of a plastic hinge with the yielding of the steel reinforcement which increases the ductility of the column and its ability to absorb energy. When the column is sufficiently confined, the plastic deformation in the steel may be sufficiently developed to lead to hardening, which causes the hinge to spread out, further increasing energy absorption capability and ductility. The confinement may also enhance the shear capacity of the concrete column. The second function of the hoop wraps is to enhance directly the shear resistance of the concrete column (Teng *et al.*, 2002, 2004; Chen and Teng 2003a, b). Methods of wrapping columns include full wrapping, partial wrapping using straps in a continuous spiral, partial wrapping in discrete rings, filament winding and prefabricated shell jacketing (Fig. 9.2).

Successful confinement of circular columns can be achieved with FRP wrapping, but this is less effective for square and rectangular columns. This is because only part of the concrete is effectively confined. The existence of the sharp corners also has a negative effect on the tensile strength of the FRP which in turn reduces the confinement. For these columns, modifying the section profile into a circular or elliptical shape before jacketing can be more effective (Teng *et al.*, 2002).

Hoop FRP wraps are usually mono-directional and so only provide restraint in the hoop direction. Additional fibres in the longitudinal direction are required if the flexure resistance of a column needs to be enhanced. Strips can be used but must be bonded to the column to work efficiently. The hoop wrap is not particularly dependent on its bond to the concrete and gaps can even occur between the hoops with little negative effect.

© Woodhead Publishing Limited, 2010

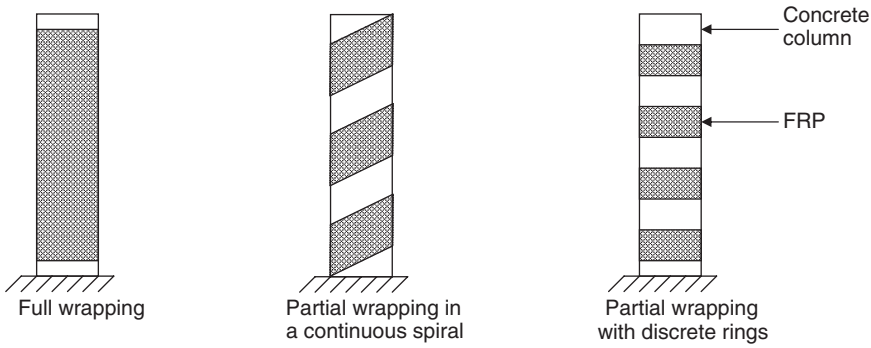

9.2 Methods of FRP column wrapping.

Increases in blast resistance of RC columns with hoop FRP wraps alone have been achieved in tests. However, to achieve simultaneous flexure and shear strengthening of columns, more than one layer of FRP composites with fibres in both circumferential and vertical directions may be required.

During experimental explosive tests it has been shown that FRP retrofitted columns require a good connection to neighbouring structural members for best performance. Typically, the column closest to the explosion is loaded with a greater force than the other columns and so its resistance has to be maximised and the load on it to be distributed to other structural members. As a result, no gap in the FRP should be left at the top or bottom of the column and the FRP retrofit should be continued to overlap with neighbouring beams and columns (Malvar *et al.*, 2007).

Experimental explosive tests have shown that control columns, without FRP retrofitting, fail mainly in diagonal shear at the columns top and bottom, with the central section relatively intact and vertical. After shear failure, the longitudinal rebar ruptures at the top and bottom thirds of the column allowing the central section of the column to displace. For example, Crawford *et al.* (2001) explosively tested 350 mm square columns without retrofit resulting in a 250 mm residual displacement at the column mid-height. By using horizontal FRP wraps for shear enhancement and vertical FRP strips for flexural enhancement, the columns under the same blast load remained elastic, with no permanent deformation (Crawford *et al.* 2001). When failure is induced in FRP retrofitted columns it is commonly by tensile rupture of the FRP due to tension in the hoop direction caused by the expansion in the concrete at peak deformation.

Potential problems noted from explosive tests are that for close-in explosions the strain capacity of FRP retrofits can be exceeded due to excessive deformation. Fragmentation has also been shown to damage the FRP wraps

© Woodhead Publishing Limited, 2010

leading to potentially premature failure (Malvar *et al.*, 2007). Possible solutions include protecting the FRP wrap or using AFRP as it has better impact resistance.

A number of numerical analyses have been conducted to predict the behaviour of FRP retrofitted columns under blast, but further research is essential to achieve a better understanding. Crawford *et al.* (1997) validated numerical analyses of 1.1 m circular RC columns against experimental trials and showed FRP composite retrofits could have a beneficial effect on the performance of columns against blast. The column without retrofit experienced a 48 mm deflection against an 18 mm deflection with a CFRP retrofit.

As a simple design tool and to rapidly assess the survivability of a column, single degree of freedom (SDOF) methods may be used and have been shown to provide reasonably accurate predictions of the response of FRP retrofitted columns against blast loads (Crawford *et al.*, 2001; Morrill *et al.*, 2004). However, it should be noted that this method involves many simplifications to obtain a SDOF system for a structure with many degrees of freedom and care must be taken in making these simplifications.

As a more advanced design tool, numerical analyses of FRP retrofitted RC column may be adopted (Crawford *et al.*, 1997). Although it is possible that this method may be used to assess the performance of various designs before being implemented on site, challenges remain on accurate modelling of the complex behaviour of concrete and its interaction with FRP under blast.

9.6.5 FRP retrofitted concrete beams

There has been very limited use of FRP composites to protect concrete beams against explosions. This may be attributed to two reasons. Firstly, exterior columns and walls, rather than beams, are most likely to be under direct blast pressure in a terrorist attack. Secondly, columns and load bearing walls may be more critical structural elements whose failure could trigger progressive collapse. Even non-load bearing walls can have a higher fragmentation hazard. However, the technique has been shown to be successful and effective despite its limited use to date.

The criteria for preventing progressive collapse can be based on the requirement that should one exterior column of a building be removed, the building should remain standing. When an exterior column is removed a perimeter beam has its spanning length increased significantly and may therefore be required to be retrofitted to prevent damage in an explosion.

The two main failure modes of conventional RC beams are flexure and shear. Flexural strengthening of beams using FRP is usually achieved using

© Woodhead Publishing Limited, 2010

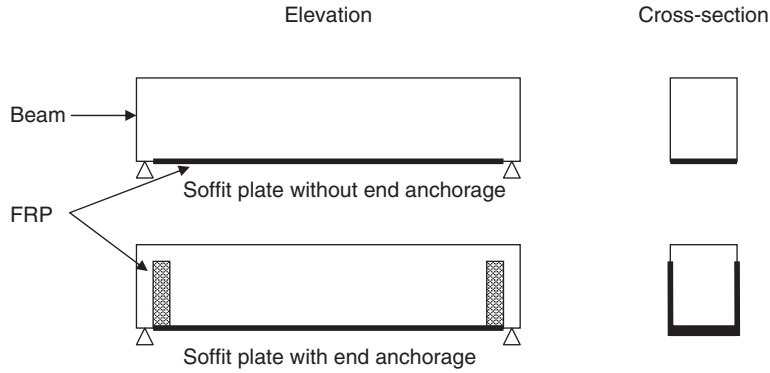

9.3 Flexural strengthening of concrete beams with FRP.

soffit plates with or without end anchorage (Fig. 9.3). In static design, the most popular method is bonding FRP plates to the tension face of the beam, without anchorage. The externally bonded FRP has a similar function to the internal tensile steel reinforcement in concrete beams in increasing the bending capacity, but debonding failure is most common in the FRP retrofitted beams. With this method, care has to be taken as an uneven or unclean bonding surface for the soffit plate can lead to rapid debonding and reduced strength.

The shear capacity of RC beams may also be increased by applying externally bonded FRP. The methods include bonding strips or continuous sheets of FRP to the vertical sides of a beam, bonding FRP U-jackets around the two sides and the tension face and wrapping FRP around the whole circumference of a beam (Fig. 9.4). FRPs bonded to the side only are most susceptible to debonding; those wrapped around the whole cross-sections are most effective with U-jacketing in between.

An extensive treatment on the flexure and shear behaviour of FRP strengthened RC beams under static loading can be found in Teng *et al.* (2002). Very limited knowledge is available for the behaviour of FRP retrofitted beams under blast loading. Based on limited experimental explosive surviving tests, control beams failed in shear and beams retrofitted with FRP on the sides and bottom of the beam have an increased blast resistance (Ross *et al.*, 1997).

There does not appear to be any publicly available literature illustrating the design of beams against blast using FRP retrofit. SDOF or advanced numerical analysis could be used for such design but further research is clearly required here. Particular attention needs to be paid to the direction of the loading, which can come from different directions leading to different behaviour from normal static gravity loading.

© Woodhead Publishing Limited, 2010

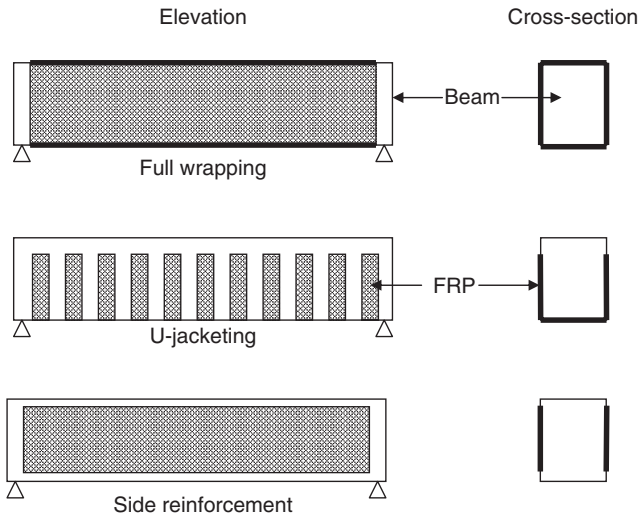

9.4 Shear strengthening of concrete beams with FRP.

9.6.6 FRP retrofitted concrete slabs

Typically, the thickness of slabs remains the same for both the interior and exterior bays of a building. However, under an explosion the exterior and lower level bays are more likely to experience a greater blast load. This is because they are closer to an external threat such as a car bomb or an internal threat such as a hand-carried device being challenged upon entry to the building. For this reason, these higher risk areas often require additional protection from blast as their failure can initiate progressive collapse in buildings. This is particularly important in areas of buildings susceptible to an internal explosion such as delivery loading areas, mail rooms and public entrances. If an explosion occurs internally, the vertical uplift of the slab is not a standard design scenario.

FRP composites may be used to enhance a slab's resistance for either downward or upward blast load. The tension face of concrete slabs is usually retrofitted by bonding an FRP sheet, one-directional FRP strips or two-directional FRP strips (Fig. 9.5). Depending on the design scenarios, FRP may need to be bonded to either the upper or lower surface or both. The ends of the FRP strips may be anchored to improve the performance. However, in two-way slabs strengthened with FRP strips in both directions, such improvement is likely to be limited as plate end debonding is unlikely.

Slabs are usually designed to resist downward gravity loads rather than an upward load from an explosion inside a building. Typically, steel reinforcements are arranged to resist normal downward static loads so the

© Woodhead Publishing Limited, 2010

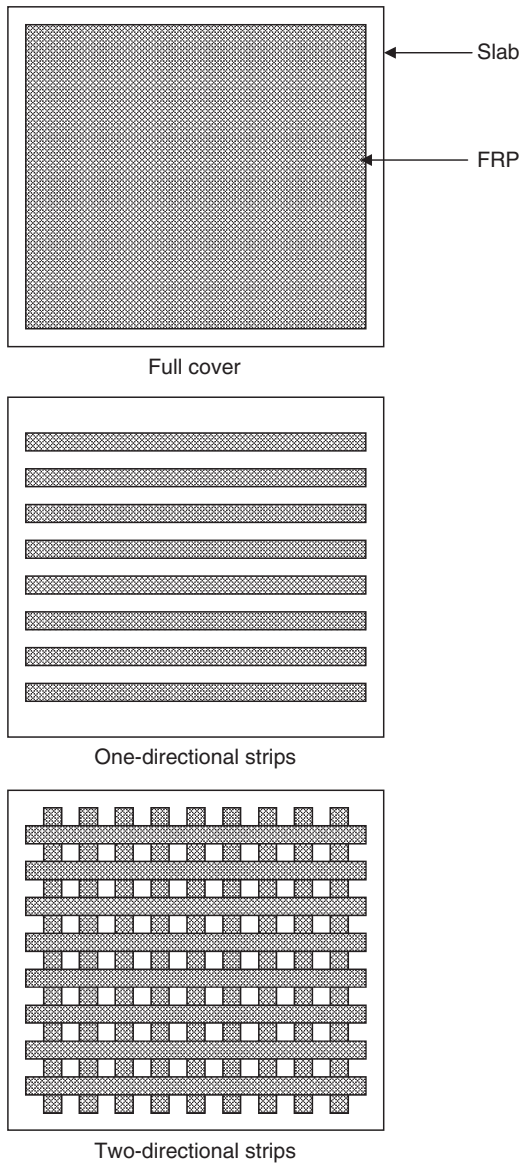

9.5 FRP strengthening of slabs.

resistance of a slab against upward loading is usually very limited. After being lifted upwards, the slab will rebound and drop with gravity acceleration which is another non-standard load. Failure of slabs is usually due to either punching shear or the loss of the moment resistance capacity. Failure may also occur locally in the slab. If the connection between the slab and

© Woodhead Publishing Limited, 2010

the column is lost, the unsupported column may buckle and the building may become laterally unstable.

Through experimental tests, FRP retrofitting has been shown to significantly improve the performance of concrete slabs against explosions. Ross *et al.* (1997) and Lawver *et al.* (2003) reported 25% decreases in the maximum deflection for FRP retrofitted slabs compared to non-retrofitted control slabs. Razaqpur *et al.* (2007) reported a 75% increase in the post-blast static strength using an FRP retrofit compared to a control slab. Higher blast resistance capacity has also been shown if the FRP is applied to both sides of a slab due to load reversal but with the disadvantage of the increase in cost (Lu *et al.*, 2005).

Care has to be taken using FRP sheets covering the entire slab surface, as it is difficult to check the quality of the bond. This can also stop the free movement of moisture out of the slab, which increases the risk of degeneration of the bond. Slabs are less prone to fragmentation than walls and so FRP strips may be used rather than fully covering the slab surface. Wide thin strips are generally preferred to narrow thick ones as the larger contact surface reduces the risk of debonding failures.

Near surface mounted (NSM) FRP bars or strips, which usually have better bond strength compared with externally bonded FRP plates or sheets, can be more suitable, but further research is required. NSM FRP bars are also advantageous is that they are embedded in concrete so they are not prone to accidental damage as are externally bonded FRP plates. This is especially true when the upper side of a slab needs to be strengthened.

On a similar theme, FRP retrofitting has been shown to improve the performance of concrete walls against blast (Muszynski and Purcell, 2003). In these studies, reduced spalling and fragmentation have also been observed when a concrete wall is retrofitted with FRP.

The behaviour of FRP retrofitted RC slabs under blast may be analysed using a simple yield line analysis of RC slabs with a modified steel reinforcement term to include the FRP (Ross *et al.*, 1997). However, the method is simplistic with significant limitations in that the effect of FRP debonding cannot be included. A number of numerical studies have produced results which are in close agreement with experiential results (Mosalam and Mosallam, 2001; Lawver *et al.*, 2003). It has been shown that they accurately predicted the damage modes and structural response.

9.6.7 FRP retrofitted masonry walls

Masonry walls are also of interest because of their frequent use in building construction. Load bearing walls may require blast protection because if they fail they can initiate progressive collapse of a building. Infill or non-

© Woodhead Publishing Limited, 2010

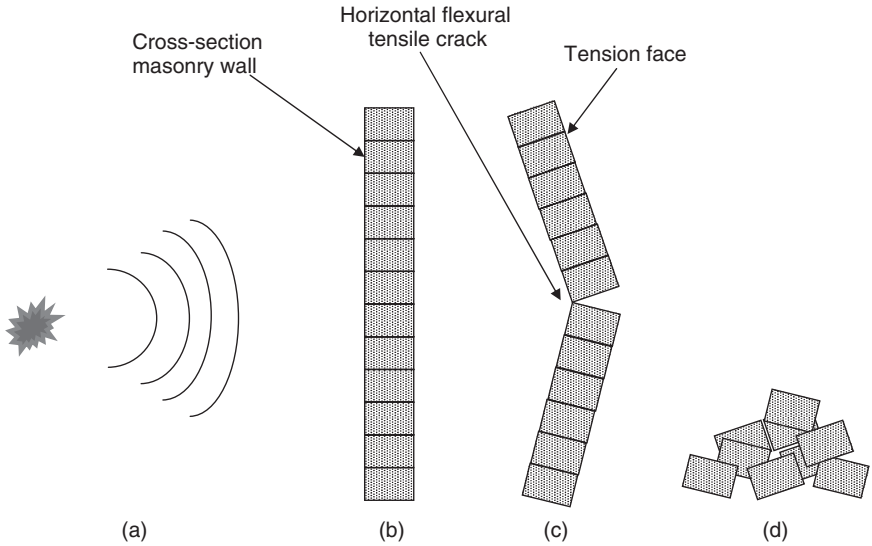

9.6 Failure of a conventional non-reinforced masonry wall under blast loading: (a) blast wave; (b) intact wall; (c) formation of a horizontal flexural crack at the mortar joint at the mid-height; (d) collapse due to snap-through of the wall.

load bearing walls may also require blast protection as they can produce secondary fragments which are a major source of casualties in an explosion. Consequently, most of the research on FRP for blast protection has been concerned with the use of FRP to increase the blast protection of masonry walls.

During an explosion a conventional masonry wall usually fails by forming a horizontal flexural crack at the mortar joint at the wall's mid-height followed by a sudden snap-through of the wall (Fig. 9.6). The failure is brittle because the tensile strength of masonry is negligible. FRP composites can be used to retrofit walls for out-of-plane blast loads. Walls are usually retrofitted by bonding strips or sheets of FRP to their tension face (Fig. 9.7). The technique can enhance both the bending capacity and the ductility because the FRP can resist the tensile stresses while the masonry usually has high compressive strength to resist compressive stresses on the compression face of the wall (Fig. 9.8).

The ends of the FRP can be anchored to increase the performance as it transfers forces from the FRP to the host structure and prevents FRP plate end debonding. Anchorage can be achieved by extending the FRP beyond the masonry wall to overlap the concrete frame, by mechanical anchors such as bolted angles or bonding (Fig. 9.9).

© Woodhead Publishing Limited, 2010

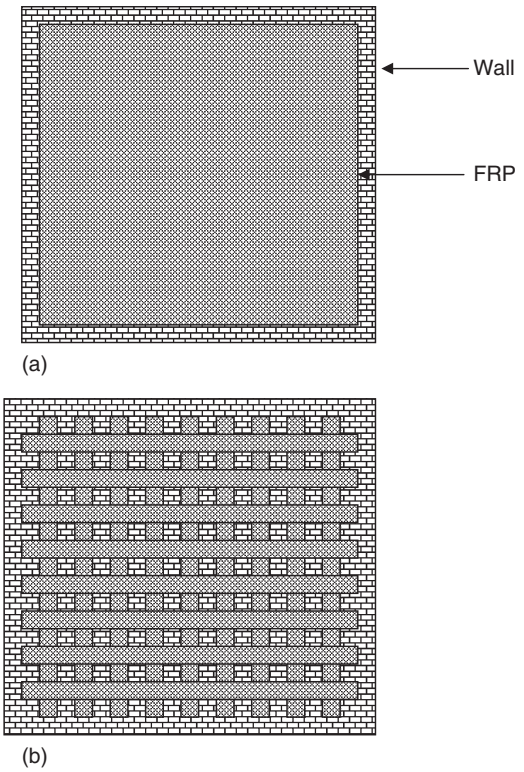

9.7 Strengthening of masonry walls with FRP: (a) strengthening with FRP sheets; strengthening with FRP strips in both directions.

It would be desirable to retrofit a load bearing wall with FRP on both sides to prevent the wall failing as it rebounds during an explosion (Oswald and Wesevich, 2001). In design, specific attention should be paid to the shear capacity of the wall along its perimeter. When the wall is enhanced in flexure, the shear capacity may be exceeded by the flexural capacity which would lead to the undesirable shear failure. In such a case the shear capacity around the perimeter may need to be enhanced.

Experimental tests have shown FRP retrofitted walls significantly improve their performance against explosions (Baylot *et al.*, 2005; Urgessa *et al.*, 2005). Muszynski and Purcell (2003) reported a 98% reduction in displacement for retrofitted walls compared to control walls. Myers *et al.* (2004) reported FRP retrofitted walls could resist a 50% increase in peak pressure. While numerical modelling by Crawford and Morrill (2003) indicated retrofitted walls limited deflection to 2% of span compared to 5% of span for the control wall. It should be noted, however, that all these numbers are

© Woodhead Publishing Limited, 2010

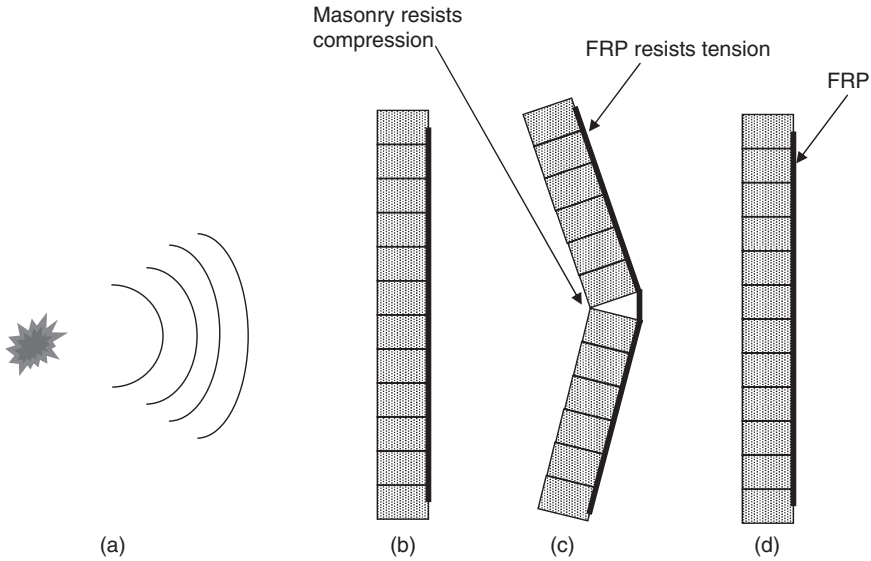

9.8 Behaviour of an FRP retrofitted masonry wall under blast loading: (a) blast wave; (b) intact wall; (c) formation of a flexural crack; (d) snap-through of the wall does not occur and the wall remains standing after explosion.

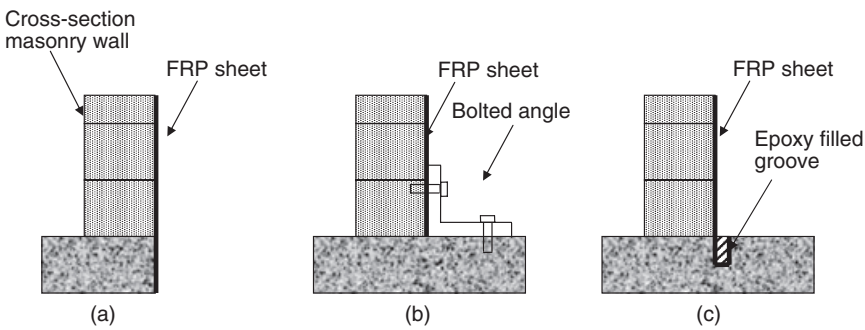

9.9 Examples of FRP anchorage: (a) extended FRP overlay; (b) bolted angles; (c) bonding.

specimen specific and would depend on the relevant material, geometrical and loading parameters.

An FRP reinforced wall may fail in a number of different failure modes. The FRP may rupture at the wall mid-height where the crack between masonry blocks exceeds the FRP's tensile capacity. This capacity can be increased by applying more plies of FRP and achieving approximately a

© Woodhead Publishing Limited, 2010

proportional decrease in its mid-height deflection. However, FRP debonding failure may occur well before that. If a large amount of FRP is applied and debonding failure does not occur first, masonry crushing failure may occur at the mid-span of the wall. As mentioned earlier, shear failure of the wall along its perimeter may also occur.

Importantly, explosive tests have shown FRP retrofit limits the fragmentation of the wall which can be lethal when projected at high velocity during an explosion (Myers *et al.*, 2004; Baylot *et al.*, 2005). The FRP retrofit also prevents primary fragments penetrating the wall and the internal space of the building. Continuous FRP sheets clearly perform better in this respect compared with FRP strips.

Whilst a few studies have been concerned with numerical analysis for predicting the performance of FRP retrofitted walls against blast (Crawford and Morrill, 2003; Tan, 2003), many more studies on this topic has been focused on using the SDOF method for predicting the blast response of such a wall (Oswald and Wesevich, 2001; Patoary and Tan, 2003; Tan, 2003; Myers *et al.*, 2004; Baylot *et al.*, 2005). Although SDOF methods may be used as fast and simple design tools, it is essential to bear in mind their limitations as discussed earlier about slabs.

9.6.8 Spray-on polymer retrofitted masonry walls

Non-load bearing walls are commonly used in construction but are susceptible to fragmentation. Spray-on polymers have been used to prevent fragmentation of these walls instead of the stiff FRP sheets. The objective of this technique is to protect occupants from fragmentation rather than supporting the wall.

The ductility of walls reinforced with stiff FRP sheets or strips is limited by either the FRP's tensile strain (FRP rupture failure) or FRP debonding when a major horizontal mortar crack forms at the mid-height of the wall. Spray-on polymers have high failure strains of greater than 100% but low stiffness. This means that non-load bearing walls retrofitted with spray-on polymer can deform significantly without compromising the building's integrity or causing fragments. A spray gun is used to apply the polymer mixture directly on to the wall, which is quicker than FRP sheets but requires protective clothing and spraying equipment. An example of such coating systems is PAXCONR® (2009).

Spray-on polymer retrofitted walls have shown improved performance against blast loads (Davidson *et al.*, 2004, 2005; Baylot *et al.*, 2005). Tests have also shown the polymer provides the same level of effectiveness for walls with window and door openings, but with an increased tendency for polymer tears at the corners of the openings. While polymer coating on both sides of the wall provides some additional blast protection compared

© Woodhead Publishing Limited, 2010

with coating on the tensile side only, it may not be sufficient to warrant the extra cost (Davidson *et al.*, 2004, 2005).

Spray-on polymers have also been used with continuous fibres to further strengthen a wall. The continuous fibres provide additional energy dissipation as the fibres rupture. However, the increase in cost for the limited increase in performance may not be justifiable (Malvar *et al.*, 2007).

When an explosion occurs, masonry bricks in spray-on polymer retrofitted walls start to fracture as the stress wave propagates through. The front face of some of the masonry blocks can fracture in the first few milliseconds of response due to the direct blast pressure. This is followed by highly localised stresses at the block to mortar interfaces closest to the supports, resulting in tearing of the polymer. The front face of some of the masonry blocks will then fracture due to flexural compression of the wall and the polymer will tear in tension as the wall flexes and mortar joints crack. Finally, the polymer may tear or lose adhesion at the connection to the host structure (Davidson *et al.*, 2004).

Experimental tests have also shown spray-on polymers being used to protect lightweight steel structures. The results show increased ductility, strength and reduced fragmentation (Knox *et al.*, 2000).

Finite element (FE) analysis has been used to aid understanding of spray-on polymer retrofitted wall behaviour under blast (Crawford and Morrill, 2003; Davidson *et al.*, 2004).

9.6.9 Practical applications

Many buildings have been retrofitted using FRPs to increase their static strength in the last decade (Concrete Society, 2004; Hollaway and Teng, 2008). However, very limited examples of buildings retrofitted with FRP for blast protection are available in the public domain. This is often due to the sensitive nature or function of these buildings and a desire not to publicise any perceived threats. Examples of buildings that use spray-on polymers for blast protection are the Pentagon building in Virginia, USA, the British Ministry of Defence building in London, the Washington Naval Yard near Washington DC, federal government buildings in downtown Manhattan, NY, National Guard facilities in Niagara Falls, NY and Canadian government buildings (Kenter, 2007).

9.7 Future developments and trends

Although FRP composites and spray-on polymers have been used to protect buildings from explosions, the technologies are far from mature. There is a lack of in-depth research in understanding the fundamental behaviour of FRP retrofitted structures under blast loading. A particular area of interest

© Woodhead Publishing Limited, 2010

is the bond behaviour between the FRP and concrete or masonry under dynamic loads. FRP debonding failure is common in experimental tests. Although extensive research has been conducted on the bond behaviour between FRP and concrete under static loading (Teng *et al.*, 2006; Chen *et al.*, 2007), little attention has been paid to the bond behaviour under dynamic loads (De Lorenzis and La Tegola, 2005) and no predictive bond model suitable for blast loads is available.

Explosive tests are expensive to conduct with high manpower, facility and instrumentation costs. With numerous combinations of construction materials, designs and retrofits, to use exclusively experimental testing to optimise design is not possible. The destructive capability and short duration of an explosion result in difficulties in fully understanding the structural response only through experimental testing. For these reasons, accurate numerical modelling of these explosive events is important and will reduce costs and time involved in assessing a design against blast loads. Many challenges exist in rigorous modelling of FRP retrofitted concrete and other structures. The problem is very complex indeed. It involves blast wave–propagation in both air and the structure, blast wave-structure interaction, very high material non-linearity, strain rate effects, strain hardening and strain softening, etc.

It is only when the fundamental behaviour of FRP retrofitted structures under blast load is well understood that an optimal design may be achieved. For example, currently there are many different FRP materials being used to protect buildings. A preferred material has not yet been established as many advantages and disadvantages are associated with each. The use of FRP hybrid materials could also be advantageous with improvements and flexibility in material properties. Anchorage has been shown to improve performance but a preferred method has not been established.

Design guidelines and best practices need to be established before FRP retrofitting can be widely implemented. Advanced numerical modelling of an integral structure under blast loads may be possible with significant challenges, and its use for practical design needs to be regulated. Simplified methods need to be established for practical design applications. Load transfer between different elements of a structure under blast loads can be much more complicated than under static loads. After a retrofitted structure is exposed to an explosion, criteria will have to be defined to determine if the FRP and the substrate need to be replaced. Further research should be carried out on methods for determining post-blast structural behaviour.

9.8 Sources of further information and advice

Several books are available in the area of static/seismic design of FRP retrofitted structures. Hollaway and Leeming (1999) is probably the first

© Woodhead Publishing Limited, 2010

book in this area which is concerned with the flexural strengthening of concrete beams with FRP composites, including constructional aspects and observations from experimental studies. Hollaway and Head (2001) discusses the properties of FRP materials, various possibilities of practical applications, and some basic design guidance. Teng *et al.* (2002) provides a systematic and comprehensive treatment of the fundamental theory on bond behaviour between FRP and concrete, flexural and shear strengthening of beams, slabs and columns using FRP with results adequately compared with those available from other researchers. Oehlers and Seracino (2004) provides a comprehensive treatment of flexural strengthening of concrete beams and slabs using steel or FRP plates with the main emphasis being on the provision of design guidance. Bank (2006) covers both the strengthening of concrete structures and new construction. This book was written as a code-based teaching text for students and engineers interested in learning about the detailed design procedures as specified by existing design guidelines. For practitioners, Hollaway and Teng (2008) is an excellent source of information covering the background, physical and mechanical properties, the use and design of FRP composites in upgrading structures in the civil infrastructure.

Several documents on the design and construction of externally bonded FRP systems for the strengthening of RC and other structures have been published in recent years. Of the guidelines that currently exist around the world, the most influential appear to be the fib (2001), JSCE (2001), ACI 440 (2008) and Concrete Society (2004) guidelines. Systematic design recommendations have also been published by independent researchers (e.g. Teng *et al.* 2002; Täljsten 2003b; Oehlers and Seracino 2004).

For an overview of the blast effects on buildings a key text is by Mays and Smith (1995). This book provides information on blast loading and structural response to blast loading. General guidance on blast protection of buildings from terrorist attacks is provided by FEMA (2003). This reference manual comprehensively covers methods to mitigate potential terrorist attacks against buildings. For an overview on research conducted on FRP retrofitting of building structures against blast, Buchan and Chen (2007) gives a thorough review of published research.

9.9 Conclusions

It has been established that there is a requirement to increase the blast protection of many buildings from explosions. This chapter has discussed the consequences of a blast load on a building and general guidance for blast protection. It considered different retrofitting methods before concentrating on FRP retrofitting of columns, beams, slabs and walls. Existing research has overwhelmingly indicated that FRP and polymer retrofitting

© Woodhead Publishing Limited, 2010

can significantly increase the blast resistance of a structure, by increasing the structural strength and ductility, with an additional advantage of reduced fragmentation. However, there is a significant lack of understanding of the fundamental behaviour of FRP retrofitted structures under blast loading. Further research is required before the technologies can be widely applied in practice.

9.10 References

ACI 440 (2008), *Guide for the Design and Construction of Externally Bonded FRP Systems for Strengthening Concrete Structures*, Committee 440, American Concrete Institute (ACI), Farmington Hills, MI.

BANK L C (2006), *Composites for Construction: Structural Design with FRP Materials*, Wiley, New York.

BAYLOT J T, BULLOCK B, SLAWSON T R and WOODSON S C (2005), *Blast response of lightly attached concrete masonry unit walls*, *Journal of Structural Engineering*, **131**(8), 1186–1193.

BUCHAN P A (2006), *FRP retrofitting of concrete and masonry structures to resist blast loads*, MSc thesis, School of Engineering and Electronics, The University of Edinburgh, UK.

BUCHAN P A and CHEN J F (2006), A review of research on blast resistance of concrete and masonry structures retrofitted with FRP, in Forde M C (ed.) *Proc. Structural Faults + Repair – 2006*, Enginering Technics Press, Edinburgh, UK, CD-ROM.

BUCHAN P A and CHEN J F (2007), Blast resistance of FRP composites and polymer strengthened concrete and masonry structures – A state-of-the-art review, *Composites: Part B*, **38**(5–6), 509–522.

CARNEY P and MYERS J (2003), Shear and flexural strengthening of masonry infill walls with FRP for extreme out-of-plane loading, in Lui, M and Parfitt KM (ed.) *Building integration solutions: Proc. 2003 Architectural Engineering Conference*, ASCE, Reston, VA, 246–250.

CHEN J F and TENG J G (2003a), Shear capacity of FRP strengthened RC beams: fibre reinforced polymer rupture, *Journal of Structural Engineering*, **129**(5), 615–625.

CHEN J F and TENG J G (2003b), Shear capacity of FRP strengthened RC beams: FRP debonding, *Construction and Building Materials*, **17**(1), 27–41.

CHEN J F, YUAN H and TENG J G (2007), Debonding failure along a softening FRP-to-concrete interface between two adjacent cracks in concrete members, *Engineering Structures*, **29**(2), 259–270.

CRAWFORD J E and MORRILL K B (2003), Retrofit techniques using polymer and FRPs for preventing injurious wall debris, in Tan, K H (ed.) *Proc., 6th Symposium Fibre-Reinforced Polymer Reinforcement for Concrete Structures*, FRPRCS-6 University of Singapore 1197–1208.

CRAWFORD J E, MALVAR J, WESEVICH J W, VALANCIUS J and RAYNOLDS A D (1997), Retrofit of reinforced concrete structures to resist blast effects, *ACI Structural Journal*, **94**(4), 371–377.

CRAWFORD J E, MALVAR L J, MORRILL K B and FERRITTO J M (2001), Composite retrofits to increase the blast resistance of reinforced concrete buildings, *10th International Symposium Interaction of the Effects of Munitions with Structures*, 1–13 May, San Diego, CA.

© Woodhead Publishing Limited, 2010

CONCRETE SOCIETY (2004), *Design Guidance for Strengthening Concrete Structures using Fibre Composite Materials*, TR 55, 2nd edn, Crowthorne, Berkshire, UK.

CORMIE D (2007), Bomb blast performance of glazed façades, *GPD Conference*, 15–18 June, Tampere, Finland.

DAVIDSON J S, PORTER J R, DINAN R J, HAMMONS M I and CONNELL J D (2004), Explosive testing of polymer retrofit masonry walls, *Journal of Performance of Constructed Facilities*, **18**(2), 100–106.

DAVIDSON J S, FISHER J W, HAMMONS M I, PORTER J R and DINAN R J (2005), Failure mechanisms of polymer-reinforced concrete masonry walls subjected to blast, *Journal of Structural Engineering*, **131**(8), 1194–1205.

DE LORENZIS L and LA TEGOLA A (2005), Bond of FRP laminates to concrete under impulse loading: a simple model, in Chen J F and Teng J G (eds), *International Symposium on Bond Behaviour of FRP in Structures (BBFS 2005)*, 7–9 December Hong Kong, 503–508.

DEPALMA R G, BURRIS D G, CHAMPION H R and HODGSON M J (2005), Blast injuries, *New England Journal of Medicine*, **352**(13), 1335–1342.

ELLIOTT C L, MAYS G C and SMITH P D (1992), The protection of buildings against terrorism and disorder, *Proc. Institution of Civil Engineers, Structures and Buildings*, **94**, 287–297.

FEMA (FEDERAL EMERGENCY MANAGEMENT AGENCY) (2003), *Reference Manual to Mitigate Potential Terrorist Attacks Against Buildings: Providing Protection to People and Buildings*, US Department of Homeland Security, Washington, DC.

FIB (2001), *Externally Bonded FRP Reinforcement for RC Structures*, Technical Report, Task Group 9.3, Bulletin No. 14, the International Federation for Structural Concrete (*fib*), Lausanne, Switzerland.

GOULD N C, WINN V and DREVINSKY D (2006), Progressive collapse analysis, retrofit design, and costs for existing structures, in Cross B and Finke J (eds), *Structures Congress 2006: Structural Engineering and Public Safety*, ASCE, Restum. VA, CD-ROM.

GSA (2003), *Progressive Collapse Analysis and Design Guidelines for New Federal Office Buildings and Major Modernization Projects*, US General Services Administration, Washington, DC.

HOLLAWAY L C and HEAD P R (2001), *Advanced Polymer Composites and Polymers in the Civil Infrastructure*, Elsevier, Oxford, UK.

HOLLAWAY L C and LEEMING M B (eds) (1999), *Strengthening of Reinforced Concrete Structures Using Externally-Bonded FRP Composites in Structural and Civil Engineering*, Woodhead Publishing, Cambridge, UK.

HOLLAWAY L C and TENG J G (eds) (2008), *Strengthening and Rehabilitation of Civil Infrastructures using Fibre-Reinforced Polymer (FRP) Composites*, Woodhead Publishing, Cambridge, UK.

JSCE (2001), *Recommendations for Upgrading of Concrete Structures with Use of Continuous Fiber Sheets*, Concrete Engineering Series 41 (English version), Japan Society of Civil Engineers (JSCE), Tokyo, Japan.

KENTER, P. (2007), Polymer spray protects building occupants, *Daily Commercial News and Construction Record*, 24 May, available at: www.dailycommercialnews.com/article/id20943, Last accessed September 2009.

KNOX K J, HAMMONS M I, LEWIS T T and PORTER J R (2000), *Polymer Materials for Structural Retrofit*, Force Protection Branch, Air Expeditionary Force Technology Division, Air Force Research Laboratory, Tyndall AFB, FL.

© Woodhead Publishing Limited, 2010

LAU K T, DUTTA P K, ZHOU L M and HUI D (2001), Mechanics of bonds in an FRP bonded concrete beam, *Composites: Part B Engineering*, **32**(6), 491–502.

LAWVER D, DADDAZIO R, JIN OH G, LEE C K B, PIFKO A B and STANLEY M (2003), Simulating the response of composite reinforced floor slabs subjected to blast loading, *ASME International Mechanical Engineering Congress*, 15–21 November, Washington, DC, 15–22.

LU B, SILVA P, NANNI A and BAIRD J (2005), Retrofit for blast resistant RC slabs with composite materials, in Shield C K, Busel J P, Walkup S L and Gremel D D (eds), *7th International Symposium on Fiber Reinforced Polymer for Reinforced Concrete Structures (FRPRCS-7). SP-230*, American Concrete Institute International, Farmington Hills, MI, 1345–1360.

MALVAR J, CRAWFORD J E and MORRILL K B (2007), Use of composites to resist blast, *Journal of Composites for Construction*, **11**(6), 601–610.

MAYS G C and SMITH P D (1995), *Blast Effects on Buildings*, Thomas Telford, London, UK.

MLAKAR SR P F, CORLEY W G and SOZEN M A (1998), The Oklahoma City bombing: Analysis of blast damage to the murrah building, *Journal of Performance of Constructed Facilities*, **12**(3), 100–112.

MORRILL K B, MALVAR L J, CRAWFORD J E and FERRITTO J M (2004), Blast resistant design and retrofit of reinforced concrete columns and walls, *Proceedings of the 2004 Structures Congress – Building on the past: Securing the future*, 22–26 May, Nashville, TN, 1–8.

MOSALAM K M and MOSALLAM A S (2001), Nonlinear transient analysis of reinforced concrete slabs subjected to blast loading and retrofitted with CFRP composites, *Composites Part B: Engineering*, **32**(8), 623–636.

MUSZYNSKI L C and PURCELL M R (2003), Use of composite reinforcement to strengthen concrete and air-entrained concrete masonry walls against air blast, *Journal of Composites for Construction*, **7**(2), 98–108.

MYERS J J, BELARBI A and EL-DOMIATY K A (2003), Blast resistance of un-reinforced masonry walls retrofitted with fibre reinforced polymers, *9th North American Masonry Conference*, 1–4 June, Clemson, SC, 312–323.

MYERS J J, BELARBI A and EL-DOMIATY K A (2004), Blast resistance of FRP retrofitted un-reinforced masonry (URM) walls with and with out arching action, *The Masonry Society Journal*, **22**, 9–26.

NATIONAL RESEARCH COUNCIL (1995), *Protecting Buildings from Bomb Damage: Transfer of Blast-effects Mitigation Technologies from Military to Civilian applications*, National Academy Press, Washington, DC.

OFFICE OF THE COORDINATOR FOR COUNTERTERRORISM (2008), *Country Reports on Terrorism*, United States Department of State, Washington, DC.

OEHLERS D J and SERACINO R (2004), *Design of FRP and Steel Plated RC Structures: Retrofitting Beams and Slabs for Strength, Stiffness and Ductility*, Elsevier, Oxford, UK

OJHA A (2001), *The execution of carbon fibre reinforced polymer strengthening work*, Thesis, Lulea University of Technology, Sweden.

OSWALD C J and WESEVICH J W (2001), Structural retrofits to increase the blast capacity of roofs and masonry walls, *Proc. SAME National Symposium on Comprehensive Force Protection*, 1–2 November, Charleston, SC.

PATOARY M K H and TAN K H (2003), Blast resistance of prototype in-built masonry walls strengthened with FRP systems, in Tan K H (ed.), *6th Symposium on Fibre-*

© Woodhead Publishing Limited, 2010

Reinforced Polymer Reinforcement for Concrete Structures, FRPRCS-6, University of Singapore, 1189–1198.

PAXCON (2009), http://www.paxcon.com/user_pages/multimedia_gallery_24.shtml?page=Multimedia&subpage=Multimedia%20Gallery (accessed September 2009).

PEARSON C and DELATTE N (2005), Ronan point apartment tower collapse and its effect on building codes, *Journal of Performance of Constructed Facilities*, **19**(2), 172–177.

RAZAQPUR A G, TOLBA A and CONTESTABILE E (2007), Blast loading response of reinforced concrete panels reinforced with externally bonded GFRP laminates, *Composites Part B: Engineering*, **38**(5–6), 535–546.

ROSS C A, PURCELL M R and JEROME E L (1997), Blast response of concrete beams and slabs externally reinforced with fibre reinforced plastics (FRP), *Building to last: Proceeding of Structures Congress XV*, 13–16 April, Portland, OR, 673–677.

START (2008), Global Terrorism Database, National consortium for the study of terrorism and responses to terrorism, http://start.umd.edu/gtd/ (last accessed September 2009).

TÄLJSTEN B (2003a), Strengthening concrete beams for shear with CFRP sheets, *Construction and Building Materials*. **17**(1), 15–26.

TÄLJSTEN B (2003b), *FRP Strengthening of Existing Concrete Structures. Design Guidelines*, 2nd edn, Division of Structural Engineering, Luleå University of Technology, Sweden.

TAN K H (2003), Blast mitigation using fibre-reinforced polymer systems, *2nd International Symposium on New Technologies for Urban Safety of Mega Cities in Asia*, 30–31 October, Tokyo, Japan, 239–246.

TENG J G, CHEN J F, SMITH S T and LAM L (2002), *FRP Strengthened RC Structures*, John Wiley & Sons, Chichester, UK.

TENG J G, LAM L and CHEN J F (2004), Shear strengthening of RC beams using FRP composites, *Progress in Structural Engineering and Materials*, **6**, 173–184.

TENG, J G, YUAN H and CHEN J F (2006), FRP-to-concrete interfaces between two adjacent cracks: theoretical model for debonding failure, *International Journal of Solids and Structures*, **43**(18–19), 5750–5778.

UFC (2005), *Design of Buildings to Resist Progressive Collapse*, Unified Facilities Criteria, US Department of Defense, Washington, DC.

URGESSA G, MAJI A and BROWN J (2005), Analysis and testing of blast effects on walls strengthened with GFRP and shotcrete, *Proc., 50th International SAMPE Symposium and Exhibition – New Horizons for Material and Processing Technologies*, 1–5 May, Long Beach, CA, 1135–1144.

US Department of Defence, http://www.defenselink.mil/DODCMSShare/NewsPhoto/1996-06/960626-N-00000-002.jpg (accessed September 2009).

WARD S P (2004), Retrofitting existing masonry buildings to resist explosions, *Journal of Performance of Constructed Facilities*, **18**(2), 95–99.

© Woodhead Publishing Limited, 2010

10

The use of composites in blast-resistant walls

L. A. LOUCA and A. S. FALLAH, Imperial College London, UK

Abstract: The use of fibrous laminated composites in blast protection is discussed in this chapter. Different ply settings, i.e. unidirectional (UD), woven roving (WR) and chopped strand mat (CSM) lamina, are considered. Three examples of the use of composites, viz. in strengthening existing corrugated blast walls and their connections, in replacement of blast walls by composite sandwich panels and in the use of fibre metal laminates (FMLs), are discussed. The examples are selected to reflect the range of applicability of composites in blast resistant design which includes offshore, defence and marine industries. The problem of connecting composite and hybrid parts is addressed. The results included are adopted from the literature on the topic or are the results of analyses conducted by authors or by their affiliated research group. It is settled that composites can be best used in conjunction with other materials. These materials can be metallic (such as aluminium) or non-metallic (such as Balsa wood). Hybrid settings can be used for low and moderate blast loading levels. The problem of designing hybrid parts using fibre-reinforced polymer (FRP) composites for use in high-pressure–high-impulse blast has not yet been fully solved and further research is required to propose set-ups which can eliminate the drawbacks of current designs.

Key words: composite, hybrid, sandwich, fibre metal laminate, deflagration, detonation.

10.1 Introduction

In recent years there has been an ever-increasing interest in the offshore, defence and marine industries to further increase the application of composite materials in primary structural applications. These applications include the construction of all-composite primary modules, substitution of an existing structural component with an equivalent one made of composites and rehabilitating, retrofitting and strengthening of existing structures. Composites have significant advantages over traditional metals by virtue of their high specific strength and stiffness,[1] buoyancy, resistance to harsh

[1]The properties of high specific strength and stiffness offer a very attractive alternative for retrofitting work in offshore and marine structures where there are usually stringent limitations on any additional loads. Lower cost and weight advantage in the order of 30% can be achieved for blast wall applications when compared to stainless steel profiled panels [5].

© Woodhead Publishing Limited, 2010

marine environment, non-magnetism and unique stealth characteristics. In the years ahead, it is expected that the use of composites will become more prevalent as improvements in military and civil structures are demanded by end users.

10.1.1 Background

Since the 1990s, application of composites in blast resistant structures has attracted much attention. There have been proposals as to how composites can be best utilised to enhance the robustness of the structure as well as to benefit from the unique aspects composites offer [1, 2]. Some successful applications [3, 4] and potential utilisation [5, 6] of composites in the marine environment have been reviewed. It must be mentioned that in a blast scenario it is usually the ultimate states which are of interest rather than stress states at service loads level. This means that plasticity, fracture, damage and large deformations are to be expected and thus the models used should have the capability to capture these effects as accurately as possible.

Although the increase in application of composites is expected to continue, predictive capability on their damage behaviour still lags behind. This has resulted in expensive testing of the material and conservative design limits. Failure prediction for composites is still very much in the research phase at different levels (micro, meso and macro) and this can be attributed to different behaviour of the composite for a wide range of parameters with respect to loading conditions as well as uncertainties and imperfections involved. In a study conducted on a number of commonly used failure theories by Soni [7], discrepancies as high as 70% in strength prediction are observed. The discrepancy in each case depends upon the type of composite and loading conditions concerned. A more recent worldwide failure exercise [8] has attempted to push the limits of some established theories for the prediction of a series of test cases. The exercise has highlighted a general lack of robustness for most theories to be adopted as a global failure criterion. Although the general responses of all test cases are reasonably predicted and the prediction of uniaxial failure is generally in good agreement, most current theories which have taken part in the survey can achieve at most 50% accuracy in final strength predictions for multi-directional laminates. In general, combined matrix, transverse and shear failures coupled with large deformation are more difficult to predict than a fibre dominated failure. It is noteworthy that no finite elements code vendors have taken part in this exercise and thus there is still no formal appraisal on the numerical algorithms of these codes for failure prediction. Some of the software, e.g. ABAQUS®, has implemented a deviatoric energy theory as Hashin's failure criteria as a built-in capability; however, all theories can be implemented via the FORTRAN subroutines available in the software. The

© Woodhead Publishing Limited, 2010

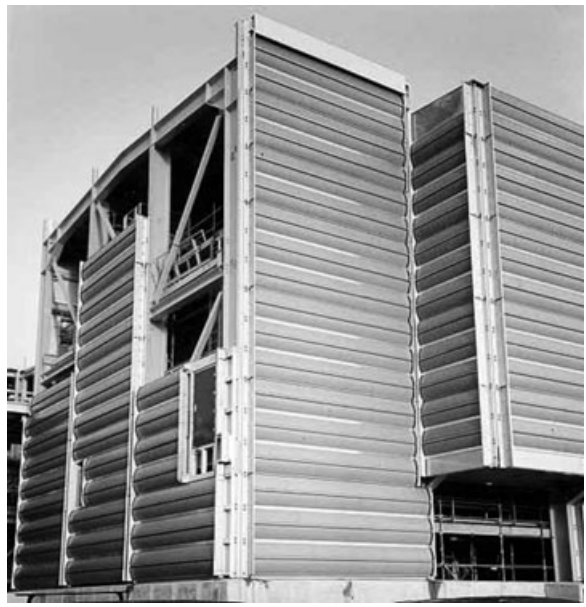

10.1 Composite blast control panels (www.offshore-technology.com).

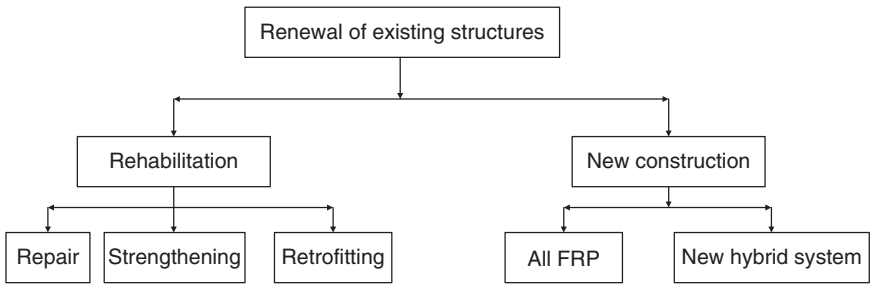

10.2 Use of fibre reinforced plastics in civil engineering applications (Van Den Einde *et al.* [10]).

reason for the discussion of this subject is the importance of material modelling in the years to come, and more rigorous models consistent with thermodynamics and with test data are yet to be introduced if the expectation of achieving better correlation with experiment is not to be abandoned.

Composites can be used as primary blast resistant structures. It has been settled by researchers that the most suitable type of composite for this type of application is glass fibre-reinforced plastic (GFRP) [3]. Figure 10.1 shows a typical all-composite blast control panel. Composites can also be used in strengthening or retrofitting existing structures and in providing alternative and parallel load paths. Figure 10.2 shows the different lines of application

© Woodhead Publishing Limited, 2010

of composites in this regard. When strengthening metallic structures is involved, the most suitable type of composite used is carbon fibre-reinforced plastic (CFRP) [9]. This is due to the close elastic moduli of steel and CFRPs which renders interfacial stresses minimal and thus reduces the probability of debonding.

10.1.2 An overview of application of composites in blast resistant design

Unarguably the most important parameter in design against a blast scenario is energy absorption. This is sometimes referred to as 'robustness' which implies the ability of a structure/structural component to survive a prescribed level of blast loading. As such, a successful blast resistant design must take account of increasing this important parameter. To investigate energy absorption one must have an understanding of different failure modes and their associated dissipated energies. The main failure modes of a composite patch in outline form are fibre breakage, fibre buckling, delamination, wrinkling, in-plane shear failure, fibre/matrix debonding and matrix cracking. In strengthening applications the debonding of the composite plate from a steel or concrete part is an important issue which is extensively studied by researchers for structures under static loads (see e.g. [11–13]). There has been some recent interest in studying debonding under dynamic loads as well as other composite failure modes at different (meso and macro) levels [14–16].

Unidirectional (UD) and woven roving (WR) fibrous laminated composites have been studied under blast loading [17, 18]. These studies are limited and do not include all material and geometric non-linear effects. In a study of blast resistance of UD fibre-reinforced composites [17] it was shown that almost 15% of the energy imparted to the structure by blast was dissipated in four different failure modes, viz. fibre breakage, fibre/matrix debonding, matrix cracking and delamination. Fibre breakage can lead to a sudden drop in load resisting capacity, especially in UD composites. The drastic tumbling in resistance element due to this mode is shown to be detrimental to the robustness of the structure [19, 20] as it increases inertia and strain rate sensitivities while concurrently bringing down the level of resisting forces. This essentially means that UD composites on their own cannot be a suitable replacement for ductile materials of construction traditionally used in the construction of conventional blast resistant structures and some modification in this regard is inevitable. This is of less significance in the case of WR composites; however, fibre breakage must be prevented as far as possible.

There are several types of modification possible to use composites in conjunction with other materials to benefit from the composite ingredients' superior properties. Some of these are as follows:

© Woodhead Publishing Limited, 2010

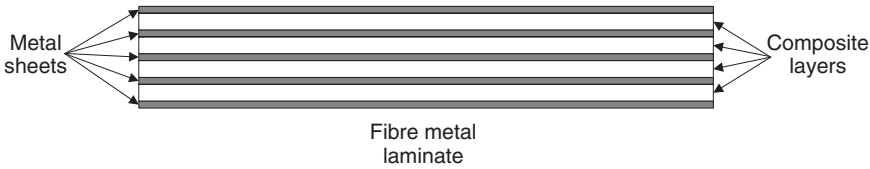

10.3 The schematic of an FML plate.

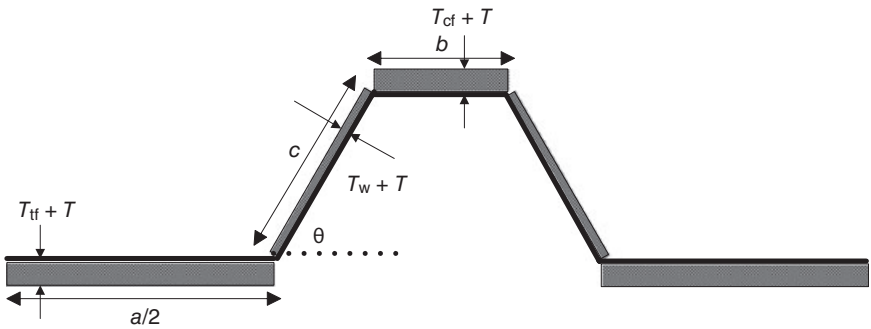

10.4 A single pitch of a profiled blast wall strengthened using composite patches with T_{ey}, T_{ty} and T_w denoting compression flange, tension flange and web thicknesses, respectively.

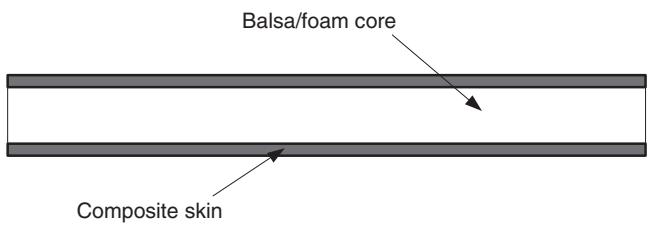

10.5 Cross-sectional view of a sandwich plate with composite skins and Balsa or foam core.

- using composites in conjunction with metals in the form of fibre metal laminates (FMLs) (Fig. 10.3).
- using composite patches for strengthening ductile structures (Fig. 10.4).
- using composite plates (as skins) along with a lightweight material such as wood or PVC foam (as core) in a sandwich beam or plate construction (Fig. 10.5).

These configurations are discussed in the present chapter.

© Woodhead Publishing Limited, 2010

10.1.3 Potential offshore and marine industry utilisation

Traditionally the materials used in the construction of marine and offshore structures are metallic. Ships and submarine hulls are made of steel with aluminium having been used in weight-sensitive applications, and offshore blast walls are made of different grades of stainless steel. In the 1960s, a comprehensive study was conducted to choose the best material for the construction of mine countermeasure vessels [21]. The study led to the choice of GFRP as the most cost-effective material given the non-magnetic and non-conducting requirements. It would be obligatory to study the effect of a possible high-rate and high-intensity dynamic load on such structures due to the environment in which these structures function.

With regard to cost in marine structures, it is true that the first (construction) cost of a fibre-reinforced plastic (FRP) structure is likely to be higher than a steel equivalent; although the difference in cost is not significant, the trade-off may still favour the use of composites. Naval ship structures must be designed to withstand shock loads from airblasts as well as from underwater explosions (UNDEX). These loads are in addition to the normal service loads as transient sea-wave and permanent static loads. Glass-reinforced plastic (GRP) composites can be specifically tailored and configured for applications to specific naval ship structures. The advantages of all-GFRP structures or hybrid arrangements compared to steel or aluminium designs are as follows:

1. elimination of fatigue cracking;
2. high strength-to-weight and stiffness-to-weight ratios;
3. better fire resistance;
4. lower maintenance cost and elimination of cracking and corrosion;
5. better weapon/ballistic protection (on a weight-to-weight basis).

There are many possible configurations with regard to the use of FRP in marine structures. These include, as mentioned before, sandwich panels with GRP skins and PVC foam or Balsa wood core and corrugated or I-beam stiffened GRP panels. Figure 10.6 shows some of the various forms of FRP composites which can be used for naval ship structures.

Each design requires an understanding of each part's role as an integral part of the structure. This is also true of the design of the associated connections. GRP structures are especially susceptible to failure under dynamic loads at bonded connections. This is due to the absence of load bearing elements as fibres across the bonded interfaces, low tensile and shear fracture energies and ductility of the adhesive as well as stress concentrations associated with joint geometry and bond imperfections. An optimised design can only be achieved if the structure and its connections have almost equal load bearing capacities. While in static design this requirement has a

© Woodhead Publishing Limited, 2010

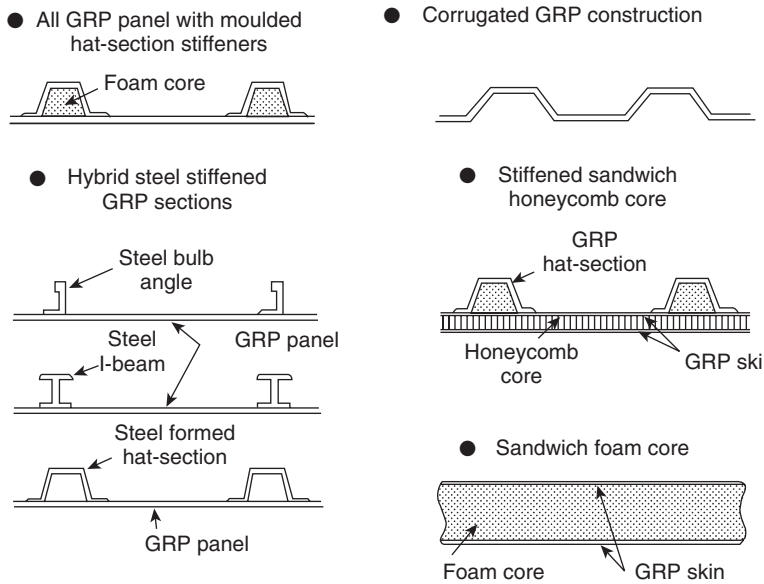

10.6 Various forms of GRP composite construction for naval ship structures (Salter [22]).

lucid meaning, in the case of dynamic extreme loading some compromise is required to achieve this goal.

In a research work conducted by a Canadian defence research establishment a UK hybrid GRP/steel I-beam stiffened panel design was selected to study for its blast resistance characteristics [22]. The unstiffened laminate fabricated from WR composite exhibited considerable strength, particularly with clamped edge conditions. The initial failure observed was in the form of interlaminar debonding and fibre breakage near the clamped boundaries (stable and controlled cracking). A plate of similar size but fabricated from CFM with lower rigidity failed catastrophically by random fibre and resin debonding/breakage (unstable and uncontrolled cracking). The 1/2-scale section of the panel fabricated and tested provided some data on the blast resistance characteristics and load level regimes for the elastic and elastic–plastic behaviour of the stiffened panel design. The steel stiffeners responded elastically to a peak blast overpressure below 250 kPa. Higher pressures caused plastic distortion of the stiffener ends. At 400 kPa, considerable permanent deflection resulted; however, the panel remained intact without breakage of welded joints or GRP laminate. The results of the complete full-size and 1/4-scale panel tests correlated well with the 1/2-scale panel section data, after it was corrected to account for free edge conditions in the orthogonal direction. Deflection of the GRP laminate

© Woodhead Publishing Limited, 2010

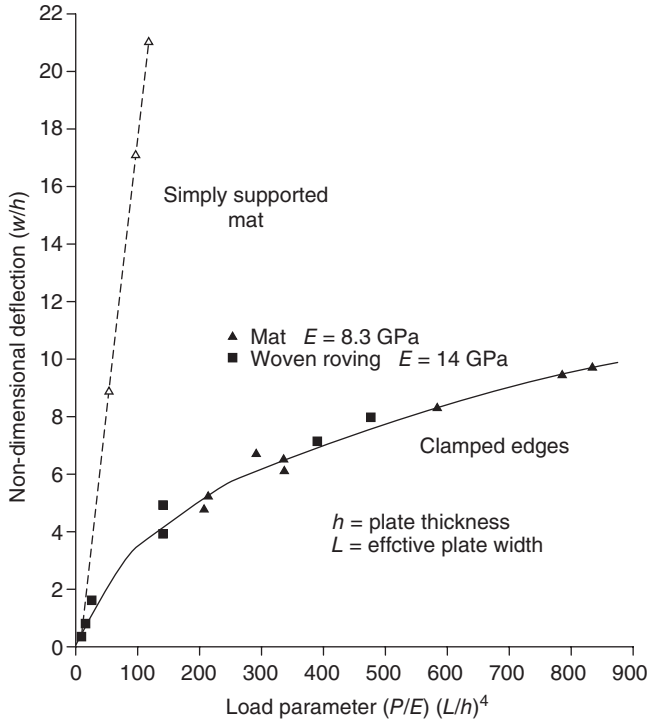

10.7 Airblast response characteristics of GRP laminates in non-dimensional form (Salter [22]).

between the stiffeners revealed that there was considerable residual strength in the composite. The blast resistance of the design was limited by the yielding and plastic distortion of the steel stiffeners. These results are shown in Fig. 10.7.

With regard to offshore industry, it must be noted that the most significant potential for using FRPs in offshore industry is in strengthening blast walls and their connections; nonetheless, strengthening main load bearing members, i.e. primary structural elements, is also sometimes considered. Blast walls are used in offshore industry to limit the destructive effects of a possible gas explosion in an offshore platform by separating the modules from one another. Due to inadequate blast resistant capacity of existing blast wall–connection systems, strengthening these structures is required [1]. One approach to solve this issue involves the use of FRP composites.

Since the objective of strengthening blast walls and their connections is to increase the energy absorption capacity, the formation of plastic hinges is not problematic and is even desirable to keep the level of forces

© Woodhead Publishing Limited, 2010

transferred to the primary structure low. Strengthening corrugated stainless steel blast walls alone could shift the plastic hinge zone to connections which would mean a non-optimized solution. In some cases it may even trigger tearing at connections. As such, both the panel and its connections must be strengthened. While strengthening connections proportional to profile would contribute to energy absorption, over-strengthening connections would shift the stress concentration zone to panel/connection weld zone and causes potential tearing. In a recent study conducted by the authors [23], a systematic method for strengthening a typical blast wall and its connections has been proposed. The method introduced is such that energy absorption is increased without material being wasted and without tearing rendering the strengthening unsuitable. This objective is satisfactorily achieved using a sequence of simple rationale in conjunction with interpretation of results obtained from the numerical general-purpose finite element code (ABAQUS® 6.6-1). However, there are cases which have not been studied in detail and the systematic method can be improved if partial strengthening is taken into account. Research is currently being conducted in Imperial College to improve the method. The particulars of the method are discussed in a later section.

10.1.4 Military and defence applications

Some of the most important applications of composites are in defence and military industries. Composites can be used in body armour design to protect military personnel against ballistic threat. Military equipment and installations can be made of composite FRPs. Ships must be protected against underwater explosions (UNDEX), and military sites must be secured against possible terrorist attacks and blasts in the vicinity of military sites such as barracks.

Protection of military sites and equipment against blast loads is of crucial importance, and composites can be used to enhance the blast resistance of existing structures and well as construction of new load bearing members to further increase the redundancy as well as capacity of the structure. Destructive effects of explosions on military sites have been studied by researchers and approximate methods of evaluation of threat have been introduced [24, 25].

Underwater explosions can have drastically detrimental effects on naval military structures such as ships and submarines. An underwater explosion causes an initial shock wave similar to that of an airblast and the subsequent bubble pulsation causes a dynamic load of much longer duration though with lower amplitude on the naval structure. In cases where there is some damage to the structure in the initial phase the second phase of loading, which usually occurs much later, can cause complete collapse. These effects

© Woodhead Publishing Limited, 2010

have been studied by researchers [26, 27]. GRP composites can be used to tackle the issue of excessive loading in this regard [3].

10.1.5 Scope of the present study

The present study deals with three examples of the use of FRP composites in blast resistant applications. These may be offshore, naval or defence related. In all these applications only the maximum response has been considered rather than a detailed time-history of the output parameters. The three examples include new design, strengthening and replacement applications. As for new design, the effects of a localised blast have been considered on an FML system. For strengthening, a corrugated stainless steel blast wall has been studied for an offshore application together with a sandwich panel with composite skins as a possible replacement. The types of explosions considered are a high explosive detonation event (e.g. TNT) and a typical deflagration process due to a hydrocarbon gas explosion. Physical explosions due to, for instance, an extremely hot liquid filling a frozen tank or pipe and nuclear explosion due to subatomic fission or fusion are not considered. Structures more familiar to the reader with a civil engineering background, i.e. buildings, are not considered here. There are several reasons for not considering buildings in a chapter of this size.

The distinction between the design of residential or commercial buildings on the one hand and offshore, marine or defence related structures on the other hand renders the use of composites in the latter group far more significant and meaningful. Composites are suitable for applications where weight sensitivity is an issue and proper blast resistance protection a key priority in design.

For most residential or commercial buildings, the effects of an explosion are not generally considered as a primary design feature, although general robustness issues are built in to many codes of practice which incorporate a certain amount of protection against progressive collapse. In more recent times, the threat of terrorist activity has increased and certain high-profile structures are given significantly more attention.

However, the costs of protection are excessive when integrated over time and space and given the low probability of occurrence of an explosion for run-of-the-mill structures. Besides costs, excessive protective designs can be aesthetically unacceptable. Integrating blast resistant design into buildings requires the consideration of many details which are too numerous to include in this chapter. However, some of these include alterations to the plan, architectural details and change to cladding that further increase the cost of design and construction. The most effective protective measure for buildings where the degree of importance is high and space permits is to

© Woodhead Publishing Limited, 2010

provide standoff from the explosive device to the building since blast waves decay significantly with distance. When blast is internal, however, the shock wave is severe and can interact with its surroundings. Furthermore, if venting is restricted the product gas can build up a quasi-static pressure in a subsequent phase to the initial shock phase which can sometimes be more severe than the initial shock phase of the detonation process. Models allowing fluid–structure interaction (FSI) must be used to effectively capture the sophisticated blast wave reflections from the surrounding surfaces, while venting and quasi-static gas pressures add to the complication. These cases are obviously not considered in the present work.

10.2 Use of composites in strengthening applications

10.2.1 Constitutive modelling of strengthening composite patches

A ply in a laminate shows linear elastic behaviour prior to failure under longitudinal (direction 1) tension or compression, transverse (direction 2) tension or compression or shear or a combination of the above. The term 'failure' can be defined in several ways. One apparent definition is the complete separation, or fracture as a result of which the component can no longer support the loads acting on it. A more accurate alternative definition is when the component can no longer fulfill the function for which it has been designed. From a mathematical point of view, failure could be associated with singularity (or ill-conditioning) of the component or structural stiffness matrix which is a result of material property degradation once a simple or interactive stress/strain-based criterion is met. Subsequent propagation of failure is associated with energy-based criteria. Progressive failure can be studied using fracture mechanics (discrete crack propagation) or damage mechanics (smeared crack model). Therefore, constitutive modelling of composite materials comprises two phases. The first is the linear elastic phase which terminates once the failure criterion (criteria) for a particular mode is met and the second is the post-failure fracture or damage model for that particular mode. Fracture models are based on fracture mechanics which studies crack extension behaviour as a function of applied loads in a discrete manner. Few finite element software packages have implemented this kind of failure model. The more common type of failure model is that of smeared crack which can be used in ABAQUS® 6.6-1 through a subroutine. The smeared crack model has been explained in this section.

The stress–strain relation for a linear elastic unidirectional composite ply can be expressed by Eq. 10.1:

© Woodhead Publishing Limited, 2010

$$\begin{bmatrix}\sigma_1\\ \sigma_2\\ \tau_{12}\end{bmatrix}=\begin{pmatrix}\dfrac{E_{11}}{1-\nu_{12}\nu_{21}} & \dfrac{\nu_{21}E_{11}}{1-\nu_{12}\nu_{21}} & 0\\ \dfrac{\nu_{12}E_{22}}{1-\nu_{12}\nu_{21}} & \dfrac{E_{22}}{1-\nu_{12}\nu_{21}} & 0\\ 0 & 0 & G_{12}\end{pmatrix}\begin{bmatrix}\varepsilon_1\\ \varepsilon_2\\ \gamma_{12}\end{bmatrix} \quad [10.1]$$

Where E is elastic moduli, υ is Poisson's ratio and G is transverse modulus. In a finite element analysis, the relevant parameters (i.e. elastic moduli and Poisson's ratios) are introduced to the software, and the calculations to find the equilibrium path are done using an incremental analysis. In such an analysis, elastic properties of the material are used to calculate the first point of equilibrium in the $N + 1$ dimensional space of N displacement coordinates and the load proportionality factor. From this point onwards, the subroutine is called per increment to check if the relevant failure criteria (which can be simple or interactive, stress or strain-based) are met. If the answer is in the negative, the final state of the first increment is taken as the initial state of the second increment and the procedure is repeated for the next increment. If the failure criterion is not met during the analysis the composite has had an elastic behaviour all along and the analysis successfully terminates. If at some increment the failure criterion is met at some point (usually integration points of elements are checked), then the material properties associated with that element would be altered accordingly. The way different material properties degrade once a failure criterion is met generally depends upon the mode of failure associated with that failure criterion. After degradation of material properties of failed elements, the same increment is reiterated until the iteration at which equilibrium is achieved and the analysis moves to the next increment. Once a material associated with an element fails, it can never regain its initial stiffness and strength properties and would be replaced by a material of much lower stiffness and strength. This is the fundamental assumption of damage mechanics. The procedure explained above is that of Riks analysis; nonetheless, it is similar to other types of implicit FE analysis procedures. This procedure is discussed in detail in [23].

Two-dimensional (2D) and three-dimensional (3D) failure criteria have been developed to deal with ply failure, i.e. fibre, matrix and in-plane shear failures. A major classification of these failure criteria categorises them as simple and interactive stress/strain-based criteria. Fibres are the most important elements of strength in a ply. As such, fibre failure in a composite ply can be viewed as the complete directional failure of that ply which causes the loss of all stiffness moduli at failed integration points. Matrix failure is not crucial on its own; however, as mentioned before, it may give rise to initiation of delamination or in-plane shear failure. In the case of

© Woodhead Publishing Limited, 2010

matrix cracking, the transverse modulus E_{22} and Poisson's ratio ϑ_{21} are reduced to zero.[2] When fibre matrix shearing is predicted at a material point, the transverse modulus G_{12} and Poisson's ratio ϑ_{21} are reduced to zero. The Tsai–Hill, Tsai–Wu and Azzi–Tsai–Hill [28] theories predict the failure using an interactive convex surface in the space of stress components. The Hashin criterion [29] directly gives the mode of failure which accounts for fibre and matrix failures. In the case of matrix failure, the in-plane shear modulus is also degraded. In the numerical analyses of this section Hashin's model has been used which is described by Eqs 10.2–10.5:

fibre failure:

$$\left(\frac{\sigma_1}{X_T}\right)^2 + \left(\frac{\sigma_{12}}{S}\right)^2 = 1, \quad \sigma_1 > 0 \qquad [10.2]$$

$$\sigma_1 = X_c, \quad \sigma_1 < 0 \qquad [10.3]$$

matrix failure:

$$\left(\frac{\sigma_2}{Y_T}\right)^2 + \left(\frac{\sigma_{12}}{S}\right)^2 = 1, \quad \sigma_1 > 0 \qquad [10.4]$$

$$\frac{1}{Y_c}\left[\left(\frac{Y_c}{2S}\right)^2 - 1\right]\sigma_2 + \left(\frac{\sigma_2}{2S}\right)^2 + \left(\frac{\sigma_{12}}{S}\right)^2 = 1, \quad \sigma_1 < 0 \qquad [10.5]$$

where $\sigma_1 > 0$ shows tension in the fibre direction and $\sigma_1 < 0$ shows compression in this direction and where X and Y show normal strengths in directions 1 and 2 and S the in-place shear strength, respectively. Subscripts T and C denote, respectively, tension and compression. For the case of 3D failure modelling, 3D failure criteria are introduced. While failure in the 1–2 plane is defined using Eqs 10.2–10.5, delamination is defined by Eq. 10.6 (this rule is introduced by Brewer and Lagace [30]):

$$\left(\frac{\sigma_{33}}{Z_T}\right)^2 + \left(\frac{\sigma_{23}}{S_{23}}\right)^2 + \left(\frac{\sigma_{13}}{S_{13}}\right)^2 = 1 \qquad [10.6]$$

where Z_T is the through-thickness tensile strength, S_{23} is the shear strength in the transverse and through-thickness plane and S_{13} is the shear strength in the through-thickness and fibre plane.

The values of these parameters for the CFRP laminate of unidirectional fibres are taken as $Z_T = 30.51$, $S_{13} = 51.96$ and $S_{23} = 51.96$ MPa. These values are extracted from Hou *et al.* [31]. The use of 3D failure criteria requires the use of continuum elements for FRP patches in an FE model. Initial

[2] In a numerical program, elastic modulus of zero will cause singularity problems. As such, small values are assigned to degraded properties.

© Woodhead Publishing Limited, 2010

study on some corrugated panels strengthened by CFRP patches on the compression and tension flanges as well as webs suggests the relative importance of delamination for the cases when stacking angle changes from one ply to another (e.g. 0/90/0). In these cases, delamination starts from free edges in the vicinity of supports and propagates towards the mid-span up to 25% of the length of the patch. However, for cases where all unidirectional plies have the same direction of fibres in a laminate, delamination is not significant and is local to the regions close to supports. As such, in the analyses of the present study shell elements are used and a 2D Hashin failure model for unidirectional laminates is considered.

In the analyses in the present study, user subroutine USDFLD is used along with static Riks and dynamic implicit analyses to capture the effects of different failure modes for composites. This subroutine has the capability of redefining the material properties and state variables in a solution-dependent manner. In numerical modelling using ABAQUS®, the values of degraded material properties are taken as 5% of the intact values for elastic moduli and 0 for Poisson's ratios. Table 10.1 shows the intact modulus values along with strength parameters for typical composites.

10.2.2 Strengthening scheme

A systematic strengthening scheme must: (i) be universally applicable, i.e. applicable to all sections considering the limitations encountered in strengthening, (ii) pinpoint the weakest part of the section and (iii) make optimal use of strengthening materials. There is some evidence of the improvement in buckling strength of CFRP-enhanced steel sections as pointed out by researchers [9]. As such, the primary function of composites in a hybrid system could be thought of as deferring buckling by a decrease in slenderness of critical compression elements. The three requirements

Table 10.1 Typical values for elastic moduli, Poisson ratios and failure stresses of unidirectionally reinforced composite material [32]

Property	Glass–epoxy	Boron–epoxy	Graphite–epoxy	Kevlar®–epoxy
E_1	54	207	207	76
E_2	18	21	5	5.5
ϑ_{12}	0.25	0.3	0.25	0.34
G_{12}	9	7	2.6	2.1
X_t	1035	1380	1035	1380
Y_t	28	83	41	28
S	41	124	69	44
X_c	1035	2760	689	276
Y_c	138	276	117	138

© Woodhead Publishing Limited, 2010

mentioned above for an ideal strengthening scheme will be satisfied if one makes use of the single parameter β proposed by Gardner and Nethercot [33]. This parameter is defined by Eq. 10.7 as follows:

$$\beta = \left(\frac{B}{t}\right)\sqrt{\frac{\sigma_{0.2}}{E_0}}\sqrt{\frac{4.0}{k}} \qquad [10.7]$$

where B is the width of the plate (flange or web), t is its thickness and k is the buckling coefficient which can be determined as a function of plate aspect ratio and edge stress distribution and can be found in tabulated form in Eurocode 3 (Table 4/ ENV 1993-1-3 [34]).

The parameter β relates the degree of criticality of a compression element (plate in compression) in buckling to geometrical and material properties for that element when the material of the section is of round-house type (e.g. aluminium or stainless steel). The equality of this parameter for web and flange thus shows that the two buckle simultaneously and the material is used optimally.

The particulars of the criteria of the selection of strengthening patches of both the profile and the connections are soon to be available in the literature [23]. In a nutshell it can be conveyed that a strengthening scheme can exist to optimally strengthen the section and its connections and to use composite materials efficiently.

Figure 10.8a shows the resistance curve of a strengthened profiled strengthened once on the compression flange and the web and once on the web and both flanges. The base design (unstrengthened profile) is included for the sake of comparison. The schematics of all three models are shown in Figs 10.8b–10.8d. As can be seen, the profile strengthened on both flanges increases the level of connection forces substantially and fails suddenly causing inertia and strain rate sensitivity. This is a major drawback which must be overcome. Currently, work is being done to further modify the method of strengthening. This includes partial strengthening of profiles and accurate modelling of residual strength and stiffness.

As for connections, two strengthening patches are required, one to reduce the level of stresses and the other to avoid large connection opening and tearing. The two patches applied on a typical connection used in offshore industry are shown schematically in Fig. 10.9a while the connection as an integral part of the structure is shown in Fig. 10.9b.

Figure 10.10 shows a failed profile where patches have failed under static uniformly distributed load over the entire span.

The conclusions drawn from the study conducted are as follows:

1. Static collapse load for a profile strengthened on both flanges and the web is considerably higher than the static collapse load of its unstrengthened counterpart.

© Woodhead Publishing Limited, 2010

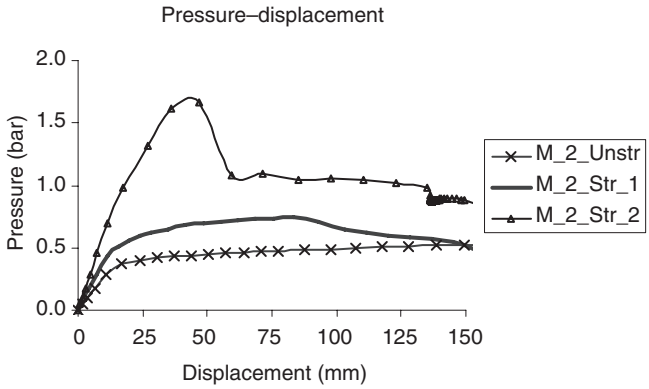

(a)

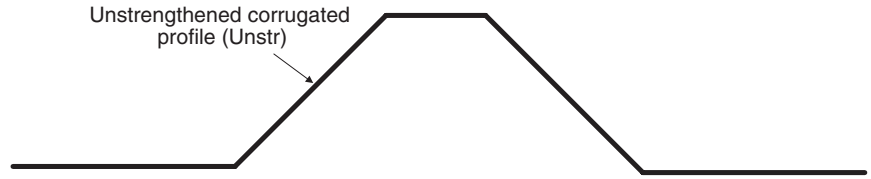

(b)

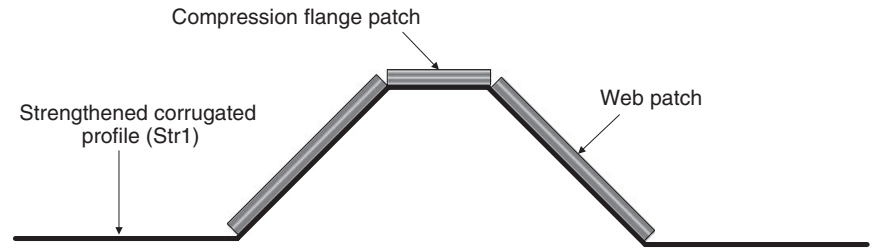

(c)

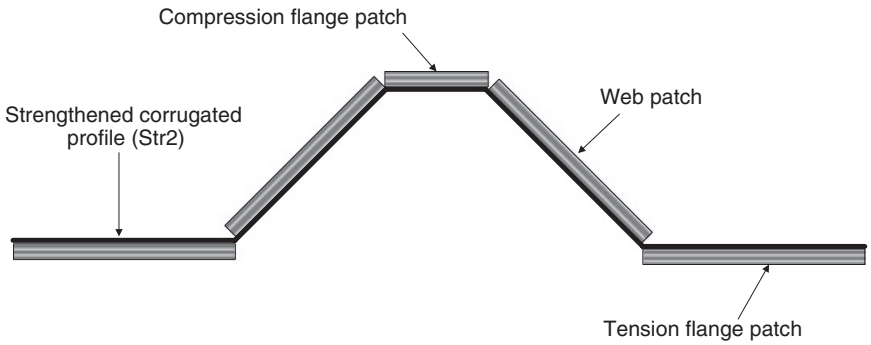

(d)

10.8 (a) Comparison of resistance curves in three cases for one of the test models (M_2) M_2_Unstr = Unstrengthened model 2, M_2_Str_1 = Model 2 strengthened on the web and compression flange only, M_2_Str_2 = Model 2 strengthened on the web and compression and tension flanges; (b) schematic of M_2_Unstr; (c) schematic of M_2_Str1; (d) schematic of M_2_Str2.

© Woodhead Publishing Limited, 2010

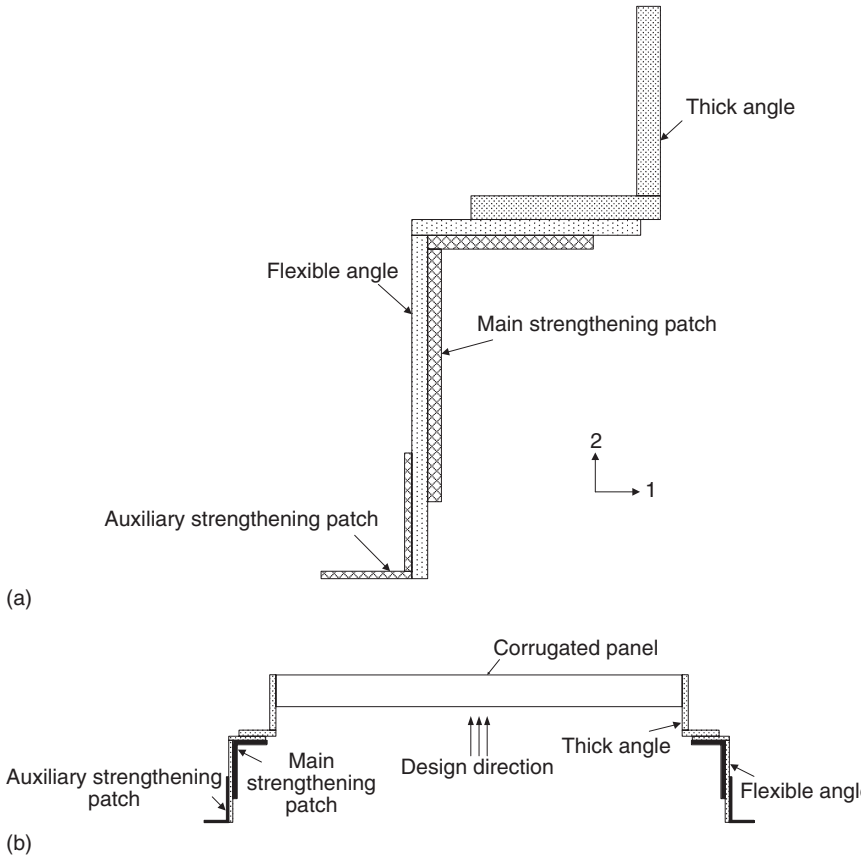

10.9 (a) The schematic of a strengthened connection used in offshore industry; (b) the panel-connection arrangement in the overall structural configuration.

2. Once fibres break in a composite patch of a strengthened hybrid system, there will be no contribution to energy absorption capacity of the hybrid system on the part of composite patches.
3. If connection and profile patches remain intact (no fibre breakage), there will be some contribution to the energy absorption capacity on the part of composites. This contribution is at the cost of large forces exerted on the connections.
4. For dynamic analyses in preliminary blast resistance assessment the conventional mass-spring SDOF (single-degree-of-freedom) model of a hybrid system would not be suitable as a substitute for the continuous system. In this case, a more sophisticated and more accurate SDOF model similar to the one proposed by Langdon and Schleyer [35] would be more suitable.

© Woodhead Publishing Limited, 2010

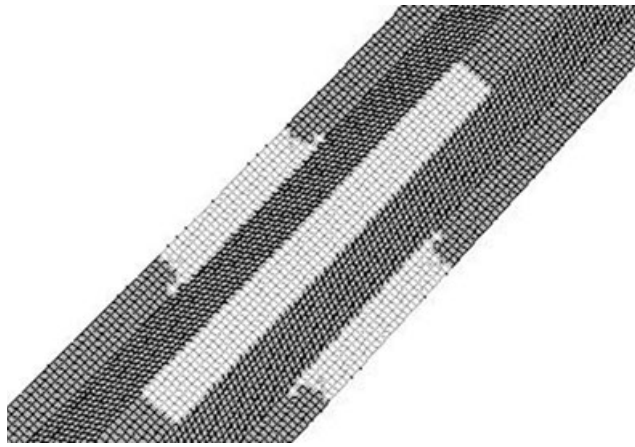

10.10 Failure of composite patches in a strengthened profiled blast wall.

10.3 Use of composites in replacement applications

Use of composites in strengthening applications was discussed in the previous section. Besides strengthening using FRPs, there has been, in recent years, an ever-increasing interest in the offshore, defence and marine industries to further increase the application of composite materials in primary structural applications. This is partly due to the significant advantages of composites over traditional metals by virtue of their high specific strength and stiffness, buoyancy, resistance to harsh marine environments, non-magnetic and unique stealth characteristics. This section includes an example study in this regard based on the work done by Boh [36].

10.3.1 Constitutive modelling of composite plates/skins

This section reviews and discusses the prediction of response and failure in large-scale composite panels subjected to blast loads and compares the results with a steel panel of the same size as the benchmark. The proposed models for the prediction of blast response of laminated composite are validated with some experimental data obtained from the literature and comments on comparisons are given. The comparison is particularly important given the weight advantages composites offer over metals.

As discussed before, different failure models can be proposed for composites. The deviatoric energy failure criterion (Tsai–Hill failure model) has been used for the purpose of the present study. It is based on Eq. 10.8 which is the extension of Hill's plasticity model into the realm of anisotropic plasticity. This model is developed based on the mathematical premise that

© Woodhead Publishing Limited, 2010

a second-order curve for all stress components is able to correlate with experimental results reasonably well.

$$(G+H)\sigma_{11}^2+(F+H)\sigma_{22}^2+(F+G)\sigma_{33}^2-2H\sigma_{11}\sigma_{22}-2G\sigma_{11}\sigma_{33}-2F\sigma_{22}\sigma_{33}+2L\sigma_{23}^2+2M\sigma_{13}^2+2N\sigma_{12}^2=1.0 \quad [10.8]$$

In this equation parameters F, G, H, L, M, N are material constants that are to be evaluated for unidirectional loading conditions. This equation can be rewritten as follows:

$$\left(\frac{1}{X^2}\right)\sigma_{11}^2+\left(\frac{1}{Y^2}\right)\sigma_{22}^2+\left(\frac{1}{Z^2}\right)\sigma_{33}^2-\left(\frac{1}{X^2}+\frac{1}{Y^2}-\frac{1}{Z^2}\right)\sigma_{11}\sigma_{22}-\left(\frac{1}{X^2}-\frac{1}{Y^2}+\frac{1}{Z^2}\right)\sigma_{11}\sigma_{33}-\left(-\frac{1}{X^2}+\frac{1}{Y^2}+\frac{1}{Z^2}\right)\sigma_{22}\sigma_{33}+\left(\frac{1}{Q^2}\right)\sigma_{23}^2+\left(\frac{1}{R^2}\right)\sigma_{13}^2+\left(\frac{1}{S^2}\right)\sigma_{12}^2=1.0 \quad [10.9]$$

where X, Y, Z, Q, R, S are the axial and shear strength parameters, respectively. The major drawback of this model is that it takes no account of the difference in tensile and compressive strengths.

In contradistinction, the interactive tensor theory proposed by Tsai and Wu [37] suggests the use of second-order polynomial strength tensors to account for the differences in tensile and compressive strength by including linear terms in the polynomial. The criterion is intrinsically anisotropic and is applicable in all coordinate systems. The failure locus exists in the scalar form of Eq. 10.10:

$$F_{ij}\sigma_{ij}+F_{ijkl}\sigma_{ij}\sigma_{kl}=1.0 \quad [10.10]$$

where F_{ij} and F_{ijkl} are tensor quantities of strength parameters.

It should be noted that neither Tsai–Hill nor Tsai–Wu failure theory is meant to model the complex failure mechanisms in composites. Subsequently, it is not possible to model progressive damage and subsequent degradation of the material properties. Despite some of the inherent inconsistencies [38], the Tsai–Wu theory remains one of the leading failure theories for composites as noted in the worldwide failure exercise [39].

As for the mechanism-based failure theories introduced to identify the various failure mechanisms of composites, a generalised quadratic failure criterion can be developed based on Fig. 10.11 where it is assumed that there exists a failure plane where all or some of associated stresses are responsible for failure on that plane and they interact in a quadratic manner.[3]

[3] Quadratic criterion is merely based on best fit of experimental observation and not on physical behaviour, though it satisfies the convexity requirement which is indispensible to any failure model consistent with thermodynamics laws.

© Woodhead Publishing Limited, 2010

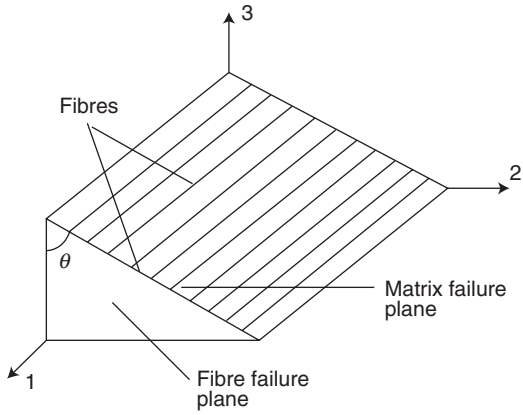

10.11 Failure planes for lamina (unidirectional) (Boh [36]).

Furthermore the fibre failure plane is perpendicular to the fibre direction and there are two matrix failure planes orthogonal to this plane if the lamina is unidirectional. For woven roving lamina, there would be two fibre failure planes and the third orthogonal plane will be in the plane of the lamina. Matrix damage may be represented by in-plane shear damage of this plane.

The equations representing this are as follows:

$$\text{(A) } \textit{Fibre failure}: \quad \left(\frac{\sigma_{11}}{X}\right)^2 + \left(\frac{\sigma_{12}}{S_{F12}}\right)^2 + \left(\frac{\sigma_{13}}{S_{F13}}\right)^2 = 1.0$$

$$\text{(B) } \textit{Matrix failure (1–3 plane)}: \quad \left(\frac{\sigma_{22}}{Y}\right)^2 + \left(\frac{\sigma_{12}}{S_{M12}}\right)^2 + \left(\frac{\sigma_{23}}{S_{M23}}\right)^2 = 1.0 \quad [10.11]$$

$$\text{(C) } \textit{Matrix failure (1–2 plane)}: \quad \left(\frac{\sigma_{33}}{Z}\right)^2 + \left(\frac{\sigma_{13}}{S_{D13}}\right)^2 + \left(\frac{\sigma_{23}}{S_{D23}}\right)^2 = 1.0$$

The generalised failure criteria may then be represented by Eqs 10.11 where X, Y and Z are the appropriate normal, tensile or compressive strength of the respective failure planes. S is the shear strength where the subscripts F, M and D denote fibre, matrix and delamination, respectively. Delamination failure is a characteristic of composites due to the effects of in-plane stress gradients and stress-free edges resulting from the compliance mismatch between plies. Delamination can be significant when thick composite laminates are subjected to transverse loads resulting in shear deformation between layers due to presence of interlaminar shear stresses. In addition, fibre and matrix failures are assumed to induce stress concentration that can promote delamination. Delamination can occur at lamina interface and at free edges which can affect the laminate mechanical properties such as tension, compression, flexure and fatigue in the form of reduced stiffness, premature failure [40, 41] or reduced residual capacity

© Woodhead Publishing Limited, 2010

[42]. Recent developments in computational mechanics of solids have allowed the implementation of cohesive elastic-damage formulation which renders modelling of an interlaminar resin-rich layer feasible. Once damage initiates, it may or may not propagate; however, the propagation follows the laws of fracture mechanics and is energy based.

After the initiation of damage indicated by the satisfaction of one of the failure criteria given above, stiffness will be reduced according to the damage mode. Stresses will be distributed to the undamaged zones and equilibrium re-established. Failure criteria will be re-checked until no further damage is detected before the analysis for the next time-step is carried out. It has been assumed that initial damage does not necessarily constitute a collapse for the composite. Instead of reducing the stiffness to zero upon damage, a residual factor approach is proposed. The reduction of stiffness to a residual factor is based on test observations where clearly there exists residual capacity for all specimens after maximum load is attained. Although the existence of the residual factor is certain, it has yet to be established how precisely such factors can be calculated. This can affect the dynamic response severely. With no measured data at our disposal, this factor will be varied to give the global load-displacement behaviour that can describe the test observation reasonably well. Factors ranging between 0.05 (for UD composites) and 0.10 (for WR composites) are found to be satisfactory for most laminated composites subjected to blast. The proposed degradation rules for UD, WR and CSM lamina are summarised in Table 10.2 with RF representing the reduced factor.

In addition, all through-thickness strengths will be reduced upon fibre or matrix damage to take account of the induced stress concentrations that promote delamination [31]. Similarly, the in-plane strengths are reduced due to delamination failure in order to take account of interaction of delamination and in-plane failure mechanisms. For simplicity, the proposed reduction factors do not take account of the difference between tensile and compressive induced failure. In addition, one would also expect the RF factors to be different for each different condition given in Table 10.2.

10.3.2 Finite element analyses of composites under blast

Once material characterisation tests have been conducted and material models implemented in numerical finite element codes the analysis can commence. In the finite element modelling of a blast or impact scenario the model must be first validated in an equivalent static loading scenario.[4] The

[4] By equivalent here is meant that the amplitude blast load or contact force must be applied statically in the same position as expected. This is different from exerting on the structure the amplified static loads based on dynamic load factors or energy equivalence.

© Woodhead Publishing Limited, 2010

Table 10.2 Property degradation for different lamina types [36]

Element status/elastic property	E_{XX}	E_{YY}	E_{ZZ}	G_{XY}	G_{XZ}	G_{YZ}
No failure	1	1	1	1	1	1
Fibre failure	RF	1	1	RF	RF	1
Matrix failure	1	RF	1	RF	1	RF
Delamination	1	1	RF	1	RF	RF

(a)

Element status/elastic property	E_{XX}	E_{YY}	E_{ZZ}	G_{XY}	G_{XZ}	G_{YZ}
No failure	1	1	1	1	1	1
Fibre failure (1)	RF	1	1	RF	RF	1
Fibre failure (2)	1	RF	1	RF	1	RF
Shear matrix failure	1	1	1	RF	1	1
Delamination	1	1	RF	1	RF	RF

(b)

Element status/elastic property	E_{XX}	E_{YY}	E_{ZZ}	G_{XY}	G_{XZ}	G_{YZ}
No failure	1	1	1	1	1	1
X-Direction	RF	1	1	RF	RF	1
Y-Direction	1	RF	1	RF	1	RF
Z-Direction	1	1	RF	1	RF	RF

(c)

response with and without damage must correspond to experimental observations. As a rule of thumb, in FE analyses the finite element mesh for cases with plasticity or damage must be finer than those without such effects. Figure 10.12 shows a thick composite panel subjected to a static load applied to the structure by placing a rigid body on the top and controlling the displacement of the rigid body reference point.

In blast resistance design the material response can be assumed to be linear if no damage occurs, but geometrical non-linearity should generally be considered. Strain rate effects on composites remain to this day a topic of research due to uncertainties, and the high sensitivity to the quality of composite and presence of voids. Figure 10.13 shows the load deflection response for a glass fibre-reinforced WR laminate subjected to short beam shear (SBS) test conducted on the beam of Fig. 10.12.

The characteristics of each model are available in Table 10.3. An interesting characteristic trait shared by all such static loading response curves is

© Woodhead Publishing Limited, 2010

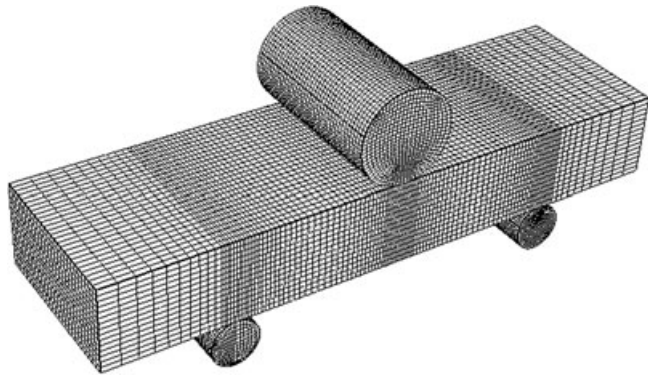

10.12 A finite element model for a laminated beam (solid elements (stacked) and a cylindrical rigid collider (tup)) (Boh [36]).

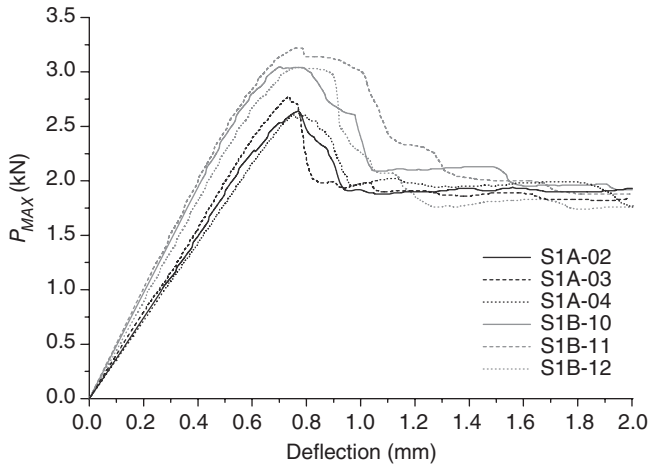

10.13 Load deflection response for different specimens of GRP WR laminates subjected to SBS test (Boh [36]).

this: the curve has linear elastic behaviour up to the point of maximum load. Then there is a steep drop to a residual value which is followed by a plateau. This characteristic was pointed out previously for over-strengthened corrugated beams. Different modes of failure are shown in Fig. 10.14.

The predicted dynamic response using finite element modelling for a $250 \times 250\ mm^2$ simply supported orthotropic panel of 50 mm thickness when subjected to a suddenly applied uniformly distributed load of 1 bar is given in Fig. 10.15. The test results reported in literature [43] are included

© Woodhead Publishing Limited, 2010

Table 10.3 Model and response characteristics

Specimen reference	Width (mm)	Length (mm)	Thickness (mm)	Load (kN)	Shear strength (MPa)
S1A-1	10.7	38.2	5.1	2.8	37.6
S1A-2	10.8	38.2	5.1	2.6	35.8
S1A-3	10.8	38.1	5.1	2.8	38.1
S1A-4	10.8	38.2	5.0	2.6	36.1
S1A-5	10.8	38.1	5.1	2.6	35.5
S1A-6	10.7	38.0	5.1	2.9	40.0
S1B-7	10.8	38.3	5.6	3.4	42.7
S1B-8	10.7	38.3	5.7	3.4	41.1
S1B-9	10.7	38.2	5.6	3.4	42.6
S1B-10	10.8	38.2	5.8	3.1	36.8
S1B-11	10.8	38.3	5.6	3.2	40.2
S1B-12	10.6	38.3	5.5	3.0	38.9

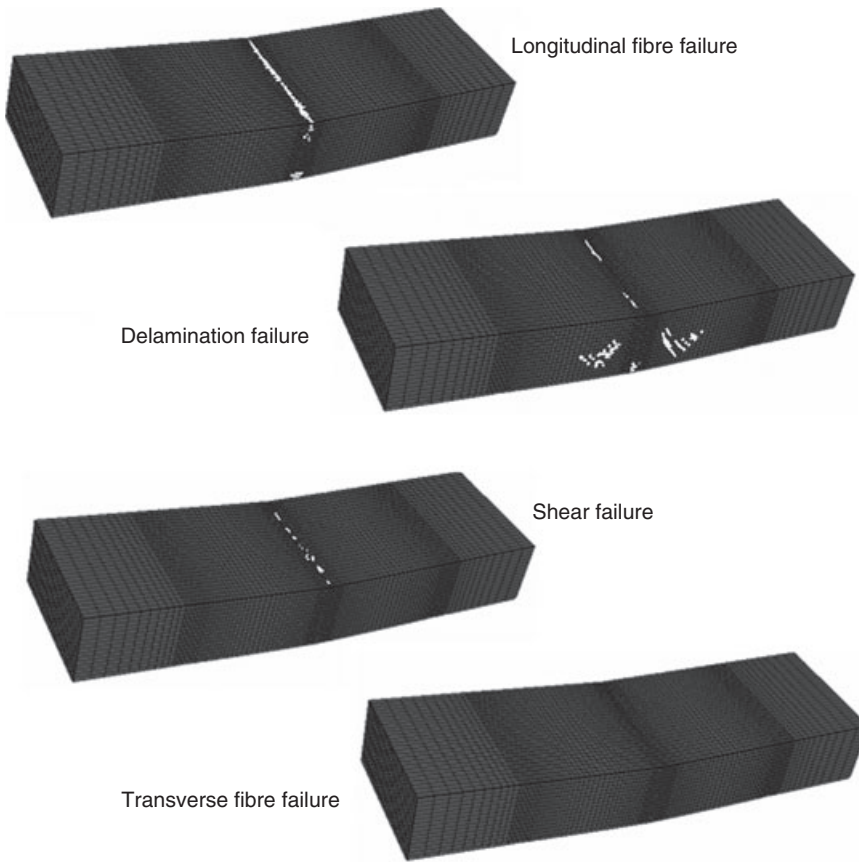

10.14 Different failure modes (brighter elements show the failed ones) (Boh [36]).

© Woodhead Publishing Limited, 2010

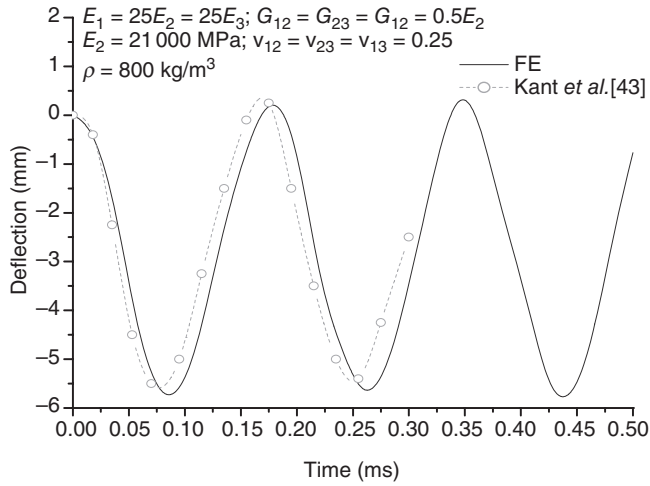

10.15 Dynamic response of an orthotropic panel (Boh [36]).

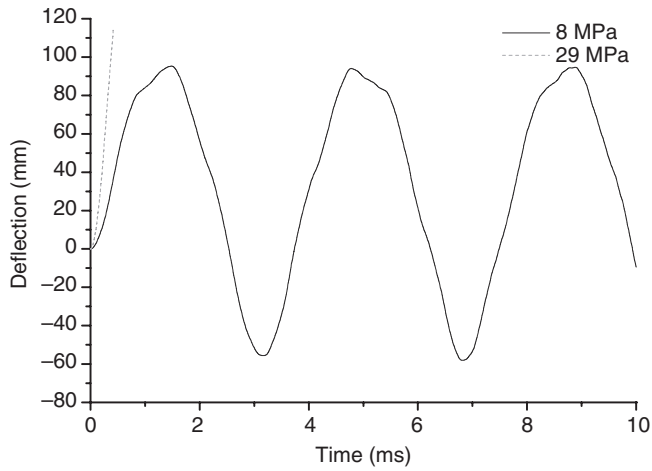

10.16 Dynamic response of a WR/CSM laminate subjected to underwater blast (Boh [36]).

in this figure for comparison. It is observed that the numerical model can predict the maximum deflection and vibration response reasonably well. The result of an underwater blast test conducted by Mouritz *et al*. [44, 45] is shown in Fig. 10.16 where the damaged response of the laminate is predicted. The adequacy of the failure and finite element models investigated are confirmed.

© Woodhead Publishing Limited, 2010

10.3.3 Composite sandwich panels and joints

This section describes an overview and considerations needed in developing a composite blast wall for applications in offshore and marine environments. This way the existing blast walls can be replaced by the proposed one. Although the main focus remains on blast resistance of the wall, other equally important considerations such as connections and fire resistance will be addressed briefly. Few possible configurations of the composite blast wall are proposed and their blast response characteristics are compared with their metal counterparts.

Selection of fibre and resin systems

E-glass has traditionally been used as the fibre system for marine composites and remains a good candidate due to its relatively low cost, ease of fabrication and good chemical resistance to salt water and engine fuel.[5] Because of its relatively low stiffness, it is appropriate to detail the connection such that the membrane resistance can be used to advantage. Vinyl ester provides good resistance to water and chemical attack and has high fracture toughness where its failure strain is approximately 5%. Composite plates can be best used as the skins in a sandwich system. The core is a lightweight material which satisfies a set of prerequisites. For illustrative purposes, Balsa wood will be used as the core in sandwich composite panel and vinyl ester will be used as matrix material in laminated composite panel.[6]

Connection system

Joining sandwich panels introduces a new challenge. One of the ways to connect vertical and horizontal sandwich components in naval vessels is to adhesively bond the two elements together. Adhesively bonded joints have been extensively used in assembling sandwich structures. This type of joint is usually termed as a T-joint due to its shape and comprises a base panel, a leg panel and two overlaminates. There is a fillet (usually made of Crestomer®) which fills in the gap between the leg and the base panels and,

[5] Other alternatives include S-2 glass which offers better mechanical strength (30%) and ballistic resistance but at a cost of up to 10 times that of E-glass. S-glass, which has even better mechanical properties, is extensively used in the aerospace industry and is about 20–30 times more expensive.

[6] Other resins that may be considered, possibly with suitable additives, are epoxy and isophthalic polyester. The former offers good mechanical properties but with high material and construction costs, and while the latter is commonly used in marine environments, it has rather poor fire performance.

© Woodhead Publishing Limited, 2010

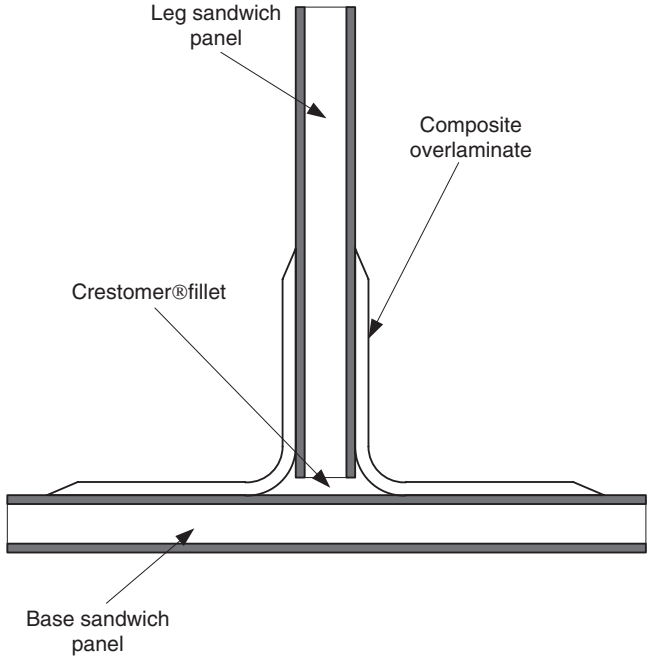

10.17 A typical T-joint connecting a vertical (leg) and a horizontal (base) panel.

along with overlaminates, provides continuity between the two parts. It was found in a number of studies that the presence of a disbond between the leg and the base altered the distribution of axial strain through the thickness of the overlaminates (see e.g. [46]). This caused an outward bending of the overlaminate when the T-joint was subjected to tensile loading, an effect which indicated that the fillet functioned as an important medium of load transfer in the joint. The fillet also helps dissipate energy from blast. A typical T-joint with the components discussed is shown in Fig. 10.17. The geometrical parameters which define the T-joint completely are those of its components. Any void in the bonding surfaces can have a detrimental effect on the ultimate capacity of the T-joint. T-joints are normally tested under tensile and 45 degree pull-off tests. The 45 degree pull-off test is particularly important since it represents the combination of lateral loads, due to for example blast, and membrane forces which develop when large deformations are involved, for instance in a blast scenario. As such, the two components are not independent of the geometry and a simple analysis cannot precisely mimic the situation.

It is shown statistically that the failure of such joints occurs more often than not at the bonded surface suggesting the inefficacy of this method of

© Woodhead Publishing Limited, 2010

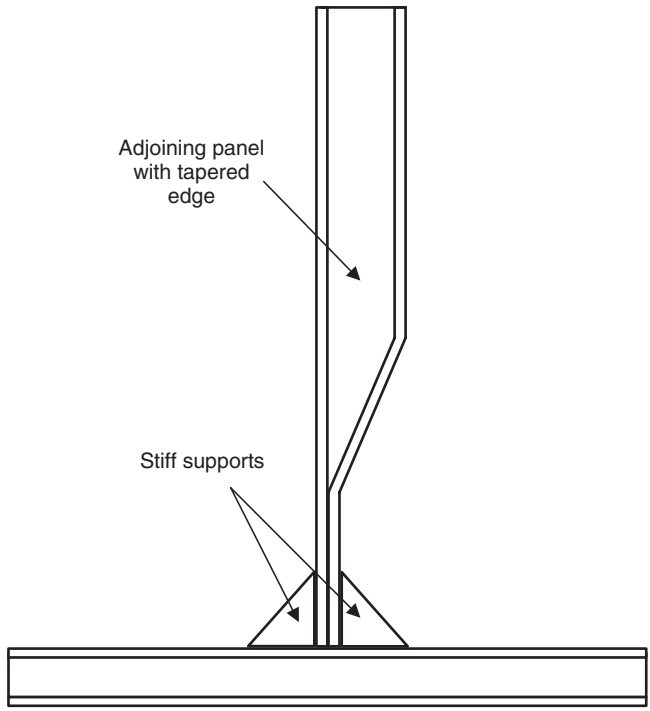

10.18 An alternative T-joint design.

bonding and the need for some modifications. Figure 10.18 shows an example modified configuration which can reduce the peel stresses but increases shear stresses substantially and is thus not a suitable solution. Other proposals have their own disadvantages. Recently some modification and improvement has been done by the authors under the auspices of the Defence Science and Technology Laboratories (DSTL); nonetheless, the results are not available in the public domain.

The connection of the panel to the main framework has also been a subject of research. As mentioned previously, it is advantageous to detail the connection such that membrane resistance can be utilised. Often the types of connection are dictated by the structural configurations of the wall and the fabrication techniques employed. From the discussion given in the literature, a pinned type connection is preferable. A possible arrangement for end connection of blast walls in typical topsides is shown in Fig. 10.19. The wall can be fully bonded to the connecting angles in addition to the minimum number of bolts. This arrangement has the advantage of acting as cracks arrester with limited stress concentration as well as maintaining

© Woodhead Publishing Limited, 2010

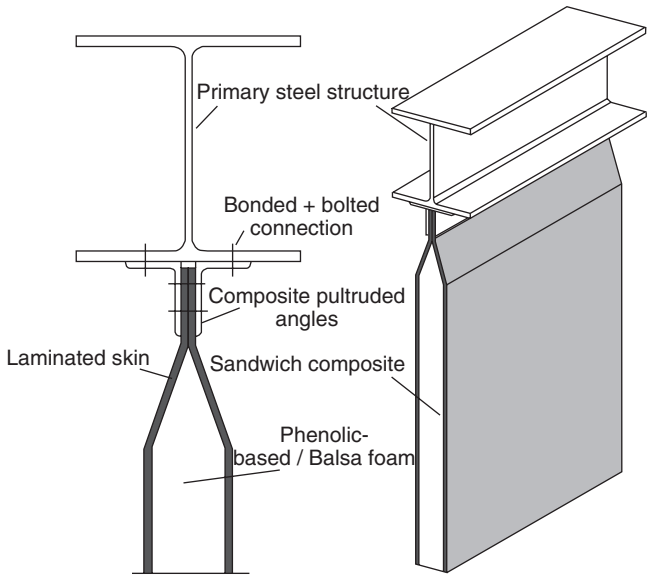

10.19 Possible connection arrangements in typical topsides (Boh [36]).

the wall in place in the event of fire and subsequent bonding failure.[7] Alternatively for hybrid system consisting of steel stiffeners and composite plate, a full rotational restraint may be provided.

Similar to the previous case, it is possible to further eliminate bond failure commonly observed between composite panel and corrugated stiffeners by tapering the panel at its ends to reduce the magnitude of peeling stresses, and to further increase the ductility a steel insert can be used [47] (see Fig. 10.20). Such an arrangement is sometimes necessary to avoid the awkward connection between an all GRP panel and steel mounting frames; however, the steel insert merely shifts the critical spot above.

With regard to fire resistance it must be said that GFRP derive their fire resistance mainly from the types of resin/core and the fibre volume fraction. The resistance can be enhanced by increasing thickness and the use of additives or sacrificial layers. Composites have a clear advantage over metals in terms of thermal conductivity, e.g. GFRP has conductivity 40 times less than that of steel and 130 times less than that of aluminium [48]. However, a major concern of GFRP is that the temperature where significant loss of strength and stiffness commences is much lower than steels.[8] For this

[7] Pure bonded joints are sometimes avoided since such joints have poor tensile and shear strengths, poor through-thickness response characteristics due to the absence of fibres and sensitivity to bond imperfection.

[8] The strength of phenolic plastics is reduced to half at around 220 °C, compared to 450 °C and 700 °C for carbon steels and stainless steel, respectively.

© Woodhead Publishing Limited, 2010

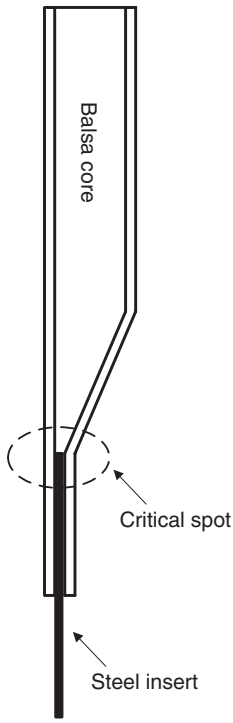

10.20 Connection between a tapered sandwich panel and steel framework.

reason, some hybrid systems consisting of the two materials have been proposed [4]. In addition, woven roving glass plies are sometimes used in the laminate skin so that they form an insulating barrier to the underlying plies when the resin is burnt off.

10.3.4 Structural system

The previous discussion provides a framework for several possible candidates for composite blast barriers as shown in Fig. 10.21. Their blast performance is judged against stiffened and profiled stainless steel panels (Fig. 10.22). All laminated skins are constructed out of GFRP and the core of the sandwich composite is made of end grain Balsa wood. All boundary connections are assumed to be effectively pinned where the plies are bonded and bolted together. All panels are approximately 2.5 m square in size and uniformly subjected to prescribed triangulated overpressures in idealised form representing a high explosive detonation load. For simplicity, failures of laminates are governed by the Hashin criterion (discussed in

© Woodhead Publishing Limited, 2010

Sandwich 50/100 panel
Core: heavy weight end grain Balsa
Skin: 6 mm thk GFRP (UD/WR/UD)
Panel size: 2.5 by 2.5 m
Weight: 174 kg
Ult. stress (WR): 260/–210 MPa
Ult. stress (UD): 735/–600 MPa
Ult. stress (core): 21 MPa
Shear stress (core): 5 MPa
Rupture strain: 5.0 %

(a)

Hat stiffened panel
Panel size: 2.4 by 2.6 m
Table: 12 mm thk GFRP (UD/WR/UD)
Panel: 6 mm thk GFRP (UD/WR/UD)
Flange: 6 mm thk GFRP (UD/WR/UD)
Web: 6 mm thk GFRP (WR;+45/–45)
Weight: 150 kg
Ult. stress (WR): 260/–210 MPa
Ult. stress (UD): 735/–600 MPa
Rupture strain: 5.0 %

(b)

10.21 (a) Tapered sandwich and (b) stiffened composite panels (Boh [36]).

the previous section) and failures of steel panels are governed by the shear failure model. These failure models are incorporated to the finite element models for the composite panels and for the steel panels.

Table 10.4 summarises the response for the various blast walls subjected to two blast pressures. The advantage in using composite panels for weight saving applications is obvious although a higher deflection limit needs to be accommodated for the lower pressure load case. Very little damage is observed for the composite panels while some yielding has occurred for the steel panels. For the higher blast pressure load case, none of the composite panels are judged to survive while the steel panels are subjected to severe yielding with rupture observed in the stiffened panel and corrugated SS2205 panel. It is interesting to note that the 100 mm core sandwich panel offers little structural advantage compared to the 50 mm core sandwich panel apart from a higher stiffness. All composite panels have higher natural periods which make them possibly more sensitive to the blast pressure characteristics of a gas explosion. The hat-stiffened panel improves the structural efficiency, although there is concern over stress concentration and debonding between the stiffener flange and the panel. The sandwich

© Woodhead Publishing Limited, 2010

G43C stiffened panel
Panel size: 2.5 by 2.5 m
Panel thk: 8 mm
Stiffener web: 140 by 7 mm
Stiffener flange: 60 by 10 mm
Weight: 421 kg
Yield stress: 220 MPa
Tensile stress: 532 MPa
Rupture strain: 5.0 %

(a)

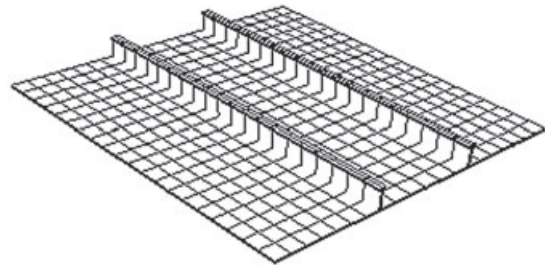

SS2205/SS316 corrugated panel
Panel size: 2.4 by 2.4 m
Panel thk: 6 mm
End plate thk: 20 mm
Weight: 578 kg
0.1 % Proof stress: 200/205 MPa
Tensile stress: 770/888 MPa
Rupture strain: 18.8/39.4 %

(b)

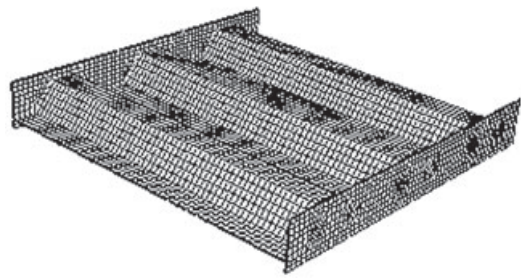

10.22 (a) Stiffened and (b) profiled steel plates (potential substitutes for composite/sandwich panels) (Boh [36]).

panels also perform relatively well when subjected to the lower blast pressure and are suitable for applications where there are stringent requirements regarding thermal performance. From this simple study, it seems that the hat-stiffened panel and the SS316 corrugated panel offer the optimum blast resistance to the lower and higher blast pressure load cases, respectively. The displacement time responses are given in Fig. 10.23, and the von Mises stress distribution plots are shown in Fig. 10.24.

10.3.5 Summary and concluding remarks

The work presented here investigates the use of composite panels as structural barriers subjected to blast loadings. Validation studies are presented and the robustness of the various composite configurations is discussed. Subroutines are developed to model the progressive damage of laminate consisting of unidirectional lamina, woven roving lamina, chopped strand mat and sandwich Balsa core. The considerations needed for the development of the composite blast wall system are discussed. Some possible composite blast wall systems are investigated and their responses are compared

© Woodhead Publishing Limited, 2010

Table 10.4 Comparison between the blast resistance of steel and sandwich/composite panels [36]

Model	Load (t_d = 0 ms)	y_{max}	$y_{residual}$	$\bar{\varepsilon}_{max}/\bar{\varepsilon}_{crit}$	$\bar{\sigma}_{max}/\bar{\sigma}_{ult}$	Critical mode
Stiffened panel	2 bar	49	15	0.11	0.86	Yielding of stiffener flange
(Wt: 421 kg; *T*: 29 ms)	5 bar	166	140	1.00	0.97	Yielding and large rotation at corners
Corrugated panel SS2205	2 bar	9	0.3	0.01	0.37	Yielding at compression flange
(Wt: 578 kg; *T*: 10.6 ms)	5 bar	378	325	0.99	0.95	Yielding at compression flange
Corrugated panel SS316	2 bar	8	0.3	0.00	0.35	Yielding at compression flange
(Wt: 578 kg; *T*: 10.6 ms)	5 bar	668	650	0.83	0.86	Yielding at compression flange
Sandwich panel, 50 mm core	2 bar	162	0.0	0.56	0.72	No fibre damage; slight shear failure of core wedge
(Wt: 174 kg; *T*: 35.1 ms)	5 bar	Collapse	–	–	–	Fibre failure of skin at connection and shear failure of core wedge
Sandwich panel, 100 mm core	2 bar	140	0.0	0.72	0.96	Transverse matrix failure
(Wt: 216 kg; *T*: 25.8 ms)	5 bar	Collapse	–	–	–	Fibre failure of skin at connection and shear failure of core wedge
Hat-stiffened panel	2 bar	60	0.0	1.06	0.73	Slight WR fibre damage; debonding at stiffener flange
(Wt: 150 kg; *T*: 30.3 ms)	5 bar	Collapse	–	–	–	Fibre damage at stiffener table

© Woodhead Publishing Limited, 2010

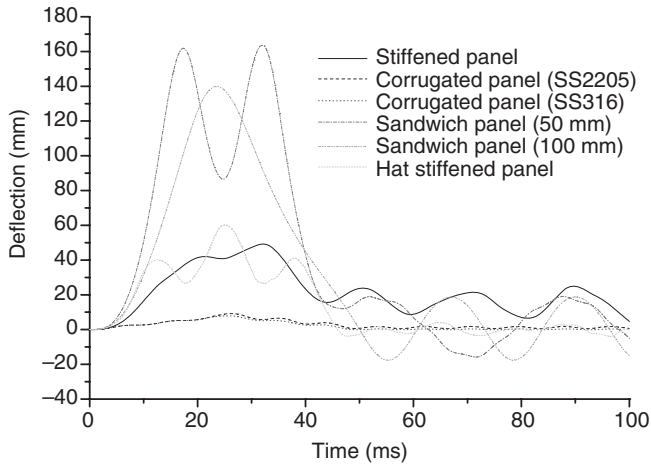

(A) P: 2 bar; t_d: 50 ms

(a)

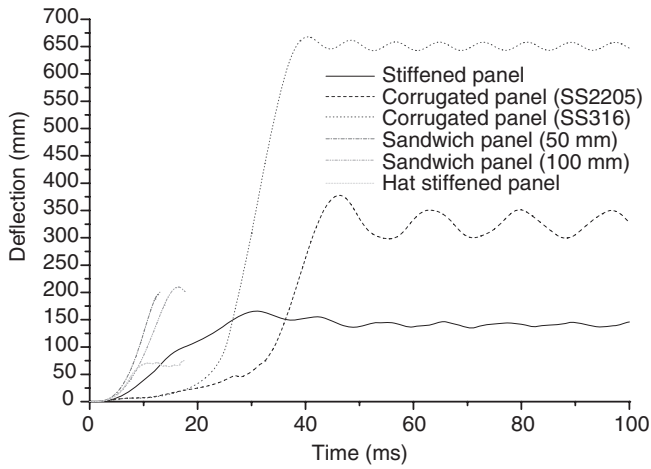

(B) P: 5 bar; t_d: 50 ms

(b)

10.23 Deflection time history plots for various blast walls: (a) load case: maximum overpressure = 2 bar; (b) load case: maximum overpressure = 5 bar (Boh [36]).

to their metal counterparts. The following presents some of the key findings from the above study.

(i) The peak capacity of the laminate is governed by the imposed failure criteria and the residual strength and stiffness are governed by the residual factors. While the maximum stress criterion correlates with

© Woodhead Publishing Limited, 2010

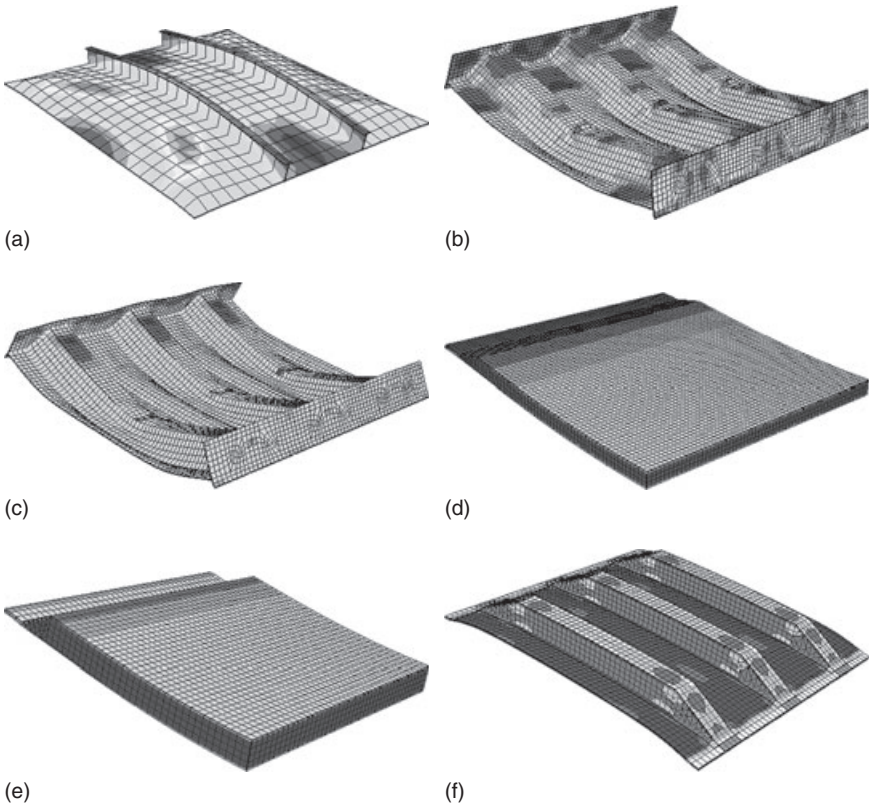

10.24 Different studied configurations: (a) stiffened panel; (b) corrugated panel (SS2205); (c) corrugated panel (SS316); (d) sandwich panel (50 mm core); (e) sandwich panel (100 mm core); (f) hat stiffened panel (Boh [36]).

tests very well for the beam models, the use of stress interactive criteria such as the Hashin criterion is required to predict the response of plate models.

(ii) The residual factor approach adopted in the analyses of this section is an effective approach based on observation that initial damage in composite often does not constitute an immediate collapse. More experimental work is required to be carried out to assess these factors based on type of composite and its corresponding failure modes. A residual factor of 5–10% of the initial stiffness gives the best fit to the test data presented here.

(iii) The proposed composite blast wall systems are developed to utilise the membrane strength of the materials which also implies that there is a high demand on the performance of the connections. The weight

© Woodhead Publishing Limited, 2010

advantage offered by the composite blast barriers is significant, although this should be reduced by the need for a more bulky connection system. Composite blast barriers are particularly appropriate for application where the there is a risk of low to moderate blast pressures. Their blast response is also more sensitive to the blast pressure parameters such as the rise time and blast duration. For high blast pressures, failure of the composite panels is often sudden and catastrophic. This poses a new challenge for designers and must be taken into consideration when novel forms are being proposed.

In conclusion the use of composites brings with it increased operational effectiveness and performance, reduced maintenance workload and reduced risk of failure in a blast scenario of moderate intensity. The stiffness-to-weight and strength-to-weight factors are considerably higher than those of steel while the strength is almost preserved in absolute terms.

10.4 Use of composites in conjunction with metals

From the study conducted so far, it can be seen that composites have superior properties compared to metals. These properties can be utilised in an efficient blast resistant design. However, the ductility of composites is still an issue and perhaps the most important single barrier against universal use of composites in protective design against blast and impact scenarios. When a ballistic load or a localised blast load is involved this issue becomes more obvious. The benefits of global response tend to be secondary in this case and through-thickness waves and tearing mode of failure become important. This is the characteristic of high-velocity–short-duration impacts where dilatational waves render the dimensions of the structure and its boundary conditions virtually irrelevant. Localised blast loading which is the result of closeness of charge to the structure has a similar effect.

With regard to an impact scenario it has been established that FRP in general can provide good armour protection, especially against fragments and small-arms attack. This can be best achieved by means of a double skin structure where the first skin upsets the ballistics of a projectile and the second catches it. Analogously, in a blast scenario the same principle holds and energy absorption can be achieved through the sacrificial or semi-sacrificial effect of the first skin accompanied by elastic deformation of the second skin subsequent to the point of contact with the first one. Even though in a high-velocity impact scenario this behaviour is feasible, there are several issues associated with this proposal when blast loads are involved. The first one is the connection of the two skins. If there is no medium in between the two skins there would be a problem transferring load from the first skin into the second one. Moreover, a layered system can provide more

© Woodhead Publishing Limited, 2010

robustness through an increase in the number of prescribed fracture surfaces in a spalling failure mode and also more in-plane strength and ductility. The requirements mentioned imply the introduction of a layered system comprising composite FRPs and steel, i.e. fibre metal laminates (FMLs).

10.4.1 Fibre metal laminates (FMLs)

Fibre metal laminates (FMLs) form a group of materials within the composite family which can be potentially utilised for the purpose of blast and impact protection. They consist of layers of metal sheets and FRP stacked in a predetermined sequence. A schematic of an FML is shown in Fig. 10.3. It is obvious that the number of metal sheets exceeds the number of blocks (grouped plies) of composite by unity. The most commonly used FML is GLARE, which comprises thin aluminium sheets and glass fibre-reinforced epoxy (GFRP) layers. Aluminium is a round-house metallic material with ductility limit lower than steel, and the resin (epoxy) used in GFRP layers is a thermoset. The main disadvantages of FMLs based on thermosetting FRPs are the long processing cycles, low fracture toughness and lack of repairability. FMLs based on thermoplastic FRPs have been successfully developed by Cantwell *et al.* [49–51] and shown to possess improved fracture toughness, shorter processing times and good impact and blast resistance.

Several variables affect the behaviour of FMLs, including plate thickness, plate composition (thickness and distribution of the aluminium and composite layers in the plate), plate area and loading parameters. The differences in composition and structure of FMLs and monolithic plates (such as steel) allow energy to be dissipated and absorbed via different mechanisms. Reyes and Cantwell [49] reported that laminated composite materials can dissipate energy through debonding, delamination and matrix cracking; however, the energy dissipated in interlaminar debonding is negligible. Elastic properties of FMLs and dynamic response can be obtained based on classical laminated plate theory (CLPT), zeroth-order and higher order shear deformation theories. Inelastic response, however, requires damage modelling at ply level and delamination at interface. Delamination requires interlaminar shear and normal stresses to be modelled subsequent to plastic deformation/matrix cracking. This is a non-trivial task and studies of this sort can in general be conducted only using non-linear finite element (NLFEA) codes.

Depending upon the type of blast load being applied to an FML, the distance of the charge and the area of the plate, the dynamic response of the plate can be different. Three regimes of response exist depending on the relative area of loading, proximity of the charge to target and plate thickness. These are the (i) response dominated by dilatational waves, (ii)

© Woodhead Publishing Limited, 2010

response dominated by flexural waves and (iii) the quasi-static response. Roughly speaking, the closer the charge to the target or the smaller the plate area affected by blast-induced overpressure, the more pronounced are the responses of types (i) and (ii). When the loading is of low intensity and with a finite rise time to maximum of the order of magnitude of the first vibration mode period, the response will fall into categories (ii) or (iii). Thus it can be concluded that the response of FMLs to high-intensity dynamic loads is in general under the influence of many parameters. When a large part of the plate is subjected to loading, the global response is of concern and boundary conditions have a significant effect on the response and the ultimate capacity; however, when a small part of the plate is affected by loading the response is of localised nature, higher modes are triggered and boundary condition effects pale into insignificance.

Research groups in Liverpool Impact Research Centre and Cape Town BISRU have paid special attention to the topic of localised blast loading. Langdon *et al.* [52] and Lemanski *et al.* [53] conducted a series of studies on the topic of localised blast loading on FMLs. These studies are important as the results may be useful for understanding of the mechanisms through which energy is dissipated from the system. The situation here can be compared to that of the ballistic loading of an FML. Three modes of failure can be identified, viz. (i) large inelastic deformation of the back of the panel, (ii) tensile tearing and (iii) transverse shear failure. The impulse associated with the transition between stages (i) and (ii) is called the threshold impulse which may be considered as analogous to the concept of the ballistic limit in an impact scenario (V_{50}).

The mechanisms active in the response of an FML to global blast loading are somehow similar to the static loading case. These mechanisms can be studied analytically and numerically without much difficulty. Nevertheless, the quantification of mechanisms active in the localised blast loading is generally much more demanding. A qualitative explanation of FML response subjected to localised blast loading was given by Franz *et al.* [54] who investigated the response of layered glass fibre laminates. It was found that the layers on the back face provided structural support to the layers on the front face. For thin plates, it is observed that the blast energy causes deformation throughout the thickness of the plate because the layers towards the back of the plate offer little structural support to the layers in front. Due to the relatively low overall bending stiffness of the plate, less energy is required to bend the whole plate than to debond the back layers from the front ones. Similar sized deformations are seen on both the front and back faces of the plate. For thick plates, it is frequently observed that the back face experiences significantly larger inelastic deformations than the front face. This is because the layers at the front of the plate are supported by the layers behind and because the flexural stiffness of the plate

© Woodhead Publishing Limited, 2010

is higher, less energy is required to debond the back layers than is required to deform the whole plate. The back face therefore debonds from the rest of the plate and its deformations are larger than those of the front face. The through-thickness waves are responsible for this debonding as tensile waves are generated as compressive waves reflect from the free back face. This phenomenon though is expected to be more pronounced in the case of localised blast loads and high-velocity impact. Figure 10.25 shows two examples corresponding to thin and thick FML panels, respectively.

10.5 Concluding remarks

It is established that composites have significant advantages over traditional metals by virtue of their high specific strength and stiffness. This arouses the expectation that they can be used in extreme loading resistant design. The use of composites on their own in blast resistant design is limited. Thus the present study deals with three examples of the use of FRP composites in conjunction with other materials in blast resistant applications. These applications may be offshore, naval or defence related. The three examples include new design, strengthening and replacement applications.

CFRP composites do not possess much ductility and can be brittle while GFRP composite panels are more suitable for use as primary blast resistant structures. There are several failure mechanisms through which blast energy is absorbed by the system. The drastic loss in post-peak resistance element of UD composites due to fibre breakage is detrimental to the robustness of the structure. This essentially means that UD composites on their own cannot be a suitable replacement for ductile materials of construction traditionally used in the construction of conventional blast resistant structures. There are several types of modification possible to enable the use of composites in conjunction with other materials in order to benefit from the composite ingredients' superior properties. The following options are discussed in the present chapter:

- using composites in conjunction with metals in the form of FMLs;
- using composite patches for strengthening ductile structures;
- using composite plates (as skins) along with a lightweight material such as wood or PVC foam (as core) in a sandwich beam or plate construction.

The three examples are adopted from the literature or are the results of analyses conducted by authors. The failure models adopted are naturally different, but in all cases correlation with test results or with literature is checked. The results of these studies are discussed in this chapter.

In the case of a strengthened corrugated profile and its connections, the static collapse load of the strengthened profile which is enhanced on both flanges and the web is considerably higher than the static collapse load of

© Woodhead Publishing Limited, 2010

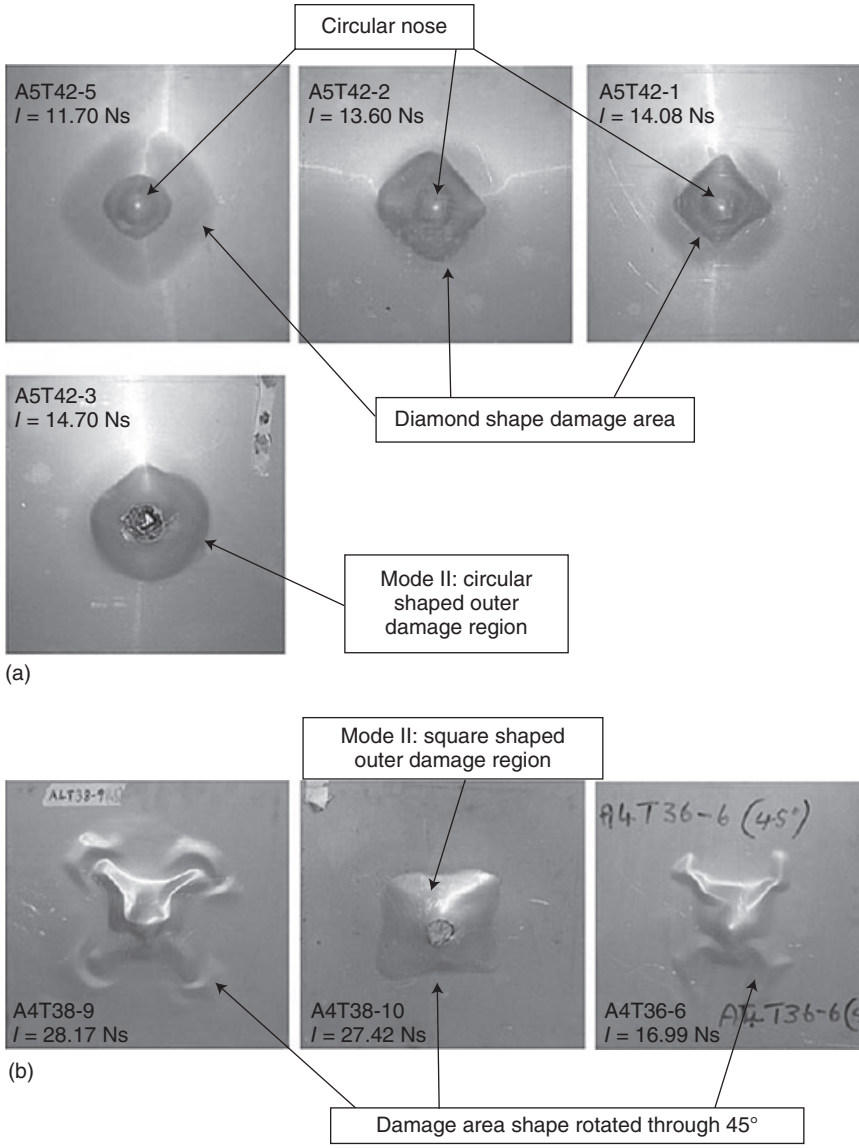

10.25 (a) Photographs of the back faces of selected FML panels (average panel thickness = 7.5 mm); (b) photographs of the back faces of selected FML panels (average panel thickness = 12.5 mm).

its unstrengthened counterpart. However, if the fibres in the composite patches of the hybrid system break there will be no contribution to energy absorption capacity of the hybrid system on the part of composites. If all composite patches remain intact with respect to fibre breakage there will be some contribution to the energy absorption capacity on the part of

© Woodhead Publishing Limited, 2010

composites. This contribution is at the cost of large forces being exerted to connections. Given that composites are mostly needed in extreme blast scenarios when metal on its own is not adequate in absorbing the blast energy, the drawback here is serious and must be overcome. Currently work is being done by researchers for instance at Imperial College Aeronautics and Civil Engineering departments to improve the situation.

In the case of a steel/metallic panel replaced by a sandwich system with composite skins, the weight advantages offered are significant although this must be reduced due to the need for a more bulky connection system. Composite blast barriers are particularly appropriate for applications where there is a risk of low to moderate blast pressures. Again the same limitation as in the case of strengthening exists. Moreover, the blast response of sandwich panels is more sensitive to the blast pressure parameters such as the rise time and blast duration. For high blast pressures, failure of the composite panels is often sudden and catastrophic and ductility negligible. This poses a new challenge for designers and must be taken into consideration when novel forms are being proposed. Some work has been done in this regard at Imperial College and some is ongoing. Some of the results obtained are to be published in the near future.

With regard to FMLs, it should be said that they possess superior performance characteristics compared to both metallic and composites when localised blast loading or high-velocity impact is of concern. Thick and thin FML panels have been considered in this chapter and energy absorption mechanisms in both cases are compared and contrasted. The reasons for dependence of damage mode and global behaviour on thickness are discussed.

Given the summary here, it can be said that composites provide good blast resistant alternatives for metals in two types of applications, i.e. when the structure is weight sensitive and when blast loading is of moderate peak pressure and impulse content. Thus the future trend in the use of composites against blast is deeply influenced by several key points: the issue of increasing ductility and whether or not this can be done within reasonable cost and construction limits; and the problem of connecting composite or sandwich parts effectively which in itself provides a challenge, and the issue of predictive capability of failure which is of no less importance. It is expected that the tendency to increase the application of composites will continue in the future if these key problems are adequately solved by researchers and implemented by manufacturers.

10.6 References

1 GALBRAITH D N and BARNES F (1995), Beryl Bravo-Blast walls conversion: development and testing of steel/carbon fibre composite. *Proceedings of the Fifth*

© Woodhead Publishing Limited, 2010

International Offshore and Polar Engineering Conference, 11–16 June, The Hague, the Netherlands, 229–236.

2 ECHTERMEYER A T, LARSEN M J and FISCHER K P (2003), A new approach to repair of FPSO's without hot work. *Proceedings of OMAE03. 22nd International Conference on Offshore Mechanics and Arctic Engineering*, 8–13 June, Cancun, Mexico: paper no. OMAE2003-37426.

3 SALTER J E (1994), Selection of a blast resistant GRP composite panel design for naval ship structures. *Marine Structures*: **7**, 417–440.

4 SMITH C S and MURPHY P (1991), Response of hybrid GRP/steel superstructures to blast loading: theory and experiment, in Smith CS and Dow RS (eds), *Advances in Marine Structures-2*, Elsevier, Amsterdam, the Netherlands: 392–415.

5 GIBSON A G (2003), *The Cost Effective Use of Fibre Reinforced Composites Offshore*. Research report 039, Health and Safety Executive (UK).

6 MOURITZ A P, GELLERT E, BURCHILL P and CHALLIS K (2003), Review of advanced composite structures for naval ship and submarines. *Composite Structures*: **53**, 21–41.

7 SONI S R (1983), A new look at commonly used failure theories in composite laminates. *24th International Conference on Structures, Structural Dynamics & Materials*, Lake Tahoe, CA: 171–179.

8 HINTON M J and SODEN P D (1998), Predicting failure in composite laminates: the background to the exercise. *Composites Science and Technology*: **58**(7), 1001–1010.

9 THE INSTITUTION OF CIVIL ENGINEERS (ICE) (2001), *ICE Design and practice guide/ FRP composites life extension and strengthening of metallic structures*. Thomas Telford, London, UK.

10 VAN DEN EINDE L, ZHAO L and SIEBLE F (2003), Use of FRP composites in civil structural applications. *Construction and Building Materials*: **17**, 389–403.

11 SMITH S T and TENG J G (2001), Interfacial stresses in plated beams. *Engineering Structures*: **23**, 857–871.

12 RASHEED H A and PERAVIZ S (2002), Bond Slip Analysis of Fibre-Reinforced Polymer-Strengthened Beams. *ASCE Journal of Engineering Mechanics*: **128**, 78–86.

13 ROBERTS T M and HAJI-KAZEMI H (1989), Theoretical study of the behaviour of reinforced concrete beams strengthened by externally bonded steel plates. *Proceedings of Institution of Civil Engineers*: **87**(Part 2), 39–55.

14 RABINOVICH O and FROSTIG Y (2000), Closed-form high-order analysis of RC beams strengthened with FRP strips. *Journal of Composites for Construction*: **4**(Part 2), 65–74.

15 HAMED E and RABINOVICH O (2005), Dynamic behaviour of reinforced concrete beams strengthened with composite materials. *Journal of Composites for Construction*: **9**(Part 5), 429–440.

16 SOLEIMAN FALLAH A, MOHAMED ALI R M and LOUCA L A (2008), Analytical-numerical study of interfacial stresses in plated beams subjected to pulse loading. *Engineering Structures*: **30**, 856–869.

17 BATRA R C and HASSAN N M (2008), Blast resistance of unidirectional fiber reinforced composites, *Composites Part B: Engineering*: **39**, 513–536.

18 KAZANCI Z and MECITOGLU Z (2008), Nonlinear dynamic behavior of simply supported laminated composite plates subjected to blast load. *Journal of Sound and Vibration*: **317**, 883–897.

© Woodhead Publishing Limited, 2010

19 TAM L L and CALLADINE C R (1991), Inertia and strain-rate effects in a simple plate-structure under impact loading. *International Journal of Impact Engineering*: **11**(Part 3), 349–377.
20 SOLEIMAN FALLAH A and LOUCA L A (2007), Pressure-impulse diagrams for elastic-plastic-hardening and softening single-degree-of-freedom models subjected to blast loading. *International Journal of Impact Engineering*: **34**(Part 4), 823–842.
21 CHALMERS D W (1994), The potential for the use of composite materials in marine structures. *Marine Structures*: **7**, 441–456.
22 SALTER J E (1994), Selection of a blast-resistant GRP composite panel design for naval ship structures. *Marine Structures*: **7**, 417–440.
23 SOLEIMAN FALLAH A and LOUCA L A (2009), Strengthening profiled blast walls and connections using FRPs, *ICE Structures and Buildings Journal* (submitted).
24 SMITH P D and HETHERINGTON J G (1994), *Blast and Ballistic Loading of Structures*, Butterworth-Heinemann, Oxford, UK.
25 BIGGS J M (1964), *Introduction to Structural Dynamics*. McGraw-Hill, New York.
26 COLE R H (1948), *Underwater Explosion*. Princeton University Press, Princeton, NJ.
27 ZONG Z (2003), Dynamic plastic response of a submerged free-free beam to an underwater gas bubble, *Acta Mechanica*: **161**, 179–194.
28 TSAI S W and HAHN H T (1980), *Introduction to Composite Materials*. Technomic, Lancaster, PA.
29 HASHIN Z (1980), Failure criteria for unidirectional fibre composites. *ASME Journal of Applied Mechanics*: **47**, 329–334.
30 BREWER J C and LAGACE P A (1988), Quadratic stress criterion for initiation of delamination. *Journal of Composite Materials*: **22**(Issue 12), 1141–1155.
31 HOU J P, PETRINIC N and RUIZ C (2001), A delamination criterion for laminated composites under low-velocity impact. *Composites Science and Technology*: **61**(Issue 14), 2069–2074.
32 JONES R M (1999), *Mechanics of Composite Materials*. 2nd Edn. Taylor and Francis, Philadelphia, PA.
33 GARDNER L and NETHERCOT D A (2004), Structural stainless steel design: a new approach. *The Structural Engineer*: **82**(Issue 21), 21–28.
34 EUROCODE 3 (1998), *Design of Steel Structures – Part 1-1: General – General Rules and Rules for Buildings*, CEN, Brussels, Belgium.
35 LANGDON G S and SCHLEYER G K (2005), Inelastic deformation and failure of profiled stainless steel Blast Wall Panels. Part II: analytical modelling considerations. *International Journal of Impact Engineering*: **31**, 371–399.
36 BOH J W (2005), *Energy Dissipating Barriers Against Hydrocarbon Explosions*, Doctoral dissertation, Department of Civil Engineering, National University of Singapore (NUS), Singapore.
37 TSAI S W and WU E M (1970), A general theory of strength for anisotropic materials. *Journal of Composite Materials*: **5**, 58–80.
38 HART-SMITH L J (2000), What the textbooks won't teach you about interactive composite failure criteria. In Grant P and Rousseau C (eds), *Composite Structures: Theory and Practice*, STP 1383, ASTM, West Conshohocken, PA: 413–436.

© Woodhead Publishing Limited, 2010

39 HINTON M J, KADDOUR A S and SODEN P D (2002), A comparison of the predictive capabilities of current failure theories for composite laminates, judged against experimental evidence. *Composites Science and Technology*: **62**(Issues 12–13), 1725–1797.

40 SMITH C S and CHALMERS D W (1987), Design of ship superstructures in fibre-reinforced plastic. *Transactions of The Royal Institution of Naval Architects*: **129**, 45–62.

41 MOURTIZ A P, SAUNDERS D S and BUCKLEY S (1994), The damage and failure of GRP laminates by underwater explosion shock loading. *Composites*: **25**(Part 6), 431–437.

42 DAVIES G A O, HITCHINGS D and ZHOU G (1996), Impact damage and residual strengths of woven fabric glass/polyester laminates. *Composites Part A*: **27A**, 1147–1156

43 KANT T, RAVICHANDRAN R V, PANDYA B N and MALLIKARJUNA A (1988), Finite element transient dynamic analysis of isotropic analysis and fibre reinforced composite plates using higher order theory. *Composite Structures*: **9**, 319–337.

44 MOURITZ A P (1996), The effect of underwater explosion shock loading on the flexural properties of GRP laminates. *International Journal of Impact Engineering*: **18**(Issue 2), 129–139.

45 MOURITZ A P, SAUNDERS D S and BUCKLEY S (1994), The damage and failure of GRP laminates by underwater explosion shock loading. *Composites*: **25**(Part 6), 431–437.

46 ZHOU D W, LOUCA L A and SAUNDERS M (2008), Numerical simulation of sandwich T-joints under dynamic loading. *Composites Part B: Engineering*: **39**, 973–985.

47 SMITH C S (1990), *Design of Marine Structures in Composite Materials*. Elsevier, London, UK.

48 THE STEEL CONSTRUCTION INSTITUTE (1991), Blast and Fire Engineering Project for Topside Structures. Work Package: G5 the Use of Alternative Materials in the Design and Construction of Blast and Fire Resistant Structures, Ascot, UK.

49 REYES G and CANTWELL W J (2000), The mechanical properties of fibre–metal laminates based on glass fibre-reinforced polypropylene. *Composites Science and Technology*: **60**, 1085–1094.

50 GUILLEN F and CANTWELL W J (2002), The influence of cooling rate on the fracture properties of a thermoplastic-based fibre metal laminate. *Journal of Reinforced Plastic Composites*: **21**, 749–772.

51 REYES G and CANTWELL W J (2004), The high velocity impact response of composite and FML-reinforced sandwich structures. *Composites Science and Technology*: **64**, 35–54.

52 LANGDON G S, LEMANSKI S L, NURICK G N, SIMMONS M C, CANTWELL W J and SCHLEYER G K (2007), Behaviour of fibre–metal laminates subjected to localised blast loading – Part I: Experimental observations *International Journal of Impact Engineering*: **34**, 1202–1222.

53 LEMANSKI S L, NURICK G N, LANGDON G S, SIMMONS M C, CANTWELL W J and SCHLEYER G K (2007), Behaviour of fibre metal laminates subjected to localized blast loading – Part II: Quantitative analysis. *International Journal of Impact Engineering*: **34**, 1223–1245.

54 FRANZ T, NURICK G N and PERRY M J (2002), Experimental investigation into the response of chopped-strand mat glass fibre laminates to blast loading. *International Journal of Impact Engineering*: **27**, 639–667.

© Woodhead Publishing Limited, 2010

11

Using composite behavior to improve the blast resistance of columns in buildings

M. P. RUTNER, Weidlinger Associates, Inc., USA

Abstract: The focus of this investigation is a load bearing column subjected to a near-proximity vehicle-borne explosive threat. The design of ground floor columns of high rise buildings has to fulfill architectural demands, such as to support long-spanned framing, which often result in a non-redundant structure. Additionally, standoff distances from the street curb line to the building's ground floor column may be insufficient and no restrictions on vehicle access within short distances to the column may be possible. This hazard requires the local resistance design approach to protect the structure of progressive collapse.

This chapter investigates the response of a representative steel column when subjected to a nearby explosive event. It discusses how composite construction technology can improve the blast response of the steel column. Additionally, structure-specific and load-dependent design parameters are derived to provide a high level of security.

Key words: composite construction, progressive collapse, non-linear analysis, shear failure, local blast resistance, specific local resistance design approach, constitutive damage model.

11.1 Introduction

In many cases, loss of a column can result in partial or full collapse of the building. A tragic example is the partial collapse of the Alfred P. Murrah Federal Building in Oklahoma City in the United States that resulted from the failure of a single ground floor column by a terrorist blast attack. Such tragic terrorist attacks have created a demand for the blast protection of civilian, as well as military/government buildings. The following sections discuss protection technologies of ground floor columns with an emphasis on composite construction. An example of ground floor columns of a high rise building in close proximity to the street is shown in Fig. 11.1.

11.2 Design specifications

Blast pressures on structures are considered accidental actions. The Eurocode 1 [1] provides the following design strategies.

© Woodhead Publishing Limited, 2010

11.1 Ground floor column of a high rise building.

1. Protecting the structure against the action.
2. Choosing structure design concepts so that local damage will not lead to progressive collapse.
3. Designing load bearing key elements, which are robust enough either to have high blast resistance or to be capable of overtaking redistributed gravity load.

This chapter deals with the third design strategy, with an emphasis on the protection of the structural member. Its importance is also expressed in [2], where alternate path design approaches and specific local resistance design approaches are compared. In certain circumstances, the specific local resistance design approach provides greater structure protection than the alternate path method [2]. The AISC 7-02 Commentary Section C2.5 [3] defines in 'Load Combinations and Extraordinary Events' that '... extraordinary events ... should be identified, and measures should be taken to ensure that the performance of key loading-bearing structural systems and components is sufficient to withstand such events.'

© Woodhead Publishing Limited, 2010

11.3 Objectives

This chapter investigates the blast resistant performance criteria of heterogeneous materials assembled in one cross-section. The composite cross-section set-up provides compression, tension or shear capacity at strategic locations of the cross-section and enables the ground floor column to sustain a vehicle-borne explosive threat with minimal damage and to carry gravity loads after the event. The advantageous behavior of the composite section is seen in the comparison with pure structural steel sections. The chapter provides insight into the theoretical background of constitutive modeling for the constituent materials, discusses the suitability of the material description, draws assumptions, and conveys consequences for the analyzed results.

The investigations of composite column types and development of protection measures include an accurate representation of the explosive effects, material properties and failure mechanisms in a realistic and non-linear manner. Analyses of the residual capacities identify the post-event axial capacity of the column under gravity loads, and they assess main design parameters that affect the blast resistance of a column member.

11.4 Simulation and experiment

Constitutive material model development necessitates numerous checks of whether all significant material parameters are included in the model to describe the realistic behavior with a high level of confidence. However, even when material models describe the material response with a high-level of accuracy, the analyzed structure's response might not reflect reality. Approximations and rough estimates in regards to the structure and within the numerical analysis may lead to meaningless results such as the following:

- **Connection detailing**: The accurate deformation/rotation capacity of connections is fundamental to realistically simulating the structural member's non-linear response. The connections are often the vulnerable part of the construction. Idealized connection models typically overstate the connection resistance.
- **The ductility of boundary conditions**: The structural member's response depends on the boundary conditions. In some cases, only experimental tests with the structural member and the adjacent structure will enable the definition of ductility level of the boundary conditions.
- **Contact**: Cross-section parts, which were separated in the unloaded state, contact and penetrate due to the large load transmission. The simulation needs to correctly consider all contact procedures from the impingement of the load.

© Woodhead Publishing Limited, 2010

- **Mesh discretization**: A poor choice in model mesh resolution can lead to aphysical results.
- **Media–structure interaction**: generates the reflected pressure due to the explosion compression wave. The accuracy of this load and the verification against experimental test results are fundamental.

11.5 Modeling

11.5.1 Material models – verification of material models

Reinforced concrete and structural steel are the materials chosen for the analytical studies described in this chapter. While steel is a homogeneous material, concrete is a heterogeneous material with its constituents cement paste, sand and aggregate. Constitutive models for concrete and steel have been investigated since the middle of the 19th century [4]. Numerous sources contributed to the development and understanding of the material behavior under static, quasi-static, dynamic and transient dynamic loads [4]. While the strain is mostly within the elastic range under static loads, the post-yield material behavior and damage mechanics are the focus of the researcher for blast loading. Constitutive models for materials that contain material softening and damage when subjected to high dynamic loads have been developed since the 1960s and the research is still ongoing. Different concepts have been set up to describe the non-linear material behavior representing material failure and damage evolution [5–8].

The material properties affect the damage behavior and the failure modes. Understanding of the constitutive models and various failure modes is essential to draw conclusions in regards to strengthening and protection measures.

Theoretical background

Blast loading locally generates stress that is beyond the material strength and causes damage. Elastic and plastic material behavior as well as material deterioration will occur. This paragraph introduces the failure and damage evolution criteria of the material within the composite section. The parameters applied are briefly introduced [9].

Hydrostatic and deviatoric stress

The stress state of every point in a body, idealized as a continuum, can be described by the stress symmetric tensor T_{ij} and is shown with its components in Eq. 11.1.

$$T_{ij} = \begin{bmatrix} T_{11} & T_{12} & T_{13} \\ T_{21} & T_{22} & T_{23} \\ T_{31} & T_{32} & T_{33} \end{bmatrix} \qquad [11.1]$$

© Woodhead Publishing Limited, 2010

If n_j is a vector which transforms under tensor T_{ij} into a vector parallel to itself, then n_j is the eigenvector and λ is the eigenvalue:

$$T_{ij}n_j = \lambda n_i = \lambda \delta_{ij} n_j \quad [11.2]$$

δ_{ij} is the Kronecker delta, which is defined as being equal to +1 if i is equal to j and 0 otherwise.

$$(T_{ij} - \lambda \delta_{ij})n_j = 0 \quad [11.3]$$

Equation 11.3 is a system of three linear homogeneous equations. The non-trivial solution for the eigenvectors exists when the determinant of the coefficients vanishes, as shown in Eq. 11.4:

$$\det(T_{ij} - \lambda \delta_{ij}) = 0 \quad [11.4]$$

The expansion of Eq. 11.4 leads to the cubic equation:

$$\lambda^3 - I_1\lambda^2 + I_2\lambda - I_3 = 0 \quad [11.5]$$

where I_1, I_2, I_3, are the invariants of the stress tensor T_{ij} and are independent of the coordinate system.

$$\begin{aligned} I_1 &= T_{ii} \\ I_2 &= \frac{1}{2} I_1^2 - \frac{1}{2} T_{ij} T_{ji} \\ I_3 &= \det(T_{ij}) = 1/6(2T_{ij}T_{jk}T_{ki} - 3I_1 T_{ij} T_{ji} + I_1^3) \end{aligned} \quad [11.6]$$

The stress tensor T_{ij} is the sum of a purely hydrostatic stress, indicated as p or σ_m.

The deviation from the hydrostatic stress, termed the deviatoric stress S_{ij}, is a stress state of pure shear and is written in Eq. 11.7:

$$s_{ij} = T_{ij} - \sigma_{\mathrm{m}} \delta_{ij} \quad [11.7]$$

where σ_m is the purely hydrostatic stress, the mean stress, which is calculated by Eq. 11.8 (compressive stress is defined negative):

$$p = \sigma_m = -1/3(T_{11} + T_{22} + T_{33}) \quad [11.8]$$

To determine the invariants of the deviatoric stress tensor S_{ij} a derivation similar to that applied to gain Eq. 11.5 is used. Thus we can write:

$$\det(s_{ij} - s\delta_{ij}) = 0 \quad [11.9]$$

This leads to the cubic equation:

$$s^3 - J_1 s^2 - J_2 s - J_3 = 0 \quad [11.10]$$

where the invariants of the deviatoric stress tensor are

© Woodhead Publishing Limited, 2010

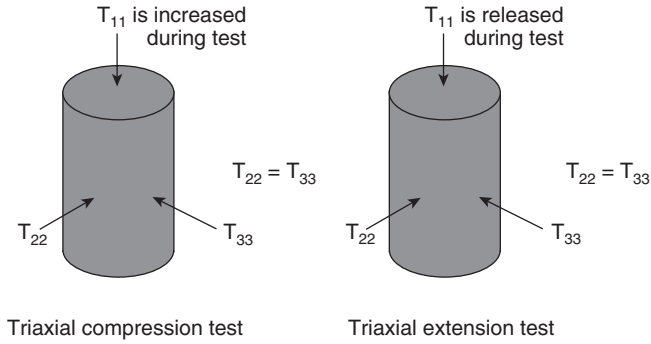

11.2 Compression and extension tests.

$$J_1 = s_{ii} = 0$$
$$J_2 = \frac{1}{2} s_{ij} s_{ji} \qquad [11.11]$$
$$J_3 = \frac{1}{3} s_{ij} s_{jk} s_{ki}$$

This paragraph introduces two more parameters which will be used in later formulations.

The shear stress $\Delta\sigma_c$ can be directly obtained from classic triaxial compression and extension tests, shown in Fig. 11.2. In both tests the principal stresses $T_{ii}, i = 1, 2, 3$ are equal at the beginning of the test, having a certain value p. In the compression test, while the principal stress components T_{22} and T_{33} are kept constant, T_{11} is increased until failure. In the extension test, while the principal stress components T_{22} and T_{33} are kept constant, T_{11} is released until failure. At failure the concrete strength in the compression test and the extension test is defined as $\Delta\sigma_c = |T_{11} - T_{22}|$ and $\Delta\sigma_t = |T_{11} - T_{22}|$ for the compression and the extension test, respectively. The ratio of the concrete strengths is determined by ψ. The strength ratio ψ has values between 0.5 and 1 depending on the confining pressure within the test piece [10]. The ratio ψ is given in Eq. 11.12:

$$\psi = \frac{\Delta\sigma_t}{\Delta\sigma_c} \qquad [11.12]$$

$\Delta\sigma_c, \Delta\sigma_t$ are measures of the shear strength of concrete. It is mentioned that the maximum shear strength is, using the three-dimensional Mohr's Circle, $|1/2(T_{11} - T_{22})|$. Thus, the factor of 0.5 should be kept in mind by evaluation of the maximum shear strength.

The shear strength can also be expressed by the second deviatoric invariant:

$$\Delta\sigma_c = \Delta\sigma_t = \sqrt{3J_2} = |T_{11} - T_{22}| > 0 \qquad [11.13]$$

© Woodhead Publishing Limited, 2010

The shear strength is defined as an absolute value, all meridian values are positive. One diagram for each case, the compression and extension test results respectively, are shown in Fig. 11.4c on p. 351. The meridians describe the path of shear strength versus the mean stress for the compression and the extension test.

Yield surface and failure surface

Depending on the stress state and the strain rate, the solid's isotropic material has a certain yield strength and fracture strength. As soon as the stress state exceeds the yield strength, the material is exposed to overstress. Within the cross-section, some fibers fail and the capacity decreases. In structural steel, the metal crystal lattice deforms along an inner layer and shear stress is the predominant cause of yielding. In concrete, microcracks appear around the aggregate and, when the load increases, these initial microcracks spread into the cement paste leading to a loosening of the material. Due to compaction of concrete pores, the concrete material generates higher strength, the so-called material hardening. While structural steel is a ductile material allowing large plastic strains before failure, concrete is brittle in tension, but can develop ductile material behavior dependent on the axial stress state under compression.

Failure surfaces in the three-axial stress state are used for analysis. The shape of the failure surface within the principal stress space is described by the invariants. A sophisticated yield surface to describe concrete material behavior in the pre- and post-failure regime is formulated using the invariants I_1, J_2, J_3:

$$f(I_1, J_2, J_3) = 0 \qquad [11.14]$$

Figure 11.3a shows the hydrostatic axis along the vector $[1\ 1\ 1]^T$ in the Cartesian coordinate system with the axes named by the three principal stress components $\sigma_1 = T_{11}$, $\sigma_2 = T_{22}$, $\sigma_3 = T_{33}$. Along the hydrostatic axis, all principal stresses are equal $\sigma_1 = \sigma_2 = \sigma_3$. Perpendicular to the hydrostatic axis, the deviatoric plane spans a region which describes the corresponding shear capacity of the solid. The yield criterion of Eq. 11.14 postulates a dependency on I_1, which demonstrates that the compaction of the material leads to increasing strength. Further, the material yielding depends on the shear strength, expressed by J_2, which grows with increasing hydrostatic pressure.

Instead of using the invariants, every stress state in an isotropic material can be expressed by the three parameters ξ, r and the angle of similarity θ, which define the solid's hydrostatic stress level, the deviatoric stress and deviatoric plane shape, as shown in Fig. 11.3b. The failure surface in Eq. 11.14 can, thus, be expressed by:

© Woodhead Publishing Limited, 2010

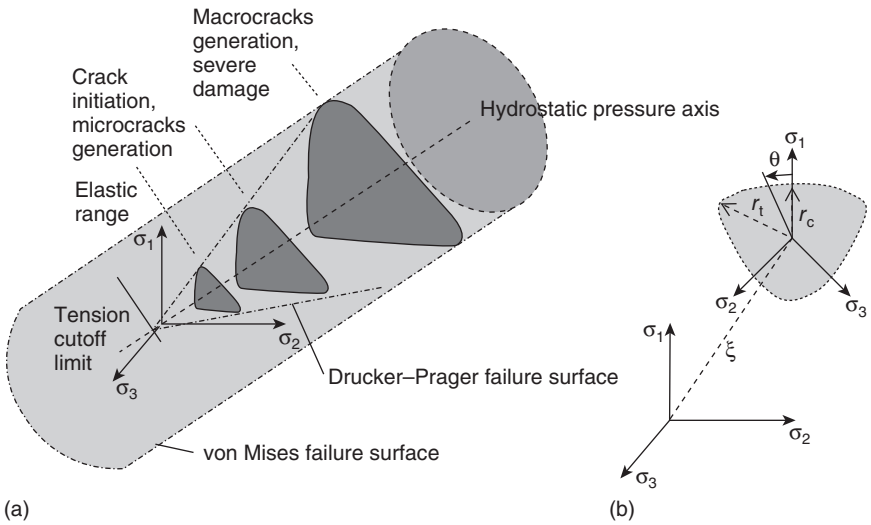

11.3 The hydrostatic and deviatoric stress: (a) three-dimensional stress state; (b) deviatoric plane.

$$f(I_1, J_2, J_3) = f(\sigma_m, \tau_m, \theta) = 0 \qquad [11.15]$$

Two early developments of a failure surface, the von Mises failure surface and the Drucker–Prager failure surface, are shown in Fig. 11.3a. The von Mises cylinder is suitable to represent materials which are pressure-independent, as e.g. structural steel. The circular deviatoric plane demonstrates a constant shear capacity. The Drucker–Prager cone mirrors a hydrostatic pressure-dependent material, such as concrete. However, the circular deviatoric plane is only valid for concrete under high hydrostatic pressure. The following failure surface characteristics are typical for concrete [4]. Point 5 has been added to the reference.

1. The failure surface is smooth.
2. The failure surface is convex.
3. The deviatoric section is triangular with rounded corners. Good approximations with an elliptic trace in 60° angles, as developed by [11].
4. The deviatoric section is somewhat triangular for the tension and the low compression range, but transitions to a circular section with increasing hydrostatic pressure, which can be described using the membrane analogy by [12].
5. Construction of a tension cutoff, as shown in Fig. 11.3a, to avoid stress beyond the tensile strength.

Yield criteria define the elastic limits of a material under combined states of stress. Since the 19th century, researchers have developed criteria to

© Woodhead Publishing Limited, 2010

describe the failure behavior of concrete, examples are the Rankine, Tresca, von Mises, Mohr–Coulomb, Drucker–Prager, Bresler–Pister, Willam–Warnke, Ottosen, Reimann, Hsieh–Ting–Chen yield criteria [4]. These failure criteria depend on up to five parameters.

Figure 11.4 defines the failure surfaces which are implemented in the material model used in this study [8] and discussed in [10]. Figure 11.4b illustrates the concept of three combined failure surfaces. As soon as the stress reaches the yield strength, the material becomes plastic. The concrete exposed to increasing compressive stress compacts, the material hardens and the strength level increases. Microcracks form around the aggregates and with increasing stress state extend into the cement paste. The maximum failure surface describes a pressure-dependent stress level, where macrocracks have formed and the concrete material is heavily damaged.

When the stress has touched the maximum failure surface, the stress is reduced gradually to a residual strength level, the residual failure surface. This reduction in material strength with increasing strain, as shown in Fig. 11.4a, defines the material softening, which comprises the material damage.

The shear stress $\Delta\sigma$, which corresponds to the yield, maximum and residual failure stress state, is analyzed by Eqs. 11.16–11.18:

$$\text{Definition of the yield failure surface: } \Delta\sigma_y = a_{0y} + \frac{p}{a_{1y} + a_{2y} p} \qquad [11.16]$$

$$\text{Definition of the maximum failure surface: } \Delta\sigma_m = a_0 + \frac{p}{a_1 + a_2 p} \qquad [11.17]$$

$$\text{Definition of the residual failure surface: } \Delta\sigma_r = \frac{p}{a_{1f} + a_{2f} p} \qquad [11.18]$$

where a_{0y}, a_{1y}, a_{2y}, a_0, a_1, a_2, a_{1f} and a_{2f} are user-defined parameters that determine the failure surface shape.

Equations 11.19 and 11.20 define the current failure surface between the yield and maximum failure surface, respectively, with dependence on η, which is a function of the accumulated effective plastic strain parameter λ, as shown in Fig. 11.4d. λ depends on the effective plastic strain increment $d\varepsilon^p$. f_t is the maximum concrete tensile strength.

$$\lambda = \int_0^{\varepsilon^p} \frac{1}{r_f \left(1 + \frac{p}{r_f f_t}\right)^{b_1}} d\varepsilon^p \quad \text{for} \quad p \geq 0 \qquad [11.19]$$

$$\lambda = \int_0^{\varepsilon^p} \frac{1}{r_f \left(1 + \frac{p}{r_f f_t}\right)^{b_2}} d\varepsilon^p \quad \text{for} \quad p < 0 \qquad [11.20]$$

© Woodhead Publishing Limited, 2010

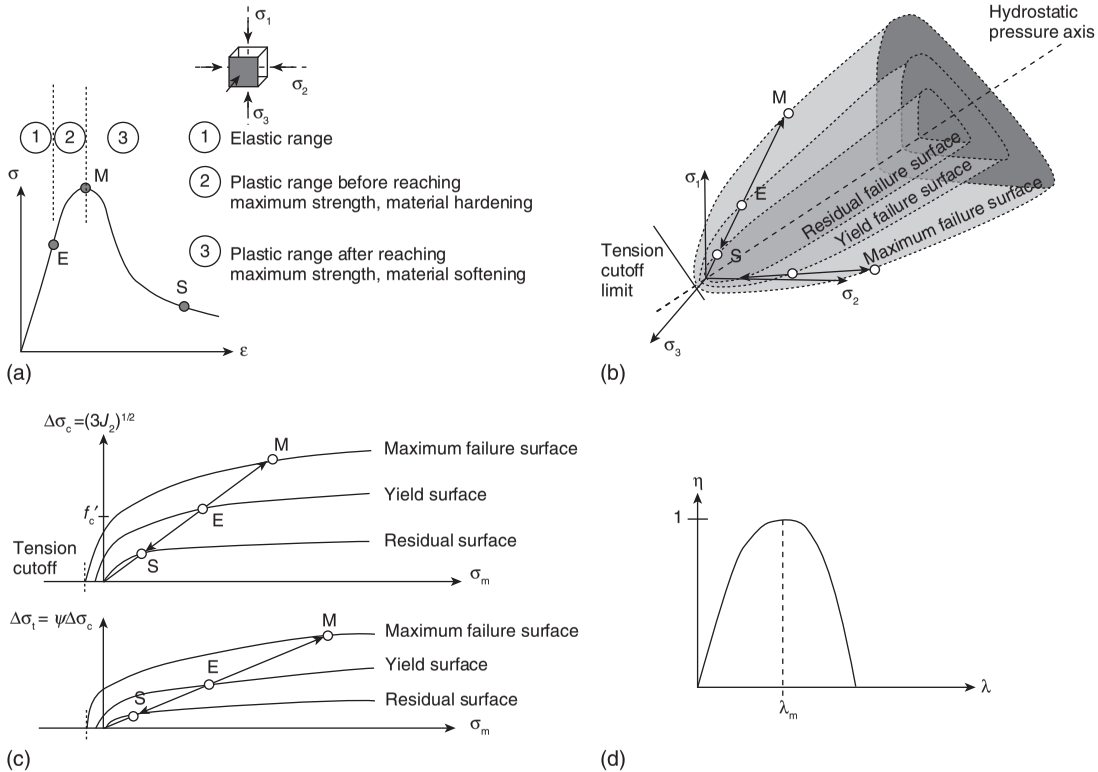

11.4 Development of failure surfaces to describe the pressure-dependent isotropic material: (a) stress–strain curve progression from elastic state to failure; (b) triaxial stress state – linear approximation to consider material hardening and softening; (c) stress–strain curve progression from elastic state to residual stress – data from compression and extension test; (d) failure evolution parameter eta (λ).

© Woodhead Publishing Limited, 2010

where the effective plastic strain increment is determined by Eq. 11.21. The concept of effective strain ε^{p} allows it to extrapolate data from uniaxial tension or compression tests into the multiaxial situation [4]:

$$\mathrm{d}\varepsilon^{\mathrm{p}} = \sqrt{\frac{2}{3}\mathrm{d}\varepsilon_{ij}^{p}\mathrm{d}\varepsilon_{ij}^{\mathrm{p}}} \qquad [11.21]$$

where $\mathrm{d}\varepsilon_{ij}^{p}$ is the plastic strain increment vector.

The values b_1, b_2 are mesh-size dependent. The current shear stress is analyzed by Eq. 11.22:

$$\begin{aligned} \Delta\sigma_{\mathrm{f}} &= \eta(\Delta\sigma_{\mathrm{m}} - \Delta\sigma_{\mathrm{y}}) + \Delta\sigma_{\mathrm{y}} \\ \Delta\sigma_{\mathrm{f}} &= \eta(\Delta\sigma_{\mathrm{m}} - \Delta\sigma_{\mathrm{r}}) + \Delta\sigma_{\mathrm{r}} \end{aligned} \qquad [11.22]$$

The abscissa value λ is applied to define a damage parameter δ:

$$\delta = \frac{2\lambda}{\lambda + \lambda_{\mathrm{m}}} \qquad [11.23]$$

Material which is subjected to high-velocity loading sustains high strain rates for blast in the range of 10^4–10^6 l/ms, depending on whether the material is exposed to direct reflected pressure or transferred shock wave pressure. Concrete strength increases with higher strain rate that is considered by the strain rate enhancement factor r_{f} in this concept. The strain rate enhancement factor pushes the shear strengths $\Delta\sigma_{\mathrm{c}}$ and $\Delta\sigma_{\mathrm{t}}$, illustrated in Fig. 11.4c, to a higher value. At the same time, there are different r_{f} factors for concrete subjected to tension and compression. Rate enhancement factors are developed, e.g. in [13]. For a strain rate of ε = 100 l/*s* the strain rate enhancement factor amounts to about 8 and 2 for concrete under tension and compression, respectively.

Flow rules

The flow rule combines the loading function and the plastic stress strain relation for a work hardening material. Equation 11.24 shows the flow rule, where the volumetric plastic strain increment $\mathrm{d}\varepsilon_{ij}^{p}$ is expressed as the partial derivative of the plastic potential function $g(T_{ij})$ over the stress state T_{ij}. The partial derivative $\partial g/\partial T_{ij}$ gives the direction of the plastic flow. The positive scalar factor λ determines the magnitude of plastic flow. λ is zero, when no plastic deformation occurs. Since on the hyper-surface, the surface of equal plastic potential, $g(T_{ij})$ is constant, the vector $\mathrm{d}\varepsilon_{ij}^{p}$ must be normal to the plastic potential surface:

$$\mathrm{d}\varepsilon_{ij}^{p} = \lambda\frac{\partial g}{\partial T_{ij}} \qquad [11.24]$$

When the plastic potential is replaced by the yield function $f(T_{ij})$, the plastic potential surface has the same shape as the yield surface and the plastic

© Woodhead Publishing Limited, 2010

strain develops normally to the yield surface. The relation shown in Eq. 11.25 is termed the associated flow rule:

$$\mathrm{d}\varepsilon_{ij}^{p} = \lambda \frac{\partial \mathrm{f}}{\partial T_{ij}} \qquad [11.25]$$

The material model utilizes a partial associated flow rule to account for the effects of shear dilatancy. The Prandtl–Reuss material model in the material library provides a non-associated flow rule and would not be able to consider the shear dilatancy, the reduction of pressure and increase in volume. Accordingly, a value ω is used to cause the direction of plastic flow to lie between the directions of the non-associated flow rule ($\omega = 0$) and the associated flow rule ($\omega = 1$).

The analysis is conducted in the explicit iteration scheme. The three energy equations and the equation of state (EOS) are solved at every time-step to solve the four unknowns which are density, pressure, internal specific energy and particle velocity. The EOS gives the volume–pressure relation.

11.5.2 Geometry of the columns

This paragraph introduces the column types investigated in this study. Square, round and octagonal geometries with multi-cell or single-cell cross-sections are considered. Comprehensive blast resistant design requires that the local strengthening does not inadvertently overburden and thereby damage the other parts of the structure. Thus, a 'balanced' design considers the transmission of increased reflected pressure into the adjacent structural elements, as well as strengthening the column exposed directly to the blast pressures.

Eight column cross-sections are investigated in a comparative analysis. All column types have an effective width of 1.52 m and a total length of 6.10 m. The first type is a single-cell steel hollow box section with two longitudinal stiffeners placed at 1/3-point on each side of the box. The stiffener plate width is 25 cm and the thickness of all plates amounts to 1.78 cm. The second column type is similar to the first but, instead of stiffeners, full plates are used at third points making the section a multi-cell cross-section with nine cells with each cell being a square cell of 50.8 cm side length. The thickness chosen for all steel plates used in the steel multi-cell cross-section is 0.92 cm. The third column type is the octagonal steel multi-cell cross-section. The geometry and steel plate thickness are identical with the square multi-cell section, but the corner cells are triangle shaped and constructed by welding the outside plate in a 45°-angle on the neighboring cells, as shown in Fig. 11.5. The fourth column type is a single-cell hollow composite cross-section consisting of an outer steel square section with the thickness

© Woodhead Publishing Limited, 2010

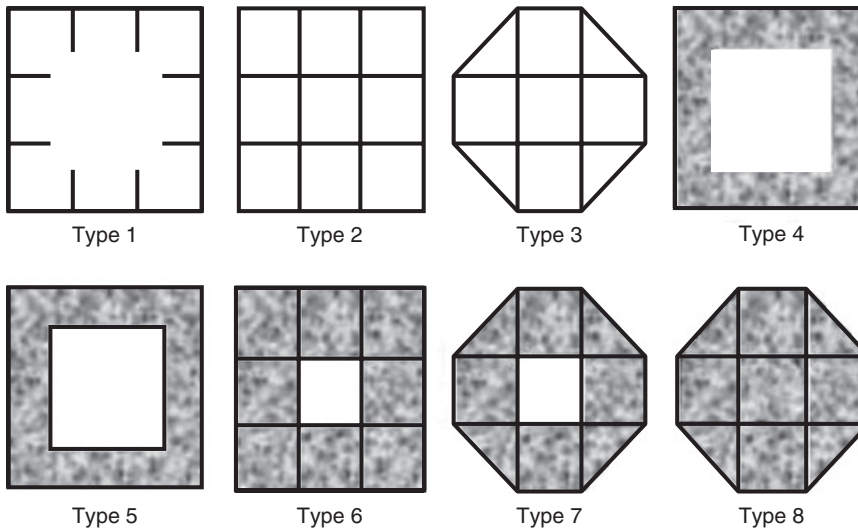

11.5 Steel and composite column cross-sections.

of 1.78 cm connected to an inner concrete square hollow section of 25 cm thickness by headed studs. In the calculation, the composite connections have been assumed to be rigidly connecting the steel outer box to the concrete inner box. The fifth section is identical with section type 4, but with an additional inner steel box section. The sixth and seventh column types in the study are composite multi-cell columns. The steel column sections introduced as column types 2 and 3 have the outer cells filled with concrete, as shown in Fig. 11.5, to make it composite sections. Again, the concrete inside the cells is connected to the steel plates using headed shear studs, simulated as rigid connections in the analyses. The eighth column type is identical with the octagonal cross-section of type seven, but has the center cell also filled with concrete.

11.5.3 Loading

The columns are subjected to a gravity load, as well as blast pressures. Each load source is described briefly in the following sections to give information about this significant parameter.

Axial load

The axial load is due to gravity. All column types introduced in Fig. 11.5 are loaded axially with 30% and 60% of the maximum axial capacity of the

© Woodhead Publishing Limited, 2010

respective cross-section. The same computations but with zero axial load are conducted and compared in order to see the effect of axial loading.

Blast pressure

The explosion is a process of rapid energy release, which generates a blast pressure wave [14]. From a spherical explosive source, this pressure wave propagates radially through the air and impinges on the column. The pressure is calculated explicitly in the Euler volume [15]. The Euler–Lagrange-coupling technique enables the pressure transfer to the solid body, in this case the column target surface. Numerous studies demonstrate the accuracy of the calculated reflected pressure pulses as compared to published experimental test data. The test data of [16,17] are used as sources for verification. The pressure reflection of the rigid ground is taken into consideration in this study. The blast source has a standoff of 1.5 m from the target surface and is positioned at 1.02 m height above rigid ground.

Temperature

Temperature plays a decisive role when fire breaks out. However, fire is not a common result of an explosion unless a secondary energetic source is ignited, e.g. gasoline within nearby vehicles. The detonation typically consumes all the oxygen in the vicinity of the burst. During the high energetic blast event, which happens within fractions of a second, the high temperature is assumed to impose limited damage to the structure in comparison to mechanical effects of the blast waves. Accordingly, temperature is not considered in the analysis of local failure in this study.

11.5.4 Boundary conditions

The boundary conditions for ground floor columns of high-rises are assumed to be rigidly connected at the base and connected to a flexible neighboring steel skeleton structure at the top. The steel skeleton structure provides a realistic horizontal boundary at the top of the column. In subsequent calculations, the boundary conditions of composite column types seven and eight, as shown in Fig. 11.5, are not assumed to be rigid in order to provide ductile response capacity to the structural member.

11.6 Results and discussion

The following sections discuss the findings for all gravity pre-loaded columns subjected to blast loads.

© Woodhead Publishing Limited, 2010

11.6.1 Square single-cell steel and composite column

When the single-cell steel section is subjected to small explosive threats, the target surface deforms plastically and transmits forces by bending and catenary action to the side plates. Even when the front face deforms significantly, the side and back plates do not sustain any permanent deformation. The cross-section does not react as a whole and thus can be characterized as inefficient and inadequate for the blast design of the vehicle-borne threat hazard. The column response is shown in Fig. 11.6a where the plastic strain contour lines are plotted over the outer column surface. There is a concentration of plastic strain visible at the base; this is the location where the column base will likely fracture if the explosive threat occurs at a higher elevation. The column target surface will fracture at the base level and deform inwards. The local damage decreases the effective load-carrying cross-section. When the target surface fails, the remaining cross-section is not able to resist the gravity load. As a result of the effective damage, the box double-symmetric section is turned into a U-shaped cross-section. A cross-section reduction to about 60% of former intact cross-section results in the collapse of the column when the gravity load amounts to more than 60% of the axial capacity of the column. Additionally, the P-Δ-effect comes into play and precipitates the collapse of the column. To improve the performance of the steel column, concrete is added to the steel single-cell section. The outer steel box girder and an inner concrete hollow section of 25 cm thickness are connected, as introduced in Section 11.5.2,

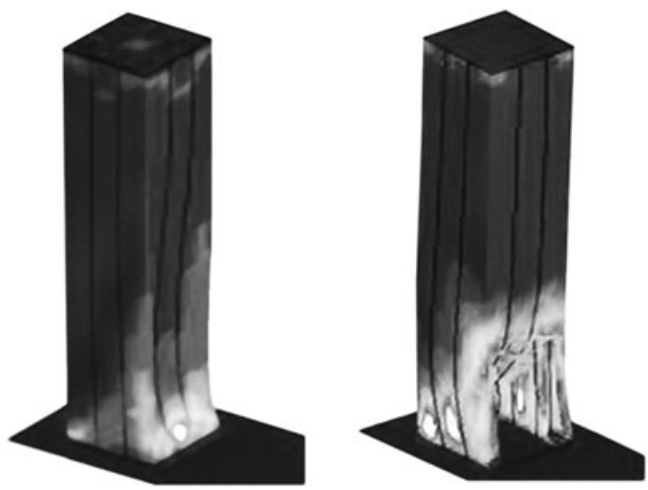

11.6 (a) Steel single-cell column type 1 (b) Composite single-cell column type 5.

© Woodhead Publishing Limited, 2010

as type 4. The concrete provides an increase in the target surface stiffness and leads to improved load distribution, which minimizes stress concentrations. Moreover, the concrete contributes in dissipating energy by deforming and developing microcracking up to complete shattering, reducing the demand on the steel plate.

Comparative analysis shows that the composite section withstands about twice the explosive threat compared with the single-cell steel column. However, the concrete partial section shatters for two reasons. First, the concrete is exposed to tensile stress when the target surface bends due to blast pressure; second, the concrete is not sufficiently confined to reach a higher compressive strength. An additional inner steel hollow box section is introduced into the column section, as is introduced with type 5 in Section 11.5.2. The comparative analysis demonstrates that this refined single-cell composite section withstands the blast pressure, while the single-cell composite section without inner steel hollow section fails under the same load. There is a steel plate positioned on both sides of the concrete section, which is capable of sustaining the tensile bending stress and further enables the concrete to develop the beneficial triaxial stress state. When the blast load is further increased, the target surface deforms inwards into the composite hollow section, which results in a reduction of intact cross-section and ultimately the collapse of the column, as shown in Fig. 11.6b. The residual cross-section is not able to withstand the combination of axial stress due to gravity, as well as combined shear and bending stresses. The side plates yield locally, shown by the plastic strain contours. However, the strengthening measure (i.e. refined single-cell composite column) results in more than four-fold increase of local blast resistance. The described failure mode leads to the conclusion that the hollow column section should be avoided and rather be designed solid, in order to avoid a situation where blast pressure punches through the composite target surface. The multi-cell composite section provides this robust level of performance. It should be mentioned that this strengthening measure can also be introduced as a retrofit for existing structures [18,19].

11.6.2 Square multi-cell steel and composite column

The multi-cell steel column is a more effective blast resistant solution than the single-cell section. The nine-cell cross-section brings stiffness into the section and leads to smaller target surface deformation than observed at the single-cell section. Furthermore, the multi-cell section responds as a whole; the inner stiffeners which interconnect target surface and back side plate transfer the blast load directly to the back plate, which improves overall impact resistance. Side plates and inner stiffener provide bracing for the target surface, which accordingly acts as a three-span plate.

© Woodhead Publishing Limited, 2010

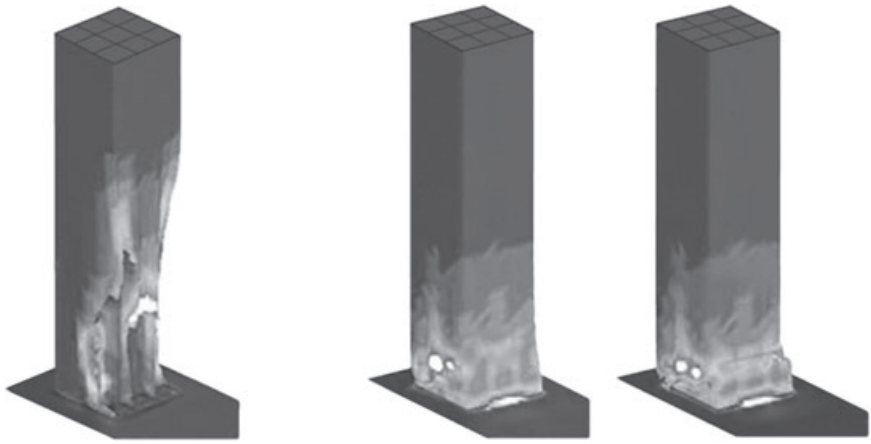

11.7 (a) Steel multi-cell column type 2 (b) Composite multi-cell column type 6.

Bending and catenary action transfer the blast pressure to the inner stiffeners, as well as to the side plates. However, the target surface, the side plates and stiffeners are damaged when the blast load is increased. Figure 11.7a shows the plastic strain contour line plot of the multi-cell steel column type, referred to as type 2 in Section 11.5.2, shortly after detonation. The failure mode of this column type 2 is caused by overstress in the residual cross-section in combination with P-Δ-effect. In order to strengthen the nine-cell steel section, the outer eight cells are filled with grout/concrete, introduced in Section 11.5.2 as section type 6. Figure 11.7b shows the multi-cell composite column at two different time-steps. The improved load distribution and stiffening effect of concrete improves the resistance of the target surface. The concrete behind the steel front face may be compacted and shattered to powder and granulate, but it is still able to carry load. Due to confinement of concrete in the cells, the section stays stable even when the blast load is increased six-fold, compared with the maximum explosive size of the respective steel section. The column is loaded with an axial load of 30% of its axial capacity. The plastic strain contour lines show that there is high local plastic strain at the bottom target surface. However, the prominent failure mechanism is initiated by shear stress failure of the longitudinal stiffener adjacent to the base. Figure 11.7b depicts the failure of the column side plate. Following this localized failure, the column's shear capacity is abruptly reduced. The lateral forces and vertical load cannot find any alternate load path and the column fails. The comparison of composite multi-cell and pure steel multi-cell column deformation and plastic strain plots demonstrates the beneficial behavior of the composite section.

© Woodhead Publishing Limited, 2010

11.6.3 The octagonal multi-cell steel and composite column

Lessons learned from wind engineering can be applied in the development of streamlined target surface shapes for blast loading. The streamlined shape attracts less blast pressure and subsequently results in reduced damage [19]. A study was conducted to change the geometric shape of the square cross-section to an eight-sided octagonal cross-section, introduced in Section 11.5.2 as type 3.

As seen at the square multi-cell section, the response of the target surface (normal to the explosive threat) indicates bending and catenary action. When the size of the explosive threat is increased, the narrow target surface plate fails. The base elements that are directly connected to the ground (idealized rigid boundary condition) fracture first. Two damage mechanisms are found to contribute to global failure of the column. The first damage mechanism includes stress concentrations in the lower part of the longitudinal stiffener. In the absence of lateral deformations at the top column connection, this is the governing failure mechanism of the column. The second failure mechanism governs when the column top undergoes displacement, as it occurs at a cantilever system. In this case, the failure is initiated by axial load, which generates P-Δ-effect and displaces the column top forward. This initiates a plastic hinge in the vicinity of the column base, as shown in Fig. 11.8. In this example the axial load amounts to 60% of the

11.8 Octagonal multi-cell steel column.

© Woodhead Publishing Limited, 2010

axial cross-section capacity. The octagonal steel section is strengthened by concrete infill, representing type 7 of Section 11.5.2. The increased stiffness of the target surface results in improved pressure distribution and reduction of stress concentration. The blast load can be increased six-fold, without any fracture of the target surface, except for the bottom target surface connected to rigid ground.

11.7 Observed failure mechanisms

The global failure of the concrete column subjected to nearby blast is initiated by local failure. Four cases of local failure were detected in this study and are shown in Fig. 11.9 [20,21]. The composite set-up of the cross-section adds strength to the cross-section at strategic locations. This Section discusses the zones of local overstress, the kinds of stress that lead to damage and initiate the specific failure pattern. It further explains the benefits of

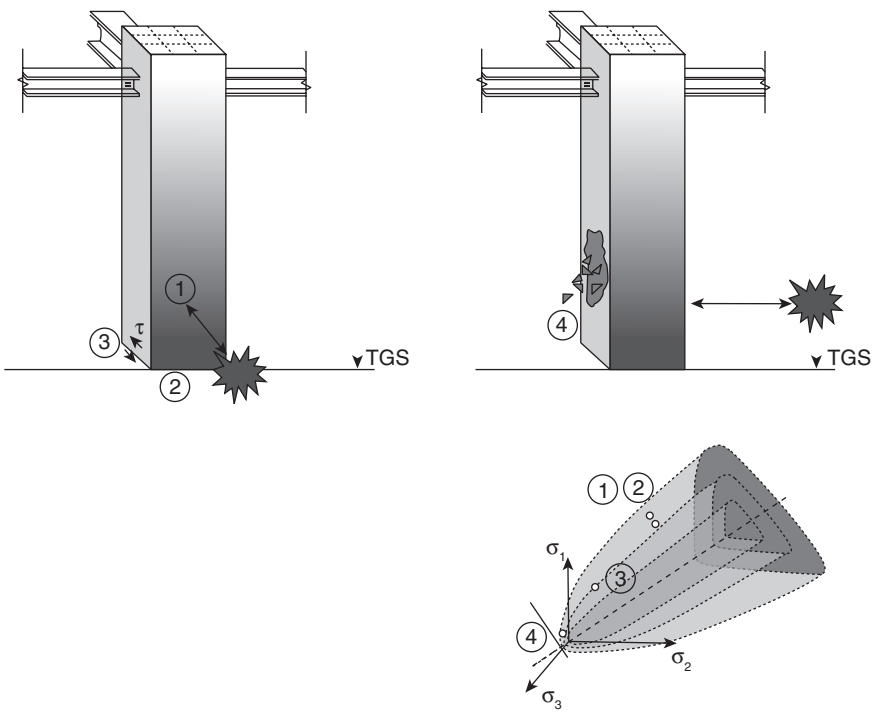

11.9 Locations of local failure: ① deterioration of infill material and subsequent fracture of target surface; ② fracture at bottom of target surface; ③ shear failure at web plate or inner stiffener; ④ spalling at column back side.

© Woodhead Publishing Limited, 2010

the composite partial section and the possible advantageous usage of fiber reinforcement.

Zone 1 of the target surface is closest to the explosive threat. Accordingly, the reflected pressure is at a maximum. The infill concrete is jacketed by steel and develops the beneficial triaxial stress state due to confinement. An example of the stress state is shown in the three-dimensional stress plot of Fig. 11.9 and marked with point 1. The concrete without the steel jacket would not reach this high level of confinement and failure strength. The use of fiber-reinforced concrete instead of normal concrete is assumed to only marginally enhance the failure strength, because the concrete is exposed to compression rather than to tension or shear, where fibers would add strength.

Zone 2 is the intersection of the target surface with the top ground surface. High reflected pressure and rigid boundary conditions result in high stress concentrations and early fracture of the bottom target surface. Because the infill concrete fails, the target surface sustains large deformations and fractures. However, as comparative analyses results will demonstrate later, a thicker steel jacket plate results in less improvement than changing the rigid boundary condition to a deformable condition.

Further review of the response indicated shear stress concentrations at the bottom of the column side plates and inner stiffeners adjacent to the intersection with the top ground surface, marked as zone 3. The magnitude of the shear stress is immediately affected by the analyst-selected boundary conditions. Reduced rigidity or a more compliant boundary is assumed to significantly reduce the peak shear stress. This failure mode highlights the importance of the vertical steel plates placed in-line with the blast pressure, providing the section with sufficient shear capacity. Fiber-reinforced concrete, instead of normal concrete, supposedly mitigates this failure mode by increasing activated shear force capacity.

The impedance mismatch at the backside of the column, marked as zone 4, generates full reflection of the shockwave and generates local tension stress. The steel jacket helps to sustain the tensile stress. The three-dimensional stress plot of Fig. 11.9 shows only reduced strength of concrete in tension. Fiber-reinforced concrete provides higher tensile strength compared to normal concrete and, accordingly, fiber-reinforced concrete infill, instead of normal concrete infill, is assumed to improve resistance against spalling by providing higher tension capacity.

11.8 Mitigation of the failure mechanisms

The following narrative provides measures to mitigate the failure mechanisms described above. The protection measures at the local level, i.e. within the column cross-section as well as at the global level, are discussed.

© Woodhead Publishing Limited, 2010

11.8.1 Global protection measure: ductile boundary conditions

Three boundary connections are investigated for cases where: (i) the column is rigidly restrained at the ground level, (ii) the column is recessed into the ground and rigidly restrained (iii) the recessed column with its base vertically pin connected and laterally restrained by a spring system.

The vulnerable portion of the column is at its base. Figure 11.10 illustrates the multi-cell steel section column base. The zone of deterioration is marked by a hatched zone on the left hand side. On the right hand side the steel section is shown cut at the height of about 1.00 m above the top ground surface (TGS), as well as along the left inner stiffener. The plastic strain contour lines plotted over the partial steel cross-section indicate the zones of local failure. The element line adjacent to the base at the bottom longitudinal stiffener is fractured and the bottom target surface is ruptured; this results in the deactivation of the first cell line. A view of the interior of the steel cross-section, depicted on the right hand side, clearly shows the bending and catenary action of the first transverse stiffener in the absence of the concrete in the center cell. The pressure impinges on the concrete in the first cell that is directly behind the target surface and against the first transverse stiffener. The strain contour lines mark the high plastic strain concentrations, which can be mitigated by also filling the inner center cell with concrete. One strengthening measure to reduce stress concentrations involves increasing the thickness of the steel plates adjacent to the base. All column base plates up to the 1.27 m-level are thickened. The steel plate thickness is increased to 25.4 mm, 38.1 mm and 50.8 mm. Further, the

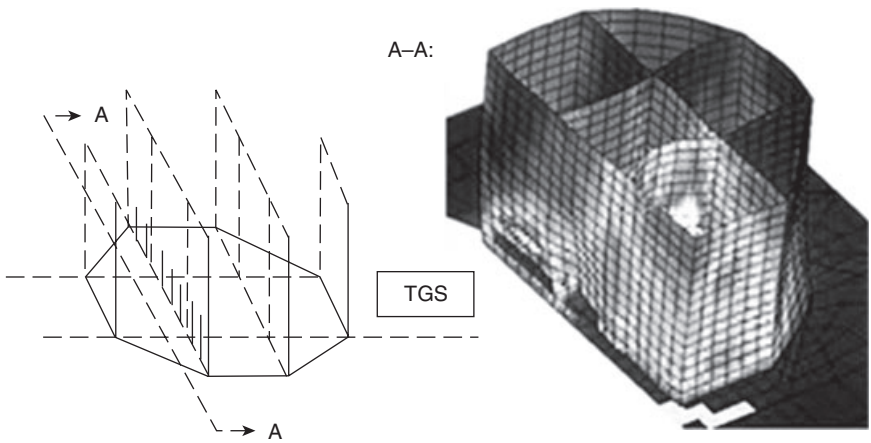

11.10 Inner stiffener at top ground surface.

© Woodhead Publishing Limited, 2010

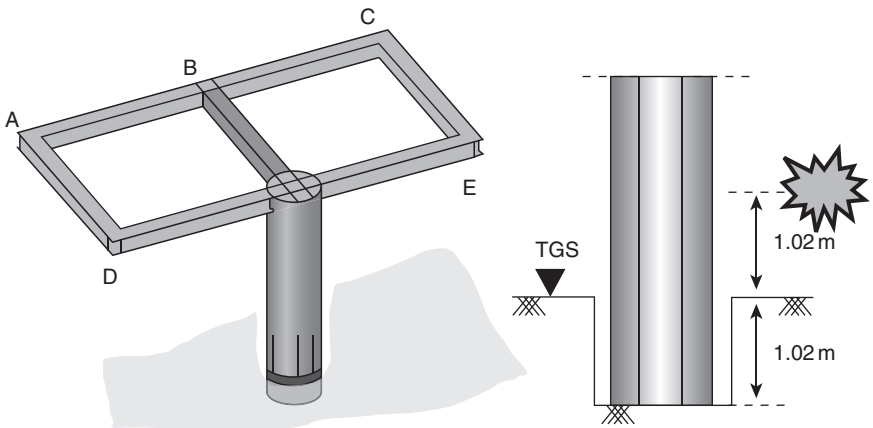

11.11 Column recessed into the ground.

center cell is filled with concrete. Extensive comparative analyses show that the local failure of inner and outer stiffener can be prevented for high blast loads by increasing the steel plate thickness. This increases the shear force capacity to transfer the large lateral loads into the floor slabs. The fully grouted section improves load distribution and creates the triaxial stress state which is beneficial for concrete to resist stresses and significantly increases the uniaxial concrete compressive strength. Both strengthening measures are incorporated in the protection technology that is introduced, as follows.

Recessing the column base in the concrete slab is one structural protective measure that avoids the concurrence of extreme reflected pressure at the TGS and the rigid connection. In this analysis, the column base is fixed rigidly at level 1.02 m below the TGS, as depicted in Fig. 11.11. The explosives detonate at the 1.02 m-level above the TGS. The left-hand side outlines the isometric view of the column. The column top is connected to the neighboring framing system. The frame system consists of a center girder, which connects the column top with bearing B, shown in Fig. 11.11. The composite girder has a square cross-section of dimensions 50.8 cm × 50.8 cm and a steel plate thickness of 38.1 mm. The frame construction consists of I-beams with flange width and web height of 50.8 cm and flange and web thickness of 12.7 mm. Stiffeners are installed at the positions of load transmission. The frame system is fixed rigidly at points A, B, C, which is comparable to the role of the staircase core in high rise buildings.

The boundary conditions specified at D and E are vertically rigid but horizontally displaceable. The maximum pressure appears at the target surface slightly above the TGS. At this level, the column is able to undergo

© Woodhead Publishing Limited, 2010

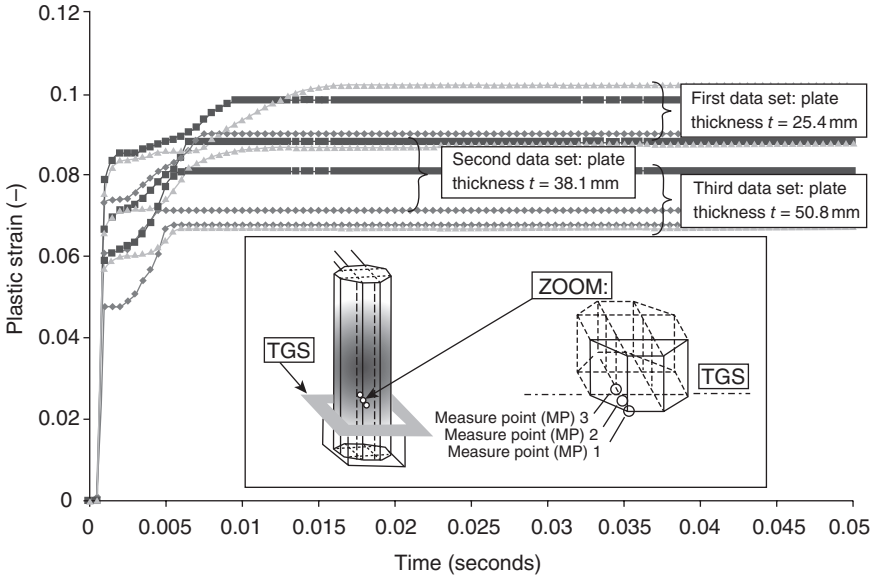

11.12 Strain measured at the inner stiffener at top ground surface (TGS) and plotted versus time.

certain rigid body deformation. The structural system dissipates energy due to both elastic and plastic deformation, which results in a significant reduction of reaction forces compared with the identical column that is connected rigidly at the TGS.

This study further considers the effect of an increase in the thickness of all plates composing the partial steel cross-section of the composite column (applied from the column bottom up to +1.27 m above TGS). The identical locations that failed at the non-strengthened column base because of shear stress concentrations are selected as areas of focus. The plastic strain time history at the first three elements of the inner longitudinal stiffener within the first cell behind the target surface is used as a measure of response. The points of interest are outlined in the diagram of Fig. 11.12. Nine curve progressions are presented, for which three curves correspond to points 1, 2 and 3 for each of three plate thicknesses. The thicknesses of t = 25.4 mm, 38.1 mm and 50.8 mm are considered in this study.

The column base is strengthened by increasing the steel plate thickness in the predefined area to 25.4 mm, as well as grouting the inner cell of the multi-cell composite section. These measures result in a maximum local limited plastic strain of about 0.1, as shown in Fig. 11.12. A further plate thickness increase, up to 38.1 mm and 50.8 mm, leads to maximum plastic strain of about 0.085 and 0.067, respectively. The improved blast resistance

© Woodhead Publishing Limited, 2010

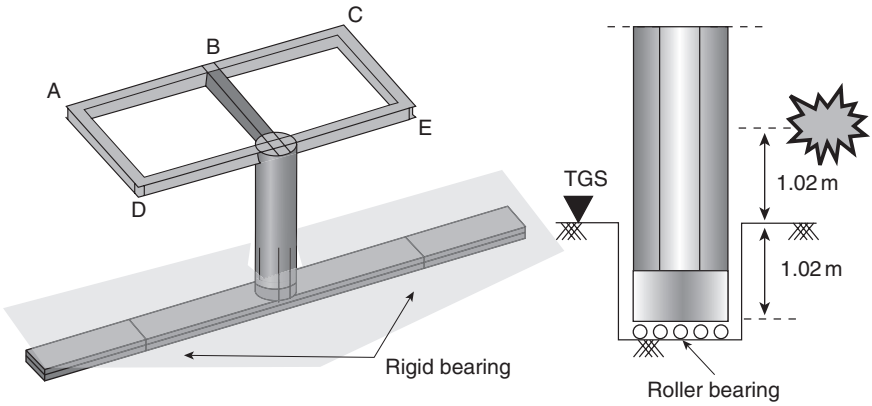

11.13 Horizontally displaceable column with arm construction.

of the octagonal column is mostly due to the ductile boundary response and the steel thickness increase. A modified connection is subsequently applied in order to study the effect of ductile boundary condition on the structural member. The octagonal column support is permitted to displace horizontally. As shown in Fig. 11.13 right, the column base is fixed by two arms, which are connected rigidly at the distance of 5.08 m from the column surface.

The arms have a composite cross-section with a dimension $h \times b$ of 50.8 cm × 152 cm. The arms consist of a hollow steel section with an additional horizontal plate installed. The horizontal and vertical steel plates have a thickness of 25.4 mm and 12.7 mm, respectively. The arm construction at the column base acts similarly to a spring and produces a time-shifted and smaller amplitude horizontal force in response to the explosive event. For the sake of convenience, this ductile boundary construction will be referred to as the horizontally displaceable column with arm construction, and can be substituted by a spring system. The column top is supported by the identical frame system as was introduced above for the recessed and rigidly connected column base. The same explosive threat is considered against the target column. The plastic strain time history is measured in the first elements of the first cell, as shown in Fig. 11.14. A steel thickness increase to 25.4 mm of all plates from the column bottom up to 1.27 m above TGS leads to a maximum plastic strain in the first cell line of about 0.11. However, the plate thickness discontinuities along the height are found to generate breaking points when the blast load increases. Accordingly, the plate thickness should be held constant over the height rather than tapering the thickness.

A further thickness increase up to 38.1 mm and 50.8 mm reduces the plastic strain to about 0.08 and 0.07, respectively. Investigations show that

© Woodhead Publishing Limited, 2010

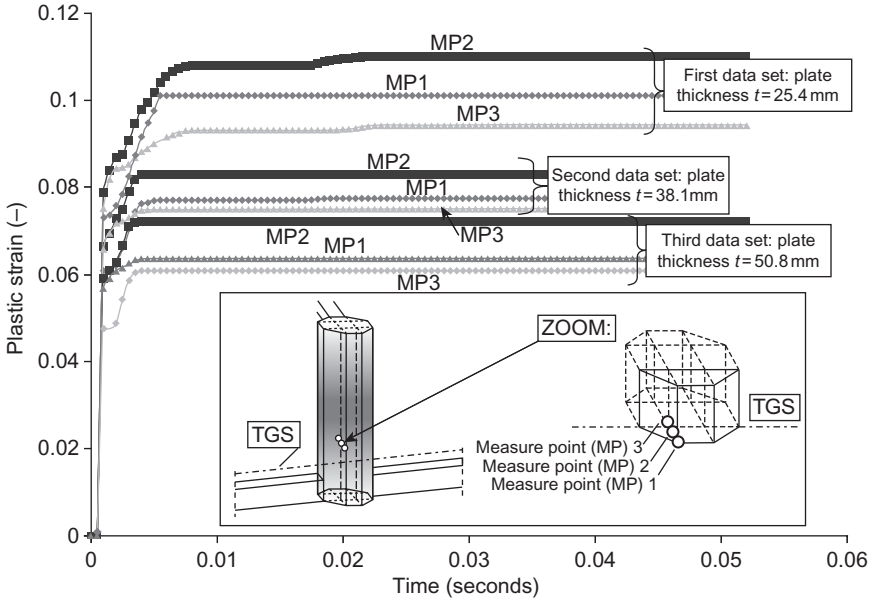

11.14 Effect of the plate thickness increase on the plastic strain in the inner stiffener at top ground surface (TGS).

the plastic strain decays over the column section from the target surface to the backside of the column. The plastic strain in the second cell line only amounts to about half the plastic strain of the first cell line. Similarly, the plastic strain in the third cell line is about one third. The comparison of the maximum plastic strain distribution at the inner stiffener within the column cross-section measured at the recessed column as well as at the horizontally displaceable column with arm construction shows that both ductile boundary conditions result in very similar reduced plastic strains.

11.8.2 Local protection measures

The blast resistance of the solid versus the hollow column cross-section is compared. Further, the effect and protection of sacrificial cells which are wrapped around the column cross-section have been investigated.

Definition of cross-section

Hollow sections within the cross-section are deficient for structural members subjected to blast. The steel cross-section filled with concrete provides the member with inertial resistance. Hollow volumes exposed to pressure

© Woodhead Publishing Limited, 2010

waves are compressed with negligible resistance capacity and small energy dissipation. A hollow volume, within the cross-section, forces the stress to flow around the hollow section resulting in stress concentrations. Further, the triaxial stress state is generated best for cross-sections without voids. Accordingly, hollow sections can detract from the column's blast resistance and should be avoided.

Sacrificial cells

Energy absorbing or energy dissipating sacrificial cells are assembled on the target surface of the load bearing column. The performance of this protective measure, protection of the target surface and energy dissipation of the sacrificial cells is discussed in the following narrative.

The extreme reflected pressure at the bottom target surface compounded by the adjacent rigid connection to the ground leads to poor performance. At higher blast pressure, concrete shatters and the target surface fractures at the interaction of the target surface with the TGS. Possible failure mechanisms that might follow are the loss of intact cross-section area, eccentricity of gravity load and P-Δ-effects. The use of a streamlined cross-section transfers less load into the section and provides a more economical solution. The beneficial effects of ductile boundary condition, as applied by the recessed column base, as well as at the horizontally displaceable column with arm construction, introduced in Section 11.8.1, do not improve the protection of the bottom target surface from fracture and deactivation of the first cell line. An alternate method to reduce the bottom target surface stress concentration is to install an energy absorbing sacrificial cell belt around the column target surface. The shape of the sacrificial cells can adapt to the column surface shape, as shown in Fig. 11.15.

The sacrificial cell section has a depth of 25.4 cm. To provide an architecturally unobtrusive solution, the sacrificial cells run from the level –0.254 m below TGS up to the column top. The steel cross-section of the cut column base and the sacrificial cell section are illustrated without the concrete infill in Fig. 11.16.

The plastic strain contour lines indicate yielding and fracturing at the sacrificial cell surface, but only slight plastic strain of the load bearing column section. The multi-cell section of the sacrificial cell construction absorbs energy outside the load bearing column cross-section by material deterioration and deformation and protects the section effectively. The results from the horizontally displaceable column with arm construction are recalled. In order to prove the effectiveness of the horizontally displaceable column with arm construction quantitatively, the plastic strain was measured at points 1–3, as previously evaluated in Fig. 11.14 of Section 11.8.1. This response is compared with the identical column with the installed

© Woodhead Publishing Limited, 2010

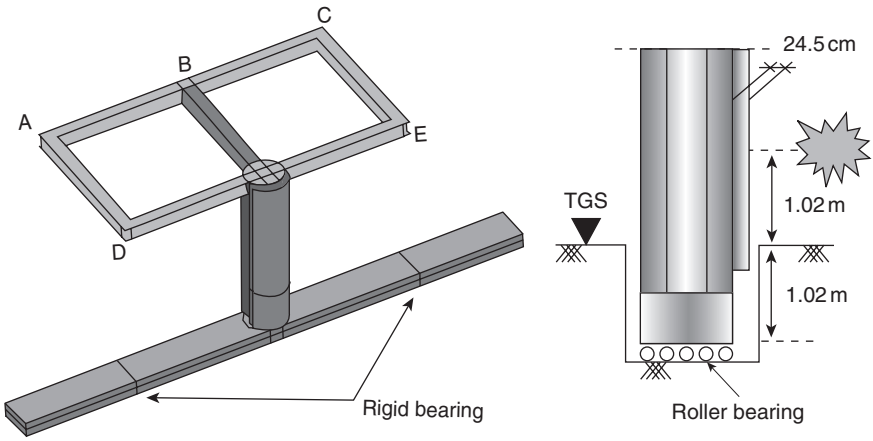

11.15 Horizontally displaceable column with arm construction and installed sacrificial cells.

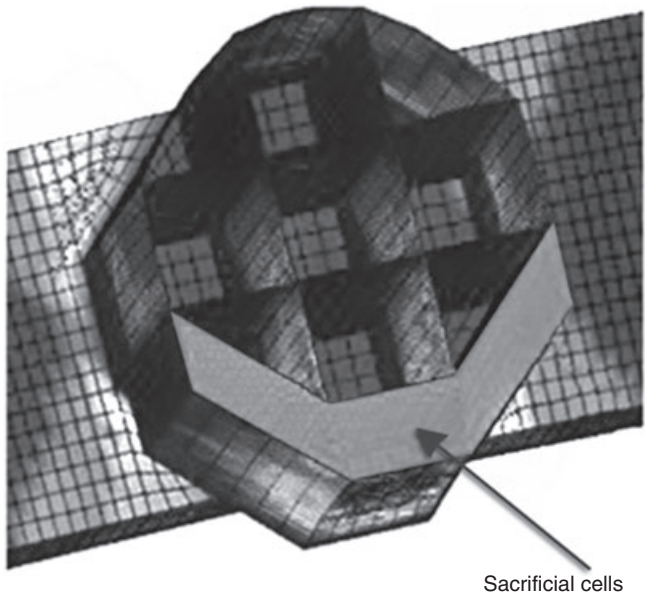

11.16 Sacrificial cells.

sacrificial cells. All steel plates at the column base have an increased thickness of 25.4 mm from the column base up to 1.27 m above rigid ground. The curves corresponding to the column with ductile arm-solution and without sacrificial cells are drawn in Fig. 11.17. The first measure point shows maximum plastic strain of about 0.11. Introducing the sacrificial cells

© Woodhead Publishing Limited, 2010

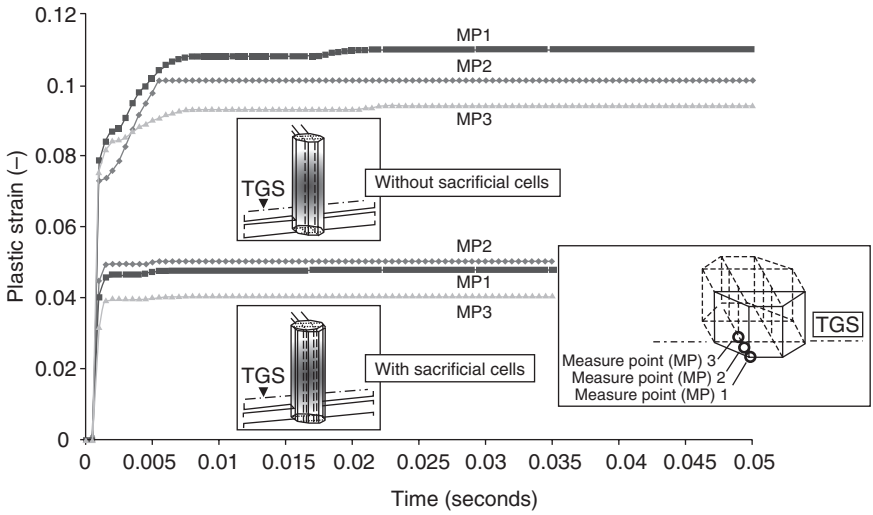

11.17 Effect of protective sacrificial cells.

reduces the plastic strain to about 0.05: a strain reduction of 55%. Further investigations show that the application of sacrificial cells not only protects the bottom target surface but also significantly reduces the plastic strain distribution within the cross-section. Extended calculations demonstrate the beneficial effects of sacrificial cell construction in steel–concrete composite elements for blast resistant design applications.

11.8.3 *P*-Δ-effects

The *P*-Δ-effect is a governing failure of steel columns subjected to blast. The blast wave leads to local cross-section damage and deactivation. The eccentricity of the gravity load results in member collapse due to *P*-Δ-effect. The composite columns are less susceptible to this failure mode. The steel jacket on the composite column, which improves load distribution and increases confinement, leads to much reduced local fracture compared to the bare steel column. The *P*-Δ-effect is further decreased when target surface damage can be diminished by using streamlined cross-section geometry and sacrificial cells.

11.9 Comparative investigation of performance and residual capacity of the load bearing column

This section considers the performance criteria of the load bearing column in a comparative analysis of all investigated columns [22]. The

© Woodhead Publishing Limited, 2010

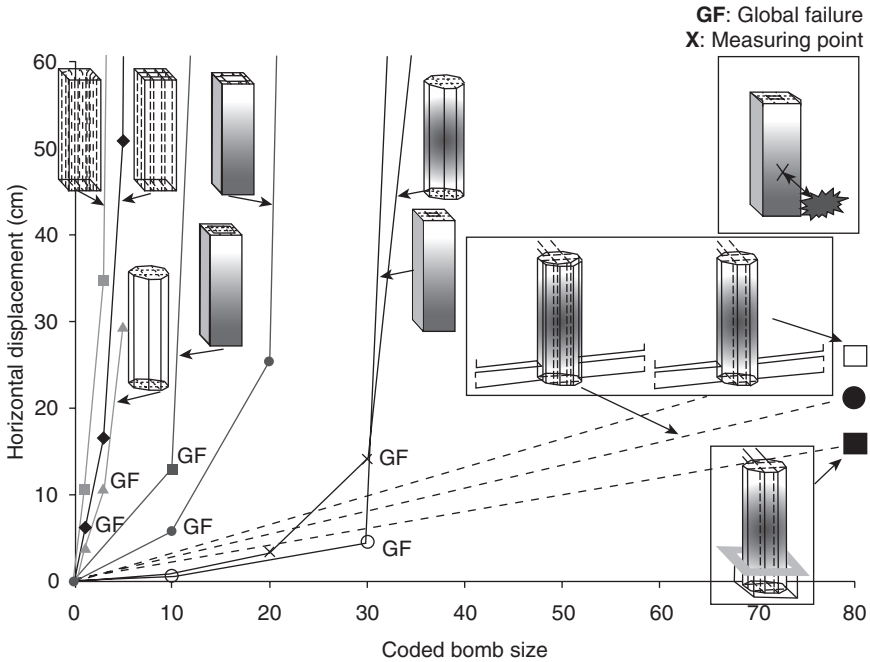

11.18 Steel and composite columns – displacement versus coded bomb size.

effectiveness of the blast resistance of the respective protective technology is evaluated and the results are summarized in the diagram of Fig. 11.18. The horizontal displacement measured at the center line on the target surface at the 1.02 m-level above the TGS is plotted against the coded size of explosive threat. The objective of this comparative analysis is to develop a qualitative means of summarizing the blast response of the column types. Accordingly, the size of the explosive threat is not important. Each curve in the diagram describes the deformation behavior of one column type and indicates the failure load GF (global failure). The composite column types 4 and 5 attain a two- to six-fold increase in blast resistance of the pure steel column types 1–3, respectively. Composite column types 6 and 7 reach about a six-fold increase in blast resistance of the pure steel column types 2–3. All these columns were rigidly connected at the TGS. When the ductile boundary conditions are applied for composite column type 8 and sacrificial cells are added, the blast resistance is more than 16 times the blast resistance capacity of the pure steel columns 1–3.

© Woodhead Publishing Limited, 2010

11.10 Establishing parameters affecting blast resistance of columns

The study demonstrates that the blast resistance of a ground floor column of a high rise building depends on structure- and load-specific parameters. The structure-specific parameters can be subdivided into local structural parameters and global structural parameters. These parameters are summarized in Fig. 11.19. The consideration of these parameters in the design process would allow the engineer to develop a desired level of blast resistance against vehicle-borne explosive threat. This in turn can lead to the prevention of column loss and catastrophic and progressive collapse of the large portions of the structure.

11.11 Summary and conclusions

The implementation of inner stiffener into the single-cell steel cross-section and its conversion into a multi-cell section is an effective blast resistant measure for small amounts of explosives. For larger explosive threats, further changes of the cross-section are necessary to ensure effective protection. The significant failure modes of steel columns include target surface damage, followed by reduction of cross-section and P-Δ-effects. Adding concrete inside the single-cell and multi-cell steel columns and converting them into composite columns significantly improves the blast resistance of the column. Inertial resistance is the key factor in the improved performance of the composite column. Because of improved load distribution and

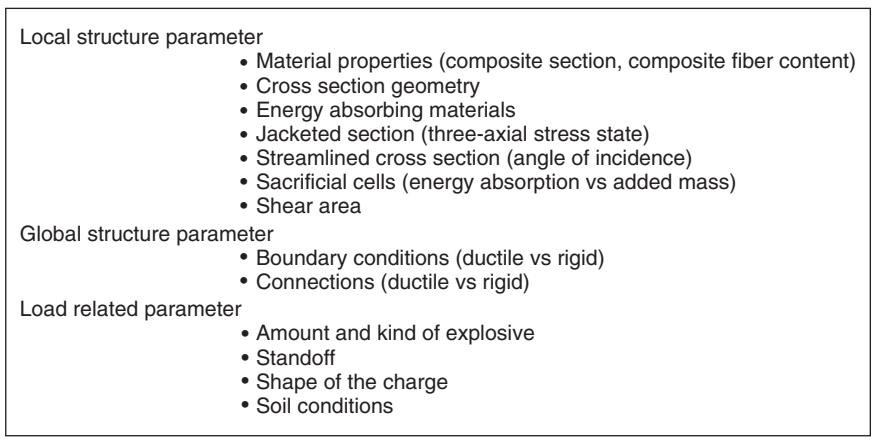

11.19 Blast resistant parameters.

© Woodhead Publishing Limited, 2010

confinement, the composite section sustains only localized plastic behavior, even under relatively large explosive threats. The multi-cell composite section is more suitable for blast resistance than the single-cell composite section. It is recognized that highly impulsive blast pressures will breach through the target surface. This failure mechanism has not been detected in multi-cell column section. The multi-cell composite cross-section responds as a whole when subjected to transient load.

Stress concentrations at the bottom longitudinal stiffener and at the bottom target surface connected to rigid ground were defined as key failure modes. Structural solutions were presented to mitigate these failure modes. The octagonal cross-section was introduced as streamlined cross-section, which reduces the reflected pressure. The increase of thickness of the longitudinal stiffener adjacent to the ground strategically improves the shear capacity of the column. The column cross-section should be totally filled with concrete, which improves distribution of the extreme lateral loads and increases the effective material strength due to generation of the triaxial stress state. The hollow center cell of the multi-cell composite section is proven to be an ineffective solution for blast resistance.

Ductile boundary conditions are a decisive and prominent tool in reducing the magnitude of lateral load transfer into the column. Two solutions of columns with ductile boundary condition were introduced and evaluated. Recessing the column base into the ground separates the locations of extreme reflected pressure and the rigidity of the connection. This effectively prevents high stress concentrations in the longitudinal stiffener. As a second ductile boundary solution, the horizontally displaceable column with arm construction was introduced. Evaluation of plastic strain distribution and comparison of the two ductile boundary conditions show that both systems lead to similar reduction of stress concentrations at the inner stiffener. The steel–concrete-composite sacrificial cell construction which is attached to the target surface emerges to be an effective measure to decrease the potential of local fracture detected at the intersection of the bottom target surface and the top ground surface.

11.12 Acknowledgements

The research presented in this chapter is based on the work conducted on various aspects of modeling and response analyses of steel and composite columns subjected to blast load during a 2-year post doctoral stay at the University of California at Berkeley, USA and the research on investigating the effect of ductile boundary condition on blast resistance of columns and developing structural solutions at the Technical University Munich, Germany. The author sincerely thanks the German Research Foundation (DFG) for the receipt of the generous DFG Research Fellowship. The

© Woodhead Publishing Limited, 2010

author further thanks his colleagues Adam W. Hapij, Dr Bob Smilowitz and Dr Ivan S. Sandler, Weidlinger Associates Inc., New York, for the discussions about the topic and the careful review of the chapter.

11.13 References

1 CEN (EUROPEAN COMMITTEE FOR STANDARDIZATION) (1997), *Eurocode 1, Part 2.7, Accidental Actions, Background Document*, Brussels, Belgium, November.
2 SMILOWITZ R (2002), Analytical tools for progressive collapse analysis, *Proceeding of National Workshop on Prevention of Progressive Collapse*, Multihazard Mitigation Council of the National Insitute of Building Sciences, Rosemont, IL, 10–12 July.
3 SEI/ASCE 7-05, *Minimum Design Loads for Buildings and Other Structures*, Section C2.5: Load Combinations for Extraordinary Events, American Society for Civil Engineers, Reston, VA, 2005, 257.
4 CHEN W F (1982), *Plasticity in Reinforced Concrete*, McGraw-Hill, New York.
5 LEVINE H (1982), A two-surface plastic and microcracking model for plain concrete, nonlinear numerical analysis of reinforced concrete, *Winter Annual Meeting*, ASME, Phoenix, AZ, 14–19 November.
6 MOULD J, LEVINE H (1987), A three-invariant viscoplastic concrete model, in Desai C S, Krempl E, Kiousis P D (eds), *Constitutive Laws for Engineering Materials: Theory and Applications*, Elsevier, New York, 707–712.
7 MOULD J C, LEVINE H S, TENNANT D (1994), Evaluation of a rate-dependent three invariant softening model for concrete, fracture and damage, in Bazant Z P, Bittnar Z, Jirasek M and Mazars J (eds), *Quasi-brittle Structures*, E & F Spon, London, UK, 231–243.
8 MALVAR L J, CRAWFORD J E, WESEVICH J W, SIMONS D, A plasticity concrete material model for DYNA3D, *International Journal of Impact Engineering*, **19**(9–10), 847–873.
9 MALVERN L E (1969), *Introduction to the Mechanics of a Continuous Medium*, Prentice-Hall, Englewood Cliffs, NJ.
10 NOBLE C, KOKKO E, DARNELL I, DUNN T, HAGLER L and LEININGER L (2005), *Concrete Model Descriptions and Summary of Benchmark Studies for Blast Effects Simulations*, UCRL-TR-215024, U.S. Department of Energy, Lawrence Livermore National Laboratory, Livermore, CA.
11 WILLAM K J, WARNKE E P (1975), Constitutive model for the triaxial behavior of concrete, *Proceedings IABSE Seminar on Concrete Subjected to Threeaxial Stresses*, Paper III-1, Instituto Sperimentali Modelli e Structure, Bergamo, Italy, 174–186.
12 CHEN W F, ATSUTA T (1977), *Theory of Beam Columns, Vol. 2, Space Behavior and Design*, McGraw-Hill, New York.
13 MALVAR L J and ROSS C A (1998), Review of strain rate effects for concrete in tension, *ACI Materials Journal*, **95**(6), 735–739.
14 BAKER W E (1973), *Explosions in Air*, University of Texas Press, Austin, TX, USA.
15 *MSC/Dytran Theory Manual*, MSC Software Corporation, Santa Ana, CA, 2002.

© Woodhead Publishing Limited, 2010

16 U.S. DEPARTMENT OF THE ARMY TECHNICAL MANUAL: TM5-1300 (1990), *Structures to Resist the Effects of Accidental Explosion*, United States Department of the Army, Navy and Air Force, Washington, DC.
17 MAYS G C, SMITH P D (1995), (eds), *Blast Effect on Buildings*, Thomas Telford, London, UK.
18 RUTNER M, ASTANEH-ASL A (2005–2006), Behavior of bridge piers subjected to blast load. Research project at the Department of Civil and Environmental Engineering, Univ. of California, Berkeley.
19 RUTNER M, ASTANEH-ASL A, SON J (2006), Blast resistant performance of steel and composite bridge piers, *Proceedings IABSE 2006 Symposium*, Budapest, Hungary, 13–15 September.
20 RUTNER M (2007), Blast resistance of structural members, *Proceedings IABSE 2007 Symposium*, Weimar, Germany, September 19–21.
21 RUTNER M (2007), The effect of ductile boundary connection to blast reysistance of gravity-bearing columns, *Proceedings, 7th Japanese-German Bridge Symposium*, Osaka, Japan, July 30–August 1, 80–81.
22 RUTNER M, GEBBEKEN N, MANGERIG I, ZAPFE O, MÜLLER R, WAGNER M, PIEZSCH A and MENSINGER M (2008), Steel Structures Subjected to Blast, in Kuhlmann U (eds), *Steel Construction Annual 2008 (Stahlbau Kalender 2008)*, Section 6, Wiley, New York, 549–646.

© Woodhead Publishing Limited, 2010

12

Retrofitting using fiber-reinforced polymer (FRP) composites for blast protection of buildings

G. S. URGESSA, George Mason University, USA

Abstract: This chapter discusses the use of fiber-reinforced polymer (FRP) composite retrofits for blast loading. The chapter reviews the history of fiber-reinforced polymer composite retrofit application for out-of-plane loadings, blast tests using FRP retrofits and notes on the analysis of FRP strengthened (retrofitted) structures. It then covers connection systems and equivalent single degree of freedom analysis. The chapter also presents a short section of resources for the use of FRP composites.

Key words: fiber-reinforced polymers, blast protection, retrofitted masonry walls, full-scale blast tests, connection systems.

12.1 Introduction

Recent events throughout the world have drawn attention to the vulnerability of infrastructure to acts of terrorism. Protecting society against terrorism requires a well-planned, layered approach that combines innovative intelligence as well as effective protective strategies. The development of protective measures against explosions is not only to create new methods for designing new structures but also to improve the capability of existing structures so that they will perform efficiently and effectively under anticipated dangers and threats. This chapter focuses on the history of the use of fiber-reinforced polymer (FRP) composite retrofits for out-of-plane loadings, overview of blast tests using FRP retrofits and notes on the analysis of FRP strengthened (retrofitted) structures.

Section 12.2 presents the need for retrofitting structures and the advantages of using FRP composites when compared to other retrofitting techniques. Section 12.3 discusses the history of FRP composites in structural engineering as a retrofit material for out-of-plane loadings including blast. The section also provides important research publications and findings in the area. Section 12.4 provides a case study of a full-scale blast test conducted on masonry walls retrofitted using FRP. Section 12.5 reviews existing knowledge on FRP connection systems and the challenges involved in transferring blast loads to surrounding strengthened structural components. Section 12.6 outlines an equivalent non-linear single degree of freedom

© Woodhead Publishing Limited, 2010

model approach for the analysis of FRP retrofitted structures. Section 12.7 provides a brief commentary on major professional organizations regarding FRP composites and available reference manuals and books.

12.2 Retrofitting structures for blast protection and the advantages of fiber-reinforced polymer (FRP) composite retrofits

The Unified Facilities Criteria (UFC 4-010-01), 'Minimum antiterrorism standards for buildings', sets design standards to seek effective ways to minimize casualties from terrorist attacks. Realizing that it would be cost-prohibitive to achieve complete protection, the main goal of the standards is to increase survival rates in buildings. The standard identifies several strategies for mitigating bomb threats with the primary strategy of maximizing the standoff distance which is the distance between a structure or inhabited portion of a structure and the potential location of an explosive detonation (Department of Defense, 2003).

Although the Unified Facilities Criteria documents have been published, there are still several challenges, especially the lack of standoff distance in existing structures. Most existing structures of essential buildings are not designed for blast loading and they have little strength to withstand blast loads. More importantly, structures made from concrete masonry units have defined joint patterns that provide readily available failure planes. Under a blast load, the failure of these structures is likely to be sudden and severe, producing injuries from fragments and shattered glass that usually exceed those produced by the blast itself.

Different approaches have been used as retrofit techniques that will allow building hardening. The main aim of building hardening is enhancing conventional construction practices that mitigate hazards where standoff distance is limited or unavailable. Some of the traditional methods used to upgrade structures include: filling of cracks and voids by grouting, stitching of large cracks and other weak areas with metallic or brick elements, single or double sided jacketing by cast *in-situ* concrete, etc. A detail showing an example of a concrete backing system is shown in Fig. 12.1. For wall retrofits, another method includes a steel column and a plate in which a number of steel columns are secured behind the wall and connected into the building frame. The steel plates will connect the flanges of the columns together thereby producing a tension membrane.

The Army Corp of Engineers at Waterway Experiment Station tested a sheet steel wall system for concrete masonry unit retrofit. The experiments consisted of a 1/4 in (63.5 mm) thick mild steel spanning from floor to ceiling and securely anchored to reinforced steel anchors that were attached to the ceiling and floor slab using concrete anchors (AMPTIAC Quarterly,

© Woodhead Publishing Limited, 2010

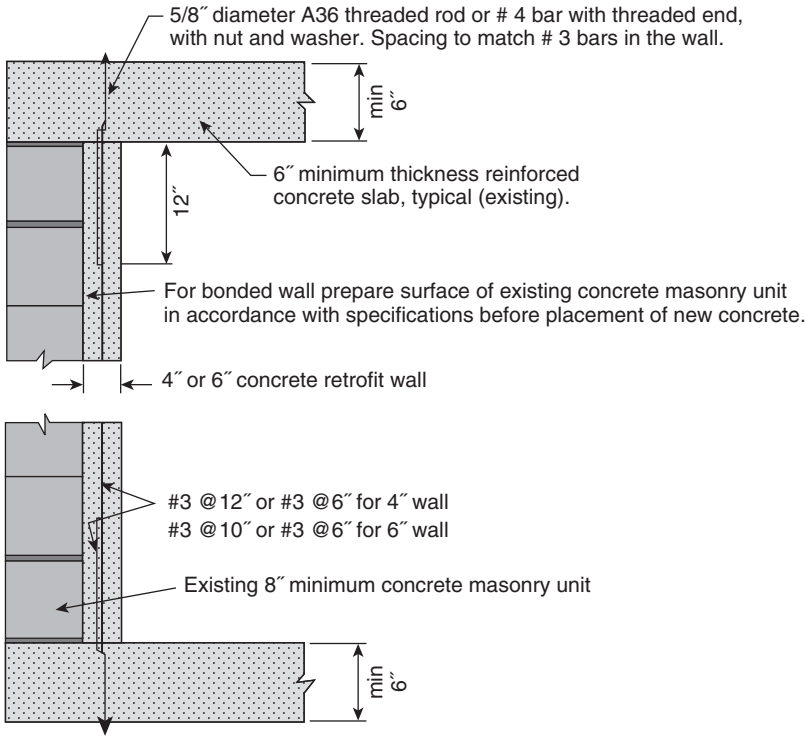

12.1 Concrete backing system.

2002). One of the key successes of this system was the detailed design of the anchorage system. The experiment was shown to contain the closed-in detonation.

Ward (2004) provided a number of different retrofitting techniques for retrofitting masonry walls against blast loads of specific impulse values. Davidson *et al*. (2004) have presented results of explosive tests on masonry walls with various polymer retrofits conducted at the Tyndall Air Force Base as well as some qualitative results of structural response of these structures.

Coltharp and Hall (2002) have shown the use of a thin steel stud system that investigated steel studs to construct an interior wall inside an existing wall. Each stud was anchored to the concrete slabs at the top and bottom using concrete anchors. Gypsum board was installed to the interior surface of the steel studs using adhesives and screws with bearing strips to prevent the gypsum board from pulling over the screw heads during blast loading. The steel stud walls prevented the exterior wall and debris from blowing into the room. Although the techniques mentioned above are effective in

© Woodhead Publishing Limited, 2010

increasing the strength and stiffness of structural components, they add considerable mass to the structure that can modify its dynamic response characteristics resulting in increased inertia forces. Another disadvantage is that the thickness added by the jackets may violate aesthetic requirements for historic building façades and reduce the free space of the structure (Triantafillou, 1998).

Recently, FRPs have attracted considerable attention in retrofitting structures. Expedient retrofits can be developed by producing a field-made composite of high-strength fabric (aramid, glass or carbon) in an epoxy matrix that is bonded to the structure for upgrading the blast loading capacity of structures. In the event of an explosion, the FRP composite enhances the out-of-plane bending strength of a structural component. In cases of wall retrofits, the FRP will prevent broken pieces of the wall from entering the protected space, thereby reducing injury to the occupants. Fiber-reinforced polymer systems were proven to provide a medium level of protection with low level of installation difficulty. The sharp price decrease in FRP composite material has made it attractive in strengthening structures for extreme loadings. Coltharp *et al*. (2002) also have presented a test on high-strength composites used for wall retrofits to catch wall debris. The retrofit fabric coverings, called geotextiles, have been discussed in their work.

Accurate prediction of the behavior of FRP as a means of strengthening structures is of great interest in protective technologies in order to provide a level of protection that is needed by security engineering standards.

12.3 The history of fiber-reinforced polymer (FRP) composites as retrofits for out-of-plane loadings

Fiber-reinforced polymers were introduced into the fields of aerospace and mechanical engineering in the 1940s. By the late 1970s, the use of composites had expanded to include applications in the automotive, sporting goods, and biomedical industries. Not until about 1985 did researchers in structural engineering begin to investigate the application of FRP to strengthen existing structures (Kuzik *et al*., 2003).

Croci *et al*. (1990) tested shear wall specimens with vertical and inclined reinforcement made of low-modulus polypropylene braids. A few years later, Sweidan (1991) demonstrated through analytical developments the high effectiveness of an FRP post-tensioning system for pre-stressing masonry. Schwegler (1994) was the first to propose and study the use of carbon fiber-reinforced polymers (CFRP) as seismic strengthening elements of masonry structures. The laminates were epoxy bonded to the masonry surface, serving as tensile reinforcement. Schwegler (1994) dem-

© Woodhead Publishing Limited, 2010

onstrated the effectiveness of this technique through full-scale in-plane behavior of CFRP strengthened walls. One of the first field applications of this technique was used in some of the load bearing walls of a six storey residential building in Zurich. Saadatmanesh (1994) later found in his investigation that external reinforcing glass fiber plates could be successfully laminated to the tension side of reinforced concrete beams, and this technique increased the flexural strength significantly. He also performed similar tests on masonry beams made of clay masonry units strengthened with external fiber composite plates. These tests proved that the retrofitting technique was effective and attractive due to the simplicity and versatility of the application.

Ehsani *et al*. (1997) also investigated the in-plane shear behavior of unreinforced masonry walls strengthened with fiber-reinforced plastic overlay. They noted that external FRP retrofit systems did not appear to increase significantly the in-plane shear strength of the walls. Further, it was found that the fiber orientation had a major influence on the stiffness of the retrofitted system.

Kolsch (1998) investigated a technique for strengthening existing buildings to resist bending stresses produced by earthquake loads. This system used an external reinforcement overlay that was added to the tension side of a given flexural element to increase the flexural strength. The overlay consisted of textile carbon fabrics embedded in a cement-based matrix. The results of this investigation showed that a significant enhancement of the load carrying capacity was achieved. The tests also showed that the overlay system prevented both partial and complete collapse of the masonry walls in the critical direction during the seismic loading.

Triantafillou (1998) presented a systematic numerical analysis procedure for the short-term strength of masonry walls strengthened with externally bonded FRP laminates under monotonic out-of-plane bending, in-plane bending, and in-plane shear. An experimental program on 12 small wall specimens was performed to validate the analysis and showed that strengthening of masonry walls with externally bonded FRP laminates appears to be an effective method for retrofitting. It was also noted that, when out-of-plane bending response dominates, the increase in the bending capacity is quite high.

Velazquez-Dimas and Ehsani *et al*. (2000) presented different methodologies for modeling the behavior of unreinforced masonry walls retrofitted with glass fiber composites and subjected to cyclic out-of-plane loading. The method was based on experimental data generated through seven tested unreinforced masonry walls. The data analyzed included several design parameters such as the amount of reinforcement, height to thickness ratio as well as the observed behavior in terms of modes of failure, maximum measured longitudinal strains in composite strips, compressive strain in

© Woodhead Publishing Limited, 2010

brickwork, and out-of-plane deflection. Based on the trends given by the experimental study, a methodology for estimating the ultimate flexural capacity of the walls was proposed.

Albert *at al*. (2001) presented a simple analytical model to characterize the load-deflection response of unreinforced masonry wall strengthened with glass fiber-reinforced polymers (GFRP) by conducting a test on ten masonry walls. The model considered a two-phase behavior, consisting of a non-linear portion (stiffness contribution of masonry) followed by a linear portion (stiffness contribution from fiber reinforcement). The tests predicted the cracking load and corresponding deflections well, but not the load and deflection at ultimate.

Hamoush *et al*. (2001) investigated the effectiveness of using fiber-reinforced composite overlays to strengthen existing unreinforced masonry walls to resist out-of-plane loads and made recommendations on the usefulness of using FRP as a means of strengthening masonry walls. They tested 15 wall panels with different retrofit schemes and used an air bag wall test apparatus to apply a uniform lateral load.

Tumialan *et al*. (2003) conducted a full-scale field assessment of unreinforced masonry walls strengthened with FRP laminates on a decommissioned building in St Louis, Missouri. They observed remarkable increase in the moment capacity and ductility of the walls with FRP reinforcements. These tests also served as a benchmark for their analytical models in predicting mid-height deflections and out-of-plane load carrying capacities.

Ward (2004) provided an overview on some of the methods available for strengthening existing masonry structures to resist the effects of blast attack and summarized the comparative advantages and disadvantages of various retrofit systems. The paper investigated methods such as using a steel column and plate, steel stud partitions, elastomeric spray, FRPs, internal concrete skin, and Durisol® brick. Tan and Patoary (2004) tested 13 masonry walls with three different FRP systems and showed an increase in the out-of-plane wall strength compared to a control wall without retrofit under static loading. They also presented simple analytical models to predict ultimate load carrying capacity.

The Air Force Research Laboratory at Tyndall Air Force Base, Florida, USA, conducted research towards expedient retrofit methods. The program involved explosive testing of unreinforced masonry walls retrofitted with sprayed-on polymers to improve blast resistance. The test program featured full-scale wall panels coated with polymer and a detonating explosive charge at designed standoff distances. The tests proved the effectiveness of the retrofit system (Davidson *et al*., 2004). Their work was also reported in a special issue 'Protecting people at risk' with additional comparative protective technologies that favor properly designed fabric overlays to minimize secondary blast damage (AMPTIAC Quarterly, 2002).

© Woodhead Publishing Limited, 2010

Odello (2002) has discussed the wet layup bonded carbon fibers in upgrading floor slabs that were originally designed for gravity loads. A threat situation in which the blast loading could be coming from below the floor slab provides a unique situation, because the designer places the reinforcement to resist downward loads. Typically, there is little steel to resist upward loadings. To resist this type of loading, workers could bond carbon or other fiber sheets to the floor surface and place a floor covering over them to protect the fibers. This involves minimal disruption to the strengthened area.

In addition to the literature on FRP retrofit and blast tests described above, there exists a fair amount of research examining the behavior of structures subject to blast and recommendations for retrofits (ASCE, 1997).

12.4 Full scale blast testing of fiber-reinforced polymer (FRP) retrofitted masonry walls

Maji *et al*. (2008) tested eight masonry wall segments 3.33 ft (1.02 m) wide × 10 ft (3.05 m) high × 8 in (203.2 mm) thick in dimension and were constructed in a circular arrangement at the Energetic Materials Research and Testing Center (EMRTC) north mount blast test site in Socorro, New Mexico, USA. The walls were made inside a 10 in (254 mm) reinforced concrete containment structure with windows for digital video imaging access. The test setup is shown in Fig. 12.2.

After the unreinforced walls cured, they were retrofitted with PANEX®35 uni-directional carbon fabric (PX35FBUD0150) from Zoltek Corporation. The carbon fabric packages came in a 109 yd (100 m) roll and were cut in

12.2 Full-scale blast test set-up.

© Woodhead Publishing Limited, 2010

the field to the desired wall height. The matrix used in four of the walls was an inorganic matrix called a geopolymer, consisting of a liquid potassium silicate solution and amorphous silica powder. Such resins were proven to have an excellent potential in many applications where high use temperatures are anticipated (Giancaspro *et al.*, 2004).The remaining four walls were retrofitted with an organic matrix consisting of thixotropic epoxy resin (Jeffco 1310-T) and a 2:1 hardener (Jeffco 3191) from Jeffco Products, Inc. This resin has a high resistance to crystallization in cold environments and so was chosen because the retrofitting application was done in a cold weather environment.

Different wall retrofit schemes were implemented by varying the amount of carbon fiber polymer sheets and type of matrix. Angle irons were used for anchoring the CFRP to the floor and roof of the test structure. The floor anchorage consisted of two angles (L 6 × 5½ × 1/2 × 30) whereas the roof anchorage consisted of two lighter angles (L 4 × 4 × 3/8 × 30) to facilitate lifting and installation to the roof structures. Execution of the connection was performed in the following sequence. Holes were punched in the steel angles and at the floor and roof of the reaction structure. After the wall was constructed, the carbon overlay was applied and taken around the corner of the wall in a tight curve. Once the matrix hardened, the steel angles were aligned over the holes and concrete anchors were installed. The CFRP overlay and connection details are shown in Figs 12.3 and 12.4.

The walls were subjected to a 1 lb (0.45 kg) Pentolite booster as shown in Fig. 12.5 with an equivalent TNT value of 1.4 lb (0.64 kg) for pressure determination. The explosive was suspended from the roof of the test

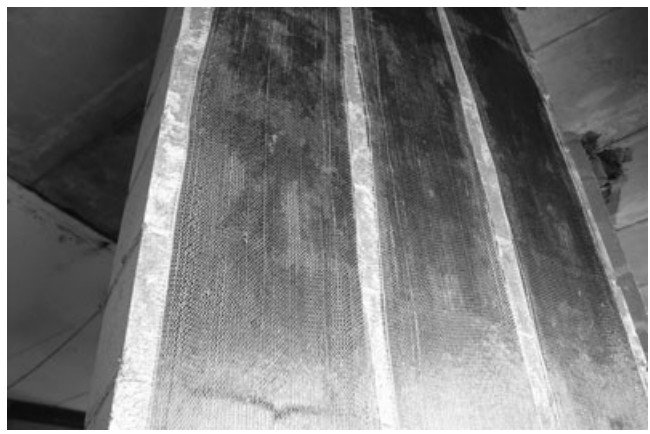

12.3 CFRP retrofitted walls.

© Woodhead Publishing Limited, 2010

12.4 CFRP connection details.

12.5 Internal explosion set-up.

© Woodhead Publishing Limited, 2010

structure and connected to a detonation device outside of the structure and was remotely controlled at a bunker. Displacement gages were mounted on each wall at mid-height to record the deflection of the walls. Two pressure gages were mounted on a steel stand (pencil pressure gages) to record the incident pressure and a third pressure gage was mounted on the roof of the test structure to capture reflected pressure. Four high-speed digital video cameras were used to capture the explosion event. Holes were cut in the test structure to facilitate lighting needed for the video imaging process. A Panasonic® CF-28 ruggedized notebook PC was used in conjunction with digital cameras for image acquisition. Once the wires were tested to work in conjunction with the station at the bunker, sand bags were used as an in-fill between the masonry wall segments to minimize the pressure wrap around effect in order to reduce the effect of stress reversal.

Post-test investigation on some of the masonry segments showed that the connections had failed during the full-scale blast test (Urgessa and Maji, 2006). A closer look at the roof of the reaction structure showed that the angle irons acted as a knife edge and tore the carbon fabric. This prompted a need for identifying a novel approach for FRP connection systems. A literature review on FRP connection systems for out-of-plane loadings is provided in the next section.

12.5 Fiber-reinforced polymer (FRP) connection systems

After a particular structure has been strengthened, one of the concerns is providing an adequate connection between the FRP and adjacent foundation or floor diaphragm. The connection is critical in establishing membrane action for structures strengthened with FRP. There are very few research findings on FRP connection systems for out-of-plane loadings including blast.

Holmberg (2000) grouted reinforcing steel bars into the foundation and into the unreinforced masonry wall a short distance to provide a pin connection. FRP was then applied to the exterior of the wall over the grouted cell containing the reinforcing bar, creating a lap splice between the FRP and the bar.

Hall *et al*. (2002) presented a scheme for testing and analysis of a ductile structural steel connection that can be used to strengthen the connection of FRP strengthened shear walls to the foundation. The test was designed to simulate the uplift experienced at the heel of an unreinforced masonry shear wall, and the authors identified several failure modes including delamination, GFRP composite rupture, glass fiber tearing and angle yielding of steel angles. The results showed the increase in energy dissipation of the

© Woodhead Publishing Limited, 2010

system and indicated that a ductile failure mode can be attained using the system.

Carney and Myers (2003) investigated a slightly different anchorage mechanism. Their method involved the anchoring of the laminate in a groove at the concrete boundary (base of a structure) by allowing the laminate strip to wrap in the groove. A GFRP bar was epoxied into the groove to hold the strips in place. First, a 0.5 in (12.7 mm) by 0.5 in (12.7 mm) groove was cut into the boundary member across the length of the wall. The wall was then constructed with the face flush with the side of the groove. The laminate strips were cut longer than the height of the wall to have enough materials to work with in the anchorage region. Once the FRP was applied to the wall, the sheet was wrapped into the groove and the groove was filled with paste and a #2 GFRP rebar was inserted in the boundary element. The connection system proved to provide an additional capacity compared to a control test without anchorage into the boundary element.

Brown and Maji (2002) provided a detail for using a metal angle iron anchorage system in a full-scale blast test. The angles were fastened to embedded channels in the test structure with bolts welded to the channels. The angles served as a clamp to the adhered GFRP fabric that was bonded to the channels and walls. A small strip of plywood was placed between the angle iron and the wall to fill the gap caused by the radius in the FRP as it turned from the wall to the floor or ceiling. The connection system was shown to remain intact following an explosion in a full-scale field test.

12.6 Equivalent non-linear single degree of freedom model for fiber-reinforced polymer (FRP) retrofitted structures

The governing dynamic equilibrium of motion for a structure with mass (m), damping coefficient (c) and stiffness (k) subjected to a loading (F) is expressed as shown in Eq. 12.1:

$$m\ddot{y} + c\dot{y} + ky = F \qquad [12.1]$$

where $\ddot{y}$ is acceleration, $\dot{y}$ is velocity, y is displacement and they are functions of time. For analyses involving blast loadings, the above equation is usually simplified by setting the damping term (c) to zero. This is due to the short time in which structures reach maximum responses when subjected to transient loads which causes a small attenuation in one cycle of displacement (Chopra, 2006). In order to predict the transient response of a structure, an incremental solution for Eq. 12.2 is sought implementing numerical integration procedures:

$$m\Delta\ddot{y}_i + k_i\Delta y_i = \Delta F_i \qquad [12.2]$$

© Woodhead Publishing Limited, 2010

Among the many methods available for the solution of the non-linear equation of motion, one of the most effective is the step by step integration using the linear acceleration method. In this method, the response is evaluated at successive increments, Δt, usually taken of equal length of time for computational convenience. At the beginning of each interval, the condition of dynamic equilibrium is established. The response for a time increment, Δt, is evaluated on the basis that the coefficient k (a function of y) remains constant during this interval. The non-linear characteristic of the stiffness is considered in the analysis by re-evaluating the value at the beginning of each time increment. The response is then obtained using the displacement and velocity calculated at the end of the time interval as the initial conditions for the next time step. The major assumption is acceleration varying linearly during the time increment. The unknown incremental displacement, Δy_i, is first calculated from the expression shown in Eq. 12.3:

$$\Delta y_i = \frac{\Delta F_i + m\left[\frac{6}{\Delta t}\dot{y}_i + 3\ddot{y}_i\right]}{\left[k_i + \frac{6m}{\Delta t^2}\right]} \qquad [12.3]$$

Once the incremental displacement is obtained, the incremental velocity ($\Delta \dot{y}_i$) is calculated using Eq. 12.4:

$$\Delta \dot{y}_i = \frac{3}{\Delta t}\Delta y_i - 3\dot{y}_i - \frac{\Delta t}{2}\ddot{y}_i \qquad [12.4]$$

In order to minimize the accumulation of errors, the acceleration at the next time step ($\ddot{y}_{i+1}$) is expressed in terms of the force, stiffness, and displacement at time $i + 1$ instead of adding the incremental acceleration to the previous step. Hence, equilibrium at each successive time step was assured using the expression in Eq. 12.5:

$$\ddot{y}_{i+1} = \frac{1}{m}[F(t_{i+1}) - k_{i+1}y_{i+1}] \qquad [12.5]$$

The above procedures are repeated at successive time intervals until the desired final value of time is reached.

Maji *et al*. (2008) had developed a resistance deflection scheme for walls retrofitted with FRP. The resistance mechanism relied principally on membrane action for concrete masonry unit walls reinforced with FRP, and a parabolic catenary shape was selected to model the deformed shape of the retrofitted walls. The resistance deflection function is non-linear and increases rapidly after a few inches of displacement. Urgessa *et al*. (2006) summarizes the findings from this test.

© Woodhead Publishing Limited, 2010

12.7 Resources for fiber-reinforced polymer (FRP) composites

The American Concrete Institute (ACI) sponsored the First International Symposium of FRPRCS (Fiber-reinforced Polymer Reinforcement for Reinforced Concrete Structures) at the 1993 convention and the international research community agreed to repeat these symposia every second year, rotating venues on various continents. The FRPRCS symposium proceedings provide a great wealth of information on FRP applications. FRPRCS-7 has a section on effects of extreme events on FRP Reinforced Concrete structures (Shield *et al.*, 2005).

Bank (2006) has a vast resource of information on properties of FRP composites, historical background, and design basis for FRP reinforcements for out-of-plane loadings. Eamon *et al.* (2004) showed numerical modeling procedures for concrete masonry walls subjected to a blast load. The method used a highly non-linear, large displacement approach that allows arbitrary element contact and separation. AMPTIAC Quarterly (2002) contains full-scale blast research on geotextiles, information on blast mitigation tools, experiments done by different federal agencies for blast hardening of structures.

12.8 References

ALBERT M L, ELWI A E and CHENG J J (2001), Strengthening of unreinforced masonry walls using FRPs, *Journal of Composites for Construction*, **5**(2), 76–84.

AMPTIAC QUARTERLY (2002), *Protecting People at Risk: How DOD Research Reduces the Impact of Terrorism*, Volume 6, Number 4, Alion Science and Technology.

ASCE (1997), *Design of Blast Resistant Buildings in Petrochemical Facilities*, Task Committee on Blast Resistant Design, New York.

BANKS L C (2006), *Composites for Construction: Structural Design with FRP Materials*, New York, Wiley.

BROWN J P and MAJI A K (2002), Blast-proofing of unreinforced masonry (URM) walls with GFRP, in Smyth A W (ed.) *Proceedings of 15th ASCE Engineering Mechanics Conference*, 2–5 June, New York.

CARNEY P and MYERS J J (2003), *Out-of-Plane Static and Blast Resistance of Unreinforced Masonry Wall Connections Strengthened with Fiber-reinforced Polymers – CIES 03-46*, Center for Infrastructure Engineering Studies, University of Missouri Rolla.

CHOPRA A K (2006), *Dynamics of Structures: Theory and Applications to Earthquake Engineering*, 3rd edn, Upper Saddle River, NJ, Prentice Hall.

COLTHARP D R and HALL R L (2002), Blast retrofit research and development: protection for walls and windows, *Amptiac Quarterly*, **6**(4), 31–37.

CROCI G, D'AYALA D, D'ASDIA P and PALOMBINI F (1990), Analysis on shear walls with reinforced fibers, *Proceedings of the IABSE Symposium on Mixed Structures Including New Materials*, 5–7 September, Brussels, Belgium, 653–658.

© Woodhead Publishing Limited, 2010

DAVIDSON J S, PORTER J R, DINAN R J, HAMMONS M I and CONNELL J D (2004), Explosive testing of polymer retrofit masonry walls, *Journal of Performance of Constructed Facilities*, **18**(2), 100–106.

DEPARTMENT OF DEFENSE (2003), *Unified Facilities Criteria (UFC 4-010-01): DoD Minimum Antiterrorism Standards for Buildings*, Washington, DC.

EAMON C D, BAYLOT J T and O'DANIEL J L (2004), Modeling concrete masonry walls subjected to explosive loads, *Journal of Engineering Mechanics*, **130**(9), 1098–1106.

EHSANI M R, SAADATMANESH H and AL-SAIDY A (1997), Shear behavior of URM retrofitted with FRP overlays, *Journal of Composites for Construction*, **1**(1), 17–25.

GIANCASPRO J, BALAGURU P and LYON R (2004), Fire protection of flammable materials utilizing geopolymer, *SAMPE Journal*, **40**(5), 42–49.

HALL J D, SCHUMAN P M and HAMILTON III, H R (2002), Ductile anchorage for connecting FRP strengthening of under-reinforced masonry buildings, *Journal of Composites for Construction*, **6**(1), 3–10.

HAMOUSH S A, MCGINLEY M W, MLAKAR P, SCOTT D and MURRAY K (2001), Out-of-plane strengthening of masonry walls with reinforced composites, *Journal of Composites for Construction*, **5**(3), 139–145.

HOLMBERG A M (2000), *FRP/Steel Strengthening of Unreinforced Concrete Masonry Shear Walls*, MS Thesis, Laramie, WY, University of Wyoming.

KOLSCH H (1998), Carbon fiber cement matrix (CFCM) overlay system for masonry strengthening, *Journal of Composites for Construction*, **2**(2), 105–109.

KUZIK M D, ELWI A E and ROGER CHENG J J (2003), Cyclic flexure tests of masonry walls reinforced with glass fiber reinforced polymer sheets, *Journal of Composites for Construction*, **7**(1), 20–30.

MAJI A K, BROWN J P and URGESSA G (2008), Full-scale testing and analysis for blast-resistant design, *Journal of Aerospace Engineering*, **21**(4), 217–225, ASCE.

ODELLO R J (2002), Polymer composite retrofits strengthen concrete structures, *Amptiac Quarterly*, **6**(4), 25–29.

SAADATMANESH H (1994), Fiber composites for new and existing structures, *Structural Journal*, **91**(3), 346–354.

SCHWEGLER G (1994), Masonry construction strengthened with composites in seismically endangered zones, in Duma G (Ed.) *Proceedings of the 10th European Conference on Earthquake Engineering*, Rotterdam, the Netherlands, Balkema, 454–458.

SHIELD C K, BUSEL J P, WALKUP S L and GREMEL D D (2005), *Fiber-Reinforced Polymer (FRP) Reinforcement for Concrete Structures*, Farmington Hills, MI, ACI.

SWEIDAN R I (1991), *The Application of Fiber-reinforced Plastics to the Strengthening of Masonry Structures*, MS Thesis, Cambridge, MA, Massachusetts Institute Technology.

TAN K H and PATOARY M K H (2004), Strengthening of masonry walls against out-of-plane loads using fiber-reinforced polymer reinforcement, *Journal of Composites for Construction*, **8**(1), 79–87.

TRIANTAFILLOU T C (1998), Strengthening of masonry structures using epoxy-bonded FRP laminates, *Journal of Composites for Construction*, **2**(2), 96–104.

TUMIALAN J G, GALATI N and NANNI A (2003), Field assessment of unreinforced masonry walls strengthened with fiber-reinforced polymer laminates', *Journal of Structural Engineering*, **129**(8), 1047–1056.

© Woodhead Publishing Limited, 2010

URGESSA G and MAJI A (2006), Blast test and analysis of carbon fiber-reinforced masonry walls, *Proceedings of XXIII Southeastern Conference on Theoretical and Applied Mechanics*, 21–23 May, Puerto Rico.

VELAZQUEZ-DIMAS J I and EHSANI M R (2000), Modeling out-of-plane behavior of URM walls reinforced with fiber composites, *Journal of Composites for Construction*, **4**(4), 172–181.

WARD S P (2004), Retrofitting existing masonry buildings to resist explosion, *Journal of Performance of Constructed Facilities*, **18**(2), 95–99.

© Woodhead Publishing Limited, 2010

13

Retrofitting to improve the blast response of masonry walls

L. MORADI, University of Alabama at Birmingham, USA

Abstract: Incidents and threats of terrorist bombings of buildings and installations have led to significant interest for blast mitigation techniques for exterior walls. Building material fragmentation is a major cause of human injury during such events. One of the most common methods of construction in buildings is the use of masonry walls. Masonry provides a fast inexpensive way to construct buildings of various heights; however, these walls are extremely vulnerable to blast pressure resulting in collapse, fragmentation, and severe injury to occupants.

Membrane retrofit materials are used to strengthen the wall's resistance to lateral pressure. In actual tests, membrane retrofit unreinforced masonry walls have experienced severe cracking and large displacements without collapse. This chapter presents resistance functions for three different scenarios of membrane retrofit unreinforced masonry walls to lateral pressure. These functions are further coupled with single degree of freedom systems to predict the wall response to blast loads. This chapter gives the structural engineer a practical tool for the design of membrane retrofit masonry walls to resist lateral pressures such as wind, and various blast charges and distances.

Key words: masonry, walls, blast, membrane, retrofit, response.

13.1 Introduction

In today's society, there is an increasing risk of terrorist attacks by radical groups, political separatists, and those people who intend to injure, and even kill, innocent people. Attacks of this nature can be carried out with relative ease by anyone who has such intent. The most widely used type of device in such an attack is an improvised explosive device (IED). The simplest of IEDs may consist only of a container carrying fuel, an oxidizer, and a detonation device. IEDs may be easily concealed and are commonly delivered by vehicles, in postal packages, and even on foot.

Terrorist attacks commonly target crowded facilities, such as office buildings and restaurants, not to mention military installations. Casualties and injuries sustained in such attacks are often caused by the disintegration and fragmentation of walls, the shattering of windows, and by non-secured objects that can be propelled at high velocities by the blast. Ensuring that

© Woodhead Publishing Limited, 2010

the exterior walls of a structure are able to withstand a blast and not produce deadly fragments is an important part of minimizing injuries to building occupants.

13.2 Types of masonry walls

Masonry construction is defined as a type of construction in which masonry units are placed by hand with mortar between them. There are many types of masonry walls, but the most common may be classified as clay masonry, stone masonry, cavity wall masonry, hollow unit masonry such as concrete masonry unit (CMU), solid masonry such as clay or concrete brick units, grouted masonry such as clay or concrete brick units filled by pouring grout between the outer and inner wythes, reinforced grouted masonry, and reinforced hollow unit masonry. These have developed in different ways and have a variety of uses in common construction.

Although masonry provides a fast and inexpensive way to construct building facilities of various heights, it is extremely vulnerable to the high pressures induced by blast, resulting in collapse, fragmentation, and severe injury to occupants. An understanding of the structural behavior of masonry walls during blast is the key to providing mitigation techniques.

Masonry walls may be constructed to be load bearing where they carry the forces of the structure above them, or non-load bearing. They may be constructed to resist lateral pressure from wind, seismic, or other sources such as blast in two-way action, or they may be constructed to carry lateral forces in one-way action. The methodology developed in this chapter is applicable to:

- walls constructed with unreinforced masonry units;
- load bearing or non-load bearing walls constructed to resist lateral pressure in one-way action.

13.3 Blast load

The load magnitude caused by a blast is determined by many factors, including charge size, type of explosive, and standoff distance. Blast can be airburst or surface burst, depending on the distance of the burst above the ground. An airblast generates a pressure sphere traveling in the radial direction at the speed of sound (Dharaneepathy *et al.*, 1995). This pressure has a positive phase and a negative phase as shown in Fig. 13.1.

The positive phase has a peak side-on pressure, and the negative phase is characterized by suction. In many studies of blast effects on structures, the negative phase is ignored (Beshara, 1994). Pressure intensity depends

© Woodhead Publishing Limited, 2010

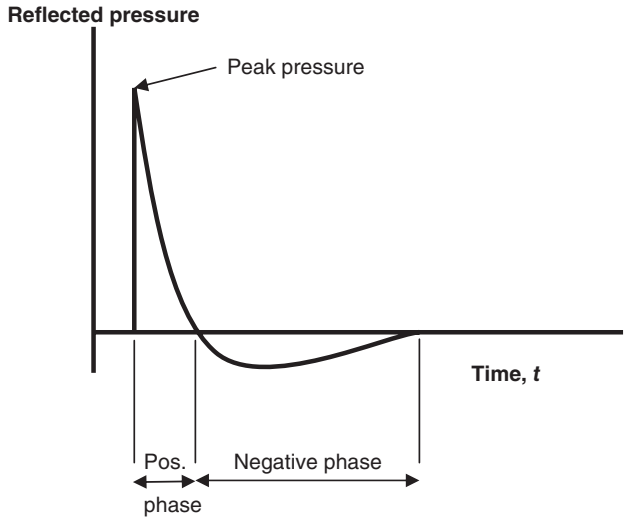

13.1 Blast load waveform.

on the location within the structure, hence the impulse depends on the standoff distance and angle of incidence. Parameters such as time of arrival, positive phase duration, wave decay coefficient, and side-on pressure depend on standoff distance. If the standoff equals the 'critical blast distance,' the transient dynamic response is maximum (Dharaneepathy *et al.*, 1995).

Explosive effects do not scale linearly. For example, a 2 lb charge does not produce the same effect as a 1 lb charge at half the distance. Scaling is generally done in terms of TNT equivalence. This equivalency is affected by the charge size, confinement, nature of source, and pressure range under consideration. General important characteristics of the blast wave, such as energy release, are measured for standard TNT tests carried out with controlled explosions. These results are then used as a benchmark to calculate data for other explosions by using the cube root scaling law, which states that 'when two charges of same explosive and geometry, but different sizes, are detonated in the same atmosphere, the shock waves produced are similar in nature to the same-scaled distances (Beshara, 1994).

The point on the ground exactly below the explosion is referred to as ground zero. Pressure time history is composed of overpressure, dynamic pressure, and reflected pressure. Overpressure is a pressure that acts on the structure in the absence of such obstacles as the ground and is hydrostatic in nature. Dynamic pressure causes drag or wind-type loads on the structure and exhibits sharper pressure decay over a longer duration. Reflected pressure is generated when the shock front hits a rigid surface.

© Woodhead Publishing Limited, 2010

The overpressure and dynamic pressure have a longer duration than reflected pressure. For conventional high explosives, the magnitude of the peak reflected pressure is higher than the peak overpressure and peak dynamic pressure. Near the ground surface, the combined effect of incident pressure and reflected pressure is considered. While studying the effect of unconfined explosions such as nuclear explosions on multi-story structures, however, peak overpressure may be more important that the reflected pressure.

Krauthammer and Otani (1997) studied the behavior and design of reinforced concrete structures subjected to blast loads and concluded that shock pressure has less of an effect on reinforced concrete structures than the lower overpressure that has a longer time duration. The function used for the load application must consider both pressures. Since the maximum dynamic pressure is very small as compared to the other two, it can be neglected in the load calculation. This load application depends on the angle of incidence, which is the angle between the line of wave propagation and the outer normal to the element.

The US Army Engineer Waterways Experiment Station developed the Conventional Weapons Effect Program (CONWEP) which provides free-field spherical and hemispherical predictions (Randers-Pehrson and Bannister, 1997). The calculations consider the blast wave angle of incidence. The BRODE model implemented in DYNA3D for modeling blast pressure excludes this feature. CONWEP, on the other hand, does not combine reflected pressure and incident pressure for the calculation of the angle of incidence. Randers-Pehrson and Bannister (1997) integrated a modified CONWEP model into DYNA2D and DYNA3D by incorporating the following equation:

$$PL = PR(\cos 2\theta) + PI(1 + \cos 2\theta - 2\cos\theta) \qquad [13.1]$$

13.4 Finite element models

The behavior of unreinforced masonry walls has been investigated using detailed finite element models. These investigations have advanced the knowledge in this field. However, the cost and time associated with the development and implementation of such models are prohibitive. Accurate, simplified, and cost-effective modeling techniques have been developed recently in the form of *resistance functions*, addressed later in this chapter. Nonetheless, a short report on the development and state of finite element modeling in this arena is worthy of mention.

Hamid and Drysdale (1988) investigated fracture of masonry structures using the finite element approach. This investigation resulted in constitutive models capable of simulating the initiation and propagation of fracture

© Woodhead Publishing Limited, 2010

under combined normal and shear stresses in both tension-shear and compression-shear regions. The models predicted the load carrying capacity of masonry assemblages and provided detailed information on the failure mode, ductility, and crack patterns.

Martini (1996a) reported a study in which a finite element model was constructed for the one-way, out-of-plane failure of unreinforced masonry walls subjected to static loading. This study was conducted as an investigative approach for two-way action walls. A discrete cracking material model involving eight-node elastic continuum elements was used to model masonry units, and eight-node surface contact elements were used to model joints. Uniform pressure was applied until the equilibrium of the analysis became unstable. Load–displacement plots were then compared with the literature to verify the suitability of the model.

In another study, Martini (1996b) developed a two-way unreinforced masonry wall panel supported at the sides and bottom. Modified yield-line theory was used for unreinforced masonry walls by considering post-cracking mechanisms of moment transfer for the horizontal and vertical directions. Models of the wall were analyzed. The modified theory predicted lower failure loads than finite element results but closely matched failure patterns.

In 1996, Karagozian and Case developed several candidate retrofit designs for increasing the blast resistance of concrete masonry walls (Wesevich and Crawford, 1996). Finite element models were developed using DYNA3D for the chosen retrofit designs so that wall response predictions could be made prior to the explosive tests. Each model used three-dimensional (3D) continuum elements and material models that were formulated to account for the extensive non-linear behaviors of material subjected to blast loads (Wesevich and Crawford, 1996). The particular concrete material model used was developed for predicting the response of concrete to explosive loads. The material model was also validated for the prediction of light and severe damage to reinforced concrete and masonry walls subjected to blast loading.

The results of the DYNA3D analysis indicated that the knee-brace and shotcrete options were the 'best retrofit candidates in that the least amount of damage occurred to the wall panels for the two designs' (Wesevich and Crawford, 1996). The structural integrity of the wall panels retrofit with these designs remained sound. The success of the shotcrete retrofit seems to indicate that the use of other materials, such as composites that can be bonded to the wall surfaces, may also provide positive results.

Crawford *et al.* (1997) evaluated the effects of explosive loads on masonry walls using a DYNA3D analytical model. The aim was to estimate the responses of lightly reinforced or unreinforced structures subjected to blast

© Woodhead Publishing Limited, 2010

loads. An analytical wall model having the width of a single cell unit that includes two half-cells and a web was studied. The analytical model was validated for pressure versus impulse diagrams by comparing it with results obtained from field tests conducted in Sweden. Load was applied using blast curves generated by BLASTX (Britt and Lumsden, 1994). The analytical model was used further to validate and update the *P–I* curves typically associated with simplified assessment codes, such as FACEDAP. Various retrofit techniques were assessed for increasing the strength of unreinforced or lightly reinforced masonry walls. It was found that retrofit designs that uniformly reinforce a masonry wall, such as composite wrap and shotcrete, were shown to provide a better enhancement to blast protection than those that discretely reinforce a wall, such as pilasters.

Krauthammer and Otani (1997) reported a study of meshing, gravity, and load effects on finite element simulations of blast loaded reinforced concrete structures using DYNA3D. The near-cubical reinforced concrete structure was considered, and symmetry was used to reduce the structure to 1/8th of true size. The model consisted of a back wall, sidewall, and roof. Ten cases were analyzed with increasing reinforcement, load, and gravity effects. The lumped mass approach was used for reinforcement in the coarse mesh model. A 'soil and foam' material model with eight-node solid elements was used for the concrete material, whereas thin shell and beam elements were used to simulate steel reinforcement bars.

Shope and Frank performed finite element analysis of blast loaded CMU walls in 1998. One-way action strip models and two-way action wall panel models subjected to blast loads were developed using the DYNA3D software package. In June 1999, a study of finite element modeling techniques for a CMU wall subjected to airblast loading was performed using the DYNA3D software (Dennis, 1999). A simplified approach was used for this study because of modeling difficulties that arise when complex algorithms are implemented without the fundamental characteristics being known.

The finite element models were based upon nominal 8 in × 8 in × 16 in hollow CMUs that contained 3/8 in mortar layers. Each masonry unit comprised eight-node solid elements. All masonry units were constructed as individual parts of a wall panel that were connected with slide surfaces that represented the mortar layers (Dennis, 1999). The material properties for the CMUs and the mortar were based upon the ACI 530-95 and ASTM C 270-89 standards. These properties were used in conjunction with material models that incorporated failure and strain-rate strengthening criterion.

The US Army Engineering Research and Development Center (ERDC) conducted experiments involving blast loaded masonry walls in 1999 with the goal of validating the finite element modeling method. A series of five ¼-scale CMU wall experiments was performed to study the response of

© Woodhead Publishing Limited, 2010

non-grouted, non-reinforced, one-way CMU walls to the blast pressure from high explosives (Dennis *et al.*, 2000). A single one-way, ¼-scale CMU wall was also statically tested. Pre-test analysis and predictions were made for the ¼-scale experiments using the previously developed DYNA3D modeling method.

The pre-test analysis was used, in part, to determine a standoff distance for the explosive charge that would ensure wall failure without the complete destruction of the test specimen. The originally calculated standoff distance was used for the first test. For the second and third tests, the standoff distance was reduced by 25%. The fourth test used the original standoff distance and was a repeat of the first test. The standoff distance for the final test was increased by 25% (Dennis *et al.*, 2000). The results showed that the analysis method slightly over-predicted the maximum static capacity of the CMU wall (Dennis *et al.*, 2000). The over-prediction was attributed to the use of average CMU properties, and it was found that the use of lower-bound properties provided a very good estimate of the load–deflection function.

13.5 Resistance function approach

Studies in the 1970s and 1980s (Yokel and Dikkers, 1971; Ewing *et al.*, 1984; Kariotis, 1985a,b) suggested that the primary concern for a wall exposed to sudden lateral loads is dynamic stability – the equilibrium of the cracked wall under the influence of applied lateral loads, self weight, and inertial loads, rather than material stress levels. In 1985, Priestley developed a similar methodology to examine the behavior of one-way unreinforced masonry walls under the action of lateral seismic loads (Priestley, 1985). The methodology was later corrected in 1986 (Priestley and Robinson, 1986), with a final publication in 1992 (Paulay and Priestley, 1992). Priestley argues that the formation of cracks does not constitute wall failure, even in unreinforced masonry walls. Failure occurs only when the resultant compression force from surcharge and wall weight above the crack is displaced outside the line of action of the applied gravity loads at the top and bottom of the wall. The method determines the non-linear load–deflection curve for a masonry wall subjected to out-of-plane loading.

In 1995, La Mendola *et al.* examined the stability conditions of masonry walls subjected to seismic transverse forces. The problem was translated into the analysis of a fixed free-ended prismatic column undergoing static, horizontal forces equivalent to maximum inertia actions. Drysdale *et al.* (1994) used a very similar approach to that employed by Yokel (1971) and Priestley and Robinson (1986) to develop resistance functions for unreinforced masonry walls under lateral loads. The approach considered arching for one-way action walls confined between rigid boundaries at their top and

© Woodhead Publishing Limited, 2010

bottom interfaces. The results showed a significant increase in the resistance of such walls to lateral loads.

Martini (1997) investigated the one-way and two-way action of unreinforced masonry walls using the finite element method and showed excellent correlation with the approach proposed by Priestley and Robinson (1986), Paulay and Priestley (1992) and La Mendola *et al.* (1995). Doherty *et al.* (2002) published their work on displacement-based seismic analysis for the out-of-plane bending of unreinforced masonry walls. The approach adapts a simplified displacement-based procedure and a trilinear characterization of the actual non-linear force displacement relationship in the analysis. The results of the seismic analysis show this method to yield significantly better predictions than the force-based method. Similar approaches have been used with the application of single degree of freedom (SDOF) system in the Wall Analysis Code (WAC Version 2) and SBEDS (2006).

As part of his research, the author developed resistance and response function equations for unreinforced one-way action masonry walls (Moradi, 2007). The remainder of this chapter is dedicated to this development.

Unreinforced masonry walls supported along their top and bottom edges resist lateral forces by spanning vertically between these supports (Drysdale *et al.*, 1994). Flexural stresses normal to the bed joints eventually result in tensile failure when a crack occurs along a course of the bed joint. The failure mechanism can be very complex and depends upon the type of supports provided at the top and bottom edges, and the magnitude of axial forces from self-weight and any superimposed loads.

In general, the weight of the wall produces a uniform compressive stress throughout the wall. Initially, any tensile stresses developing from the bending of the wall due to lateral loads will be suppressed by the compressive stresses due to the weight of the wall. As the lateral forces increase, the impact of compressive stresses decrease on the tension face of the wall, and eventually tensile stresses begin to develop. Because the flexural strength of the mortar joints is quite variable and depends on construction techniques and weather, it is possible that cracks will initiate at the early stages of tensile stresses. Therefore, it may conservatively be assumed that the wall cannot resist tensile stresses.

Once tensile stresses develop on the tension side of the wall, cracks will initiate (Baker, 1977, 1980) along two or three units in the course and then immediately propagate for the full length of the wall. The formation of cracks does not constitute wall failure, even in an unreinforced masonry wall (Paulay and Priestley, 1992). The resultant compressive force R in the compression zone of the central crack counteracts the vertical loads due to wall weight and surcharge, and creates a balancing moment against lateral loads (Fig. 13.2). As lateral loads increase so do lateral displacements and compressive stresses that cause R, and subsequently the wall resistance. The

© Woodhead Publishing Limited, 2010

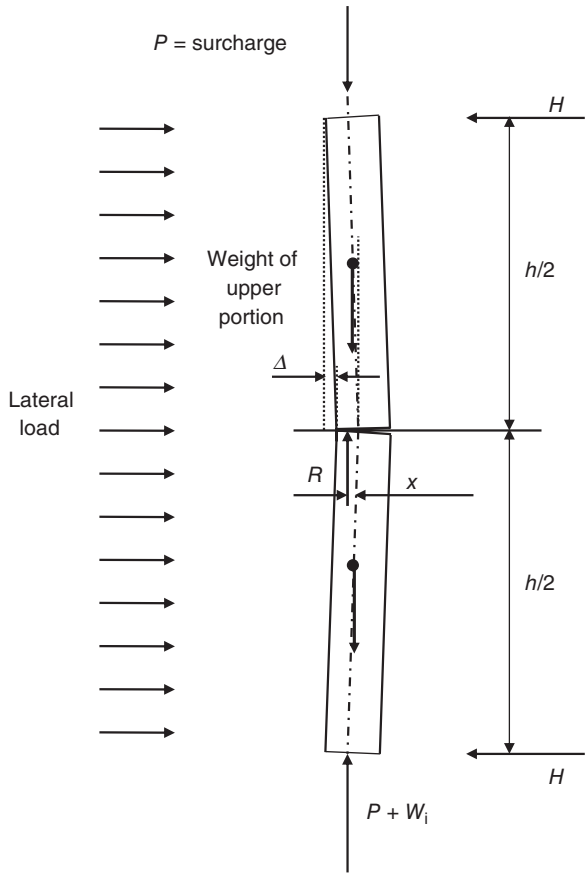

13.2 Equilibrium of face-loaded wall.

increase in the lateral displacement and compressive stresses causes R to move more and more toward the compression face of the wall. A maximum compressive stress block will develop in the compression side of the wall that equals the masonry compressive strength. The wall collapses when R moves outside of the line of action of the vertical loads, namely wall weight and surcharge.

13.5.1 Unreinforced masonry wall – analytical model

In beginning to develop the equations to predict conditions for wall failure, some simplifying assumptions are necessary:

1. The wall experiences one-way bending action.
2. The wall may be load bearing.

© Woodhead Publishing Limited, 2010

3. The wall is not reinforced with steel bars.
4. The tensile strength of concrete masonry and mortar joints is ignored.
5. The lateral load on the wall is constant over the wall height (h).
6. The wall may be partially fixed at the top and bottom interfaces.

The last assumption is made to help develop the necessary equations for wall failure with varying degrees of end fixity. Although most unreinforced masonry walls are simply supported at the top and bottom supports, the ability to specify end fixity makes it convenient when a specific wall design develops moment capacity at the top and bottom supports. The design engineer can determine the degree at which the top and bottom supports develop moment in the wall and determine the percent end fixity for the analysis. The designer can also be conservative and assume simply supported conditions at the top and bottom supports.

Consider the free-body diagram of an unreinforced masonry wall shown in Fig. 13.3. The static equations of equilibrium will lead to a final equation for wall displacement versus lateral load as shown below:

$$\Delta = \frac{t}{6} + \frac{y}{3} - \frac{(3-2\alpha)\,ph^2}{12W_i + 24P} \qquad [13.2]$$

It may be assumed conservatively that the displacement Δ increases in proportion with the central curvature, thus the following equation (Paulay and Priestley 1992) is derived for the wall curvature as crack grows:

$$\Phi_{cr} = \frac{\sigma_{crG}}{E_c\,(t-y)}$$

$$\text{Also:} \quad \sigma_{cr} = \frac{2R_{cr}}{t} \quad \text{and} \quad \sigma_{crG} = \frac{2R_{crG}}{(t-y)} \qquad [13.3]$$

$$\text{Setting:} \quad \beta = \frac{\Phi_{crG}}{\Phi_{cr}} = \frac{R_{crG}t^2}{R_{cr}\,(t-y)^2}$$

$$\text{Then:} \quad \Delta_{crG} = \beta\Delta_{cr}$$

The wall resistance function in terms of displacement versus lateral load can now be derived in an iterative fashion using Eqs 13.2 and 13.3. The result is the full resistance function of the wall through failure, as shown in Fig. 13.4.

13.5.2 Membrane retrofit concrete masonry wall – analytical model

The assumptions made for the unreinforced case apply for this case as well. Consider the wall in Fig. 13.5, with partially fixed-end conditions at top and

© Woodhead Publishing Limited, 2010

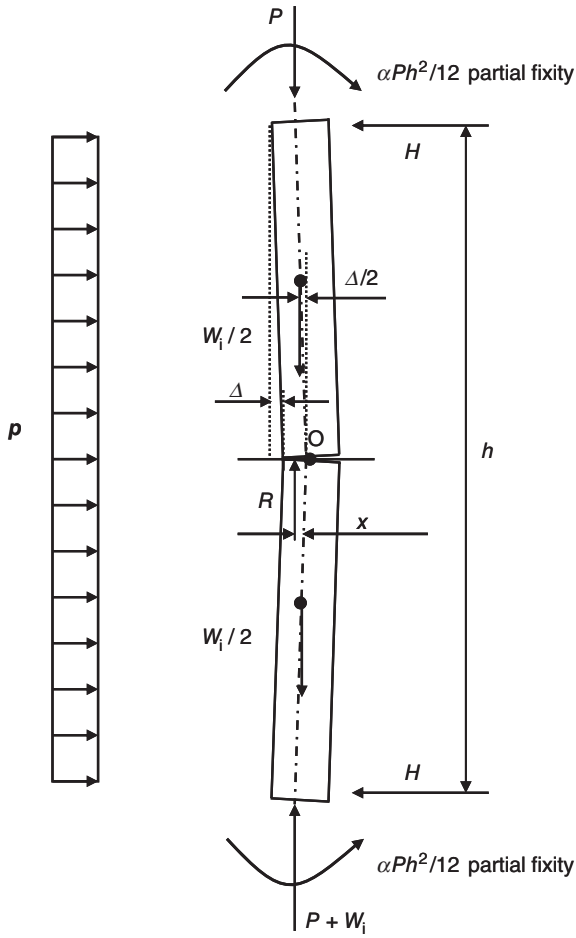

13.3 Free-body diagram of wall.

bottom, and lateral pressure p. The added parameter is the membrane retrofit at the crack opening. Although the membrane retrofit covers the entire inside surface of the wall, the tributary length (l) of the membrane affected by the crack opening is far less than the height of the wall. The tributary length depends on how the membrane retrofit is attached to the concrete masonry and how far the membrane strain extends past the crack opening. The shorter the tributary length, the higher the membrane strain due to the crack opening. The approximate tributary length of the polymer membrane retrofit may be assumed equal to the height of one masonry unit.

More accurate estimates of the tributary length of specific polymers may be obtained by test or analysis and used in the analytical model. For metal

© Woodhead Publishing Limited, 2010

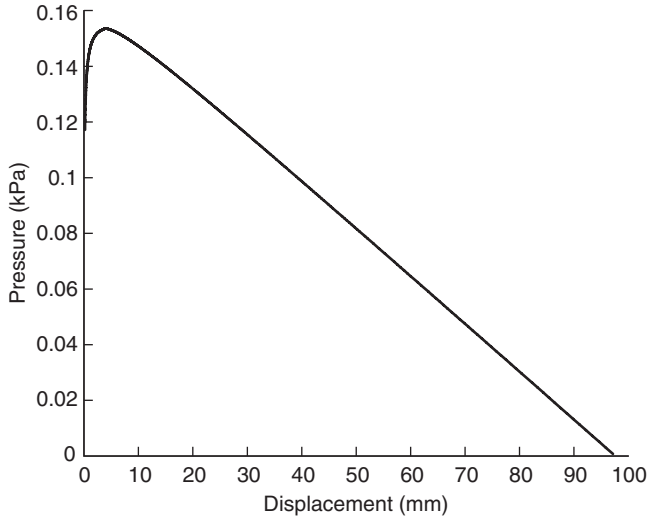

13.4 Resistance function – unreinforced CMU wall.

membrane retrofits discretely fastened to the masonry wall, the tributary length is the vertical distance between fasteners.

A final equation for wall displacement in terms versus lateral load is derived by Moradi (2007) as shown below:

$$\Delta = \frac{\left(\frac{t}{6} + \frac{y}{3} - \frac{(3-2\alpha)\,ph^2}{12W_i + 24P}\right)}{1 - \left(\frac{4E_r t_r t}{lh}\right)\left(\frac{4t + 2y}{3W_i + 6P}\right)} \qquad [13.4]$$

The wall resistance function in terms of displacement versus lateral load is derived in an iterative fashion using Eqs 13.4 and 13.3. Figure 13.6 shows the resistance function for a typical wall with two different thicknesses of polymer.

13.5.3 Arching action of membrane retrofit concrete masonry wall – analytical model

When a wall is built between and in tight contact with supports that serve as restraints against outward movement, elongation of the tension face due to bending cannot occur without inducing a compressive force (Drysdale *et al.*, 1994). Under lateral load, this induced in-plane compressive force results in arching, which increases the cracking load significantly. With increased loading, flexural cracking occurs at the supports and the mid-span.

© Woodhead Publishing Limited, 2010

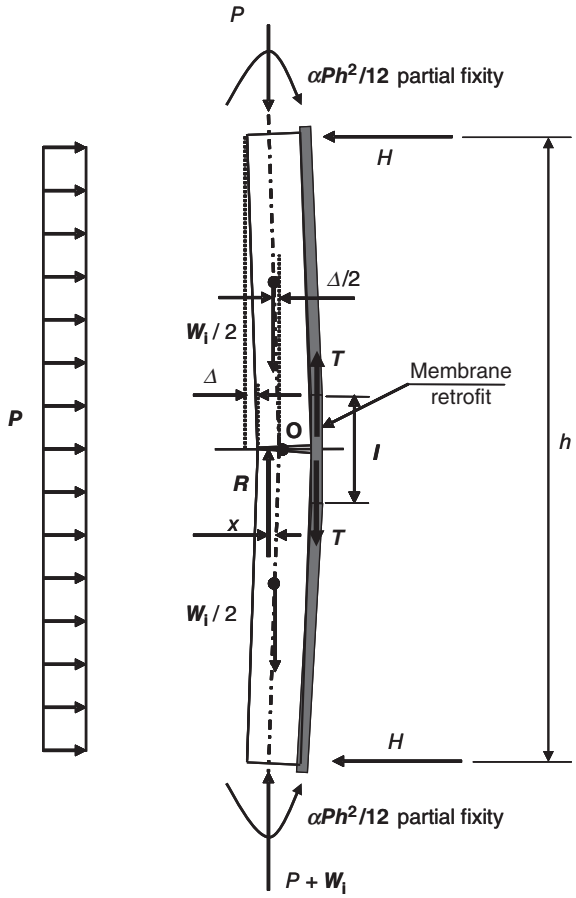

13.5 Free-body diagram of polymer retrofit concrete masonry wall.

As the load increases, the wall is pushed against the unyielding supports, creating thrust forces at the ends. A three-hinged arch is formed with one hinge at each end and one hinge in the middle of the wall. The arching force is a function of the material properties of the mortar joint and the contact area.

Consider the wall in Fig. 13.7, with thrust forces at top and bottom due to arching, and membrane retrofit on the tension face. The tributary length (l) of the membrane retrofit is treated in the same manner as in the previous case. The width of the arching area is shown by a simplified equation proposed by Drysdale *et al.* (1994):

$$\alpha = 0.1t \qquad [13.5]$$

The final resistance function equation is shown next:

© Woodhead Publishing Limited, 2010

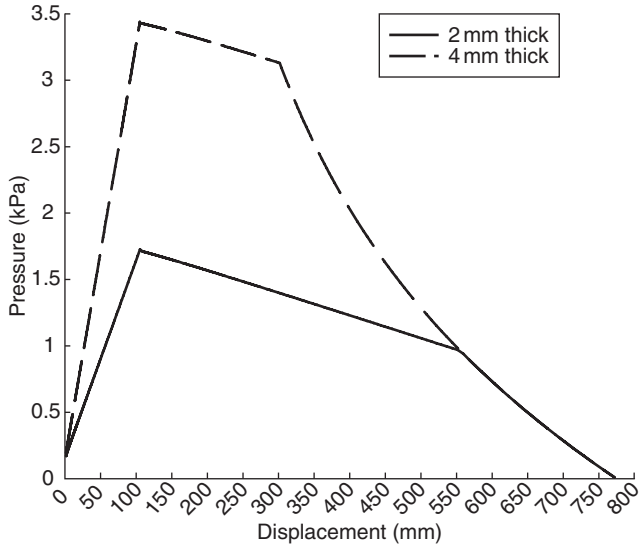

13.6 Resistance function – polymer retrofit.

$$p = -\frac{8}{h^2}\left(P\left(\frac{t-a}{2}\right)+\frac{W_i}{2}\left(\frac{t-a}{2}-\frac{\Delta}{2}\right)-\left(T+P+V_{\text{Top}}+\frac{W_i}{2}\right)\left(x+\frac{t-a}{2}-\Delta\right)-T\left(\frac{a}{2}+\Delta\right)\right) \quad [13.6]$$

As mentioned in the earlier cases, it may be assumed conservatively that the displacement Δ increases in proportion with the central curvature. The wall resistance function in terms of displacement versus lateral load can now be derived in an iterative fashion using Eqs 13.6 and 13.3. Figure 13.8 is a typical plot of the arching resistance function of an unreinforced CMU wall and Fig. 13.9, is a typical plot of the arching resistance function of the unreinforced CMU wall with polymer retrofit.

13.5.4 Catcher system resistance function development

In the cases studied in this research thus far, the membrane retrofit was firmly attached to the unreinforced concrete masonry wall. Another system of interest is when the membrane retrofit is not firmly attached to the wall. This system will be referred to as the catcher system and resists blast pressure in three distinct phases. In the first phase, the unreinforced concrete masonry wall goes through the initial elastic response, the subsequent initiation of cracks, the non-linear rocking response, and eventual failure and

© Woodhead Publishing Limited, 2010

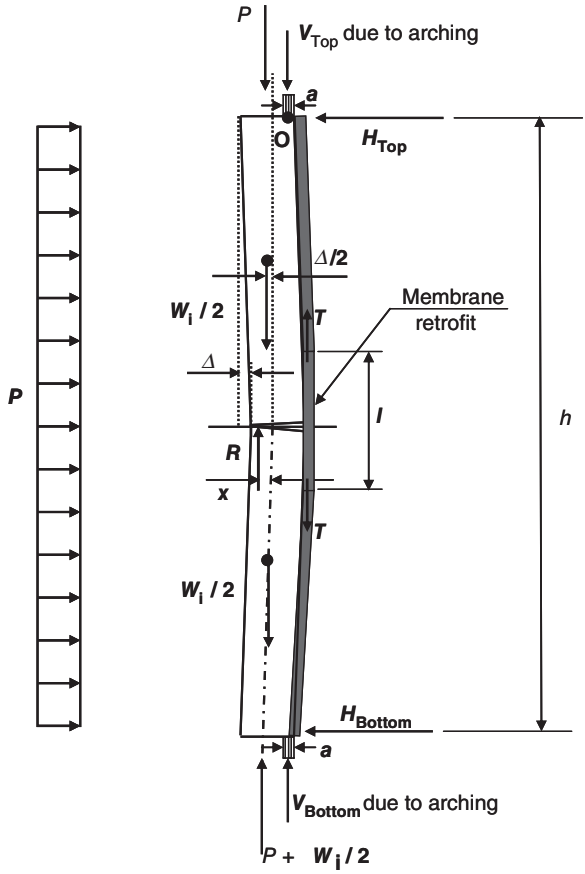

13.7 Free-body diagram of wall.

collapse. In the second phase, the membrane retrofit responds as an elastic membrane. In the third phase, the membrane retrofit reaches yield and responds as a plastic membrane. Each phase is examined separately, and deflection versus pressure equations are developed for each phase. The final resistance function of the system is the summation of the resistance functions for the three phases.

For phase I, the equations for the resistance function of unreinforced concrete masonry walls were developed earlier. For phase II, the retrofit is assumed to behave elastically like a thin, flexible membrane supported on both ends and loaded uniformly along its length. The membrane deflects elastically until yield. The pressure-deflection relation is found in Roark and Young (1975):

© Woodhead Publishing Limited, 2010

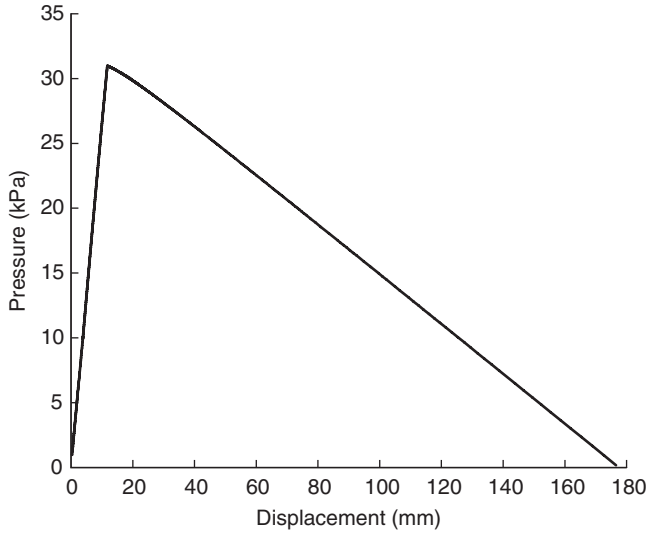

13.8 Arching resistance – unreinforced CMU wall.

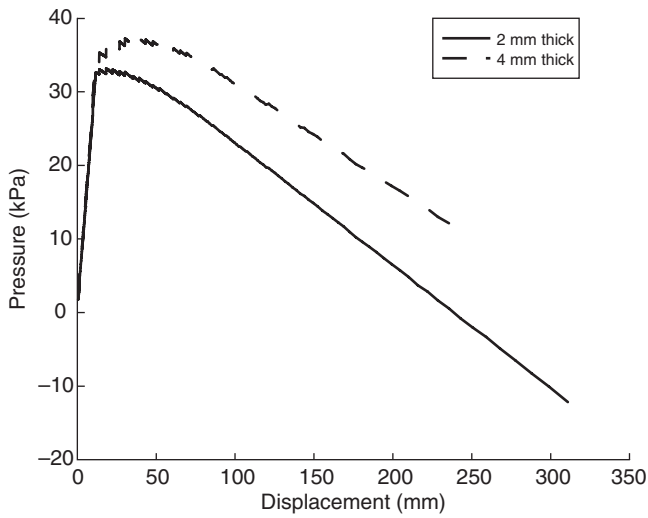

13.9 Arching resistance – polymer retrofit.

$$p = \frac{64 E_r t_r \Delta^3}{3h^4} \qquad \text{[cubic equation]}$$

In phase III, for elastic, perfectly plastic materials the post-yield behavior can be defined by (Lane, 2003):

© Woodhead Publishing Limited, 2010

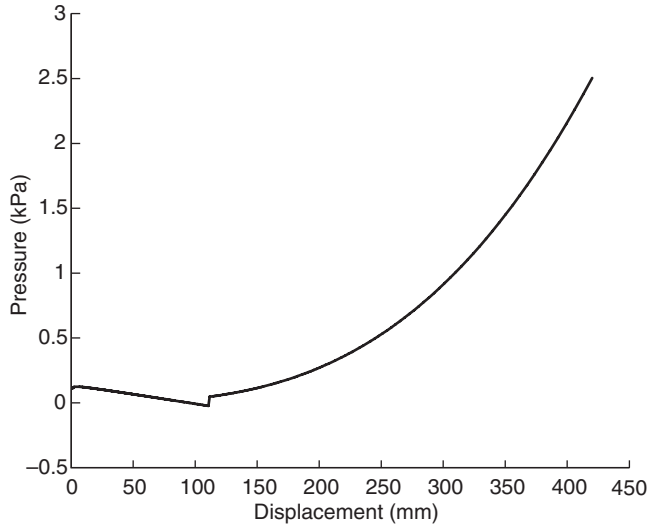

13.10 Resistance function – polymer catcher system retrofit.

$$p = \frac{8\sigma\Delta t_r}{h^2} \qquad \text{[linear equation]}$$

For materials that are defined by a general nonlinear stress-strain relationship, this equation would be used in an iterative solution that defines the resistance function of the sheet. A deformed shape is assumed for the tension membrane sheet, and a compatibility relationship for the material is used to arrive at the magnitude of stress for each increment of deflection. In all cases, this value of stress is used for σ in the above equation.

These phases are used in the resistance function calculations in order to arrive at the complete resistance function plot of the unreinforced concrete masonry wall with a membrane catcher system (Fig. 13.10).

13.6 Response model development

13.6.1 Single-degree-of-freedom (SDOF) system

An approximate design method first suggested by Biggs (1964) is adopted in this study for idealization of the one-way masonry wall as a SDOF system. To remain consistent, the nomenclature used by Biggs will also be used. A mass, spring, and damper system is depicted in Fig. 13.11 to simulate the wall system, and the general equation of motion for forced vibration is:

$$M_e\ddot{z}(t) + C_e\dot{z}(t) + K_e z(t) = F_e(t) \qquad [13.7]$$

© Woodhead Publishing Limited, 2010

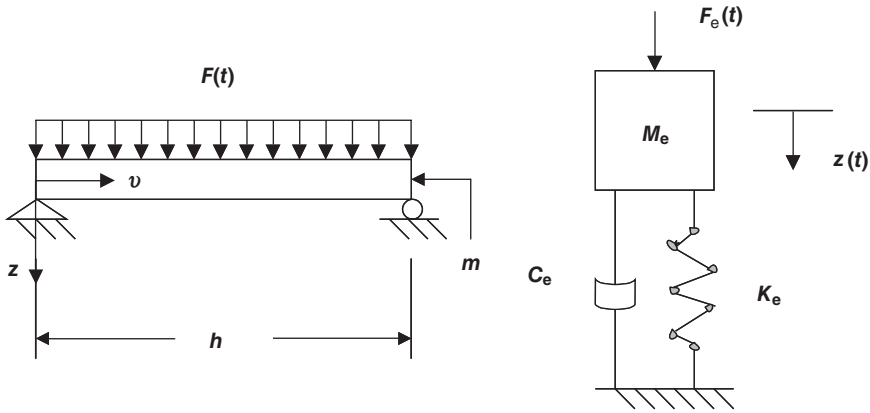

13.11 Beam idealized as mass-spring-damper system.

The equivalent system parameters are used to better match the deflection of the concentrated mass in the SDOF with some point on the structure, generally the mid-span deflection. Damping was considered by Moradi (2003) in his analysis of a single CMU as well as CMU walls. The impact of damping on the wall displacements and stresses proved to be insignificant in all cases.

In addition, structural damping during plastic response cannot be clearly defined or verified experimentally and has no physical significance during the plastic deformation of the structural element (Kiger and Salim, 1999). Therefore, the effects of structural damping will not be considered in the plastic region of response. For the purposes of this study, the damping coefficient is assumed to be zero, and Eq. 13.7 reduces to:

$$M_e\ddot{z}(t) + K_e z(t) = F_e(t) \qquad [13.8]$$

Following the methodology outlined in Biggs (1964), the final equation of motion in terms of displacement time steps was derived by Moradi (2007) and shown below:

$$z(t+\Delta t) = \frac{F_t \Delta t^2}{KLMM_t} + \left(2 - \frac{R_z \Delta t^2}{KLMM_t}\right) z(t) - z(t-\Delta t) \qquad [13.9]$$

The central difference method is an explicit time scheme, because the unknown $\ddot{z}(t)$ is only a function of known values. Equation 13.9 allows for the displacement at the next time increment $z(t + \Delta t)$ to be calculated in terms of system constants and the current and previous displacement values $z(t)$ and $z(t - \Delta t)$. Note that F_t is non-zero only when a load is being applied to the structure and that R_z is a function of the displacement. For the SDOF analysis, the actual or estimated time histories of the blast loads are required.

© Woodhead Publishing Limited, 2010

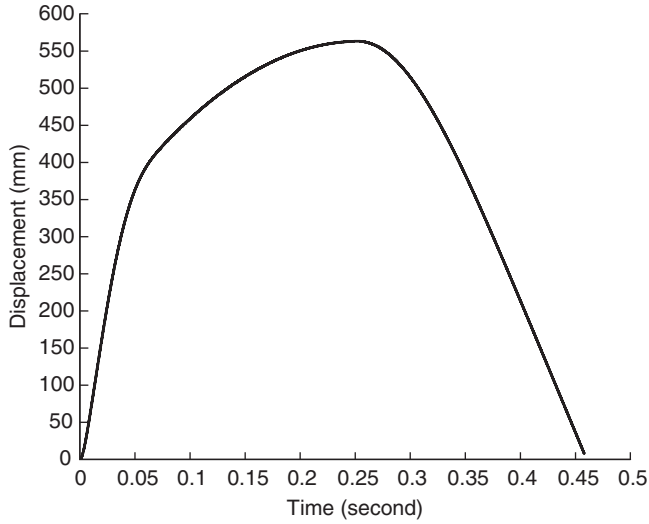

13.12 Typical SDOF analysis result.

Both positive and negative phases of the time histories may be used to calculate the response.

13.6.2 Analysis results of the SDOF system

The resistance functions developed in Section 13.5 and Eq. 13.9 can be programmed into Microsoft Excel and solved for different wall heights, material properties, and blast time histories. The wall height is the actual unsupported length from the top support to the bottom support. A typical SDOF response is shown in Fig. 13.12.

13.7 Summary

This chapter provides the formulation for the resistance of membrane retrofit masonry walls to lateral uniform pressure. Resistance functions are provided for three separate cases.

1. Unreinforced masonry walls.
2. Masonry walls with attached membrane retrofit.
3. Masonry walls with detached membrane retrofit.

In addition, each case was developed with arching action. These results can be used to design unreinforced masonry walls exposed to lateral pressure loads induced by natural or man-made events. The results may be used in high-risk areas to enhance the construction of new buildings using unreinforced concrete masonry walls, as well as to retrofit similar walls in existing

© Woodhead Publishing Limited, 2010

buildings or homes. For arching action to develop, care must be taken to ensure gaps are not present between the wall and its top and bottom interfaces.

13.8 Notation

a	width of arching area
A	area
α	wall support degree of fixity
β	ratio of wall curvature
C_e	equivalent damping coefficient of the SDOF
Δ	wall lateral displacement, mm
E	elastic modulus, kPa
E_c	concrete masonry elastic modulus, kPa
E_r	polymer retrofit elastic modulus, kPa
ε	strain
f_c	compressive stress
$F_e(t)$	equivalent load–time history applied to the SDOF
F_{yr}	yield strength of membrane retrofit
h	height of wall, m
H	horizontal reaction force, N/mm
I	moment of inertia
K_e	equivalent stiffness of the SDOF
KLM	effective load mass factor
l	tributary length of membrane retrofit
M	moment
M_e	equivalent mass of the SDOF
p	lateral pressure, kPa
P	wall surcharge, N/mm
PI	incident pressure in blast (psi)
PL	pressure load in blast (psi)
PR	reflected pressure in blast (psi)
Φ	wall curvature
Φ_{cr}	wall curvature at cracking
Φ_{crG}	wall curvature as crack grows
R	resultant force of the compressive stresses in the wall, N/mm
σ	stress (kPa)
σ_{cr}	stress at cracking
σ_{crG}	stress as crack grows
t	wall thickness
t	time (Section 13.6)
t_r	membrane retrofit thickness, mm
T	tension in the polymer retrofit, N/mm

© Woodhead Publishing Limited, 2010

θ	angle of incidence
V_{Top}	arching force at top support
V_{Bottom}	arching force at bottom support
W_{i}	wall weight, N/mm
x	distance from R to the wall centerline
y	crack length, in
z	displacement
$z(t)$	time dependent displacement

13.9 References

BAKER L R (1977), The failure criterion of brickwork in vertical flexure, *Proc. 6th International Symposium on Loadbearing Brickwork*, December, London, UK, 203–216.

BAKER L R (1980), Lateral Loading of Masonry Panels: *Structural Design of Masonry*, Cement and Concrete Association of Australia, Sydney, Australia.

BESHARA F B A (1994), Modelling of blast loading on aboveground structures-I. General phenomenology and external blast, Technical paper, *Computers and Structures*, **51**(5), 585–596.

BIGGS J M (1964), *Introduction to Structural Dynamics*, McGraw-Hill Book Company, New York.

BRITT J R and LUMSDEN M G (1994), *Internal blast and thermal environment from internal and external explosions: A user's guide for BLASTX Code, Version 3.0*, Report No. SAIC 405-94-2, Science Applications International Corporation, St Joseph, LA.

CRAWFORD J E, BOGOSIAN D D and WESEVICH J W (1997), Evaluation of the effects of explosive loads on masonry walls and an assessment of retrofit techniques for increasing their strength, *Proc. 8th International Symposium on Interaction of the Effects of Munitions with Structures*, 22–25 April, McLean, VA.

DENNIS S T (1999), Masonry Walls Subjected to Blast Loading-DYNA3D Analysis, U.S. Army Engineer Waterways Experiment Station, Vicksburg, MS.

DENNIS S T, BAYLOT J T and WOODSON S C (2002), Response of 1/4-scale concrete masonry unit (CMU) walls to blast, *Journal of Engineering Mechanics*, **128**(2), 134–142.

DHARANEEPATHY M V, KESHAVA RAO M N and SANTHAKUMAR A R (1995), Critical distance for blast-resistant design, *Computers and Structures*, **54**(4), 587–595.

DOHERTY K, GRIFFITH M C, LAM N and WILSON J (2002), Displacement-based seismic analysis for out-of-plane bending of unreinforced masonry walls, *Earthquake Engineering and Structural Dynamics*, **31**(4), 833–850.

DRYSDALE R G, HAMID A A and BAKER L R (1994), *Masonry and Structures: Behavior and Design*, Prentice Hall, Englewood Cliffs, NJ.

EWING R D, JOHNSON A W and KARIOTIS J C (1984), *Methodology for Mitigation of Seismic Hazards in Existing Unreinforced Masonry Buildings: the Methodology*, ABK-TR-08, ABK, El Sugundo, CA.

FACEDAP (FACILITY AND COMPONENT EXPLOSIVE DAMAGE ASSESSMENT PROGRAM) (1994), Version 1.2, Theory Manual, Technical Report 92-2, Department of the Army, Corps of Engineers, Omaha District, Omaha, NE.

© Woodhead Publishing Limited, 2010

HAMID A A and DRYSDALE R G (1988), Flexural tensile strength of concrete block masonry, Technical paper, *Journal of Structural Engineering*, **114**(1), 50–66.

KARIOTIS J C, EWING R D and JOHNSON A W (1985a), Predictions of stability for unreinforced brick masonry walls shaken by earthquakes, in McNeilly T and Scrivener J C (eds), *Proc. 7th International Brick Masonry Conference*, 17–20 February, Melbourne, VIC, **2**, 1175–1184.

KARIOTIS J C, EWING R D, JOHNSON A W and ADHAM S A (1985b), Methodology for mitigation of earthquake hazards in unreinforced brick masonry buildings, in McNeilly T and Scrivener J C (eds), *Proc. 7th International Brick Masonry Conference*, 17–20 February, Melbourne, VIC, **2**, 1339–1350.

KIGER S and SALIM H (1999), Use and misuse of structural damping in blast response calculations, *Concrete and Blast Effects, ACI Special Publication SP-175*, American Concrete Institute, Farmington Hills, MI, 121–130.

KRAUTHAMMER T and OTANI R K (1997), Mesh, gravity and load effects on finite element simulations of blast loaded reinforced concrete structures, Technical paper, *Computers and Structures*, **63**(6), 1113–1120.

LA MENDOLA L L, PAPIA M and ZINGONE G (1995), Stability of masonry walls subjected to seismic transverse forces, *Journal of Structural Engineering*, ASCE, **121**(11), 1581–1587.

LANE J W (2003), *Modeling and Design of Explosion-Resistant Steel Stud Wall System*, MSCE Thesis, University of Missouri, Columbia, MO.

MARTINI K (1996a), *Research in the Out-of-Plane Behavior of Unreinforced Masonry*, Ancient Reconstruction of the Pompeii Forum, School of Architecture, University of Virginia, Charlottesville, VA.

MARTINI K (1996b), *Finite Element Studies in the Two-Way Out-of-Plane Behavior of Unreinforced Masonry*, Ancient Reconstruction of the Pompeii Forum, School of Architecture, University of Virginia, Charlottesville, VA.

MARTINI K (1997), *Research in the Out-of-Plane Behavior of Unreinforced Masonry*, Department of Architecture and Civil Engineering, University of Virginia, Charlottesville, VA.

MORADI L (2003), *Constitutive Properties for a Single Concrete Masonry Unit (CMU) Subjected to Blast*, MS Project, University of Alabama at Birmingham, Birmingham, AL.

MORADI L (2007), *Resistance of Membrane Retrofit Concrete Masonry Walls to Lateral Pressure*, PhD Dissertation, The University of Alabama at Birmingham, Birmingham, AL.

PAULAY T and PRIESTLEY M J N (1992), *Seismic Design of Reinforced Concrete and Masonry Buildings*, Wiley, New York.

PRIESTLEY M J N (1985), Seismic behaviour of unreinforced masonry walls, *Bulletin of the New Zealand National Society for Earthquake Engineering*, **18**(2), 191–205.

PRIESTLEY M J N and ROBINSON L M (1986), Discussion: seismic behaviour of unreinforced masonry walls, *Bulletin of the New Zealand National Society for Earthquake Engineering*, **19**(1), 65–75.

RANDERS-PEHRSON G and BANNISTER K A (1997), *Airblast Loading Model for DYNA2D and DYNA3D*, ARL-TR-1310, Army Research Laboratory, Adelphi, MD.

SHOPE R and FRANK R (1998), *Preliminary Finite Element Analysis of Masonry Walls*, Applied Research Associates, Inc., Raleigh, NC.

© Woodhead Publishing Limited, 2010

SINGLE-DEGREE-OF-FREEDOM BLAST EFFECTS DESIGN SPREADSHEETS (SBEDS) (2006), U.S. Army Corps of Engineers, Protective Design Center Technical Report, PDC-TR 06-02.

SINGLE-DEGREE-OF-FREEDOM STRUCTURAL RESPONSE LIMITS FOR ANTITERRORISM DESIGN (2006), U.S. Army Corps of Engineers, Protective Design Center Technical Report, PDC-TR 06-08.

WESEVICH J W and CRAWFORD J E (1996), *Candidate Retrofit Designs for Increasing the Blast Resistance of Conventional Wall Panels*, Technical report, TR-96-32.1, Karagozian and Case, Glendale, CA.

YOKEL F Y (1971), Stability and load capacity of members with no tensile strength, *Proc. American Society of Civil Engineers, Journal of the Structural Division*, **97**(7), 1913–1926.

YOKEL F Y and DIKKERS R D (1971), Strength of load bearing masonry walls, *Proc. American Society of Civil Engineers, Journal of the Structural Division*, **97**, 1593–1609.

YOUNG W D (1989), *Roark's Formulas for Stress and Strain*, McGraw Hill, New York.

© Woodhead Publishing Limited, 2010

Index

ABAQUS, 122, 213, 299
ABAQUS 6.6–1, 308
ABAQUSR, 394
ACAVP *see* Advanced Composite Armoured Vehicle Platform
accidental explosions, 22–3
ACI 530-95, 395
Advanced Composite Armoured Vehicle Platform, 244, 256, 257, xviii
  lower hull moulding, 258
advanced composites, 55
AFV *see* armoured fighting vehicles
air shock, 19
alumina, 236, 237
alumina-zirconia ceramics, 236
aluminium, 334
  foam, 167
  foil, 138, 139
ammonium nitrate and fuel oil, 10, 121
ANSYS, 122
ANSYS AUTODYN, 263
aramid, 55, 240
  fibre-reinforced polymers, 278
ARAMIS system, 95
Arena Satchel-Bomb Test, 47
armoured fighting vehicles, xviii
  composite materials in vehicles, 255–9
    civil protected vehicles, 259
    composite AFV development, 256–9
  composite vehicle structures mine blast loading, 259–67
    blast only model, 264
    design tools for mine protection, 263–7
    example of fully coupled model, 264
    fully coupled blast model, 265
    mine blast testing of composites, 261–3
    small-scale trials arena, 262
  integrated vehicle survivability, 252–5
    BAE Systems RG31, 253
    debris cone within a vehicle from armour overmatch event, 254
    requirement for lighter weight AFVs, 255
    spall liners, 253–4
    survivability onion, 252
  joints location in metal and composite hull designs, 257
  occupant injury mechanisms, 251
  protection from mine blasts by using composites, 244–67
Army Standard TM 5-853-3, 46
ASTM C 270-89, 395
ASTM E2639-09, 47
ASTM F2247, 47
A3T22 panel, 104
axial load, 354–5
Azzi-Tsai Hill theory, 310

BAES RG31, 253
Balsa wood core, 136, 138, 152, 158, 167, 178, 183

© Woodhead Publishing Limited, 2010

bead model, 14
behind armour effects, 249
Bernstein approximation polynomial, 125, 128, 140
Bernstein polynomial basis functions, 128, 132, 206, 208
  x-. y- and z-directions, 130
binder yarns, 123
Bingham fluid, 107
blast, 101–2
blast focussing, 261
blast loading, 3–41, 247, 335, 345, 391–3
  categories, 15–17
    confined explosions, 16–17
    representative, 17
    unconfined explosions, 15–16
  waveform, 392
blast pressure, 221, 355
  wave, 271
blast protection
  buildings using FRP composites, 269–94
    assessment, 272
    explosion consequences, 271–2
    future developments and trends, 291–2
    general design guidance, 272–5
  polymer matrix composites, 54–78
  retrofitting buildings, 275–7
    catcher system, 276
    fibre reinforced polymer composites, 277
    reinforced concrete, 275–6
    steel plates, 276–7
    steel stud walls, 276
  retrofitting buildings using FRP composites, 277–91
    application procedure, 278–9
    column wrapping methods, 281
    concrete beam shear strengthening, 284
    concrete beams, 282–3
    concrete columns, 279–82
    concrete flexural strengthening, 283
    concrete slabs, 284–6
    conventional non-reinforced masonry wall failure, 287
    masonry walls, 286–90
    masonry walls strengthening, 287
    materials used, 277–8
    practical applications, 291
    slabs strengthening, 285
    spray-on polymer retrofitted masonry walls, 290–1
  retrofitting using FRP composites for buildings, 375–87
    advantages of FRP composite retrofits, 376–8
    equivalent non-linear single degree of freedom model, 385–6
    FRP connection systems, 384–5
    full scale blast testing of FRP retrofitted masonry walls, 381–4
    history of FRP composites as retrofits, 378–81
    resources for FRP composites, 387
  standards and specifications, 44–52
    future trends, 51–2
    interpretation, 45–8
    relevant parts, 48–50
    time of usage, 50–1
blast resistant design
  advanced and new materials for impact and energy absorption, 89–100
    literature review, 90–100
    problem significance, 100
  advanced composites, 88–9
  blast wall strengthened using composite patches, 302
  case studies, 103–11
    metal and foam sandwich panels under blast, 105–7
    MR fluids under blast, 107
    multilayer composite structures under blast loading, 103–4
    porous NiTi SMA under blast, 107, 111
  design philosophy for blast protection, 101–3
  failure mechanisms mitigation, 361–9
    P-Δ-effects, 369

© Woodhead Publishing Limited, 2010

global protection measure, 362–6
arm solution, 365
column recessed into the ground, 363
inner stiffener at top ground surface, 362
plate thickness increase, 366
strain measured and plotted *versus* time, 364
high energy absorbing materials, 88–114
local protection measures, 366–9
cross-section definition, 366–7
sacrificial cells, 367–9
material models, 345–55
modelling, 345–55
boundary conditions, 355
column geometry, 353–4
loading, 354–5
material models verification, 345–53
multilayer and sandwich structures, 89
parameters, 371
sandwich plate with composite skins, 302
using composites to improve resistance of building columns, 342–72
design specifications, 342–3
establishing parameters, 371
failure mechanisms mitigation, 361–9
load bearing column, 369–70
local failure locations, 360
objectives, 344
observed failure mechanisms, 360–1
results and discussion, 355–60
simulation and experiment, 344–5
blast resistant walls
composite patches, 302
use of composites, 298–338
background, 299–301
in conjunction with metals, 333–6
military and defense applications, 306–7
offshore and marine industry utilisation, 303–6
overview, 301–2
replacement conditions, 315–33
scope of study, 307–8
strengthening applications, 308–14
blast response
characteristics comparison for longer time interval, 191–5
maximum displacement and strains values, 194
maximum transient magnitudes, 194
time variations computed at the centre of top surface of 3 panels, 191–3
effect of internal material damping, 195–201
u_z time variations until t = 50 μsec, 196–8
u_z time variations until t = 500 μsec, 199–200
four panels characteristic response, 178–89
centre of the top surface of Balsa core, 184–5
centre of the top surface of upper composite layer, 182–3
results for transverse displacement, 179
time variations at the centre of bottom surface of ceramic layer, 189–90
time variations at the centre of top surface of lower composite layer, 187–8
variations of in-plane strain at centre of the top surface of each panel, 180–1
hybrid laminated composite plates response modelling, 120–208
mitigation materials, 123–5
numerical results of response for the four panels, 140–78
computational meshes description, 141

© Woodhead Publishing Limited, 2010

convergence study and accuracy control of numerical results, 140–2
panel # 1 numerical results, 142–52
panel # 2 numerical results, 152–7
panel # 3 numerical results, 158–67
panel # 4 numerical results, 167–78
phenomena modelling and predictive analysis tools, 120–3
retrofitting of masonry walls, 390–409
blast load, 391–3
finite element models, 393–6
notations, 408–9
resistance function approach, 396–406
response model development, 406–8
typical pressure–time variation for incident blast pulse, 122
blast testing, 38–41
blast loads measurements, 40–1
general considerations, 38–9
measurements, 40
primary configurations
blast chamber, 40
open-arena, 40
shock tube, 40
structural response/performance measurements, 41
blast threats, 3–41
blast wave pressure loadings
all clamped panel with unidirectional plies
impulse and initial pressure magnitude, 224
slope vs impulse for two different meshes, 227
slope vs impulse for two different time increments, 228
all clamped panel with woven plies, 226–9
analysis results using material damage model, 230
impulse and initial pressure magnitude, 229
mechanical properties, 228
slope vs impulse, 229
strain-rate dependent strength properties, 228
composite panels response, 212–31
comprehensive methodology for damage assessment, 214–16
failure criteria for unidirectional and woven ply composites, 215–16
non-linear solid shell element formulation for dynamic problems, 215
validation, 216
deflection vs time, 219
future trends, 231
non-dimensional centre deflection vs time
eleven blast wave pressure loadings, 225
three blast wave pressure loadings, 224
numerical tests on flat laminated composite panels, 223–30
panel subjected to blast pressure wave
non-dimensional *w/h* vs impulse, 220
slope vs impulse, 220
simplified methodology for failure assessment, 216–22
deformed configurations of plate centreline at first peaks, 221
maximum displacement at plate centre vs impulse, 218
numerical analysis and test for maximum displacement at plate centre, 217
numerically observed structural responses of composite panels, 217–21
structural failure criterion, 222
two-step approach, 221–2
simply supported–free panel with woven plies, 229–30
analysis results using material damage model, 231
slope vs impulse, 230

© Woodhead Publishing Limited, 2010

blast waves, in free air, 11–15
  blast wind and gaseous burning, 14–15
  ideal free-air explosion, 11
  shock pressure and impulse, 11–14
blast wind, 14
BLAST-X, 38, 395
boron carbide, 237
boron carbide plate, 96
boundary conditions, 355, 362–9
  ductile, 362–9, 372
boundary element method, 63, 64
boundary-fitted coordinate transformation, 63
BRODE model, 393
BS EN 13123 – 2:2004, 46
BS EN 13124 – 1:2001, 46
buildings, blast protection using FRP composites, 269–94
Bureau Veritas *see* Det Norske Veritas

CAP4 Al_2O_3, 137
Carbon Armoured Fighting Vehicle, 244, 259, 261
carbon composites, 212
carbon fibre reinforced composites, 277–8
carbon fibre-reinforced polymer, 93, 258, 301, 378
  connection details, 383
  retrofitted walls, 382
carbon fibres, 55
catcher system, 276, 403–6
CAV 100 vehicle, 255
centre of burst, 11
ceramic, 158, 183, 189
  armours, 96–7
  whiskers, 239
ceramic matrix composites
  ballistic protection of vehicles and personnel, 235–42
  ballistic test results
    7.62 AP M2 threats, 238
    7.62 ball threats, 238
  improved, impact for ballistic protection, 240–2
    other military and law enforcement applications, 241–2
    primary military applications, 240–1
  properties, 239
  technology approach for improved ballistic protection, 238–40
  technology overview, 236–7
    ceramic composite materials and ballistic results, 237
    reaction bonded SiC and B4C properties, 237
  toughening effects of SiC in alumina matrix composite, 240
Chapman Jouguet state parameters, 6, 7, 38
chemical energy weapons, 249
CHNO explosives, 5
chopped strand mat, 322
classical plate theory, 213
clearing effects, 28
CMU *see* concrete masonry unit
coal-based carbon foam, 89
coal energy absorbing system, 89
columns
  geometry, 353–4
  high rise building ground floor column, 343
  loading, 354–5
    axial load, 354–5
    blast pressure, 355
    boundary conditions, 355
    temperature, 355
  response, 356
  steel and composite
    cross-section, 354
    displacement vs coded bomb size, 370
    multi-cell types, 358
    octagonal multi-cell, 359
    square multi-cell, 357–8
    square single cell, 356–7
    types 1 and 5, 356
Composite Design for Armoured Fighting Vehicles, xviii
composites
  see also specific composite
  advanced, as blast absorbing materials, 88–9

© Woodhead Publishing Limited, 2010

and sandwich structures for blasting protection, 92–6
blast control panels, 300
blast loading on composite target structure, 260–1
  blast focussing, 261
  impulse, 260–1
  peak overpressure, 260
elastic unidirectional ply stress-strain relation, 308–9
improving blast resistance of building columns, 342–3, 342–72
  compression and extension testing, 347
  design specifications, 342–3
  establishing parameters affecting column blast resistance, 371
  failure mechanisms mitigation, 361–9
  hydrostatic and deviatoric stress, 349
  load bearing column, 369–70
  modelling, 345–55
  objectives, 344
  observed failure mechanisms, 360–1
  simulation and experiment, 344–5
layered armour system with ceramic facing, 97
military vehicles protection from mine blasts, 244–67
  composite materials in vehicles, 255–9
  integrated vehicle survivability, 252–5
  mine blast loading of composite vehicle structures, 259–64, 266–7
  occupant injury mechanisms, 251
multilayer structures under blast loading, 103–4
sandwich panels and joints, 323–7
  connection arrangements in typical topsides, 326
  connection between tapered sandwich panel and steel framework, 327
  connection system, 323
  fibre and resin systems selection, 323
  stiffened and profiled steel plates, 329
  tapered sandwich and stiffened composite panels, 328
  vs steel blast resistance, 330
use in blast resistant walls, 298–338
  background, 299–301
  fibre reinforced plastics in civil engineering applications, 300
  military and defense applications, 306–7
  offshore and marine industry utilisation, 303–6
  overview, 301–2
  scope of study, 307–8
use in conjunction with metals, 333–6
  fibre metal laminates, 334–6
use in replacement applications, 315–33
  blast walls deflection time history plots, 331
  constitutive modelling of plates/skins, 315–18
  different studied configurations, 332
  failure modes, 321
  finite element analysis under blast, 318–22
  lamina failure planes, 317
  lamina types property degradation, 319
  laminated beam finite element model, 320
  load deflection response, 320
  model and response characteristics, 321
  orthotropic panel dynamic response, 322
  sandwich panels and joints, 323–7
  structural system, 327–9
  WR/CSM laminate dynamic response, 322

© Woodhead Publishing Limited, 2010

use in strengthening applications, 308–14
constitutive modelling of patches, 308–11
elastic moduli, Poisson ratios and failure stresses values, 311
failure of patches in strengthened profiled blast wall, 315
resistance curves, 313
strengthening patches used in offshore industry, 314
strengthening scheme, 311–14
compression test, 347
computational fluid dynamics, 38, 39
computational solid mechanics, 38, 39
concrete beams, 282–3
concrete columns, 279–82
concrete masonry unit, 391, 395–6, 401
concrete slabs, 284–6
confined explosions, 16–17
Construction Industry Research and Information Association, 52
continuous fibres, 55
control-volume finite element method, 64–5
control-volume method, 64
conventional stiffness averaging method, 135
Conventional Weapons Effect Program, 393
CoorsTek CAp4 Al_2O_3, 136
core crushing, 93–5
coupled analysis, 38
Crestomer, 323
CRYSTALOY, 238, xviii
cube-root scaling law, 25–6
cure-kinetic model, 67
curing reaction, 56, 58
Cymat aluminium foam, 105

3D hexahedral finite element analysis, 125
3D MOSAIC, 123, 125, 138
computer code, 207
dynamic analysis tools, 204, 207
generic solid model, 126
model, 132, 135, 136
synopsis of approach, 126–32
3D mosaic parallelepiped, 126
two levels of applied discretisation, 128
3D stress wave propagation processes, 126
damping coefficients, 134, 195
Darcy velocities, 65
Darcy's law, 61, 63, 64, 71
deflagration, 6
delamination, 317, 334
failure, 317
Department of Defense, 46
Det Norske Veritas, 45
detonation, 6, 7
deviatoric stress, 345–8, 349
DIN C5-SF AP, 235
direct shock, 19
DIS 16933, 47
discontinuous fibres, 55
discrete element, 127
Drucker–Prager yield criterion, 91
dual-scale porous media flow, 68
Durisol, 380
DYNA 2D, 393
DYNA 3D, 122, 393, 394, 395
dynamic boundary value, 125
3D problem formulation, 134–9
panel # 1 description, 135–6
panel # 2 description, 136
panel # 3 description, 136–7
panel # 4 description, 138–9
panel geometry and boundary conditions, 134–5
Dynamic Photomechanics Laboratory, 201
dynamic pressure, 392, 393

E-glass, 323
composite, 177, 178
3D woven fabric, 138, 167
vinyl ester, 212
E-glass/polyester, 223
unidirectional laminate
analysis results using material damage model, 226

© Woodhead Publishing Limited, 2010

deformed configurations of plate centreline, 227
mechanical properties, 224
slope vs impulse, 226
Energetic Materials Research and Testing Centre, 381
energy absorption, 301
energy balance, 66
energy dissipation mechanisms, 91
engineering composites, 55
epoxy, 57, 59
epoxy-vinyl ester resin, 135
ERODING SINGLE SURFACE, 105
ERODING SURFACE TO SURFACE, 105
Eulerian algorithm, 62–3
Eulerian fixed mesh, 67
Eurocode, 343
explicit mould-filling simulation, 65
explosion, 101
and high explosives, 3–5
consequences, 201–2
explosive effects, xv
explosive cutting, 20
explosively formed projectile, 248
extension test, 347

FACEDAP, 395
failure criteria, 308–9, 318
failure surface, 348–51
Drucker-Prager, 349
pressure-dependent isotropic material, 351
von Mises, 349
family of medium tactical vehicles, 241
ferromagnetic ultrafine particles, 98
fibre failure, 309, 317
fibre metal laminates, 103–4, 334–6, xviii
failure under explosive loading, 104
thin and thick panels, 337
fibre-reinforced plastics, 54
use in civil engineering applications, 300
fibre reinforced polymer composites, 277, xiii, xix
materials used to protect buildings from explosion, 277–8
retrofitted masonry walls full scale blast testing, 381–4
internal explosion set-up, 383
test set-up, 381
retrofitting buildings, 275–7, 277–91
application procedure, 278–9
column wrapping methods, 281–2
composite materials, 277–8
concrete beams, 282–3
concrete beams shear strengthening, 284
concrete columns, 279–81
concrete slabs, 284–6
flexural strengthening of concrete beams, 283
FRP anchorage examples, 289
masonry walls, 286–90
masonry walls strengthening, 288
non-reinforced masonry wall under blast loading failure, 287
practical applications, 291
retrofitted masonry wall behaviour under blast loading, 289
slabs strengthening, 285
spray-on polymer masonry walls, 290–1
retrofitting for blast protection of buildings, 375–87
concrete backing system, 377
equivalent non-linear single degree of freedom model, 385–6
FRP connection systems, 384–5
history as retrofits for out-of-plane loadings, 378–81
retrofitting structures and advantages of FRP composite retrofits, 376–8
use in buildings blast protection, 269–94
assessment, 272
explosion consequences, 271–2
future developments and trends, 291–2
general design guidance, 272–5
retrofitting buildings, 275–7, 277–91
fibreglass, 240

© Woodhead Publishing Limited, 2010

field test data, 133
finite difference method, 63
finite element analysis, 38, 63, 263, 291
finite element/control-volume method, 64, 65
finite element models, 393–6
first-order shear deformation theory, 213
flow analysis network method, 62
1D flow method, 76
flow rule, 352–3
FML *see* fibre metal laminates
FORTRAN, 299
fragmentation, 19
free-air explosion, 18, 32–3
Friedlander decay function, 213, 215, 221, 223, 227, 230
Friedlander's equation, 103
front-tracking algorithm FAN, 65
FRP composites *see* fibre reinforced polymer composites
full scale blast, 381–4

Galerkin FEM, 64, 67
gas impulse, 29–30
gas pressure, 20
gaseous burning, 20
German Standard DIN 52290, 46
GLARE, 334
glass fibre reinforced plastic, 256, 300
glass fibre-reinforced polymer composite, 93, 277
glass fibres, 55
glass reinforced plastic
  composite construction for naval ship structure, 304
  laminates airblast response characteristics, 305
  woven roving laminates load deflection response, 320
global-impregnation model, 71
graphical user interface, 231, xvii
graphite, 55
Green's strain, 215
ground shock, 19
ground zero, 392
GSA C/ISO EXV 25, 46
GSA C/ISO EXV 45, 46
GSA-TS01-2003, 46

Hagen–Poiseuille flow equation, 78
Hamilton's variational principle, 128, 131
Hardened Unit Loading Devices, 48
Hashin criterion, 310
Hashin's model, 310
  2D failure model, 311
heat of combustion, 5
heat of detonation, 6, 8, 9
heat of reaction, 5
height of burst, 16
hidden underground device, 244
high-alumina ceramics, 236
high energy absorbing materials
  advanced and new materials, 89–100
  blast impact on sandwich composite, 106
  blast resistant design, 88–114
  braided composite failure modes, 92
  case studies, 103–11
  design philosophy for blast protection, 101–3
  energy absorbed in SMA rod
    under adiabatic conditions, 113
    under twinning conditions, 114
  failure modes in face sheet 1, 108–9
  foam restricted for all degrees of freedom along the corners, 105
  hysteresis loops of stress–strain curves for porous NiTi material, 101
  initial yielding force and viscosity index variation, 111
  layered armour composite system with ceramic facing, 97
  literature review, 90–100
    ceramic armours, 96–7
    composite and sandwich structures for blasting protection, 92–6
    lattice and truss structures, 97–8
    MR fluids, 98–100
    porous NiTi SMA, 100

© Woodhead Publishing Limited, 2010

strain rate-dependent metal plates and polymer matrix composites, 90–2
momentum of face sheets and foam with different amounts of TNT, 106
porous SMA material system, 100
pressure vs time plot of typical blast wave, 103
sandwich beams failure modes under impact forces, 94
sandwich composite showing dishing, 110
square honeycomb sandwich energy absorbing system, 97
stress evolution in SMA rod
under adiabatic conditions, 113
under twinning conditions, 114
types under blast, 102
high explosives
additional resources, 37–41
analytical methods for blast load computation and structural response, 37–8
blast professional consultation, 41
blast testing, 38–41
computer programs for blast load prediction and structural response simulation, 39
technical documents, 37
basics, 3–7
composition and oxidation, 5–6
confinement, size, shock sensitivity and density effects, 6–7
explosions and high explosives, 3–5
traditional uses, 5
blast-induced load types and load cases, 17, 19–22
blast-induced load cases, 21–2
blast-induced load types, 19–21
load types for above ground structure, 22
traditional load types and combinations, 17, 19
blast loading categories, 15–17
confined explosions, 16–17
representative blast loading categories, 17
unconfined explosions, 15–16
blast threats and blast loading, 3–41
blast waves in free air, 11–15
blast wind and gaseous burning, 14–15
ideal free-air explosion, 11
shock pressure and impulse, 11–14
generic explosive device, 10–11, 11
incident and reflected blast pressure pulses, 12
properties and physical forms, 7–10
heats of combustion, detonation and afterburn, 7–8
physical forms, 10
representative densities, heats of detonation and TNT-equivalencies, 9
TNT equivalency, 8–10
reflected pressure coefficient, 14
simplified blast load computation, 24–32
numerical examples, 32–7
threat assessment for design, 22–4
accidental or intentional explosions, 22–3
threat assessment of aggression, 23–4
hoop wraps, 280
Hopkinson–Cranz scaling, 26
HOSDB Publication No. 70/06, 47
hybrid laminated composite plates
blast mitigation materials, 123–5
blast phenomena, modelling and predictive analysis tools, 120–3
blast response characteristics
comparison for longer time interval, 191–5
comparison of four panels, 178–89
blast response modelling, 120–208
3D dynamic boundary value problem formulation, 134–9
3D Mosaic analysis approach synopsis, 126–32

© Woodhead Publishing Limited, 2010

deflection vs time variations of stitched sandwich panel exposed to shock pressure loading, 205
experimental strain recorded by strain gage and strain history, 203
internal material damping effect, 195–201
multi-layer panel exposed to local pressure pulse, 134
numerical results of four panels blast response, 140–78
numerical simulations of blast structural response, 132–4
panel # 1
  computational model of two-layer S-2 glass 3D woven composite, 135
  convergence of time variations for (0, 50 μsec), 143–5
  convergence of time variations for (0, 500 μsec), 148–9
  description, 135–6
  numerical results, 142–52
  time variations for (0, 3000 μsec), 150–1
  transverse normal stress comparison, 146
panel # 2
  cross-section scheme and computational model of sandwich panel, 137
  description, 135–6, 136
  numerical results, 152–7
  time variations computed at the centre of lower interface, 156–8
  time variations computed at the centre of upper interface, 153–5
panel # 3
  cross-section scheme and computational model of four-layer panel, 138
  description, 136–7
  numerical results, 158–67
  time variations computed at the centre of the first from top interface, 159–61
  time variations computed at the centre of the second from top interface, 161–3
  time variations computed at the centre of the third from top interface, 164–6
panel # 4
  cross-section scheme and computational model of five-layer panel, 139
  description, 138–9
  numerical results, 167–78
  time variations computed at the centre of the first from top interface, 167–9
  time variations computed at the centre of the fourth from top interface, 175–7
  time variations computed at the centre of the second from top interface, 170–2
  time variations computed at the centre of the third from top interface, 172–4
scope of chapter, 125–6
smooth approximation of experimental blast pressure history, 202
theoretical vs experimental results, 201–5
  sandwich panel with 3D woven composite skins and stitched foam core, 204–5
  shock wave loading laboratory studies, 201–2
  two-ply 3D woven S-2 glass composite plate, 202–3
hydrocodes, 38, 122
hydrostatic stress, 345–8, 349
hysteresis loops, 107

improvised explosive device, 244, 390
impulse, 260–1
in-situ resin-infusion method, 55
incident pressure pulse, 135
incident wave, 102

© Woodhead Publishing Limited, 2010

Industrial Ceramic Technology, Inc, 240
infinite diameter detonation velocity, 6–7
integration points, 132
intentional explosions, 22–3
internal material damping, 195–201
International Maritime Organisation, 49
ISO 6517, 47
ISO 16933:2007, 46
ISO 16935:2007, 46
isothermal filling simulation, 61

Jeffco 3191, 382
Jeffco 1310-T, 382
Jeffco Products, Inc., 382
jetting, 20

Kevlar, 90, 240
Khobar tower, partial collapse after terrorist attack 1996, 270
Kozeny-Carman's permeability, 76

lab simulation results, 133
Lagrange function, 128, 131, 195
Lagrangian algorithm, 61–3
Laplace equation, 61
LCM *see* liquid composite moulding
leakage, 16
lightweight aluminium, 177
linear elasticity, 127
liquid composite moulding, 54, 58–60, 78, xv
  1D flow in flat rectangular mould, 68
  experimental inlet-pressure history vs theoretical prediction using Darcy's law, 69
  mould-filling stage modelling, 60–74
    conventional modelling and simulation, 61–7
    dual-scale modelling and simulation, 68–74
  permeability measurement, 74–8
    based on 1D and radial flow techniques, 75
  snapshot of impregnation of fibre mats in 1D flow mould, 70
  unsaturated flow within dual-scale fibre preforms, 70
  volume-averaged governing equations
    set for gap region, 73
    set for tow region, 74
Lloyd's Register of Shipping, 45
LNG plant, 49
Lockerbie bombing of Pan Am flight 103, 45
LS-DYNA, 90, 91, 95, 105, 122, 263
  crushable foam, 93
  non-linear finite element code, 92

Mach stem, 102
magneto-rheological fluid, 88, 89, 107
  Bingham-plastic behaviour, 110
  impact damper MR fluid system, 99
  literature review, 98–100
  typical force–displacement and force–velocity curves, 112
  under blast, 107
marker-and-cell method, 62
Martin Marietta Composites, 125, 201
masonry walls, 286–91
  analytical model
    arching action of membrane retrofit concrete, 401–3
    membrane retrofit concrete, 399–401
    polymer retrofit concrete free-body diagram, 402
    unreinforced masonry wall, 398–9
    wall free-body diagram, 400
  arching resistance
    polymer retrofit, 405
    unreinforced CMU wall, 405
  resistance function approach, 396–406
    catcher system development, 403–6
    face-loaded wall equilibrium, 398
    polymer catcher system retrofit, 406
    polymer retrofit, 403

© Woodhead Publishing Limited, 2010

unreinforced CMU wall, 401
wall free-body diagram, 404
response model development
beam idealised as mass-spring damper system, 407
retrofitting to improve blast response, 390–408, 390–409
blast load, 391–3
finite element models, 393–6
notations, 408–9
resistance function approach, 396–406
types, 391
matrix failure, 316, 317
mean stress, 346, 348
MIL-STD-662F, 237
mine resistant armoured patrol vehicles, 252–3, 258
mine weapons
blast mines, 245–8
characteristic blast wave parameters, 246
mine blast event schematic view, 247
pressure–time histories for free air and subsoil blast events, 247
TMM1 blast mine, 246
composite vehicle structures mine blast loading, 259–67
composites for military vehicles protection from blasts, 244–67
historical developments, 244–5
occupant injury mechanisms, 251
position relative to target structure for blast test procedures, 260
shaped charge and fragmentation mines, 248–51
liner shape on weapon effects, 248
shaped charge warhead on vehicle interior, 249
TMRP-6 mine sectioned view, 250
Mises strains, 95
Misznay Schardin principle, 248, 250
Mohr's circle, 347
multi-cavity parallel flow technique, 76
Munroe shaped charge principle, 248

National Consortium for the Study of Terrorism and Responses to Terrorism, 270
national Norwegian oil industry standards, 49
7.62 mm NATO M80 ball round, 235
Navy Standard MIL-HDBK-1013, 46
7.62 mm NIJ IV, 235
NiTi shape memory alloys, 100, 107, 111
non-isothermal filling simulation, 61
non-zero sink term, 72
numerical integration step, 132

overpressure, 392, 393

P-Δ-effect, 369
Panasonic CF-28, 384
PANEX 35, 381
partial differential equations, 63
partially confined explosion, 18, 35–7
particulate loading, 247
PAXCONR, 290
PE4 plastic explosive, 104
peak incident pressure, 11–12
peak overpressure, 260
peridynamic method, 92
phenolic, 57, 59
pipe bomb, 6
Piper Alpha platform disaster, 45, 49
Poisson's ratio, 309, 310, 311
polyester, 57, 59
polyethylene, 57
polymer matrix composites, 88
processing for blast protection, 54–78
LCM, 58–60
mould-filling stage modelling in LCM, 60–74
permeability measurement, 74–8
polymer resins, 56
polypropylene, 57
polystyrene pad, 104
polyvinyl chloride, 57
Prandtl-Reuss material model, 353
prefabricated plates, 278
prepregs, 57
pressure pulse history, 125

© Woodhead Publishing Limited, 2010

primary fragments, 21
pseudo-concentration method, 62
pultruded plates, 278
PX35FBUD0150, 381

quadratic interpolation, 219

race tracking, 75
Rayleigh–Taylor-type instability, 30
reacting shock wave, 6
reaction bonded SiC, 237
reaction injection moulding process, 59
reflected blast pressure, 121
reflected pressure, 392
reflected wave, 102
reflection factor, 121
reinforced concrete, 275–6
resin transfer moulding, 60, 256
  manufacturing steps, 58
resistance functions, 393
retrofitting
  improving blast response of masonry walls, 390–409
    concrete masonry wall types, 391–2
    finite element models, 393–6
    notations, 408–9
    resistance function approach, 396–406
    response model development, 406–8
Riks analysis, 309
robustness, 301
rocket propelled grenade, 249
Ronan point tower block, 269

S-2 glass composite, 201
S-2 glass fibre, 135, 217, 227
S-2 glass, 240
sacrificial cells, 367–9, 372
  arm solution, 368
  cross-section, 368
  protective effect, 369
saturated permeability, 75
SC-15 epoxy resin, 217, 226
SCRIMP *see* Seemann composites resin infusion moulding process
SDOF system *see* single-degree-of-freedom system
second Piola–Kirchhoff stress, 215
secondary fragments, 21
Seemann composites resin infusion moulding process, 59–60
  manufacturing steps, 59
shape memory alloys
  energy absorbed in rod
    under adiabatic conditions, 113
    under twinning conditions, 114
  NiTi, 100, 107, 111
  porous material system, 100
  stress evolution in rod
    under adiabatic conditions, 113
    under twinning conditions, 114
shaped charge mines, 256
shear strength, 347, 348, 352
shear stress, 347, 348, 350, 352, 358, 361, 364
shock holing, 261
shock physics program, 38
silicon carbide, 237, 238
simplified blast load computation, 24–32
  airblast, 26–8
  approximate pressure pulse, 31
  blast load simplifications for design, 31–2
  blast scaling, 25–6
  gas pressure, 29–31
  numerical examples, 32–7
    free-air explosion, 32–3
    partially confined explosion, 35–7
    surface explosion, 33–5
  peak gas pressure from TNT detonation in partially confined chamber, 29
  positive phase shockwave parameters
    hemispherical TNT explosion on surface at sea level, 27
    spherical TNT explosion in free air at sea level, 26
  primary parameters, 24–5
  scaled gas impulse and vent opening without cover, 30
  shock fronts interaction, 28–9

© Woodhead Publishing Limited, 2010

single-degree-of-freedom system, 122, 406–7
  analysis results, 407–8
    typical response, 408
sink terms, 73
slope *S,* 219
slug, 250
SMA *see* shape memory alloys
solidification process, 58
spall, 249
spark plasma sintering method, 100
square honeycomb sandwich system, 97–8
stagnation pressure, 19
STANAG 4569, 263
steel, 139, 177, 183, 189
  perforated, 167
  plates, 276–7
  square multi-cell column types, 358
  stud walls, 276
  vs sandwich/composite panels blast resistance, 330
stereolithography, 77
Stokes and Brinkman equations, 71
streamline upwind Petrov–Galerkin, 67
stress tensor, 346
structural reaction injection moulding, 58
subunitary power index, 99
supraunitary power index, 99
surface explosion, 18, 33–5
survivability onion, 255

T-joint, 323–4
  alternative design, 325
  typical design, 324
3TEX, 123, 201, 202
theoretical maximum density, 24
thermal explosion, 6
thermal–hydrodynamic model, 6
thermochemical phenomena, 61
thermoplastics, 56
thermosets, 56
threat
  assessment for design, 22–4
  design criteria, 23
titanium diboride, 237
TMPR-6 mine, 250
TNT equivalency, 8–10, 9, 24
total Lagrangian description, 215
tow-impregnation model, 71, 72
TRANSONITE, 125
  sandwich samples, 204
  technology, 201
trapezoidal rule, 215
TRYMER 200 L foam, 125, 201
Tsai-Hill failure model, 315
Tsai Hill theory, 310
Tsai-Wu theory, 310, 316

UFC 4-010-01, 376
unconfined explosions, 15–16
Unified Facilities Criteria, 376
unit-cell flow model, 72
unsaturated permeability, 75
US Army Engineer Waterways Experiment Station, 393
US Army Engineering Research and Development Centre, 395
user defined materials, 91

vacuum assisted resin transfer moulding, 59–60
  manufacturing steps, 59
vacuum infusion moulding, 256
vinylester, 59
volume averaging method, 73
volume of fluid method, 62
von Karman assumption, 213

WAC Version 2, 397
waiting link concept, 98
Wall Analysis Code, 397
3WEAVE E-glass fibre preforms, 201
3WEAVE fabric, 123, 125
wet lay-up, 278, 279
WK1902, 47

yield criterion, 348, 349–50
yield surface, 348, 352–3

Z yarns, 123
Zoltek Corporation, 381

© Woodhead Publishing Limited, 2010